

# Electrification

2019 Annual Progress Report

Vehicle Technologies Office

(This page intentionally left blank)

## Disclaimer

This report was prepared as an account of work sponsored by an agency of the United States government. Neither the United States government nor any agency thereof, nor any of their employees, makes any warranty, express or implied, or assumes any legal liability or responsibility for the accuracy, completeness, or usefulness of any information, apparatus, product, or process disclosed or represents that its use would not infringe privately owned rights. Reference herein to any specific commercial product, process, or service by trade name, trademark, manufacturer, or otherwise does not necessarily constitute or imply its endorsement, recommendation, or favoring by the United States government or any agency thereof. The views and opinions of authors expressed herein do not necessarily state or reflect those of the United States government or any agency thereof.

## Acronyms

### A

AC	Alternating Current
ACC	Adaptive Cruise Control
accel	Acceleration
ACS	Advanced Combustion Systems
ACSforEVER	Advanced Climate Systems for EV Extended Range
AER	All-electric range
AFV	Alternative Fuel Vehicle
AMI	Advanced Metering Infrastructure
AMT	Automated Mechanical Transmission
ANL	Argonne National Laboratory
ANN	Artificial Neural Network
AOI	Areas of Interest
APEC	Asia Pacific Economic Council
APRF	Advanced Powertrain Research Facility
APT	Pressure Sensor
ASD	Aftermarket Safety Device
AVTA	Advanced Vehicle Testing Activity
AVTE	Advanced Vehicle Testing and Evaluation

### B

BaSc	Baseline and Scenario
Batt	Battery
BEB	Battery Next-Generation Electric Transit Bus
BEC	Bussed Electrical Center
BEMS	Building Energy Management System
BET	Battery Electric Truck
BEV	Battery Electric Vehicle
BMW	Bayerische Motoren Werke AG
BSFC	Brake Specific Fuel Consumption
BTE	Brake Thermal Efficiency

### C

CAC	Charge Air Cooler
CACC	Cooperative Adaptive Cruise Control
CAE	Computer-Aided Engineering
CAFE	Corporate Average Fuel Economy
CAN	Controller Area Network
CAV	Connected and automated vehicles
CARB	California Air Resources Board
CBD	Central Business District
CCS	Combined Charging System
CW, CCW	Clockwise, Counter Clockwise

CD	Charge-Depleting
CERV	Conference on Electric Roads and Vehicles
CFD	Computational Fluid Dynamics
CFDC	Commercial Fleet Data Center
CFL	Combined Fluid Loop
CH <sub>4</sub>	Methane
CHTS	California Household Travel Survey
CIP	Common Integration Platform
Cm <sup>3</sup>	Cubic
CNG	Compressed Natural Gas
CO	Carbon monoxide
CO <sub>2</sub>	Carbon Dioxide
COMM	Commuter
Conv	Conventional Vehicle
COP	Coefficient of Performance
CRADA	Cooperative Research and Development Agreement
CS	Charge Sustaining
Cs	Cold start
CV	Conventional vehicle

**D**

D3	Downloadable Dynamometer Database
DC	Direct current
DCFC	Direct Current Fast Charge
DCT	Dual-clutch transmission
decel	Deceleration
DER	Distributed energy resource
DFGM	Digital Flux Gate Magnetometer
DFMEA	Design of Failure Modes Analysis
DGE	Diesel Gallon Equivalent
DOE	U.S. Department of Energy
DOHC	Dual overhead cam
DS	Down speeding
DSM	Distributed Security Module
DSM	Diagnostic Security Module
DSP	Digital Signal Processor
DSRC	Dedicated Short Range Communications
dt	Change in time
dv	Change in velocity
Dyno	Dynamometer

**E**

EAVS	Electrically Assisted Variable Speed Supercharger
EC	European Commission
EDV	Electric Drive Vehicle
EDT	Electric Drive Technologies

EDX	Energy dispersive x-ray spectroscopy
EERE	Energy Efficiency and Renewable Energy
EGR	Exhaust Gas Recirculation
EG/W	Ethylene glycol/water
EOL	End of life
EPA	Environmental Protection Agency
ePATHS	Electrical PCM Assisted Thermal Heating System
EREV	Extended-Range Electric Vehicles
ESIF	Energy Systems Integration Facility
ESS	Energy Storage System
ETT	Electric Transportation Technologies
E-TREE	Electric Truck with Range Extending Engine
EUMD	End-Use Measurement Device
EV	Electric Vehicle
EV2G	Electric Vehicle-to-Grid
EVSE	Electric Vehicle Service Equipment
EXV	Electronic Expansion Valve

## F

F	Force
FASTSim	Future Automotive Systems Technology Simulator
FC	Fuel cell
FC	Fast charge
FCons	Fuel consumption
FCTO	Fuel Cell Technologies Office
FE	Fuel Economy
FEA	Finite Element Analysis
FEX	Front-end Heat Exchanger
FHWA	Federal Highway Administration
FLNA	Frito-Lay North America
FM	Friction Modifier
FMEP	Friction Mean Effective Pressure
FOA	Funding Opportunity Announcement
FTIR	Fourier transform infrared spectroscopy
FTP	Federal Test Procedure
FWD	Four wheel drive
FY	Fiscal year

## G

g	gram
GB	Gigabyte
GCEDV	Grid Connected Electrical Drive Vehicles
GEM	Gas Emissions Model
GHG	Greenhouse Gas
GITT	Grid Interaction Tech Team
GMLC	Grid Modernization Lab Consortium

GnPs	graphene nanoplatelets
GO	Graphene Oxide
GPRA	Government Performance and Results Act
GPS	Global Positioning System
GREET	Greenhouse gases, Regulated Emissions, and Energy use in Transportation
GSF1	Generic Speed Form 1
GSU	Grid side unit
GUI	Graphic User Interface
GVW	Gross Vehicle Weight

## H

h-APU	hybrid Auxiliary Power Unit
HATCI	Hyundai America Technical Center, Inc.
HC	Unburned hydrocarbons
HD	Heavy Duty
HEV	Hybrid-Electric Vehicle
H-GAC	Houston-Galveston Area Council
HHDDT	Heavy Heavy-Duty Diesel Truck
HHV	Hydraulic Hybrid Vehicle
HIL	Hardware-In-the-Loop
HP	Heat Pump
Hp	Horsepower
HTML	HyperText Markup Language
HV	High Voltage
HVAC	Heating Ventilating and Air Conditioning
HWFET	Highway Fuel Economy Test
HPMS	Highway Performance Monitoring System
HVTB	High Voltage Traction Battery
HWY	Highway Program or Highway Fuel Economy Test Cycle
HPC	High Performance Computing
HTR	Heater
Hz	Hertz

## I

I	Inertia
IC	Internal Combustion
ICD	Interim Component Durability
ICDV	Internal Combustion Drive Vehicles
ICE	Internal Combustion Engine
ICTF	Intermodal Container Transfer Facility
ICU	Inverter-Charger Unit
IEB	Information Exchange Bus
IEC	International Electrotechnical Commission
IGBT	Insulated Gate Bipolar Transistors
IHX	Internal Heat Exchanger
INL	Idaho National Laboratory

INTEGRATE	Integrated Network Testbed for Energy Grid Research and Technology
IOT	Internet of Things
IR	Infrared Radiation
ISO	International Organization for Standardization
ITS	Intelligent Transportation Systems

## J

JIT	Just-in-Time
-----	--------------

## K

kg	Kilogram
km	Kilometer
kW	Kilowatt
kWh	Kilowatt hour

## L

L	litre
L1	Level 1 benchmark
L2	Level 2 benchmark
Lbf	Pounds force
LCC	Liquid-Cooled Condenser
LD	Light-duty
LH	line haul
Li	Lithium
LIB	Lithium ion battery
LLNL	Lawrence Livermore National Laboratory
LNG	Liquefied natural gas
LTC	Lockport Technical Center
LV	Leading Vehicle

## M

M	Mass
MBSE	Model Based System Engineering
MD	Medium Duty
mpg	Miles per gallon
MMTCE	Million Metric Tons of Carbon Equivalent
MIIT	Ministry of Industry and Information Technology
mi	Mile
MJ	Megajoules
MOSFET	Metal-Oxide Semiconductor Field-Effect Transistor
mph	Miles per hour
MPGe,	Miles per gallon equivalent, Miles per gallon gasoline equivalent
MTDC	Medium Truck Duty Cycle
MOVES	Motor Vehicle Emission Simulator
MRF	Moving Reference Frame
MURECP	Medium-Duty Urban Range Extended Connected Powertrain
MY	Model year



M2 Meters squared

## N

NACFE North American Council for Freight Efficiency  
 NDA Non-Disclosure Agreement  
 NETL National Energy Technology Laboratory  
 NHTS National Household Travel Survey  
 NHTSA National Highway Transportation Safety Administration  
 NM Newton meters  
 NOx Nitrogen oxides  
 NR Natural Rubber  
 NRE Non Recurring Engineering  
 NREL National Renewable Energy Laboratory  
 NRT National Retail Trucking  
 NVH Noise, vibration, and harshness  
 NVUSD Napa Valley Unified School District  
 NYSERDA New York State Energy Research Development Authority

## O

OBC On-board charger  
 OCBC Orange County Bus Cycle  
 OEM Original Equipment Manufacturer  
 OneSAF One Semi-Automated Forces  
 ORNL Oak Ridge National Laboratories

## P

P Active Power  
 PC Polycarbonate  
 PCM Phase-Change Material  
 PCU Power Control Unit  
 PCU Powertrain Control Unit  
 PEEM Power Electronics and Electric Motor  
 PFC Power factor correction  
 PFI Port fuel injection  
 PGW Pittsburgh Glass Works  
 PHEV Plug-in Hybrid Electric Vehicle  
 PHEV## Plug-in hybrid electric vehicle with ## miles of all-electric range  
 PI Principal Investigator  
 PM Permanent Magnet  
 PM Particulate Matter  
 ppm Parts per Million  
 PTC Positive Temperature Coefficient (Electric Heater)  
 PTO Power Take-Off  
 PVP Polyvinylpyrrolidone  
 PWWM Public Works and Waste Management Department  
 $\lambda$  Power Factor

$\varphi$	Power Angle
<b>Q</b>	
Q	Reactive power
QA	Quality assurance
QC	Quality control
<b>R</b>	
R2	Coefficient of Determination
R/D	Receiver / Dryer
REV	New York State's Reforming the Energy Vision Initiative
REx	Range Extending Engine
rGO	reduced graphene oxide
RH	Relative Humidity
RMS	Root Mean Square
ROL	Ring-On-Liner
rpm	Revolutions Per Minute
RSU	Road Side Unit
RWDC	Real-World Drive-Cycle
<b>S</b>	
S	Apparent power
SAE	Society of Automotive Engineers
SBR	Styrene-Butadiene Rubber
SC03	SC03 Supplemental Federal Test Procedure
SCAG	Southern California Association of Governments
SCAQMD	South Coast Air Quality Management District
SCIG	Southern California International Gateway
SCR	Silicon Controlled Rectifier
SCR	Selective Catalytic Reduction
SDO	Standards Definition Organizations
SI	<a href="#">Système International d'Unités</a>
SI	Gasoline Spark Ignition
SNR	Sensor
SOC	State of Charge
SPL	Sound Pressure Level
SR	Speed Ratio
SS	Steady State
SPaT	Signal Phase and Timing
StAR	Storage-Assisted Recharging
<b>T</b>	
T	Torque
TA	Technical Area
TA	Torque Assist
TC	Thermocouple
TE	Thermoelectric

TE	Transmission Error
TES	Thermal Energy Storage
TGA	thermogravimetric analysis
THC	Total hydrocarbon emissions
TIM	Thermal Interface Materials
TLRP	Thermal Load Reduction Package
TN	Testing Network
TOU	Time-Of-Use
TSDC	Transportation Secure Data Center
TSI	Turbocharged stratified injection
TUSD	Torrance Unified School District
TXVs	Thermal Expansion Valves

## U

U.S. DRIVE	U.S. Driving Research and Innovation for Vehicle Efficiency and Energy Sustainability
UA	Transfer Coefficient
UC	Ultra-capacitor
UCR	University of California, Riverside
UDDS	Urban Dynamometer Driving Schedule
UN ECE	United Nations Economic Council for Europe
UPS	United Parcel Service
URL	Uniform Resource Locator
US06	Environmental Protection Agency US06 or Supplemental Federal Test Procedure
USABC	United States Advanced Battery Consortium
USCAR	U.S. Council for Automotive Research
Util	Battery capacity utilization

## V

V	Voltage
V2G	Vehicle-to-Grid
VAr	Volt-Amp-reactive
VGI	Vehicle-Grid Integration
VGT	Variable Geometry Turbocharger
VIP	Vacuum Insulated Panels
VMT	Vehicle Miles Traveled
VS	Vehicle Systems
VSATT	Vehicle Systems Analysis Technical Team
VSI	Vehicle Systems Integration
VSST	Vehicle Systems Simulation and Testing
VTCab	Vehicle Thermal Cab Simulator
VTIF	Vehicle Testing and Integration Facility
VTO	Vehicle Technologies Office

## W

dw	Change in Angle W
WCC	Water Cooled Condenser

WEC	World Endurance Championship
WEG	Water/Ethylene Glycol
Wh	Watt hour
WHR	Waste Heat Recovery
WPT	Wireless Power Transfer
WTW	Well-to-Wheels
<b>X</b>	
XPS	x-ray photoelectron spectroscopy
<b>Z</b>	
ZECT	Zero-emissions cargo transport

## Executive Summary

During fiscal year 2019 (FY 2019), the U.S. Department of Energy (DOE) Vehicle Technologies Office (VTO) funded early stage research & development (R&D) projects that address Batteries and Electrification of the U.S. transportation sector. The VTO Electrification Sub-Program is composed of Electric Drive Technologies, and Grid Integration activities. The Electric Drive Technologies group conducts R&D projects that advance electric motors and power electronics technologies. The Grid and Charging Infrastructure group conducts R&D projects that advance grid modernization and electric vehicle charging technologies. This document presents a brief overview of the Electrification Sub-Program and progress reports for its R&D projects. Each of the progress reports provide a project overview and highlights of the technical results that were accomplished in FY 2019.

# Table of Contents

Acronyms .....	iv
Executive Summary.....	xiii
Vehicle Technologies Office Overview .....	1
Electric Drive Technologies Program Overview.....	3
Grid and Infrastructure Program Overview .....	5
<b>I Electric Drive Technologies Research .....</b>	<b>15</b>
I.1 Highly Integrated Power Module (ORNL) .....	15
I.2 High-Voltage, High-Power Density Traction Drive Inverter (ORNL) .....	22
I.3 High-Fidelity Multiphysics Material Models for Electric Motors (ORNL).....	30
I.4 Non-Heavy Rare Earth High-Speed Motors (ORNL).....	38
I.5 Integrated Electric Drive (ORNL).....	48
I.6 Ultra-Conducting Copper (ORNL) .....	59
I.7 Power Electronics: Active Device and Passive Component Evaluation (SNL).....	68
I.8 Bottom-Up Soft Magnetic Composites (SNL).....	74
I.9 Component Modeling, Co-Optimization, and Trade-Space Evaluation (SNL) .....	80
I.10 Power Electronics: Vertical GaN Device Development (SNL) .....	87
I.11 Advanced Packaging Designs – Reliability and Prognostics (NREL).....	95
I.12 Electric Motor Thermal Management (NREL).....	102
I.13 Integrated Traction Drive Thermal Management (NREL).....	109
I.14 Power Electronics Materials and Bonded Interfaces – Reliability and Lifetime (NREL) .....	116
I.15 Power Electronics Thermal Management (NREL) .....	124
I.16 Magnetics for Ultra-High Speed Transformative Electric Motor (Ames Lab) .....	133
I.17 Integration Methods for High-Density Integrated Electric Drives (University of Arkansas) .....	139
I.18 Design, Optimization, and Control of a 100 kW Electric Traction Motor Meeting or Exceeding DOE 2025 Targets (Illinois Institute of Technology) .....	148
I.19 Cost Competitive, High-Performance, Highly Reliable (CPR) Power Devices on SiC (SUNY Polytechnic Institute) .....	156
I.20 Cost Competitive, High-Performance, Highly Reliable (CPR) Power Devices on GaN (SUNY Polytechnic Institute) .....	162
I.21 Device- and System-Level Thermal Packaging for Electric-Drive Technologies (Georgia Institute of Technology).....	170
I.22 Next-Generation, High-temperature, High-frequency, High-efficiency, High-power-density Traction System (University of California, Berkeley) .....	179
I.23 Heterogeneous Integration Technologies for High-temperature, High-density, Low-profile Power Modules of Wide Bandgap Devices in Electric Drive Applications (Virginia Tech).....	187
I.24 Integrated Motor and Drive for Traction Application (University of Wisconsin – Madison) .....	196

I.25	Multi-Objective Design Optimization of 100 kW Non-Rare-Earth or Reduced-Rare Earth Machines (Purdue University).....	205
I.26	Implementation of WBG devices in circuits, circuit topology, system integration as well as SiC devices (The Ohio State University).....	213
I.27	Rugged WBG Devices and Advanced Electric Machines for High Power Density Automotive Electric Drives (North Carolina State University).....	222
<b>II</b>	<b>Electric Drive Technologies Development .....</b>	<b>226</b>
II.1	High Speed Hybrid Reluctance Motor Utilizing Anisotropic Materials (General Motors LLC)....	226
II.2	Dual Phase Soft Magnetic Laminates for Low-cost, Non/Reduced-Rare-Earth Containing Electrical Machines (GE Global Research).....	234
II.3	Cost Effective 6.5% Silicon Steel Laminate for Electric Machines (Iowa State University) .....	241
II.4	Mapping the North American Light Duty Electric Vehicle (LDEV) Charging Market and Supply Chain: Assessment of Suppliers, Technology Developments and Gaps. (Synthesis Partners, LLC).....	251
II.5	Highly Integrated Wide Bandgap Power Module for Next Generation Plug-In Vehicles (General Motors LLC) .....	259
II.6	V2G Electric School Bus Commercialization Project (Blue Bird Corporation).....	265
<b>III</b>	<b>Grid and Infrastructure Industry Awards.....</b>	<b>270</b>
III.1	Emission Drayage Trucks Demonstration (ZECT I).....	270
III.2	Zero Emission Cargo Transport II San Pedro Bay Ports Hybrid & Fuel Cell Electric Vehicle Project (South Coast Air Quality Management District).....	278
III.3	Medium-Duty Urban Range Extended Connected Powertrain (MURECP), (Robert Bosch LLC)	287
III.4	Medium Duty Vehicle Powertrain Electrification and Demonstration (McLaren Engineering)....	293
III.5	Wireless Extreme Fast Charging for Electric Trucks.....	298
III.6	Bidirectional Wireless Power Flow for Medium-Duty Vehicle-to-Grid Connectivity .....	302
III.7	Development and Demonstration of Medium-Heavy Duty PHEV Work Trucks (Odyne Systems).....	309
III.8	Cummins Electric Truck with Range-Extending Engine (ETREE) (Cummins, Inc.).....	315
III.9	Comprehensive Assessment of On-and Off-Board Vehicle-to-Grid Technology Performance and Impacts on Battery and the Grid (EPRI) .....	319
III.10	Enabling Extreme Fast Charging with Energy Storage (Missouri University of Science and Technology) .....	332
III.11	Intelligent, Grid-Friendly, Modular Extreme Fast Charging System with Solid-State DC Protection (NCSU) .....	338
III.12	Direct Current Conversion Equipment Connected to the Medium-Voltage Grid for XFC Utilizing a Modular and Interoperable Architecture (EPRI).....	347
III.13	High-Efficiency, Medium-Voltage-Input, Solid-State-Transformer-Based 400-kW/1000-V/400-A Extreme Fast Charger for Electric Vehicles (Delta Electronics (Americas) Ltd).....	350
<b>IV</b>	<b>Grid and Infrastructure Grid Interoperability and Control .....</b>	<b>356</b>
IV.1	Smart Vehicle-Grid Integration (ANL).....	356
IV.2	Scalable Electric Vehicle Smart Charging Using Collaborative Autonomy (LLNL).....	362

<b>V</b>	<b>Grid and Infrastructure Fast Charging Enabling Technologies</b> .....	<b>368</b>
V.1	Fast Charging: Interoperability and Integration Technologies (ANL).....	368
V.2	Fast Charging: Grid Impacts and Cyber Security (INL).....	373
V.3	Demand Charge Mitigation Technologies (NREL).....	379
V.4	Smart Electric Vehicle Charging for a Reliable and Resilient Grid (NREL).....	386
V.5	Smart Electric Vehicle Charging for a Reliable and Resilient Grid (Idaho National Laboratory)..	392
V.6	Smart Electric Vehicle Charging for a Reliable and Resilient Grid (Recharge) (SNL).....	398
V.7	Development of a Multi-port 1+ Megawatt Charging System for Medium-and Heavy-Duty Electric Vehicles (ORNL).....	403
V.8	Development of a Multiport 1+Megawatt Charging System for Medium- and Heavy-Duty Electric Vehicles (NREL).....	410
V.9	Development of a Multiport 1+ Megawatt Charging System for Medium and Heavy-Duty Electric Vehicles (ANL).....	419
V.10	High-Power Inductive Charging System Development and Integration for Mobility (ORNL).....	425
<b>VI</b>	<b>Grid and Infrastructure High Power Wireless Charging</b> .....	<b>433</b>
VI.1	High Power and Dynamic Wireless Charging of EVs (ORNL).....	433
VI.2	High Power and Dynamic Wireless Charging for EVs (INL).....	440
<b>VII</b>	<b>Grid and Infrastructure Cyber Security</b> .....	<b>445</b>
VII.1	Consequence-Driven Cybersecurity for High-Power Charging Infrastructure (INL).....	445
VII.2	CyberX: Cybersecurity for Grid Connected eXtreme Fast Charging Station (Idaho National Laboratory).....	452
VII.3	Threat Model of Vehicle Charging Infrastructure (ANL).....	456
VII.4	Securing Vehicle Charging Infrastructure.....	458



## List of Figures

Figure I.1.1 Electrical layout of the half-bridge module.....	16
Figure I.1.2 Layer details and isometric view of IMS substrate. ....	17
Figure I.1.3 Cross section of DBC (left), IMS (middle), and IMS with TPG (right).....	17
Figure I.1.4 Steady-state thermal performance of DBC (left), IMS (middle), and IMSwTPG (right). ....	18
Figure I.1.5 Transient thermal impedance of SiC MOSFET dies placed on DBC (left), IMS (middle), and IMSwTPG (right).....	19
Figure I.1.6 Thermal evaluation board (left); assembled substrate with cold plate, interconnects, and SiC MOSFETs (middle); setup for thermal characterization of DBC, IMS and IMSwTPG under different load and temperature conditions (right).....	19
Figure I.1.7 Thermal imaging results of IMS (left) and IMSwTPG (right) at 250 W total power loss and 65°C coolant temperature.....	19
Figure I.1.8 IMS-based half-bridge power module.....	20
Figure I.1.9 Chip-to-chip and board-to-board interconnect examples with quilt packaging. ....	20
Figure I.1.10 Test sample design for interconnect evaluation. ....	20
Figure I.1.11 Fabricated silicon samples with quilt nodules.....	21
Figure I.2.1 A standard 3-phase inverter-based drive. ....	23
Figure I.2.2 Segmented inverter-based drive. ....	23
Figure I.2.3 Rearrangement of the segmented inverter-based drive. ....	24
Figure I.2.4 PWM schemes for the segmented inverter-based drive to reduce the DC bus ripple current: (a) phase-shifted carrier-based schemes, (b) space vector modulation with optimal placement of zero vectors for sector 1, (c) alternate space vector modulation.....	24
Figure I.2.5 Simulated operating waveforms for the segmented inverter with a capacitor ripple current of 17.5 Arms (a) and standard inverter with a capacitor ripple current of 62.1 Arms (b) at $M=0.6$ , $pf=0.9$ , $I_{ph}=100$ Arms. ....	25
Figure I.2.6 Comparison of normalized capacitor ripple current (a) and busbar current (b) vs. modulation index for 3-phase and segmented inverters at various power factors. ....	26
Figure I.2.7 Block diagram for a 5-phase inverter (a) and simulation waveforms for switching at $m=0.65$ and $pf=0.9$ (b). ....	26
Figure I.2.8 Block diagram (a) and simulation waveforms for a symmetrical 6-phase inverter at $m=0.65$ and $pf=0.9$ (b). ....	27
Figure I.2.9 Block diagram (a) and simulation results for an asymmetrical 6-phase inverter at $m=0.65$ and $pf=0.9$ (b). ....	27
Figure I.2.10 Block diagram for driving cycle–based DC bus capacitor life-expectancy prediction and sizing tools.....	28
Figure I.2.11 Modeling results for a film capacitor under US06 driving cycle (left) and FUDDS (right). ....	28
Figure I.2.12 Inverter power stage design (left) and power module baseplate temperature profile (right). ....	29
Figure I.3.1 Nine-magnet permanent magnet array for accurate 3-axis demagnetization testing of low-energy-product and HRE-free permanent magnets. Two 3-axis magnetic field sensors are used to measure the normal	

flux density and tangential field intensity of the central magnet. The orbiting magnets are used to provide field continuity, which minimizes the impact of edge effects on the measurements. .... 32

Figure I.3.2 Simulation comparison of single cubic magnet measurement versus nine-magnet array measurement. The intrinsic curve is the permanent magnet data input into the simulation. The “Single” and “Array” markers are the expected measurements in each of the configurations. The array configuration measurements more closely match the intrinsic characteristic. .... 32

Figure I.3.3 One-eighth section cutaway simulation of the optimized permanent magnet testing fixture. The peak aperture airgap flux density is 1.8 T with uniformity of better than 1%. The peak winding temperature under constant 24 A excitation is less than 110°C when it is cooled by silicon oil at a flow rate of 10 L/min. .... 34

Figure I.3.4 Disassembled permanent magnet array assembly. .... 34

Figure I.3.5 Permanent magnet test fixture subassemblies and components; (Left) One of the two excitation coils after removal from bobbin. (Center) ferromagnetic yoke with excitation coils housed in Ultem oil cooling jackets. (Right) Permanent magnet assembly installed on one half of the magnetic core. .... 35

Figure I.3.6 Complete permanent magnet testing system including power supply, inverter, magnetic field sensors, current sensors, and oscilloscope. .... 35

Figure I.3.7 Comparison of measured AlNiCo 8HC hard and easy axis magnetization characteristics; (Right) normal curves, (left) intrinsic curves. A computed estimate of the expected characteristic when a field is applied at 45 degrees between the hard and easy axes is superimposed on both plots. .... 36

Figure I.4.1 Proposed rotary transformer-based excitation system with resonant compensation only on the primary side. .... 39

Figure I.4.2 Robustness of the field current against the variation of field winding resistance due to temperature (for a temperature swing from -50 to 150°C). .... 39

Figure I.4.3 Resistance of the HRE-free outer rotor SPM to demagnetization under 3-phase short circuit at 20,000 rpm. .... 40

Figure I.4.4 Mechanical assembly and stress analysis at 20,000 rpm. .... 41

Figure I.4.5 AC loss in winding and eddy current loss in permanent magnets at 100 kW and 20,000 rpm operation. .... 44

Figure I.4.6 Thermal simulation results at 20krpm with high thermal conductivity winding potting, winding spray cooling, slot wedge liquid cooling, and rotor liquid cooling (*Refer to project elt214 “Electric Motor Thermal Management” by Kevin Bennion (NREL)*). .... 45

Figure I.4.7 Analyzed motor topologies. .... 45

Figure I.4.8 Impact of winding conductivity on the motor active volume. .... 46

Figure I.4.9 Impact of winding conductivity on the speed range and efficiency. .... 46

Figure I.5.1 Motor and inverter integration techniques: (a) radial housing mount, (b) radial stator mount, (c) axial endplate mount, (d) axial stator mount. .... 49

Figure I.5.2 One-sixth of 2016 BMW-i3 stator. .... 50

Figure I.5.3 DBC structure for thermal simulation. .... 50

Figure I.5.4 Power loss data: (a) experimental motor power loss; (b) inverter power loss (simulation-based). 51

Figure I.5.5 Identification of required thermal performance of radial stator mount IMD system.  $h_{tc}$  = heat transfer coefficient. .... 51

Figure I.5.6 Capacitance density of the selected capacitor ..... 52

Figure I.5.7 Experimental setup. .... 53

Figure I.5.8 Change in ESR and capacitance with DC bias voltage ( $f = 1\text{kHz}$ , $T = 23^\circ\text{C}$ ).	54
Figure I.5.9 Change in ESR and capacitance of different capacitor technology in terms of frequency, bias voltage, and temperature.	55
Figure I.5.10 The volume of the selected capacitor technologies compared with that of a 2016 BMW-i3 450 V 475 $\mu\text{F}$ film capacitor.	57
Figure I.6.1 Schematic illustration of the process flow for producing Cu-CNT-Cu multilayer composite tapes.	61
Figure I.6.2 Scanning electron microscopy images and G-band intensity variations on single-walled CNT-coated copper tapes at various inclination angles during ultrasonic spray coating. Inset shows a schematic of the tape inclination angle.	62
Figure I.6.3 Scanning electron microscopy images displaying the shear-induced alignment of CNTs with increased CNT loading on copper tapes.	62
Figure I.6.4 (Left) Electrical properties of single-layer and three-layer Cu-CNT-Cu composite architectures as a function of temperature ranging from 0 to $120^\circ\text{C}$ , displaying reduced resistivity compared with the reference Cu substrate. (Right) Representative Z-contrast STEM cross-sectional microstructures of single and 3-layer UCC composites using similar processing conditions.	63
Figure I.6.5 Energy diagram showing the density of states for metallic, semiconducting, and Cu-doped semiconducting CNTs (left panel). Z-contrast STEM image of a Cu-CNT-Cu sample, displaying Cu nanoparticles within the CNT layer (right panel). Inset shows the schematics of the undoped metallic, and semiconducting, and Cu-doped semiconducting CNTs used in the first-principles density functional theory calculations.	64
Figure I.6.6 Cross-sectional schematic illustration of the three topologies of heavy rare-earth-free permanent magnet traction motors.	65
Figure I.6.7 Reduction in active volume as a function of winding conductivity for different motor topologies.	65
Figure I.6.8 Photograph of the newly designed roll-to-roll CNT deposition system.	66
Figure I.7.1 Oxygen vacancy migration under applied bias can lead to degradation of ceramic capacitors.	69
Figure I.7.2 The evaluation of prototype devices in a custom testbed can inform both device designers on the strengths/weaknesses of their prototypes, as well as validate device models for simulation.	70
Figure I.7.3 Schematic for WBG device testbed with embedded motor control.	70
Figure I.7.4 The lifetime of DC capacitors can be increased through the implementation of a bipolar switching scheme.	71
Figure I.7.5 Design layout for capacitor test setup which allows for stress and evaluation of a population of 40 capacitors under bipolar switching.	71
Figure I.7.6 Breadboard of 3-phase DC motor drive power stage (left) and embedded controller (right).	72
Figure I.7.7 (left) Thermal image of one leg of the power stage showing the temperature of power switches (centered at the crosshairs) and gate driver (just below the crosshairs) at 200 V and 7.5 A. (right) Gate drive signaling at 200V and 7.5 A.	73
Figure I.8.1 Temperature-dependent XRD data of commercially available mixed phase iron nitride powder and its conversion to nearly phase pure $\text{Fe}_4\text{N}$ .	75
Figure I.8.2 1,6-hexanediamine.	76
Figure I.8.3 N,N-diglycidyl-4-glycidyl-oxyaniline.	76
Figure I.8.4 Magnetic composite toroidal cores wound for B-H analysis.	76

Figure I.8.5 B-H hysteresis loop for a magnetic composite toroid. This hysteresis loop was collected at a frequency of 10 kHz. ....	77
Figure I.8.6 3D printed magnetic composite rotor (1/6 of total rotor design).....	77
Figure I.8.7 4-aminophenyl sulfone.....	78
Figure I.8.8 Three differently-sized magnetic composite rotor teeth and a magnetic composite toroid.....	78
Figure I.9.1 Comparison of power loss in SiC MPS, GaN PiN, and GaN JBS diodes showing (left) preferred device as a function of voltage and frequency at 50% duty cycle, and (right) the comparison of loss at 650 V, 50% duty cycle .....	82
Figure I.9.2 Comparison of $R_{on}$ in MOSFETs made in Silicon, SiC, and GaN showing (left) the device structure and (right) the predicted results. ....	83
Figure I.9.3 Circuit topology for co-optimization.....	83
Figure I.9.4 Candidate design considers a flat integrated form factor that includes module and DC link capacitor.....	84
Figure I.9.5 Module volume estimate as a function of voltage and frequency for Ceramic X7R and Ceralink Capacitors. ....	84
Figure I.9.6 Co-optimization results for (left) 10 kW boost converter and (right) 100 kW inverter module + capacitor.....	85
Figure I.10.1 (top) Schematic drawing of JBS diode. (bottom) Schematic drawing of Trench MOSFET.....	87
Figure I.10.2 Simulated reverse-bias curves of GaN Schottky diodes using various transport models (courtesy of Lehigh University).....	88
Figure I.10.3 Schematic drawings of (top) trench MOSFET and (bottom) double-well MOSFET. ....	89
Figure I.10.4 (top) IV curves of GaN Schottky Barrier Diodes, and (bottom) extracted ideality factors of the same diodes.....	90
Figure I.10.5 (top row) Simulated breakdown voltage and (bottom row) on-resistance of GaN JBS diodes. Left column is a design with a narrow current-carrying channel, while right column is a design with a wide current-carrying channel. The middle column represents the device performance. ....	91
Figure I.10.6 Simulated Baliga Figure of Merit for JBS diodes with three different p-layer widths.....	91
Figure I.10.7 TCAD simulations of D-MOSFETS, examine four design parameters: (top left) JFET region width, epilayer (drift layer) doping (top right), current spreading layer doping (bottom left), and JFET region doping (bottom right).....	92
Figure I.10.8 (left) Schematic drawing of T-MOSFET. (middle) Simulated internal electric field of the same device. (right) simulated breakdown characteristic of the same device.....	92
Figure I.11.1 A traditional power electronics package (left), and double-sided-cooled power electronics packages from Toyota and General Motors (right).....	96
Figure I.11.2 Power device within a second-generation Chevy Volt [2] (left), and example double-sided cooling structure [3] (right).....	97
Figure I.11.3 Traditional package with metalized polyimide substrate (left), and with polyimide substrate bonded directly to baseplate/heat exchanger with no bottom metallization layer (right). ....	98
Figure I.11.4 Double-sided cooled package with polyimide substrate (left), and with stacked devices in a 3D package design (right).....	98
Figure I.11.5 Manufacturing process for a traditional power electronics module [4] (top), and a simplified process for the novel power electronics package (bottom).....	99

Figure I.11.6 Sample design with QP. ....	100
Figure I.12.1 Overview of ASTM D5470 method for measuring the thermal resistance of a sample placed between two metering blocks. (Source: Emily Cousineau, NREL).....	104
Figure I.12.2 Example analysis for locating temperature measurement locations within bottom metering block. Example temperature profile through metering block showing uniform temperature gradient beyond 25.4 mm from the bottom of the block (left). Example showing the calculated heat flux through the metering block, highlighting the heat flux variation towards the bottom of the metering block. (Source: Emily Cousineau, NREL).....	105
Figure I.12.3 Example analysis for including a copper spreader to the metering block with different metering block materials. Drawing of metering block with copper spreader (left). Example results showing the calculated spatial temperature variation within the temperature measurement plane for different metering block materials and spreader thicknesses. (Source: Emily Cousineau, NREL).....	106
Figure I.12.4 Constructed experimental hardware inside environmental chamber. (Source: Emily Cousineau, NREL).....	107
Figure I.13.1 Electric motor and power electronics integration concepts: (a) Separate enclosures for motor and power electronics, (b) Power electronics mounted or distributed radially on the motor outer case with shared cooling, (c) Power electronics integrated axially in the motor’s front or back plate (Figures by Shajjad Chowdhury, ORNL) .....	110
Figure I.13.2 Experimental setup for jet impingement heat transfer characterization: (a) General view of large fluid test loop (Photo by Bidzina Kekelia, NREL), (b) Large fluid test loop schematic .....	110
Figure I.13.3 Electric machine with mounted heat target assembly within the end-windings (Computer-aided design (CAD) model by Emily Cousineau, NREL).....	111
Figure I.13.4 FEA thermal simulations of a single slot of stator windings in ANSYS: (a) Heat flux distribution, (b) Temperature distribution (Figures by Bidzina Kekelia, NREL). .....	111
Figure I.13.5 ATF jet impingement on heated target (Photo by Bidzina Kekelia, NREL).....	112
Figure I.13.6 Experimentally measured convective heat transfer coefficients for 50°C ATF at various jet impingement velocities and cooled-surface temperatures .....	113
Figure I.13.7 CFD modeling of orifice and fan-shaped jet impingement on heated copper target.....	113
Figure I.14.1 Pressureless sintering profile at VT (left) and NREL (right) .....	117
Figure I.14.2 Circular coupons ( $\Phi$ 25.4mm) for reliability evaluation – Cu (bottom) bonded to Invar (top) using sintered silver.....	118
Figure I.14.3 C-SAM images of pressureless sintered silver samples fabricated at VT (left and center) and NREL (right).....	118
Figure I.14.4 Pressure-assisted sintering profile .....	118
Figure I.14.5 C-SAM images of pressure-assisted sintered silver samples fabricated at VT. Bond diameter of 22 mm (left), 16 mm (center), and 10 mm (right).....	119
Figure I.14.6 Round sintered silver samples arranged on a thermal platform for thermal cycling .....	119
Figure I.14.7 C-SAM images of pressureless sintered silver before (left) and after 10 thermal cycles (right) – Cu-side images (top) and Invar-side images (bottom).....	120
Figure I.14.8 C-SAM images of pressure-assisted sintered silver before (left) and after 100 thermal cycles (right), Cu-side images (top) and Invar-side images (bottom).....	121
Figure I.14.9 Crack growth in pressure-assisted samples (3 MPa).....	121
Figure I.14.10 Cross-sectional image of a pressure-assisted sintered silver sample.....	122

Figure I.14.11 Strain energy density results of sintered silver samples.....	122
Figure I.15.1 Schematic showing the dielectric fluid cooling strategy for a planar-style module.....	125
Figure I.15.2 CFD results showing the effects of varying the fin thickness (left), fin height (middle), and the slot jet width (right). .....	126
Figure I.15.3 CFD temperature contours for the optimal fin and slot jet design using the device scale model. Model predicts 220°C maximum junction temperature at 716 W/cm <sup>2</sup> device heat flux. ....	126
Figure I.15.4 CFD-predicted flow distribution for the 12 slot jets. A ±5% flow variation is predicted. ....	127
Figure I.15.5 CAD drawing of the heat exchanger designed to cool 12 (25 mm <sup>2</sup> ) devices (left). 3D printed heat exchanger fabricated for experimental validation (right). Total volume for the conceptual heat exchanger and power module is 120 ml.....	127
Figure I.15.6 Temperature contours for inverter-scale (12 devices) CFD simulations for 2.2 kW of heat dissipation (716 W/cm <sup>2</sup> per device) and total flow rate (Alpha 6 fluid) of 4.1 lpm. Maximum junction temperatures of 222°C are predicted.....	128
Figure I.15.7 Image of the finned ( $w_f = 0.2$ mm, $w_c = 0.43$ mm, and $h_f = 4$ mm) heat spreader (left) and cartridge heater block (middle). FE-analysis-predicted temperatures for the cartridge heater block at the 716 W/cm <sup>2</sup> heat flux condition (right). ....	128
Figure I.15.8 Picture of the dielectric fluid flow loop fabricated and used to measure the thermal performance of the dielectric fluid heat exchanger. The flow loop can accommodate various dielectric fluids and can control fluid temperatures and flow rates.....	129
Figure I.15.9 Schematic of the 1D transient thermal FEA model (left). FEA temperature versus time results for a simulated short-circuit fault condition (right). ....	130
Figure I.15.10 Predicted thermal resistance for the double-side-cooled module design indicating substantial thermal performance enhancements compared to the single-side-cooled design. ....	130
Figure I.16.1 Dependence of coercivity on grain size. ....	134
Figure I.16.2 Micromagnetic simulation of the demagnetization field near the permanent magnets in motor. ....	135
Figure I.16.3 MH curves of the bulk magnet prepared using feedstock powders that were ball-milled for different time. The longer the ball milling hours, the finer the particle size.....	135
Figure I.16.4 MH curves of the assemblies listed in Table I.1.16.1. ....	136
Figure I.16.5 a) the large melt-spinner capable of producing 500 gram thin sheet steel; b) the 10 mm ribbon of 6.5% Si steel prepared using only 10 gram of ingot; c) The new two-body crucible design allowing quick change of orifice; d) new muffin fan for bus-bar and modified cooling lines; e) newly added insulation materials to protect cooling lines from radiation heating by the coil; f) the custom designed BN crucible. ....	137
Figure I.17.1 Simplified SiC CMOS gate driver schematic and layout with programmable drive strength.....	142
Figure I.17.2 Simplified SiC NMOS gate driver schematic and layout with programmable drive strength. ...	143
Figure I.18.1 Representative interior permanent magnet synchronous machines from optimization Pareto front.....	150
Figure I.18.2 Pareto fronts to identify target performance gaps using state of the art motor topologies and materials.....	151
Figure I.18.3 Magnetic only topology optimization, (a) design domain, (b) synchronous reluctance rotor, (c) interior permanent magnet rotor with fixed permanent magnet.....	152
Figure I.18.4 Synchronous reluctance rotor magneto-structural topology optimization results for (a) formulation I 4,000 RPM, (b) formulation II 4,000 RPM, (c) formulation I 12,000 RPM, and (d) formulation II 12,000 RPM. ....	154

Figure I.18.5 Interior permanent magnet synchronous machine rotor magneto-structural topology optimization with fixed position and size permanent magnet, (a) normalized electrical steel density, (b) Von Mises stress, (c) displacement. ....	155
Figure I.18.6 Multi-layer IPM rotor verification of the proposed design approach, (a) cross-section of barriers and magnets, (b) flux density distribution at no-load. ....	155
Figure I.19.1 Cross-sectional view of proposed 1.2kV 4H-SiC MOSFETs. ....	157
Figure I.19.2 Optimization of the JFET doping concentration to minimize the on-resistance and electric field in gate oxide and PN junction. ....	157
Figure I.19.3 Optimization of the JFET width to minimize the on-resistance and electric field in gate oxide and PN junction. ....	158
Figure I.19.4 Top view for Mask.....	158
Figure I.19.5 1 <sup>st</sup> lot fabrication status .....	159
Figure I.20.1 AFM scans of (a) AlGa <sub>N</sub> /Ga <sub>N</sub> on sapphire and (b) AlGa <sub>N</sub> /Ga <sub>N</sub> on Si .....	164
Figure I.20.2 in situ curvature measurement during growth.....	164
Figure I.20.3 Output and gate leakage characteristics for HEMT on sapphire. Device Dimensions: $W_g=150\ \mu\text{m}$ ; $L_g=7\ \mu\text{m}$ ; $L_{gs}=4\ \mu\text{m}$ ; $L_{dg}=10\ \mu\text{m}$ ; $L_{ds}=21\ \mu\text{m}$ .....	165
Figure I.20.4 Output and gate leakage characteristics for HEMT on sapphire. Device Dimensions: $W_g=150\ \mu\text{m}$ ; $L_g=7\ \mu\text{m}$ ; $L_{gs}=4\ \mu\text{m}$ ; $L_{dg}=10\ \mu\text{m}$ ; $L_{ds}=21\ \mu\text{m}$ .....	165
Figure I.20.5 Frequency-dependent C-V measurements for samples annealed at (a) 350°C for 1 min, (b) 350°C for 10 min, (c) 350°C for 20 min, (d) 600°C for 1 min, (e) 475°C for 10 min, (f) 600°C for 20 min, and (g) as-deposited. Threshold voltage is indicated by a dashed line. The insets show frequency dispersion close to threshold voltage. A large negative shift in threshold voltage is observed in the sample annealed at 600°C for 1 min relative to the other curves, and the effect observed after annealing at 600°C for 20 min indicate poor oxide and/or interface quality. ....	166
Figure I.20.6 C-V measurement data collected at 100 kHz AC signal. The arrows indicate the direction of the DC bias sweep. Insets show zoomed in area of hysteresis to show changes in $\Delta V$ from sweep up to sweep down. The largest reduction in hysteresis is observed after annealing at 350°C for 20 min. ....	167
Figure I.20.7 EDS elemental maps showing the spatial distribution of (a) O in the as-deposited sample, (b) Al in the as-deposited sample, (c) O in the sample annealed at 350°C for 10 min, (d) Al in the sample annealed at 350°C for 10 min, (e) O in the sample annealed at 600°C for 20 min, and (f) Al in the sample annealed at 600°C for 20 min. No diffusion of Al or O is observed.....	168
Figure I.21.1 Illustration of steps for commercial stochastic foam characterization .....	172
Figure I.21.2 Comparison of ERG foam versus AM foam (left) and reduced computational domains (right) 172	172
Figure I.21.3 Pressure drop per unit length (left) and Nusselt number (right) for the ERG and AM samples. 173	173
Figure I.21.4 Nusselt numbers recalculated with varying TIM thermal conductivities.....	174
Figure I.21.5 50 mm ×50 mm prototype of AlSiC heat sink bonded to AlN and Al foam with liquid header. 174	174
Figure I.21.6 (a) Assemble packaged prototype (b) Liquid coolant loop setup showing essential sensors and DAQ.....	175
Figure I.21.7 Failed Cu-invar bond.....	175
Figure I.21.8 SEM and EDS results of Cu-Al bond between a) Cu-Invar coupons b) Invar-Invar coupons c) Cu-Cu coupons .....	176

Figure I.21.9 (a) Maximum Shaft Torque, (b) Maximum Shaft Power, (c) Maximum Stator Winding Current and (d) Maximum Efficiency, with a temperature threshold of 200°C and for six different flow rates. These results have been extracted from Motor-CAD simulation. ....	177
Figure I.21.10 (a) Maximum Shaft Torque, (b) Maximum Shaft Power, (c) Maximum Stator Winding Current and (d) Maximum Efficiency, with a temperature threshold of 200°C, a fixed 9 Lpm flow rate and for four different liquid coolant materials. These results have been extracted from Motor-CAD simulation. ....	177
Figure I.22.1 Comparison in output waveforms of a conventional two-level design (left), and a 9-level, dual-interleaved FCML design (right). The latter are from results in [2], and illustrate reduced dv/dt, interleaving and high effective frequency.....	180
Figure I.22.2 Top: schematic and current waveforms for a dual-interleaved, 10-level FCML inverter. Bottom: hierarchical control strategy and system diagram of paralleled converters of the modular (i.e., segmented) approach.....	181
Figure I.22.3 Left: measured overshoot of the commutation loop in this design. Right: measured experimental performance of the prototype inverter module across various load impedances and dc bus voltages. ....	182
Figure I.22.4 Left: an annotated hardware prototype of the 10-level, dual-interleaved inverter module for this project. Right: a 9-module, segmented inverter paralleled across three winding phases assembled for initial motor testing. ....	183
Figure I.22.5 Left: experimental setup showing the thermal test assembly for this air-cooled inverter iteration. Right: CFD results showing relatively a relatively uniform pressure front across the inlet window of each modular heat sink.....	184
Figure I.22.6:Nonlinear simulation of the flying capacitor voltages during dc bus startup. ....	185
Figure I.22.7 Calorimetric test setup used in evaluating large-signal loss characteristics for passive devices. The entire assembly is loaded into a temperature-controlled chamber during component evaluation. ....	185
Figure I.23.1. A schematic of the hardware to be developed in this project.....	188
Figure I.23.2. Summary of recommended high temperature packaging materials for power modules. ....	189
Figure I.23.3. High temperature gate driver IC from Cissoid.....	189
Figure I.23.4. Air-core inductors. ....	190
Figure I.23.5. The layout design of a 1.2kV, 149 A SiC MOSFET planar module with double-side cooling. ....	192
Figure I.23.6. Terminals of the power module for gate driver and current sensor.....	192
Figure I.23.7. (a) Equivalent circuit of power MOSFET model, and (b) Current sensing with short-circuit protection and current reconstruction. ....	193
Figure I.23.8. Sensor waveforms (scaled) in comparison to the actual current waveforms.....	193
Figure I.23.9. Reconstructed current waveform. ....	193
Figure I.23.10. Short-circuit protection. ....	193
Figure I.24.1 Integrated Modular Motor Drive (IMMD) concept [4].....	198
Figure I.24.2 IMD Topologies [6],[7].....	199
Figure I.24.3 Alternative traction inverter drive configurations: a) VSI excitation; and b) CSI excitation.....	200
Figure I.24.4 Typical line-to-neutral voltage waveforms for (a) VSI and (b) CSI .....	200
Figure I.24.5 Typical switch voltage and current waveforms for (a) VSI and (b) CSI.....	202
Figure I.24.6 Electric machine categorization segregating machine types with and without permanent magnets.....	202



Figure I.24.7 Flux-weakening performance comparison of the CSI-excited and VSI-excited SPM machines for CPSR=6.25 .....	203
Figure I.25.1 Homopolar AC Machine .....	207
Figure I.25.2 HAM magnetic equivalent circuit. ....	207
Figure I.25.3 HAM phase MMF waveforms. ....	208
Figure I.25.4 Preliminary HAM Pareto-optimal front. ....	209
Figure I.25.5 Preliminary HAM design. ....	209
Figure I.25.6 (a) Surface meshed linear materials and (b) volume-meshed nonlinear materials for a PMSM model. ....	210
Figure I.25.7 Pareto-optimal front from an MoM-based optimization. ....	211
Figure I.26.1 SiC MOSFET Reliability Issues .....	213
Figure I.26.2 Key Partnerships .....	214
Figure I.26.3 Gate leakage current-voltage characteristics at three different temperatures.....	216
Figure I.26.4 Weibull distribution of vendor E' for four different gate voltages at 28°C and 175°C.....	217
Figure I.26.5 Degradation of the 3 <sup>rd</sup> quadrant I <sub>D</sub> -V <sub>D</sub> characteristics for built-in body diode of one selected 1.7 kV SiC DMOSFET from each vendor.....	218
Figure I.26.6 Reverse bias characteristics at gate voltage of V <sub>GS</sub> = 0 V of one selected 1.7 kV SiC DMOSFET from each vendor at room temperature before and after stress of the body diode.....	218
Figure I.26.7 Time-dependent threshold voltage shifts for (a) positive bias-stress of +20 V, (b) +30 V, and (c) negative bias-stress of -10 V for 50 hours. ....	219
Figure I.26.8 Temperature-dependent (a) threshold voltage values and (b) I <sub>D</sub> -V <sub>G</sub> transfer characteristics of device E' and C.....	219
Figure I.26.9 Block diagram of gate drive circuit.....	220
Figure I.26.10 Load transient response, Propagation delay waveform, Relationship between the output voltage levels of outputs and switching frequency.....	220
Figure I.27.1 Design-I.....	224
Figure I.27.2 Design-II .....	224
Figure I.27.3 Design-III.....	224
Figure I.27.4 Short circuit at 18,000 rpm.....	224
Figure I.27.5 Short circuit at 18,000 rpm.....	224
Figure I.27.6 Short circuit at 18,000 rpm.....	224
Figure I.27.7 Slotless motor using thermal plastic.....	225
Figure I.27.8 Slotless motor using Alumina .....	225
Figure II.1.1 Variant 1, 2, and 3 rotors shown from left to right .....	228
Figure II.1.2 Variant 1, 2, and 3 stators shown from left to right .....	229
Figure II.1.3 Rotor casting simulations for improved Al-Cu interface strength .....	229
Figure II.1.4 Average rotor bar improvement from baseline (Casting #15) based on pull force. Casting numbers represent different parameters in the design of experiment .....	229

Figure II.1.5 Cost analysis of Variants 1, 2, and 3. Variant 1 only was estimated to be below the DoE cost target of \$4.7/kW. ....	230
Figure II.1.6 Stress life curves for materials “A”, “B”, and “C”. ....	231
Figure II.1.7 Example of fracture analysis with SEM for material A, sample #2. ....	231
Figure II.1.8 Rotor bar casting sample. ....	232
Figure II.1.9 X-ray CT scanning results from rotor bar sample. ....	232
Figure II.2.1. Illustration of the dual phase structure in a laminate used to manufacture a SynRel machine. The left image shows where the non-magnetic (orange) regions are patterned into the magnetic (green) laminate. The middle image shows an actual laminate in which a ceramic mask has been applied. The exposed regions will become non-magnetic after nitrogenation. The right image shows a laminate after nitrogenation, placed underneath a magnetic indicator film. The stripe domains shine through the regions which have been made non-magnetic. ....	235
Figure II.2.2 Manufacturing sequence for prototypes containing dual phase magnetic laminates. ....	236
Figure II.2.3 a) Fully assembled full-scale prototype motor. b) exterior dimensions of the prototype motor. ....	237
Figure II.2.4 Full-scale prototype motor on a dynamometer test stand. ....	238
Figure II.2.5 Measured continuous shaft torque and power output of the full-scale dual phase synchronous reluctance prototype made from the dual phase laminate rotor. ....	239
Figure II.2.6 Measured efficiency of the full-scale dual phase synchronous reluctance prototype made from the dual phase laminate rotor. ....	239
Figure II.3.1 Magnetization vs. applied field at different temperature of the bulk magnet fabricated using the newly developed CIP process. Note that the coercivity increases with increasing temperature, resulting in a series of B-H curves that are overlaid on top of each other. This is the most desired magnet feature for motor design. ....	243
Figure II.3.2 Photo of 5 wt% epoxy bonded core after curing. The surface epoxy coat has not been applied. ....	245
Figure II.3.3 Iron loss of epoxy bonded, flake core ring samples as a function of flux density for a number for frequencies (a) 5 wt% epoxy, flux area by dimension; (b) 3 wt% epoxy, flux area by dimension; (c) 5 wt% epoxy, flux area by density; (d) 3 wt% epoxy, flux area by density. ....	246
Figure II.3.4 (a) MgO laminated ring, the bright features are MgO agglomerations. (b) Cross-section optical image of the MgO laminated ring sample, the dark strips are MgO layers, while the gray bands are FeSi. ....	246
Figure II.3.5 Magnetic properties of MgO laminated rings. (a) Flux density as a function of magnetic field for both the DC and AC400Hz condition using dimension method; (b) flux density as a function of magnetic field for both the DC and AC400Hz condition using density method; (c) AC400Hz iron loss as a function of flux density. ....	247
Figure II.3.6 Picture of the prototype rotor (left) and stator (middle), and fully assembled motor. ....	247
Figure II.3.7 Motor test setup at UTRC. ....	248
Figure II.3.8 Comparison between the predicted back EMF results and the actual measurements. ....	249
Figure II.4.1 Organizations That Are Publicly Held and Actively Engaged in the NA EVSE Supply Chain, Ranked by Annual Revenues (Dollar Millions, Calendar Year 2018). ....	254
Figure II.4.2 NA EVSE Supply Chain Organizations, By Product or Service Category (Represents 170 organizations, both public and private.*) As of July 2019. ....	255
Figure II.5.1 Automotive SiC power module with 900V SiC die. ....	261

Figure II.5.2 Switch resistance: (left) measured through pcb flex circuit (right) measured through module terminals .....	261
Figure II.5.3 Hardware set-up for the thermal impedance measurements .....	262
Figure II.5.4 Thermal impedance curves for $V_{gs}=-8V$ : (left) $Z_{th}$ for switch UHI, (middle) $Z_{th}$ for switch VHI, (right) $Z_{th}$ for switch WHI.....	262
Figure II.5.5 Equivalent 6 <sup>th</sup> order Cauer impedance network to represent thermal impedances .....	263
Figure II.6.1 Dynamometer results for bus P1' vs. bus P1. Provided by NREL based on P1' dynamometer testing on May 29, 2019. ....	268
Figure III.1.1 TransPower EDD Battery Electric Trucks .....	272
Figure III.1.2 US Hybrid Battery Electric Truck No. 1 .....	273
Figure III.1.3 US Hybrid Battery Electric Truck No. 2 .....	273
Figure III.1.4 TransPower CNGH-1 .....	274
Figure III.1.5 Route containing hills during Q4 2018 tests.....	275
Figure III.1.6 TransPower - CNGH-2 (APU view) .....	275
Figure III.1.7 .....	275
Figure III.1.8 TransPower - CNGH-2 with trailer .....	275
Figure III.1.9 US Hybrid LNGH.....	276
Figure III.1.10 US Hybrid LNGH pulling a container for TTSI.....	276
Figure III.2.1 CTE/Kenworth Fuel Cell Truck .....	279
Figure III.2.2 TransPower Fuel Cell Truck in Foreground & CNG Truck in Background .....	279
Figure III.2.3 U.S. Hybrid Truck: Design to Fabrication.....	279
Figure III.2.4 Kenworth/BAE - CNG Hybrid System Architecture .....	280
Figure III.3.1 Mutual verification of simulation and powertrain dyno measurements .....	288
Figure III.3.2 Fluids box redesign to improve space utilization, ease assembly on truck chassis .....	289
Figure III.3.3 Consolidation of separate 12V 24V and HVIL fuse relay boxes into one.....	289
Figure III.3.4 Performance vs. Speed simulation results in different modes including transmission spin losses.....	291
Figure III.3.5 1MEV to Powersplit Transient including Hybrid Start .....	291
Figure III.3.6 1MEV to Powersplit Transient including Hybrid Start .....	292
Figure III.4.1 Hybrid System vehicles in Build Shop.....	295
Figure III.4.2 Complete eAxle System on McLaren Test Rig .....	295
Figure III.4.3 1st Design Demonstrator On Real World Commissioning Drive.....	296
Figure III.4.4 Vehicle, Being Returned to Shop for Adjustments/Updates .....	296
Figure III.5.1 WXFC project activities. ....	299
Figure III.5.2 Project design and implementation approach. ....	299
Figure III.5.3 System block diagram. ....	300

Figure III.6.1 System level diagram of the proposed architecture for the bidirectional wireless charging system.....	304
Figure III.6.2 System level diagram of the proposed architecture for the bidirectional wireless charging system.....	304
Figure III.6.3 System level diagram of the proposed architecture for the bidirectional wireless charging system.....	304
Figure III.6.4 Primary and secondary coils with their resonant tuning components (a) and Bode 100 frequency response analyzer used for voltage gain characterization of the system.....	305
Figure III.6.5 Resonant voltage gain of the system using the analytical model (a) and the experimental validation (b).....	305
Figure III.6.6 Resonant voltage gain of the system using the analytical model (a) and the experimental validation (b).....	306
Figure III.6.7 Experimental test results for G2V mode with 20 kW power transfer to the vehicles-side battery emulator: Operational waveforms (a) and power analyzer measurements (b).....	306
Figure III.6.8 Experimental test results for V2G mode with 20 kW power transfer to the primary-side DC link.....	307
Figure III.7.1 Odyne powertrain configuration.....	310
Figure III.7.2 Odyne hybrid architecture .....	311
Figure III.7.3 Odyne / Oak Ridge HIL powertrain test stand .....	312
Figure III.7.4 Torqeedo 11.6 kWh battery pack .....	313
Figure III.7.5 Test chassis design layout .....	313
Figure III.7.6 Completed test chassis and hydraulic test stand.....	314
Figure III.8.1 ETREE powertrain test cell located at Cummins Technical Center, Columbus, Indiana.....	317
Figure III.8.2 ETREE alternate battery—drivers side enclosure (shown without cover) .....	317
Figure III.9.1 NRTC Lab Equipment Set Up with SPIN Rack System .....	323
Figure III.9.2 Power Analyzer Test Trace Showing Sequential Execution of All of the SPIN Operating Modes (Source: ORNL NTRC).....	323
Figure III.9.3 SPIN DC Communications Control Module (CCM) with J1772 Combo Coupler Assembly....	324
Figure III.9.4 IoTecha EVCC and SECC Card Facilitates SPIN to PHEV DC Charging Communications (Source: IoTecha, Inc) .....	324
Figure III.9.5 SPIN Product Concept 3D-Layout including DC CCM and Charging Cable .....	325
Figure III.9.6 SPIN Application Scenarios being Designed for Verification .....	326
Figure III.9.7 SPIN Integrated Ecosystem Software Architecture: In-Cloud, On-Vehicle and On-SPIN .....	326
Figure III.9.8 Combined IEEE2030.5 and DIN 70121 Communications Sequence Diagram.....	328
Figure III.10.1. Block-diagram schematic of the XFC station.....	333
Figure III.10.2. Hierarchical control architecture. ....	333
Figure III.10.3. Comparison between full model and estimator for two CCCV cycles at 1C with constant diffusivities. ....	334
Figure III.10.4. Experimental results for open-circuit potential and solid-phase lithium diffusivity of half-cells. ....	335

Figure III.10.5. Prototype module to construct cascaded H-bridge .....	335
Figure III.10.6. Virtual inertia control scheme. ....	336
Figure III.10.7. Improved performance of the NN-MPC virtual inertia compared to PI controllers. ....	336
Figure III.10.8. Bus voltage and current without (Case I) and with (Case II) reactive power injection. ....	337
Figure III.11.1 System Layout showing the key components: MV SST, DC distribution network, and DC node that contains the DC/DC converter and vehicle interface.....	339
Figure III.11.2 MV SST Converter topology. The SST is made up of 6 Levels connected in input-series output-parallel configuration.....	341
Figure III.11.3. [Left] Small-scale prototype of the SST stage used for control validation [Right] Experimental results showing the behavior of the single module connected to an ac source and a variable DC load. The controller response shows the ability of the DAB stage to handle the power pulsations present in the single phase system .....	342
Figure III.11.4 Fault scenarios under investigation .....	343
Figure III.11.5. [Left] IGCT stack for 500 A class breaker B2 with forced air cooling system [Right] Air flow analysis for design validation of cooling system for 500 A class breaker B2.....	344
Figure III.11.6 [Left] Advanced thermosyphon design and operating principle [Right] First batch of manufactured advanced thermosyphon for breaker B1 .....	344
Figure III.11.7 Example of high di/dt current transient during a short circuit event .....	345
Figure III.11.8 [Left] Mechanical design of SS DCCB B1; [Right ] Mechanical design of power stack for unidirectional SS DCCB B2 .....	345
Figure III.13.1 XFC System Architecture.....	351
Figure III.13.2 Circuit Diagram of Power Module .....	351
Figure III.13.3 Picture of an SST Module at left, and Charging Controller (Buck) Module at right.....	352
Figure III.13.4 SST's AC/DC Stage Waveforms (CH1 brown: $V_{ph}$ , CH2 blue: $V_{AC}$ , CH3 purple: $V_L$ , CH4 green: $I_{AC}$ ).....	353
Figure III.13.5 SST's DC/DC Stage Waveforms (CH1 brown: $V_{GS}$ , CH2 blue: $V_{DS}$ , CH3 purple: $I_{Lr}$ , CH4 green: $V_{Cr}$ ) .....	353
Figure III.13.6 1-Phase Series SST and Buck Module Test Setup (up to 45-kW).....	354
Figure III.13.7 1-Phase Series SST and Buck Module Efficiency Test Result (up to 45-kW).....	354
Figure IV.1.1 SAE J1772 charge connector w/DEVA .....	360
Figure IV.1.2 SpEC module 2.0 alpha board.....	360
Figure IV.1.3 Multi-unit sub-meter (w/o current sensors).....	360
Figure IV.2.1 ADMM allows groups of distributed computers to jointly solve optimization problems .....	364
Figure IV.2.2: Charging station demand and net load for an 8,000 kVA distribution grid based on CAISO data.....	366
Figure IV.2.3: 100 CS show valley filling; net load from 6-10 pm cannot be flattened by reducing charging load. ....	366
Figure V.1.1 200 kW DC EVSE Interoperability Testing .....	369
Figure V.1.2 BTC Power SLAC-based Communication .....	370
Figure V.1.3 BTCP DCFC Communication Log.....	370

Figure V.1.4 Comemso EV Charge Analyzer..... 371

Figure V.2.1 350-kW XFC charging a 2014 BMW i3 in INL’s Electric Vehicle Infrastructure Lab ..... 374

Figure V.2.2 350-kW XFC charging a New Flyer 60-foot electric transit bus in INL’s Electric Vehicle Infrastructure Lab ..... 374

Figure V.2.3 Efficiency of the 350-kW XFC..... 375

Figure V.2.4 Charge profile of the 2014 BMW i3 connected to the 350-kW XFC ..... 376

Figure V.2.5 Charge initialization ramp-up characteristics when charging with a 350kW capable XFC ..... 376

Figure V.2.6 Comparison of charge event initialization and power ramp-up: 50kW DCFC and 350kW XFC 377

Figure V.2.7 Power ramp-down at the end of a charge on the 350-kW XFC..... 377

Figure V.2.8 Schematic of vehicle emulator that uses the XFC’s Combined Charging System (CCS) connector (Source: INL)..... 378

Figure V.3.1 Energy envelop of each device and aggregated energy envelop ..... 380

Figure V.3.2 Structure of distributed control with hierarchy..... 380

Figure V.3.3 Architecture of integrated control system for EVSE and ESS at NREL ..... 381

Figure V.3.4 Computed plots at (a) 9:00am (top) and (b) 11:00am (bottom) of the energy constraints and optimal energy profile (left) and the resulting L2 EVSE power profile plan compared to the forecasted load with/without the L2 EVSE load (right)..... 382

Figure V.3.5 Test results of the DCFC control ..... 383

Figure V.3.6 Test results of the stationary ESS ..... 384

Figure V.4.1 Example of a 5-trip vehicle simulation..... 389

Figure V.4.2 Hosting capacity analysis for four feeders in the MSP region..... 390

Figure V.5.1 Simulation architecture used in RECHARGE project..... 394

Figure V.5.2 Caldera charging profiles for PEV charging models in when the PEVs are connected to a 350-kW capable XFC unit ..... 395

Figure V.5.3 Feeder demand profiles when PEV charging not controlled and when it is controlled using the centralized charging control strategy ..... 395

Figure V.5.4 Real and reactive power profiles for Atlanta and Minneapolis used in scenario 1 ..... 396

Figure V.5.5 Real and reactive power profiles for Atlanta and Minneapolis used in scenario 2..... 397

Figure V.6.1 Hosting capacity result for a residential feeder..... 401

Figure V.7.1 Topology of candidate 1+MW System Architectures ..... 404

Figure V.7.2..... 405

Figure V.7.3 Expected voltage drop introduced by multiple XFCs in a distribution system..... 408

Figure V.8.1 Example of a 5-trip vehicle simulation..... 413

Figure V.8.2 Testing results for IEEE 34-bus system..... 414

Figure V.8.3 Station load profiles for stations with 30 vehicles / day ..... 414

Figure V.8.4 (a) Deformation of connector after insertion process, and (b) temperature distribution of the connector with constant current ..... 415

Figure V.8.5 (a) A schematic of the pin/socket coupler showing various locations to apply the convective heat transfer boundary condition, and (b) Results of temperature rise variation with combination of locations to apply heat transfer boundary condition.....	416
Figure V.8.6 Composition of Waste Heat.....	417
Figure V.9.1 Set of topics covered in the requirements study .....	420
Figure V.9.2 four station charging mezzanine charging installation at the Daimler bus factory .....	423
Figure V.10.1 System level diagram of the proposed XFC inductive charging system. ....	427
Figure V.10.2 Rendered 3-D image of the inverter design (a) and the actual prototype fabricated (b).....	427
Figure V.10.3 Simulation model of the two-layer coupler design (a) and the fabricated prototype.....	428
Figure V.10.4 Simulation model of the front-end rectifier and buck converter.....	429
Figure V.10.5 Simulation model of the two-layer three-phase couplers with three-phase inverter/rectifier. ....	429
Figure V.10.6 Computational model images of the ground and vehicle couplers. ....	430
Figure V.10.7 Computational model images of the ground and vehicle couplers. ....	430
Figure V.10.8 Computational model images of the ground and vehicle couplers. ....	430
Figure V.10.9 Experimental test setup.....	431
Figure V.10.10 Results for an example test case with 50 kW output. ....	431
Figure VI.1.1 Percentage of total paved miles and annual driven road-miles for primary, secondary, and local roadways in USA. ....	434
Figure VI.1.2 Dynamic wireless EV charging in an electrified roadway .....	435
Figure VI.1.3 Dynamic wireless EV charging in an electrified roadway .....	435
Figure VI.1.4 Reference wireless power transfer pads showing coil layout and peak ferrite flux density (mT):(Left) Square pad, (Right) DD pad.....	436
Figure VI.1.5 Reference pad transmitter showing coil layout, peak ferrite flux density (mT), and travel direction:(Left) Square pad system, (Right) DD pad system.....	436
Figure VI.1.6 Dynamic wireless EV charging in an electrified roadway. ....	436
Figure VI.1.7 Dynamic power transfer level and efficiency of the SOA DWPT systems. ....	437
Figure VI.1.8 Dynamic power transfer level and surface power density of the vehicle coil of the SOA DWPT systems.....	437
Figure VI.1.9 Reference pad profiles assuming a vehicle velocity of 75 mph. ....	438
Figure VI.1.10 Grid current, active and reactive power and current spectrum for vehicle traveling at 20 mph with DWPT .....	438
Figure VI.1.11 Grid current, active and reactive power and current spectrum for vehicle traveling at 70 mph with DWPT .....	438
Figure VI.1.12 The phase of the derived and simulated control-signal-to-coil current transfer function as a function of frequency.....	438
Figure VI.1.13 The magnitude of the derived and simulated control-signal-to-coil current transfer function as a function of frequency. ....	438
Figure VI.2.1 Light duty 200kW WPT with Tooth-Edge ferrite design.....	441

Figure VI.2.2 Magnetic field magnitude for 200kW light duty WPT with and without Tooth-Edge ferrite design..... 442

Figure VI.2.3 Representative electrical waveform during in-motion wireless power transfer ..... 443

Figure VII.1.1 Project tasks flow chart..... 446

Figure VII.1.2 350kW Extreme Fast Charger at Idaho National Lab ..... 449

Figure VII.1.3 350kW Extreme Fast Charger stop charge response characteristics..... 450

Figure VII.2.1 Charging power profile for a fast charging site with high fidelity models for six 350 kW ABB Terra HP fast chargers over a 24-hour period..... 454

Figure VII.2.2 Charging power profile for a fast charging site with high fidelity models for six 350 kW ABB Terra HP fast chargers over a 2-hour period..... 454

Figure VII.2.3 ABB Terra HP extreme fast charger installed in the EVIL lab located at INL..... 455

Figure VII.4.1 Electric vehicle communication systems to different components and entities. .... 459

Figure VII.4.2 Project tasking..... 460

Figure VII.4.3 Threat Model..... 461

Figure VII.4.4 Attack graph..... 462

Figure VII.4.5 Different distribution voltage profiles for coordinated charging/discharging of EVSEs totaling 2.25 MW. .... 462

Figure VII.4.6 WECC light spring: system values through time. .... 463



## List of Tables

Table I.1.1 Standard Layer Thickness of Insulators and Fundamental Properties.....	17
Table I.3.1 Summary of Test Results for AlNiCo 8HC Magnet Samples .....	36
Table I.4.1 Motor Candidates .....	42
Table I.4.2 Performance Comparison .....	43
Table I.4.3 Summary of Pros and Cons .....	44
Table I.5.1 Advantages and Disadvantages of Various Integration Techniques.....	49
Table I.5.2 Selected Capacitor’s Parameter Comparison.....	53
Table I.5.3 Advantages and Disadvantages of Selected Capacitor Technologies.....	56
Table I.6.1 Comparison of the Properties of Single Walled CNTs versus Cu.....	60
Table I.10.1 .....	90
Table I.11.1 Nodule Dimensions .....	100
Table I.12.1 Summary of Measurement Error with Different Metering Block Materials for High Thermal Resistance Sample .....	106
Table I.13.1 Parameters varied during jet impingement heat transfer characterization experiments .....	112
Table I.16.1 Magnetic properties of the magnet assembly with different configuration. ....	136
Table I.17.1 Power Electronics Requirements.....	140
Table I.18.1 EDT Consortium Electric Motor Targets .....	148
Table I.18.2 Optimization Target Specifications and Constraints .....	150
Table I.19.1 Summary of Process flow for 1 <sup>st</sup> lot .....	159
Table I.19.2 Summary of simulation models.....	160
Table I.20.1 A comparison of the most commonly used substrates for GaN epitaxy [1] .....	163
Table I.21.1 Comparison of foam properties for analysis, literature <sup>3</sup> , and AM unit cell.....	172
Table I.22.1 Key Inverter Prototype Experimental Results .....	183
Table I.23.1 Power Electronics Requirements.....	187
Table I.23.2 Commercially Available High Temperature Resistors.....	190
Table I.23.3 Commercially Available High Temperature Capacitors .....	191
Table I.24.1 Power Electronics and Motor Requirements .....	196
Table I.24.2 Production Electric Vehicle Power Density Metrics [1]-[3] .....	197
Table I.24.3 Key Advantages/Disadvantages of Major IMD Topologies [6],[7] .....	199
Table I.24.4 Calculated Efficiency Comparison of VSI and CSI Power Converters.....	201
Table I.26.1 TESTED COMMERCIAL SIC POWER MOSFETS .....	215
Table I.27.1 Summarized Electromagnetic Results .....	223
Table II.1.1 Summary of motor performance results for all three variants.....	228
Table II.1.2 Rotor overspeed testing.....	230

Table II.2.1 The coolant flowrate, inlet pressure, coolant pressure drop, and temperature at continuous power. ....	238
Table II.2.2 Target vs. calculated and measured performance of the full-scale dual phase synchronous reluctance motor prototype. ....	240
Table II.3.1 Properties of magnets prepared by compacting melt-spun MnBi-based alloys at $T_{comp}$ and subsequently annealing them in magnetic field of 30 kOe. ....	244
Table II.3.2 Per-phase resistance and inductance measurements.....	248
Table II.4.1 NA EVSE Supply Chain Overview .....	252
Table II.4.2 Priority Gap Areas, by Frequency of Gap Statements .....	255
Table II.5.1 SiC power module switch resistances, $T=25C$ , $V_{gs}=15V$ .....	262
Table II.5.2 Thermal impedance parameters for equivalent Cauer Network.....	263
Table II.5.3 Thermal impedance parameters for equivalent Cauer Network.....	263
Table II.6.1 Results of P1' Dynamometer Testing .....	267
Table III.1.1 2012 Zero Emission Cargo Transport Demonstration Portfolio .....	271
Table III.1.2 Average Daily Use – TransPower BETs.....	272
Table III.1.3 Summary across all cycles for chassis dyno testing of CNGH-2.....	276
Table III.2.1 Hydrogenics Vehicle Systems Specifications.....	280
Table III.7.1 Oak Ridge Driving Simulation Fuel Economy Improvement Summary .....	312
Table III.8.1 Summary of ETREE Powertrain Components.....	316
Table III.8.2 Summary J1526 Testing Results.....	318
Table III.9.1 Pacifica PHEV Battery Impact Energy Consumption for Test Protocol (Source: FCA, NREL). ....	329
Table III.9.2 Battery Test Cycle for Grid Services Impact Evaluation.....	329
Table IV.2.1 Performance characteristics of widely-used charging station communications media.....	365
Table IV.2.2: ChargePoint CT4000 specifications .....	365
Table V.4.1 Feeder descriptions .....	389
Table V.5.1 Types of High-Powered EVSE Used in the Recharge Project.....	394
Table V.5.2 Types of PEVs in the RECHARGE Project.....	395
Table V.6.1 Feeder descriptions .....	400
Table V.7.1 1+MW Architecture Evaluation Metrics.....	403
Table V.7.2 System Level Terminal Specifications .....	404
Table V.7.3 Summary Metrics for top three candidate topologies .....	409
Table V.8.1 Driving analysis of roadway segments .....	412
Table V.8.2 Waste Heat by Cable/Connector Type.....	417
Table V.10.1 High-frequency Power Inverter Parameters.....	427
Table V.10.2 Inductances of the Polyphase Coupler Prototype.....	428
Table V.10.3 Specifications of the 300 kW Polyphase Couplers .....	429
Table V.10.4 Experimental test results .....	431

Table VI.1.1 Comparison of simulation results of DD and square coil three-coil transmitter system for 200 kW dynamic WPT ..... 438

Table VI.2.1 Four Sample Rate Ranges for dWPT Evaluation ..... 442

Table VII.1.1 Impact Severity Scoring Matrix ..... 447

Table VII.1.2 Top Dozen Prioritized High Consequence Events ..... 448

(This page intentionally left blank

## Vehicle Technologies Office Overview

Vehicles move our national economy. Annually, vehicles transport 11 billion tons of freight—about \$35 billion worth of goods each day<sup>1</sup>—and move people more than 3 trillion vehicle-miles.<sup>2</sup> Growing our economy requires transportation and transportation requires energy. The transportation sector accounts for approximately 30% of total U.S. energy needs<sup>3</sup> and 70% of U.S. petroleum consumption.<sup>4</sup> The average U.S. household spends over 15% of its total family expenditures on transportation, making it the most expensive spending category after housing.<sup>5</sup>

The Vehicle Technologies Office (VTO) has a comprehensive portfolio of early-stage research to enable industry to accelerate the development and widespread use of a variety of promising sustainable transportation technologies. The research pathways focus on fuel diversification, vehicle efficiency, energy storage, and mobility energy productivity that can improve the overall energy efficiency and efficacy of the transportation or mobility system. VTO leverages the unique capabilities and world-class expertise of the National Laboratory system to develop innovations in electrification, including advanced battery technologies; advanced combustion engines and fuels, including co-optimized systems; advanced materials for lighter-weight vehicle structures; and energy efficient mobility systems.

VTO is uniquely positioned to address early-stage challenges due to strategic public-private research partnerships with industry (e.g., U.S. DRIVE, 21<sup>st</sup> Century Truck Partnership) that leverage relevant expertise. These partnerships prevent duplication of effort, focus DOE research on critical R&D barriers, and accelerate progress. VTO focuses on research that industry does not have the technical capability to undertake on its own, usually due to a high degree of scientific or technical uncertainty, or that is too far from market realization to merit industry resources.

## Annual Progress Report

As shown in the organization chart (below), VTO is organized by technology area: Batteries & Electrification R&D, Materials Technologies, Advanced Engine & Fuel R&D, Energy Efficient Mobility Systems, Technology Integration, and Analysis. Each year, VTO's technology areas prepare an Annual Progress Report (APR) that details progress and accomplishments during the fiscal year. VTO is pleased to submit this APR for Fiscal Year (FY) 2019. In this APR, each project active during FY 2019 describes work conducted in support of VTO's mission. Individual project descriptions in this APR detail funding, objectives, approach, results, and conclusions during FY 2019.

---

<sup>1</sup> Bureau of Transportation Statistics, Department of Transportation, Transportation Statistics Annual Report 2018, Table 4-1. <https://www.bts.gov/tsar>.

<sup>2</sup> Transportation Energy Data Book 37<sup>th</sup> Edition, Oak Ridge National Laboratory (ORNL), 2019. Table 3.8 Shares of Highway Vehicle-Miles Traveled by Vehicle Type, 1970-2017.

<sup>3</sup> Ibid. Table 2.1. U.S. Consumption of Total Energy by End-use Sector, 1950-2018.

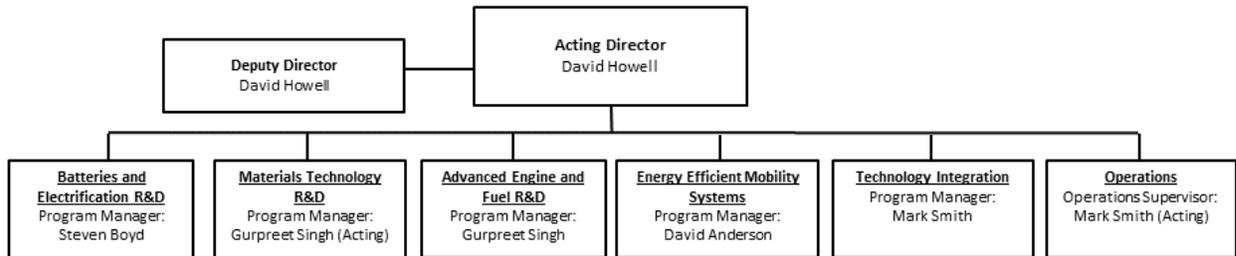
<sup>4</sup> Ibid. Table 1.12. U.S. Transportation Petroleum Use as a Percent of U.S. Petroleum Production, 2018.

<sup>5</sup> Ibid. Table 10.1. Average Annual Expenditures of Households by Income, 2016.

## Organization Chart

### Vehicle Technologies Office

February 2020



# Electric Drive Technologies Program Overview

## Introduction

The Electric Drive Technologies (EDT) program's mission is to conduct early stage research and development on transportation electrification technologies that accelerate the development of cost-effective and compact electric traction drive systems that meet or exceed performance and reliability requirements of internal combustion engine (ICE)-based vehicles, thereby enabling electrification across all light-duty vehicle types.

## Goals and Objectives

The goal of the EDT program is to develop an electric traction drive system at a cost of \$6/kW for a 100 kW peak system by 2025. In addition, the program has a 2025 power density target of 33 kW/L for a 100 kW peak system. While achieving these targets will require transformational technology changes to current materials and processes, it is essential for enabling widespread electrification across all light-duty vehicle platforms.

## Program Design and Execution

The EDT program provides support and guidance for many cutting-edge automotive technologies now under development. Researchers focus on developing revolutionary new power electronics (PE), electric motor (EM), and traction drive system (TDS) technologies that will leapfrog current on-the-road technologies. This will lead to lower cost and better efficiency in transforming battery energy to useful work. Research and development (R&D) is also aimed at achieving greater understanding of, and improvements in how the various components of tomorrow's automobiles will function as a unified system.

In supporting the development of advanced vehicle propulsion systems, the EDT program fosters the development of technologies that will significantly improve efficiency, costs, and fuel economy.

The EDT program directs early-stage research through a three-phase approach intended to

- Identify overall propulsion- and vehicle-related needs by analyzing programmatic goals and reviewing industry recommendations and requirements, and then develop and deliver the appropriate technical targets for systems, subsystems, and component R&D activities
- Develop, test, and validate individual subsystems and components, including EMs and PE
- Estimate how well the components and subsystems work together in a vehicle environment or as a complete propulsion system and whether the efficiency and performance targets at the vehicle level have been achieved.

The research performed under this program addresses the technical and cost barriers that currently inhibit the introduction of advanced propulsion technologies into hybrid electric vehicles (HEVs), plug-in HEVs, battery electric vehicles (BEVs), and fuel cell powered automobiles that meet the DOE goals.

A key element in making these advanced vehicles practical is providing an affordable electric TDS. This will require attaining weight, volume, efficiency, and cost targets for the PE and EM subsystems of the TDS. Areas of development include:

- Novel traction motor designs that result in increased power density and lower cost

- Inverter technologies that incorporate advanced wide bandgap (WBG) semiconductor devices to achieve higher efficiency while accommodating higher-temperature environments and delivering higher reliability
- Converter concepts that leverage higher-switching-frequency semiconductors, nanocomposite magnetics, higher-temperature capacitors, and novel packaging techniques that integrate more functionality into applications offering reduced size, weight, and cost
- New onboard battery charging electronics that build from advances in converter architectures for decreased cost and size
- More compact and higher-performing thermal controls achieved through novel thermal materials and innovative packaging technologies
- Integrated motor-inverter TDS architectures that optimize the technical strengths of the underlying PE and electric machine subsystems.

VTO competitively awards funding through funding opportunity announcement (FOA) selections, and projects are fully funded through the duration of the project in the year that the funding is awarded. The future direction for direct-funded work at the National Laboratories is subject to change based on annual appropriations.

## Electric Drive Technologies Lab Consortium

The multi-lab EDT Consortium will leverage U.S. research expertise and facilities at the National Labs and universities to improve the power density of electric drives by 10X compared with the 2015 numbers while reducing the cost by 50% and doubling the lifetime miles within the next 5 years. The final objective of the consortium is to develop a 100 kW traction drive system that achieves a power density of 33 kW/L, has an operational life of 300,000 miles, and a cost of \$6/kW. The system will be composed of a 100 kW/L inverter and a >20,000 rpm, 50 kW/L electric motor.

Research will be performed within the framework of a new research consortium consisting of a multi-disciplinary team that will plan, establish, conduct, and manage a portfolio of multi-lab and multi-university research efforts to advance the state-of-the-art in electric drive technologies.

The consortium is organized around three Keystone projects: (1) Power Electronics; (2) Electric Motors; and (3) Traction Drive System. The consortium will focus on early-stage research projects on advanced materials, high-density integration of dissimilar layers/materials, multifunctional subcomponents, and optimized and new thermal/electrical/magnetic architectures. New materials such as wide-bandgap semiconductors, soft magnetic materials, and ceramic dielectrics, merged using multi-objective co-optimization design techniques, will be utilized to achieve the program goals. Moreover, integration of components and subcomponents will further propel the research toward the goals of the consortium.

Consortium National Laboratory members include Ames Laboratory, The National Renewable Energy Laboratory (NREL), Oak Ridge National Laboratory (ORNL), and Sandia National Laboratory (SNL). University consortium partners include: North Carolina State University, The University of Arkansas, Virginia Polytechnic Institute, University of Wisconsin-Madison, Georgia Institute of Technology, University of California-Berkeley, Illinois Institute of Technology (IIT), Purdue University, The State University of New York (SUNY), and The Ohio State University.



# Grid and Infrastructure Program Overview

## Introduction

The Grid and Charging Infrastructure (G&I) program's mission is to conduct early stage research and development on transportation electrification technologies that enable reduced petroleum consumption by light, medium, and heavy duty vehicles. The program identifies and enables the role of vehicles in the future electrical grid.

## Goals and Objectives

**Program Goal:** The G&I Program identifies systems pathways and conducts research to facilitate the development and harmonization of a robust, interoperable, and cyber secure, electric vehicle charging and grid infrastructure which incorporates advanced charging technologies, distributed energy resources, grid, and grid services.

The program achieves its goal by accomplishing the following objectives:

- **EV Grid Integration and Services:** Identify system requirements and research Grid to Vehicle power transfer and storage (V1G) and Vehicle to Grid power transfer (V2G) technologies that optimize vehicle charging efficiency, minimize systems disruptions, and facilitate integration of distributed energy resources
- **High Power Static / Dynamic Wireless Charging:** Conduct feasibility studies and technology research and development of high power static and dynamic wireless charging to enable additional consumer charging options and greater vehicle autonomy
- **EV / Electric Vehicle Service Equipment (EVSE) / Grid Interoperability & Control:** Research and develop technologies and tools to enable seamless interoperability (connectivity and communications) and control that maximize charging convenience and minimize impacts to the grid
- **Extreme Fast Charging (XFC):** Identify and assess system requirements and conduct research to enable extreme fast charging while minimizing impacts to the grid.
- **Cyber Security:** Address on-road vehicle and charging infrastructure related cyber security gaps.

### *Program Design and Execution*

The G&I Program carries out its mission by focusing its R&D investments on early stage, medium and long-term technology projects that are unlikely to be pursued by industry alone, but have significant potential public benefit.

## G&I R&D Functions

- Perform R&D that focuses on defining requirements, designing, prototyping, and validating the enabling technologies that are needed. Document and share the results in public and industry forums where appropriate and feasible.
- Perform modeling and evaluation activities that provide objective, publicly available data to identify the most appropriate Federal investments and pathways for technology improvements and lessons learned for cost-effective future activities.

- Initiate outreach that provides technical assistance, tools, and resources to help stakeholders understand the technologies.
- Engage in research partnerships with industry to leverage technical expertise, prevent duplication, ensure public funding remains focused on the most critical barriers to technology commercialization, and accelerate progress. G&I will work collaboratively with its industry partners in the U.S. DRIVE Partnership (Grid Interaction Technical Team (GITT)) to analyze and identify technical R&D opportunities for passenger vehicles.
- Coordinate with other programs in EERE and across the DOE complex – National Laboratories, DOE’s Office of Science, Office of Electricity Delivery and Energy Reliability (OE), and the Advanced Research Projects Agency-Energy (ARPA-E) to ensure the effective use of resources while avoiding duplication and facilitates the transfer of successful technologies across the research and development continuum. (i.e., Grid Modernization Initiative)
- Collaborate via strategic partnerships with end-users and other key stakeholders.

The G&I program was established in January 2017. The program inherited a few of its FY 2019 projects from VTO’s Vehicle Systems program. These inherited G&I projects have been assigned to Grid Modernization, Industry Awards, or Fast Charging Enabling Technologies sections of this Electrification Annual Progress Report (APR). The Grid Modernization section contains project reports that were awarded to members of the Grid Modernization Laboratory Consortium (GMLC). The Industry section describes projects that were awarded to commercial industry performers via DOE’s Funding Opportunities Announcement (FOA) solicitation process. The Fast Charging Enabling Technologies projects were awarded to National Laboratories via direct funding agreements.

## State of the Art

### *Electric Vehicle Charging*

It is desirable to reduce EV refueling times to be competitive with conventional vehicle refueling times. The table below lists the refueling characteristics of several types of installed commercial EVSEs and a conventional gasoline fueling pump. The technologies employed in the EV charging stations are shown in the figure below.

Currently the most advanced Light Duty vehicle charging equipment is a proprietary system that can recharge the Tesla EV to 80% of battery capacity (and vehicle range capability) in approximately one-half hour of charging. This is accomplished by a charge rate of 140 KW.

The two open fast charging standards on the market today CCS and CHAdeMO were both originally designed to work at 400V. The Combined Charging System (CCS) was developed by seven carmakers and designed for charging up to 80KW at 400V. The standard is backed by major European and US OEMs and is positioned as the preferred option for a European network. CHAdeMO was an initiative of Japanese car companies and was originally designed to charge at up to 50KW at 400V.

The mid-term objective of XFC is to reduce LD charging time to approximately 10 minutes via a charge rate of approximately 350 to 400 KW. The long-term objective is to achieve charge rates of greater than 1 MW that will enable fast charging of both LD and Heavy Duty (HD) vehicles.

**Table 1 Light Duty Conventional and Electric Vehicle Refueling Characteristics**

Type of Refueling	Gasoline	Level 1 110V (~1.4kW)	Level 2 220V (~7.2kW)	DC Fast Charger (50kW)	Tesla SuperCharger (140kW)
Range per Charge Time	400 miles /5 mins	3-5 miles /60 mins	25 miles /60 mins	150 miles /90 mins	330 miles /60 mins
Time to Charge for 200 miles	<5 mins	<b>37 hours</b>	<b>8 hours</b>	<b>2 hours</b>	<b>25 mins</b>
Number of U.S. stations circa 2016	153,000	1,600	10,600	1,600	<b>705</b>

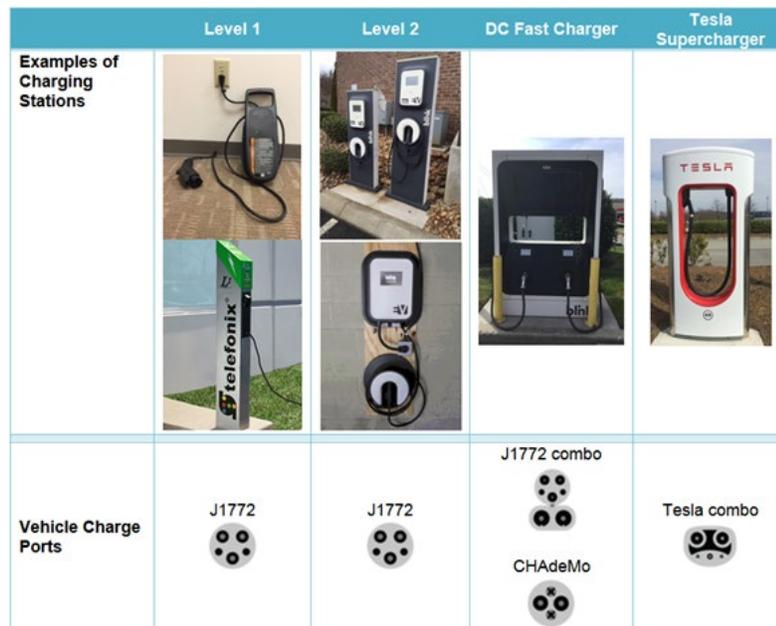


Figure 1 Examples of EV Charging Stations

## Grid and Infrastructure Research Highlights

Accomplishments	Organization	Focus Area	Project Title
<b>Designed a Novel High Power WPT device:</b> The team worked on modeling, simulations, analysis, and design of the system power conversion stages and control systems and completed the design and simulations of the 300 kW inductive charging system. Since proposed concept is new, a relatively low-power, scaled-down version of the couplers were developed and tested to validate the concept and the operation. The prototype was tested with ~95% dc-to-dc efficiency with ~50 kW output.	ORNL	High Power Wireless Charging	High-Power Inductive Charging System Development and Integration for Mobility
<b>Built and demonstrated zero emission capable electric truck technologies for drayage operations:</b> As of 2019, all eleven electric trucks funded under this project were constructed with two trucks continuing demonstration efforts until March 2020. Overall, the trucks that have completed demonstration have proven successful in demonstrating their feasibility in various drayage operations and handling daily loads and many routine schedules. The trucks have generated significant interest from trucking companies, which helps to promote and to accelerate market adoption of electric truck technologies in cargo transport operations.	South Coast Air Quality Management District	Industry Awards	Zero Emission Drayage Trucks Demonstration (ZECT I)
<b>65% Reduction in Fuel Consumption via Electrification:</b> The Electric Truck with Range Extending Engine (ETREE) project team has developed an EV powertrain and related systems and completed J1526 fuel consumption testing that demonstrated 65% reduction in fuel consumption on a modified NREL80 cycle over a baseline vehicle. The test exceeded the project goal of 50% reduction in fuel consumption.	Cummins	Industry Awards	Cummins Electric Truck with Range-Extending Engine (ETREE)
<b>McLaren built and tested a novel eAxle system, energy storage &amp; range extender systems for installation and final calibration in four MD demonstration vehicles.</b> There have been continued challenges to achieve the desired reliability for demonstration routes. The current system with the two-speed transmission feature will continue to be developed for demonstration in FY20.	McLaren Engineering	Industry Awards	Medium Duty Vehicle Powertrain Electrification and Demonstration
<b>Delta designed and tested a high-efficiency, medium-voltage-input, solid-state-transformer-based 400-kW XFC for EVs achieving better than 96.5 percent efficiency.</b> The XFC system consists of a Solid-State Transformer (SST), a Charge Controller (in power cabinet), a Charge Dispenser (A.K.A. User Unit) and an optional Energy Storage System (ESS). The test result shows that the SST module and the Buck module meet the specification. The integration of the series SST and Buck module is successful. The program objectives of FY19 were completely met.	Delta Electronics (Americas) Ltd)	Industry Awards – Fast Charging Enabling Technologies	High-Efficiency, Medium-Voltage-Input, Solid-State-Transformer-Based 400-kW/1000-V/400-A Extreme Fast Charger for Electric Vehicles

Accomplishments	Organization	Focus Area	Project Title
<p><b><u>Bosch progressed development of a commercially viable PHEV powertrain for MD vehicles that reduces fuel consumption by 50% on a real-world drive cycle by utilizing an advanced dual-planetary gear transmission with multiple clutches, coupled with cost-optimized electric machines. The integration phase of the PHEV powertrain continued throughout the year. A dual 24V power pack was installed for electro-hydraulic power steering and braking while the ICE is not running. Thermal management is accomplished using an integrated fluids box from VOSS including new thermally controlled valves. Fluids box installed on the chassis, filled and commissioned for initial chassis dyno testing. E/E Architecture was frozen and the 12V 24V and HVIL (High Voltage InterLock) systems were integrated into a single Power Distribution Unit for convenient access and space considerations. In parallel, engine dyno test results with a downsized diesel engine assembled to a hybrid transmission successfully demonstrated mode switches between one and two motor EV as well as Powersplit during transient cycles.</u></b></p>	<p>Robert Bosch LLC</p>	<p>Industry Awards</p>	<p>Medium-Duty Urban Range Extended Connected Powertrain (MURECP), ()</p>
<p><b><u>High Power Wireless System Development: The CALSTART project made significant progress in developing systems for high power and high-efficiency wireless charging of an electric medium duty delivery trucks. Team developed the resonant stage components and verified the resonant voltage gains that would optimize the power transfer between the ~750-800V primary dc bus voltage and the nominal 420V secondary. As of September 2019 the team was working on vehicle integrations and preparations to demonstrate the operation of the technology on the UPS research truck.</u></b></p>	<p>CALSTART, ORNL, UPS</p>	<p>Industry Awards-High Power Wireless Charging</p>	<p>Bidirectional Wireless Power Flow for Medium Duty Vehicle Grid Connectivity</p>
<p><b><u>Odyne progressed the development of a new class of PHEV Work Truck which will be modularized and customized to provide optimal ROI across multiple customers and applications. The work initially focused to demonstrate this technology as a Utility Work Truck variant. The project completed the final analytical drive optimization, selection of the primary path battery system. The project also built the prototype test chassis and ORNL Hardware-in-Loop (HIL) powertrain dynamometer test system fixturing and assembly.</u></b></p>	<p>Odyne Systems</p>	<p>Industry Awards</p>	<p>Development and Demonstration of Medium-Heavy Duty PHEV Work Trucks</p>
<p><b><u>NREL developed technology to mitigate demand charges via a charge management system integrating many different types of controllable loads for demand charge mitigation. The central controller only needs to add a list of MQTT message topics that are required for the new controllable loads and aggregate the forecasted energy needs of them into the optimization.</u></b></p>	<p>NREL</p>	<p>Fast Charging Enabling Technologies</p>	<p>Demand Charge Mitigation Technologies</p>
<p><b><u>WAVE developed a HP WPT System Requirements to develop and integrate a new 500kW WXFC system into a</u></b></p>	<p>WAVE, Utah State</p>	<p>Industry Awards-</p>	<p>High-Power Inductive Charging</p>

Accomplishments	Organization	Focus Area	Project Title
<p><b>Class 8 electric drayage truck developed by Cummins so that it can automatically and wirelessly charge at a high charging rate (c-rate) during their dwell times. The proposed wireless charger features a direct connection to the Medium Voltage (MV) 3-phase grid developed by Utah State University and Schneider Electric and the final prototype will be deployed at Total Transportation Services Inc. (TTSI), which is a truck operator at the Port of Los Angeles (POLA).</b></p>	<p>University, Schneider Electric, Total Transportation Services</p>	<p>High Power Wireless Charging</p>	<p>System Development and Integration for Mobility</p>
<p><b><u>EPRI progressed V2G technology to improve the value of owning a Plug-in Electric Vehicle (PEV) in the form of an off-vehicle Smart Power Integrated Node (SPIN) system. SPIN enables increased renewable generation on the grid and providing Vehicle to Home type services in conjunction with on-vehicle and off-vehicle storage. A fully functional SPIN unit was delivered to NREL NTRC for acceptance testing of its operational modes. The project defined DC DER software and communications strategy—an industry first, that will inform both the IEC/ISO and SAE standards. The project defined a control and communications architecture for information exchange between the grid and SPIN as well as the SPIN and PEV. The project developed the SPIN master controller and integrated the IoTecha EVCC and SECC cards on Pacifica PHEV and SPIN. Setup of an End to end communications bench to verify system-level communications and control functions began. Off-board V2G functionality of the Pacifica PHEVs have been accomplished by refreshing the on-board V2G program. from the on-board V2G program have been refreshed to A battery test cycle has been defined and the battery has been provided by FCA to NREL where the test set up has been completed and the battery testing has commenced.</u></b></p>	<p>EPRI</p>	<p>Industry Awards-</p>	<p>Comprehensive Assessment of On- and Off-Board Vehicle-To-Grid Technology Performance and Impacts On Battery and The Grid (EPRI SPIN)</p>
<p><b><u>MUST began advancing the state of the art in EV charging by addressing the three key challenges of 1) battery charging algorithms for minimal damage during extreme fast charging, 2) medium-voltage power conversion for rapid, inexpensive deployment, and 3) grid compatibility to mitigate the impact of charging transients on the grid. The project produced preliminary results on sub-scale analysis, design, and construction that are to be completed in FY20 and scaled up in future years.</u></b></p>	<p>Missouri University of Science and Technology (MUST)</p>	<p>Industry Awards – Fast Charging Enabling Technologies</p>	<p>Enabling Extreme Fast Charging with Energy Storage</p>
<p><b><u>NCSU has made significant progress in all key aspects of the XFC station design. The team has selected the MV SST topology; completed the system-level control simulations,</u></b></p>	<p>North Carolina State</p>	<p>Industry Awards – Fast</p>	<p>Intelligent, Grid-Friendly, Modular Extreme Fast</p>

Accomplishments	Organization	Focus Area	Project Title
<p>and has constructed a small proof-of-concept prototype to validate the system control. In addition, the team has made significant progress in designing the full-scale SST module and has identified a vendor for the DC/DC stage that will make up the DC node for the system. The team has made significant progress in developing the DC solid-state breaker and has completed a number of system-level protection coordination studies, which will drive the design of the DC distribution system. Finally, the team has selected the deployment site for the system and is making progress on completing the detailed engineering drawings for the system site.</p>	<p>University (NCSU)</p>	<p>Charging Enabling Technologies</p>	<p>Charging System with Solid-State DC Protection</p>
<p><u>The EPRI led project team initiated development and validation of a system of PEV XFC equipment with a direct connection to the medium-voltage utility grid with a novel, modular, and interoperable approach.</u> The objective of the project is to develop and demonstrate medium voltage SiC-based AC-DC conversion equipment and the DC-to-DC head unit for use in XFC equipment capable of simultaneously charging multiple light duty PEVs at rates of <math>\geq 350</math> kW and a combined power level of <math>\geq 1</math> MW while minimizing the impact on the grid and operational costs.</p>	<p>Electric Power Research Institute (EPRI), Eaton Corporation., NREL, Tritium, ANL</p>	<p>Industry Awards – Fast Charging Enabling Technologies</p>	<p>Direct Current Conversion Equipment Connected to the Medium-Voltage Grid for XFC Utilizing a Modular and Interoperable Architecture</p>
<p><u>Argonne collaborated with the European Union’s JRC to uncover ‘childhood diseases’ in new XFC technology</u> and inform the manufacturers accordingly. The project addressed identification and resolution of issues associated with a 200 kW XFC system. had a few technical issues early on, but when these issues were addressed by the manufacturer it was found to communicate according to the standards using an industry-standard interoperability test tool. The results showed the EVSE to be backward compatible with EVs below 50 kW charge levels. The DC communication analysis showed consistent messaging and timing. The results imply that integration of higher power charging stations in communication networks via OCPP should be accomplished with no more effort than lower power EVSE that communicate using OCPP.</p>	<p>ANL</p>	<p>Fast Charging Enabling Technologies</p>	<p>Fast Charging: Interoperability and Integration Technologies</p>
<p><u>INL developed XFC Technology Requirements:</u> This project completed important preliminary research that is necessary for understanding the impact of fast charging on grid stability and identifying and mitigating cybersecurity vulnerabilities. A transient characteristic of a prototype commercial 350KW XFC was discovered – namely ramp-down rate at the end of charge events – that has the potential to impact grid stability.</p>	<p>INL</p>	<p>Fast Charging Enabling Technologies</p>	<p>Fast Charging: Grid Impacts and Cyber Security</p>
<p><u>ORNL identified technology targets to achieve an economically feasible dynamic wireless EV charging system applicable to LD vehicles and primary roadways.</u> The performance targets are:                      1) Power transfer level for range extension: 150 kW – 235 kW                      2) Efficiency: 90 %</p>	<p>ORNL, INL, NREL</p>	<p>High Power Wireless Charging</p>	<p>High Power and Dynamic Wireless Charging for EVs</p>

Accomplishments	Organization	Focus Area	Project Title
<p>3) Surface power density (SPD): 400 kW/m<sup>2</sup>                      The project also analyzed                      a) Minimum roadway coverage solution for primary roadways for a LD vehicle,                      b) Current capabilities of SOA dynamic wireless systems,                      c) Performance of two candidate coil reference design as applied to 200KW systems, and                      d) Derived a control-to-coil-current transfer function for a DWPT controller.  <u>INL WPT EM-field Shaping and Shielding Solutions</u>                      Advanced magnetics 3-D finite element modeling tools were used to develop and analyze the EM field surrounding a 200-kW light-duty WPT system. The new EM-field shaping design uses innovated geometry of ferrite placement around the WPT to effectively shape the EM field therefore reducing the stray EM field surrounding the WPT system.</p>			
<p>The GMLC 1.4.2 Grid Services from Devices project has <u>completed the specification of the general battery-equivalent interface for eight device models</u> and is preparing to publish the models in the form of an open-source Python-based software library. The project is in the final stages of completing the grid services software that will be used for exercising the models and provide insights into devices' abilities to respond to a range of prototypical grid services. The project has analyzed how existing appliance standards test procedures could be leveraged to provide equipment parameters useful for characterizing how well devices can supply grid services, and has developed plans for testing example devices from three device classes—electric vehicles, commercial refrigeration, and water heaters—to validate their device models.</p>	<p>GMLC - PNNL, with ANL, INL, LBNL, LANL, NREL, ORNL, SNL</p>	<p>Grid Modernization</p>	<p>GMLC 1.4.2 – Definitions, Standards and Test Procedures for Grid Services from Devices</p>
<p><u>Developed Grid-XFC Requirements to promote a reliable and resilient electric grid:</u>                      NREL quantified the effects of uncontrolled charging to understand how increased PEV adoption may negatively impact the grid. Progress considered the limitations of the grid and the impacts of PEV adoption. After acquiring distribution feeder data, the hosting capacity analysis displayed the grid's ability to serve larger loads, such as xFC. This analysis leads into uncontrolled charging simulations in which high levels of PEV adoption begin to create voltage and line loading violations throughout the</p>	<p>NREL, INL, SNL</p>	<p>Fast Charging Enabling Technologies</p>	<p>Smart Electric Vehicle Charging for a Reliable and Resilient Grid (RECHARGE)</p>



Accomplishments	Organization	Focus Area	Project Title
<p>feeder. These challenges make the case for controlled charging as a way to mitigate these problems. INL quantified the effects of uncontrolled charging to understand how increased PEV adoption may negatively impact the grid, and to analyzed the effectiveness of multiple control strategies in mitigating negative grid impacts introduced by PEVs at scale. High-fidelity charging models were integrated into Caldera to supplement existing control strategies developed in past projects. INL began work to develop new PEV charging control strategies.</p>			
<p><b><u>NREL Developed MultiPort 1+MW Charging Requirements -:</u></b>                      The first year work of the project included -1) considered various use cases and travel patterns to develop / quantify expected vehicle loads at a multi-MW station, 2) analyzed and optimized charge port control and battery requirements in a multi-MW station, 3) developed a framework to analyze grid impacts of various multi-MW stations at the distribution level, 4) Analyzed and quantified connector and charging system electrical and thermal requirements.</p> <p><b><u>ANL Developed MultiPort 1+MW Charging Requirements:</u></b>                      The work-in-progress CharIN HPCCV coupler specification covers MD/HD electric truck charging connections, with similar remaining requirements gaps in communication reliability, safety interlocks, cooling, and cord handling including robotic insertion/removal processes. A draft MW+ multiport charging requirements document was compiled. A concise digest was created to highlight the state of readiness of stake holders to plan deployment of MW+ multiport EV charging systems, including gaps in standards or data.</p> <p><b><u>ORNL assessed candidate 1+MW charging architectures:</u></b>                      The three candidate architectures listed below were selected for in-depth study:                      1) DC Coupled architecture: components are interconnected through a common 2kV DC bus                      2) AC-Coupled architecture: components are interconnected through a common 480V, 60Hz AC bus                      3) Medium Voltage(MV) Architecture: connects directly to the medium voltage distribution grid using a cascaded H-Bridge (CHB) converter                      Each of these approaches were investigated from the grid conversion and impact as well as the interaction with DERs and EV load converters. The MV topology using the CHB converter was selected as the most suitable.</p>	<p>NREL, ANL, ORNL</p>	<p>Fast Charging Enabling Technologies</p>	<p>Development of a Multiport 1+Megawatt Charging System for Medium- and Heavy-Duty Electric Vehicles</p>
<p><b><u>Developed charging infrastructure cyber threat prioritization system:</u></b> Research efforts for this project were focused on trying to prevent high consequence manipulation and misuse of EV charging infrastructure. In order to effectively do so, researchers first conceptualized events that could be brought about by cyber manipulation to create a physically adverse effect on high-powered charging infrastructure, EVs, and/or the electric grid. Researchers then quantitatively scored the events using an impact severity scoring matrix and complexity multiplier. The high consequence events (HCEs) were scored and prioritized based upon this quantitative method. This prioritization ranking allows</p>	<p>INL</p>	<p>Cyber Security</p>	<p>Consequence-Driven Cybersecurity for High-Power Charging Infrastructure</p>

Accomplishments	Organization	Focus Area	Project Title
<p>researchers to focus their efforts on identifying and securing attack pathways enabling the most severe HCEs, then working to develop mitigation solutions to prevent and identify the cyber threats potentially leading to those HCEs.</p>			
<p><b><u>Began Developing EVSE Cyber Security Threat Models:</u></b>                      There is no comprehensive EVSE cybersecurity approach and limited best practices have been adopted by the EV/EVSE industry. For this reason, there is an incomplete industry understanding of the attack surface, interconnected assets, and unsecured interfaces. Thus, comprehensive cybersecurity recommendations founded on sound research are necessary to secure EV charging infrastructure. This project is providing the automotive industry with a strong technical basis for securing this infrastructure by developing threat models, prioritizing technology gaps, and developing effective countermeasures. Specifically, the team is creating a cybersecurity threat model and performing a technical risk assessment of EVSE assets, so that automotive, charging, and utility stakeholders can better protect customers, vehicles, and power systems in the face of new cyber threats.</p>	SNL, PNNL, ANL	Cyber Security	Securing Vehicle Charging Infrastructure
<p><b><u>ANL progressed incorporating EVs and EVSE with ‘smart’ communication capabilities</u></b> in the network at the Smart Energy Plaza; use cases have been demonstrated for controlled and emulated smart charging, EVs and EVSE have been acquired with high level language (i.e., smart capability and the common integration platform, CIP.io, has been enhanced to enable charge scheduling using ISO 15118. However the GMLC use cases that depend on smart charging have not been demonstrated on schedule due to delays in overcoming the proprietary interfaces of the EVSE, The beta version of the Diagnostic Electric Vehicle Adapter (DEVA) was demonstrated on schedule.</p>	ANL, INL	Fast Charging Enabling Technologies	Smart Vehicle-Grid Integration (Smart-VGI)
<p><b><u>LLNL progressed development of a decentralized, collaborative algorithm that will enable local groups of charging station controllers to coordinate the load reduction responses required by the centralized grid command center,</u></b> while meeting technological, policy, and contractual constraints imposed at the level of the smart charging stations and possibly at the level of the individual electric vehicles. The work developed charge management algorithms.</p>	LLNL	Grid and Infrastructure Grid Interoperability and Control	Scalable Electric Vehicle Smart Charging Using Collaborative Autonomy

# I Electric Drive Technologies Research

## I.1 Highly Integrated Power Module (ORNL)

### **Emre Gurpinar, Principal Investigator**

Oak Ridge National Laboratory  
1 Bethel Valley Road  
Oak Ridge, TN 37830  
E-mail: [gurpinare@ornl.gov](mailto:gurpinare@ornl.gov)

### **Susan Rogers, DOE Technology Development Manager**

U.S. Department of Energy  
E-mail: [Susan.Rogers@ee.doe.gov](mailto:Susan.Rogers@ee.doe.gov)

Start Date: October 1, 2018  
Project Funding: \$700,000

End Date: September 30, 2019  
DOE share: \$700,000

Non-DOE share: \$0

### **Project Introduction**

This project covers the design and development of next-generation wide-bandgap (WBG) power modules and associated components within the system. Various component challenges in the system that were addressed—such as substrates, interconnects, and gate driver circuitry to advance the power density—reduced the footprint of the system and increased the level of integration.

### **Objectives**

The overall objective of the project is to develop technologies for next-generation advanced integrated power electronic systems enabling high power density and reliability to achieve the Department of Energy (DOE) Electrification (ELT) 2025 technical targets: 100 kW/L, \$2.70/kW, and 300,000-mile lifetime. Under the overall objective, two main streamlines have been identified: (1) power module design and (2) gate driver and auxiliary components. Two evaluations were conducted under the power module design streamline: the feasibility of quilt packaging (QP) as an interconnect solution in power modules, and the thermal performance and design challenges of an insulated metal substrate (IMS) with a thermally annealed pyrolytic graphite (TPG) insert as a substrate solution. Under the gate driver and auxiliary components streamline, radio frequency (RF)-based solutions for ultra-compact isolated signal and power transfer were investigated.

### **Approach**

The main approach is to increase the power density and reliability of power electronics to meet DOE ELT 2025 targets (100 kW/L, \$2.70/kW, and 300,000-mile lifetime) by focusing on power electronic module and gate driver research.

Under the power module design streamline, investigations were conducted of substrates for power electronic modules that allowed increased power density and high reliability for WBG device-based power modules via better coefficient of thermal expansion (CTE) matching between WBG devices and power module materials, improved heat extraction, and enhanced thermal and power cycling capability. Furthermore, interconnects with high power density were evaluated and investigated for low profile, high-current density, and reliable chip-to-chip and chip-to-package interconnects for power modules and auxiliary circuits (e.g., gate drivers). These enabled reduced parasitic inductance in the system for optimum switching performance, reduced power module size, and enhanced reliability by moving to wire bondless solutions.

Under gate driver research for WBG devices, novel architectures for combined signal and power transfer were developed with advanced functionalities that enabled high power density via the minimization of auxiliary

components; integration of gate drive circuitry to WBG modules; and advanced gate drive functionality for improved electromagnetic interference, short circuit protection, and loss distribution.

## Results

### *IMS with TPG Insert*

The substrate design evaluated in this study was based on a half-bridge silicon carbide (SiC) metal-oxide semiconductor field-effect transistor (MOSFET) power module, in which three SiC MOSFET dies were paralleled per switch and placed on a substrate electrically isolated from the coolant. The electrical schematic of the half-bridge module is presented in Figure I.1.1. A Kelvin connection was used for the gate and source terminals of the SiC MOSFETs to optimize the switching performance independent of the load current. The SiC MOSFET dies used in this work were rated at 900 V, 30 m $\Omega$  (CPM3-0900-0030A) at room temperature and manufactured by CREE. Traditionally, such a design is realized on a direct bonded copper (DBC) substrate that provides electrical isolation by using an aluminum nitride (AlN) dielectric layer between two copper planes. The dies were soldered on different copper islands and then connected via bond wires to form the three terminal half-bridge structure.

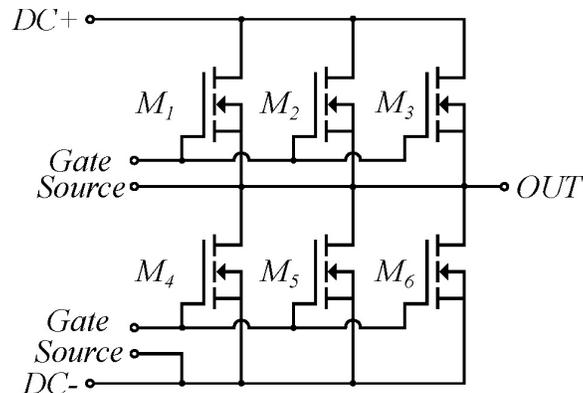


Figure I.1.1 Electrical layout of the half-bridge module.

In this work, an IMS was used to replace the DBC. The DBC was formed by a 640  $\mu\text{m}$  AlN ceramic insulator sandwiched with 300  $\mu\text{m}$  copper on both sides. The substrate provided flexibility to the designer in terms of the number of stacked layers and thickness of each layer to optimize thermal and electrical isolation performance. Therefore, the flexibility of the design was used to overcome some of the challenges of an IMS, such as the low thermal conductivity of the dielectric layer, as stated in Table I.1.1. The isometric view and cross section of the insulated metal structure, which was targeted to replace the DBC, are presented in Figure I.1.2 and Figure I.1.3, respectively. The SiC MOSFET dies were soldered on two electrical isolated copper cores, designed to spread heat laterally across the substrate to improve the transient thermal performance and steady state thermal resistance. These two copper cores were isolated from the bottom copper layer using an HT-07006 dielectric film, and from each other with a nonconductive epoxy-based filler. The copper core thickness was 1.6 mm, the dielectric film thickness was 152  $\mu\text{m}$ , and the bottom layer copper thickness was 70  $\mu\text{m}$ . The expanded view of the IMS is presented in Figure I.1.2, where the structure of each layer can be seen clearly. Once the copper core, dielectric layer 1, and bottom layer were bonded, additional layers could be added to the structure. In this case, dielectric layer 2 and the top layer were added to the design to accommodate isolated electrical terminals for the gate-source connections of the SiC MOSFETs and DC terminal for the half-bridge design. In the third design, the copper core in the traditional IMS was filled with thermally annealed pyrolytic graphite (TPG) to enhance the heat spreading and thermal conductivity.

**Table I.1.1 Standard Layer Thickness of Insulators and Fundamental Properties**

Material	Standard Thickness [μm]	Heat Transfer Coefficient [W/(cm <sup>2</sup> K)]	Breakdown Voltage [kV]
Al <sub>2</sub> O <sub>3</sub>	381	6.3	5.7
AlN	635	28.3	12.7
Si <sub>3</sub> N <sub>4</sub>	635	11	8.9
HT-07006	152	1.41	11

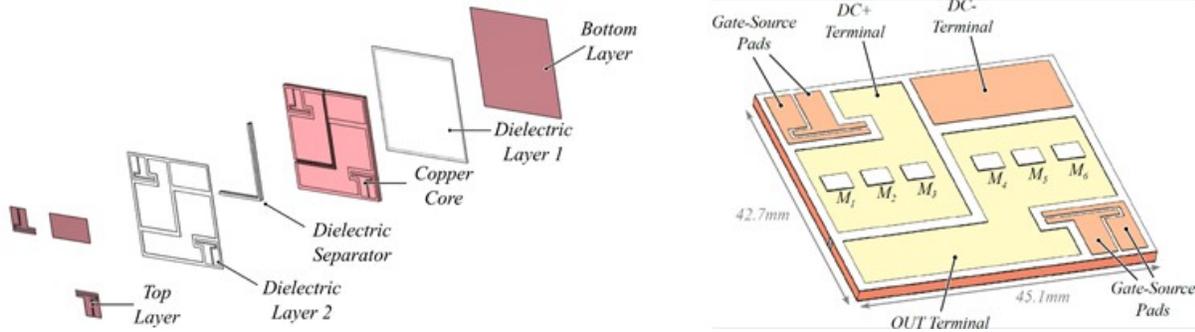


Figure I.1.2 Layer details and isometric view of IMS substrate.

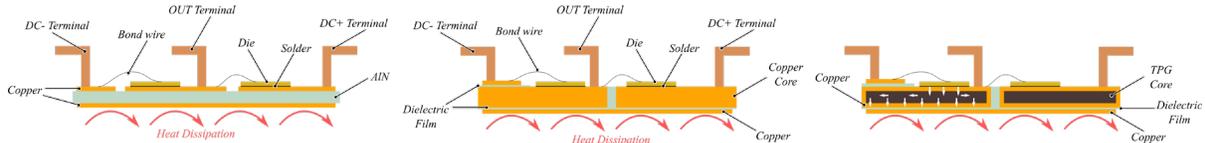


Figure I.1.3 Cross section of DBC (left), IMS (middle), and IMS with TPG (right).

The analysis of the substrates was conducted in the COMSOL Multiphysics finite element simulation tool and based on representative electrical and thermal operating conditions of a WBG power module. The base temperature of the substrates was set to 65°C, which is the typical coolant temperature in automotive systems. The heat transfer coefficient between the coolant and the base of the substrate was defined as 5000 W/m<sup>2</sup>K to represent the cooling performance of a typical liquid-cooled cold plate and the interface thermal resistance between the substrate and the cold plate. Each of the SiC MOSFET dies shown in Figure I.1.2 was considered as an individual heat source, with a 45 W constant heat source on the top surface of the die for steady-state thermal analysis. Once the system reached steady state, the heat sources were set to 0 W, and the cooling profile of the system was analyzed in a time-dependent simulation for transient thermal response analysis.

For the meshing of the substrates, a free triangular mesh was applied at the surface of the system with a 0.2 mm maximum feature size on the die surface and a 0.5 mm maximum feature size on the surface of the substrate. The surface mesh was then distributed to 5 layers in the die, 5 layers in the die attach, 20 layers in the copper core, 5 layers in the dielectric layer and 5 layers in the bottom layer to capture head spreading and temperature distribution across the substrate under test with high accuracy and resolution. Similar settings were applied to the DBC model for consistency.

The steady-state thermal analysis results for the DBC, IMS, and IMSwTPG are presented in Figure I.1.4 with surface temperature distribution for three different solutions under the same operating conditions. The DBC provided symmetrical temperature distribution among the top and bottom switches in the half-bridge with a 144°C maximum junction temperature on the surface of the die M<sub>2</sub>. Furthermore, the temperature distribution presented in Figure I.1.4 shows that the heat spread across the DBC was limited, resulting in hot spot areas around the heat sources. Such a temperature distribution across the DBC is one of the reasons that base plates are included in conventional power modules. As the DBC had limited heat spreading capability, the base plate provided a larger surface area for the heat transfer from the dies to the heat sink. On the other hand, for the IMS and IMSwTPG, the maximum junction temperature across the half-bridge module reached 152°C and 141.2°C on the surface of die M<sub>2</sub>. The surface temperature distribution for the IMS and IMSwTPG showed that there was an asymmetry in temperature distribution between the top and bottom switches in the half-bridge. Dies M<sub>4</sub>–M<sub>6</sub> had lower temperatures than dies M<sub>1</sub>–M<sub>3</sub> under same loading condition. This asymmetry can be explained by the design of the copper core in the insulated metal substrate. As shown in Figure I.1.2, the copper core was divided into two pieces and separated with a dielectric separator to provide isolated copper islands for the top and half switches in the half-bridge configuration. The thermal conductivity of the dielectric separator was less than 0.6 W/m·K; therefore, the separator also acted as a thermal insulator between two sections of the copper core. Furthermore, it can be seen from Figure I.1.2 that the right side of the copper core was slightly larger than the left side to accommodate the wire bonding of dies M<sub>1</sub>–M<sub>3</sub> and the output terminal of the half-bridge. The increase in the copper- or TPG-based core volume led to improved heat spreading for dies M<sub>4</sub>–M<sub>6</sub>, and the thermal separation with the dielectric separator limited the heat transfer between the isolated islands within the copper core.

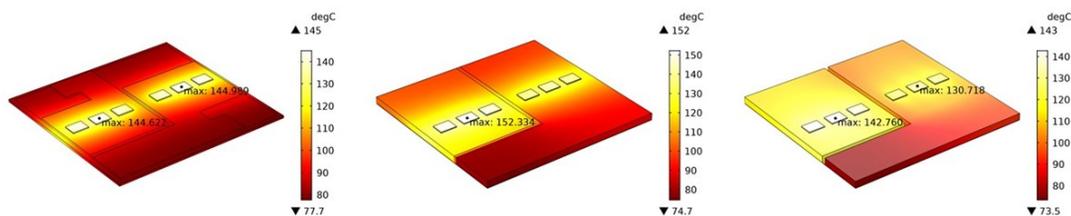


Figure I.1.4 Steady-state thermal performance of DBC (left), IMS (middle), and IMSwTPG (right).

The transient thermal impedance of each SiC MOSFET die on IMS and DBC substrates was obtained by recording the cooling performance of each die in a time-dependent simulation. The time-dependent simulation was run for 100 seconds (s), and the initial conditions for the transient analysis were defined as the results of the presented steady state analysis. As the junction temperature of each die was recorded, the base temperature was fixed at 65°C and the initial heat loss across each die was fixed to 45 W; the transient thermal impedance could be calculated at every time step. The transient thermal impedance values of six dies placed on DBC, IMS and IMSwTPG substrates are presented in Figure I.1.5. The thermal impedance curves presented in Figure I.1.5 show that the symmetrical thermal performance presented in Figure I.1.5 was achieved by the well-matched steady state thermal impedance for individual dies on the DBC. The steady state thermal impedance difference among the six dies was less than 0.1°K/W. On the other side, the transient thermal impedance for the dies on the IMS and IMSwTPG showed the impact of asymmetrical copper and the TPG-based core design discussed previously. Although the thermal impedance difference between the parallel dies could be considered negligible, there was approximately 0.2°K/W between the parallel die groups. Finally, the transient thermal impedance between 10 ms and 1 s was significantly improved with IMS and IMSwTPG compared with the DBC-based solution. The results showed that if the copper core area was sufficiently large, then the steady state thermal impedance of a SiC MOSFET die on an AlN-based DBC could be matched by that of an IMS or IMSwTPG solution with improved transient thermal impedance below 1 s. The improved transient thermal impedance performance led to a reduction in junction temperature operation under high-torque, low-speed operating conditions, which had a positive impact on power cycling and therefore the reliability of the power module structure.

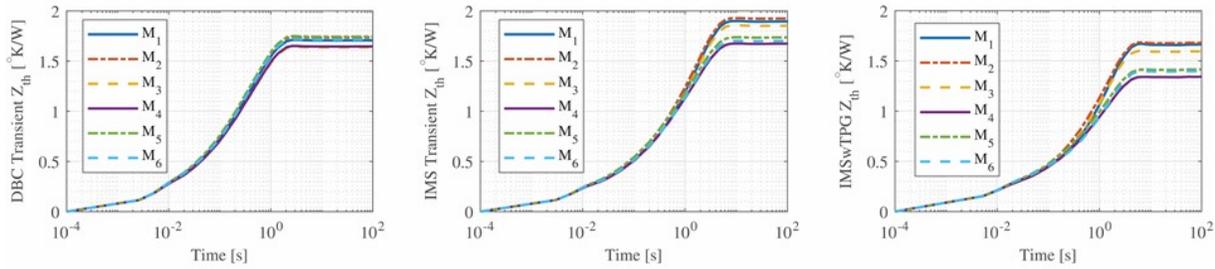


Figure I.1.5 Transient thermal impedance of SiC MOSFET dies placed on DBC (left), IMS (middle), and IMSwTPG (right)

For the experimental characterization of the substrates, a thermal evaluation board was developed to accommodate the gate driver circuitry, high-voltage/current DC input, and infrared (IR) thermal imaging area. The developed board is presented in Figure I.1.6. Each substrate with completed die, wire bond, and interconnect assembly, as shown in Figure I.1.6, was painted with flat black spray paint for maximum emissivity and minimum reflection.

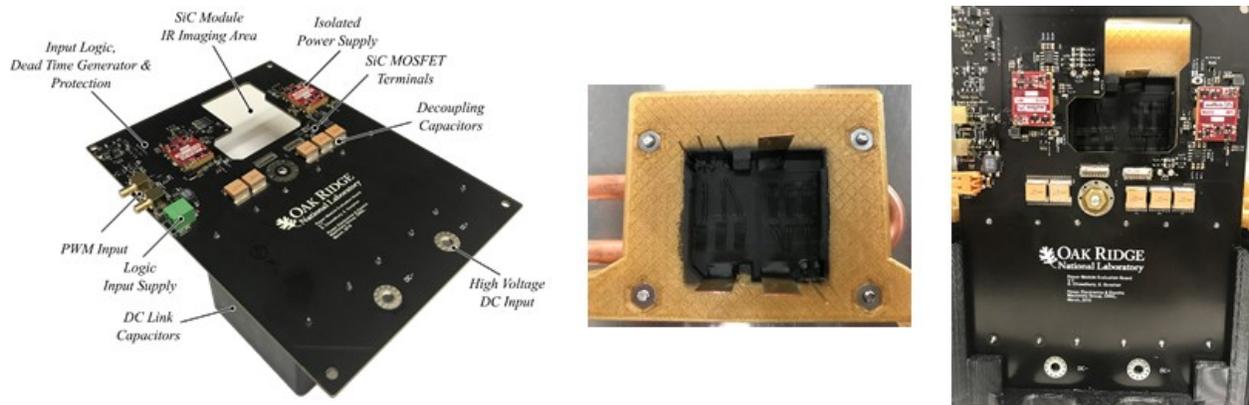


Figure I.1.6 Thermal evaluation board (left); assembled substrate with cold plate, interconnects, and SiC MOSFETs (middle); setup for thermal characterization of DBC, IMS and IMSwTPG under different load and temperature conditions (right).

The thermal imaging results for the IMS and IMSwTPG substrates, at 250 W total power loss across six SiC MOSFETs and 65°C coolant temperature, are presented in Figure I.1.7. The die temperature distribution shows that the TPG embedded core in the IMS provided improved thermal resistance and reduced junction temperature, as predicted by finite element analysis.

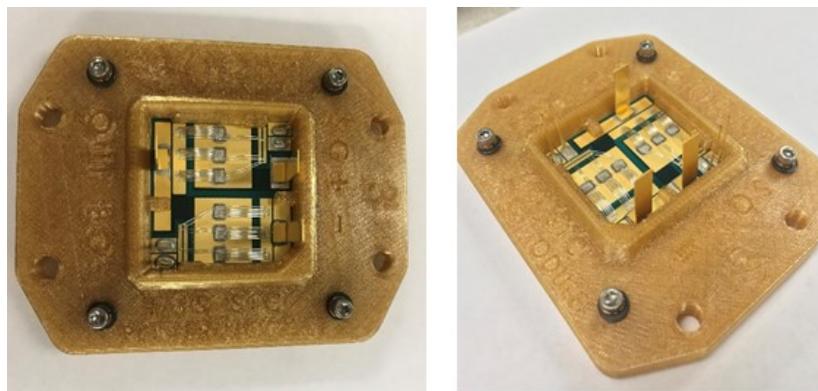


Figure I.1.7 Thermal imaging results of IMS (left) and IMSwTPG (right) at 250 W total power loss and 65°C coolant temperature.

The IMS-based half-bridge power module was encapsulated and packaged for electrical characterization. The image of the prototype is presented in Figure I.1.8.

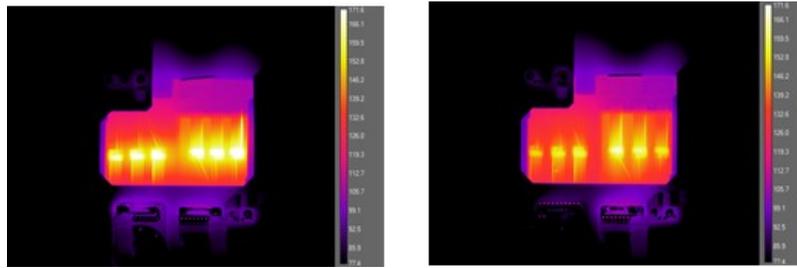


Figure I.1.8 IMS-based half-bridge power module.

### Quilt Interconnects

QP is a chip-to-chip interconnect technology that incorporates conductive metal “nodules” on the sides of chips. These nodules are typically copper, and the width can vary from 5 to 500  $\mu\text{m}$ , the thickness can be between 20 and 50  $\mu\text{m}$ , and a 10  $\mu\text{m}$  nodule pitch is possible with the standard manufacturing process. Typical examples of QP in low-power, low-voltage chip-to-chip and board-to-board interconnect solutions are presented in Figure I.1.9, [1].

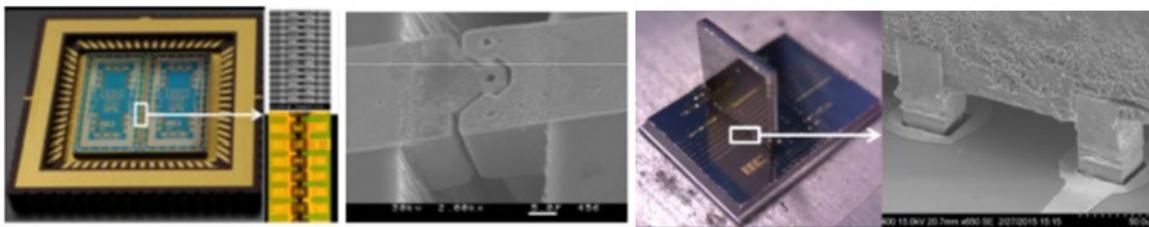


Figure I.1.9 Chip-to-chip and board-to-board interconnect examples with quilt packaging.

Under this task, a silicon-based test sample for quilt interconnect evaluation was designed to evaluate the electrical, thermal, and mechanical performance of different nodule designs under different operating conditions. The test sample design for interconnect evaluation is presented in Figure I.1.10. Two silicon chips with quilt nodules on the device edges were designed to be mounted on an insulated substrate (DBC in this scenario) with Al wire bonds for connecting the samples to test equipment. Such a design provides a flexible platform for evaluation of the nodules for electrical performance and thermo-mechanical reliability.

On four sides of the chip, four different nodule widths (100, 300, 500, and 700  $\mu\text{m}$ ), two different nodule spacings (100 and 250  $\mu\text{m}$ ), two different nodule length (30 and 70  $\mu\text{m}$ ), and two different nodule geometries (rectangular and triangular) were implemented in various samples. Some of the quilted samples are presented in Figure I.1.11.

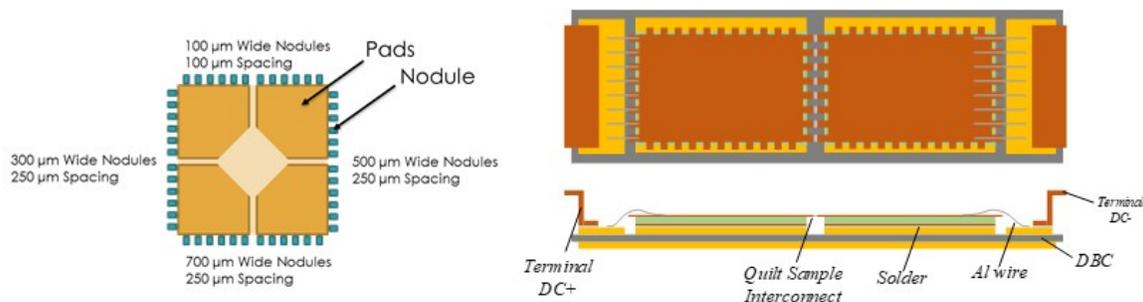


Figure I.1.10 Test sample design for interconnect evaluation.



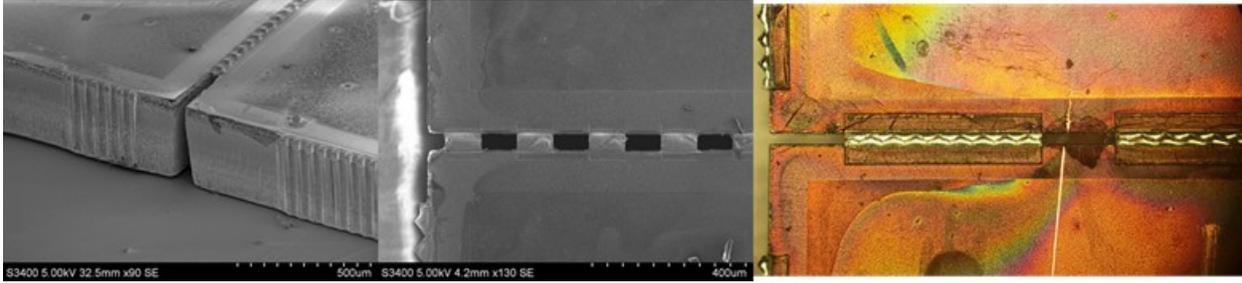


Figure I.1.11 Fabricated silicon samples with quilt nodules.

## Conclusions

This report introduces new substrate, integration, and interconnect technologies for next-generation advanced integrated power electronic systems enabling high power density and reliability to achieve DOE ELT 2025 technical targets (100 kW/L, \$2.7/kW, and 300,000-mile lifetime).

Conventional AlN-based DBC was compared with copper core-based and TPG core-based IMSs in steady-state and transient thermal analysis. It was shown that an IMSwTPG can provide a lower junction temperature under transient and steady-state operating conditions for SiC MOSFET switches compared with IMS- and DBC-based solutions. A thermal characterization setup was built for evaluation of different substrates under various power loss and cooling temperature conditions. It was shown that the IMSwTPG provided reduced junction temperatures for SiC MOSFETs at rated power loss and coolant temperatures. Furthermore, the IMS-based half-bridge power module was constructed with full encapsulation and housing for evaluation of the system under traction drive operating profile.

A quilt interconnect-based test sample, which can accommodate different nodule size and geometries, was designed to evaluate the electrical, thermal, and mechanical performance of quilt nodules under different operating conditions. The test sample with various design options was manufactured and quilted successfully. Experimental evaluation of these substrates will be conducted for electrical and thermal performance and mechanical reliability assessment.

## Key Publications

1. E. Gurpinar and B. Ozpineci, “Design, Analysis and Comparison of Insulated Metal Substrates for High Power Wide-Bandgap Power Modules,” *2019 International Technical Conference and Exhibition on Packaging and Integration of Electronic and Photonic Microsystems*, ASME2019 InterPack, 2019.
2. Wei Fan, G. Wexler, E. Gurpinar, and B. Ozpineci, “Improving Heat Conduction of Insulated Metal Substrate with Thermal Pyrolytic Graphite Core for SiC Power Module Packaging,” *International Conference on Silicon Carbide and Related Materials 2019*, Kyoto, Japan, 2019
3. E. Gurpinar, S. Chowdhury, “Integrated Power Module,” Invention Disclosure 81915581, 13 Aug 2019.

## References

1. Indiana IC, <https://www.indianaic.com/>.

## Acknowledgements

The author wishes to thank the project team members: Randy Wiles and Jon Wilkins for mechanical design support, Starra Gribble for thermal camera setup and imaging, Shajjad Chowdhury and Larry Seiber for printed circuit board design and assembly. The author wishes to thank Wei Fan from Momentive for the TPG samples, Garry Wrexler for IMS manufacturing, Jason Kulick and Jackson Lu from Indiana IC, and Doug DeVoto from National Renewable Energy Laboratory for QP support.

## I.2 High-Voltage, High-Power Density Traction Drive Inverter (ORNL)

### Gui-Jia Su, Principal Investigator

Oak Ridge National Laboratory  
1 Bethel Valley Road  
Oak Ridge, TN 37830  
E-mail: [sugj@ornl.gov](mailto:sugj@ornl.gov)

### Susan Rogers, DOE Technology Development Manager

U.S. Department of Energy  
E-mail: [Susan.Rogers@ee.doe.gov](mailto:Susan.Rogers@ee.doe.gov)

Start Date: October 1, 2018  
Project Funding: \$300,000

End Date: September 30, 2019  
DOE share: \$300,000

Non-DOE share: \$0

### Project Introduction

One of the barriers to meeting the DOE ELT 2025 power electronics targets for power density, 100kW/L and cost, \$2.7/kW is the dc bus capacitor in the inverter. The dc bus capacitor is an indispensable component for maintaining a stable dc bus voltage and smooth battery current for the voltage source inverters (VSI) in electric vehicles (EVs) traction drive systems. The widely used three-phase VSI switches the battery dc voltage according to a chosen pulse width modulation (PWM) scheme to produce a desired set of three-phase ac voltages to regulate the motor current and control the motor torque. In doing the switching operations, the inverter generates large ripple components with root-mean-square (rms) values over 60 % of the motor currents in the dc link current, thus necessitating the use of the dc bus filter capacitor to absorb the ripple currents and suppress voltage transients, which, if not sufficiently constrained, are detrimental to the battery life and reliability of the semiconductor switches in the inverter. Concerns about the reliability of electrolytic capacitors have forced EV makers to use self-healing film capacitors, and currently available film capacitors that can meet the demanding requirements are costly and bulky, making up one-fifth of the volume and cost. The dc bus capacitor, therefore, presents a significant barrier to meeting the requirements of the electrification program goals for inverter volume, lifetime, and cost established by DOE and its industrial partners [1]. There is thus an urgent need to minimize this bulky component by significantly reducing the inverter ripple current. A much smaller dc bus capacitor would also enable inverters to operate at higher temperatures. Unlike in dc-dc converter applications, increasing the switching frequency with wide-bandgap (WBG)-based switches has little impact on the rms value of the bus capacitor ripple currents, although increasing switching frequency does reduce the dc bus voltage and motor current ripples.

The goal for this project is to increase traction drive power electronics system power density to meet DOE ELT 2025 targets (100kW/L) by focusing on power inverter architecture research and busbar designs for reducing the requirements for passive components.

### Objectives

The overall objective of this project is to develop technologies for next generation traction drive power electronic systems with 8x increase in power density to achieve DOE ELT 2025 target of 100 kW/L through novel traction drive inverter architecture, optimization of busbar design, and minimization of passive components.

The two objectives for FY 2019 are: (1) evaluate and select traction drive inverter architecture and (2) produce a design for 100kW inverter using the selected inverter topology and commercially available components and access via simulation the gaps for meeting the power density target.

**Approach**

The following technical approaches are considered in this project. The first is selecting inverter architectures that can reduce the dc bus capacitor requirements. Multiphase inverters and segmented inverter arrangement are evaluated [2]. The second is increasing the inverter dc bus voltage to 800V or higher. This will better utilize Silicon Carbide (SiC) switching devices' inherently higher voltage ratings, reduce the size of SiC dies (and thus lowering the cost), and reduce phase and dc bus currents. The last one is optimizing designs for the inverter dc busbars (to be carried out in FY2020) by employing embedded and distributed capacitors and direct cooling of dc busbars.

**Results**

Figure I.2.1 shows a standard three-phase inverter-based drive, in which the switches are typically comprised of multiple switch and diode dies connected in parallel. The segmented inverter (shown in Figure I.2.2) is formed by separating the inverter switch and diode dies and motor stator windings into two sets of drive unit. Further interleaving the switching timings between the drive units through modifying the PWM scheme is introduced to reduce the dc bus ripple current. There are no changes in the motor control algorithms.

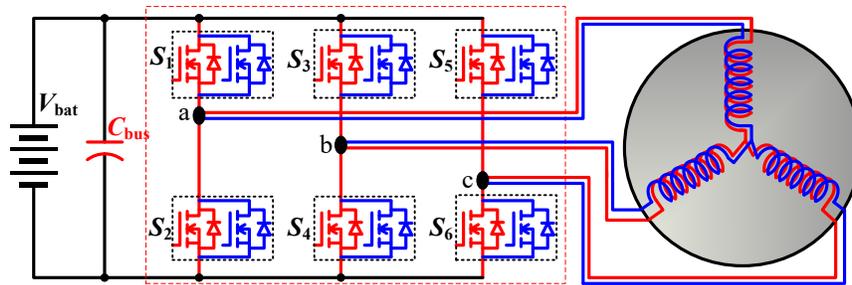


Figure I.2.1 A standard 3-phase inverter-based drive.

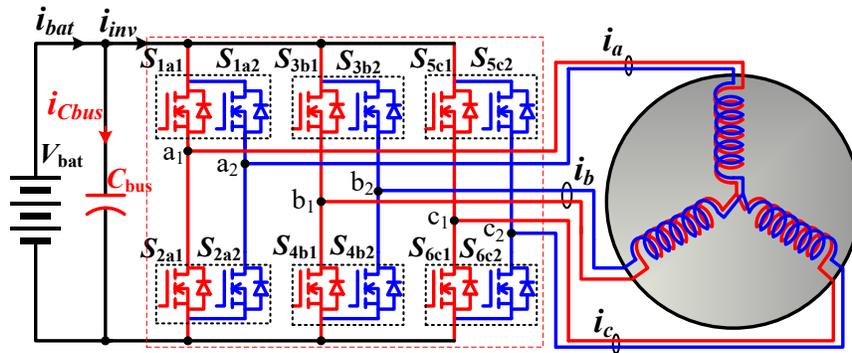


Figure I.2.2 Segmented inverter-based drive.

Figure I.2.3 shows a rearrangement of the segmented inverter depicting the two 3-phase inverter units, Inv1 and Inv2. The DC bus currents for the two inverters,  $i_{inv1}$  and  $i_{inv2}$ , and the combined inverter current  $i_{inv}$  at switching frequency  $f_{sw}$  and fundamental frequency  $f_m$  consist of a DC component  $I_{dc}$  and many harmonic components. It can be expressed by

$$\begin{cases} i_{inv1} = 0.5 \left( I_{dc} + \sum_{k=0}^{\infty} \sum_{n=1}^{\infty} I_{n,k} \sin[2\pi(nf_{sw} \pm kf_m)t + \alpha_{n,k}] \right) \\ i_{inv2} = 0.5 \left( I_{dc} + \sum_{k=0}^{\infty} \sum_{n=1}^{\infty} I_{n,k} \sin[2\pi(nf_{sw} \pm kf_m)t + \beta_{n,k}] \right) \\ i_{inv} = I_{dc} + \sum_{k=0}^{\infty} \sum_{n=1}^{\infty} \sqrt{\frac{1 + \cos(\beta_{n,k} - \alpha_{n,k})}{2}} I_{n,k} \sin\left(2\pi(nf_{sw} \pm kf_m)t + \frac{\alpha_{n,k} + \beta_{n,k}}{2}\right) \end{cases}$$

where  $I_{n,k}$  represents the amplitude, and  $\alpha_{n,k}$  and  $\beta_{n,k}$  the phase angles of the harmonic components of the two inverters identified by the integers  $n$  and  $k$ . As shown in the equations, the amplitude of each combined ripple component can be reduced by introducing a phase shift into the corresponding ripple components of the two drive units to make  $\alpha_{n,k} \neq \beta_{n,k}$ . In particular, the combined ripple current components can be reduced to zero by introducing a 180 electrical degree phase shift into the corresponding ripple components of the two drive units. Shifting the relative phase angle of the carrier signals as shown in Figure I.2.4(a) can introduce phase shifts in the harmonic components and thus lead to canceling some of the ripple current components while reducing others. The net effect is a significantly reduced DC bus ripple current to be filtered out by the DC bus capacitor. The optimal phase-shift angle is 90° for triangle carriers and 180° for sawtooth carriers.

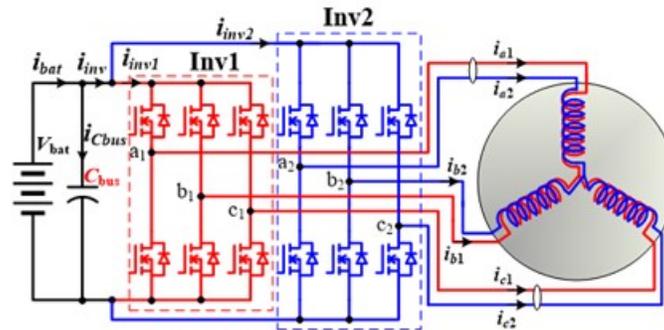


Figure I.2.3 Rearrangement of the segmented inverter-based drive.

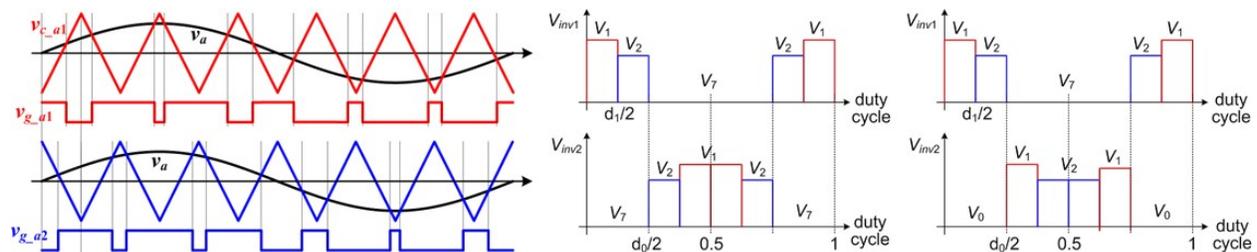


Figure I.2.4 PWM schemes for the segmented inverter-based drive to reduce the DC bus ripple current: (a) phase-shifted carrier-based schemes, (b) space vector modulation with optimal placement of zero vectors for sector 1, (c) alternate space vector modulation.

Figure I.2.5a and Figure I.2.5b show space vector modulations in sector 1 for the segmented inverter, which use optimal placement of the zero voltage vectors to reduce the inverter DC ripple current, where  $V_1$ – $V_6$  are the six active voltage vectors,  $V_0$  and  $V_7$  are the two zero vectors,  $d_0$  and  $d_1$  are the duty ratios for  $V_0/V_7$  and  $V_1$ , and  $V_{inv1}$  and  $V_{inv2}$  are the output voltage vectors for Inv1 and Inv2, respectively.

Figure I.2.5 shows a comparison of simulated operating waveforms for the segmented inverter with a capacitor ripple current of 17.5 Arms (a) and a standard inverter with a capacitor ripple current of 62.1 Arms (b) at modulation index  $M=0.6$ , power factor  $pf=0.9$ , and phase current  $I_{ph}=100$  Arms. The results show a significant reduction (71.8%) in DC bus ripple current with the space-vector PWM schemes for the segmented inverter.

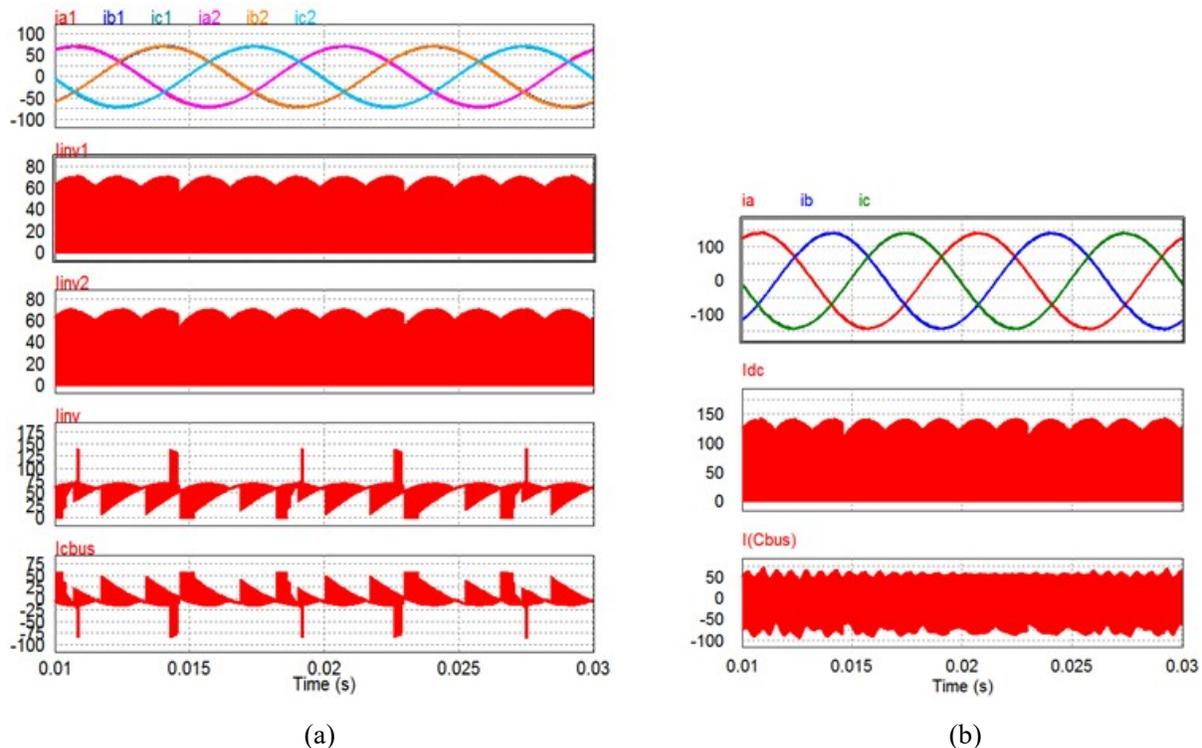


Figure I.2.5 Simulated operating waveforms for the segmented inverter with a capacitor ripple current of 17.5 Arms (a) and standard inverter with a capacitor ripple current of 62.1 Arms (b) at  $M=0.6$ ,  $pf=0.9$ ,  $I_{ph}=100$  Arms.

A switching timing-based tool for computing the DC bus currents was developed and implemented in Matlab. The advantages of the method were that it (1) was faster than circuit simulation, (2) implemented various PWMs more accurately and more easily than analytical formulae, and (3) was easier to use in optimizing inverter designs. Figure I.2.6 plots a comparison of normalized capacitor ripple current (a) and busbar current (b) vs. modulation index for 3-phase and segmented inverters at various power factors. More than 50% reductions in the maximum ripple currents were possible with the segmented inverter. A maximum reduction of over 25% was also possible in the DC bus current. These reductions in currents translated to a smaller DC bus capacitor and busbars. Further, the DC link currents were inversely proportional to the DC bus voltage. For example, when the bus voltage was increased from 400 V to 800 V, the DC bus ripple currents were reduced by a factor of 2.

A feasibility study was conducted of multi-phase inverter and motor systems for traction drive applications. In general, for a given power level, more phases result in lower phase current, which, however, leads to only moderate reductions in the DC bus ripple current. Multi-phase drive systems may also increase fault tolerance.

A 5-phase system demands complex control methods; whereas a 6-phase system can operate as a dual 3-phase system, so the same simpler control method used for a 3-phase drive can be used. Moreover, segmented PWMs can be used in 6-phase systems to reduce the DC bus ripple current.

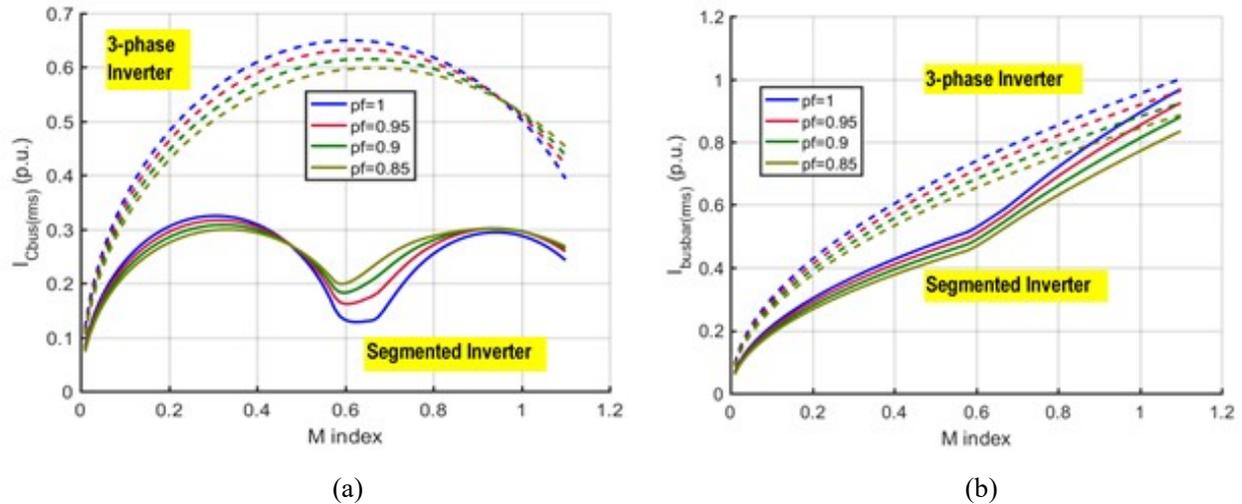


Figure I.2.6 Comparison of normalized capacitor ripple current (a) and busbar current (b) vs. modulation index for 3-phase and segmented inverters at various power factors.

Simulation results for a 5-phase drive, a symmetrical 6-phase inverter, and an asymmetrical 6-phase drive with a phase shift of  $30^\circ$  in the stator windings are shown in Figure I.2.7, Figure I.2.8, and Figure I.2.9, respectively. The DC bus ripple currents are 40.4 Arms for the 5-phase inverter, 38.3 Arms for the symmetrical 6-phase inverter, and 43.9 Arms for the asymmetrical 6-phase inverter. Compared with 53.8 Arms for a 3-phase inverter, moderate reductions in the DC bus ripple currents were achieved with the multi-phase inverters.

Segmented PWM techniques were used in the asymmetrical 6-phase drive system to reduce the DC bus ripple current. Simulation results gave a DC bus ripple current of 24.5 Arms, a reduction of 44% compared with using non-segmented PWM and a reduction of 54% compared with using the 3-phase inverter.

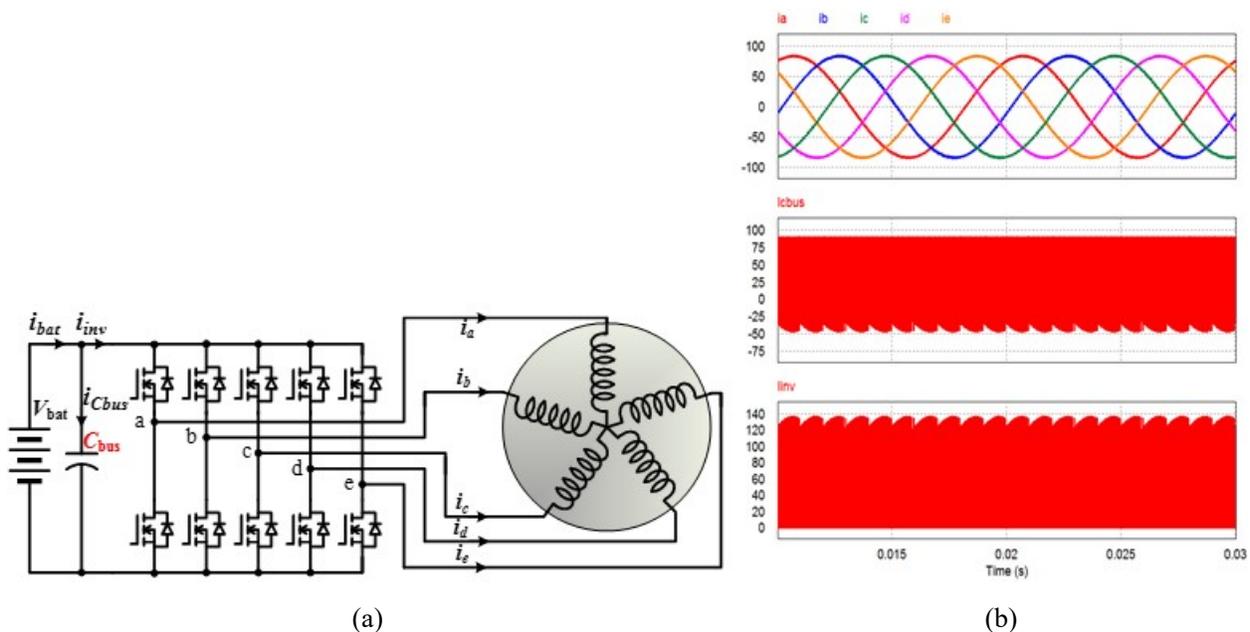
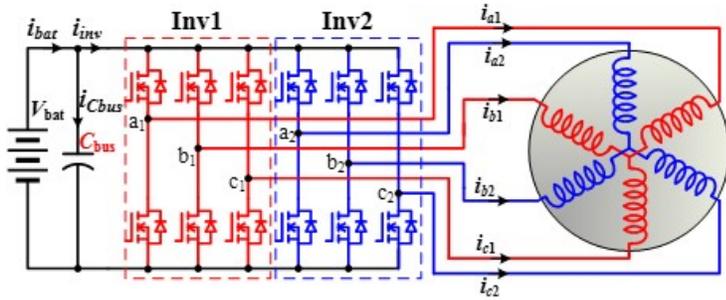
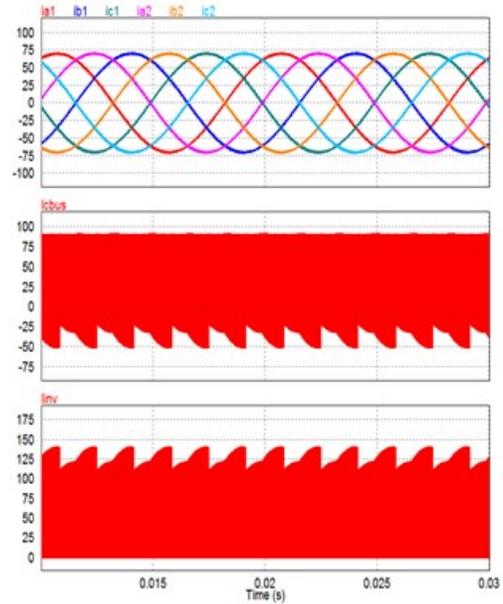


Figure I.2.7 Block diagram for a 5-phase inverter (a) and simulation waveforms for switching at  $m=0.65$  and  $pf=0.9$  (b).

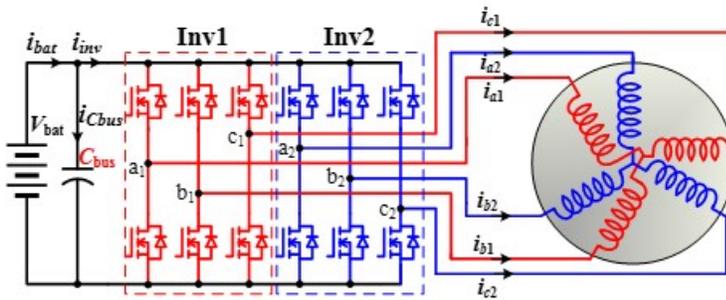


(a)

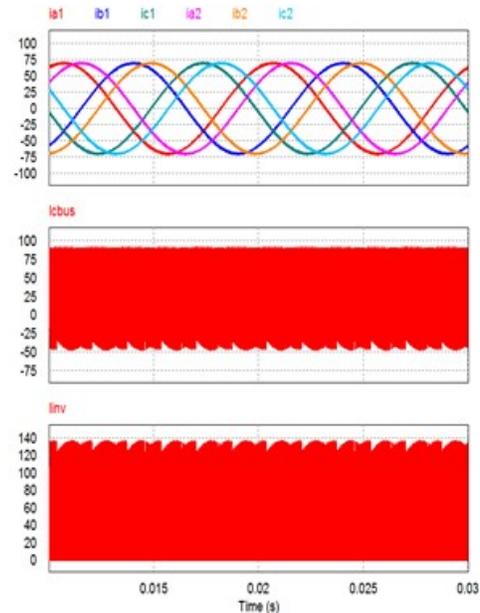


(b)

Figure I.2.8 Block diagram (a) and simulation waveforms for a symmetrical 6-phase inverter at  $m=0.65$  and  $pf=0.9$  (b).



(a)



(b)

Figure I.2.9 Block diagram (a) and simulation results for an asymmetrical 6-phase inverter at  $m=0.65$  and  $pf=0.9$  (b).

A DC bus capacitor life-expectancy prediction and sizing tool was also developed in Matlab based on driving cycle hot spot temperatures and voltage stress profile (instead of a single temperature and voltage stress point). Figure I.2.10 shows a block diagram for the prediction tool, which includes a vehicle model, permanent magnet (PM) motor with optimal current control block, inverter switching model, capacitor loss and thermal model, and capacitor reliability and sizing block. Figure I.2.11 shows modeling results for capacitor ripple current,  $I_{ripple}$ , temperature,  $T_h$ , and lifetime,  $L_t$ , for a film capacitor under the US06 driving cycle and the Federal Urban Dynamometer Driving Schedule (FUDDS). Under US06, the capacitor life expectancy is

L=50,235h for a conventional 3-phase inverter vs. L=67,164h for the segmented inverter. Under FUDDS, the numbers are L=101,668 h for a conventional 3-phase inverter vs. L=107,782 h for the segmented inverter.

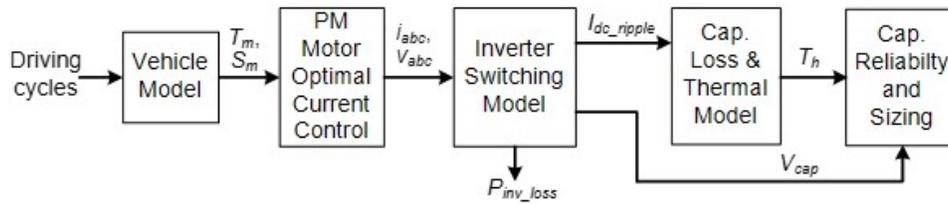


Figure I.2.10 Block diagram for driving cycle-based DC bus capacitor life-expectancy prediction and sizing tools.

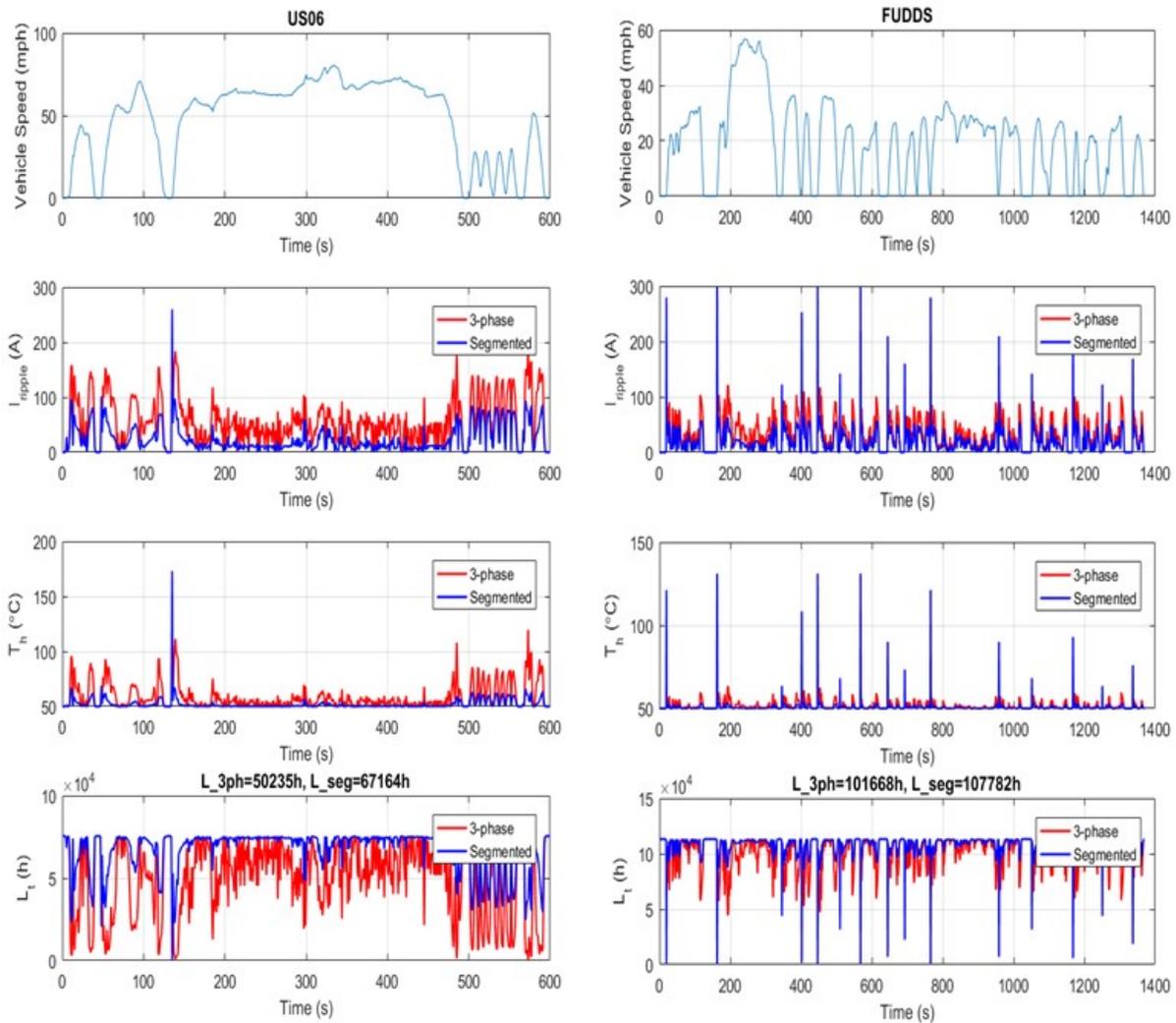


Figure I.2.11 Modeling results for a film capacitor under US06 driving cycle (left) and FUDDS (right).

A 100kW inverter power stage design was conducted using commercially available components: Cree SiC metal oxide semiconductor field effect transistor modules and gate drivers, TDK Ceralink capacitors, and a Microcool coldplate to access the gaps for meeting the DOE ELT 2025 target. Figure I.2.12 shows a 3-dimensional drawing for the inverter power stage design and power module baseplate temperature profile. The design has a power density of 66 kW/L with the following component volume distributions: coldplate 31%, gate drivers 14%, power modules 10%, DC bus capacitors 9% (with most of the remaining space unused).



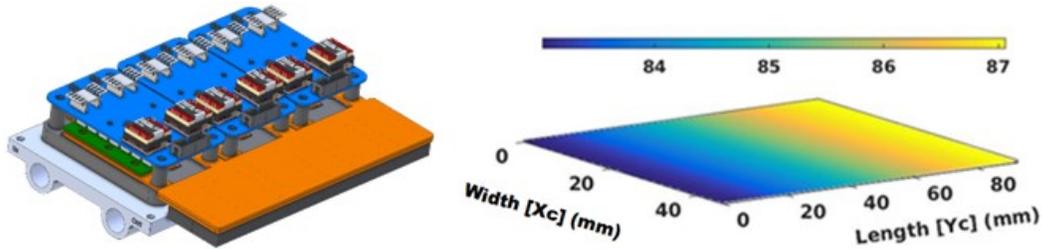


Figure I.2.12 Inverter power stage design (left) and power module baseplate temperature profile (right).

### Conclusions

To help achieve the ELT 2025 targets of 100 kW/L and 300,000 mile lifetime, this project aims to reduce the sizes of inverter DC bus components in inverter designs by developing novel inverter topologies, increasing the DC bus voltage, and investigating direct bus cooling to minimize the inverter DC busbar design.

Segmented 3-phase and asymmetrical 6-phase inverter systems were shown to significantly reduce the DC link ripple current and the DC link capacitor. Other major technical accomplishments included these: (1) developed a space vector-based segmented PWM switching schemes, (2) developed tools in Matlab to accurately and speedily compute inverter DC bus ripple current, (3) verified increasing the DC bus voltage and proportionally reducing the DC bus ripple current and busbar current, (4) developed bus capacitor life-expectancy prediction and sizing tool based on driving profiles, and (5) generated a gap analysis for inverter power stage designs using commercially available components.

### Key Publications

1. S. Chowdhury, E. Gurpinar, G.-J. Su, T. Raminosoa, T. Burrell, and B. Ozpineci, “Enabling Technologies for Compact Integrated Electric Drives for Automotive Traction Applications,” *2019 IEEE Transportation Electrification Conference and Expo*, June 19–21, 2019, Novi, Michigan.

### References

1. *Electrical and Electronics Technical Team Roadmap*, U.S. DRIVE, Department of Energy, October 2017.
2. G. J. Su and L. Tang, “A Segmented Traction Drive System with a Small dc Bus Capacitor,” *4th IEEE Energy Conversion Congress and Exposition (ECCE 2012)*, pp. 2847–2853, September 16–20, 2012, Raleigh, North Carolina.

### Acknowledgements

ORNL team members: Shajjad Chowdhury, Emre Gurpinar, and Randy Wiles

DOE Technology Manager: Susan Rogers

ORNL Program Manager: Burak Ozpineci

### I.3 High-Fidelity Multiphysics Material Models for Electric Motors (ORNL)

#### Jason Pries, Principal Investigator

Oak Ridge National Laboratory  
1 Bethel Valley Road  
Oak Ridge, TN 37830  
E-mail: [priesjl@ornl.gov](mailto:priesjl@ornl.gov)

#### Susan Rogers, DOE Technology Development Manager

U.S. Department of Energy  
E-mail: [Susan.Rogers@ee.doe.gov](mailto:Susan.Rogers@ee.doe.gov)

Start Date: October 1, 2018

End Date: September 30, 2019

Project Funding: \$400,000

DOE share: \$400,000

Non-DOE share: \$0

#### Project Introduction

Permanent magnets with heavy-rare-earth (HRE) materials offer superior magnetic properties in terms of remanence, coercivity, and energy product compared with non-rare earth alternatives. The superior magnetic properties of these materials yield electric traction motors with unmatched power density and torque density. Additionally, the inclusion of HRE elements into permanent magnet chemistries provide greatly improved stability at elevated temperatures. The improved high-temperature properties yield highly reliable motors.

For these reasons, HRE permanent magnets are the standard material choice for automotive traction motors in hybrid and electric vehicles. Most traction motors on the road today are of the internal permanent magnet (IPM) type since IPM motors achieve the best performance per dollar over several metrics, including mass, volume, reliability, efficiency, and noise. Several suppliers have developed surface permanent magnet (SPM) designs, which have seen limited application in higher-power application (e.g., buses); but these have not made their way into the light-duty passenger vehicle space because of the cost associated with the increased permanent magnet usage.

HRE permanent magnets, however, are not without their drawbacks. HREs are expensive materials; the refinement process is lengthy and costly. Furthermore, supply chain issues with respect to the sourcing and refinement of HREs have caused significant price volatility. This uncertainty has piqued interest in developing competitive HRE-free traction motor alternatives to secure the US automotive industry against the uncertainties related to HREs.

HRE-free traction motor designs come in several flavors. Competitive permanent magnet-free designs include induction, wound field, switched reluctance, and synchronous reluctance motors. However, all these motors have their drawbacks. Motors with rotor excitation (induction, wound field) are limited by lower efficiency due to conduction losses in the rotor coils/bars. Switched reluctance motors have high noise and vibration levels and thus are not favored for automotive applications. Synchronous reluctance motors can achieve noise and vibration characteristics as good as those of permanent magnet machines but a theoretical limit on their power factor requires them to use additional electronics to meet both low-speed torque and high-speed power design specifications [1].

Because of the drawbacks of the alternatives, there is still broad interest in developing HRE-free permanent magnet motors. However, because of the limited performance of HRE-free permanent magnets, motors designed using these materials are more prone to reliability issues related to heating and demagnetization. Therefore, to design a reliable HRE-free permanent magnet motor, modeling of the demagnetization characteristics is of utmost importance. For standard permanent magnet materials using HREs, existing modeling tools work quite well. Unfortunately, this is not true for HRE-free permanent magnets.

The issue stems from a combination of (1) the complex demagnetization fields present in electric motors and (2) the nonlinear, anisotropic, and hysteretic nature of the magnetization/demagnetization process of permanent magnets. Permanent magnets have different characteristic directions. One, called the “hard” axis, is parallel to the designed magnetization direction; two “easy” axes are perpendicular to the hard axis. Typical manufacturer and simulation data sets consider only the nonlinear characteristics of the hard axis, while the easy axes are modeled as ideal linear soft magnetic materials. This approach works well when either (1) the magnet has a very large coercivity or (2) the demagnetizing field is parallel to the hard axis. When the HREs are removed from the permanent magnet material, assumption (1) is violated. In IPM traction motors, the magnets are placed at an angle with respect to the radial direction of the motor, meaning that any demagnetization field applied during field-weakening operation will not appear parallel to the hard axis. In SPM traction motors, the low coercivity of the permanent magnets requires that Halbach arrays be used to prevent demagnetization, requiring that certain magnet segments be magnetized circumferentially instead of radially. This leads to a similar problem as in IPMs. In any case, it can be almost guaranteed that in any competitive permanent magnet traction motor, assumption (2) will also be violated.

The issue with vector demagnetization (as opposed to uniaxial demagnetization) in electric motors has received little attention. The publications that have examined the problem have put estimates on the magnitude of the errors but have done little to improve modeling tools. One publication examining this issue found that when a field was applied at a  $52^\circ$  angle to the hard axis of the magnet, no demagnetization was predicted in simulations, but more than 20% demagnetization was measured [2]. The design margins required to develop a reliable motor in the face of this uncertainty mean that improved modeling could reduce electric motor costs by more than 10% through reduced permanent magnet consumption.

### Objectives

The objective of this project is to increase the accuracy of the material models used to design electric motors in order to improve the efficiency, reliability, and power density of HRE-free motors. The two key areas of investigation are (1) electrical steel core losses and (2) HRE-free permanent magnet modeling. Electrical steel core losses include hysteresis losses and eddy current losses, which may be caused by a combination of sinusoidal current waveforms, pulse width modulation (PWM) harmonics, and rotating field vector losses. Accurately modeling these losses is important for improving electric motor and system efficiency. HRE-free permanent magnet modeling focuses on vector demagnetization modeling for improved reliability.

This effort has focused on the design of test methodologies and modeling techniques for HRE-free permanent magnets. This path was chosen because, currently, it is impossible to accurately determine the feasibility and reliability of any HRE-free motor designed to meet DOE’s 2025 power density targets through simulation alone. Because of this, expensive prototypes must be built for validation. Even so, if a prototype fails, without proper modeling tools, it is difficult to understand why the prototype failed and what design parameters can be changed to make improvements.

### Approach

Gathering the data required to implement high-fidelity permanent magnet demagnetization models. There are two reasons a customized approach is necessary: (1) standard sample geometry is not conducive to measuring both hard- and easy-axis demagnetization characteristics on the same coupon, and (2) the accuracy of demagnetization methods is limited by sharp increases in differential permeability near the intrinsic coercivity of the material.

The standard sample geometry for testing permanent magnets is a small flat cylinder on which the hard axis runs parallel to the axis of the cylinder. Because of the curved geometry of the cylinder parallel to the easy axes, this geometry is unsuitable for testing those directions. Therefore, a cubic magnet shape is desirable for testing all three of the magnetization axes. However, the sharp edges of the cubic shape lead to undesirable boundary effects that cause severe measurement errors. Therefore, we have proposed a nine-magnet array configuration as depicted in Figure I.3.1. The magnets are separated by thin gaps to allow the insertion of 3-axis magnetic field sensors to measure the normal flux density and tangential field intensity. The well-known field continuity conditions of electromagnetics imply that moving similar materials adjacent to one another will reduce the variation of the materials in the gaps [3].

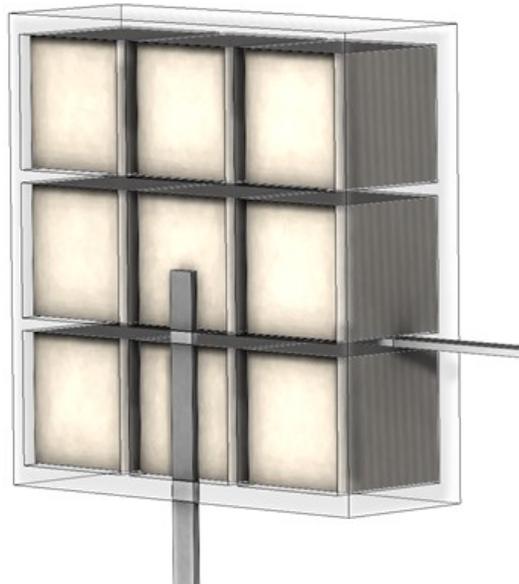


Figure I.3.1 Nine-magnet permanent magnet array for accurate 3-axis demagnetization testing of low-energy- product and HRE-free permanent magnets. Two 3-axis magnetic field sensors are used to measure the normal flux density and tangential field intensity of the central magnet. The orbiting magnets are used to provide field continuity, which minimizes the impact of edge effects on the measurements.

Figure I.3.2 shows simulation results for the measurements that would be expected from a single-magnet configuration versus a magnet array configuration. These are compared against the “intrinsic” magnet properties that serve as the ground truth. This simple example shows that measurement errors are reduced from over 50% in the single-magnet configuration to less than 10% in the magnet array configuration. These errors could be reduced even further using analytical correction terms for magnetic field distributions in thin airgaps.

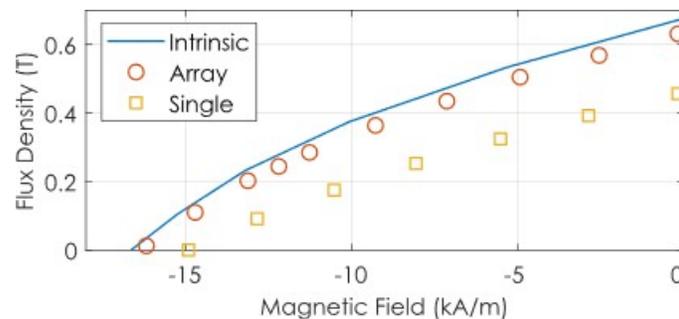


Figure I.3.2 Simulation comparison of single cubic magnet measurement versus nine-magnet array measurement. The intrinsic curve is the permanent magnet data input into the simulation. The “Single” and “Array” markers are the expected measurements in each of the configurations. The array configuration measurements more closely match the intrinsic characteristic.

Finally, the proposed approach has the advantage of correcting a certain measurement error that occurs in measuring low-coercivity magnets (regardless of sample geometry). A typical way of measuring the field applied to a permanent magnet test specimen is to characterize the yoke and coil system without any sample and then correlate the measured field to the current applied to the coil. The theory is that there is a one-to-one mapping between coil current and applied field, independent of the sample. This approach only works, however, if the sample has a relatively low permeability. When permanent magnets are demagnetized, they transition through a region of high differential permeability occurring around the coercivity. For permanent magnets containing HREs, this region is not particularly interesting since it typically occurs in the third quadrant and is bounded away from the maximum energy product location.

This is not the case for HRE- free permanent magnets. Typically, the maximum energy product location is close to the coercivity. Thus, the differential permeability increase impacts both estimation of the coercivity (which is critical in this case) and the maximum energy product measurement. By directly measuring the tangential field intensity using the magnet array technique, the demagnetizing field can be precisely known without any pre-calibration and despite any permeability variations.

Our approach requires the design and fabrication of a custom testing fixture suited to implementing the measurement technique. We wanted to apply a field of up to 1.8 T, which is the saturation flux density of standard silicon steel and about 50% higher than the peak flux density of the highest-remanence permanent magnets at 1.2 T. The core was to be made from M19 steel laminates to eliminate core eddy currents. Generally, a greater than 10:1 ratio of gap to permanent magnet material is desirable. The thinnest magnet field sensor available has a nominal dimension of 0.5 mm. Therefore, we chose a magnet sample geometry of 3/8 inch, giving a ratio of about 19:1. Combined magnetic and thermal optimization was performed to reach the target airgap flux density while limiting the winding losses to less than 1200 W, which is the maximum power typically available from a DC power supply and the typical cooling rate from a heat exchanger using standard single-phase outlets.

Figure I.3.3 shows simulation results for the final optimized structure. The core dimensions are 331 by 276 by 72 mm. The peak airgap flux density of 1.8 T was achieved with a better than 1% field variation over the body of the magnet under test. The peak winding temperature was 110°C in the extreme case of constant maximum current excitation. Because the fields are time-varying, the losses and temperature rise should be about half of the simulated values. Because of the relatively low winding temperature, it became possible to use a high-temperature thermoplastic (Ultem) to 3D print the winding housing with coolant inlet and outlet channels. The windings were constructed of 12 AWG square wire for maximum fill factor, with some space allowed for coolant flow.

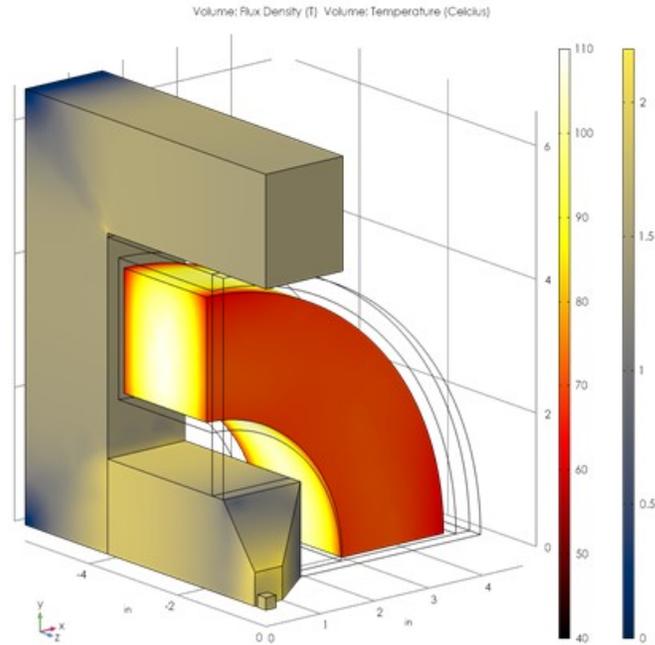


Figure I.3.3 One-eighth section cutaway simulation of the optimized permanent magnet testing fixture. The peak aperture airgap flux density is 1.8 T with uniformity of better than 1%. The peak winding temperature under constant 24 A excitation is less than 110°C when it is cooled by silicon oil at a flow rate of 10 L/min.

Based on the simulated design, all the key subsystems were fabricated and assembled. Figure I.3.4 shows the 3D printed magnet array holder. The tray containing magnets is disassembled from the body of the assembly. The groove for the normal flux density sensor can be seen in the body on the right. Figure I.3.5 shows a few different views of the various test fixture subsystems. The rightmost image is one of the two coils before being placed in its housing. The middle image shows the coils in their 3D printed Ultem housing installed on the ferromagnetic core. The leftmost image shows the permanent magnet subassembly installed on one-half of the core. Figure I.3.6 shows the entire system assembled with power supply, inverter, magnetic field sensors, current sensors, and oscilloscopes for real-time monitoring and data acquisition.



Figure I.3.4 Disassembled permanent magnet array assembly.

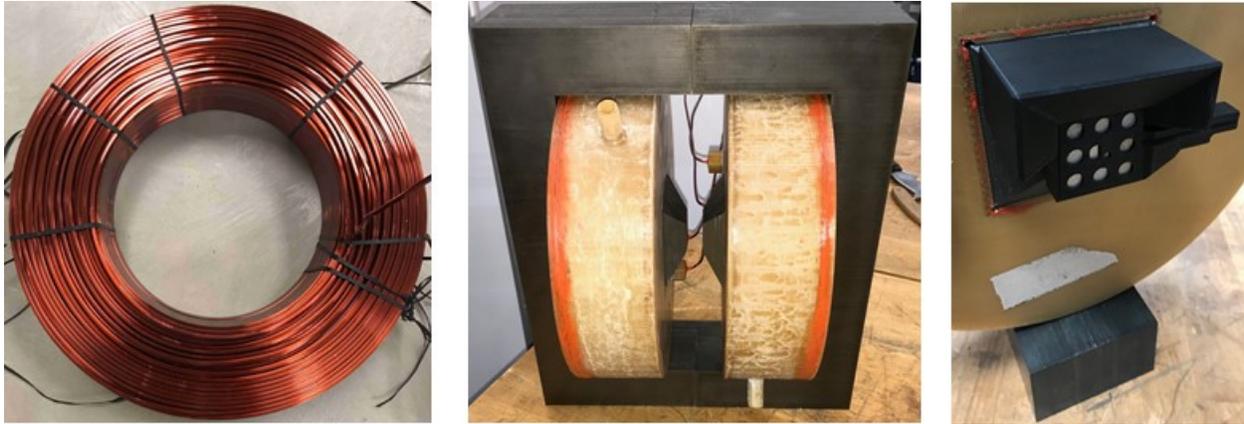


Figure I.3.5 Permanent magnet test fixture subassemblies and components; (Left) One of the two excitation coils after removal from bobbin. (Center) ferromagnetic yoke with excitation coils housed in Ultem oil cooling jackets. (Right) Permanent magnet assembly installed on one half of the magnetic core.

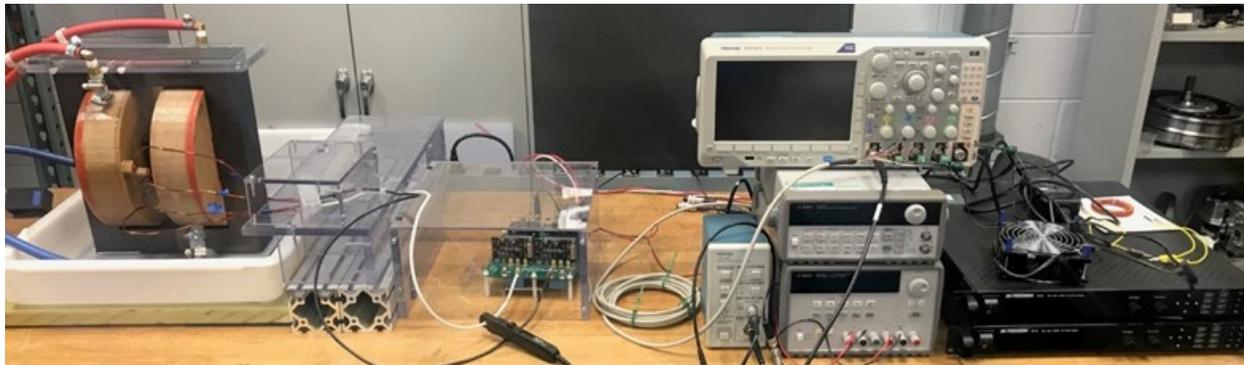


Figure I.3.6 Complete permanent magnet testing system including power supply, inverter, magnetic field sensors, current sensors, and oscilloscope.

## Results

The completed permanent magnet testing system was used to characterize aluminum-nickel-cobalt (AlNiCo) 8HC permanent magnet test samples. The hard axis of each sample was first tested in the single-magnet configuration and compared against the nominal data sheet values for the samples. Note that the data sheet values are not necessarily the true values for the permanent magnet samples. These properties can vary significantly as a result of small changes in processing parameters. For example, since the samples are cut from larger blocks of processed materials, the location in the block from which a sample is taken can impact the resulting performance greatly.

The single magnet remanence was measured at 0.4 T versus 0.72 T nominal. That this value was significantly lower than the datasheet value was expected because of the demagnetizing boundary effects impacting the measured property of the single magnet. The coercivity of the single magnet sample was measured at 149 kA/m vs. 150 kA/m nominal. Likewise, it is expected that the single magnet coercivity measurement should be fairly close to the real value of the coercivity because this measurement is not highly dependent on the sample geometry. Finally, the measured energy product was 22 kJ/m<sup>3</sup> versus 36 kJ/m<sup>3</sup> nominal. The measured value was significantly lower owing to a combination of differential permeability increase and sample geometry impacts on demagnetization. The measured normal and intrinsic curves for the single magnet sample are shown in Figure I.3.7.

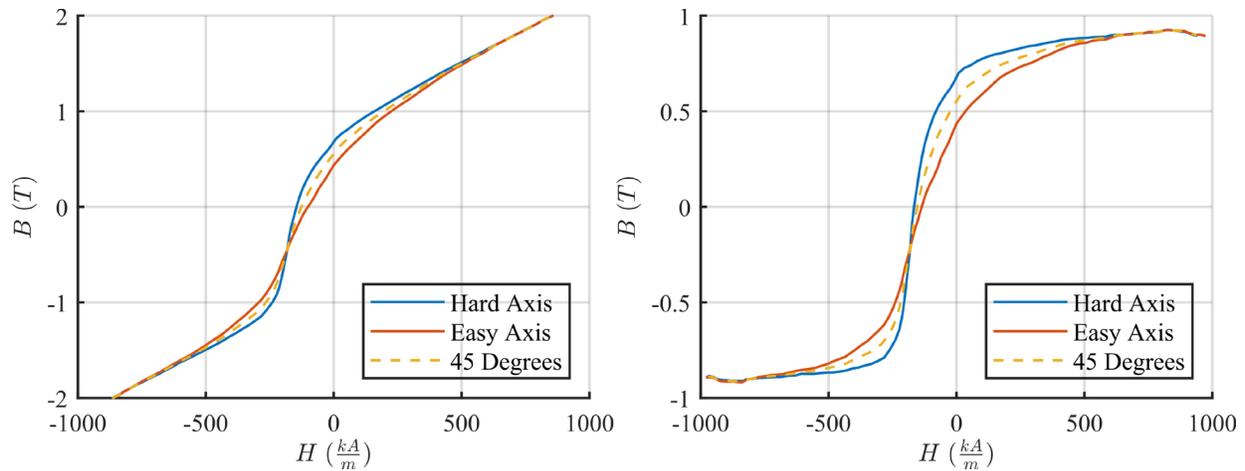


Figure I.3.7 Comparison of measured AlNiCo 8HC hard and easy axis magnetization characteristics; (Right) normal curves, (left) intrinsic curves. A computed estimate of the expected characteristic when a field is applied at 45 degrees between the hard and easy axes is superimposed on both plots.

Next, the hard axes of the magnet samples were tested in the array configuration. This saw the remanence increase to 0.68 T (0.72 T nominal), the coercivity increase to 166 kA/m (150 kA/m nominal), and the maximum energy product increase to 44 kJ/m<sup>3</sup> (36 kJ/m<sup>3</sup> nominal). The measured characteristics of the magnets in the array configuration are much closer to the nominal values than are the test results from the single-magnet tests. This validates the testing procedure accuracy improvements provided by the magnet array technique.

Finally, the easy axis magnetic properties were tested and compared against the hard axis properties. This test revealed that, compared with the hard axis, the easy axis had 37% lower remanence (0.43 T), 18% lower coercivity (136 kA/m), and 64% lower maximum energy product (16 kJ/m<sup>3</sup>). A summary of the three test cases and nominal values for the AlNiCo 8HC are given in Table I.3.1.

**Table I.3.1 Summary of Test Results for AlNiCo 8HC Magnet Samples**

	Remanance	Coercivity	Maximum Energy Product
<b>Nominal (Hard)</b>	0.72 T	150 kA/m	36 kJ/m <sup>3</sup>
<b>Single Magnet (Hard)</b>	0.40 T	149 kA/m	22 kJ/m <sup>3</sup>
<b>Magnet Array (Hard)</b>	0.68 T	166 kA/m	44 kJ/m <sup>3</sup>
<b>Magnet Array (Easy)</b>	0.43 T	136 kA/m	16 kJ/m <sup>3</sup>

Figure I.3.7 compares the measured three-quadrant normal and intrinsic curves of the easy and hard axes from the magnet array test. In both plots, the convergence of the measured flux density for the easy and hard axis tests indicates that the applied field is large enough to completely saturate the magnets. This means that the tested magnets will have reached their maximum possible magnetization state. While the easy axis does exhibit much better linearity in the second quadrant, the overall characteristic is still highly nonlinear. For designs in which the magnitude of the applied field projected onto the easy axis is small, it may be enough to model the easy axis characteristic with a linear permeability. However, note that this parameter is not supplied by permanent magnet manufacturers.



In contrast, when the applied field is no longer primarily against the magnet hard axis, one might expect to encounter a characteristic closer to the “45 degree” curve superimposed on the measured data in Figure I.3.7. This continuous gradation of magnetic properties as the applied field is rotated is missing from current simulation, analysis, and design procedures. The developed test system and procedures provides a method for obtaining the necessary data for implementing high-fidelity demagnetization models for HRE- free permanent magnets.

### Conclusions

This project successfully developed a permanent magnet testing system for the evaluation of anisotropic properties of heavy-rare earth free permanent magnets. The system and methodologies were validated through full three-quadrant magnetization and demagnetization testing of AlNiCo 8HC magnet samples. A failed magnetic field sensor precluded more detailed testing of the AlNiCo 8HC samples or testing of additional samples before the end of the fiscal year. However, enough data were obtained to demonstrate the functionality and correctness of the test system and methodologies. Therefore, the system that has been developed will be able to aid in the design and analysis of HRE-free permanent magnet motors by providing more detailed magnetization characteristics.

### Key Publications

1. J. Pries, E. Gurpinar, L. Tang, and T. A. Burress, “Continuum Modeling of Inductor Magnetic Hysteresis and Eddy Currents in Resonant Circuits,” *IEEE Journal of Emerging and Selected Topics in Power Electronics* 7(3), 1703–14, 2019. Available at <https://doi.org/10.1109/jestpe.2019.2908894>.

### References

1. Electrification 2017 Annual Progress Report. Vehicle Technologies Office, US Department of Energy, 2017. DOI:10.2172/1440304. <https://www.osti.gov/servlets/purl/1440304>.
2. P. Peng, H. Xiong, J. Zhang, et al. “Effects of External Field Orientation on Permanent Magnet Demagnetization.” *IEEE Transactions on Industry Applications* 53(4), 3438–46 (2017). <https://doi.org/10.1109/tia.2017.2686344>.
3. D. Fleisch. *A Student’s Guide to Maxwell’s Equations*. Cambridge: Cambridge University Press, 2011.

### Acknowledgements

Special thanks are owed to the following people and groups: Randy Wiles and Jon Wilkins for assistance in the design and fabrication of the magnetic test fixture; researchers at Ames Laboratory, including Iver Anderson, Matt Kramer, and Jun Cui for technical discussions relating to magnetic material physics, testing, and manufacturing.

## I.4 Non-Heavy Rare Earth High-Speed Motors (ORNL)

### **Tsarafidy Raminosoa, Principal Investigator**

Oak Ridge National Laboratory  
1 Bethel Valley Road  
Oak Ridge, TN 37831  
E-mail: [raminosoat@ornl.gov](mailto:raminosoat@ornl.gov)

### **Susan A. Rogers, DOE Technology Development Manager**

U.S. Department of Energy  
E-mail: [Susan.Rogers@ee.doe.gov](mailto:Susan.Rogers@ee.doe.gov)

Start Date: October 1, 2018  
Project Funding: \$438,000

End Date: September 30, 2019  
DOE share: \$438,000

Non-DOE share: \$0

### **Project Introduction**

The overall objective of this project is to (1) enable the adoption of high-speed and high-power density non-heavy-rare-earth (HRE) traction motors and (2) analyze the impact of new advanced materials for non-heavy-rare-earth electric motors. For the first objective, two motor technology options were considered: permanent magnet (PM) motors using non-HRE magnet materials and motors not using PMs, such as wound field synchronous motors. For the second objective, the impact of emerging nanotube-copper composite conductors, also called ultra-conducting copper (UCC), on the power density and efficiency of non-HRE motors was investigated. One non-HRE motor technology that has the potential to meet the DOE ELT 2025 targets of 50kW/L, \$6/kW, and 300,000-mile lifetime was down-selected, and mechanical assembly design and thermal analysis were carried out to confirm its viability.

### **Objectives**

- Evaluate the power density of non-HRE traction motors and their ability to operate under a wide speed range and at a top speed of 20,000 rpm
- Investigate the impact of the conductivity of UCC winding on the power density and efficiency of traction motors

### **Approach**

Two options were considered to enable the adoption of non-HRE electric motors for traction to achieve the DOE ELT 2025 targets:

*Option 1: HRE-free PM motors:* With dysprosium and terbium-free PMs, PM motors can keep the high-power density and high efficiency that make them so popular for electric vehicle traction while lowering the cost and reducing the supply reliability risk. The challenge here is to design the non-HRE PM motor to be resistant to demagnetization despite the lower coercivity of HRE-free PMs compared with HRE PMs.

*Option 2: Non-PM motors:* Wound rotor synchronous motors use electromagnets instead of PMs. Hence, they are very cost effective and can help achieve the 30% cost reduction DOE ELT target for 2025. The rotor field winding is excited via a stable, robust, and high-speed-capable rotary transformer-based contactless system.

In addition, emerging high-conductivity composite conductors based on carbon nanotubes (CNTs) and UCC have opened a new degree of freedom to improve electric motor performance: the conductivity of the winding. Their potential for improving the power density and performance of non-HRE traction motors to achieve the DOE ELT target of 50 kW/L was evaluated.

**Results**

Demonstrated the stability of the open-loop control of the proposed contact-less excitation system for the wound rotor synchronous motor.

In this task, the impact of resonant compensation on the power transfer capability and stability of the proposed rotary transformer-based contact-less excitation system was analyzed. It was theoretically demonstrated that open-loop control of the field winding current is stable. This key finding brings a significant simplification by eliminating any need for current sensors on the rotating parts. Furthermore, this study has shown that series resonant compensation on the primary side alone is enough to ensure both high power transfer capability and stability. This significantly simplifies the excitation by eliminating the need to integrate a resonant capacitor on the rotating secondary winding (Figure I.4.1).

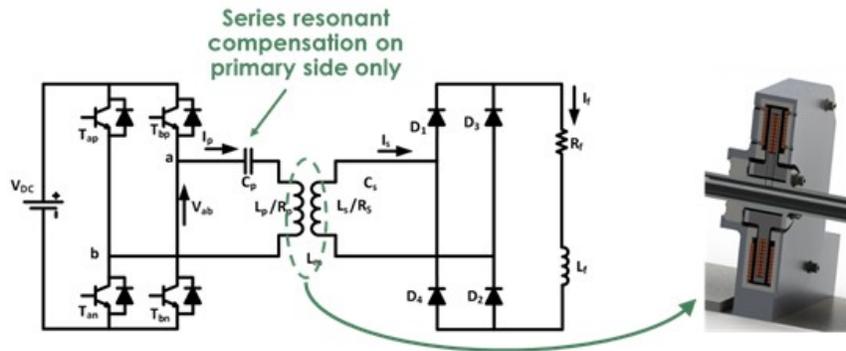


Figure I.4.1 Proposed rotary transformer-based excitation system with resonant compensation only on the primary side.

The condition of stability of the field current control under open-loop operation was theoretically established. If this condition is verified, the stability of the zero dynamics is independent of the value of the field winding resistance. The field winding current can be controlled with the inverter phase shift angle and is not affected by the variation of field winding resistance due to temperature (for a temperature swing from  $-50$  to  $150^{\circ}\text{C}$ ), Figure I.4.2.

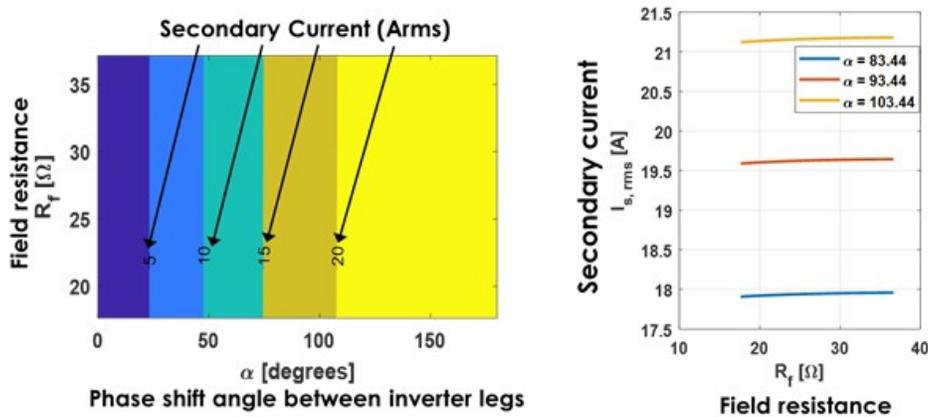


Figure I.4.2 Robustness of the field current against the variation of field winding resistance due to temperature (for a temperature swing from  $-50$  to  $150^{\circ}\text{C}$ ).

**Completed design of HRE-free PM motors**

Under this task, four non-HRE motor technologies were evaluated and compared. These attributes of these motor candidates are summarized in Table I.4.1. They are compared for the same outer diameter of 242 mm, 0.76 mm airgap length, copper current density of  $20 \text{ Arms}/\text{mm}^2$  under peak power operation, base speed of

4750 rpm, and top speed of 20,000 rpm. Motor technologies with distributing windings were assumed to be using bar windings with a slot fill factor of 65%. Those using tooth windings were assumed to have a slot fill factor of 45%.

The performances of the motor candidates are summarized and compared in Table I.4.2. Their pros and cons are described in Table I.4.3. From these tables, it was found that:

- The outer rotor Halbach surface PM (SPM) motor has the highest power density. Its mechanical assembly and bearing system are, however, more complex.
- The dysprosium-free spoke internal PM motor has slightly lower power density and has a conventional bearing system. However, its rotor assembly is complex and may not be robust at 20,000 rpm.
- The wound rotor synchronous motor has acceptable power density, but it is lower than the two PM motors mentioned above. It also has a satisfactory but lower efficiency. Its advantage is mainly its cost-effectiveness.
- Slotless PM motor topologies are not suitable for wide speed range applications because of their very low inductances.

Based on these conclusions, it was decided to select the outer rotor Halbach SPM motor. Since the PM material used in the Halbach SPM motor does not include HREs, it is more prone to demagnetization. Hence, the demagnetization resistance was carefully analyzed under a worst-case scenario of a 3-phase short-circuit fault at 20,000 rpm and 150°C. The result is presented in Figure I.4.3: the loss of magnetization under was only 7% under such an extreme fault. This confirms the robustness of the outer rotor Halbach SPM motor against demagnetization.

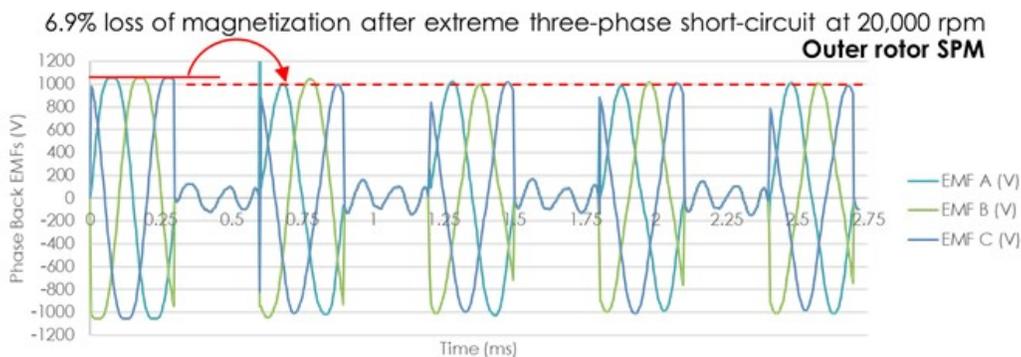


Figure I.4.3 Resistance of the HRE-free outer rotor SPM to demagnetization under 3-phase short circuit at 20,000 rpm.

The mechanical assembly of the motor and the analysis of the mechanical stress on the rotor at 20,000 rpm are presented in Figure I.4.4. The maximum stress is within the stress limit for 410 stainless steel (1475 MPa tensile strength and 1005 MPa yield strength), confirming the mechanical viability of the assembly.

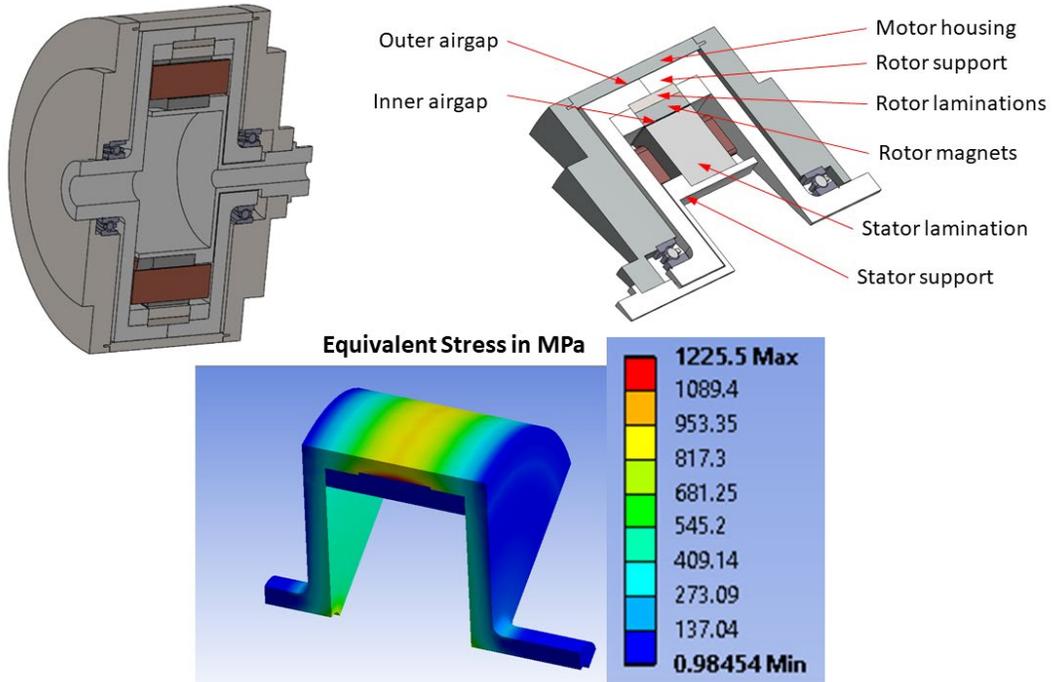


Figure I.4.4 Mechanical assembly and stress analysis at 20,000 rpm.

Table I.4.1 Motor Candidates

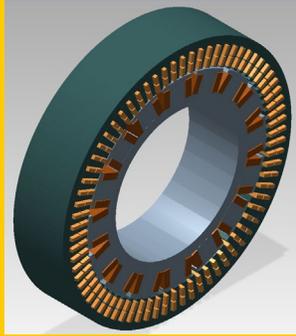
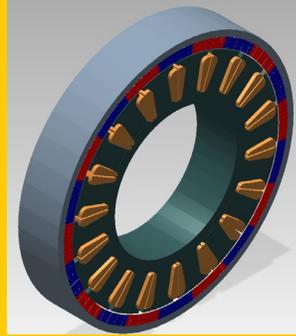
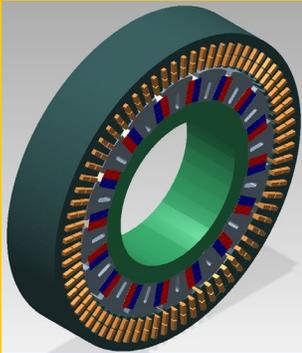
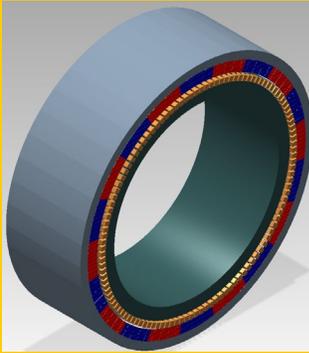
<p><b>Wound Rotor Synchronous Motor</b></p> <p><b>Inner rotor</b></p> <p><b>72 slots, 16 poles</b></p> <p><b>Distributed winding</b></p> <ul style="list-style-type: none"> <li>• Non-permanent magnet: Cost effective</li> <li>• No demagnetization issue</li> <li>• Fractional 1.5 slots per pole per phase to reduce torque ripple (no skewing)</li> </ul>		<p><b>HRE-free Outer Rotor SPM Motor</b></p> <p><b>18 slots, 20 poles</b></p> <p><b>Concentrated tooth winding</b></p> <ul style="list-style-type: none"> <li>• Natural magnet retention by rotor yoke</li> <li>• Airgap radius at the outermost possible to maximize the torque density</li> <li>• Tooth winding: high direct inductance for flux weakening and low torque ripple</li> <li>• Halbach magnet arrangement: Maximize airgap flux density and reinforce demagnetization resistance</li> </ul>	
<p><b>HRE-free Inner rotor Spoke Internal PM Motor</b></p> <p><b>72 slots, 16 poles</b></p> <p><b>Distributed winding</b></p> <ul style="list-style-type: none"> <li>• Reluctance torque helps maximize torque density</li> <li>• Low exposure of the lower coercivity HRE-free PMs to demagnetizing armature field</li> <li>• Fractional 1.5 slots per pole per phase and rotor pole shaping to reduce torque ripple (No skewing)</li> </ul>		<p><b>HRE-free Outer rotor Slotless Surface Permanent Magnet</b></p> <p><b>120 slots, 20 poles</b></p> <p><b>Distributed winding</b></p> <ul style="list-style-type: none"> <li>• Natural magnet retention by rotor yoke</li> <li>• Airgap radius at the outermost possible to maximize the torque density</li> <li>• Slotless winding: extremely low torque ripple</li> <li>• Halbach magnet arrangement to maximize flux density and to have a near sinusoidal flux density distribution in the airgap</li> </ul>	

Table I.4.2 Performance Comparison

Very Good	Good	Neutral	Insufficient	Bad	Very Bad
Criteria	Wound Rotor Synchronous Motor	Inner Rotor Spoke HRE-free IPM	Outer Rotor Tooth Wound HRE-free SPM	Outer Rotor Slotless HRE-free SPM	
Active volume (L) – (lamination stack)	2.40	2.15	1.88	3.55	
Max current (at peak torque)	232.77	232.77	192	192	
Efficiency at peak power base speed (%) (150°C)	93.8	95.6	96.9	96.6	
Efficiency at 20% load base speed (%) (150°C)	94.9	95.6	96.4	98.4	
Efficiency at 20% load top speed (%) (150°C)	96.1	95.0	97.0	Cannot achieve 20,000 rpm	
Power factor at peak power base speed	0.83	0.86	0.81	0.99	
Torque ripple at peak power base speed (%)	8.62	4.8	3.2	0.60	
Mechanical robustness at high speed	Proven robust at 20,000 rpm in industry (aircraft generator applications)	Complex rotor assembly	Complex assembly and bearing system	Complex assembly and bearing system	
Simplicity of control	Additional DC-DC converter with rotary transformer for the field winding	Standard	Standard	Standard	
Wide speed range capability (4,750 to 20,000rpm)	Capable	Capable	Capable	Limited speed range	
Resistance to demagnetization (under 3-phase short-circuit)	No permanent magnets	2.5% demagnetization	7% demagnetization	65% demagnetization	
Cost effectiveness	No permanent magnets	Cost of HRE-free PM material	Cost of HRE-free PM material	65 to 89% more HRE-free PM material	

**Table I.4.3 Summary of Pros and Cons**

Motor Candidates	Pros	Cons
<b>Wound Rotor Synchronous Motor</b>	Proven mechanically robust at 20,000 rpm in industry (aircraft generator); cost effective; wide speed range capable; field excitation can be disabled in case of fault; no demagnetization issue	Lower power density; lower efficiency; complex control algorithm; additional DC/DC converter and rotary transformer for the field winding
<b>Inner Rotor Spoke HRE-free IPM</b>	Proven mechanically robust in laboratory for speed up to 14,000 rpm; wide speed range capable; can be designed to be resistant to demagnetization; high power density; high efficiency; standard 3-phase inverter; standard control algorithm; standard bearing system	Rotor assembly is relatively complex
<b>Outer Rotor Tooth Wound HRE-free SPM</b>	Proven mechanically robust in laboratory for speed up to 15,000 rpm; wide speed range capable; can be designed to be resistant to demagnetization; highest power density; high efficiency; standard 3-phase inverter; standard control algorithm	Complex overall motor assembly; complex bearing system
<b>Outer Rotor Slotless HRE-free SPM</b>	Proven mechanically robust in laboratory for speed up to 15,000 rpm; high efficiency; standard 3-phase inverter; standard control algorithm	Limited speed range; vulnerable to demagnetization; lowest power density; uses up to 89% more permanent magnets (expensive); complex overall motor assembly; complex bearing system

The thermal analysis and cooling system design were conducted in collaboration with National Renewable Energy Laboratory (NREL). ORNL evaluated the loss distribution in the motor, including the AC losses in the winding and the eddy current losses in the magnets (Figure I.4.5). The finite element thermal modeling was done at NREL based on the mechanical assembly file from ORNL. NREL analyzed and compared several cooling options. It was found that with aggressive oil spray cooling on all exposed faces of the stator lamination and winding, combined with spray cooling of the rotor, and oil cooling of the slot wedges, the hot spots in the winding and magnets could be kept within the 150°C temperature limit at the highest heat-load scenario of continuous 55 kW operation at 20,000 rpm (Figure I.4.6).

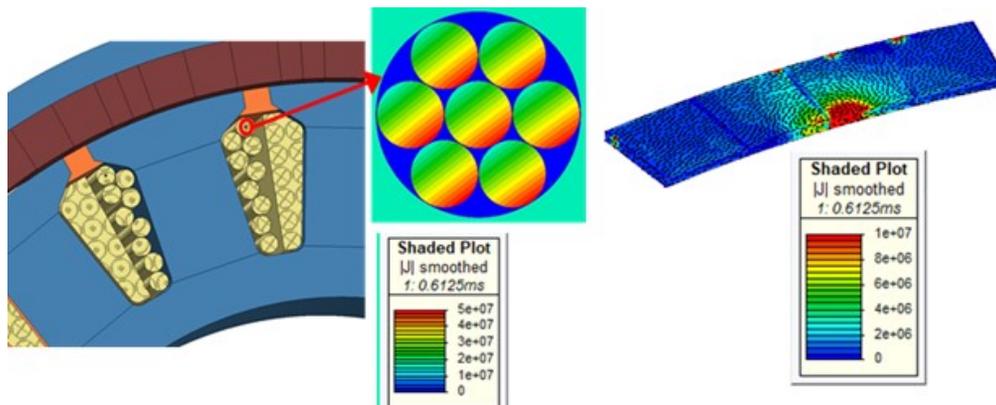


Figure I.4.5 AC loss in winding and eddy current loss in permanent magnets at 100 kW and 20,000 rpm operation.



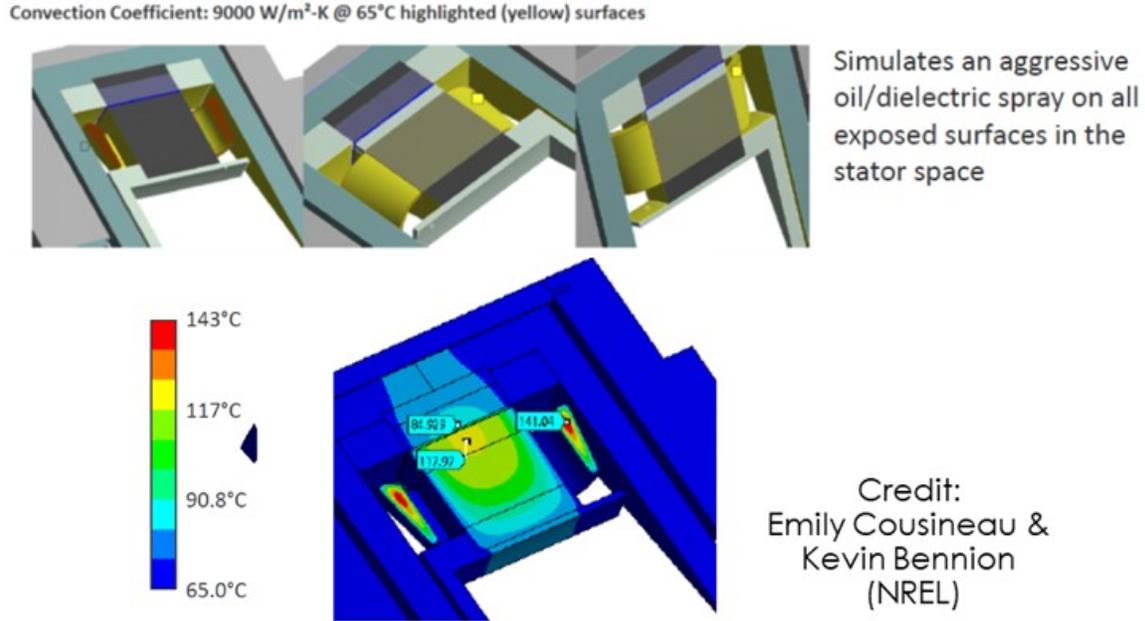


Figure I.4.6 Thermal simulation results at 20krpm with high thermal conductivity winding potting, winding spray cooling, slot wedge liquid cooling, and rotor liquid cooling (Refer to project elt2.14 “Electric Motor Thermal Management” by Kevin Bennion (NREL)).

***Evaluated the impact of UCC winding conductivity on traction motor performance***

The emergence of carbon nanotube-copper composite conductors has opened a new degree of freedom in electric machine design to improve machine performance: the conductivity of the winding. The goals of this study are (1) to determine how much improvement in power per unit of volume and performance can be achieved with an increase in winding conductivity and (2) to investigate any physical limitations on the effectiveness of this degree of freedom in improving the power per unit of volume and performance of electric traction motors. Three topologies of HRE-free PM motors were analyzed. The motors had the same outer diameter of 242 mm and were designed for 100 kW peak power (Figure I.4.7). The conductivity of the winding is varied up to 2 times the conductivity of copper. The heat loads in the slots were kept constant across all the designs.

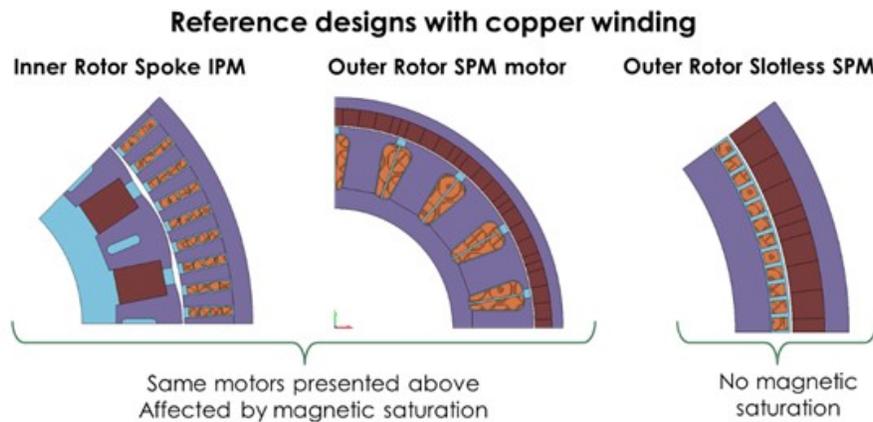


Figure I.4.7 Analyzed motor topologies.

The impacts of the winding conductivity on the power densities of the spoke internal PM motor and the outer rotor SPM motor were similar. With increasing winding conductivity, the volume reduction was lower than the

ideal forecast because of the magnetic saturation effect in the steel. With a 30% improvement in UCC conductivity, a 10% reduction in active volume was achieved.

The outer rotor slotless SPM had a low magnetic loading because of the long magnetic airgap. As a result, its power density was lower than that of the two previous conventional motors. However, since it was not affected by magnetic saturation, the impact of the winding conductivity reached the theoretical expectation. Therefore, with a 30% improvement in UCC conductivity, a 12% reduction in active volume was achieved. In addition, because of its low inductance, the slotless SPM could not achieve constant power operation up to 20,000 rpm (Figure I.4.8). This type of machine is better suited for fixed speed or narrow speed range, and the higher the winding conductivity, the wider the speed range is.

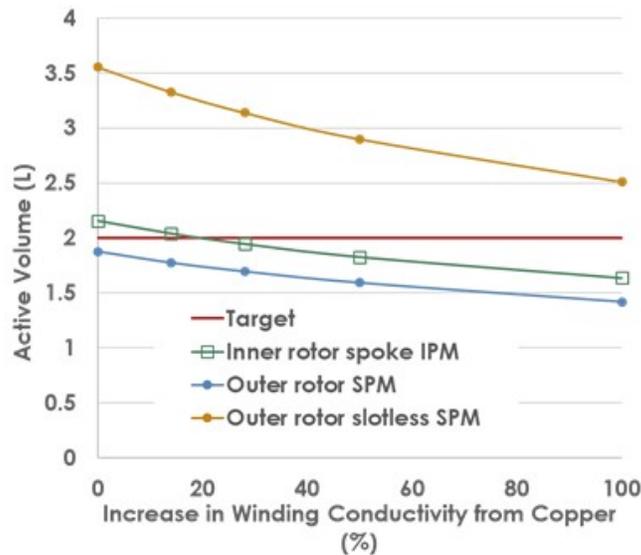


Figure I.4.8 Impact of winding conductivity on the motor active volume.

In all cases, as the winding conductivity increased, the high-efficiency operating area ( $\geq 97\%$ ) was enlarged toward light loads and high speeds (Figure I.4.9).

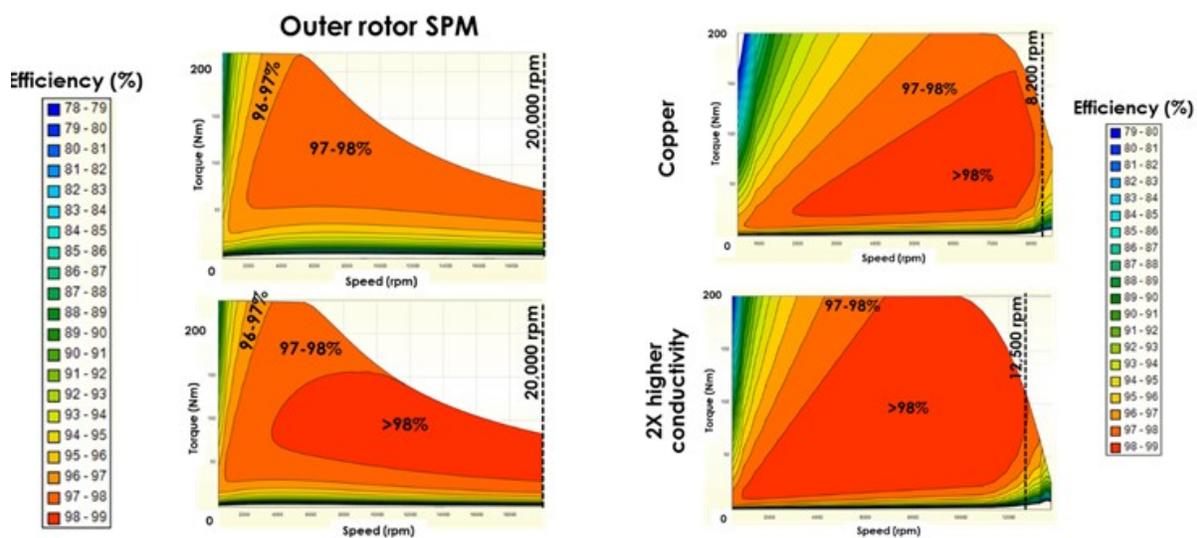


Figure I.4.9 Impact of winding conductivity on the speed range and efficiency.

## Conclusions

This work has shown that non-HRE high-speed traction motors have the potential to meet the DOE ELT 2025 targets of 50 kW/L, \$6/kW, and 300,000-mile lifetime. Two paths were considered. The first one proposes a contact-less excitation system to enable the adoption of non-PM motors and low-cost wound rotor synchronous motors for vehicle traction. The second one proposes PM motors using non-HRE magnet materials. The study has concluded that non-HRE PM motors offer the best compromise among power density, efficiency, and cost. The outer rotor SPM topology was selected because it had the best power density, efficiency, and robustness for high-speed operation. A Halbach magnet arrangement was used to maximize the power density as well as to provide resistance to demagnetization. Electromagnetic, mechanical, and thermal designs were carried out and confirmed the feasibility of the selected motor.

In addition, the impact of UCC winding conductivity on the power density and performance of several traction motor topologies was investigated. It was found that the currently reported 30% improvement in UCC conductivity can lead to a 10% reduction in a traction motor's active volume.

## Key Publications

1. T. Raminosoa, T. Aytug, "Impact of Ultra-Conducting Winding on the Power Density and Performance of Non-Heavy Rare Earth Traction Motors," *2019 IEEE International Electric Machines and Drives Conference (IEMDC)*, San Diego, May 12–15, 2019.
2. J. Haruna, T. Raminosoa, "Modeling and Steady-State Analysis of a Rotary Transformer-Based Field Excitation System for Wound Rotor Synchronous Machine," *2019 IEEE Transportation Electrification Conference and Expo (ITEC)*, Seogwipo-si, South Korea, May 8–11, 2019.
3. J. Haruna, T. Raminosoa, O. Ojo, "Stability Analysis and Control of a Rotary Transformer-Based Synchronous Motor Field Excitation System," *2019 IEEE International Electric Machines and Drives Conference (IEMDC)*, San Diego, May 12–15, 2019.
4. J. Haruna, T. Raminosoa, J. Wilkins, "Enhanced Rotary Transformer-Based Field Excitation System for Wound Rotor Synchronous Motor," *2019 IEEE Energy Conversion Congress and Exposition (ECCE)*, Baltimore, Maryland, September 29–October 3, 2019.
5. T. Raminosoa, "Non-Heavy Rare-Earth High-Speed Motors," 2019 DOE Vehicle Technologies Office Annual Merit Review, Project ID: ELT212.

## Acknowledgements

The principal investigator would like to thank ORNL's Randy Wiles for the design of the mechanical assembly of the outer rotor SPM motor and the mechanical stress analysis, and NREL's Emily Cousineau and Kevin Bennion for the thermal analysis and design (Refer to project elt214 "Electric Motor Thermal Management" by Kevin Bennion (NREL)).

## I.5 Integrated Electric Drive (ORNL)

### Shajjad Chowdhury, Principal Investigator

Oak Ridge National Laboratory  
1 Bethel Valley Road  
Oak Ridge, TN 37830  
E-mail: [chowdhurys@ornl.gov](mailto:chowdhurys@ornl.gov)

### Susan Rogers, DOE Technology Development Manager

U.S. Department of Energy  
E-mail: [Susan.Rogers@ee.doe.gov](mailto:Susan.Rogers@ee.doe.gov)

Start Date: October 1, 2018  
Project Funding: \$270,000

End Date: September 30, 2019  
DOE share: \$270,000

Non-DOE share: \$0

### Project Introduction

In recent years, DOE has announced technical targets for light-duty electric vehicles. DOE targets reaching a power density of 33 kW/L for a 100 kW traction drive system by 2025 [1]. It translates to an increment of a factor of 8 times of the state of the art. To achieve the target, this project focuses on the tight integration of motor and inverter components to improve power density. In addition to integration, this project focuses on optimizing the volume of the bulky DC link capacitor by identifying high energy density capacitor technology.

### Objectives

The overall objective of this project is to research technologies that will allow the integration of the inverter with the motor, resulting in a high-power-density integrated traction drive. Specific objectives for FY 2019 include the following:

- Identify the gaps and challenges in current integrated electric drive technologies for electric vehicle (EV) traction application
- Identify various integration techniques to integrate an electric motor and an inverter to meet the DOE 2025 power density target
- Compare the advantages and disadvantages of different integration technologies
- Build finite element (FE) models to analyze thermal effects in collaboration with National Renewable Energy Laboratory (NREL)
- Identify and characterize capacitor technologies for volume optimization

### Approach

Our approach to achieving the objectives is:

- Understand current integration techniques and identify challenges for tight integration of motor and inverter
- Find all the possible integration methods and assess their thermal performances using a finite element (FE) platform
- Identify and characterize high-energy-density capacitors for volume optimization

## Results

### Integration of Motor and Inverter

An integrated motor drive (IMD) involves physical integration of all the components of an electric drive unit into a single casing, thus reducing volume, cost, and complexity of installation. The elimination of separate casings, busbars, and long wires, along with sharing of the cooling system, are the catalysts behind achieving increased power density for an IMD. A tightly integrated drive can increase power density by 10–20% with a concomitant reduction of manufacturing and installation costs by 30%–40% [2].

The state of the art of integration techniques identified through a literature search [3],[4],[5] is depicted in Figure I.5.1. The most common integration technique is a radial housing mount, in which the inverter is manufactured in a separate casing and then mounted on top of the motor casing, Figure I.5.1a. This type of integration has the lowest power density because of the geometry, additional casing, and busbars. A radial stator mounting inverter system uses the stator's outer periphery. In this type of integration, the inverter and the motor share the same cooling system, as shown in Figure I.5.1b. The other two integration techniques noted in the literature are axially mounted inverters, which are either directly connected to the endplate or connected between the stator lamination and endplate. The latter suffers from an extreme environment, as the inverter is mounted next to the major heat source (stator winding). The advantages and disadvantages of the identified integration techniques are shown in Table I.5.1 Advantages and Disadvantages of Various Integration Techniques. It is evident from the literature that integration of the motor and inverter reduces the component count of a traction drive system, resulting in an overall reduction of system cost and volume.

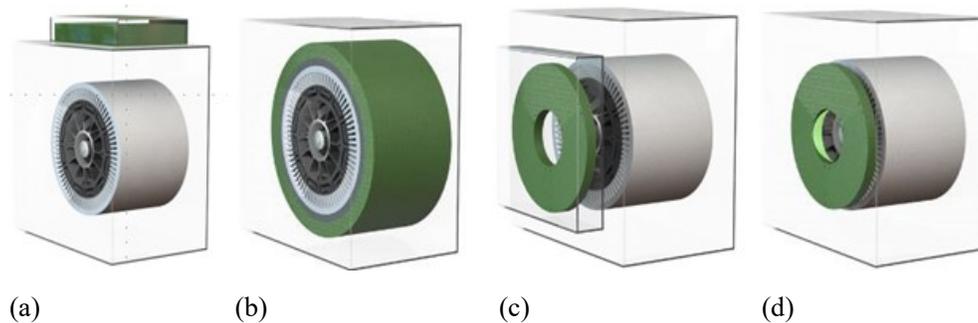


Figure I.5.1 Motor and inverter integration techniques: (a) radial housing mount, (b) radial stator mount, (c) axial endplate mount, (d) axial stator mount.

**Table I.5.1 Advantages and Disadvantages of Various Integration Techniques**

Integration Techniques	Advantages	Disadvantages
<b>Radial Housing Mount</b>	Better thermal isolation between the inverter and motor Ease of implementation and manufacturing process	May require a separate cooling system Achieving high power density is difficult
<b>Radial Stator Mount</b>	Can share the motor cooling jacket Tight integration due to sharing of the cooling jacket	Flat surface is required to accommodate inverter components
<b>Axial Endplate Mount</b>	Endplate provides thermal isolation Ease of inverter design on top of a flat circular disk	A separate cold plate is required

Integration Techniques	Advantages	Disadvantages
Axial Stator Mount	Can share the same cold plate Shared cold plate will act as a thermal shield	Winding losses must conduct axially if the motor is cooled from end-windings

Although combining the physical structure of the motor and inverter into a single casing reduces the physical size of the overall system, heat extraction becomes a challenge. Adopting a traditional separate cold plate design increases the volume and cost of the overall system, thus reducing the attractiveness of the IMD system. Therefore, the design of an efficient cooling system for an IMD requires extensive thermal analysis of the system.

To identify the required thermal performance of these integration techniques, a motor and an inverter were modeled. The motor model is shown in Figure I.5.2. In the figure, one-sixth of a 2016 BMW-i3 traction motor can be seen. A portion of the stator was modeled to reduce the computational burden, with the assumption that one-sixth of the total losses would be dissipated through the modeled section. One phase leg of the segmented inverter [6] was also modeled, as shown in Figure I.5.3. The inverter was designed using a SiC-based chip mounted on a direct bonded copper (DBC) substrate; the structure and layer thickness of the DBC are also shown in Figure I.5.3. The experimental loss data of the motor and loss data of the inverter (simulation-based) are shown in Figure I.5.4.

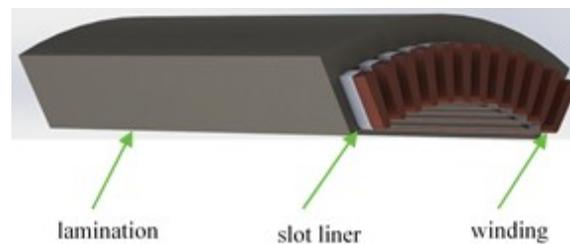


Figure I.5.2 One-sixth of 2016 BMW-i3 stator.

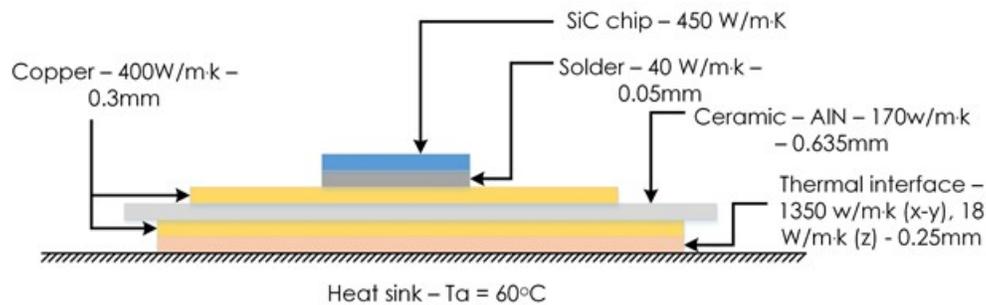


Figure I.5.3 DBC structure for thermal simulation.

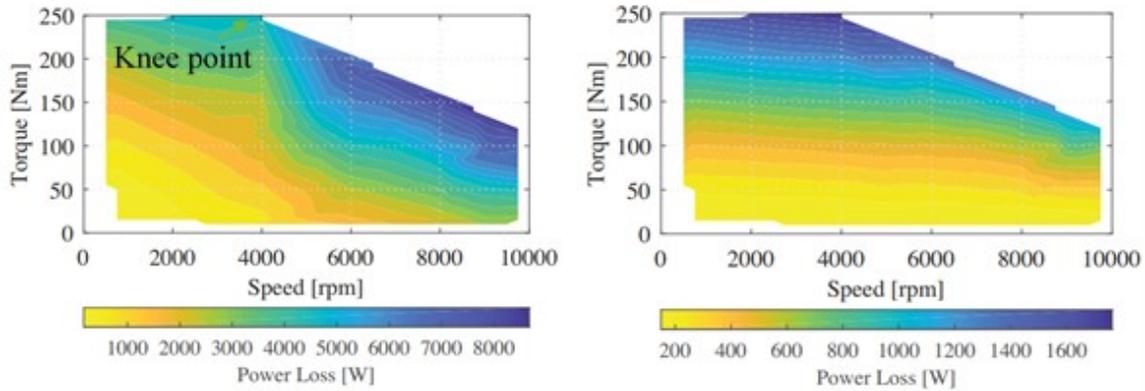


Figure I.5.4 Power loss data: (a) experimental motor power loss; (b) inverter power loss (simulation-based).

An FE-based model of the radial housing mount inverter was created in COMSOL for thermal analysis. The winding and the core losses were evenly distributed among the motor winding and stator laminations, respectively. The inverter losses were evenly distributed among the SiC chips. The inverter module was assumed to be connected to the heat sink using a thermal interface material with thermal conductivity of 28 W/m.k. The heat transfer coefficient was applied to the inner hollow surface of the heat sink. To identify the required thermal performance, the heat transfer coefficient was varied from 1 kW/m<sup>2</sup>·K to 10 kW/m<sup>2</sup>·K for various operating conditions, and the ambient temperature was set to 60°C. The results are shown in a 3D surface plot in Figure I.5.5. It can be seen from the simulation results that the winding temperature of the motor and the inverter junction temperature would remain within the limits, below 200°C and 150°C, respectively, for the worst-case condition if the heat transfer coefficient were 6kW/m<sup>2</sup>·K or higher.

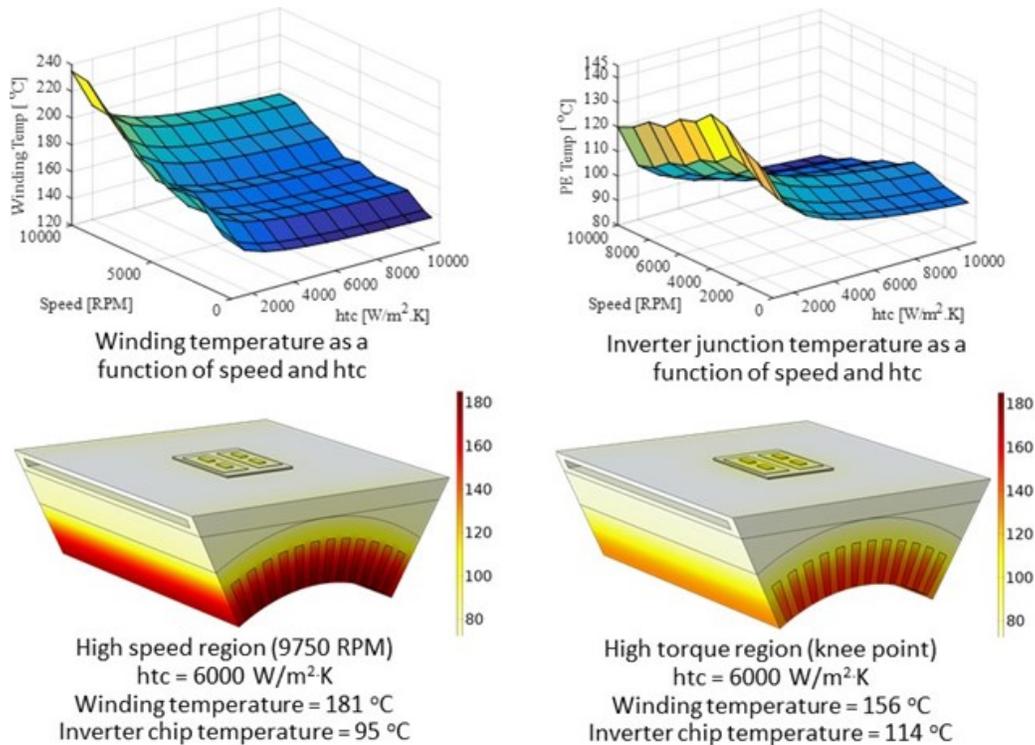


Figure I.5.5 Identification of required thermal performance of radial stator mount IMD system. htc = heat transfer coefficient.

### Capacitor Characterization

A DC bus capacitor imposes an obstruction to meet high-power-density demand in voltage source inverters employed in electric traction drives. The purpose of the DC bus capacitor is to decouple the load from the DC supply unit, thus absorbing a large ripple current and retaining the voltage transients resulting from the inverter switching action. These capacitors use substantial space, about 20% of an inverter, requiring better capacitor technology to optimize power density.

There are several capacitor technologies available in the market. The most commonly used ones are electrolytic, ceramic, and film capacitors. Among the three, the film capacitor is widely used as a DC bus capacitor for EV traction drive applications. Although these capacitors have lower capacitances per unit of volume than electrolytic capacitors, they are of interest because of their reliability, high current capability, and lower equivalent series resistance (ESR).

The other candidate for a DC bus capacitor is the ceramic capacitor. These use ceramic dielectric and have a very high dielectric constant. They can be constructed using a single-layer capacitor for small capacitance or by stacking multiple units together to form multilayer ceramic capacitors (MLCCs). The ceramic capacitor has a much higher rms current rating per unit of volume, has higher capacitance density, and can withstand higher temperatures than film capacitors. The most common dielectric used in MLCCs is barium titanate ( $\text{BaTiO}_3$ ), which is a class II dielectric material.

Another type of ceramic capacitor available in the market is the CeraLink, a trademark of TDK. This capacitor has all the advantages of MLCCs coupled with increased reliability achieved by using a series connection of two MLCC geometries in one component. These capacitors use an antiferroelectric material (PLZT) as the dielectric; thus, their capacitance increases with DC bias.

To realize high energy density, 55 samples of ceramic, CeraLink, and film capacitors were chosen; their capacitances per unit of volume are plotted in Figure I.5.6. These are off-the-shelf capacitors readily available in the market and have a voltage range of 450–1000 V. It is evident from Figure I.5.6. that CeraLink capacitors have the highest capacitance density and can be used to optimize the volume of traction inverters. To further support this hypothesis, film, MLCC, and CeraLink capacitors were selected for detailed experimental characterization. The parameters of the selected capacitors are shown in Table I.5.2.

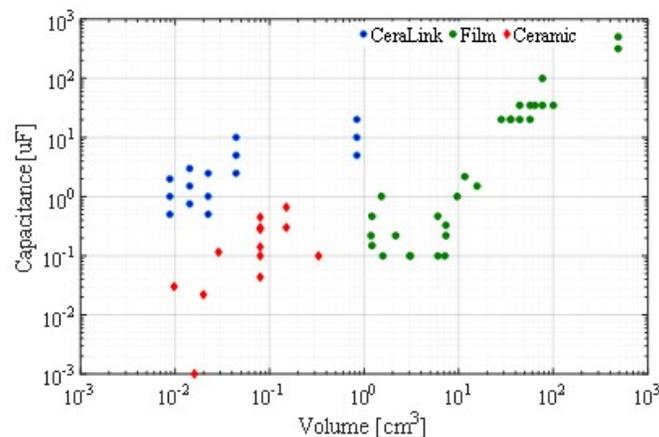


Figure I.5.6 Capacitance density of the selected capacitor



Table I.5.2 Selected Capacitor's Parameter Comparison

	Panasonic Film ECW-FE2W105J [7]	TDK MLCC C5750X7T2W105K250KA [8]	TDK CeraLink B58031U5105M062 [9]
Material	Metallized polypropylene	BaTiO <sub>3</sub>	PLZT
Capacitance	1 $\mu$ F <sup>1</sup>	1 $\mu$ F <sup>1</sup>	0.6 $\mu$ F <sup>2</sup>
Dimensions	17.6 × 7 × 12.5 mm	5.6 × 4.9 × 2.5 mm	7.5 × 8.3 × 4.5 mm
Current rating @ 50 kHz, Tamb = 85 °C	3.5 A	5 A	8 A
Maximum Voltage	450 V	450 V	650 V
Maximum Temperature	105 °C	125 °C	150 °C

<sup>1</sup> Nominal capacitance at 0 V DC bias.

<sup>2</sup> Nominal capacitance at 400 V DC bias.

The performance of the selected capacitors was determined under various operating conditions. The ESR and the capacitance variation were determined under 0 and 400 VDC bias along with varying device temperatures (25, 50, 75, and 100°C). The test setup used to adjust the operating point of the capacitors is shown in Figure I.5.7. A small sinusoidal signal was injected using a frequency response analyzer, and then the current and voltage across the capacitor under test (CUT) were measured to calculate the ESR and the capacitance variation during different operating conditions.

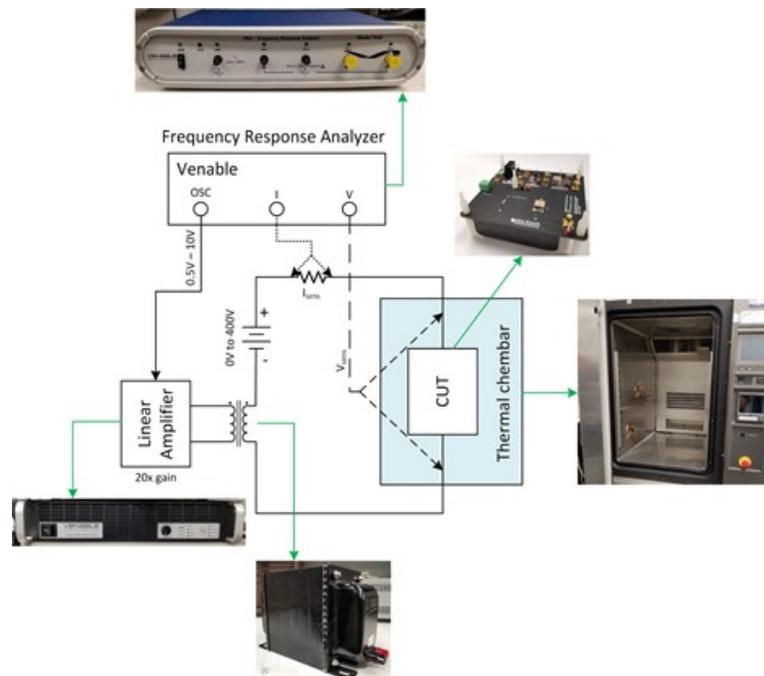


Figure I.5.7 Experimental setup.

The frequency of the AC signal varied between 5 and 200 kHz, and a 500VDC source was used in series with the AC source to vary the bias voltage of the CUT. A linear amplifier was used to control the amplitude of the AC signal, in conjunction with an isolation transformer to protect the oscillator port of the frequency response analyzer. The current and voltage ports of the analyzer were isolated up to 600 V; thus, no isolation was

required for this test. The CUT was enclosed in a laboratory oven to determine the characteristics under various operating temperatures. To average the tolerances between individual capacitors, test results for two samples were averaged and then plotted in Figure I.5.8 and Figure I.5.9.

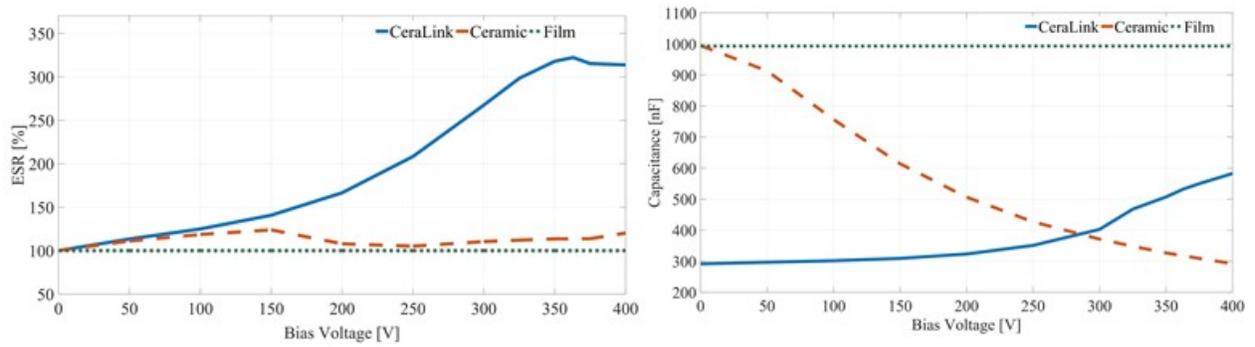


Figure I.5.8 Change in ESR and capacitance with DC bias voltage ( $f = 1\text{kHz}$ ,  $T = 23^\circ\text{C}$ ).

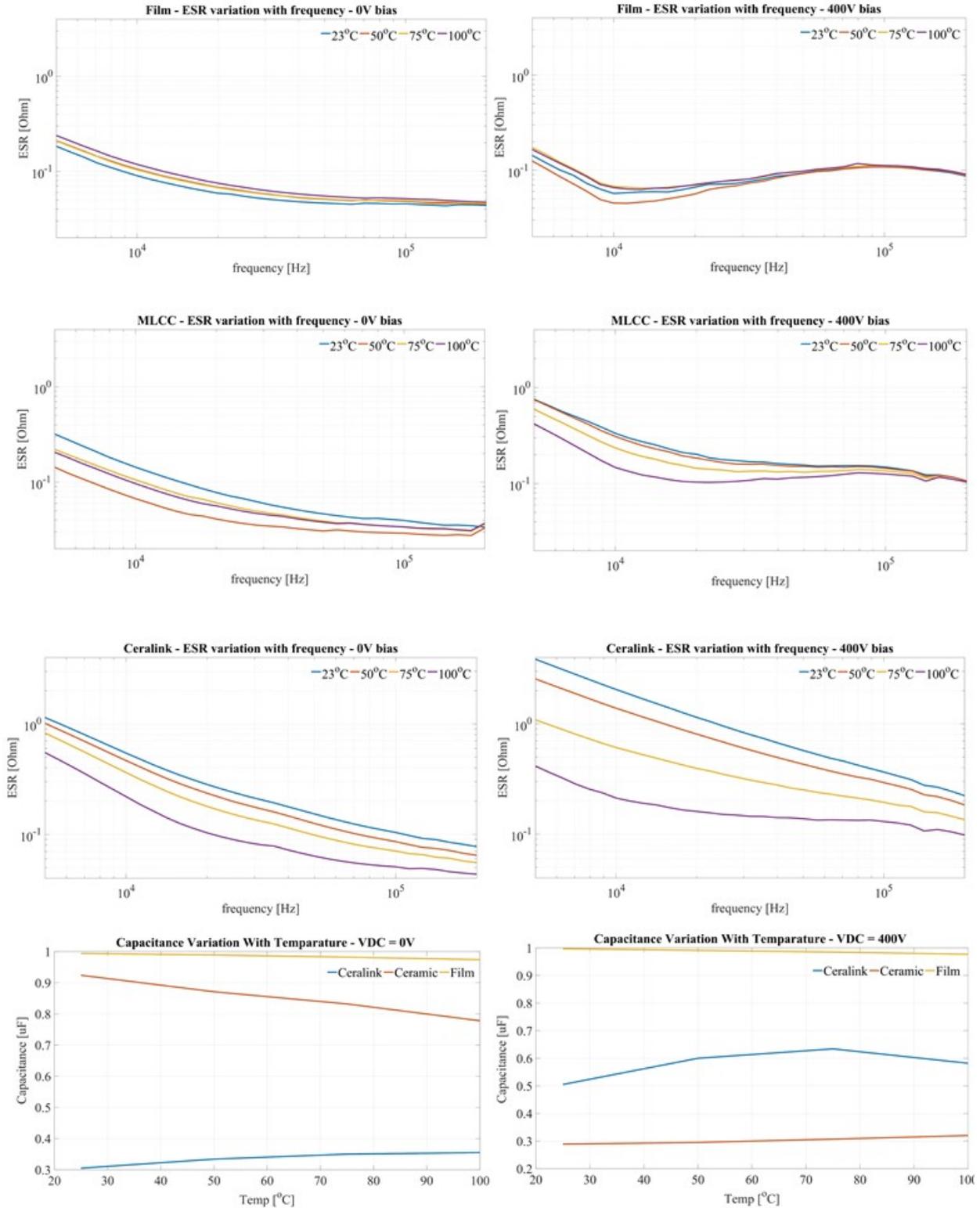


Figure I.5.9 Change in ESR and capacitance of different capacitor technology in terms of frequency, bias voltage, and temperature.

The results indicated that the ESR of the film capacitor was the lowest, meaning the losses in the capacitor would be lower. However, the bottleneck for the film capacitor was the fixed temperature rise due to self-heating, 20°C for the selected capacitor. The limited temperature rise significantly reduced the current conduction capability of the capacitor. The selected film capacitor could conduct only 4 A of current, necessitating a heat sink to support a higher current or higher-temperature operation. On the other hand, the CeraLink and ceramic capacitor had much higher maximum operating temperatures and had no obstruction on the self-temperature rise. Thus, ceramic and CeraLink capacitors could conduct a much higher current.

It is also evident from Figure I.5.8 and Figure I.5.9 that the capacitance of the film capacitor was nearly independent of the DC bus voltage and temperature. On the other hand, the capacitance of the ceramic capacitor decreased by 70% with the DC bias voltage. The CeraLink capacitor showed opposite characteristics; unlike the ceramic capacitor, the capacitance of the CeraLink increased with the bias voltage and temperature. The capacitance reached a maximum value (0.63  $\mu$ F) at 400 VDC bias and 75°C device temperature.

The impedance of the capacitor increases after a certain temperature (capacitance decrease after 75°C) and the hottest capacitor takes less current. This ensures natural current balancing through parallel capacitor branches. The advantages and disadvantages of three selected capacitor technologies are shown in Table I.5.3.

**Table I.5.3 Advantages and Disadvantages of Selected Capacitor Technologies.**

		Film	Ceramic	CeraLink
<b>Energy Density</b>		80J/dm <sup>3</sup>	350J/dm <sup>3</sup>	172 J/dm <sup>3</sup>
<b>Capacitance Density</b>	0.47 mf/dm <sup>3</sup>	4.37 mF/dm <sup>3</sup>	2.25 mF/dm <sup>3</sup>	
<b>Thermal Runaway</b>	Immune	Prone	Immune	
<b>Reliability</b>	High	Low	Medium	
<b>Temperature</b>	105 °C	125 °C	150 °C	
<b>Inductance [ESL]</b>	High	Medium	Low	
<b>Current Carrying Capability</b>	Low	Medium	High	
<b>ESR</b>	Low	Medium	Medium	

Finally, the volumes of the three capacitors were compared with the film capacitor used inside a 2016 BMW i3 inverter, shown in Figure I.5.10. It can be seen that the capacitor volume can be reduced by 76% and by 81% if CeraLink and ceramic capacitors are used. The results established that the CeraLink capacitor represents the best choice among the three capacitor technologies as a DC bus capacitor for traction inverters because of its higher energy density, higher current conduction capacity, and redundancy.

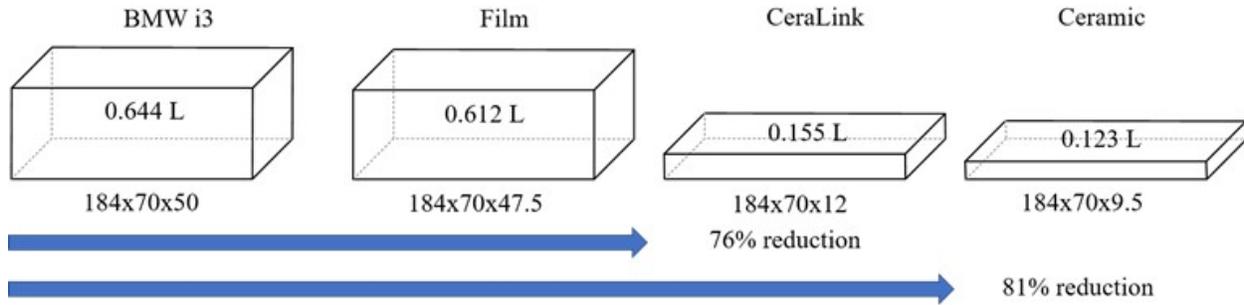


Figure I.5.10 The volume of the selected capacitor technologies compared with that of a 2016 BMW-i3 450 V 475 uF film capacitor.

## Conclusions

In this report, four integrated drive systems were identified from the literature. A brief review of the identified integrated electric drive systems, along with their advantages and disadvantages, is presented. It is evident from the literature that tight integration of the motor and inverter will result in a high-power-density traction drive system, thus introducing cooling challenges.

To understand the required cooling performance of these tightly integrated systems, an FE-based simulation model was created to analyze the radial stator mount IMD. The simulation results showed that the required heat transfer coefficient to cool the motor and inverter for a radial stator mount system is  $6 \text{ kW/m}^2\text{K}$ , which is not a very aggressive target and can be achieved.

Furthermore, to reduce the DC bus capacitor volume, three capacitor technologies were selected for detailed characterization. The CeraLink capacitor showed superior characteristics compared with the ceramic and film capacitors. It can be concluded that the CeraLink capacitor technology will be a viable solution for optimizing overall electric drive volume.

## Key Publications

1. S. Chowdhury, E. Gurpinar, G. Su, T. Raminosa, T. A. Burrell and B. Ozpineci, “Enabling Technologies for Compact Integrated Electric Drives for Automotive Traction Applications,” pp. 1–8 in *2019 IEEE Transportation Electrification Conference and Expo (ITEC)*, Detroit, MI, USA, 2019. DOI: 10.1109/ITEC.2019.8790594

## References

1. Electrical and Electronics Technical Team Roadmap, U.S. DRIVE, Department of Energy, October 2017. Available at <https://www.energy.gov/sites/prod/files/2017/11/f39/EETT%20Roadmap%2010-27-17.pdf>, 2017 [2017, Dec. 12].
2. F. M. D. Throne, R. Marguire, D. Arens, “Integrated Motor/Drive Technology with Rockwell Connectivity.” Available at <http://www.cmafh.com/enewsletter/PDFs/IntegratedMotorDrives.pdf>, [Dec. 14,].
3. J. Wang, Y. Li, and Y. Han, “Integrated Modular Motor Drive Design With GaN Power FETs,” *IEEE Transactions on Industry Applications*, 51(4), pp. 3198–3207, 2015. DOI: 10.1109/TIA.2015.2413380.
4. W. Lee, S. Li, D. Han, B. Sarlioglu, T. A. Minav, and M. Pietola, “A Review of Integrated Motor Drive and Wide-Bandgap Power Electronics for High-Performance Electro-Hydrostatic Actuators,” *IEEE Transactions on Transportation Electrification*, 4(3), 684–693, 2018. DOI: 10.1109/TTE.2018.2853994.

5. R. Abebe et al., “Integrated Motor Drives: State of the Art and Future Trends,” IET Electric Power Applications, 10(8), 757–771, 2016. DOI: 10.1049/iet-epa.2015.0506.
6. G. Su and L. Tang, “A Segmented Traction Drive System with a Small DC Bus Capacitor,” in 2012 IEEE Energy Conversion Congress and Exposition (ECCE), pp. 2847–2853, 2012. DOI: 10.1109/ECCE.2012.6342375.
7. “Metallized Polypropylene Film Capacitor,” Available at [https://www.mouser.ca/datasheet/2/315/panasonic\\_06262019\\_Capacitor\\_Film\\_Leaded\\_\(ECW-F\(E\)-1609057\).pdf](https://www.mouser.ca/datasheet/2/315/panasonic_06262019_Capacitor_Film_Leaded_(ECW-F(E)-1609057).pdf), 2019 [2019, Sep, 09].
8. C5750X7T2W105K250KA, Available at [https://product.tdk.com/info/en/documents/chara\\_sheet/C5750X7T2W105K250KA.pdf](https://product.tdk.com/info/en/documents/chara_sheet/C5750X7T2W105K250KA.pdf), 2016 [2016, Sep, 26].
9. “Capacitors for Fast-switching Semiconductors,” Available at [https://www.tdk-electronics.tdk.com/inf/20/10/ds/B58031\\_LP.pdf](https://www.tdk-electronics.tdk.com/inf/20/10/ds/B58031_LP.pdf), 2019 [2019, Sep, 26].

### Acknowledgements

This work is supported by the DOE Office of Energy Efficiency and Renewable Energy, Vehicle Technologies Office, under contract number DE-AC05-00OR22725. The author wishes to thank the project team members—Emre Gurpinar, Gui-Jia Su, Tsarafidy Raminosoa and Jon Wilkins of ORNL—for their contributions, and Bidzina Kekelia of NREL for collaboration.

## I.6 Ultra-Conducting Copper (ORNL)

### **Tolga Aytug, Principal Investigator**

Oak Ridge National Laboratory  
National Transportation Research Center  
2360 Cherahala Boulevard  
Knoxville, TN 37932  
E-mail: [aytugt@ornl.gov](mailto:aytugt@ornl.gov)

### **Susan A. Rogers, DOE Technology Development Manager**

E-mail: [Susan.Rogers@ee.doe.gov](mailto:Susan.Rogers@ee.doe.gov)

Start Date: October 1, 2018  
Project Funding: \$392,000

End Date: September 30, 2019  
DOE share: \$392,000

Non-DOE share: \$0

### **Project Introduction**

This project focuses on the design, study, and evaluation of scalable and high-throughput synthesis approaches and material technologies for the fabrication of a new class of high-performance copper (Cu) tape conductors using carbon nanotubes (CNT) (i.e., ultra-conductive copper, or UCC, composites). These conductors will have higher electrical (and possibly thermal) conductivity than pure Cu to increase the power density and higher-temperature operation reliability of electric motors while improving their overall efficiency. The new concepts and methods developed under this project are expected to help meet the DOE 2025 cost and performance targets for electric motors. After a decade of global research and development (R&D) efforts [1],[2],[3],[4],[5],[6] the most promising UCC composites are composed of 1-dimensional CNTs and Cu, but the room-temperature performance of these composites is inconsistent. Although a few Cu-CNT composites with increased conductivities (by up to 30% compared with the International Annealed Cu Standard) have been demonstrated, those improvements were limited to micrometer-long sample pieces. Further improvements have been hampered by the lack of controlled alignment of CNTs along the direction of current flow, as well as unstable/irreproducible processing strategies that rendered these processes to laboratory research. Thus, these composites are unsuitable for scalable commercial development and production.

The power losses associated with the electrical resistance of Cu adversely impact the efficiency and performance of all electric devices. Ballistic electrical transport in CNTs (the charge carriers can travel over approximately 500 nm in nanotubes without scattering) is expected to improve the conductivity of the Cu matrix with additional CNT-enabled benefits, including low-weight, flexibility, and better thermal management (Table I.6.1).

**Table I.6.1 Comparison of the Properties of Single Walled CNTs versus Cu**

	Cu	CNT
<b>Electrical Conductivity</b>	59.6 MS/m	100 MS/m
<b>Thermal Conductivity</b>	400 W/m-K	4000 W/m-K
<b>Current Density</b>	$10^6$ A/cm <sup>2</sup>	$10^8$ A/cm <sup>2</sup>

A few promising Cu-CNT composites with improved conductivities have been demonstrated, but only on micrometer-long sample pieces [1],[2],[3],[4],[5]. Further improvement of these UCCs has been hampered by poor fundamental understanding of Cu-CNT interactions affecting bulk electrical and thermal transport properties. In addition, most of the present UCC processing strategies are unstable (leading to inconsistent results) and are limited to laboratory-scale operation, rendering them unsuitable for large-scale commercial development and production. The current approaches to making Cu-CNT composites include electrolytic processes, either to produce a composite deposit containing Cu-ions and CNTs on a cathode, or forming powders that may be consolidated later into usable wire forms; die-casting, to metal forming, by mixing liquid Cu with CNTs; acoustic-assisted coating by which CNTs that are suspended in a fluid are agitated/deposited around a central Cu wire; high-pressure laser chemical deposition with simultaneous laser-induced cladding with Cu; and a powder metallurgical approach using spark plasma sintering to form a Cu composite.

The main problems associated with these methods are (1) the lack of controlled alignment of CNTs along the direction of the current flow, (2) the phase segregation of CNTs from the Cu during wire processing, and (3) the lack of fundamental understanding of how nanotube properties and CNT-Cu interfaces/interactions affect macroscale properties. Based on a theory-aided experimental approach, this project addresses these fundamental challenges to successful development of UCCs with electrical conductivities exceeding that of pure Cu.

### Objectives

Cost and size are the key barriers to achieving the Electrical and Electronics Technical Team 2025 electric traction drive systems technical R&D targets. In the case of electric motors, reductions in volume and improvements in efficiency are limited in part by the electrical conductivity limitations of copper windings. In addition, considering that the stator with copper winding constitutes nearly 40% of the total motor cost, the main R&D strategy is currently focused on reducing cost by using new materials with improved capabilities and performance, and applying them in motor design innovations [6]. The overall objective of this project is to design and develop a new class of high-performance Cu wires, using CNTs that are higher in electrical and thermal conductivity, to increase the power density of electric motors while improving the overall efficiency. Specific R&D efforts in FY 2019 included (1) optimization of processing protocols and identification of the two most promising scalable approaches for the prototyping of carbon nanomaterial-enabled UCC conductors, (2) integration of additional Cu-CNT stack(s) on the first Cu-CNT-Cu architecture and investigation of their influence on the electrical performance, (3) theoretical modeling to understand metal-nanocarbon interface properties for optimized electronic/thermal transport characteristics, (5) understanding the impact of UCC winding conductivity on traction motor performance, (6) establishing a roll-to-roll deposition capability for applying CNTs on Cu tapes.



## Approach

Using scalable fabrication approaches, our overall approach is to couple theoretical and experimental efforts to enable the design and reproducible assembly of CNT-Cu multilayer composites that have electrical and thermal conductivity exceeding that of pure Cu and current Cu-CNT composites. To achieve this, two interrelated and equally important tasks are being pursued: (1) development of controllable processing techniques for the design and scalable, reproducible fabrication of advanced multilayer composites and (2) theory-guided optimization for high-performance Cu-CNT multilayer composites. Figure I.6.1 schematically describes the process flow for producing UCC tapes, starting with formulation of stable CNT dispersions, deposition of uniform CNT coatings using solution-based commercially viable practices, homogeneous deposition of thin films of Cu overlayers onto CNT-coated tapes, and post-thermal treatment procedures to produce multilayer Cu-CNT-Cu composite architectures.

Samples were characterized by scanning electron microscopy (SEM) for microstructural investigations. Nanotube alignment was analyzed by both SEM and polarized confocal Raman spectroscopy using a Renishaw in Via Raman microscope (Wotton-under-Edge, UK) with a linearly polarized 532 nm laser source. Cross-sectional microstructures of samples were studied by Z-contrast scanning transmission electron microscopy (STEM). Specimen preparation was carried out by focused ion beam methods, and STEM images were recorded using a Nion Ultra STEM operating at 200 kV. The electrical conductivity of the new composites was characterized in the temperature range from 4 to 400 K using a physical property measurement system (PPMS).

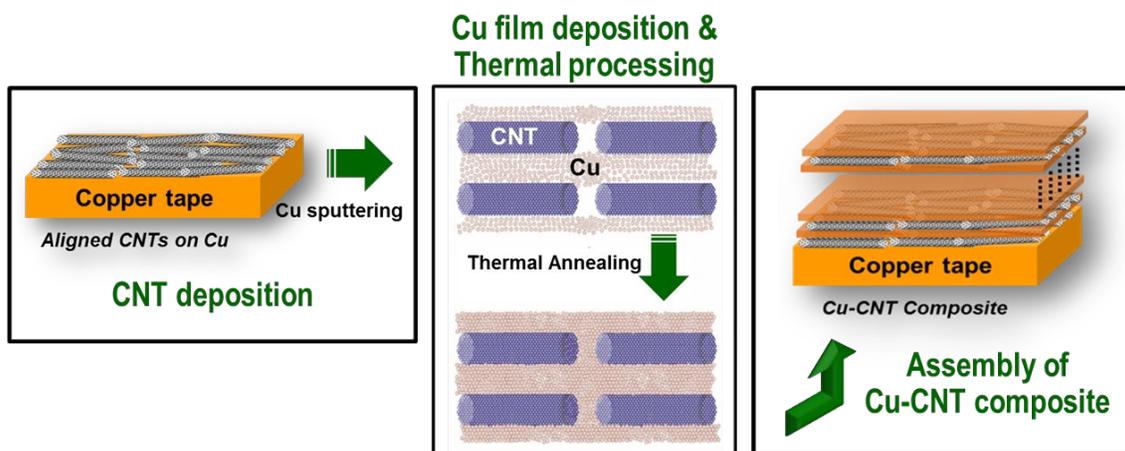


Figure I.6.1 Schematic illustration of the process flow for producing Cu-CNT-Cu multilayer composite tapes.

## Results

### *Sonospray process optimization*

Understanding the influence of the substrate inclination angle on CNT alignment is essential to attaining reproducible UCC properties. Note that the techniques identified in this study are expected to result in alignment of nanotubes with their axes parallel to the shear or flow-field direction induced between the droplets and the Cu substrate. In the case of sonospray, shear-induced alignment originates from shearing of the droplets containing CNTs against the inclined Cu surface. In the electrospinning approach, it is expected that elongation of the droplets during suspension extrusion under a high voltage applied between the syringe and the rotating collector should provide alignment of CNTs on the Cu collector. SEM and polarized Raman spectroscopy results from sonospray samples confirmed that shear-induced alignment of CNTs can occur at all experimentally accessible Cu tape inclination angles. Figure I.6.2 compares and correlates the surface morphologies and changes in the G-band intensity (from Raman spectroscopy) of three sonospray samples, processed at different Cu tape inclination angles. Corroborating with SEM images, for all the inclination angles studied (e.g., 5°, 15°, 30°) the Raman data show variations in the intensity of the G-band at approximately 180° intervals, indicating alignment of CNTs along the coating direction with respect to the

sample orientation. In addition, irrespective of the substrate inclination angle, we observed that preferential shear-induced alignment initiates with an increase in the deposited CNT amount on the Cu surface (Figure I.6.3). The samples coated with low CNT loading display nonuniform, random surface coverage with no obvious alignment, whereas the ones with higher loading show alignment parallel to the flow-field direction.

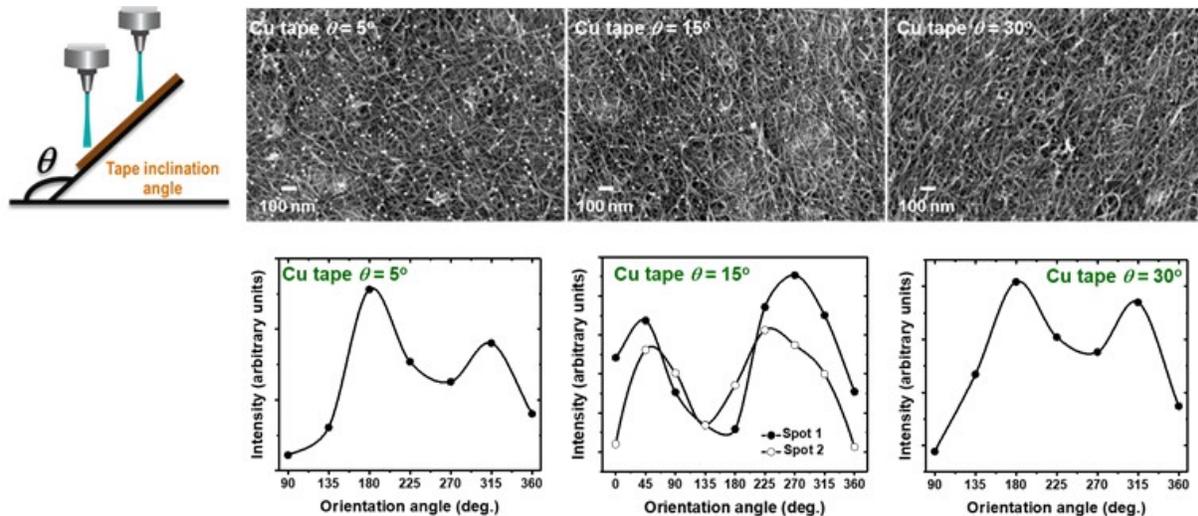


Figure I.6.2 Scanning electron microscopy images and G-band intensity variations on single-walled CNT-coated copper tapes at various inclination angles during ultrasonic spray coating. Inset shows a schematic of the tape inclination angle.

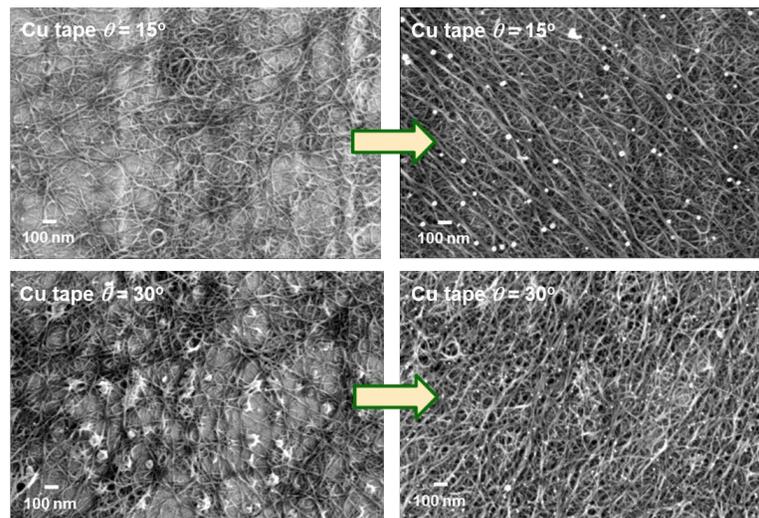


Figure I.6.3 Scanning electron microscopy images displaying the shear-induced alignment of CNTs with increased CNT loading on copper tapes.

### ***Prototyping of multilayered carbon nanomaterial enabled UCC conductors using a sonospray approach***

Understanding the electrical properties of the composite at high temperatures is particularly important for reliable and efficient operation of electric motors. Therefore, using PPMS, temperature-dependent electrical properties of single-layer and multilayer Cu-CNT-Cu samples processed at relatively optimized parameters were measured at various temperatures ranging from 0 to 125°C. Results shown in Figure I.6.4 (left panel) verified a reduction of electrical resistivity of >10% for a multilayer Cu-CNT-Cu (3 stacks) prototype over the entire temperature range compared with reference pure Cu samples. However, note that this performance did not scale linearly with the additional number of Cu-CNT stacks. That is, compared with the observed 5–6% decrease in resistivity for the single-layer UCC composite, the decrease in resistivity of the three-layer

counterpart was expected to exceed 15%. We think this behavior was highly dependent on the uniformity and structural quality of each additional Cu and CNT layer. To evaluate this idea, Z-contrast STEM investigations were conducted to analyze the cross-sectional microstructure of the select multilayer UCC samples (Figure I.6.4, right panel). Z-contrast STEM provided detailed information related to thickness, microstructural defects, and possible doping effects throughout the thickness of the samples. Note that the higher-Z elements (Cu with  $Z = 29$ ) appear brighter than the lower-Z elements (C with  $Z = 6$ ) in this imaging mode, revealing darker CNT layers and brighter regions of Cu. For analysis, two different UCC specimens (single-layer and 3-layer) were prepared using focused ion beam milling. While cross-sectional images show relatively dense and homogenous Cu coverage over the first and second CNT layers, a less dense and defective Cu microstructure is observed on the third CNT layer, most likely degrading the electrical performance of the samples. Hence, it was not surprising to observe a nonlinear improvement in conductivity with increasing numbers of Cu/CNT stacks. These results underscore the importance of process optimization to obtain the best possible electrical performance characteristics of multilayer UCC prototypes. Another notable observation was the presence of Cu nanoparticles inside the CNT matrix (Figure I.6.4, right panel). Cu diffused within the CNT layers either during the sputter deposition or through the post-annealing process of the Cu and CNT layers at high temperatures ( $\sim 500^\circ\text{C}$ ), or through both. Diffusion of Cu not only is important to realize a highly percolative conductive network throughout the entire CNT/metal matrix ensemble, but also is essential to facilitate modification of CNTs via Cu doping. Doping mainly (1) improves transport across interparticle contacts by reducing tunneling barriers or to provide conducting shunts around defective nonconducting regions and (2) affects the electronic structure of CNTs through charge-transfer doping.

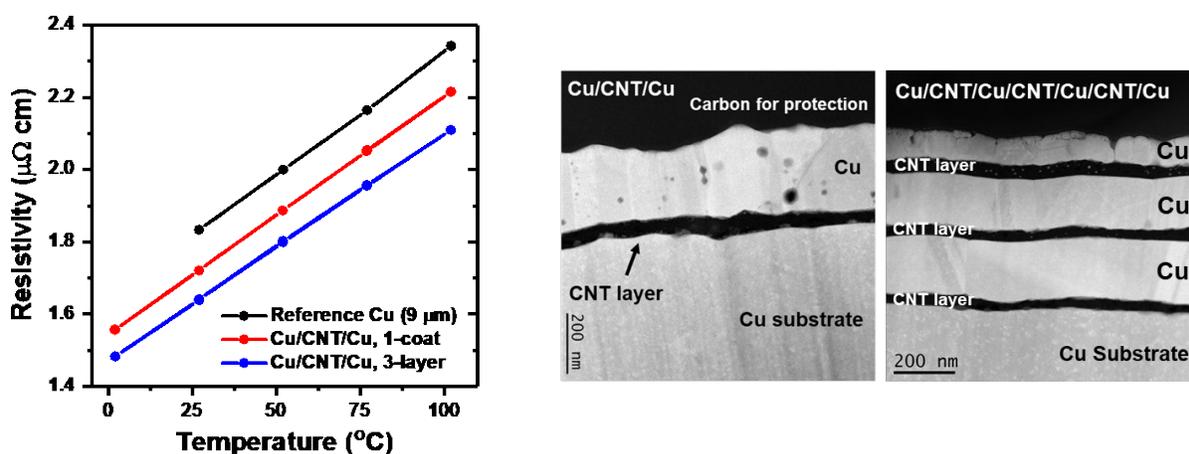


Figure I.6.4 (Left) Electrical properties of single-layer and three-layer Cu-CNT-Cu composite architectures as a function of temperature ranging from 0 to  $120^\circ\text{C}$ , displaying reduced resistivity compared with the reference Cu substrate. (Right) Representative Z-contrast STEM cross-sectional microstructures of single and 3-layer UCC composites using similar processing conditions.

While metallic tubes show a constant electronic DOS around the Fermi level, there exists an energy gap for the semiconducting tubes. However, even with a very small amount of Cu doping (e.g., 0.75 at. %), the DOS for the semiconducting tubes peaks at the Fermi energy; and at higher doping levels (e.g., 50 at. %) the gap disappears. This result indicated an increase in the conduction electrons and the conversion of initially semiconducting CNTs into metallic tubes, while the metallic ones became better conductors with higher DOS at the Fermi level (the latter data are not included in Figure I.6.5).

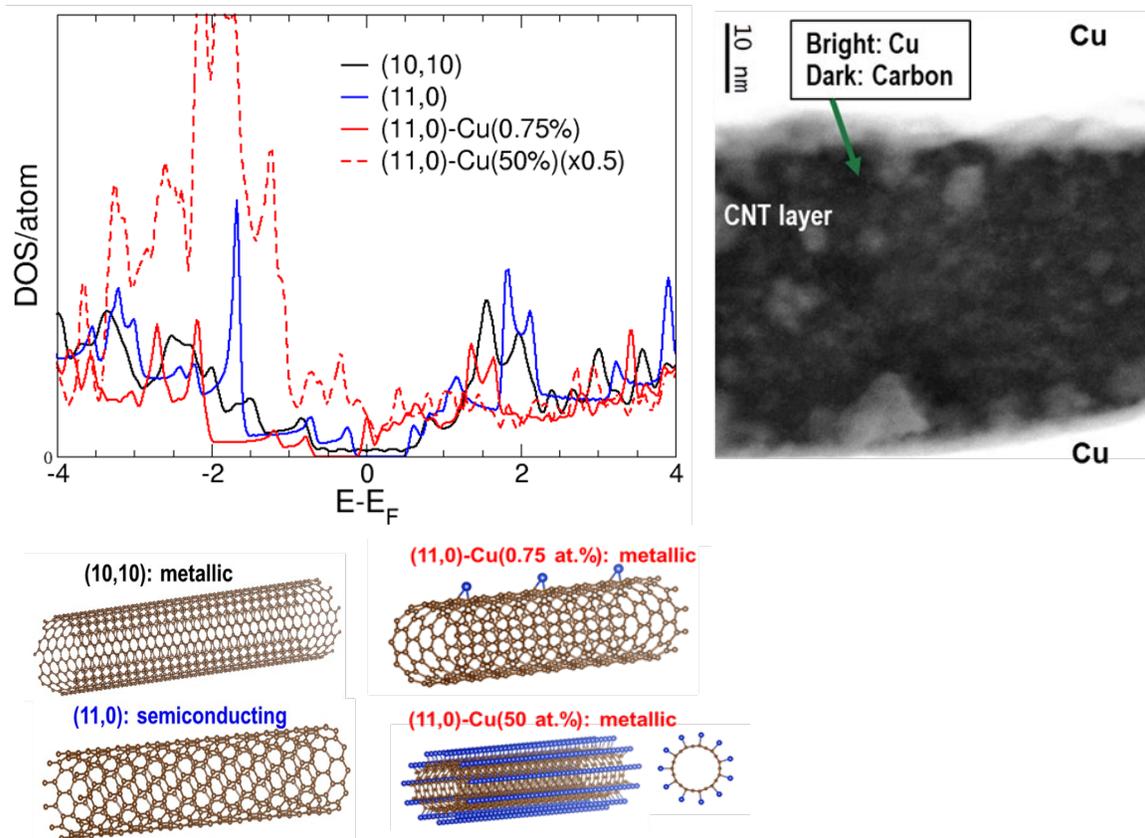


Figure I.6.5 Energy diagram showing the density of states for metallic, semiconducting, and Cu-doped semiconducting CNTs (left panel). Z-contrast STEM image of a Cu-CNT-Cu sample, displaying Cu nanoparticles within the CNT layer (right panel). Inset shows the schematics of the undoped metallic, and semiconducting, and Cu-doped semiconducting CNTs used in the first-principles density functional theory calculations.

Developing materials with improved capabilities and performance and applying them in motor design innovations are particularly important to meet DOE ELT 2025 performance and cost targets. Hence, we investigated the feasibility of using UCC composite tapes for the windings of traction motors. Three motor types were studied (1) a spoke internal permanent magnet motor (IPM) with distributed winding; (2) an outer rotor surface permanent magnet motor (SPM) with tooth winding, and (3) a slotless outer rotor SPM with distributed winding (Figure I.6.6). Note that, while the ferromagnetic saturation affects the former two topologies, it does not influence the latter. It was found that the ferromagnetic saturation of the lamination materials reduced the effectiveness of the highly conductive winding to improve the power per unit of volume. For machine topologies that were not affected by ferromagnetic saturation, the power density improvement reached the theoretical expectation. It was found that a UCC composite with 30% higher conductivity than Cu could enable a 10% reduction in the active volume for conventional motors and a 12% reduction for motors for which the magnetic saturation is not an issue (Figure I.6.7). However, it is worth noting that the volume reduction was lower than the theoretical expectation because of the magnetic saturation effect in the steel. In both cases, highly conductive winding materials can also provide other important benefits, such as reduced PM material usage, that can lead to significant cost reductions as well as overall improvement in the efficiency by extending the high efficiency operating area into light loads and high speeds.

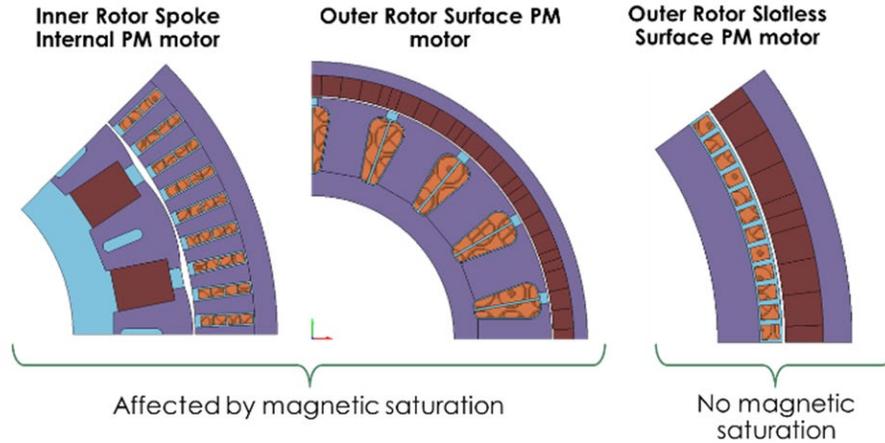


Figure I.6.6 Cross-sectional schematic illustration of the three topologies of heavy rare-earth-free permanent magnet traction motors.

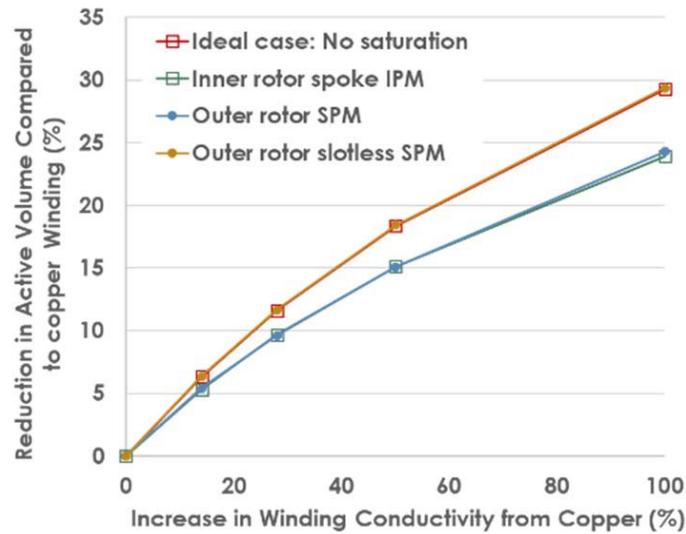


Figure I.6.7 Reduction in active volume as a function of winding conductivity for different motor topologies.

As a part of the UCC development efforts, we recently integrated roll-to-roll processing capability with the sonospray equipment to enable scalable deposition of CNTs and produce long pieces ( $\geq 1$  m) of UCC composites for commercial testing and optimization. For this, we designed and assembled a compact tape handling system that includes a radiant heater, for roll-to-roll multi-coat CNT deposition on 0.50 in. wide and up to 25 ft long Cu tapes (Figure I.1.6.8). To facilitate CNT alignment, the spray angle can be varied by adjusting the idler spool. The radiant heater continuously cures the CNT coating and enables multi-coat deposition. The tape speed can be varied from 0.5 mm/sec to 100 mm/sec. Long-length prototyping has been started.

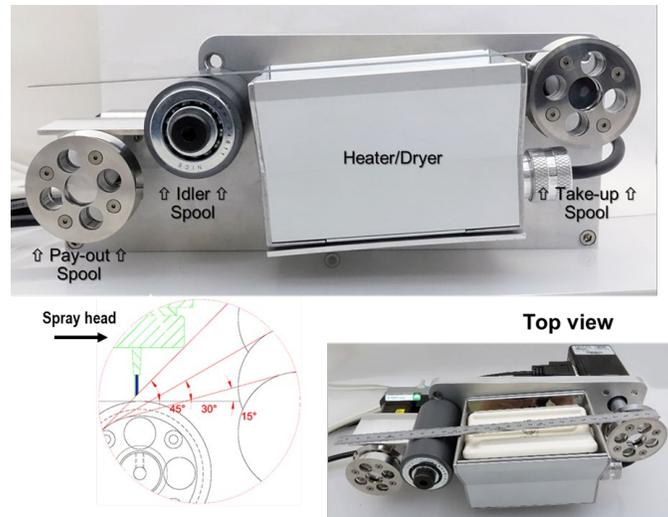


Figure I.6.8 Photograph of the newly designed roll-to-roll CNT deposition system.

### Conclusions

Advanced materials with higher electrical conductivity are needed to increase power density and reduce cost while improving the performance and reliability of electric motors. Under this multiyear project, using scalable, cost-effective, and commercially viable processing methods, we have demonstrated the feasibility of a novel materials/computational modeling platform that can facilitate the design and fabrication of advanced UCC materials for a broad range of industrial applications. The benefits that will be gained from this research can lead to high-efficiency, high-density, reduced-volume/weight electric motors beyond the limits of what is achievable today. Specific accomplishments include (1) identified the viability of two scalable processing techniques for CNT deposition—sonospray and electrospinning; (2) demonstrated that theoretical modeling can support experimental efforts; (3) analyzed the influence of the CNT interface on the in-plane thermal transport properties; (4) integrated additional Cu-CNT layers on the first Cu-CNT-Cu architecture, performed electrical characterizations, and demonstrated improved conductivity compared with the reference pure Cu; (5) evaluated the impact of UCC winding conductivity on various traction motor topologies. Because of the multistep processing and the associated parameter space for producing UCC tapes, future work will involve the optimization of processing protocols and provisions to attain reproducible results along with the highest possible performance characteristics. Future efforts will also include the production of long-length UCC composites and computational feasibility studies to support the integration of UCCs in electric drive components.

### Key Publications

1. Tolga Aytug, “Ultra-Conducting Copper,” presented at the 2019 DOE Vehicle Technologies Office Annual Merit Review, June 2017, Washington, DC.
2. T. Raminosa and T. Aytug, “Impact of Ultra-Conducting Winding on the Power Density and Performance of Non-Heavy Rare Earth Traction Motors,” *IEEE International Electric Machines and Drives Conference (IEMDC)*, 2019.
3. K. Li, L. Skolrood, S. Ozcan, M. McGuire, F. List, A. Lupini, B. Ozpineci, and T. Aytug, “Electrospinning Enabled Ultra-Conductive Copper-Carbon Nanotube Composites” (in progress).

### References

1. H. Stillman, and M. Burwell, “Ultraconductive Copper Wire: Overview of Worldwide Research and Development,” *Copper 2013*, International Copper Association, Santiago Chile, December 1–4, 2013.

2. D. F. Lee, M. Burwell, and H. Stillman, *Priority Research Areas to Accelerate the Development of Practical Ultra-conductive Copper Conductors*, ORNL/TM-2015/403, 2015.
3. C. Subramaniam, T. Yamada, K. Kobashi, A. Sekiguchi, D.N. Futaba, M. Yumura, and K. Hata, “One Hundredfold Increase in Current Carrying Capacity in a Carbon Nanotube–Copper Composite,” *Nat. Commun.* 4, 2202, 2013.
4. C. Subramaniam, A. Sekiguchi, T. Yamada, D.N. Futaba, and K. Hata, “Nano-scale, Planar and Multi-tiered Current Pathways from a Carbon Nanotube–Copper Composite with High Conductivity, Ampacity and Stability,” *Nanoscale*, 8, 3888, 2016.
5. T. Holesinger, *Development of Carbon Nanotube Composite Cables for Ultra-Deepwater Oil and Gas Fields*, RPSEA Phase II Final Report, 2013.
6. *Electrical and Electronics Technical Team Roadmap*, U.S. DRIVE, Department of Energy, 2017.

## I.7 Power Electronics: Active Device and Passive Component Evaluation (SNL)

### Jack Flicker, Principal Investigator

Sandia National Laboratories  
 P.O. Box 5800, MS 1033  
 Albuquerque, NM 87123  
 E-mail: [jdflick@sandia.gov](mailto:jdflick@sandia.gov)

### Susan Rogers, DOE Technology Development Manager

U.S. Department of Energy  
 E-mail: [susan.rogers@ee.doe.gov](mailto:susan.rogers@ee.doe.gov)

Start Date: October 1, 2018	End Date: September 30, 2023	
Project Funding (FY19): \$275,000	DOE share: \$275,000	Non-DOE share: \$0

### Project Introduction

This project is part of a multi-lab consortium that leverages U.S. research expertise and facilities at National Labs and universities to significantly advance electric drive power density and reliability, while simultaneously reducing cost. The final objective of the consortium is to develop a 100 kW traction drive system that achieves 33 kW/L, has an operational life of 300,000 miles, and a cost of less than \$6/kW. One element of the system is a 100 kW inverter with a power density of 100 kW/L and a cost of \$2.7/kW. New materials such as wide-bandgap semiconductors, soft magnetic materials, and ceramic dielectrics, integrated using multi-objective co-optimization design techniques, will be utilized to achieve these program goals. This project focuses on a subset of the power electronics work within the consortium, specifically the evaluation of wide-bandgap power semiconductor devices (primarily SiC) as well as passive elements (primarily ceramic capacitors).

### Objectives

Silicon Carbide (SiC) is a wide-bandgap (WBG) semiconductor that has matured to the point where power electronic devices are now commercially available. However, it remains to be seen whether such devices can be used to construct a power converter (inverter) that meets the consortium's goals for performance and reliability. As such, in collaboration with consortium partners (other National Labs as well as universities), this project is focused on the performance and reliability evaluation of these devices. Additionally, the passive elements within power electronic converters must be concurrently developed and evaluated to ensure that the performance promised by SiC can be realized in a real converter, and this project addresses that need as well. Note that another WBG semiconductor, Gallium Nitride (GaN), is addressed under a different project under the consortium. Similarly, magnetic materials, which are likewise critical to the performance of WBG-based power converters as well as electric motors, are addressed under a different project. Details regarding SiC device and capacitor testing, as well as the test circuit developed to perform this work, are described below.

### SiC Testing

WBG semiconductors will be necessary to achieve the performance targets of the inverter, and the most mature WBG semiconductor (SiC) will be used extensively the near future to achieve advances in electric drive technology. In conjunction with university partners, state-of-the-art SiC devices (switches and diodes) will be evaluated. Further, a strong focus will be placed on design for reliability, which to date has often been traded for high performance and low cost. While the latter two attributes are necessary for automotive applications, reliability is also of paramount importance. Thus, designs that meet all three criteria specific to the traction drive inverter of interest will be created, and devices based on these designs will be fabricated. In conjunction with NREL and ORNL, these devices will then be incorporated into power modules featuring advanced thermal management and minimized electrical parasitics to meet the performance goals of the program.



### Capacitor Testing

Passive components (inductors and capacitors) are also of high importance to the overall consortium metrics. Ceramic dielectric capacitors are preferred because of their high energy density and reliability. However, achieving high performance and long lifetime at elevated temperatures has proven elusive for ceramic dielectrics. Instead of addressing this deficiency through alterations in material composition (which have not yet proven fruitful), an innovative bipolar switching strategy to periodically clear a build-up of oxygen vacancies at electrode surfaces has been implemented. This allows for ceramic dielectrics to exhibit long lifetime at high temperature. The dynamics of this strategy will be explored and optimized through the design and fabrication of a large-scale testbed for capacitor degradation evaluation.

### WBG Device Test Circuit

In order to evaluate fabricated devices within the consortium (including the SiC active devices and ceramic capacitors described herein, and also GaN devices and inductors), Sandia has designed an advanced component test-bed that reproduces the functionality of an end-use vehicle inverter that is consistent with the consortium's targets. This allows for analysis of device performance and reliability under realistic scenarios. Once fabricated devices are available, the realistic evaluation of the operation of devices in the test-bed will be used by device designers to identify performance or reliability issues before incorporation into a high-power, high-density consortium exemplar inverter. Additionally, the test-bed provides validation opportunities for the development of realistic device models under varied usage scenarios for incorporation into system topology optimization.

## Approach

### SiC Testing

Sandia has been consulting with consortium university partners (primarily OSU and SUNY) and providing feedback on device designs and testing. Design criteria have focused on field-shaping within SiC devices through the design of the junction termination extension (JTE), as well as evaluating current commercial SiC devices for reliability. Pending the completion of the test circuit and receipt of devices from the university partners, evaluation of SiC devices will be carried out in the testbed.

### Capacitor Testing

In order to reduce costs, ceramic capacitors are typically fabricated using base-metal electrodes such as Ni [1]. During the fabrication process, these require a reducing environment during sintering to avoid oxidation. An unintended side-effect of this reducing environment is that oxygen vacancies are created in the ceramic material [2]. As with any charged species, these vacancies will migrate under an applied voltage and preferentially collect at the electrode/dielectric interface (see Figure I.1.7.1). This gettering of defects results in a loss of insulation resistance and an increase in the DC leakage of the capacitor, which negatively affects the performance of the power electronics [3]. Furthermore, this leakage will increase operational temperature, resulting in quicker diffusion of vacancies. This process is a positive feedback loop that leads to an accelerating failure mechanism.

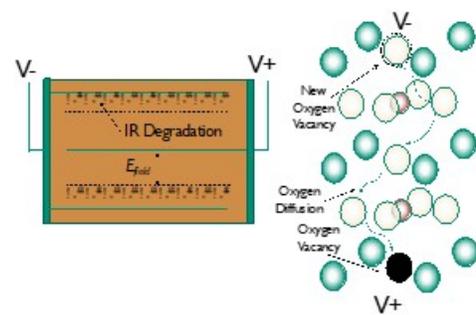


Figure I.1.7.1 Oxygen vacancy migration under applied bias can lead to degradation of ceramic capacitors.

The conventional wisdom for increasing capacitor reliability is to alter the fabrication process or materials properties of the capacitor. This is a long, complicated process that requires significant cost and effort to achieve. Instead of altering the capacitor properties, we are investigating the ability to heal capacitors periodically via reverse biasing. This reverse biasing should allow for re-distribution of oxygen vacancies to lengthen the lifetime of the component. To evaluate this mechanism, we propose a method of altering the

typical DC-field highly accelerated lifetime tests on the capacitor to an AC field variety. This reversing electric field can limit the transport of oxygen vacancies.

**Test Circuit**

Fabrication of new laboratory-scale devices can be beset with many reliability and performance challenges that are not present in commercialized devices. In order to move forward to a next generation of prototype device, it is necessary to understand its strengths and weaknesses in an appropriate end-use testbed. This testbed must deliver realistic stresses on the device that it will see in field use, but at a lower stress level than would be experienced in the field. By having realistic usage data available to device designers and fabricators, the process of developing a device can be accelerated and weaknesses of past devices can be addressed quickly in future generations (Figure I.7.2).

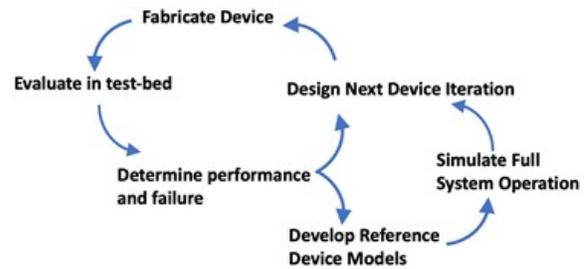


Figure I.7.2 The evaluation of prototype devices in a custom testbed can inform both device designers on the strengths/weaknesses of their prototypes, as well as validate device models for simulation.

In order to evaluate fabricated devices in the consortium, SNL is developing a scaled motor drive test-bed that can be tailored to prototype devices (both in voltage and current stress delivered) while still applying realistic end-use stress profiles that the device will see when mature. In order to carry this out, a 3-phase DC motor drive was designed (Figure I.7.3). This design is split into two sections, a control section and a power stage section. The control section applies a realistic PWM profile to the device using an embedded microcontroller specifically for motor drive applications. The three-phase power stage contains a single stage that is daughter-carded. This daughter card can be quickly removed and replaced with a card containing new device types. By daughter-carding the entire stage, parasitic inductance is kept commensurate with the other two stages to minimize asymmetric operation and get a better view of the device performance.

**Prototype Motor Controller Component Testbed Design**

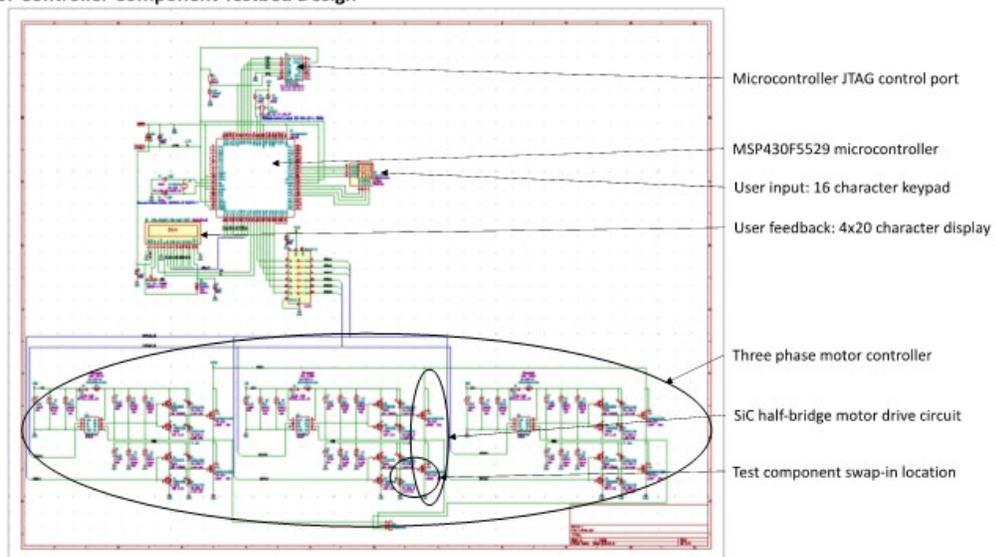


Figure I.7.3 Schematic for WBG device testbed with embedded motor control.

**Results**

**SiC Testing**

As discussed above, testing of SiC power devices is awaiting the receipt of consortium-fabricated devices as well as the completion of the motor-drive testbed.

**Capacitor Testing**

SNL carried out preliminary bipolar switching testing on commercially available X7R capacitors. A DC bias of 10x the rated voltage was applied at a temperature 125°C above the rated temperature. These voltage and temperature levels are characteristic of highly-accelerated DC life tests for capacitors. The leakage current of the devices was monitored at DC bias (no switching) and bipolar operation with switching frequencies of 0.1 and 2.5 Hz. These preliminary results (subset shown in Figure I.7.4) show that bipolar switching can result in significantly increased time-to-failure for ceramic capacitors. The 2.5 Hz bipolar switching scheme (blue trace) demonstrated a ~4x lifetime increase compared to the DC voltage stress (black trace).

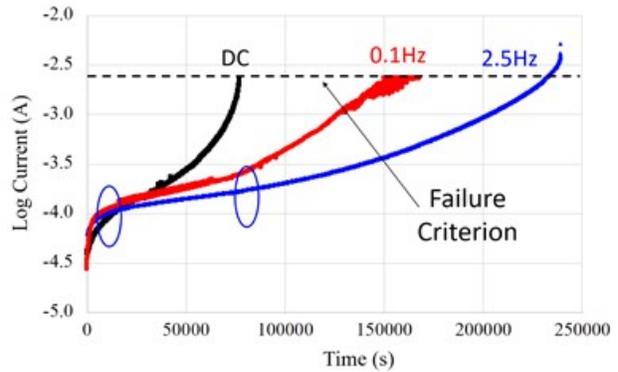


Figure I.7.4 The lifetime of DC capacitors can be increased through the implementation of a bipolar switching scheme.

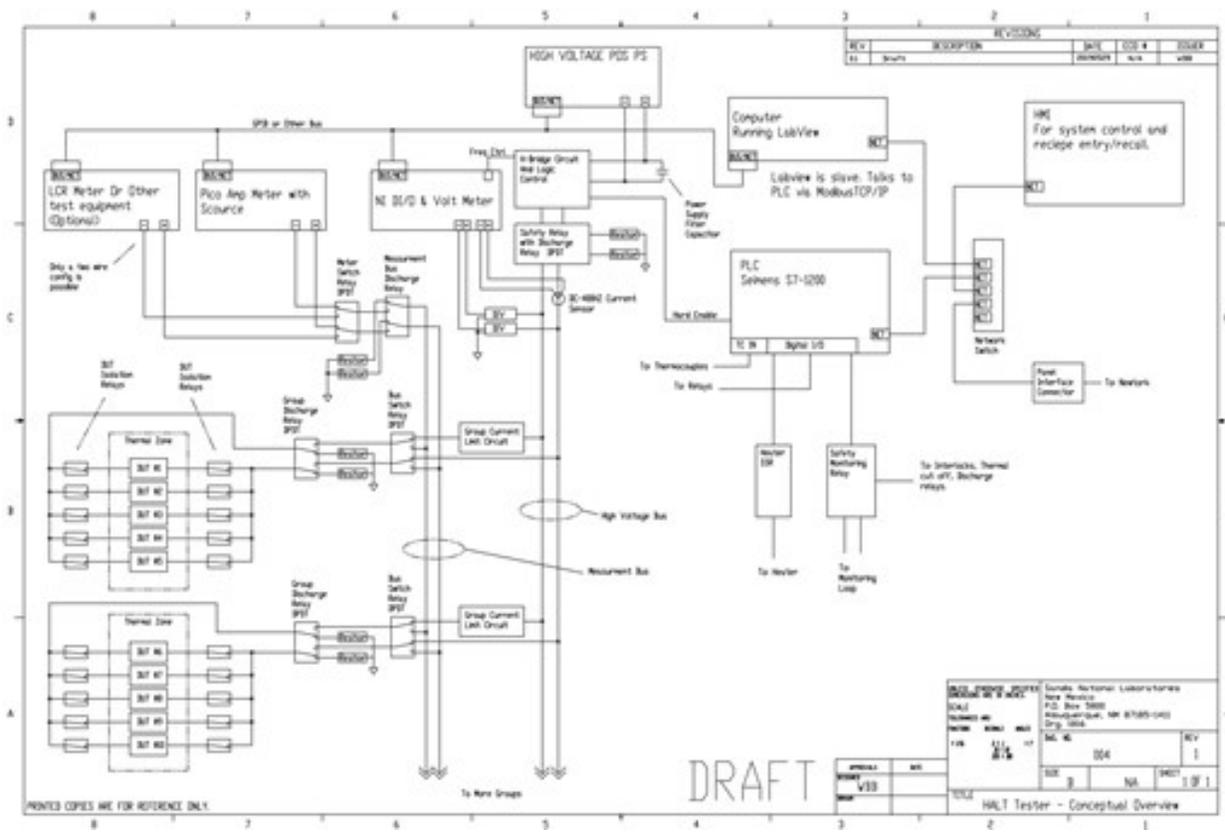


Figure I.7.5 Design layout for capacitor test setup which allows for stress and evaluation of a population of 40 capacitors under bipolar switching.

While this initial testing shows promise, further work is needed both to elucidate the exact mechanisms for this bipolar switching and evaluate if the effect is large enough for real-world practical application. The necessary frequency of healing procedures should decrease significantly at less accelerated conditions. Larger sample sets are required to both obtain Weibull statistics and, simultaneously, explore changes in MTTF within a wide temp/field/frequency space. To accomplish this, a test setup with more flexibility for application of stress (both

voltage and temperature) and large sample population is needed. SNL has been in the process of designing this second-generation test setup for bipolar capacitor switching (Figure I.7.5).

This test setup will be able to carry out a stress-and-measure protocol for a population of 40 capacitors. The system is divided into two buses, one for stressing and one for measurement. Each of the DUTs are divided into 5-10 groups and one group may be measured while the rest can be stressed. Failed DUTs will be detected by a combination of voltage/current monitoring and power supply compliance monitoring. Upon a DUT failure, the DUT will be identified during the measurement sequence, then isolated. All cycle times between stress and measure are user-controllable with a maximum temperature of 300°C (with 25°C/min ramp rate) and a voltage stress of 600 V (2.6 A/1.5 kW).

The design review of this test setup has been completed and fabrication and procurement of the bill of materials is underway.

### *Test Circuit*

The motor drive test circuit has been fabricated on a breadboard to ensure correct functionality before the PCB design files are sent to a fabrication house. Figure I.7.6 shows the as-fabricated power stage board and daughter-card (left) as well as the embedded motor control with user input (right).

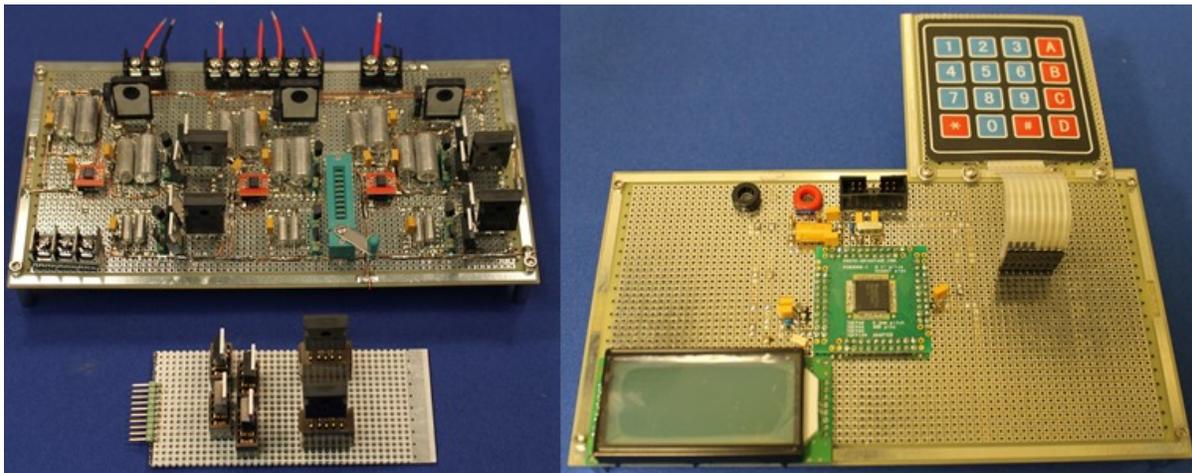


Figure I.7.6 Breadboard of 3-phase DC motor drive power stage (left) and embedded controller (right).

The motor drive power stage and controller were tested to ensure correct functionality. Power was supplied by a 1000 V, 10 A DC power supply and a three-phase controllable load was placed on the drive output. The board functioned correctly up to a level of 200 V (see Figure I.7.7). At this level, the load consumed 7.5 A (1500 W or ~2 HP), the temperature of the discrete gate driver (without heat-sinking) rose to 105°C, and the

power switches (also without heat-sinking) rose to 80°C. In a full PCB-fabricated setup with surface-mount parts and proper heat-sinking, there should be no issues achieving the ~1000 V DC bias level.

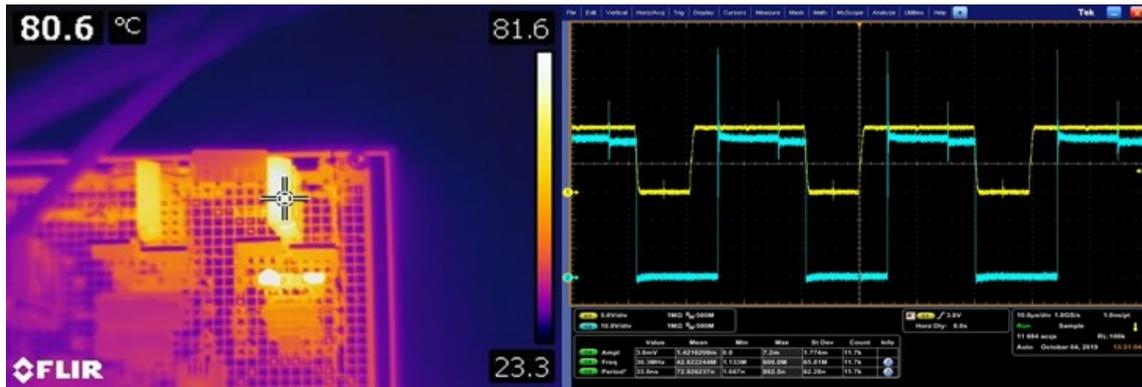


Figure 1.7.7 (left) Thermal image of one leg of the power stage showing the temperature of power switches (centered at the crosshairs) and gate driver (just below the crosshairs) at 200 V and 7.5 A. (right) Gate drive signaling at 200V and 7.5 A.

## Conclusions

During FY19, we have demonstrated the ability of a bipolar switching scheme to improve ceramic capacitor lifetime. This proof-of-concept result is being expanded through the fabrication of a test setup that will allow for testing of a large population of capacitors (40) under a variety of temperature and voltage stresses and bipolar switching profiles. This will allow for full characterization of the activation energy for oxygen vacancy migration as a function of voltage/temperature as well as the efficacy of different bipolar switching profiles. Such information will allow for incorporation of ceramic capacitors with bipolar switching into an electric traction drive.

Additionally, in FY19 a three-phase motor drive component test-bed was fabricated. This test-bed allows for the application of realistic operational stress to prototype devices fabricated within the consortium. A preliminary breadboard of the circuit has been fabricated and tested to ensure operation. A fully-integrated version is being constructed and will be used to test both SiC and GaN devices fabricated by Sandia as well as consortium partners.

## References

1. D Donahoe and C Hillman. Failures in base metal electrode (bme) capacitors. In 23rd Capacitor and Resistor Technology Symposium, pages 129–138, 2003.
2. T Nomura, Y Nakano, and A Satoh. Multilayer ceramic chip capacitor. US Patent 5,319,517, 1994.
3. X Zhang, T Hashimoto, and DC Joy. Electron holographic study of ferroelectric domain-walls. *Applied Physics Letters*, 60(6):784–786, 1992.

## Acknowledgements

This work is supported by the DOE Office of Energy Efficiency and Renewable Energy, Vehicle Technologies Office. Sandia National Laboratories is a multi-mission laboratory managed and operated by National Technology and Engineering Solutions of Sandia, LLC., a wholly owned subsidiary of Honeywell International, Inc., for the U.S. Department of Energy's National Nuclear Security Administration under contract DE-NA0003525. The views expressed in the article do not necessarily represent the views of the U.S. Department of Energy or the United States Government.

## I.8 Bottom-Up Soft Magnetic Composites (SNL)

### Todd Monson, Principal Investigator

Sandia National Laboratories  
 P.O. Box 5800, MS 1415  
 Albuquerque, NM 87185  
 E-mail: [tmonson@sandia.gov](mailto:tmonson@sandia.gov)

### Susan Rogers, DOE Technology Development Manager

U.S. Department of Energy  
 E-mail: [susan.rogers@ee.doe.gov](mailto:susan.rogers@ee.doe.gov)

Start Date: October 1, 2018

End Date: September 30, 2023

Project Funding (FY19): \$125,000

DOE share: \$125,000

Non-DOE share: \$0

### Project Introduction

In order to meet 2025 goals for enhanced peak power (100 kW), specific power (50kW/L), and reduced cost (3.3 \$/kW) in a motor that operates at >20,000 rpm, improved soft magnetic materials must be developed. Additionally, improved soft magnetic materials will enable high performance motors that do not rely on rare earth materials. In fact, replacement of permanent magnets with soft magnet materials was highlighted in the Electrical and Electronics Technical Team (EETT) Roadmap [1] as a potential R&D pathway for meeting 2025 targets. At the higher targeted rotational speeds, eddy current losses in conventional soft magnetic materials, such as silicon steel, will begin to significantly decrease motor efficiency. One possible solution is to use soft magnetic composites (SMCs), which combine magnetic particles with an insulating matrix to increase electrical resistivity ( $\rho$ ) and decrease eddy current losses, even at higher operating frequencies (or rotational speeds). Currently, SMCs are being fabricated with values of  $\rho$  ranging between  $10^{-3}$  to  $10^{-1}$   $\mu\text{ohm}\cdot\text{m}$  [2], which is significantly higher than 3% silicon steel ( $\sim 0.5$   $\mu\text{ohm}\cdot\text{m}$ ) [3]. Additionally, the isotropic nature of SMCs is ideally suited for motors with 3D flux paths. Furthermore, the manufacturing cost of SMCs is low and they are highly amenable to advanced manufacturing and net-shaping into complex geometries, which would significantly reduce or eliminate manufacturing costs. However, there is still significant room for advancement in SMCs, which will allow for improved performance in electrical machines. For example, despite the inclusion of non-magnetic insulating material, their electrical resistivities are still far below that of ferrites ( $10 - 10^8$   $\mu\text{ohm}\cdot\text{m}$ ).

In this project, we are developing SMCs from the bottom up, with a final objective of creating composites with high volume loading (and therefore high saturation magnetization) while increasing the value of  $\rho$  several orders of magnitude over the current state-of-the-art in SMCs. We are accomplishing our goals by starting with particles of the  $\gamma'$ -Fe<sub>4</sub>N phase of iron nitride, which has a saturation magnetic polarization ( $J_s$ ) slightly greater than Si steel (1.89 T) [4] and a  $\rho$  of  $\sim 2$   $\mu\text{ohm}\cdot\text{m}$  [5]. In our bottom-up approach we begin by coating the magnetic particles with a diamine, which can chemically react directly with epoxide terminated monomers and form a cross-linked epoxy composite. This “matrix-free” approach to composite formation will not suffer from the same nanoparticle aggregation and phase separation effects commonly observed in conventional nanocomposites [6]. Furthermore, it should ensure better separation between magnetic particles and significantly reduce or eliminate inter-particle eddy currents. There is already an established precedent for the use of epoxies in electrical machine construction [7],[8]. Also, it is possible to design epoxy systems with glass transition temperatures ( $T_g$ ) well in excess of the target motor operating temperature of 150°C [9]. Furthermore, composites have been successfully demonstrated in high-speed motors [10] and even flywheels rotating at speeds up to 60,000 rpm [11].

## Objectives

The project objective is to develop high-magnetization, low-loss iron-nitride-based soft magnetic composites for electrical machines. These new SMCs will enable low eddy current losses and therefore efficient motor operation at rotational speeds up to 20,000 rpm. Additionally, our iron nitride and epoxy composites will be capable of operating at temperatures of 150°C or higher over a lifetime of 300,000 miles or 15 years.

## Approach

A high-level overview of our approach is:

1. Convert commercially available mixed-phase iron nitride powder to nearly phase-pure  $\gamma'$ -Fe<sub>4</sub>N
2. Coat iron nitride particles with diamine molecules (part A of epoxy chemistry)
3. Combine surface functionalized particles with epoxide terminated monomers (part B of epoxy chemistry)
4. Fabricate SMC part by pouring mixture from #3 into a mold. In future years of the project, hot pressing can be used to increase the volume loading of the magnetic particles.
5. Evaluate and test the fabricated SMC part.

Each of these steps involves many possible optimization steps such as processing conditions, epoxy monomer selection and curing conditions, and hot-pressing conditions.

## Results

### 1. Production of phase-pure $\gamma'$ -Fe<sub>4</sub>N

We demonstrated the conversion of mixed-phase commercially available iron nitride powder to nearly phase-pure  $\gamma'$ -Fe<sub>4</sub>N. Our starting material was commercially available iron nitride powder, acquired from Alfa Aesar. This commercial iron nitride powder is a mixture of both Fe<sub>3</sub>N and Fe<sub>4</sub>N. We developed a straightforward heat treatment to convert almost all of the Fe<sub>3</sub>N phase to the higher Js Fe<sub>4</sub>N at a temperature slightly above 550°C, conducted in an inert atmosphere. Temperature-dependent X-ray diffraction (XRD) data of this process, collected under flowing nitrogen, is displayed in Figure I.8.1. This data shows that at a temperature slightly above 550°C the diffraction peaks associated with the Fe<sub>3</sub>N disappear, leaving nearly phase-pure Fe<sub>4</sub>N.

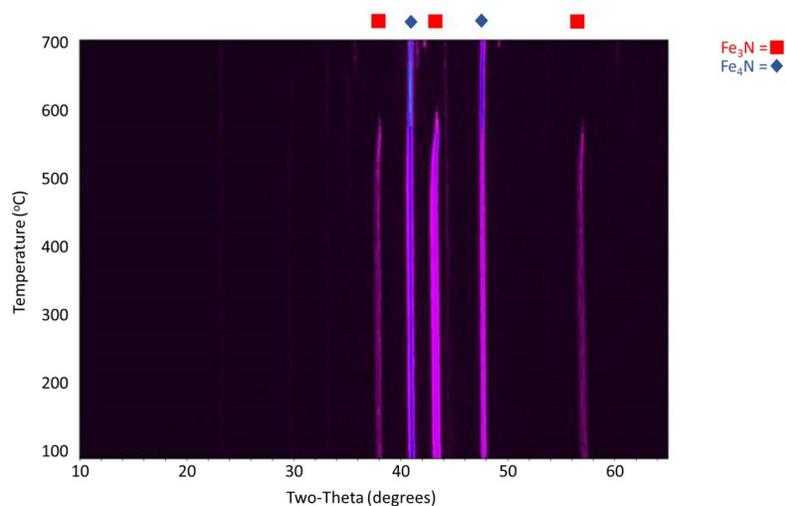


Figure I.8.1 Temperature-dependent XRD data of commercially available mixed phase iron nitride powder and its conversion to nearly phase pure Fe<sub>4</sub>N.

## 2. Coating of Iron Nitride Particles and Composite Formation

To fabricate iron-nitride-based magnetic composites, iron nitride powder and 1,6-hexanediamine (see Figure I.8.2) were added to a SPEX high-energy ball mill and were milled until the particles were coated by the diamine, as confirmed by infrared (IR) spectroscopy. Next, the diamine coated particles were mixed with one of a number of different epoxides: neopentyl glycol diglycidyl ether (which has two epoxide groups); trimethylpropane triglycidyl ether (three epoxide groups); or *N,N*-diglycidyl-4-glycidyoxyaniline (3 epoxide groups). For the sake of brevity, only an image of *N,N*-diglycidyl-4-glycidyoxyaniline is displayed (see Figure I.8.3). After mixing the amine functionalized particles with one of the three epoxide-terminated monomers listed above, the mixture was poured into a mold and cured. We fabricated a 3D-printed toroidal mold (9 mm O.D.) for this project. The toroidal geometry is ideal for characterization on our Iwatsu B-H analyzer.

All three epoxide-terminated monomers formed suitable epoxy-based composites. The collection of additional data in the upcoming fiscal year ( $T_g$ , mechanical strength, thermal conductivity, and  $\rho$ ) will allow us to down-select to the epoxide-terminated monomer that yields the best properties for electric motor implementation. An image of three cured magnetic composite cores wound for B-H analysis is shown in Figure I.8.4. A B-H loop collected at 10 kHz for a magnetic composite toroid is displayed in Figure I.8.5. We fully expect that magnetic properties will be significantly enhanced in the future as we optimize processing conditions and volume loading of the magnetic particles.



Figure I.8.2 1,6-hexanediamine.

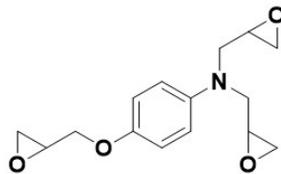


Figure I.8.3 *N,N*-diglycidyl-4-glycidyoxyaniline.

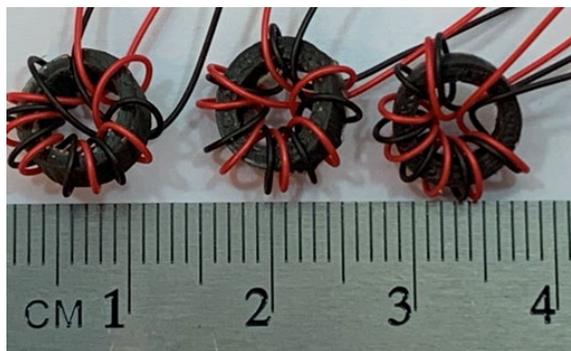


Figure I.8.4 Magnetic composite toroidal cores wound for B-H analysis.



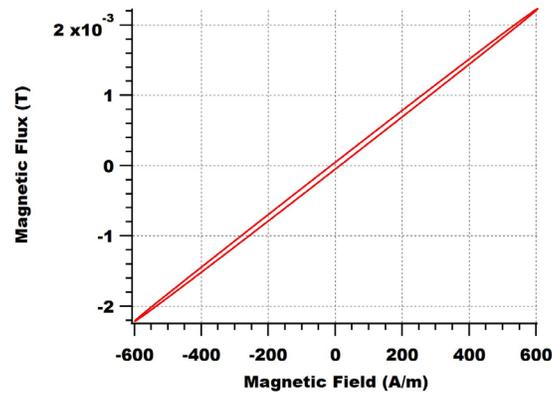


Figure I.8.5 B-H hysteresis loop for a magnetic composite toroid. This hysteresis loop was collected at a frequency of 10 kHz.

### 3. Magnetic Composite Rotor Fabrication

We fabricated portions of a rotor design from Oak Ridge National Lab (ORNL) via two different methods. First, a commercially available magnetic composite filament (purchased from Proto-pasta) was used to 3D print a portion of Oak Ridge's rotor design (see Figure I.8.6). Manufacturing this part serves as a demonstration of our capability to 3D-print magnetic parts for both electric drive power electronics and motors. Although this first 3D-printed rotor part used a commercially available magnetic filament, we are developing our own high magnetization magnetic composite filament. To this end we have purchased, assembled, and tested a Filastruder and Filawinder, which will allow us to create printable magnetic composite filaments using iron nitride particles and any suitable polymer of our choice. This will be an important capability both for the fabrication of inductors for power electronics and soft magnetic motor components.

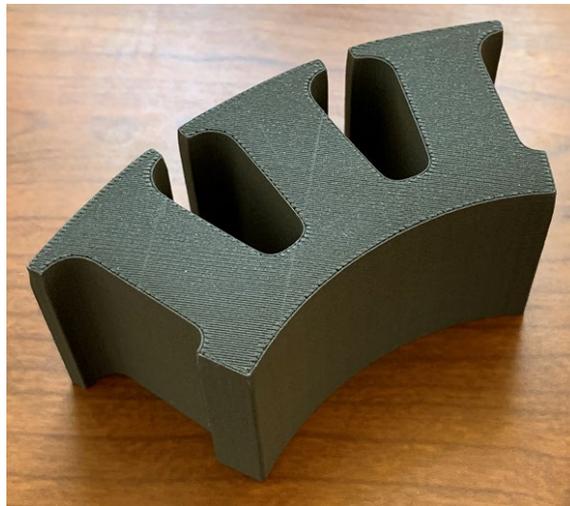


Figure I.8.6 3D printed magnetic composite rotor (1/6 of total rotor design).

Second, an iron nitride and epoxy composite was prepared, mixed (as described above), and poured into a silicone mold for curing. In curing these larger epoxy-based composites, it was discovered that 1,6-hexanediamine reacted too vigorously with the epoxide monomers and led to an exothermic cure. This resulted in excessive heating of the curing epoxy. We switched from using 1,6-hexanediamine to 4-aminophenyl sulfone (see Figure I.8.7) which cures more slowly and does not result in an overly aggressive exothermic cure. In fact, when 4-aminophenyl sulfone is used as the diamine, the uncured epoxy mixture must be heated to a temperature of 130°C to initiate the curing process. We incrementally increased the size of the parts we were

fabricating in order to ensure we were controlling the curing process adequately, gradually approaching a full-sized rotor tooth. An image of three different sized magnetic composite rotor teeth, along with a composite toroid, is displayed in Figure I.8.8.

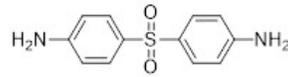


Figure I.8.7 4-aminophenyl sulfone.



Figure I.8.8 Three differently-sized magnetic composite rotor teeth and a magnetic composite toroid.

### Conclusions

During FY19, we successfully demonstrated the fabrication of iron nitride ( $\gamma'$ -Fe<sub>4</sub>N) based magnetic composite parts for electric motors. These parts will also be suitable as inductor cores for electric drive power electronics. Custom epoxy chemistries were selected, evaluated, and used to fabricate magnetic composite toroids and rotors. Additionally, we demonstrated the capability of not only fabricating complex shapes using molds but also via 3D printing. We expect this capability to be particularly fruitful in the fabrication of inductor cores for power electronics. Future work will focus on improving processing conditions and magnetic material volume loading in the fabrication of magnetic composites to enhance magnetic performance for motor and power electronic applications.

### Key Publications

1. T. C. Monson *et al.*, Soft Magnetic Multilayered FeSiCrB-Fe<sub>4</sub>N Metallic Glass Composites Fabricated by Spark Plasma Sintering. *IEEE Magnetics Letters* **10**, 1-5 (2019).
2. J. M. Silveyra, E. Ferrara, D. L. Huber, T. C. Monson, Soft magnetic materials for a sustainable and electrified world. *Science* **362**, eaao0195 (2018).

### References

1. U.S. Drive, "Electrical and Electronics Technical Team Roadmap," Partnership Plan, Roadmaps, and Other Documents 2017.
2. H. Shokrollahi and K. Janghorban, "Soft magnetic composite materials (SMCs)," *Journal of Materials Processing Technology*, vol. 189, no. 1-3, pp. 1-12, 2007.
3. J. S. Corporation, "Super Core™ Electrical steel sheets for high-frequency application," J. S. Corporation, Ed., ed: JFE Steel Corporation, 2017.

4. J. M. Coey, Magnetism and magnetic materials. Cambridge university press, 2010.
5. T. C. Monson et al., "Soft Magnetic Multilayered FeSiCrB-Fe<sub>4</sub>N Metallic Glass Composites Fabricated by Spark Plasma Sintering," IEEE Magnetics Letters, vol. 10, pp. 1-5, 2019.
6. M. Qu et al., "Magneto-photo-acoustic imaging," Biomedical Optics Express, vol. 2, no. 2, pp. 385-396, 2011/02/01 2011.
7. M. Magazine. Available: <https://magneticmag.com/new-structural-adhesive-from-delo-for-magnet-bonding-has-high-temperature-stability/>
8. Crosslinktech. Available: <http://www.crosslinktech.com/products-by-application/featured-electric-motor-products.html>
9. M. Bond. Available: <https://www.masterbond.com/techtips/how-optimizing-glass-transition-temperature-tg>
10. A. Schoppa and P. Delarbre, "Soft Magnetic Powder Composites and Potential Applications in Modern Electric Machines and Devices," IEEE Transactions on Magnetics, vol. 50, no. 4, pp. 1-4, 2014.
11. P. Mason, K. Atallah, and D. Howe, Hard and soft magnetic composites in high speed flywheels. 1999.

#### **Acknowledgements**

This work is supported by the DOE Office of Energy Efficiency and Renewable Energy, Vehicle Technologies Office. Sandia National Laboratories is a multi-mission laboratory managed and operated by National Technology and Engineering Solutions of Sandia, LLC., a wholly owned subsidiary of Honeywell International, Inc., for the U.S. Department of Energy's National Nuclear Security Administration under contract DE-NA0003525. The views expressed in the article do not necessarily represent the views of the U.S. Department of Energy or the United States Government. The author wishes to thank Tyler Stevens, Melinda Hoyt, and Emily Johnson for their development of epoxy chemistries and implementation of composite fabrication techniques, Robert Delaney and Charles Pearce for their assistance with magnetic characterization, and Mark Rodriguez for his help with X-ray diffraction data collection and analysis.

## I.9 Component Modeling, Co-Optimization, and Trade-Space Evaluation (SNL)

### Jason Neely, Principal Investigator

Sandia National Laboratories  
 P.O. Box 5800, MS 1152  
 Albuquerque, NM 87185  
 E-mail: [jneely@sandia.gov](mailto:jneely@sandia.gov)

### Susan Rogers, DOE Technology Development Manager

U.S. Department of Energy  
 E-mail: [susan.rogers@ee.doe.gov](mailto:susan.rogers@ee.doe.gov)

Start Date: October 1, 2018	End Date: September 30, 2023	
Project Funding (FY19): \$200,000	DOE share: \$200,000	Non-DOE share: 0

### Project Introduction

This project is intended to support the development of new traction drive systems that meet the targets of 100 kW/L for power electronics and 50 kW/L for electric machines with reliable operation to 300,000 miles. To meet these goals, new designs must be identified that make use of state-of-the-art and next-generation electronic materials and design methods. Designs must exploit synergies between components, for example converters designed for high-frequency switching using wide band gap devices and ceramic capacitors. This project includes: (1) a survey of available technologies, (2) the development of design tools that consider the converter volume and performance, and (3) exercising the design software to evaluate performance gaps and predict the impact of certain technologies and design approaches, i.e., GaN semiconductors, ceramic capacitors, and select topologies. Early instantiations of the design tools enable co-optimization of the power module and passive elements and provide some design guidance; later instantiations will enable the co-optimization of inverter and machine.

### Objectives

- Identify performance measures corresponding to consortium design targets
- Develop metrics for performance/reliability of power electronics and electric motors
- Evaluate reliability/performance of state-of-the-art power devices and identify gaps
- Evaluate state-of-the-art/baseline traction drive system
- Utilize optimization tools to inform designs
  - Identify co-optimized designs
  - Evaluate parameter sensitivities and identify target specifications

### Approach

The approach includes four strategies for generating design guidance and optimal designs, listed in order of increased fidelity and resources:

1. **Empirical and First-Principles Analysis:** This uses first-principles knowledge, such as physical models, as well as comparative designs to inform the design.
2. **High-Fidelity Modeling and Analysis:** This uses higher-order models that consider the component equivalent circuits, dimensions, reliability calculations, etc.

3. **Global Co-Optimization:** With the definition of one or more performance metrics, components are simulated together and their performance is measured and compared.
4. **Hardware Iteration:** Using optimal designs identified in software, hardware exemplars are built and evaluated; 3 and 4 are iterated to create the best results.

In FY19, the project focused on the first three strategies. Strategy 1 entailed an extensive literature search and the use of first principles to define metrics and down-select the design space. Models were then created for select components, and co-optimization software was developed to identify Pareto-optimal designs. Hardware iteration will begin in FY20.

For co-optimization, the team used the Genetic Optimization System Engineering Tool (GOSET) developed by Purdue University [1]. This MATLAB<sup>®</sup>-based software package consists of several scripts for implementing and solving a genetic algorithm optimization problem. The genetic algorithm is a probabilistic method for optimizing multi-input systems with non-convex solution spaces using the principles of genetics and a user-defined fitness function. GOSET allows for multiple fitness functions to be co-optimized into a Pareto front. To set up the optimization, the circuit schematic and physical layout must be partially defined, and the dimensions of and between components, thicknesses of insulators, lengths of conductors, etc. must be formulated and linked to the schematic definition in order to compute a volume and evaluate the circuit/system performance using a dynamic simulation. In FY19, optimization efforts focused on the electric drive; future efforts will seek to merge the models with those of the machine currently being developed at Purdue, to enable co-optimization.

## Results

### *Performance Measures/Targets*

The targets indicate a 100 kW/L power density for the electric drive and 50 kW/L for the machine. Though this project will primarily rely on optimization to select the actual component dimensions, it is convenient to generate initial targets for component volumes for down-select. Using the U.S. Drive 2017 Roadmap, component volumes were estimated for the BMW i3 and interpolated to these new targets. These include, for example, a volume target for the power module + DC link capacitor of < 175 cm<sup>3</sup>.

To clarify the reliability metrics in terms of what can be measured and validated through laboratory measurements and lifetime models, the DOE Targets were mapped to performance criteria based on recent driving statistics as follows:

- Establish a range of 300,000 miles (DOE target); assuming 13,456 miles/year average [2] and 435 hours/year in vehicle [3], this becomes 22.3 years reliability (roadmap indicates 15 years), and 9702 hours of operation
- Process approximately 102 MWh [4] over 300,000-mile lifetime

Many reliability metrics were considered for integration into the co-optimization code. In general, reliability models can range from highly specific failure-based mechanisms that rely on models of physical process to reproduce lifetime, to more statistical measures. Failure-based mechanisms are the most realistic, but only apply for a specific failure mechanism in a specific component. Statistical-based methods, on the other hand, do not rely on a given failure mechanism, but on the aggregate behavior of many competing failure mechanisms in a large population of devices. These types of statistics typically give information on *mean time between failure* (MTBF). This, in itself, is a statistical measure of the reliability of an aggregation of devices and gives an idea of the “useful life” of a device but does not predict end-of-life. For example, a statistical measurement may give an MTBF reliability of 100,000 hours for a system. This does not mean that any given system may have a lifetime of 100,000 hours, but that one expects an average failure rate of 1 per hour per 100,000 devices. In light of this, and in order to balance the tractability of the calculation needed for optimization and accuracy, we chose to incorporate MIL-HDBK-217F calculations [5]. This statistical measure

of MTBF is simple, conservative, and specifically designed for high-reliability systems, but is not as accurate as other methods (physics-of-failure, telecordia, etc.) For every component, a 217F-style calculation takes the generic form of:  $\lambda = n \cdot \lambda_b \pi_T \pi_A \pi_Q \pi_E$

where  $\lambda$  is the failure rate,  $n$  is the number of units in the system,  $\lambda_b$  is the base failure rate,  $\pi_T$  is the temperature factor,  $\pi_A$  is the electrical stress factor,  $\pi_Q$  is the quality factor, and  $\pi_E$  is the environmental factor. Each factor can be determined either through look-up tables in the handbook or via calculations based on physical phenomena.

### Design Space

The inverter design space includes the selection of semiconductor material, the capacitor technology, circuit topology, and layout scheme. As part of this effort, the feasibility of using Gallium Nitride (GaN) devices for the drive train was investigated. In [6], an empirical analysis predicts that GaN-based converters can realize an improvement in power density over SiC-based converters by approximately 2x. GaN is already being considered for charging applications [7]. However, in [8], a genetic optimization of a converter + machine design showed only marginal gains in specific power with GaN compared to SiC. However, the circuit in [8] contained a passive rectifier with six GaN PiN diodes operating at low frequency, and the higher turn-on voltage (and hence loss) of these diodes drove up the circuit volume. Thus, to predict the impact of vertical GaN Junction Barrier Schottky (JBS) diodes (in development within the consortium), a comparative analysis presented in [9] was applied to compare optimally-designed GaN PiN, GaN JBS and SiC Merged PiN Schottky (MPS) diodes under operating conditions for the vehicle environment. Figure I.9.1 illustrates the difference in predicted power loss in vertical GaN JBS diodes compared to SiC MPS diodes for a 50% duty cycle. In fact, at relevant voltages and frequencies, GaN JBS diodes show a considerable advantage over SiC MPS diodes, with about 1/3 the electrical loss. Likewise, for a vertical FET device, assuming a fixed device structure (for comparison), the predicted  $R_{on}$  was computed as a function of breakdown voltage for devices based on Silicon, SiC, and GaN (see Figure I.9.2). Therein,  $R_{on}$  for the GaN device is approximately 1/2 that of the SiC device. Based on these results, vertical GaN technology may provide significant gains over SiC at higher voltage and frequency. Further work is ongoing for a full switching-based device loss analysis.

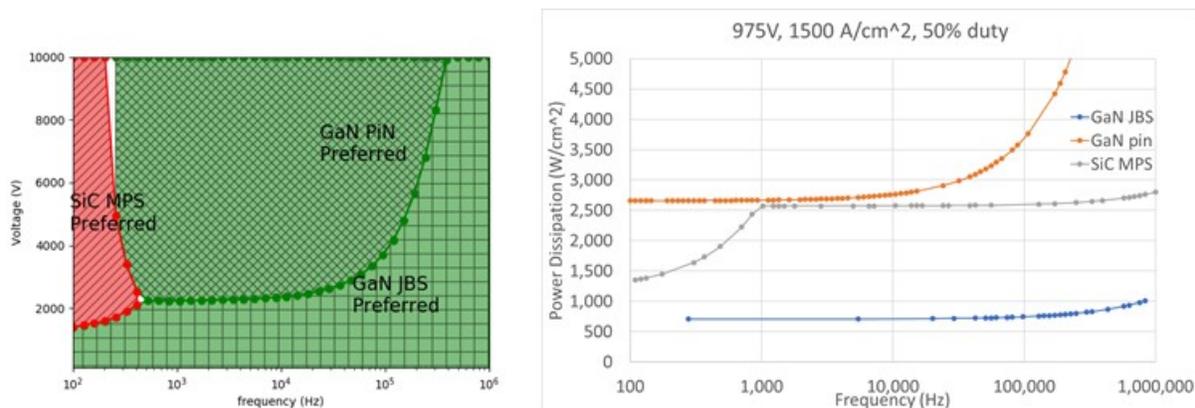


Figure I.9.1 Comparison of power loss in SiC MPS, GaN PiN, and GaN JBS diodes showing (left) preferred device as a function of voltage and frequency at 50% duty cycle, and (right) the comparison of loss at 650 V, 50% duty cycle

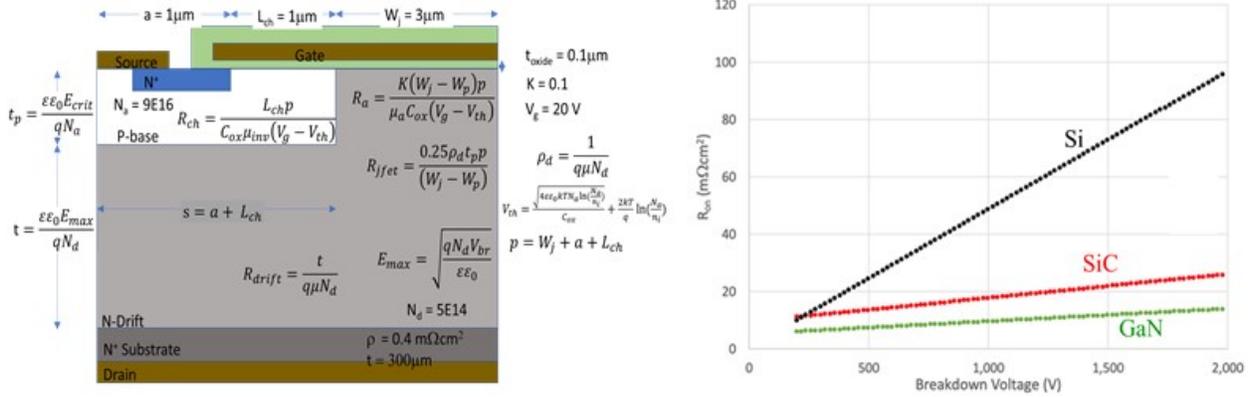


Figure I.9.2 Comparison of  $R_{on}$  in MOSFETs made in Silicon, SiC, and GaN showing (left) the device structure and (right) the predicted results.

### Topologies and Capacitor Technologies

Several converter topologies were considered including the combined DC-DC ↔ DC-AC architecture identified in [10] as well as multi-phase topologies [11], and more exotic configurations [12]. Given the higher projected available battery voltage, the team focused on direct-connect DC-AC (no DC-DC boost). Due to the beneficial effect of additional phases on required dc-link capacitance and dc-link capacitor current ripple [11], the team focused our design on the multi-phase topology. Figure I.9.3 shows the selected circuit topology used in the co-optimization problem consisting of a multi-phase inverter, DC-link capacitor, input inductor, and multiple parasitic terms which vary with component selection and layout. The design parameters included in the optimization are the battery open-circuit voltage  $V_{in}$ , the input inductance  $L_{in}$ , the link capacitance  $C_{link}$ , the number of phases  $N_\phi$ , the switching frequency  $f_{sw}$ , the fundamental frequency of the output voltage  $\omega_r$ , and the AC filter inductance  $L_f$ , resistance  $R_f$ , and capacitance  $C_f$ . A MATLAB<sup>®</sup> script was developed that took these parameters, solved a set of differential equations for the circuit, and then post-processed the behavior of the voltages and currents in the circuit to determine the volume and losses of the design as well as the voltage and power loss in specified components. The form factor selected for the principal converter elements is shown in Figure I.9.4. Therein, the module with the devices, conductors, and flat capacitor assembly are packaged together. This form factor was used as a basis for the dimensional analysis. This approach has several advantages discussed in [13].

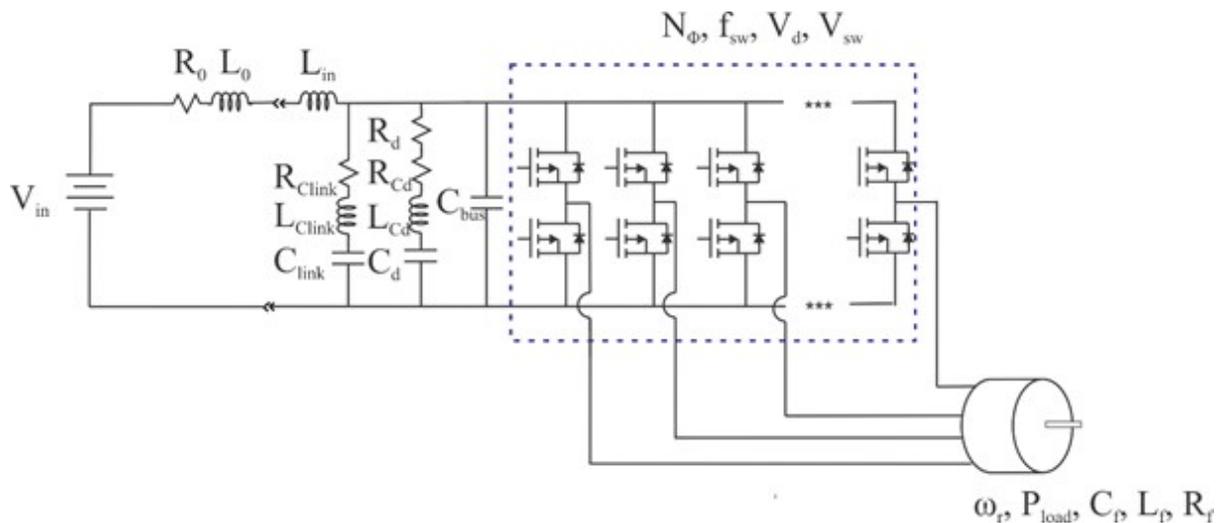


Figure I.9.3 Circuit topology for co-optimization.

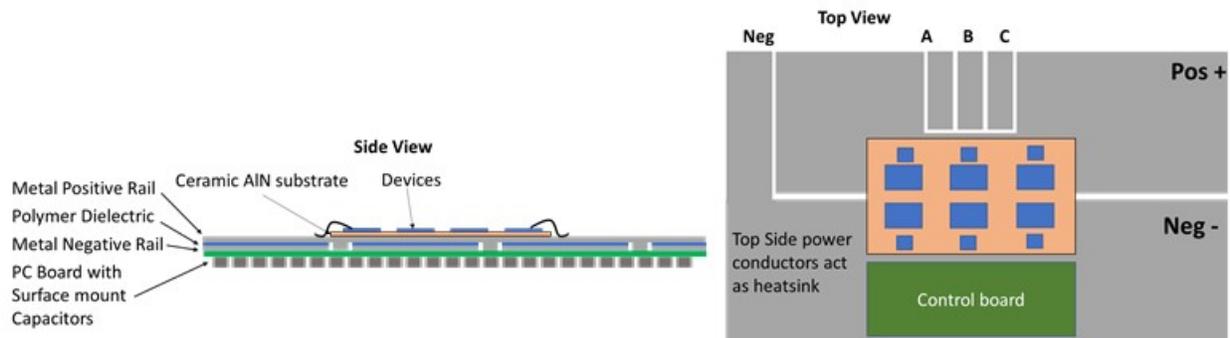


Figure I.9.4 Candidate design considers a flat integrated form factor that includes module and DC link capacitor.

Using these dimensional models and different capacitor technologies, initial estimated sizes for the module + capacitor were generated as a function of voltage, frequency, capacitor type, and number of phases. See Figure I.9.5, left panel. When checked against the target volume, this estimate aids in the identification of the achievable design space; see Figure I.9.5, right panel for designs complying with 175 mL volume. Additional factors must be considered, however. For example, the Ceralink capacitors indicate a high energy density and a favorable C-V characteristic, but this is achieved at very high field strengths which may impact their reliability. Reliability considerations are factored into the design within the optimization.

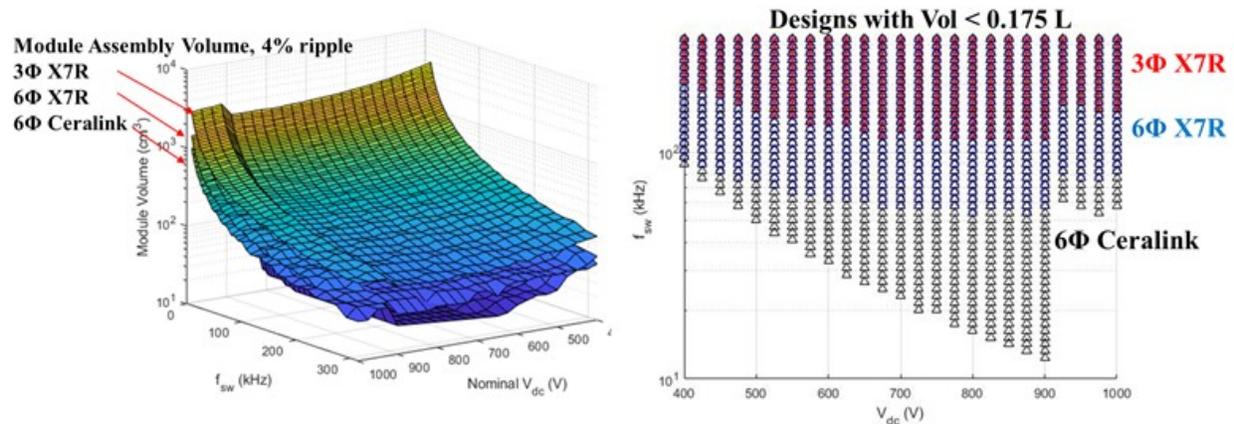


Figure I.9.5 Module volume estimate as a function of voltage and frequency for Ceramic X7R and Ceralink Capacitors.

### Machine Design

Highly desirable features of electric vehicle drive motors are high starting torque, high power density, and high efficiency over the full operating range. These requirements place significant limits on motor type as well as the materials used in their construction. Using hard permanent magnet materials in the motor construction is the current preferred approach to addressing volume and weight requirements. NdFeB magnets offer the highest residual induction, coercive force, and energy product compared to Ferrites, AlNiCo, and SmCo. NdFeB magnets, however, do pose potential supply-chain issues necessitating new magnetic materials and motor designs. Recently, motors based on different magnetic materials have been compared based on machine constant of mechanical power [14] (MCMP is defined as  $P_{\text{mech}} / [\text{motor volume}] \times [\text{rotor frequency in Hz}]$ ) which gives a measure of potential output mechanical power. The comparison includes both prototypes and simulation data. While NdFeB-based IPMSM demonstrate  $\sim 0.9$  kW/L of MCMP with 96% efficiency, various ferrite-based PMSMs also show performance approaching this limit with MCMP ranging from 0.7-0.8



kWs/L with an efficiency range of 93-97% with rotor speeds ranging from 1500-2800 rpm. Taking rotor speed into account, these motors provide 20-40 kW/L. For comparison, the BMW i3 was evaluated to be 9.2 kW/L with a top speed of 11.5 krpm. To meet DOE targets (50 kW/L) while eliminating permanent magnets, the team plans to consider new homopolar motor designs, which establish a rotor field using a static field winding and may achieve speeds > 20 krpm. Next year's work will include a collaborative effort with Purdue University; Purdue is developing design codes for the homopolar machine and is investigating the feasibility of meeting the DOE targets using this approach.

### Co-Optimization

Two co-optimization examples are presented here. The first considers a simple bi-directional 10 kW boost converter, like one that might connect a battery to an inverter. Therein, the converter was optimized for DC link capacitor MTBF versus converter volume. Results are shown in Figure I.9.6. The optimization pulls the solutions to the upper left of the trade-space, showing a clear trade-off between reliability and size. The second optimization was performed on a 100 kW inverter (Figure I.9.3 and Figure I.9.4) module and DC link capacitor (no thermal management) with the parameters noted above. The genetic optimization algorithm was run on a population of 50 individuals in this parameter space over 100 generations with fitness functions to maximize the power density of the module + link capacitor size and minimize loss. There was also a constraint placed on the maximum RMS of the DC bus voltage ripple. The resulting Pareto front is shown to the right in Figure I.9.6. The genetic optimization pulls all the individuals towards the lower right. Examining the parameter values for the individuals on the Pareto front shows a tendency of the individuals to have a 450 V input, 9 phases, and over 250 kHz switching. Since only the volumes of the capacitor and module were considered in the optimization, voltage was minimized to minimize the number of capacitors needed to stand off the voltage. After adding the magnetics and thermal management components to the model, solutions with higher DC-link voltage are expected.

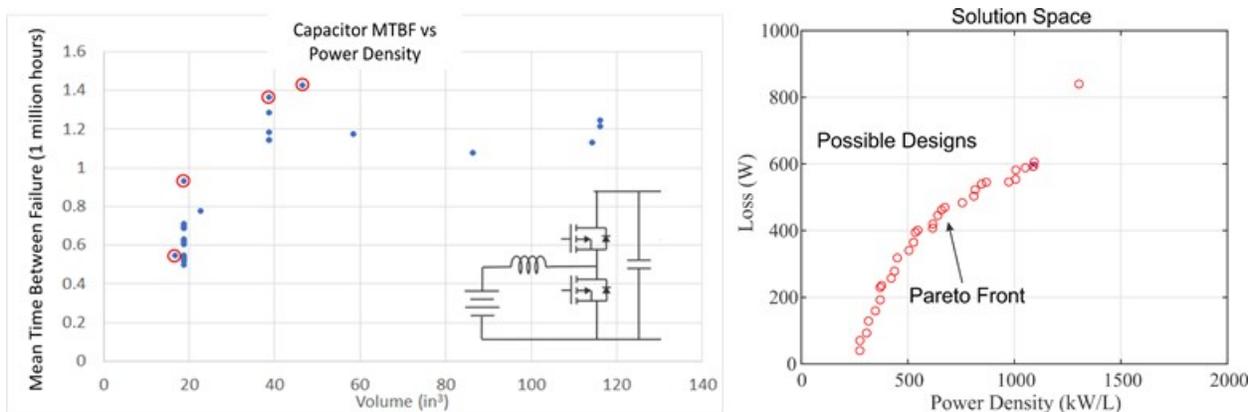


Figure I.9.6 Co-optimization results for (left) 10 kW boost converter and (right) 100 kW inverter module + capacitor.

### Conclusions

This project first focused on down-selecting the design space for future traction drive systems; combined, the use of GaN devices, ceramic capacitors, high-frequency switching, and multi-phase designs may enable considerable improvements in power density. This work also developed tools to perform multi-objective optimizations on electric drive designs. Unlike previous work, these include optimizations that consider component reliability. Future work will refine these tools and extend their use to co-optimize the inverter and machine designs.

### References

1. S. D. Sudhoff, GOSET: Genetic Optimization System Engineering Tool: For Use with MATLAB®, version 2.6, January 1, 2014.

2. US Department of Transportation Federal Highway Administration driving statistics; URL: <https://www.fhwa.dot.gov/ohim/onh00/bar8.htm>
3. Sean Szymkowski; Study: Americans spend 18 days in their car per year, forge close bonds with a vehicle; April 2019; URL: [https://www.thecarconnection.com/news/1122782\\_study-americans-spend-18-days-in-their-car-per-year-forge-close-bonds-with-a-vehicle](https://www.thecarconnection.com/news/1122782_study-americans-spend-18-days-in-their-car-per-year-forge-close-bonds-with-a-vehicle)
4. US Department of Energy, Alternative Fuels Data Center; URL: [https://afdc.energy.gov/fuels/electricity\\_charging\\_home.html](https://afdc.energy.gov/fuels/electricity_charging_home.html)
5. Military Handbook: Reliability prediction of electronic equipment, 1991. Available: <https://snebulos.mit.edu/projects/reference/MIL-STD/MIL-HDBK-217F-Notice2.pdf>
6. R. J. Kaplar, J. C. Neely, D. L. Huber and L. J. Rashkin, “Generation-After-Next Power Electronics: Ultrawide-bandgap devices, high-temperature packaging, and magnetic nanocomposite materials,” in *IEEE Power Electronics Magazine*, vol. 4, no. 1, pp. 36-42, March 2017.
7. G. Liu et al., “Comparison of SiC MOSFETs and GaN HEMTs based high-efficiency high-power-density 7.2kW EV battery chargers,” *2017 IEEE 5th Workshop on Wide Bandgap Power Devices and Applications (WiPDA)*, Albuquerque, NM, 2017.
8. B. Zhang et al., “Prediction of Pareto-optimal performance improvements in a power conversion system using GaN devices,” *2017 IEEE 5th Workshop on Wide Bandgap Power Devices and Applications (WiPDA)*, Albuquerque, NM, 2017, pp. 80-86.
9. J. Flicker and R. Kaplar, “Design optimization of GaN vertical power diodes and comparison to Si and SiC,” *2017 IEEE 5th Workshop on Wide Bandgap Power Devices and Applications (WiPDA)*, Albuquerque, NM, 2017, pp. 31-38.
10. M. Olszewski, Evaluation of the 2010 Toyota Prius Hybrid Synergy Drive System, Oakridge National Laboratory, Oak Ridge, TN, Tech Report. ORNL/TM-2010/253, March 2011.
11. Nie, Zipan; Schofield, Nigel: 'Multi-phase VSI DC-link capacitor considerations', *IET Electric Power Applications*, 2019, DOI: 10.1049/iet-epa.2019.0062 IET Digital Library, <https://digital-library.theiet.org/content/journals/10.1049/iet-epa.2019.0062>
12. L. Chen and B. Ge, “High Power Traction Inverter Design and Comparison for Electric Vehicles,” *2018 IEEE Transportation Electrification Conference and Expo (ITEC)*, Long Beach, CA, 2018.
13. J. Stewart, J. Neely, J. Delhotal and J. Flicker, “DC link bus design for high frequency, high temperature converters,” *2017 IEEE Applied Power Electronics Conference and Exposition (APEC)*, Tampa, FL, 2017, pp. 809-815.
14. J.-R. Riba, C. López-Torres, L. Romeral, and A. Garcia, “Rare-earth-free propulsion motors for electric vehicles: A technology review,” *Renewable and Sustainable Energy Reviews* 57 (2016).

## Acknowledgements

This work is supported by the DOE Office of Energy Efficiency and Renewable Energy, Vehicle Technologies Office. Sandia National Laboratories is a multi-mission laboratory managed and operated by National Technology and Engineering Solutions of Sandia, LLC., a wholly owned subsidiary of Honeywell International, Inc., for the U.S. Department of Energy’s National Nuclear Security Administration under contract DE-NA0003525. The views expressed in the article do not necessarily represent the views of the U.S. Department of Energy or the United States Government.

## I.10 Power Electronics: Vertical GaN Device Development (SNL)

### Greg Pickrell, Principal Investigator

Sandia National Laboratories  
P.O. Box 5800, MS 1086  
Albuquerque, NM 87185  
E-mail: [gpickre@sandia.gov](mailto:gpickre@sandia.gov)

### Susan Rogers, DOE Technology Development Manager

U.S. Department of Energy  
E-mail: [susan.rogers@ee.doe.gov](mailto:susan.rogers@ee.doe.gov)

Start Date: October 1, 2018

End Date: September 30, 2023

Project Funding (FY19): \$800,000

DOE share: \$800,000

Non-DOE share: \$0

### Project Introduction

This project is part of a multi-lab consortium that leverages U.S. research expertise and facilities at National Labs and universities to significantly advance electric drive power density and reliability, while simultaneously reducing cost. The final objective of the consortium is to develop a 100 kW traction drive system that achieves 33 kW/L, has an operational life of 300,000 miles, and a cost of less than \$6/kW. One element of the system is a 100 kW inverter with a power density of 100 kW/L and a cost of \$2.7/kW. New materials such as wide-bandgap semiconductors, soft magnetic materials, and ceramic dielectrics, integrated using multi-objective co-optimization design techniques, will be utilized to achieve these program goals. This project focuses on a subset of the power electronics work within the consortium, specifically the design, fabrication, and evaluation of vertical GaN power devices suitable for automotive applications.

### Objectives

Gallium Nitride (GaN) is a promising wide-bandgap (WBG) semiconductor material that could enable higher-performance power electronic devices than traditional Silicon (Si) or even its WBG counterpart, Silicon Carbide (SiC). This is based on the increased critical electric field of GaN, which would enable lower-resistance devices with the same hold-off voltage as devices fabricated from the other materials. This is a key performance metric for power devices. While laterally-oriented, High Electron Mobility Transistors (HEMTs) based on AlGaN and GaN materials are common in high-frequency applications and are being established in lower-voltage power switching applications (approximately 600 V and below). However, with the emerging commercial maturation efforts for GaN substrates using various methods, traditional vertically-oriented device structures (such as are common in Si and SiC) can now be realized in GaN, with several promising demonstrations of high-voltage PN diodes and vertical transistors appearing in the literature [1],[2],[3]. While GaN PN diodes may be of interest, the ~3 V turn-on voltage, determined mainly by the bandgap of the material, discourages their use in some power-switching circuits due to the loss of power conversion efficiency resulting from this high turn-on voltage. Instead, more promising candidates for these power conversion systems, including automotive inverters, are GaN Schottky barrier diodes (SBDs) and Junction Barrier Schottky (JBS) diodes,

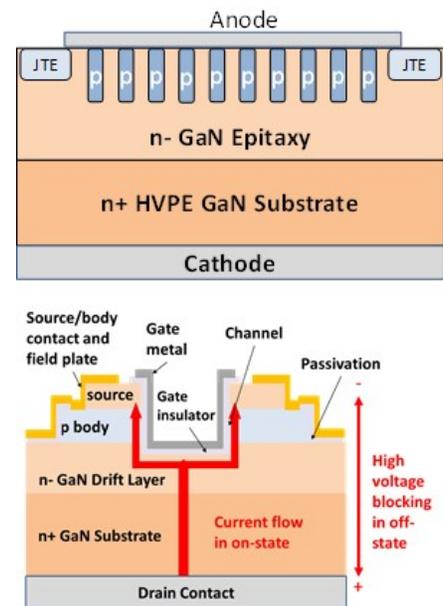


Figure I.10.1 (top) Schematic drawing of JBS diode. (bottom) Schematic drawing of Trench MOSFET.

shown in Figure I.10.1(top), which have turn on voltages of  $\sim 1$  V as determined by the Schottky barrier height of the metal to the semiconductor material, rather than the semiconductor bandgap.

Similarly, vertically-oriented GaN transistors promise high-performance power electronic devices if several key growth and fabrication challenges are overcome for the GaN material system. Interestingly, several different types of vertical GaN transistors have been demonstrated including Metal Oxide Semiconductor Field-Effect Transistors (MOSFETs) in the trench configuration (T-MOSFET, shown in the bottom portion of Figure I.10.1), the double-well (D-MOSFET) configuration, and the Current Aperture Vertical Electron Transistor (CAVET) configuration [4],[5],[6]. Each of these device topologies has benefits and challenges associated with fabrication and performance, but the MOSFET designs show the most promise for power switching applications and will be investigated during this effort. With the MOSFET device designs, challenges exist in making the semiconductor/insulator (or oxide) interface due to the lack of a good native oxide for GaN (Si and SiC both have native oxides). In addition, selective-area doping control, which is needed to form lateral PN junctions, cannot be easily achieved in GaN. Current state-of-the-art GaN devices use techniques such as ion implantation with special anneal processes (high-pressure and high-temperature) [7] or epitaxial regrowth [8] to realize selective-area doping control. Both techniques are relatively immature in GaN, and their behavior needs to be studied and techniques need to be developed to control these processes for eventual use in power systems for electric vehicles.

The first year of this effort focused on the development of simulation and modeling capabilities to help drive the designs of future GaN diodes and transistors. In parallel, epitaxial growth and fabrication processes were initiated toward realizing and demonstrating these devices. Once devices of sufficient performance are achieved, these will be further characterized in a performance and reliability test-bed (created under a different project within the consortium) to evaluate their suitability for electric drive applications, especially regarding their ability to meet the DOE consortium targets. Also, with increasing maturity, the devices can be shared with the consortium partners, who will evaluate them in electric drive systems and provide feedback to us for further improvement in their performance for power electronics.

## Approach

### Vertical GaN Diodes

To understand the designs for development of the vertical GaN diodes, Technology Computer-Assisted Design (TCAD) models were co-developed at Sandia National Laboratories and Lehigh University (subcontract to Professor Jon Wierer) using the Silvaco software suite. The first efforts focused on simulations of the Schottky barrier diodes in forward and reverse bias operating modes while using various models for leakage currents available in Silvaco. Figure I.10.2 shows the simulated reverse-bias current-voltage behavior of a GaN SBD with different models being used in the TCAD simulation. These included the thermionic emission, thermionic emission with barrier lowering, universal Schottky tunneling, and phonon-assisted tunneling models. GaN material was grown using Sandia's Metal-Organic Chemical Vapor Deposition (MOCVD) facilities and SBDs were fabricated and tested using a simple shadow-mask process where metal is deposited onto the surface of the GaN through a perforated metal mask to form circular devices. With the fabrication and testing of these simple GaN SBDs during the first year, these models were evaluated based on their ability to match experimental results and were optimized to allow predictive behavior of the diodes. This iterative process will be continued in future modeling and simulation efforts to drive realistic simulation capabilities to help with future, more complicated device designs.

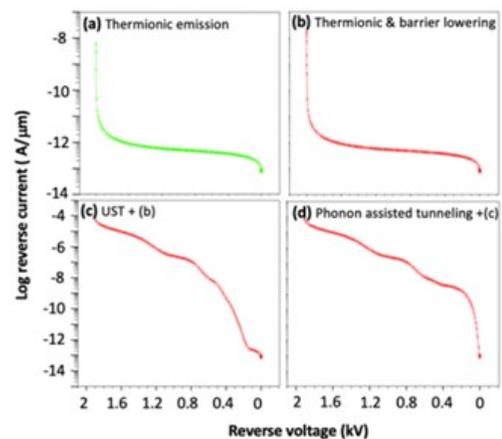


Figure I.10.2 Simulated reverse-bias curves of GaN Schottky diodes using various transport models (courtesy of Lehigh University).

With the successful modeling of SBDs and previous work in GaN PN junctions, Junction Barrier Schottky (JBS) diode models were also developed during the first year. The JBS diode is a hybrid between a SBD and PN junction diode that combines the best of both, namely high breakdown voltage and low forward turn-on. To drive design optimization of the fabrication efforts for future JBS diodes, a systematic study of the JBS parameter space was conducted to evaluate different device designs. The parameters analyzed included the width of the n-GaN and p-GaN layers, the Mg-doping level of the p-GaN layer, and the thickness of the p-GaN layer. To optimize the design, simulated device performance parameters including the breakdown voltage, the forward specific on-resistance, and the Baliga Figure of Merit (BFOM) which is equal to the breakdown voltage squared divided by the specific on-resistance, were used to evaluate the different designs and to gauge the parameter space best for future fabrication efforts.

To begin to develop the vertical GaN diodes, work was performed in material synthesis using Sandia MOCVD GaN growth capabilities, coupled with device fabrication process development to assemble the tools necessary to fabricate these devices. For the material synthesis portion, thick n-type GaN layers were grown on commercially available GaN substrates, and the net carrier concentration was measured using capacitance-voltage techniques to optimize the processes for the designed values. Using these grown structures, SBDs were fabricated using standard lithographic patterning, etching, and metallization processes, and were subsequently characterized to understand their performance. With the development of the JBS designs, photolithographic mask sets were designed and fabricated for the first generation of the JBS diode effort. Fabrication short loops were begun to develop the fabrication processes needed to realize the JBS devices. These included investigations of contact lithography and etch processes to form the small patterns in the JBS device area.

### Vertical GaN Transistors

Due to the increased complexity of the vertical GaN transistors, the work in the first year was primarily focused on the simulation of two candidate device structures, and work was also started to develop and understand the dielectric/semiconductor interface that is critical to the gate control of the devices. Cross-sectional diagrams of the two types of MOSFETs are shown with the T-MOSFET at the top and the D-MOSFET at the bottom of Figure I.10.3. Using TCAD simulations, the sensitivity of the device performance to various parameters was investigated to understand the performance trade-offs of the different devices and to look for possible limitations in the theoretical device performance imposed by material growth and device fabrication challenges. Based on the results of the simulations, it was clear that both device architectures are viable for automotive drivetrain applications, and we continue to investigate both during the fabrication process development. This is not surprising since both device architectures are commercially produced using SiC, with no obvious advantage to either choice at this time.

To begin the development of the transistors, investigation of the dielectric/semiconductor interface was studied to develop and optimize this process using Atomic Layer Deposition (ALD) of Silicon Dioxide ( $\text{SiO}_2$ ) as a starting point. GaN wafers were grown, similar to those used for GaN SBDs, and various surface treatments were investigated before deposition of the ALD  $\text{SiO}_2$  film. Next circular metal contacts were deposited on the ALD films to form MOS capacitor structures. These MOS capacitors were characterized using current-voltage, and variable frequency capacitance-voltage techniques to evaluate and understand the interface trap density between the dielectric and semiconductor layer, which will eventually limit the performance of the transistors.

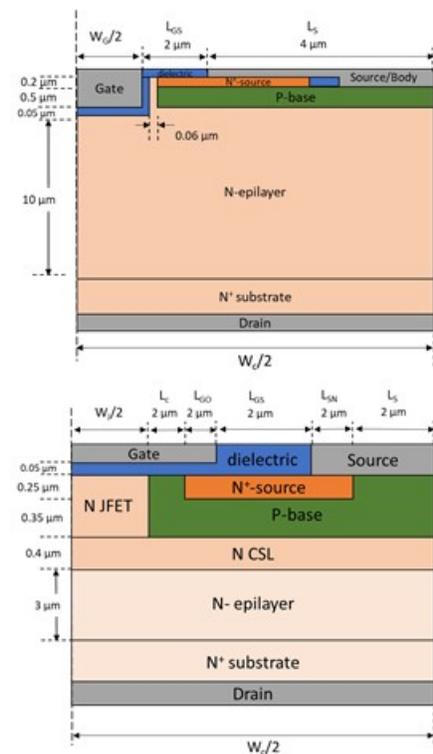


Figure I.10.3 Schematic drawings of (top) trench MOSFET and (bottom) double-well MOSFET.

## Results

### Vertical GaN Diodes

To evaluate the GaN SBD simulations that were developed, actual devices were fabricated to compare their performance to predicted results. Initially, simple shadow-masked devices were made by depositing a Pd Schottky contact through a perforated metal screen to form circular devices. While this method can help to give understanding of device performance, it will not allow for more complicated device structures to be made that would eventually be needed to yield devices for electric drive systems. More complicated devices would include thick wire-bond pads, surface passivation, device identifier numbers, and other features to enable large-scale parallel processing, characterization, singulation, and packaging for insertion into circuits. To realize GaN SBDs using these more traditional methods was not straightforward due to the effects of GaN surfaces on device performance. Inherently, SBDs are sensitive to surfaces, and care must be maintained to develop a robust and stable process. Eventually, we were able to realize photolithographically-defined GaN SBDs using a blanket metal layer with a pattern-and-etch used to define the metal. Using this process, we were able to realize high-performance GaN SBDs with highly uniform results for devices of 250  $\mu\text{m}$  diameter. The forward IV curves for representative devices are shown in Figure I.10.4(top) along with the extracted ideality factors for these devices (bottom). These devices show ideality factors of 1.05 to 1.10, which is good for state of the art GaN SBDs (the ideality factor is a measure of the quality of the diode, with a value of 1.00 being ideal).

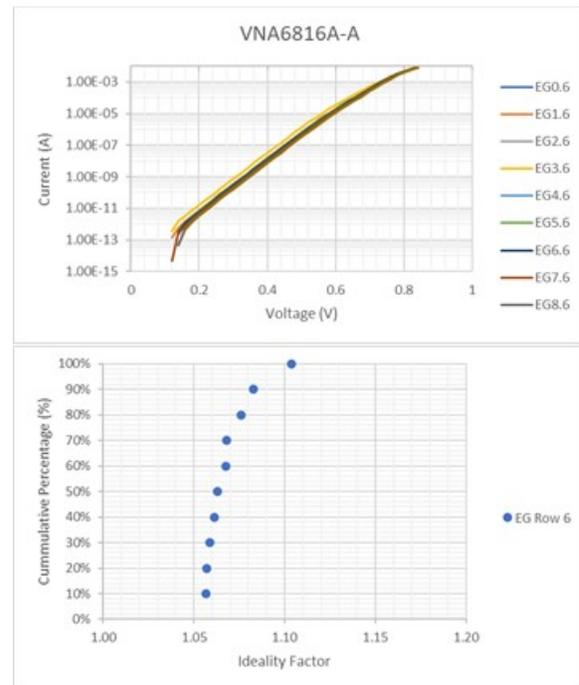


Figure I.10.4 (top) IV curves of GaN Schottky Barrier Diodes, and (bottom) extracted ideality factors of the same diodes.

These devices show ideality factors of 1.05 to 1.10, which is good for state of the art GaN SBDs (the ideality factor is a measure of the quality of the diode, with a value of 1.00 being ideal).

Table I.10.1

Parameter	Variation in Simulation
p-GaN thickness ( $T_p$ ) ( $\mu\text{m}$ )	0-2, spaced by 0.5 $\mu\text{m}$
p-GaN trench width ( $W_p$ ) ( $\mu\text{m}$ )	0-5, spaced by 0.5 $\mu\text{m}$
p-GaN Mg doping concentration ( $\text{cm}^{-3}$ )	$10^{17}$ - $10^{19}$
n-GaN trench width ( $W_n$ ) ( $\mu\text{m}$ )	0-5, spaced by 0.5 $\mu\text{m}$

Using the empirical results from the GaN SBD work, simulations for the JBS diodes were performed as described above. For the parameters swept in the simulation work, Table I.10.1 defines the variables. The n-GaN drift layer for the device was kept constant at a thickness of 10  $\mu\text{m}$  with a net carrier concentration of  $2 \times 10^{16} \text{ cm}^{-3}$ . From these simulations, charts were constructed for analyzing various performance parameters by color-coding the performance metric on a 2-dimensional plot with two of the parameters swept in the simulations. For each colored dot, a forward and reverse IV curve have been simulated and the performance metric extracted to represent the color. The scale for the color is along the side of the plot as shown in Figure I.10.5. The analysis showed that the performance was highly sensitive to the widths of the p-GaN and n-GaN as expected. Other parameters such as the p-GaN doping level and p-GaN thickness also had effects. The BFOM was chosen as the operating parameter because it includes both forward and reverse performance

metrics, and the desired outcome was to have as large a parameter space as possible for the p-GaN and n-GaN widths to allow for process variations in the growth and fabrication of the diodes. A Mg doping level for the p-GaN layers of  $1 \times 10^{18} \text{ cm}^{-3}$  was chosen for several reasons, including empirical results with good device performance for GaN PN diodes. Doping levels higher than this reduce the parameter space over which good simulated results are obtained, and doping levels lower than this pose some risk for device operation. Figure I.10.6 shows the color plots for the BFOM plotted as a function of p-GaN and n-GaN trench width for three different p-GaN layer thicknesses at a Mg doping level of  $1 \times 10^{18} \text{ cm}^{-3}$ . The results indicate that there is potentially a wide set of p-GaN and n-GaN widths that can give good BFOM results, with a thickness of  $0.5 \mu\text{m}$  giving the best BFOM values (these are encircled by the dashed lines). These data were used to bound the designs of the mask sets to fabricate the JBS diodes, and these masks have been made. Experiments are underway to develop the processes (growth and fabrication) needed to realize these designs. In addition, design methodologies and fabricated device results for SiC devices were obtained through the subcontract with Jim Cooper (Sonrisa) to allow us to further refine the design space for the GaN devices.

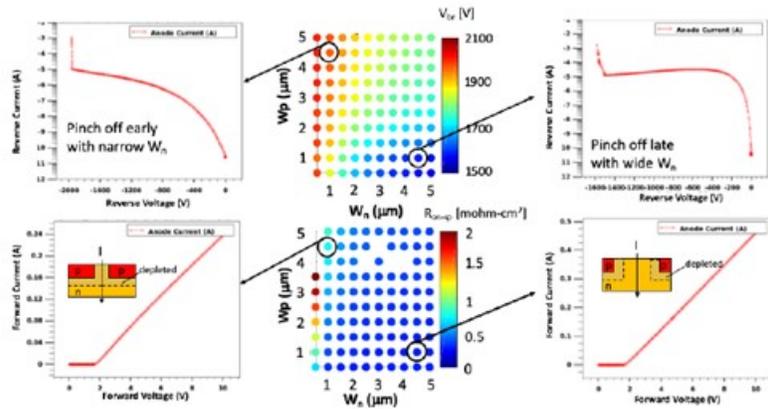


Figure I.10.5 (top row) Simulated breakdown voltage and (bottom row) on-resistance of GaN JBS diodes. Left column is a design with a narrow current-carrying channel, while right column is a design with a wide current-carrying channel. The middle column represents the device performance.

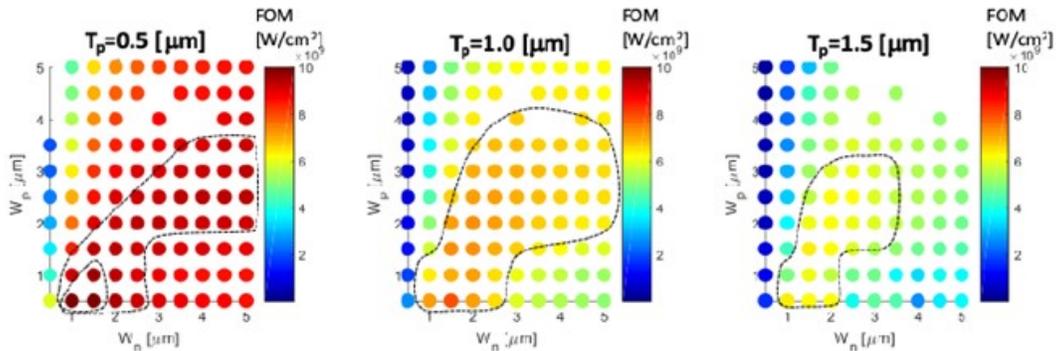


Figure I.10.6 Simulated Baliga Figure of Merit for JBS diodes with three different p-layer widths.

**Vertical GaN Transistors**

As mentioned previously, TCAD simulations were used to investigate the performance of the T-MOSFET and D-MOSFET devices. To limit the simulation space, a gate dielectric composed of Silicon Nitride ( $\text{SiN}_x$ ) was chosen, and the forward and reverse bias performance of the transistors was simulated to examine changes in parameters such as layer thickness and doping. Performance metrics including breakdown voltage, forward specific on-resistance, and the BFOM were evaluated as they were in the diode simulations to find the optimal designs. Figure I.10.7 shows the optimization information for the D-MOSFET analyzing four parameters: JFET region width (area under the gate), epilayer (drift layer) doping, current spreading layer (CSL) doping, and JFET region doping. To bound the simulations, a p-GaN (source) layer doping of  $1 \times 10^{18} \text{ cm}^{-3}$  and a source layer doping of  $5 \times 10^{18} \text{ cm}^{-3}$  were chosen. The blue lines represent the simulated breakdown voltage as determined by either the breakdown of the GaN or the peak field in the gate dielectric reaching  $4 \text{ MV/cm}$  (a

known limit to reliability for SiC devices). The black lines represent the forward specific on-resistance, and the red lines represent the BFOM for the devices. Using the BFOM as the design optimization parameter, the ideal GaN D-MOSFET would have a JFET width less than or equal to 1  $\mu\text{m}$ , a JFET doping level of  $5 \times 10^{17} \text{ cm}^{-3}$  (n-type), an epilayer (drift layer) doping level of  $\sim 1\text{-}1.5 \times 10^{16} \text{ cm}^{-3}$ , and a CSL doping levels of  $1\text{-}2 \times 10^{17} \text{ cm}^{-3}$ , all of which are achievable using our GaN MOCVD capability. Based on these simulations, the D-MOSFET looks like a promising candidate for a vertical GaN transistor for an automotive drivetrain, and process development is underway to realize this device.

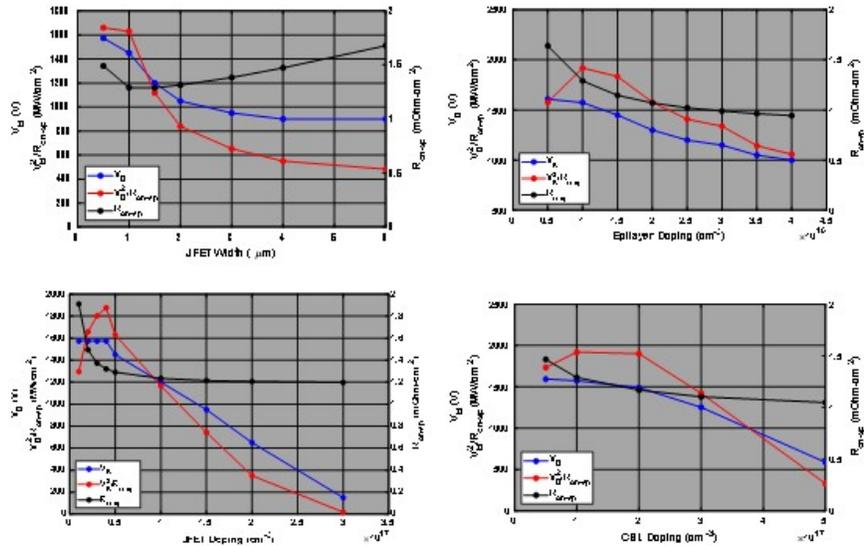


Figure I.10.7 TCAD simulations of D-MOSFETS, examine four design parameters: (top left) JFET region width, epilayer (drift layer) doping (top right), current spreading layer doping (bottom left), and JFET region doping (bottom right).

Additionally, T-MOSFETs were simulated and show promise for vertical GaN transistors. A set of similar simulations was performed to investigate the forward and reverse bias performance of the device as well as the internal electric fields within the device, which might limit performance. For a device with the cross-section as defined in the top portion of Figure I.10.8, the reverse-bias operation was simulated and the resulting internal electric field profile (middle) and IV performance (bottom) are shown. The inputs for the simulation are: source doping of  $5 \times 10^{18} \text{ cm}^{-3}$ , base doping of  $1 \times 10^{19} \text{ cm}^{-3}$ , epilayer doping of  $1 \times 10^{16} \text{ cm}^{-3}$ , p<sup>+</sup> trench doping of  $3 \times 10^{19} \text{ cm}^{-3}$ , buffer layer doping of  $5 \times 10^{18} \text{ cm}^{-3}$ , and CSL doping of  $3 \times 10^{16} \text{ cm}^{-3}$ . The peak electric field occurs near the corner of the trench area and has a value of 7 MV/cm, resulting in a breakdown voltage for the device of over 1.7 kV. The peak electric field in the gate dielectric layer is 2.6 MV/cm which is below the threshold of concern for device reliability. The same device was simulated in forward-bias operation and showed good performance with a threshold voltage of 2.1 V, a specific on-resistance value < 1 m $\Omega\text{-cm}^2$ , and a maximum drain current of nearly 0.5 A/mm. These results are similar to the simulated D-MOSFET performance.

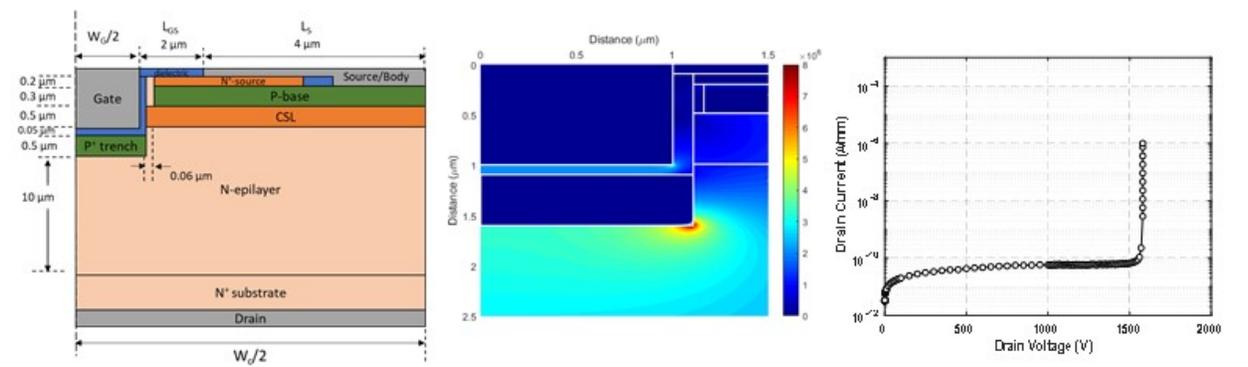


Figure I.10.8 (left) Schematic drawing of T-MOSFET. (middle) Simulated internal electric field of the same device. (right) simulated breakdown characteristic of the same device.



Because of the good performance of both types of MOSFETs, a down-select to one of the topologies does not make sense at this time. Instead, both structures are being considered for additional evaluation by looking at other constraints, including thermally-induced degradation in performance using additional thermo-electric simulations and growth and/or fabrication concerns that might limit the performance of a realistic device. To evaluate the growth and fabrication limitations to device realization, a series of short experiments is planned to demonstrate and evaluate the process capability needed. After further consideration, one of the structures will be selected on which to focus the resources of a single device development effort.

## Conclusions

GaN offers the promise of power electronic devices with performance that exceeds conventional Si and even SiC-based devices. This is due to its advantageous material properties, chiefly its higher breakdown electric field. Due to the increased maturity of GaN substrates, vertical GaN devices showing promising performance are being demonstrated and are being considered for insertion into power conversion applications. This project has focused on the design, simulation, and fabrication processes needed to build vertical GaN diodes and transistors for use in electric drive traction systems. GaN SBDs have been simulated, and simple devices have been fabricated to help improve predictive ability of the models. GaN SBDs with excellent ideality factors of 1.05 were characterized and are indicative of the high quality of the metal/semiconductor junction using with our fabrication processes. JBS diodes were then simulated using the SBD models and existing PN diode models as input to develop a design optimization for future fabrication of these devices. Using the outcome of the simulations, experiments have begun to further develop the growth and fabrication processes necessary for realization of these devices. For GaN transistors, a careful simulation study was done to understand the performance comparison between T-MOSFETs and D-MOSFETs. Based on these results, both device topologies look promising for future automotive applications and are being considered as potential candidates for the traction drive system. Future work will focus on demonstrating and characterizing prototypes of GaN JBS diodes and demonstrating gate control on GaN MOSFETs. The characterization of the first prototypes will help provide feedback into the design efforts to continually improve the devices.

## Key Publications

1. L. Yates, A. Binder, J. Dickerson, G. Pickrell, and R. Kaplar, "Electro-thermal Simulation and Performance Comparison of 1.2 kV, 10 A Vertical GaN MOSFETs," Rio Grande Symposium on Advanced Materials, Albuquerque, NM (September 2019).

## References

1. I. C. Kizilyalli, A. P. Edwards, O. Aktas, T. Prunty, and D. J. I. T. o. E. D. Bour, "Vertical power pn diodes based on bulk GaN," vol. 62, no. 2, pp. 414-422, 2014.
2. A. Armstrong et al., "High voltage and high current density vertical GaN power diodes," vol. 52, no. 13, pp. 1170-1171, 2016.
3. H. Ohta, K. Hayashi, F. Horikiri, M. Yoshino, T. Nakamura, and T. J. J. J. o. A. P. Mishima, "5.0 kV breakdown-voltage vertical GaN p-n junction diodes," vol. 57, no. 4S, p. 04FG09, 2018.
4. T. Oka, Y. Ueno, T. Ina, and K. J. A. P. E. Hasegawa, "Vertical GaN-based trench metal oxide semiconductor field-effect transistors on a free-standing GaN substrate with blocking voltage of 1.6 kV," vol. 7, no. 2, p. 021002, 2014.
5. H. Otake, S. Egami, H. Ohta, Y. Nanishi, and H. Takasu, "GaN-Based Trench Gate Metal Oxide Semiconductor Field Effect Transistors with Over 100 cm<sup>2</sup>/(V s) Channel Mobility," Japanese Journal of Applied Physics, vol. 46, no. 25-28, p. L599, 2007.
6. S. Chowdhury, M. H. Wong, B. L. Swenson, and U. K. J. I. E. D. L. Mishra, "CAVET on bulk GaN substrates achieved with MBE-regrown AlGaIn/GaN layers to suppress dispersion," vol. 33, no. 1, pp. 41-43, 2011.

7. T. Anderson et al., “Activation of Mg implanted in GaN by multicycle rapid thermal annealing,” vol. 50, no. 3, pp. 197-198, 2014.
8. G. Pickrell et al., “Regrown Vertical GaN p–n Diodes with Low Reverse Leakage Current,” vol. 48, no. 5, pp. 3311-3316, 2019.

### **Acknowledgements**

This work is supported by the DOE Office of Energy Efficiency and Renewable Energy, Vehicle Technologies Office. Sandia National Laboratories is a multi-mission laboratory managed and operated by National Technology and Engineering Solutions of Sandia, LLC., a wholly owned subsidiary of Honeywell International, Inc., for the U.S. Department of Energy’s National Nuclear Security Administration under contract DE-NA0003525. The views expressed in the article do not necessarily represent the views of the U.S. Department of Energy or the United States Government.

## I.11 Advanced Packaging Designs – Reliability and Prognostics (NREL)

### **Douglas DeVoto, Principal Investigator**

National Renewable Energy Laboratory  
15013 Denver West Parkway  
Golden, CO 80401  
E-mail: [douglas.devoto@nrel.gov](mailto:douglas.devoto@nrel.gov)

### **Susan Rogers, DOE Technology Development Manager**

U.S. Department of Energy  
E-mail: [susan.rogers@ee.doe.gov](mailto:susan.rogers@ee.doe.gov)

Start Date: October 1, 2018      End Date: September 30, 2021  
Project Funding (FY19): \$175,000      DOE share: \$175,000      Non-DOE share: \$0

### **Project Introduction**

The Vehicle Technologies Office and the Electrical and Electronics Technical Team have proposed aggressive research and development targets [1] aimed at improving power electronics technology to enable the mass market penetration of electric-drive vehicles. Achieving these aggressive power electronics targets will require a decrease in cost (year 2025 cost target: \$2.70/kW) and an increase in power density (year 2025 power density target: 100 kW/L) as compared with current, on-road technology. Replacing traditional silicon device-based components with more efficient and higher temperature wide-bandgap semiconductor device-based components will enable increasing the power density. However, meeting the power density target will also require innovative packaging and thermal management solutions to increase the heat fluxes dissipated, and allow for compact electronics packaging.

Decreasing the thermal resistance pathway in power electronics packages is a primary objective for maximizing the performance of wide-bandgap devices. This can be accomplished by either replacing package layers with new materials that enable greater thermal, electrical, and reliability performance, or eliminating layers and components through new packaging designs. Safe and robust operation of the power electronics requires electrical isolation of the high voltage circuitry within the power electronics module. For example, typical power electronics modules use a ceramic material within the package for electrical isolation and wire bonds for electrical connections.

### **Objectives**

The primary deliverable for this project will be to construct a power electronics package utilizing an organic electrically insulating substrate material with a direct chip-to-chip interconnect technology and demonstrate superior thermal performance and greater reliability under thermal cycling, thermal aging, vibration, power cycling, and electrical high-potential evaluation over traditional packages. This will be accomplished through the following tasks:

- *Design optimization of a power electronics package.* A multiphysics optimization process will incorporate the electrically insulating substrate alternative into a novel power electronics package. Electrical, thermal, and mechanical constraints will be balanced through this optimization.
- *Prototype construction.* Example power electronics packages based on an electrically insulating substrate alternative with devices joined by Quilt Packaging (QP) will be developed.

### **Approach**

The project aim is to develop a power-dense, reliable, and cost-effective 3D power electronics package enabled by an alternative electrical isolation material. This material provides equivalent electrical isolation to current

technologies while providing high thermomechanical reliability at high device junction temperatures, as well as enabling higher power densities. In addition, elimination of design constraints associated with traditional ceramic substrates reduces device-to-coolant thermal resistance, simplifies package design, and offers more design flexibility. This package design will eliminate component layers in a new, low cost, simplified manufacturing process for a packaging design that will allow for higher power densities and reliability. Additionally, the new circuit board structure will transport heat out of encapsulated component areas within a 3D structure. This work is being performed in collaboration with Oak Ridge National Laboratory (ORNL) and DuPont.

QP is a chip-to-chip interconnect technology that incorporates conductive metal “nodules” on the sides of the chips. The technology has been commercialized by Indiana Integrated Circuits, LLC (IIC) from research originating at the University of Notre Dame. IIC will design and fabricate QP test chips for NREL to evaluate the electrical characteristics of the interconnect technology as a replacement for traditional wire bond interconnects. Design work with IIC has also involved collaboration with ORNL.

## Results

### *Power Electronics Module Design with Organic Insulating Substrate*

Figure I.11.1 shows a typical state-of-the-art power electronics package stackup. During operation, a significant amount of heat is generated by the semiconductor device that needs to be removed to keep temperatures within limits. However, due to the roughness of the component surfaces in contact with each other, air gaps are formed between the surfaces and can cause a large resistance to heat transfer, which in turn results in large increases in temperatures in the package. Bonded materials ensure an efficient path for heat transfer at the interfaces by closing these air gaps. Hence, the semiconductor device is typically attached by a bonded material such as solder at the die-attach level to a metallized substrate. The substrate is composed of a ceramic bounded by copper layers on either side and provides electrical isolation. This substrate is then mounted onto a baseplate or directly to a heat exchanger, typically made of copper or aluminum, via a substrate-attach, typically another solder alloy or a grease. Efforts to improve the thermal management design of the traditional power electronics package has led to cooling both sides of a semiconductor device. Figure I.11.1 also shows two examples of packages utilizing double-sided cooling. Wire bonds are replaced with metal terminals to allow for cooling of the top side of a device. Variations of these designs have been commercialized in several automotive applications from both General Motors and Toyota.

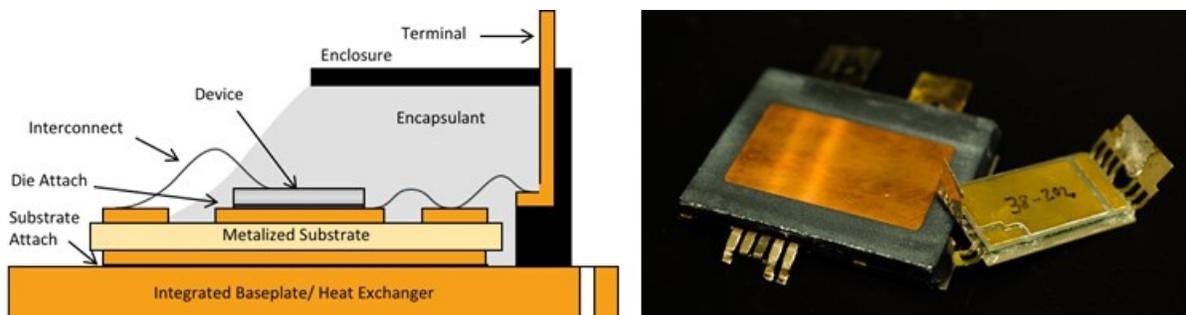


Figure I.11.1 A traditional power electronics package (left), and double-sided-cooled power electronics packages from Toyota and General Motors (right).

General Motors has implemented a double-sided cooling design within the second-generation Chevy Volt as shown in Figure I.11.2. The design sandwiches the semiconductor devices and electrical connections between two ceramic substrates, then attaches heat sinks to both sides of the package. Toyota has designed a similar

commercial package where ceramic substrates are placed on either side of a semiconductor device for double-sided cooling, also shown in Figure I.11.2.

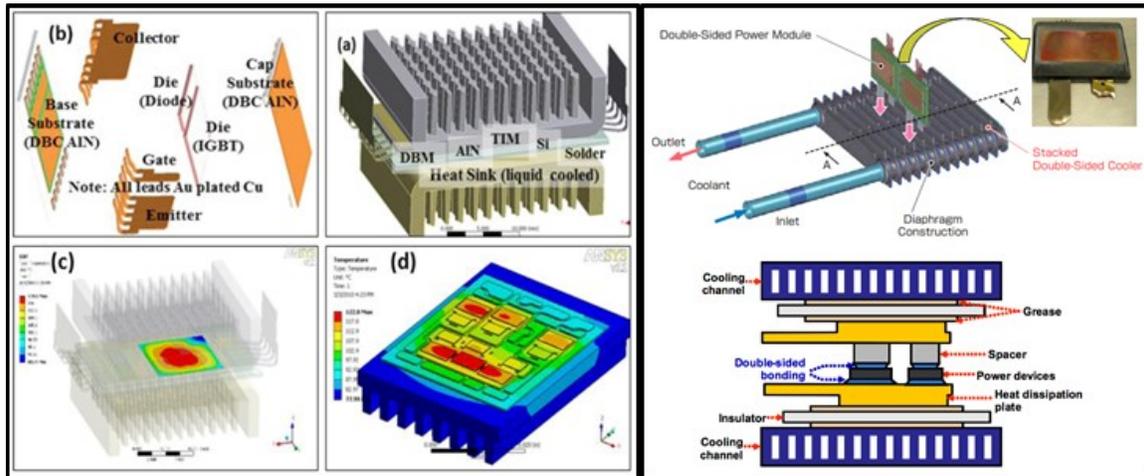


Figure I.11.2 Power device within a second-generation Chevy Volt [2] (left), and example double-sided cooling structure [3] (right).

In both single- and double-sided cooling designs employing water-ethylene glycol as the coolant, ceramic substrates are used to isolate the electrically active components from the thermal management system. The ceramic substrates typically are composed of aluminum oxide ( $\text{Al}_2\text{O}_3$ ), aluminum nitride (AlN), or silicon nitride ( $\text{Si}_3\text{N}_4$ ).  $\text{Al}_2\text{O}_3$ -based substrates have been utilized as an industry standard for electrical insulation for many years, and recently AlN and  $\text{Si}_3\text{N}_4$  are being used for improved thermal and mechanical properties. However, their improved performance comes at a significant cost increase, with  $\text{Si}_3\text{N}_4$  substrates costing several times more than their  $\text{Al}_2\text{O}_3$  counterparts. Thin copper (Cu) layers are bonded to either side of the substrate using a direct-bond-Cu (DBC) or active metal brazing (AMB) process. These processes involve bonding metallization layers symmetrically to both sides of the ceramic at a high temperature, as bonding to only one side would cause deformation during the cooling phase. The metal bonded to either side of the ceramic is between 0.3 and 0.8 mm in thickness, as the high-temperature manufacturing process does not allow very thick metals to be bonded. This limits the heat spreading capability of the thermal substrate and the current-carrying capacity of the metallization layer that is bonded with the semiconductor device. The metallization layer adjacent to the heat spreader or cold plate is bonded via a solder or grease layer. This layer is a common failure location within a power electronics package as cracks and voids in solder or pump-out/dry-out in grease can propagate over time, causing an increase in package thermal resistance and device junction temperature.

Replacement of a traditional brittle ceramic substrate with a robust and flexible polyimide film for electrical isolation allows for direct bonding to a heat exchanger or cold plate and eliminates the need for an intermediate bonding layer, typically solder. Elimination of the brittle ceramic enables higher operating temperatures, reduces thermomechanical stresses, and allows for higher bonding pressures and temperatures during the manufacturing of the package. Implementation of this film enables the simplification of the manufacturing process allowing for time and cost reductions. These benefits will be demonstrated by the conclusion of the project and will allow for existing power electronics manufacturers to transition to polyimide film with reduced research and development time and expense. A direct replacement of the ceramic substrate with the polyimide film is shown in Figure I.11.3. The bonding process of polyimide films does not require matching top and bottom metallization layers. Each metallization layer can be optimized independently, and different thicknesses and materials can be selected. The polyimide film can be directly bonded to a cold plate or heat spreader, eliminating the requirement for the bottom metallization layer and the substrate-attach solder layer. This reduces the thermal resistance pathway between the device and coolant, eliminates the common failure

mechanism of solder fatigue, allows for higher-temperature operation above the reflow temperature of solder, and reduces manufacturing time and material costs. This direct bonding design is demonstrated in Figure I.11.3.

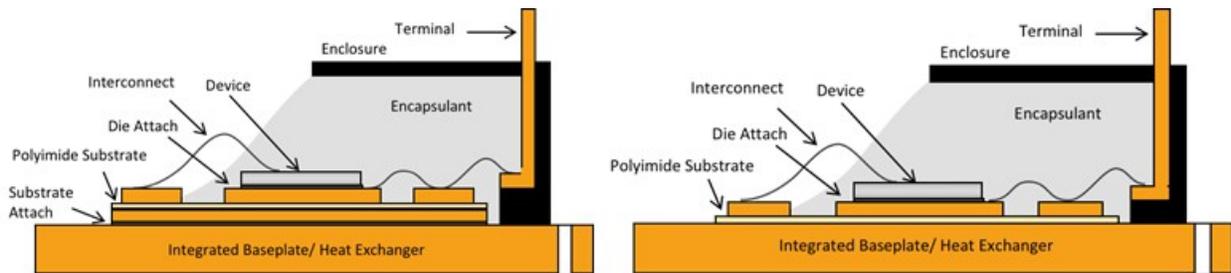


Figure I.11.3 Traditional package with metalized polyimide substrate (left), and with polyimide substrate bonded directly to baseplate/heat exchanger with no bottom metallization layer (right).

A double-sided cooling package will also benefit from the elimination of the outer metallization layer and substrate attach layer. This is demonstrated in Figure I.11.4. In addition, a polyimide-based design can be incorporated into new circuit board structures to transport heat out of encapsulated component areas within a 3D structure, as defined as stacking semiconductor devices vertically. Presently, only 2D architectures have been commercialized for automotive power electronics.

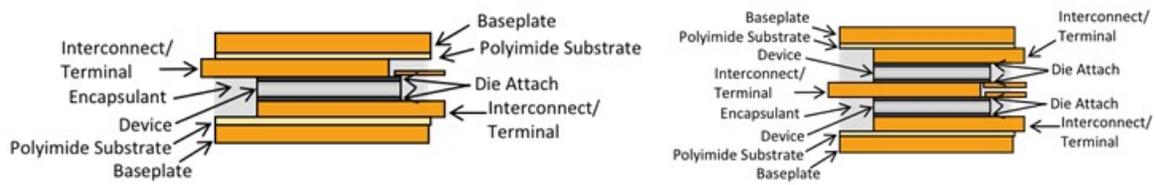


Figure I.11.4 Double-sided cooled package with polyimide substrate (left), and with stacked devices in a 3D package design (right).

The traditional manufacturing process, shown in Figure I.11.5, bonds layers together in sequential steps, requiring two solder reflow processes, separate polymer and silicone cures, and several electrical attachment steps. The steps also do not include the costly energy-intensive manufacturing process for the DBC substrate. The improved packaging design and manufacturing process are documented in the NREL Record of Invention (ROI) No. 19-15 “Organic Electrically Insulating Layers for Electronics Packaging” and the corresponding U.S. provisional patent application number 62/776,506. Figure I.11.5 also demonstrates the reduction in processing steps for the novel power electronics module.



Figure I.11.5 Manufacturing process for a traditional power electronics module [4] (top), and a simplified process for the novel power electronics package (bottom).

Both sintered silver and polyimide require an elevated temperature and pressure to complete their synthesis. After initial assembly, silver sintering and polyimide bonding would take place simultaneously in the fifth step, with all bonding and electrical connecting steps completed simultaneously. Encapsulation of the electrical components would complete the synthesis of the package, followed by electrical evaluation.

Thermal cycling, thermal aging, power cycling, and electrical high-potential evaluations were completed to validate the performance of this polyimide-based substrate. The conditions are summarized below.

- Thermal Shock: -40°C to 200°C, 5-minute dwells, for 5,000 cycles
- Thermal Aging: 175°C for 1,900 hours
- Power Cycling: 40°C to 200°C for 2,200 cycles.

No mechanical or electrical performance degradation was observed after the completion of each evaluation. The results show that polyimide-based substrate exceeds the mechanical capabilities of traditional ceramic substrates while still maintaining the necessary electrical isolation. Additional evaluations, such as 85% relative humidity and 85°C temperature conditions, are planned for FY20.

**Direct Chip-to-Chip Electrical Connection within a Power Electronics Module**

Alternative electrical interconnect designs are required as switching devices are reduced in size and spacing between devices is minimized. By joining devices with the QP technique, the need for wire bonds or other external electrical connection technology is eliminated. The QP technique has been demonstrated for microwave applications [5] and proposed for power electronics designs [6], but to date has not been experimentally validated. For this project, traditional wire interconnects will be replaced with direct chip-to-chip edge interconnect technology in a two-device package. An example of this sample design is shown in Figure I.11.6.

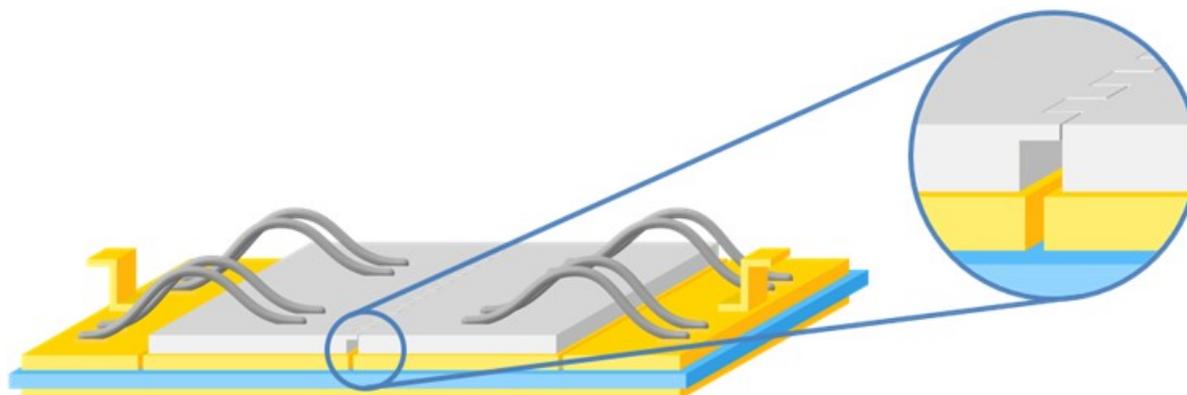


Figure I.11.6 Sample design with QP.

Experimental samples were designed in collaboration with IIC and ORNL, and a design of experiments was established based on previous QP packaging experience to optimize the size and shape of the connecting nodules. Nodules were fabricated in four different widths—100, 300, 500, and 700 μm—in both rectangular and triangular shapes. The length of the nodules extending into the chips were also varied to two lengths, 30 and 70 μm. The nodule dimensions are summarized in Table I.11.1.

**Table I.11.1 Nodule Dimensions**

Nodule Interlocking Geometry		Nodule Width (μm)			
		100	300	500	700
Nodule Length (μm)	30	Rectangular/ Triangular	Rectangular/ Triangular	Rectangular/ Triangular	Rectangular/ Triangular
	70	Rectangular/ Triangular	Rectangular/ Triangular	Rectangular/ Triangular	Rectangular/ Triangular

Reliability evaluation will be performed at NREL in FY20 after the QP devices have been mounted to substrates. Samples will be subjected to thermal shock, thermal aging, and vibration experiments. The maximum current-carrying capability of the nodule interconnects will also be determined.

**Conclusions**

The project aim is to develop a power-dense, reliable, and cost-effective 3D power electronics package enabled by an alternative electrical isolation material and electrical interconnect method. The project accomplishments for FY19 are summarized below.



- Thermal impact of polyimide-based substrate designs was modeled and experimentally evaluated. A thicker topside metallization in a polyimide-based substrate allows for enhanced thermal spreading over traditional substrate designs.
- Reliability evaluations of the polyimide-based substrate found no significant decrease in electrical or thermal performance after 5,000 thermal shock cycles, 1,900 thermal aging hours, and 2,200 power cycles.
- In collaboration with ORNL and IIC, initial device geometry—for evaluation of the QP device—was designed and fabricated. Devices will be mounted to substrates, and the package will undergo electrical and reliability evaluations in FY20.

### Key Publications

1. DeVoto, D. “Advanced Power Electronics Designs – Reliability and Prognostics.” 2019 DOE VTO Annual Merit Review, Washington, D.C., June 2019.
2. DeVoto, D. “Advanced Power Electronics Designs – Reliability and Prognostics.” 2019 presentation to the DOE VTO Electrical and Electronics Technical Team, August 2019.

### References

1. USDRIVE, 2017, *Electrical and Electronics Technical Team Roadmap*, USDRIVE. Available: <https://www.energy.gov/eere/vehicles/downloads/us-drive-electrical-and-electronics-technical-team-roadmap>
2. Anwar, M., Hayes, M., Tata, A., Teimorzadeh, M., and Achatz, T. (2015). “Power Dense and Robust Traction Power Inverter for the Second-Generation Chevrolet Volt Extended-Range EV.” *SAE International Journal of Alternative Powertrains*, 4(1), 2015–01–1201–8. <http://doi.org/10.4271/2015-01-1201>
3. Yoon, S.W., Shiozaki, K., and Kato, T. (2014). “Double-Sided Nickel-Tin Transient Liquid Phase Bonding for Double-Sided Cooling.” *IEEE Applied Power Electronics Conference and Exposition – APEC*, 527-530.
4. Horowitz, K., Remo, T., and Reese, S. (2017). *A Manufacturing Cost and Supply Chain Analysis of SiC Power Electronics Applicable to Medium-Voltage Motor Drives*. Technical Report TP-6A20-67694, National Renewable Energy Laboratory. doi:10.2172/1349212.
5. Lu, T., Kulick, J., Lannon, J., Bernstein, G., and Fay, P. (2016). “Heterogeneous Microwave and Millimeter-Wave System Integration using Quilt Packaging,” *2016 IEEE MTT-S International Microwave Symposium (IMS)*, San Francisco, CA, 2016, pp. 1-4. doi: 10.1109/MWSYM.2016.7540247
6. Lu, T., Ortega, C., Kulick, J., Bernstein, G. H., Ardisson, S., and Engelhardt, R. “Rapid SOC Prototyping Utilizing Quilt Packaging Technology for Modular Functional IC Partitioning,” *2016 International Symposium on Rapid System Prototyping (RSP)*, Pittsburgh, PA, 2016, pp. 1-7. doi: 10.1145/2990299.2990313

### Acknowledgments

The significant contributions of Joshua Major, Paul Paret, and Gilbert Moreno are acknowledged.

## I.12 Electric Motor Thermal Management (NREL)

### Kevin Bennion, Principal Investigator

National Renewable Energy Laboratory  
15013 Denver West Parkway  
Golden, CO 80401  
E-mail: [kevin.bennion@nrel.gov](mailto:kevin.bennion@nrel.gov)

### Susan Rogers, DOE Technology Development Manager

U.S. Department of Energy  
E-mail: [susan.rogers@ee.doe.gov](mailto:susan.rogers@ee.doe.gov)

Start Date: October 1, 2018

End Date: September 30, 2021

Project Funding (FY19): \$250,000

DOE share: \$250,000

Non-DOE share: \$0

### Project Introduction

This project is part of a multi-lab consortium including the National Renewable Energy Laboratory (NREL), Oak Ridge National Laboratory (ORNL), Sandia National Laboratories, and Ames Laboratory that leverages research expertise and facilities at the National Labs, universities, and industry to significantly increase electric drive power density and reliability while simultaneously reducing cost. The project is organized around three Keystone projects: (1) Power Electronics, (2) Electric Motors, and (3) Traction Drive System. The Electric Motors Keystone project at NREL focuses primarily on improvements (reductions) in the passive thermal resistance of the electric motor to increase power density in line with the most recent research priorities outlined in the U.S. DRIVE Electrical and Electronics Technical Team (EETT) Roadmap (U.S. DRIVE 2017).

In the area of electric drive motors, the EETT Roadmap highlights the importance of reducing the thermal resistance of the motor packaging stack-up to increase power density. The Roadmap also mentions that the thermal conductivity of the materials within the motor influence the amount of material necessary to generate the required mechanical power. The Roadmap emphasizes research areas with a focus on material physics-based models, improved materials, and thermally conductive epoxy and fillers. In addition, the Roadmap highlights a research gap in that the material performance characterization techniques are not well known or identified in the literature.

Heat transfer and thermal management are critical to electric motors since - as mentioned in the EETT Roadmap - thermal constraints place limitations on how electric motors ultimately perform, and “an optimized thermal design can help increase machine rated power substantially” (Lipo 2007). The thermal management of electric motors for vehicles is complex because of the multiple heat transfer paths within the motor, the variation in heat due to motor operating conditions, and the multiple material interfaces through which heat must pass through to be removed. For these reasons, “heat transfer is as important as electromagnetic and mechanical design” (Hendershot and Miller 1994) for solving research challenges to improve the electric motor power density, cost, and reliability as outlined by the EETT Roadmap.

### Objectives

Research under this project will be performed within the framework of a new research consortium consisting of a multi-disciplinary team that will plan, establish, conduct, and manage a portfolio of multi-lab and multi-university research efforts to advance the state of the art in electric drive technologies. The final objective of the consortium is to develop a 100-kW traction drive system that achieves a power density of 33 kW/L, has an operational life of 300,000 miles, and a cost of \$6/kW. The system will be composed of a 100-kW/L inverter and a >20,000 rpm, 50-kW/L electric motor. Building on the research experience and capabilities within each laboratory, the multi-lab consortium will focus on achieving research objectives within three Keystone projects: Power Electronics, (2) Electric Motors, and (3) Traction Drive System.

For the Motors Keystone project, key consortium objectives will focus on research on motor technology gaps to enable increased power density and reliability supporting research pathways in power electronics technologies. As power electronics technologies develop to enable higher operating temperatures, higher system voltages, and higher switching frequencies, motor technologies will also be necessary to realize the electric drive system benefits. Key consortium motor research pathways include motor material improvements (electrical, magnetic, and thermal), higher motor operating speeds, and higher system voltages. NREL research will provide motor researchers—within the consortium and outside—with the data and models to enable motor innovations and the use of novel materials and designs. The work supports broad demand for data, analytical methods, and experimental techniques to improve and better understand motor thermal management. It also combines unique capabilities, facilities, and expertise in addition to the data, analysis methods, and experimental techniques to improve and better understand heat transfer within electric motors to meet the demands of electric drive vehicles. NREL’s focus in FY19 included:

- Develop thermal characterization experiment for measuring thermal resistance of high-thermal-resistance materials and interfaces with improved experimental uncertainty at higher temperatures to support motor material development efforts
- Develop models and simulation tools in support of consortium team members in quantifying thermal performance and heat transfer technologies to support motor development efforts.

### Approach

The ability to remove heat from an electric motor depends on the passive stack heat transfer within the motor and the convective cooling heat transfer of the selected cooling technology. In addition, as new materials are developed, it is important to characterize temperature-dependent material properties and thermal interface properties. Characterization of new materials enables motor designers to evaluate the potential performance tradeoffs of new materials for motor applications. For this reason, the approach for the research project splits the efforts between two primary areas. The first focus area for NREL during FY19 was the development of experimental methods to measure high-thermal-resistance materials and interfaces at elevated temperatures, which is relevant to motor winding materials, core materials, and magnet materials. The second focus area involves thermal model development to support electric motor design and development research efforts performed within the consortium. Each of these efforts is summarized below.

#### *Thermal Resistance Characterization Experimental Methods*

Although methods and apparatuses exist to measure low thermal conductivity materials, the currently existing solutions do not have well-defined uncertainty and typically require large sample sizes (6x6 inches). For many of the samples NREL wants to test (electric machine components, high-resistance insulation), it is extremely expensive or impossible to construct material samples with a cross-sectional footprint of 6x6 inches. Furthermore, without well-defined uncertainty on the measurements, it is not possible to rigorously compare materials. For this reason, a thermal conductivity apparatus was designed to test high-thermal-resistance samples with a small sample size of 2x2 inches, which requires one-ninth the material than other available test methods. The apparatus also has very well-defined uncertainty.

The root of the uncertainty in the ASTM D5470 (D09 Committee 2012) method is due to the intrinsic accuracy of temperature measurement (shown as resistance temperature detectors (RTDs) in Figure I.12.1). The difference between two RTDs in each metering block provides the data to derive the heat flux going through the metering blocks, which have known thermal conductivity. The approach for measuring the thermal resistance of the sample is shown in Figure I.12.1. If the temperature difference between two RTDs at any point approaches their accuracy, the uncertainty in the temperature difference will quickly become large. This

results in a U-shaped uncertainty interval versus sample thermal resistance, where there is an optimal thermal resistance the apparatus can measure with reasonable uncertainty.

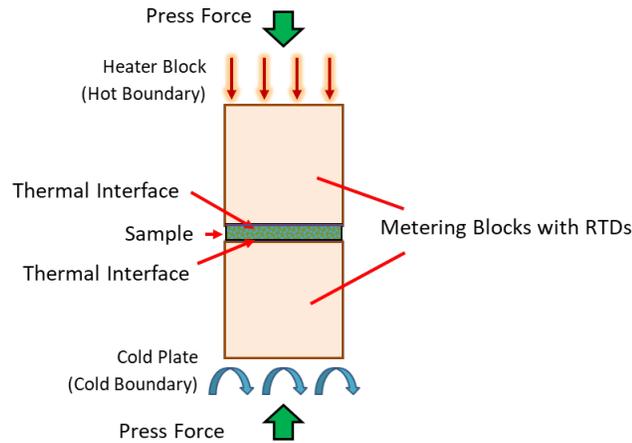


Figure I.12.1 Overview of ASTM D5470 method for measuring the thermal resistance of a sample placed between two metering blocks. (Source: Emily Cousineau, NREL)

Different approaches are required to reduce the experiment uncertainty at each end of the U-shaped uncertainty interval versus sample thermal resistance. When the thermal resistance of the sample is very low (high thermal conductivity), the temperature gradient across the sample is also very low, resulting in high uncertainty in the temperature gradient. The solution to this is to increase the heat flux going through the sample, which can be done either by increasing the current to the heat source or concentrating the heat using smaller metering blocks. However, these approaches will not work for high-thermal-resistance (low thermal conductivity) samples.

When the thermal resistance of the sample is very high (low thermal conductivity), the temperature gradient across the metering blocks will become very small because of the lower heat flux that can pass through the samples within the temperature limits of the apparatus. When the thermal resistance of a sample surpasses a certain point ( $\sim 5,000 \text{ mm}^2\text{-K/W}$  for copper metering blocks), the heat flux reduces to a point where convection and radiation effects begin to become a concern. One solution is to use larger area metering blocks. Increasing the size of the metering blocks can reduce convection and radiation effects; however, this also requires larger sample sizes, which may become expensive or even impossible (in the case of motor windings) to manufacture.

Besides improving the measurement uncertainty, another key goal of the experiment is to enable the measurement of thermal resistance at elevated temperatures within a controlled environment. As the power density of the motors increases, the materials within the motor can be exposed to high temperatures (over  $150^\circ\text{C}$ ). For this reason, we designed the experiment to enable materials to be measured up to a temperature of  $200^\circ\text{C}$ . In addition to the ability to measure materials at elevated temperatures, the experiment also accurately measures the pressure and thickness of the sample to capture the impact of distance and pressure when measuring interface thermal resistances.

### ***Consortium Team Member Thermal Analysis Collaborations***

With the initiation of the multi-lab consortium, NREL also provided thermal analysis support to consortium team members. This included discussions for thermal and mechanical characterization of material samples with collaborators, as well as performing thermal modeling and simulation in support of partner-led efforts related to electric motor designs. For example, NREL worked closely with ORNL researchers to model potential heat transfer and thermal management strategies for new motor designs led by ORNL. The initial work during FY19 focused on creating thermal finite element analysis models to study the sensitivity of

alternative motor materials and cooling strategies on the overall temperature profile within the electric motor under multiple operating conditions. This work supported ORNL in identifying potential thermal management strategies to meet the motor performance objectives.

## Results

The results for both the thermal resistance experimental methods and the consortium team member thermal analysis collaborations are summarized below.

### *Thermal Resistance Characterization Experimental Methods*

Building on past experience with thermal resistance measurements, NREL created a finite element analysis thermal model of the experimental design to study possible approaches to reduce the measurement uncertainty. The model enabled analysis to study the influence of the metering block (Figure I.12.1) thermal properties and geometry in combination with conduction, convection, and radiation heat transfer. Figure I.12.2 provides one example of analysis that was performed to locate the best temperature measurement locations within the metering blocks for calculating the heat flux through the block. The figure highlights the need to place the temperature measurements at least 25.4 mm away from the bottom of the metering block.

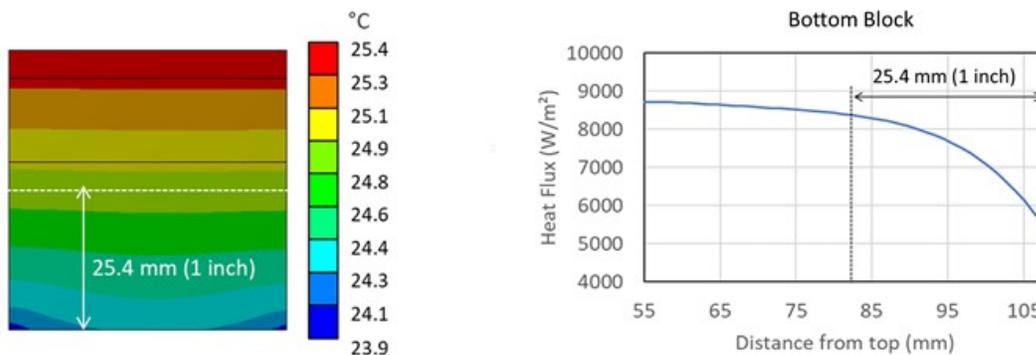


Figure I.12.2 Example analysis for locating temperature measurement locations within bottom metering block. Example temperature profile through metering block showing uniform temperature gradient beyond 25.4 mm from the bottom of the block (left). Example showing the calculated heat flux through the metering block, highlighting the heat flux variation towards the bottom of the metering block. (Source: Emily Cousineau, NREL)

Figure I.12.3 provides another example comparing the impact of alternative metering block materials and a copper spreader. As seen in the figure, the lower thermal conductivity materials increase the temperature variation along the analysis plane where the temperature is measured. This can increase the experiment measurement uncertainty. As also seen in the figure, attaching a copper spreader block to the bottom of the metering block does not improve the spatial temperature variation. For this reason, the new experimental setup was not designed to include a copper spreader block.

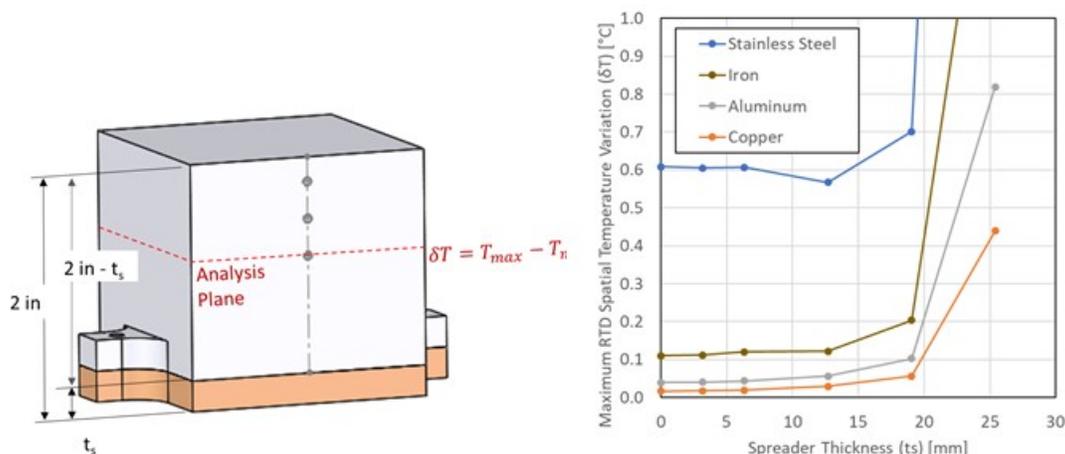


Figure I.12.3 Example analysis for including a copper spreader to the metering block with different metering block materials. Drawing of metering block with copper spreader (left). Example results showing the calculated spatial temperature variation within the temperature measurement plane for different metering block materials and spreader thicknesses. (Source: Emily Cousineau, NREL)

Table I.12.1 summarizes the impact of the metering block material on the overall systematic measurement error caused by the RTD uncertainty and the in-plane temperature variation. As seen in the table, even though the lower thermal conductivity metering blocks do increase the in-plane temperature variation (Figure I.12.3), the overall measurement error is reduced as compared to the use of standard copper metering blocks.

**Table I.12.1 Summary of Measurement Error with Different Metering Block Materials for High Thermal Resistance Sample**

Metering Block Type	Thermal Conductivity [W/m-K]	Sample Rth (Actual) [mm <sup>2</sup> -K/W]	Systematic Error (Including RTD uncertainty and in-plane temperature variation)
Copper	391 (“Copper Alloys - Copper C101 Properties, Fabrication and Applications” 2005)	17780	18.4%
Al-6061	154 (Lau and Pao 1997)	17780	9.60%
Iron	58 (Engineering Toolbox 2005)	17780	3.30%
Stainless Steel	14 (Engineering Toolbox 2005; Incropera and DeWitt 1981)	17780	1.20%

In addition to building the experimental hardware (shown in Figure I.12.4), a calibration procedure was also developed during FY19 for the new experiment. To do a general calibration, a sample with a known thermal conductivity is measured as a test standard. The test standard selected is yttria-stabilized zirconia, which has been rigorously characterized by the National Institute of Standards and Technology (Slifka, Filla, and Stalick 2000) and has a thermal conductivity of 2.19 W/m-K, which is close to the thermal conductivity range of the materials of interest (e.g., motor laminations, motor windings). The thermal conductivity of yttria-stabilized zirconia is also very stable across a wide temperature range, making it an ideal test standard. Additional details of the experimental design and calibration will be included in a planned future manuscript submission to a journal.

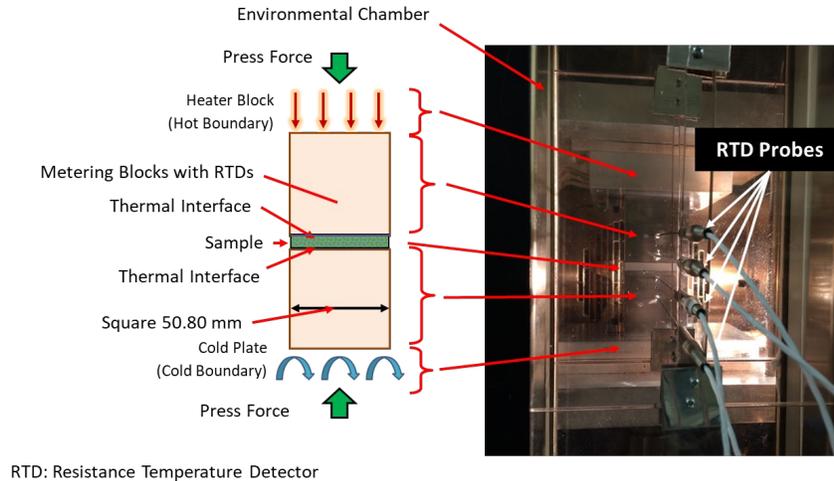


Figure I.12.4 Constructed experimental hardware inside environmental chamber. (Source: Emily Cousineau, NREL)

### ***Consortium Team Member Thermal Analysis Collaborations***

The collaborative work within the multi-lab consortium is ongoing and is planned to continue into FY20. Plans are underway to use the newly developed experimental capabilities to support both thermal and mechanical characterization of materials developed within the consortium through other research efforts led by ORNL, Sandia National Laboratories, and Ames Laboratory. During FY19, NREL worked with ORNL to support thermal analysis of motor research efforts led by ORNL. Working collaboratively, ORNL and NREL identified potential materials and cooling strategies to enable the ORNL-led motor research to achieve the desired performance metrics. Planned work into FY20 will continue the collaboration with ORNL to refine the thermal management design of the selected motor. Additional details related to the ORNL-led motor research can be found in its report related to its Keystone 2-led research efforts.

### **Conclusions**

During FY2019, research was performed to improve the understanding of motor material and material interfaces related to electric motors and heat transfer technologies. The work supports ongoing research efforts within a multi-lab consortium focused on electric drive technologies related to power electronics, electric motors, and traction drive systems. This included the design, construction, and calibration of an improved experimental setup for measuring high thermal resistance materials and interfaces at elevated temperatures. This work will support potential future planned work within the consortium to develop materials to improve electric motor performance. Also, work is underway to publish a paper in open literature describing the experimental approach and methods. In addition to the material characterization efforts, NREL is also supporting the consortium through thermal modeling and analysis support, which builds on past experiments and data measured at NREL for both convective motor cooling and materials, such as a paper published in FY2019 describing experimental measurements and modeling of electric motor lamination materials (Cousineau et al. 2019).

### **Key Publications**

1. Cousineau, J. Emily, Kevin Bennion, Douglas DeVoto, and Sreekant Narumanchi. "Experimental Characterization and Modeling of Thermal Resistance of Electric Machine Lamination Stacks." *International Journal of Heat and Mass Transfer*, vol. 129, pp. 152–159, Feb. 2019.
2. Bennion, Kevin. "Thermal Management in Electrical Applications – Electric Motors," Presented at the 2019 IEEE International Electric Machines & Drives Conference (IEMDC), 11–15 May 2019, San Diego, California

3. Bennion, Kevin. “Electric Motor Thermal Management R&D.” 2019 DOE VTO Annual Merit Review, Washington D.C., June 2019.

## References

1. “Copper Alloys - Copper C101 Properties, Fabrication and Applications.” 2005. AZoM.Com. May 11, 2005. <https://www.azom.com/article.aspx?ArticleID=2850>.
2. Cousineau, J. Emily, Kevin Bennion, Douglas DeVoto, and Sreekant Narumanchi. 2019. “Experimental Characterization and Modeling of Thermal Resistance of Electric Machine Lamination Stacks.” *International Journal of Heat and Mass Transfer* 129 (February): 152–59. <https://doi.org/10.1016/j.ijheatmasstransfer.2018.09.051>.
3. D09 Committee. 2012. “Test Method for Thermal Transmission Properties of Thermally Conductive Electrical Insulation Materials.” West Conshohocken, PA: ASTM International. <http://www.astm.org/Standards/D5470.htm>.
4. Hendershot, J. R., and Timothy John Eastham Miller. 1994. *Design of Brushless Permanent-Magnet Motors*. Oxford, UK: Magna Physics Publishing.
5. Incropera, Frank, and David DeWitt. 1981. *Fundamentals of Heat and Mass Transfer*. 4th ed. John Wiley & Sons.
6. Lau, John H., and Yi-hsin Pao. 1997. *Solder Joint Reliability of BGA, CSP, Flip Chip, and Fine Pitch SMT Assemblies*. McGraw-Hill.
7. Lipo, Thomas A. 2007. *Introduction to AC Machine Design*. 3rd ed. Wisconsin Power Electronics Research Center, University of Wisconsin.
8. Slifka, Andrew J., Bernard J. Filla, and Judith K. Stalick. 2000. “Thermal Conductivity of Two Compositions of Yttria-Stabilized Zirconia.” In *Thermal Conductivity 25/Thermal Expansion 13*, 147–54. CRC Press.
9. Engineering Toolbox. 2005. “Thermal Conductivity of Metals, Metallic Elements and Alloys.” 2005. [https://www.engineeringtoolbox.com/thermal-conductivity-metals-d\\_858.html](https://www.engineeringtoolbox.com/thermal-conductivity-metals-d_858.html).
10. U.S. DRIVE. 2017. “Electrical and Electronics Technical Team Roadmap.” U.S. DRIVE. <https://www.energy.gov/sites/prod/files/2017/11/f39/EETT%20Roadmap%2010-27-17.pdf>.

## Acknowledgments

The significant contributions from Emily Cousineau, Doug DeVoto, Xuhui Feng, Bidzina Kekelia, Joshua Major, Gilbert Moreno, and Jeff Tomerlin (NREL) to the project are acknowledged. The support, collaboration, and motor design details provided by Tsarafidy Raminosoa and Randy Wiles (ORNL) are also acknowledged.



## I.13 Integrated Traction Drive Thermal Management (NREL)

### **Bidzina Kekelia, Principal Investigator**

National Renewable Energy Laboratory  
15013 Denver West Parkway  
Golden, CO 80401  
E-mail: [bidzina.kekelia@nrel.gov](mailto:bidzina.kekelia@nrel.gov)

### **Susan A. Rogers, DOE Technology Development Manager**

U.S. Department of Energy  
E-mail: [susan.rogers@ee.doe.gov](mailto:susan.rogers@ee.doe.gov)

Start Date: October 1, 2018

End Date: September 30, 2021

Project Funding (FY19): \$250,000

DOE share: \$250,000

Non-DOE share: \$0

### **Project Introduction**

To enable the mass market penetration of electric-drive vehicles and to meet consumer electric vehicle performance expectations, the U.S. DRIVE 2017 Electrical and Electronics Technical Team Roadmap [1] proposes aggressive research and development targets aimed at reducing cost and increasing electric traction drive *system power density* to 33 kW/L by 2025. The target includes high-voltage power electronics and a single traction-drive electric motor. Achieving this level of system power density would most likely require integration of the inverter and the electric motor into a single traction module. However, this approach will also require innovative thermal management solutions to provide adequate cooling to more densely packed electrical components and keep their operating temperatures within optimal range.

### **Objectives**

The main objectives of this project are to:

- Research and evaluate motor-integrated power electronics topologies and thermal management solutions for electric traction drives
- Identify candidate driveline fluids suitable for direct cooling of traction drive components and high-voltage power electronics
- Characterize selected driveline fluids by measuring convective cooling and, if appropriate and feasible, electrical properties.

### **Approach**

To evaluate and compare different thermal management solutions for an integrated traction drive, a literature review was performed and current state-of-the-art concepts developed by the automotive Research and Development community and original equipment manufacturers were surveyed [2],[3],[4],[5],[6],[7],[8],[9],[10],[11]. Several integration concepts were identified and assigned to the following main categories:

- Separate enclosures for motor and power electronics (Figure I.13.1 a)
- Power electronics mounted on the motor outer case or distributed radially with shared cooling (Figure I.13.1 b)
- Power electronics integrated axially in the motor's front or back plate (Figure I.13.1 c).

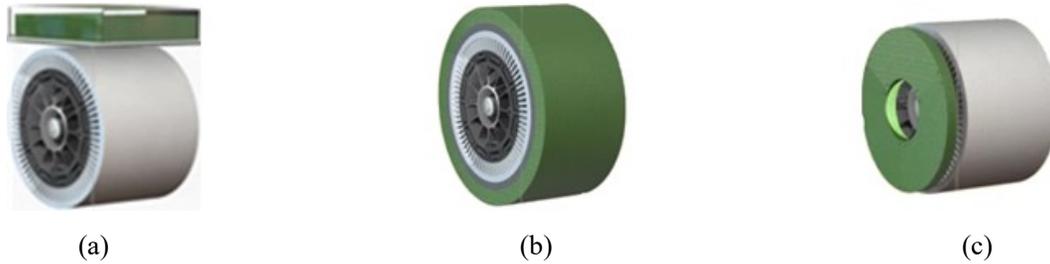


Figure I.13.1 Electric motor and power electronics integration concepts: (a) Separate enclosures for motor and power electronics, (b) Power electronics mounted or distributed radially on the motor outer case with shared cooling, (c) Power electronics integrated axially in the motor's front or back plate (Figures by Shajjad Chowdhury, ORNL)

For the integration concepts shown in Figure I.13.1, respective models will be built, and numerical simulations will be carried out. Namely, the approach includes finite element analysis (FEA) and computational fluid dynamics (CFD) modeling of the thermal management solutions (different cooling approaches) for electric traction drives. A range of heat transfer coefficient (HTC) values will be applied to cooled surfaces, including highly efficient direct jet impingement cooling of end-windings and power devices, and component temperature distributions based on BMW's i3 electric motor and power module geometries with corresponding thermal loads from Oak Ridge National Laboratory's (ORNL's) benchmarking data will also be evaluated.

Another area of focus for the project is a thermal characterization of direct cooling of temperature-sensitive components with driveline fluids. The current work is a continuation of NREL's efforts in free-surface jet impingement heat transfer characterization for cooling of electric machines with automatic transmission fluid (ATF). Previous work focused on the influence of target surface topography and physical enhancements on the heat transfer performance [12]. An experimental fluid test loop (Figure I.13.2) is used to perform in-situ jet impingement experiments with heated target embedded in the cutout of electric machine end-windings (Figure I.13.3).

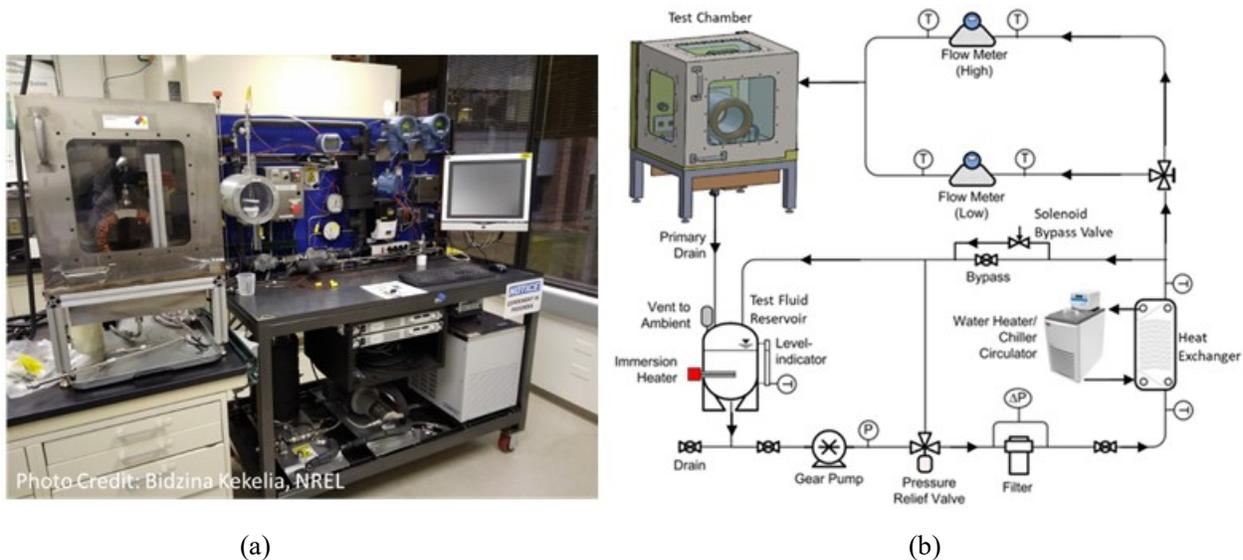


Figure I.13.2 Experimental setup for jet impingement heat transfer characterization: (a) General view of large fluid test loop (Photo by Bidzina Kekelia, NREL), (b) Large fluid test loop schematic

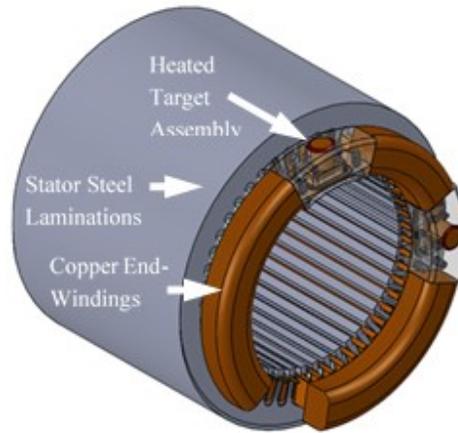


Figure I.13.3 Electric machine with mounted heat target assembly within the end-windings (Computer-aided design (CAD) model by Emily Cousineau, NREL)

## Results

### *Modeling Integrated Traction Drive*

Initial modeling efforts were focused on building an FEA model (Figure I.13.3) of an electric traction drive (based on BMW's i3 traction drive component geometries) with separate enclosures for electric motor and power electronics.

Thermal steady-state simulations of a single slot (due to symmetry) of stator windings were initiated (Figure I.13.4), to be followed by FEA thermal simulations of respective power electronics. The goal is to compare benefits and drawbacks of different concepts of integrated cooling solutions, their impact on optimal temperature distribution, and on enabling higher power output of the electric traction drive.

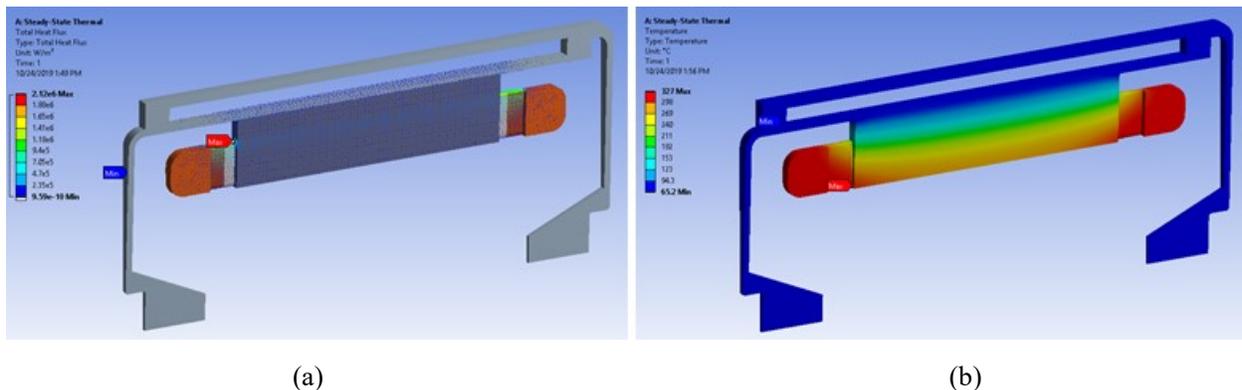


Figure I.13.4 FEA thermal simulations of a single slot of stator windings in ANSYS: (a) Heat flux distribution, (b) Temperature distribution (Figures by Bidzina Kekelia, NREL).

Figure I.13.4 illustrates cooling with fluid circulating in a cooling jacket around the motor enclosure. Other cooling concepts, including direct jet impingement on stator end windings and power electronics, applying corresponding HTCs to respective surfaces, will be also evaluated.

### *Jet Impingement Cooling with Driveline Fluids*

During recent in-situ jet impingement experiments (Figure I.13.5), Ford Mercon LV ATF was used to evaluate the impact on HTCs of varying parameters as shown in Table I.13.1.

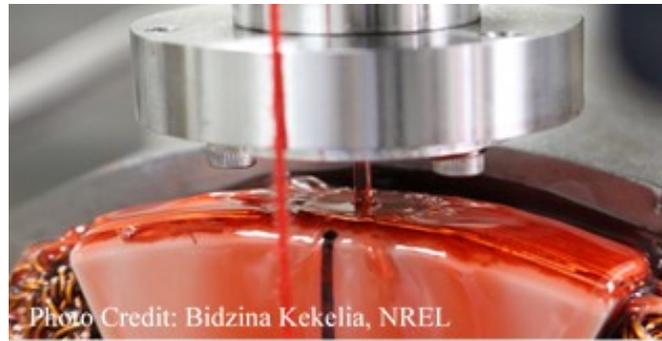


Figure I.13.5 ATF jet impingement on heated target (Photo by Bidzina Kekelia, NREL)

**Table I.13.1 Parameters varied during jet impingement heat transfer characterization experiments**

Parameter	Values
Fluid Temperature (T <sub>fluid</sub> )	50 °C, 70 °C, 90 °C
Fluid Flow Rate (Average Jet Velocity)	0.1 lpm (0.5 m/s)* 0.15 lpm (0.75 m/s)** 0.25 lpm (1.25 m/s) 0.5 lpm (2.5 m/s) 1.0 lpm (5.0 m/s) 1.5 lpm (7.5 m/s)
Target Surface Temperature (T <sub>surface</sub> )	90 °C*, 100 °C, 110 °C, 120 °C
Jet Incidence Location	Center, Edge
*Only for experiments with 50 °C and 70 °C fluid temperatures. **Only for experiments with 90 °C fluid temperature.	

It was found that the target surface temperature significantly affects convective HTC's. Namely, increasing surface temperature from 90°C to 120°C enhanced HTC values by up to 15% (see Figure I.13.6). The discovered effect is likely due to elevated fluid film temperature near the heated surface, resulting in reduced viscosity (strongly temperature-dependent property for ATF) above the hot surface. Lower viscosity leads to a thinner viscous boundary layer, increasing fluid flow and reducing the thermal boundary layer as well. Consequently, this results in a higher HTC due to higher temperature gradients in the thinner thermal boundary layer.

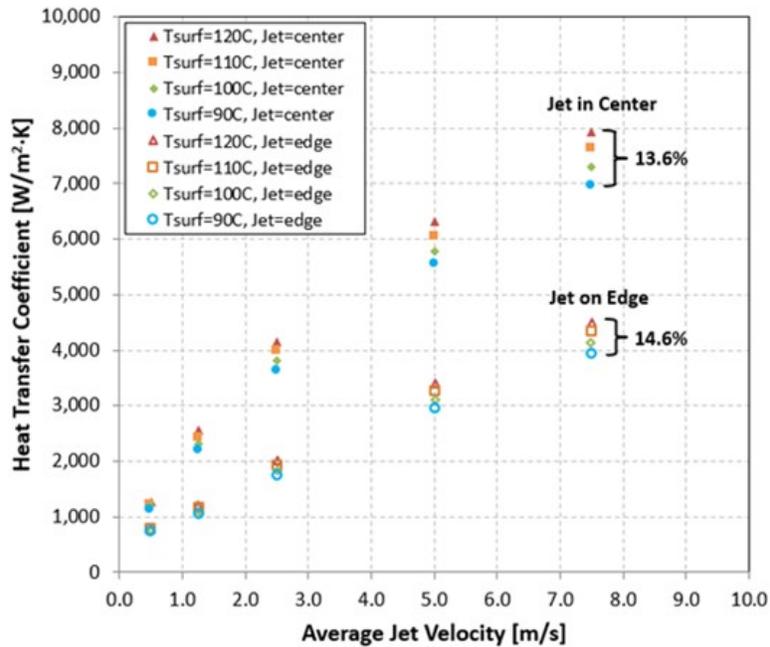


Figure I.13.6 Experimentally measured convective heat transfer coefficients for 50°C ATF at various jet impingement velocities and cooled-surface temperatures

These initial findings highlighting the target surface temperature impact on the HTCs were summarized in a technical paper published and presented at the 2019 ASME InterPACK Conference in October, 2019.

In addition to experimental HTC measurements, CFD modeling was performed for fan-shaped and orifice jet impingement with ATF (Figure I.13.7). Derived HTCs from modeling orifice jet impingement showed good agreement with experimental results.

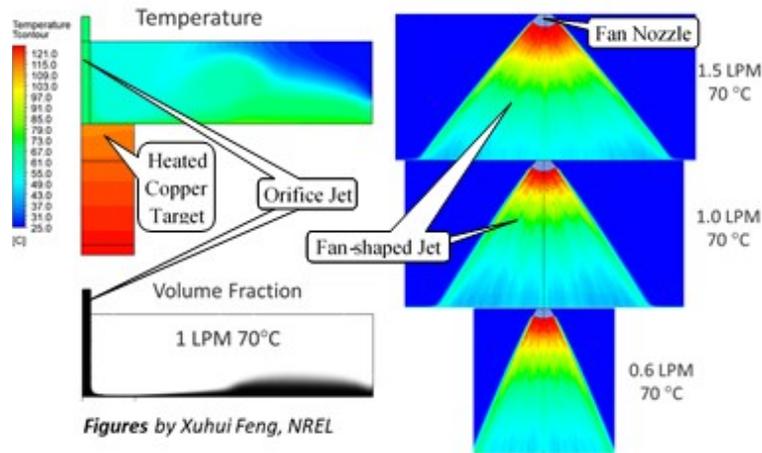


Figure I.13.7 CFD modeling of orifice and fan-shaped jet impingement on heated copper target.

**Conclusions**

The project accomplishments and conclusions for FY19 are summarized as follows:

- CAD model components of an integrated traction drive were developed for a baseline model with separate cooling enclosures for electric motor and power electronics module.

- Thermal steady-state FEA simulations of a single stator windings slot with maximum thermal loads (provided by ORNL) were initiated in ANSYS.
- Different thermal management approaches, as outlined in Figure I.13.1, are planned to be evaluated in FY2020. In addition, a concept of an internal-stator and outer-rotor integrated traction drive, currently being developed by ORNL, will also be explored.
- A large set of measured HTC's for ATF jet impingement cooling at various temperatures and flow rates was collected and published. Cooled target surface temperature impact on heat transfer effectiveness was highlighted in presentations at the IEEE ITherm 2019 and ASME InterPACK 2019 conferences. A paper was also published at the ASME 2019 InterPACK Conference. The measured HTC's are useful for understanding factors influencing performance of driveline fluid-based cooling systems for electric machines and aids automotive original equipment manufacturers and electric machine manufacturers, as well as the broader research and development community in the design and development of compact, high-performance, reliable machines. The higher temperatures of today's more powerful electric machines and power electronics would be beneficial for the performance of ATF-based cooling systems, and in turn the cooling system would have a bigger impact on increasing the power- or current density of the machines.
- CFD modeling for fan-shaped and orifice ATF jet impingement cooling of electric machines was carried out, and the results were presented at the ASME InterPACK 2019 conference.

#### Key Publications

1. Kekelia, B., "Jet Impingement Cooling of Electric Machines with Driveline Fluids," invited presentation at Technology Talks Session at the 2019 IEEE ITherm Conference, May 2019.
2. Kekelia, B., "Integrated Traction Drive Thermal Management," 2019 DOE VTO Annual Merit Review, Washington, D.C., June 2019.
3. Kekelia, B., "Surface Temperature Effect On Convective Heat Transfer Coefficients For Jet Impingement Cooling Of Electric Machines With Automatic Transmission Fluid," presented and published at the 2019 ASME InterPACK Conference.
4. Feng, X., "Thermal Performance Investigation of Jet Impingement Cooling of Electric Machines Using Automatic Transmission Fluid," presented at the 2019 ASME InterPACK Conference.

#### References

1. U.S. DRIVE. 2017. *Electrical and Electronics Technical Team Roadmap*, October 2017  
<https://www.energy.gov/sites/prod/files/2017/11/f39/EETT%20Roadmap%2010-27-17.pdf>.
2. Bosch e-axle: <https://www.bosch-presse.de/pressportal/de/en/the-start-up-powertrain-for-electric-cars-the-bosch-e-axle-offers-greater-range-121216.html>.
3. Siemens SIVETEC MSA 3300:
  - a. <https://insideevs.com/news/323281/siemens-integrates-electric-car-motor-inverter-into-single-unit/>.
  - b. <https://phys.org/news/2014-10-space-weight-electric-cars.html>.
  - c. [https://w3.siemens.com/topics/global/de/elektromobilitaet/PublishingImages/antriebe-pkw/pdf/innovative-technology-hybrid-ecar\\_en.pdf](https://w3.siemens.com/topics/global/de/elektromobilitaet/PublishingImages/antriebe-pkw/pdf/innovative-technology-hybrid-ecar_en.pdf).

4. Danfoss DCM 1000 power module: <https://www.danfoss.com/en/about-danfoss/our-businesses/silicon-power/danfoss-dcm-1000-power-module-technology-platform/>.
5. Hybrid traction unit by Fraunhofer Institute for Integrated Systems and Device Technology IISB: [https://www.iisb.fraunhofer.de/en/research\\_areas/vehicle\\_electronics/drive\\_inverters\\_mechatronics/projects/hybrid\\_traction\\_unit.html](https://www.iisb.fraunhofer.de/en/research_areas/vehicle_electronics/drive_inverters_mechatronics/projects/hybrid_traction_unit.html).
6. Abebe, Robert, et al., “Integrated motor drives: state of the art and future trends,” *IET Electr. Power Appl.*, 2016, Vol. 10, Iss. 8, pp. 757–771.
7. Wang, Jiyao, et al., “Integrated Modular Motor Drive Design With GaN Power FETs,” *IEEE Transactions on Industry Applications*, 2015, Vol. 51, No. 4.
8. Engelmann, Georges, et al., “A Highly Integrated Drive Inverter using DirectFETs and Ceramic DC-Link Capacitors for Open-End Winding Machines in Electric Vehicles,” 2015 IEEE Applied Power Electronics Conference and Exposition (APEC).
9. Tenconi, Alberto, et al., “Temperatures Evaluation in an Integrated Motor Drive for Traction Applications,” *IEEE Transactions on Industrial Electronics*, 2008, Vol. 55, No. 10.
10. Nikouie, Mojgan, et al., “A Highly Integrated Electric Drive System for Tomorrow’s EVs and HEVs,” *2017 IEEE Southern Power Electronics Conference (SPEC)*.
11. Energetics, “Literature Review: Thermal Management Approaches for Electric Vehicle Traction Motors,” 2017. Report prepared for NREL.
12. Bennion, K., and Moreno, G., “Convective heat transfer coefficients of automatic transmission fluid jets with implications for electric machine thermal management,” *ASME 2015 International Technical Conference and Exhibition on Packaging and Integration of Electronic and Photonic Microsystems*, San Francisco, CA, United States, 2015, Vol 3. doi:10.1115/IPACK2015-48382.

### Acknowledgments

The author would like to acknowledge the significant contributions of Kevin Bennion, Emily Cousineau, Xuhui Feng, and Gilbert Moreno from NREL. Valuable input and technical data from Shajjad Chowdhury and Raminosa Tsarafidy from ORNL are also appreciated.

## I.14 Power Electronics Materials and Bonded Interfaces – Reliability and Lifetime (NREL)

### Paul Paret

National Renewable Energy Laboratory (NREL)  
 15013 Denver West Parkway  
 Golden, CO 80401  
 Phone: (303) 275-4376  
 Email: [paul.paret@nrel.gov](mailto:paul.paret@nrel.gov)

### Susan A. Rogers, DOE Technology Development Manager

U.S. Department of Energy  
 E-mail: [susan.rogers@ee.doe.gov](mailto:susan.rogers@ee.doe.gov)

Start Date: October 1, 2018

End Date: September 30, 2021

Project Funding (FY19): \$175,000

DOE share: \$175,000

Non-DOE share: \$0

### Project Introduction

Robust and reliable power electronics packaging technologies are critical for the safe operation of wide-bandgap devices such as silicon carbide and gallium nitride, particularly at high temperatures. The unique characteristics of wide-bandgap devices that prove to be challenging for their packaging are high switching speed ( $dV/dt$  and  $di/dt$ ), high operation temperature, and high electric field (Chen, Luo, and Kang 2017). The cost, weight, and power density targets for these packages or modules only increase the challenges associated with their design and development. Material selection and component design within a package play a key role in determining its reliability and lifetime under high-temperature operating conditions. Advanced packaging layouts, such as 3D packaging, planar interconnects, and direct-lead-bonding are considered by researchers and engineers to minimize loop parasitics and to reduce the junction-to-coolant thermal resistance. Materials in the right combination need to be properly integrated to address the inherent coefficient of thermal expansion and stiffness mismatch issues within packaging (Khazaka et al. 2015).

For a traditional silicon device-based power electronics package, bonded interfaces, i.e., die-attach and substrate-attach, are prone to failure under environmental loading conditions such as thermal cycling and power cycling. The reliability of the package is dictated—to a significant extent—by the ability of these interface materials to withstand the stress imposed on them under long-term exposure to high temperatures and thermal gradients. While the maximum operating temperature of Si devices is around 150°C, the 200°C – 250°C desired operating temperature range of wide-bandgap devices places a more stringent requirement on the reliability and lifetime of the bonded interfaces. Solders such as SAC305 and 63Sn37Pb are not suitable for operation at these extreme temperatures. Among the high-temperature-compatible bonded interfaces, sintered silver and transient liquid phase bonded materials are regarded as strong candidates; however, their reliability and failure mechanisms at high temperatures needs to be investigated.

This report describes research at the National Renewable Energy Laboratory (NREL) in assessing the reliability and lifetime prediction model development of sintered silver and the copper (Cu)-aluminum (Al) transient bonded interface material. In collaboration with Virginia Tech (VT), samples with sintered silver as the bonded material were fabricated and subjected to accelerated thermal cycling. Also, the reliability of sintered silver material with a different microstructure, which was purchased from an industry partner, was evaluated using the same sample configuration. In addition, thermomechanical modeling results that demonstrate the impact of thickness of adjacent coupons on sintered silver are reported. Along with sintered silver, collaborative efforts between NREL and Georgia Tech—on the fabrication of Cu-Al bonded interface samples—are discussed.



## Objectives

The major objectives of this project are to:

- Evaluate the reliability of sintered silver by subjecting coefficient of thermal expansion (CTE)-mismatched coupons—with sintered silver as the bonded interface material—to accelerated thermal cycling. Crack propagation or any other failure mechanisms that originate and evolve under thermal cycling will be periodically monitored through scanning acoustic microscopy imaging.
- Develop thermomechanical models to obtain theoretical parameters such as von Mises stress, strain-energy density, and J-integral, and formulate a lifetime prediction model based on these modeling outputs and experimental data.
- Synthesize Cu-Al bond samples with less than 5% void fraction and subject these samples to accelerated thermal cycling. Explore the bonding strength of the Cu-Al bond with the same coupons used in the sintered silver samples and finalize the configuration of the Cu-Al bond samples for thermal cycling.

## Approach

### Sintered Silver

- Pressureless sintering

Two types of sintered silver pastes—synthesized using the pressureless sintering approach—were explored. Sintered silver paste purchased from NBE Tech and an industrial partner was used to bond 4- $\mu\text{m}$ -thick silver-plated copper and Invar coupons that were 25.4 mm (1 inch) in diameter and 2 mm in thickness. Cu and Invar were chosen as the adjacent coupons materials due to their large CTE-mismatch, and so under thermal cycling, the high stress induced on the sintered silver bond would eventually result in its failure. Sample fabrication with the silver paste from NBE Tech was conducted at VT, while the other paste was used to develop samples at NREL. Also, three different bond diameters (10 mm, 16 mm, and 22 mm) were synthesized at VT, whereas a single bond diameter (10 mm) was followed across the samples at NREL. The two pastes differed mainly in their microstructure, additives, and solvent composition. Consequently, different sintering profiles, as shown in Figure I.14.1, were adopted for these pastes. A schematic of the circular samples for reliability evaluation is provided in Figure I.14.2.

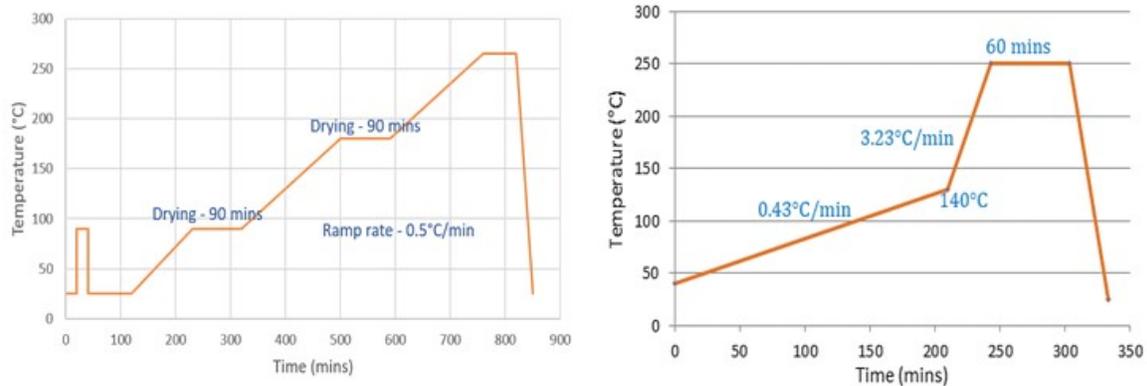


Figure I.14.1 Pressureless sintering profile at VT (left) and NREL (right)

After sample synthesis and prior to thermal cycling, the bond quality of these samples was assessed using C-mode scanning acoustic microscope (C-SAM). Most of these samples at VT had an initial void fraction greater than 20% and as such, by definition, failed. Nevertheless, these samples were subjected to thermal cycling to see if the existing voids or cracks would propagate under those conditions and thus calculate the rate of crack growth. These C-SAM images are shown in Figure I.14.3.



Figure I.14.2 Circular coupons ( $\Phi 25.4\text{mm}$ ) for reliability evaluation – Cu (bottom) bonded to Invar (top) using sintered silver

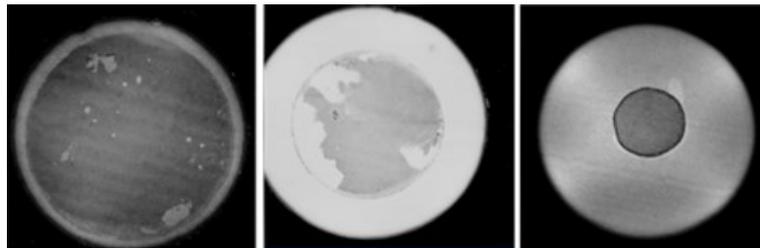


Figure I.14.3 C-SAM images of pressureless sintered silver samples fabricated at VT (left and center) and NREL (right)

### ***Pressure-assisted sintering***

In addition to the pressureless sintering approach, the impact of applying a mild pressure on the silver paste during the sintering phase of the synthesis process was explored. The same sample structure as described above for pressureless sintering was adopted for pressure-assisted sintering. The sintering profile that was selected based on the bonding quality of trial samples is shown in Figure I.14.4. Two different pressures—3 MPa and 10 MPa—were applied. Identical to the pressureless phase, samples with different bond diameters—22 mm, 16 mm, and 10 mm—were fabricated to study the impact of geometrical variations on the loading scenario and thus the crack initiation and propagation behavior in the sintered silver layer. The bond thickness in each sample was measured and varied between 110  $\mu\text{m}$  and 140  $\mu\text{m}$ . Overall, the pressure-assisted sintering process resulted in much better bond quality as indicated by the C-SAM images in Figure I.14.5. It is to be noted that samples with pressure-assisted sintering profile were fabricated only at VT. Both pressureless and pressure-assisted samples were subjected to a thermal cycle of  $-40^{\circ}\text{C}$  to  $200^{\circ}\text{C}$ .

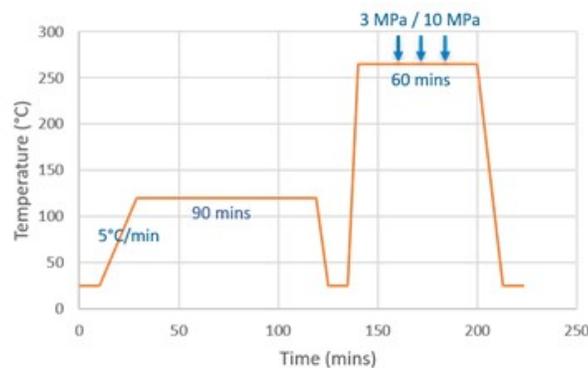


Figure I.14.4 Pressure-assisted sintering profile

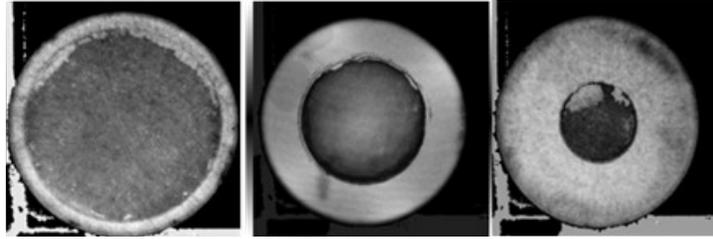


Figure I.14.5 C-SAM images of pressure-assisted sintered silver samples fabricated at VT. Bond diameter of 22 mm (left), 16 mm (center), and 10 mm (right)

Figure I.14.6 shows the round sintered silver samples arranged on a thermal test platform for thermal cycling. Custom alterations were made to the platform to enable uniform heating and cooling for all the samples under thermal cycling. A thermocouple was used to monitor the temperature to ensure that the desired thermal cycling profile targets were followed within acceptable variance.

### *Thermomechanical modeling*

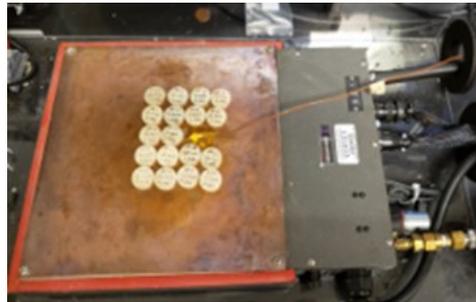


Figure I.14.6 Round sintered silver samples arranged on a thermal platform for thermal cycling

Non-linear finite element analyses were conducted on the circular sintered silver samples to compute various theoretical parameters such as stress, strain, and strain energy density and how these vary as the stiffness of the overall sample is altered. The sample stiffness was changed by varying the thickness of the Cu and Invar coupons. Simulations were run in ANSYS, and the results reported are accurate to within 2% after mesh-independence. These output parameters offer an insight into the reliability of the sintered silver material and combining them with the cycles-to-failure experimental results would result in the formulation of lifetime prediction models.

### *Cu – Al transient liquid phase bond*

A transient liquid phase bond was developed at Georgia Tech using a Cu-Al eutectic (Pahinkar et al. 2018), which can be used as a bonded material in high-temperature power electronics applications. To create this bond, Cu and Al foils are joined in a specific bulk ratio and heated above their eutectic point, but below the melting temperature of the constituent metals. While this material has demonstrated potential for high reliability under certain specific configurations in other projects, its reliability—when used for bonding in CTE-mismatched samples under a thermal cycle of  $-40^{\circ}\text{C}$  to  $200^{\circ}\text{C}$ —needs to be evaluated. To this end, attempts were made at Georgia Tech to bond Cu-Al alloy between Cu and Invar coupons; however, the weak diffusion between the Invar and Cu-Al alloy resulted in poor samples that delaminated even prior to thermal cycling. The current proposed plan is to synthesize a Cu-Al bond between Cu and AlSiC coupons and then subject the samples to thermal cycling at NREL.

## Results

### *Reliability evaluation*

#### *Pressureless sintering*

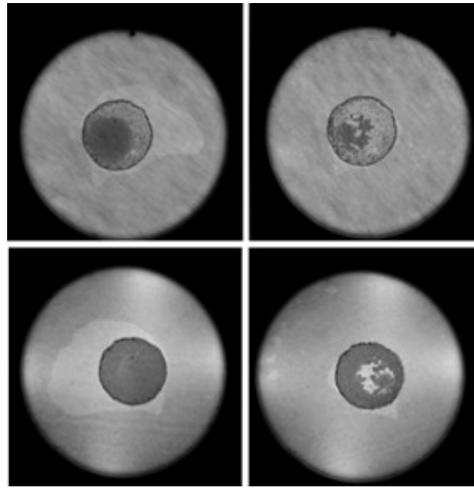


Figure I.14.7 C-SAM images of pressureless sintered silver before (left) and after 10 thermal cycles (right) – Cu-side images (top) and Invar-side images (bottom)

Figure I.14.7 shows the C-SAM images of the pressureless sintered silver samples that were fabricated at NREL prior to thermal cycling and after 10 cycles. These images show that while a solid bond was obtained between the sintered silver and the Invar coupon, voids or minor cracks existed at the other side and directly resulted in a higher rate of crack propagation. The white patches surrounding the bond region in the images prior to thermal cycling likely correspond to the presence of traces of organic solvents that did not dry out completely in the synthesis process. As these samples failed in 10 cycles, additional samples were made using the same sintering profile and subjected to slightly less severe thermal cycles from  $-40^{\circ}\text{C}$  to  $175^{\circ}\text{C}$  and  $-40^{\circ}\text{C}$  to  $150^{\circ}\text{C}$ ; however, the C-SAM images of these samples indicated a similar result with clear signs of cracks occurring in just 10 cycles.

#### ***Pressure-assisted sintering (3 and 10 MPa)***

In the case of pressure-assisted sintered silver samples, a good bonding was achieved at the interface between the Cu and Invar coupons where most of these samples showed less than 3% voiding or cracking. However, when subjected to thermal cycling, cracks initiated and propagated to beyond the failure criterion of 20% in less than 50 cycles regardless of the bond diameter, as shown in Figure I.14.8. Failure in these samples may have occurred in 10 or 20 cycles, similar to the pressureless case. From the C-SAM images in Figure I.14.8, it is evident that on the Cu side, cracks initiated at the periphery of the bond and propagated towards the inner regions whereas cracks within the bond with no connection to the outer edge were present on the Invar side. Also, a few speckled white patterns can be spotted on the Invar side, which possibly indicates the occurrence of multiple uncorrelated crack formations.

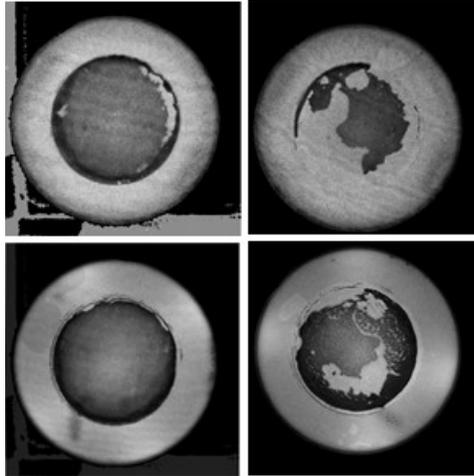


Figure I.14.8 C-SAM images of pressure-assisted sintered silver before (left) and after 100 thermal cycles (right), Cu-side images (top) and Invar-side images (bottom)

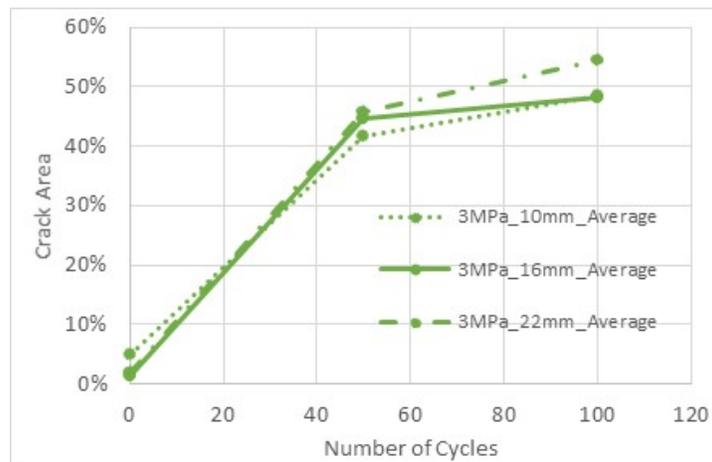


Figure I.14.9 Crack growth in pressure-assisted samples (3 MPa)

Figure I.14.9 shows the measured crack growth at cycling intervals in samples on which the applied sintering pressure was 3 MPa. Data obtained from all three bond diameter cases are presented. A common observation among these three cases is that despite the high rate of crack propagation in the first 50 cycles, crack growth occurred at a relatively lower pace from 50 to 100 cycles. This observed shift in crack growth rate could be due to the reduction in stress that is induced on a failed sample as compared to a solid bond. The initiation and propagation of cracks in the sintered silver layer within the first 50 cycles led to a weak contact at the interface between the bond and the adjacent coupons, thereby disrupting the stiffness of the entire configuration. Thus, the bond layer became less constrained by the adjacent coupons under thermal cycling and as a result, the stress values dropped.

### Failure Mechanisms

To understand the failure mechanisms occurring within the sintered silver layer under thermal cycling, a few samples were cross-sectioned and high-resolution microscopic images taken. Figure I.14.10 shows the cross-sectional image of a sample with a sintering pressure of 3 MPa and a bond diameter of 16 mm after completing 100 thermal cycles. A detailed observation of this figure reveals the presence of adhesive and cohesive failure modes within the bond layer. The zoomed-in figure on the right side indicates a connection between these two failure modes which therefore are not mutually exclusive events. In this case, the crack likely occurred first at the interface between the silver plating on the Cu coupon and the bond layer, propagated to the other side in a near-vertical path and then continued through the interface between the silver plating and the Invar coupon. The vertical trajectory of the crack possibly forced its extension into the silver plating on the Invar side. Similar failure patterns were observed for other sample types as well.

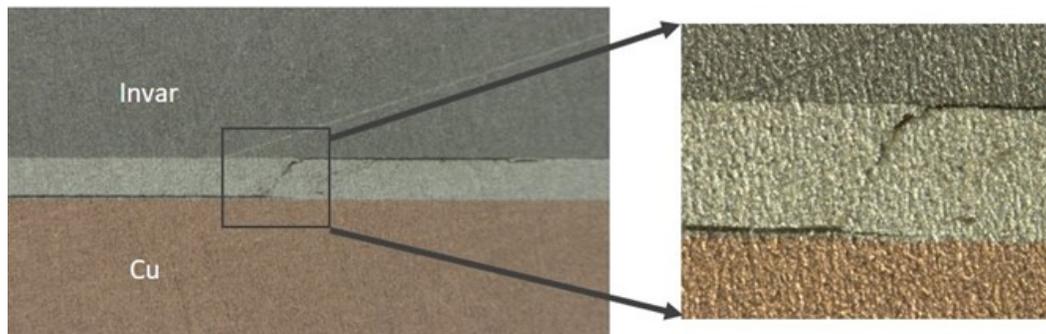


Figure I.14.10 Cross-sectional image of a pressure-assisted sintered silver sample

### Thermomechanical Modeling

Simulations were performed in the ANSYS Workbench platform to compare the impact of the thickness of the adjacent coupons on the sintered silver layer. A thermal cycle load of  $-40^{\circ}\text{C}$  to  $200^{\circ}\text{C}$  was applied on the model four times in succession based on a convergence study. After solution, the volume-averaged strain energy density of the entire bond pad region was computed for the different cases. The major effect of reducing coupon thickness is to minimize the stiffness of the overall sample configuration, and based on the results in Figure I.14.11, a longer lifetime can be extracted from the sintered silver samples by altering the thickness of Cu and Invar coupons to 1 mm. Also, the difference between the two cases is more apparent at larger bond diameters. Another possible benefit of reducing the coupon thickness is inducing distinct and separate crack propagation rates between samples with different bond diameters as opposed to the 2-mm-thick cases, as shown in Figure I.14.9.

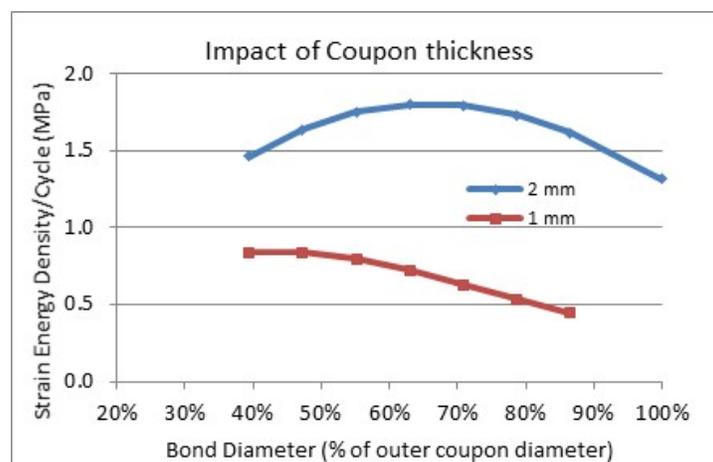


Figure I.14.11 Strain energy density results of sintered silver samples

## Conclusions

Power electronics packaging for safe operation of wide-bandgap devices at high temperatures is a challenging research goal. This project is focused on the mechanical characterization, reliability evaluation and lifetime prediction of bonded materials to determine their applicability in high-temperature packaging. The bonded materials of interest are sintered silver, sintered copper, and a transient liquid phase Cu-Al bond.

Experimental evaluation of the reliability of sintered silver material bonded between CTE-mismatched coupons were conducted through accelerated thermal cycling. Samples fabricated using different sintering profiles—pressure-less and pressure-assisted—failed in as few as 50 cycles despite the initial crack percentage by area being less than 5%. Cross-sectional images of the failed samples revealed a combination of adhesive and cohesive crack formations as the failure mechanisms. A thermomechanical modeling study explored the impact of thickness of the sample configuration and concluded that thinner coupons are likely to result in longer lifetime for sintered silver under thermal cycling. In addition to sintered silver, a transient liquid phase Cu-Al bond and sintered copper are currently being explored for their reliability in high temperature packaging.

## Key Publications and Presentations

1. Paret, P., D. DeVoto, and S. Narumanchi. “Thermomechanical Modeling of High-Temperature Bonded Interface Materials.” Book Chapter in *High Temperature Die Attach Materials for Microelectronics: Materials, Processes, Equipment, Modelling and Reliability*, Springer Nature.
2. Paret, P. “Performance and Reliability of Bonded Interfaces for High-Temperature Packaging” DOE VTO Annual Report, 2018.
3. Paret, P. “Power Electronics Materials and Bonded Interfaces – Reliability and Lifetime” DOE VTO Annual Merit Review, Washington D.C., June 2019.
4. Paret, P. “Power Electronics Materials and Bonded Interfaces – Reliability and Lifetime” Presentation to the Electrical and Electronics Technical Team, August 2019.

## References

1. C Chen, F Luo, and Y Kang. 2017. “A Review of SiC Power Module Packaging: Layout, Material System and Integration.” *CPSS Transactions On Power Electronics And Applications* 2 (3): 17.
2. R Khazaka, L Mendizabal, D Henry, and R Hanna. 2015. “Survey of High-Temperature Reliability of Power Electronics Packaging Components.” *IEEE Transactions On Power Electronics* 30 (5): 9.
3. D Pahinkar, W Puckett, S Graham, L Boteler, D Ibitayo, S Narumanchi, P Paret, D DeVoto, and J Major. 2018. “Transient Liquid Phase Bonding of AlN to AlSiC for Durable Power Electronic Packages.” *Adv. Eng. Mater.*, 9.

## Acknowledgements

The contributions of Joshua Major and Douglas DeVoto in conducting the several reliability evaluation experiments are acknowledged. The author also would like to thank Yansong Tan and G-Q. Lu at VT, and Chidinma Imediegwu, Darshan Pahinkar, and Samuel Graham at Georgia Tech for their valuable technical inputs and help with sample synthesis.

## I.15 Power Electronics Thermal Management (NREL)

### **Gilbert Moreno, Principal Investigator**

National Renewable Energy Laboratory  
15013 Denver West Parkway  
Golden, CO 80401  
E-mail: [gilbert.moreno@nrel.gov](mailto:gilbert.moreno@nrel.gov)

### **Susan Rogers, DOE Technology Development Manager**

U.S. Department of Energy  
E-mail: [susan.rogers@ee.doe.gov](mailto:susan.rogers@ee.doe.gov)

Start Date: October 1, 2018	End Date: September 30, 2021	
Project Funding (FY19): \$350,000	DOE share: \$350,000	Non-DOE share: \$0

### **Project Introduction**

The 2017 Electrical and Electronics Technical Team (EETT) Roadmap [1] proposes aggressive research and development targets aimed at improving power electronics technology to enable the mass market penetration of electric-drive vehicles. Achieving these aggressive targets will require a decrease in cost (year 2025 cost target: \$2.70/kW) and an increase in power density (year 2025 power density target: 100 kW/L) as compared with current on-road technology. Replacing traditional silicon device-based components with more efficient and higher temperature wide-bandgap (WBG) semiconductor device-based components will enable increasing the power density. However, meeting the power density target will also require innovative thermal management solutions to increase the heat fluxes dissipated and allow for compact electronics packaging.

This project conducts research to develop new power electronics thermal management technologies to increase power density, enable high WBG temperature operation, and decrease cost. One of the main challenges to achieving high power densities is associated with packaging of high-temperature (250°C) WBG devices near lower-temperature-rated components (e.g., electrical boards and capacitors). Additionally, the high junction temperatures of the WBG devices will result in large temperature gradients through the power module layers that will present reliability challenges and require higher-temperature substrates and bonding materials.

This project also supports a collaborative research effort between NREL and John Deere to research and develop advanced cooling technologies (two-phase cooling) for power electronics in heavy-duty vehicles. This work is part of a collaborative research and development agreement (CRADA) and, due to the proprietary nature of the work, the results of this task are not provided in this report.

### **Objectives**

The primary project objective is to develop thermal management technologies to enable achieving 100-kW/L power density target. Additional project objectives are to:

- Develop cooling solutions that enable high-temperature (250°C) WBG operation and low-temperature, low-cost capacitors
- Decrease cost by proposing low-cost cooling technologies that enable decreasing the number of semiconductor devices and use automotive-qualified fluids (e.g., water-ethylene glycol [WEG], transmission fluids [ATF], or air-conditioning refrigerants).

### **Approach**

A power electronics thermal metric that is predicted to enable reaching a power density of 100 kW/L was first computed and used as a design target for the power electronics heat exchanger. The thermal target was defined



in terms of a volumetric thermal resistance metric where the junction-to-coolant thermal resistance was scaled by the cold plate and power module volume requirements. The volumetric thermal resistance target value was computed to be 21 cm<sup>3</sup>-K/W, and the predicted heat load for a 100-kW WBG inverter was estimated to be 2,150 W [2]. Modeling analyses were then conducted to evaluate different cooling technologies and identify the best-performing cooling strategy. The selected cooling configuration was designed and optimized to meet the thermal target using detailed computational fluid dynamics (CFD) and finite element (FE) simulations. The optimized design was then fabricated via 3D printing for experimental validation.

**Results**

*Designing the Dielectric Fluid Heat Exchanger*

Prior work (see [2]) compared the thermal performance of various power electronics cooling strategies and identified a dielectric-fluid (single-phase heat transfer) cooling concept as a promising thermal configuration to enable greater power density. Dielectric fluids have poor properties compared to WEG (a typical power electronics coolant), but they enable a redesign of the power module that allows for a decrease of the package stack conduction resistance and thus a decrease in the junction-to-coolant thermal resistance. Dielectric fluids also enable direct cooling of the electrical interconnections within the inverter, which can be an effective method to reduce capacitor and electrical board temperatures. Alpha 6 dielectric fluid was used for most of the modeling work. AmpCool-100 is another potential dielectric fluid that is being considered. Ultimately, ATF would be an ideal coolant because it is readily available on a vehicle and enables integrating the inverter with the motor; however, its dielectric properties are not fully understood. It should be noted that all the fluids listed above can only be used for single-phase cooling applications.

The dielectric fluid cooling concept eliminates the metalized ceramics substrates that are typical in power modules and impinges dielectric fluid jets on heat spreader plates bonded to the devices (Figure I.15.1). The heat spreader plates have a dual functionality as both heat spreaders and electrical conductors. Fins are fabricated on the heat spreader to increase surface area and heat transfer (fins are not shown in Figure I.15.1). CFD was conducted to optimize the fins structures to increase heat transfer and minimize pumping power. Smaller unit-cell models were used for the CFD analysis to decrease computation time. Once optimized (via the unit-cell model), the final fin design was used for the larger device-scale and inverter-scale (12 device) models.

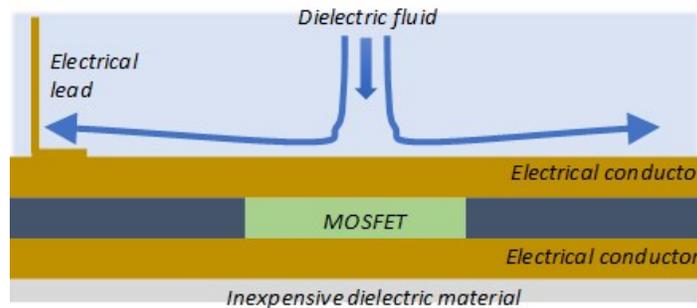


Figure I.15.1 Schematic showing the dielectric fluid cooling strategy for a planar-style module.

Figure I.15.2 shows the thermal resistance versus pumping power (flow rate × pressure drop) results from the CFD optimization analyses using Alpha 6 dielectric fluid at  $T_{inlet} = 65^{\circ}\text{C}$ . The thermal resistance ( $R''_{th}$ ) is the resistance computed at the fin base and is defined by the equation below.

$$R''_{th} = \frac{Area_{fin\ base}(\overline{T_{fin\ base}} - T_{inlet})}{Heat}$$

where  $Area_{fin\ base}$  is the surface area computed at the fin base, which includes the area of the channel and fins;  $T_{fin\ base}$  is the area-averaged temperature computed at the fin base;  $T_{inlet}$  is the fluid inlet temperature; and  $Heat$  is the heat dissipated. The results show that thinner fins are ideal because they produce lower thermal resistance (enabling higher fin densities) and lower pumping power (allowing for larger channel sizes). Based on these results, a fin thickness ( $w_f$ ) of 0.2 mm was selected. Thinner fin geometries ( $w_f < 0.2$  mm) may provide better performance but would likely not have the mechanical strength required for reliable operation. Figure I.15.2 also shows the effect of fin height ( $h_f$ ) on performance for a 0.2-mm-thick fin. These results indicate that increasing the fin height beyond 4 mm does not produce any significant enhancements and thus 4-mm-tall fins were selected. Figure I.15.2 shows the effect of varying the minor slot jet dimension ( $w_s$ ) while keeping the fin dimensions constant ( $w_f = 0.2$  mm,  $w_c = 0.43$  mm,  $h_f = 4$  mm). The major slot jet dimension was maintained at 10 mm for all cases—equal to the finned area footprint. The results show that increasing the slot width from 1 mm to 1.75 mm provides lower thermal resistance when compared at the same pumping power. Based on these results, a slot width of 1.75 mm was selected.

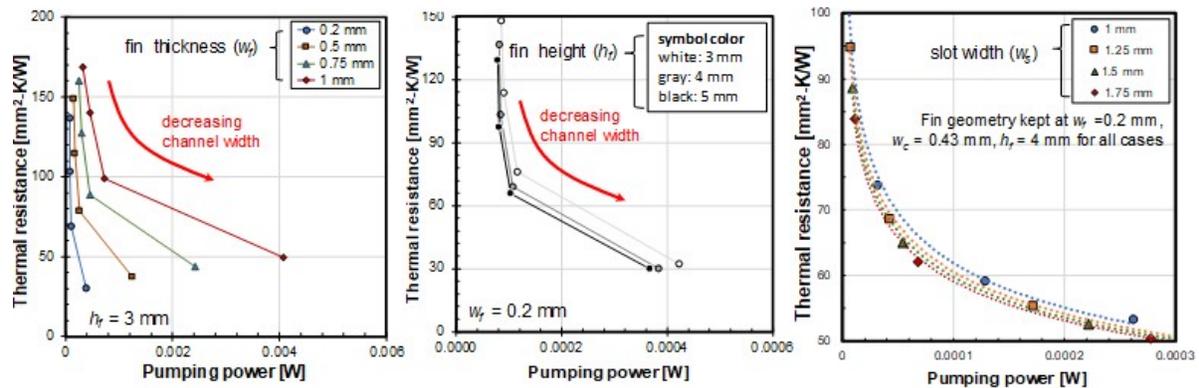


Figure I.15.2 CFD results showing the effects of varying the fin thickness (left), fin height (middle), and the slot jet width (right).

The effect of channel size ( $w_c$ , distance between fins) is more complex with smaller channels decreasing thermal resistance at the expense of higher pumping power. The channel size was selected so that its thermal resistance provided  $T_j < 250^\circ\text{C}$  under the maximum heat load condition of 2,150 W (assuming two devices per switch for a three-phase inverter—12 devices total). FE analysis of the planar package provided the target thermal resistance value required to achieve  $T_j < 250^\circ\text{C}$ . Two channels sizes were selected that meet the thermal resistance condition—0.3 mm and 0.43 mm. The CFD-predicted thermal resistance values for the 0.3-mm- and 0.43-mm-wide channels were  $44\text{ mm}^2\text{-K/W}$  and  $58\text{ mm}^2\text{-K/W}$ , respectively (for  $w_f = 0.2$  mm,  $h_f = 4$  mm,  $w_s = 1.75$  mm). Most of the simulations were conducted using the 0.43-mm-wide channels because that design requires a lower pumping power.

A device-scale CFD model (half-symmetric model) was run using the final design (fin, slot jet, channel) dimensions to compute the maximum junction temperatures. The model used a  $5 \times 5 \times 0.18$  mm silicon carbide (SiC) device placed between two 2-mm-thick copper plates. Alpha 6 fluid at  $T_{inlet} = 65^\circ\text{C}$  impinged on the top finned heat spreader plate at an average, relatively low, jet velocity of 0.3 m/s. At the maximum heat load (heat flux =  $716\text{ W/cm}^2$ , 2,150 W distributed between 12 devices) the maximum junction temperature is predicted to be  $220^\circ\text{C}$  (Figure I.15.3).

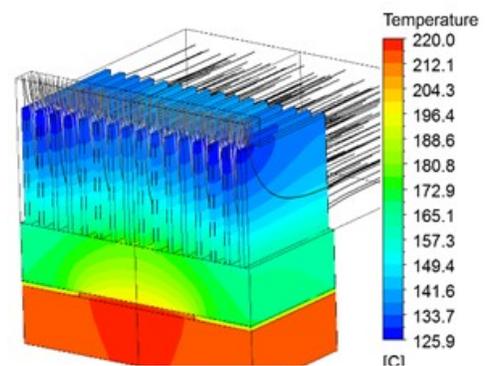


Figure I.15.3 CFD temperature contours for the optimal fin and slot jet design using the device scale model. Model predicts  $220^\circ\text{C}$  maximum junction temperature at  $716\text{ W/cm}^2$  device heat flux.

CFD modeling was used to design a heat exchanger to deliver dielectric fluid to 12 devices (inverter-scale heat exchanger). The concept was to design the heat exchanger with 12 slot jets—one per SiC device. The total flow rate requirements for the heat exchanger are 4.1 lpm to provide an average jet velocity of 0.3 m/s for all 12 jets. Extensive modeling was conducted to design the internal channels to evenly distribute dielectric fluid to the 12 SiC devices and to minimize the pressure drop. Figure I.15.4 shows the flow distribution for the final design where a  $\pm 5\%$  flow variation is predicted.

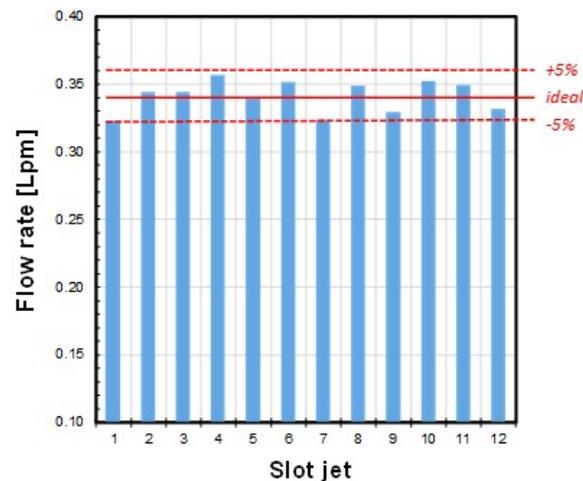


Figure I.15.4 CFD-predicted flow distribution for the 12 slot jets. A  $\pm 5\%$  flow variation is predicted.

A computer-aided design (CAD) image of the final heat exchanger and power module concept is shown in Figure I.15.5. The total volume for the conceptual inverter and heat exchanger is 120 ml. The 2018 Power Electronics Thermal Management Report [2] estimated that the total volume for the power electronics and heat exchanger needed to be  $< 240$  ml to achieve the 100-kW/l inverter power density target; therefore the current design meets the volume requirements. Figure I.15.6 shows the CFD-computed temperatures for the 12 devices for the inverter-scale CFD model using Alpha 6 at  $T_{inlet} = 65^{\circ}\text{C}$  and a total flow rate of 4.1 lpm. Maximum junction temperatures are predicted to be  $222^{\circ}\text{C}$  for the 2.2 KW of heat dissipation and  $716 \text{ W/cm}^2$  device heat flux. A  $2^{\circ}\text{C}$  temperature variation between the devices is predicted and is associated with the flow variations shown in Figure I.15.6. The total pressure drop from the inlet to the outlet is predicted to be minor (2,214 Pa, 0.32 psi) resulting in a pumping power of 0.2 W. Compared to the 2014 Honda Accord Hybrid [3], the dielectric fluid heat exchanger has 50% lower specific junction-to-coolant thermal resistance (per device area) and 80% lower pumping power. The thermal resistance combined with the total volume (120 ml) for the conceptual inverter and heat exchanger results in a volumetric thermal resistance of  $8.7 \text{ cm}^3\text{-K/W}$ . The volumetric thermal resistance of the dielectric-fluid heat exchanger outperforms (is lower) the  $21 \text{ cm}^3\text{-K/W}$  thermal target, and for this reason, it is predicted to enable reaching an inverter power density of 100 kW/l. A Record-of-Invention has been submitted to describe the dielectric-fluid cooling concept.

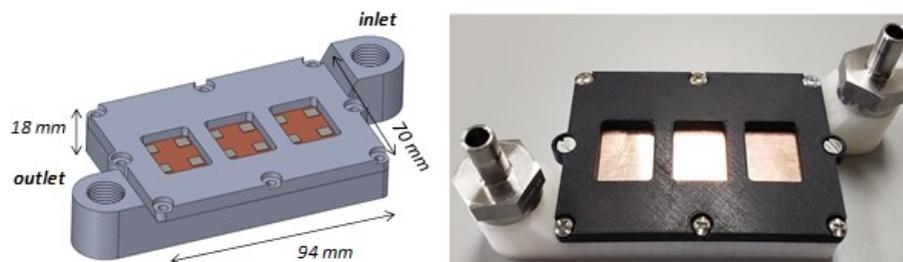


Figure I.15.5 CAD drawing of the heat exchanger designed to cool 12 ( $25 \text{ mm}^2$ ) devices (left). 3D printed heat exchanger fabricated for experimental validation (right). Total volume for the conceptual heat exchanger and power module is 120 ml.

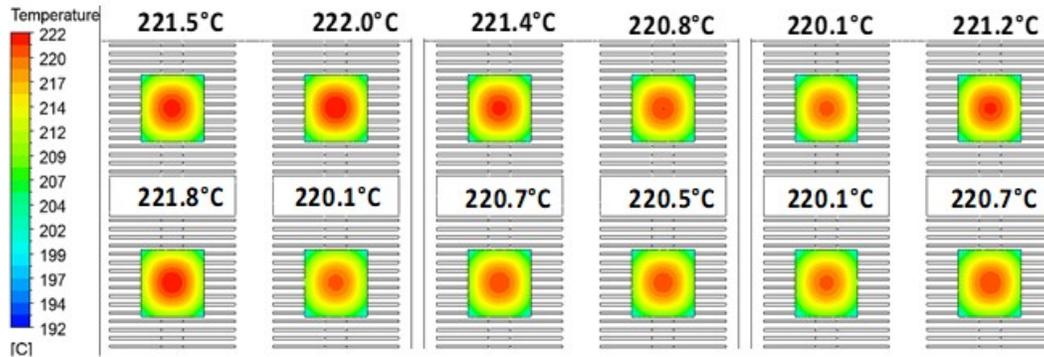


Figure I.15.6 Temperature contours for inverter-scale (12 devices) CFD simulations for 2.2 kW of heat dissipation (716 W/cm<sup>2</sup> per device) and total flow rate (Alpha 6 fluid) of 4.1 lpm. Maximum junction temperatures of 222 °C are predicted.

### Experimental Validation

A prototype of the dielectric fluid heat exchanger was 3D printed out of polycarbonate to experimentally measure its performance and confirm the model results (Figure I.15.5). The prototype is composed of two parts. The lower half is the heat exchanger that distributes the fluid to the 12 devices (white component in Figure I.15.5) and the top part (black component in Figure I.15.5) holds the finned heat spreader plates (fins facing downward within the heat exchanger) and simulates the power electronics. The prototype used O-rings to provide a fluid seal between the various components. It should be noted that although 3D printing was used for the prototype, the design can be fabricated using more conventional mass-manufacturing methods (e.g., injection molding).

Figure I.15.7 shows an image of the finned heat spreaders ( $w_f = 0.2$  mm,  $w_c = 0.43$  mm, and  $h_f = 4$  mm) fabricated using Wolverine's MicroCool Technology. The fins are somewhat angled, and their dimensions slightly vary from the model design. Future tests will reveal the effect of these manufacturing variations on performance. Cartridge heaters embedded within oxygen-free copper blocks were used to simulate the heat from the SiC devices. Four cartridge heaters are inserted into each copper block (using thermal grease), and a total of three copper blocks will be used to simulate the 12 SiC devices during the experiments. The copper block design includes "foot" extensions below each cartridge heater that are the same footprint as the 5×5 mm SiC they represent. Two thermocouples are inserted into holes machined into the 5×5 mm protrusions to measure temperatures and compute heat for each heater assuming 1D, steady-state heat transfer. The copper blocks are soldered to the smooth side of the finned heat spreader. Figure I.15.7 shows an image of the copper block and FE analysis (FEA) temperature contours for the 716 W/cm<sup>2</sup> heat flux condition.

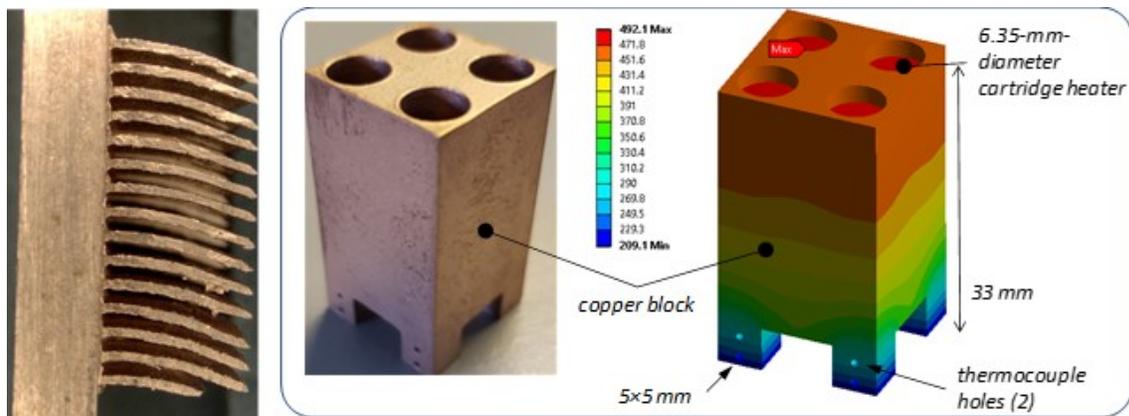


Figure I.15.7 Image of the finned ( $w_f = 0.2$  mm,  $w_c = 0.43$  mm, and  $h_f = 4$  mm) heat spreader (left) and cartridge heater block (middle). FE-analysis-predicted temperatures for the cartridge heater block at the 716 W/cm<sup>2</sup> heat flux condition (right).

A new flow loop was fabricated to measure the thermal performance of the heat exchanger using dielectric fluids (Figure I.15.8). The flow loop was designed to accommodate various fluids and can control the fluid flow rate and temperatures ( $-40^{\circ}\text{C}$  to  $100^{\circ}\text{C}$ ). A LabVIEW program was written to control and monitor the experiments. A 3.5-kW DC power supply, controlled via LabVIEW, is used to power the 12 cartridge heaters. Initial experiments with the dielectric fluid heat exchanger have shown good energy balance between the total power supply output, a summation of heat computed through the 12 cartridge heaters (measured via thermocouples embedded in the copper blocks), and the sensible heat gain from the fluid. Tests are currently underway to characterize the thermal performance of the heat exchanger.

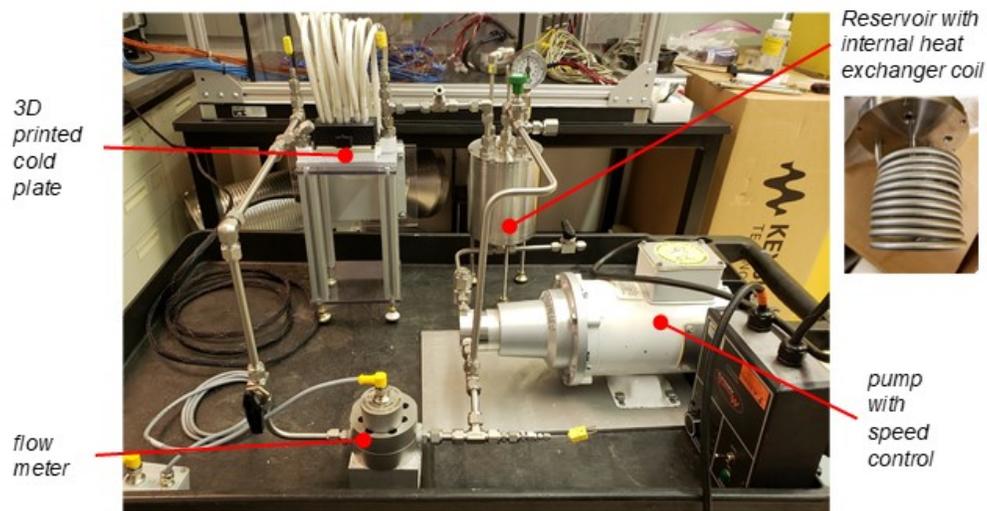


Figure I.15.8 Picture of the dielectric fluid flow loop fabricated and used to measure the thermal performance of the dielectric fluid heat exchanger. The flow loop can accommodate various dielectric fluids and can control fluid temperatures and flow rates.

### ***Short-Circuit Evaluation***

A transient thermal model was created to evaluate the temperature response for the proposed dielectric-fluid planar package cooling strategy during a short-circuit fault condition. We were interested in evaluating the effect of top-side (source side of metal oxide semiconductor field effect transistor [MOSFET]) cooling of the device via dielectric-fluid jet on short-circuit response time. A 1D FE transient thermal model was created that represented a sliver on a MOSFET device and included the various micrometer-size layers (Figure I.15.9). A short-circuit fault condition was simulated by imposing heat at the device junction layer for two different device configurations—dielectric fluid-top-side cooled and a conventional device (wire bond design, shown as red line in Figure I.15.9) with no top side cooling. Results show that the current design slightly decreases the temperature rise during the fault condition, but the temperature decrease is relatively minor. Delaying the temperature rise during the short-circuit fault condition likely requires modifications within the device, and any external changes to the substrate or cooling system will likely not have a significant effect.

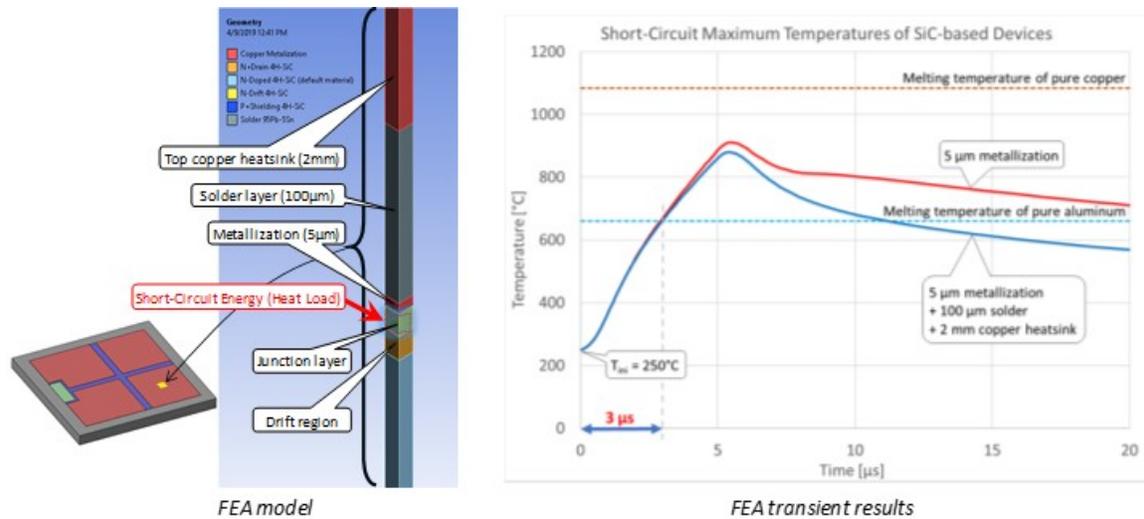


Figure I.15.9 Schematic of the 1D transient thermal FEA model (left). FEA temperature versus time results for a simulated short-circuit fault condition (right).

### *Double-Side, Dielectric-Fluid-Cooled Module Evaluation for Increased Power Density*

Planar-style packages eliminate wire/ribbon connections and offer the ability to cool modules on both sides. The 2008 Lexus Hybrid [4] and 2016 Volt [5] use double-side cooled power modules, which enables performance enhancements. However, these vehicles' systems utilize thermal grease at the power module-cold plate interfaces (both sides), which can be the largest single thermal bottleneck in the stack-up [6]. The use of dielectric fluids can allow for eliminating thermal greases and greater performance enhancements. FEA was conducted to evaluate applying a dielectric cooling strategy to a double-side-cooled planar module. Figure I.15.10 shows FEA results comparing the performance of the current design (single-side-cooled planar module) with that of various double-side dielectric-cooled configurations. The modeling shows that if the convective resistance value of  $58 \text{ mm}^2\text{-K/W}$  (equivalent to  $17,300 \text{ W/m}^2\text{-K}$ ) from the current design (single-side dielectric fluid case) is applied to both sides of the double-side cooled modules, then the thermal resistance can be reduced by 50% as compared to the single-side cooled case—a result of the two-fold increase in surface area. However, if a two-phase convective heat transfer coefficient of  $\sim 100 \text{ kW/m}^2\text{-K}$  was applied to the double-side cooled module, then the resistance can be reduced by approximately 80%. These results indicated greater power density values beyond those predicted for the current design. Future work will be dedicated to developing double-side-cooled strategies using dielectric fluids.

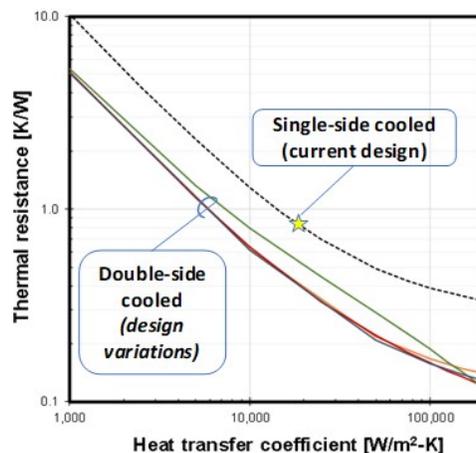


Figure I.15.10 Predicted thermal resistance for the double-side-cooled module design indicating substantial thermal performance enhancements compared to the single-side-cooled design.

## Conclusions

Research is being conducted to develop power electronics thermal management strategies to enable reaching 100 kW/L power density (2025 DOE power density target). The project's major conclusions are summarized below.

- Designed (via modeling) a novel power electronics cooling configuration that uses dielectric fluid jets impinging on a planar package that is predicted to enable reaching 100-kW/L power density. In addition, the cooling configuration is predicted to have 50% lower thermal resistance and 80% lower pumping power as compared with the 2014 Honda Accord Hybrid.
- Fabricated (via 3D printing) a prototype of the dielectric fluid heat exchanger and the finned-heat spreaders for experimental validation. A dielectric fluid flow loop was fabricated to enable testing the heat exchanger with different dielectric fluids at various flow rates and fluid temperatures (-40°C – 100°C).
- Evaluated the short-circuit fault condition response for the dielectric-fluid planar package cooling concept. Results show that the top-side dielectric cooling concept has minimal effect (slight temperature decrease) in delaying the temperature rise during the short-circuit condition.
- Modeled the effect of incorporating dielectric cooling (single phase and two phase) on double-side cooled packages, which predicted significantly lower (as much as 80% lower) thermal resistance values that will result in higher power density values.

## Key Publications and Presentations

1. Moreno, G. "Power Electronics Thermal Management Research." 2019 presentation to the DOE VTO Electrical and Electronics Technical Team, July 2019.
2. Moreno, G. "Power Electronics Thermal Management Research." 2018 DOE VTO Annual Report, 2018.

## References

1. U.S. DRIVE, 2017, Electrical and Electronics Technical Team Roadmap, U.S. DRIVE.
2. "Electrification FY2018 Annual Progress Report," Energy.gov [Online]. Available: <https://www.energy.gov/eere/vehicles/downloads/electrification-fy2018-annual-progress-report>. [Accessed: 23-Sep-2019].
3. Moreno, G., Bennion, K., King, C., and Narumanchi, S., 2016, "Evaluation of Performance and Opportunities for Improvements in Automotive Power Electronics Systems," 2016 15th IEEE Intersociety Conference on Thermal and Thermomechanical Phenomena in Electronic Systems (ITherm), pp. 185–192.
4. Sakai, Y., Ishiyama, H., and Kikuchi, T., 2007, Power Control Unit for High Power Hybrid System, 2007-01-0271, SAE International, Warrendale, PA.
5. Anwar, M., Hayes, M., Tata, A., Teimorzadeh, M., and Achatz, T., 2015, "Power Dense and Robust Traction Power Inverter for the Second-Generation Chevrolet Volt Extended-Range EV," SAE Int. J. Altern. Powertrains, 4(1).
6. Bennion, K., and Kelly, K., 2009, "Rapid Modeling of Power Electronics Thermal Management Technologies," 2009 IEEE Vehicle Power and Propulsion Conference, IEEE, pp. 622–629.

## **Acknowledgments**

The significant contributions of Kevin Bennion, Xuhui Feng, Bidzina Kekelia, Ramchandra Kotecha, and Jeff Tomerlin are acknowledged. A portion of the research was performed using computational resources sponsored by the Department of Energy's Office of Energy Efficiency and Renewable Energy located at the National Renewable Energy Laboratory.



## I.16 Magnetics for Ultra-High Speed Transformative Electric Motor (Ames Lab)

### Iver Anderson, Principal Investigator

Ames Laboratory (USDOE), Iowa State University  
222 Metals Development, Iowa State University  
Ames, IA 50011  
E-mail: [andersoni@ameslab.gov](mailto:andersoni@ameslab.gov)

### Matthew Kramer, Principal Investigator

Ames Laboratory (USDOE), Iowa State University  
125 Metals Development, Iowa State University  
Ames, IA 50011  
E-mail: [mjkramer@ameslab.gov](mailto:mjkramer@ameslab.gov)

### Jun Cui, Principal Investigator

Ames Laboratory (USDOE), Iowa State University  
106 Wilhelm, Iowa State University  
Ames, IA 50011  
E-mail: [cuijun@ameslab.gov](mailto:cuijun@ameslab.gov)

### Susan A. Rogers, DOE Technology Development Manager

U.S. Department of Energy  
E-mail: [susan.rogers@ee.doe.gov](mailto:susan.rogers@ee.doe.gov)

Start Date: October 1, 2018

End Date: September 30, 2019

Project Funding (FY19): \$600,000

DOE share: \$600,000

Non-DOE share: \$0

### Project Introduction

The DOE 2025 target on electric motor power density is 50 kW/L. Such aggressive target limits the choices on permanent magnet (PM) to the most powerful Nd-Fe-B based magnets, whose magnetic properties is strongly temperature dependent. Better thermal stability can be achieved by adding significant amount of Co and Dy [1]. Unfortunately, Dy is scarce and expensive. The U.S. Department of Energy (DOE) highlighted Dy as the single most critical strategic metal not only in the U.S., but world-wide. According to the 2014 and 2019 USGS Minerals Commodities Summaries, the average price of Dy<sub>2</sub>O<sub>3</sub> jumped from \$295/kg in 2010 to \$1410/kg in 2011, then retreated to \$180/kg in 2018. Its price and availability remain volatile, with the price back to \$247 in 2019. Currently, over 70% of rare earth (RE) metals is produced in China. In 2017, some European countries and China announced that internal combustion engine will be phased out in one to two decades. With foreseeable large increase in the number of electrical vehicles and their dependence on permanent magnet traction motors, the supply risk for Nd, Pr and Dy is expected to remain at high level with their projected demand to more than double by 2030 [2]. Strategies to mitigate the RE materials criticality issues include increasing and diversifying the supply, and reducing demand. While several mines outside of China—in Australia, Vietnam and the US—have opened and have begun production of RE elements, the most desired heavy RE elements, in particular, Dy and Tb, remain low in supply because none of these newly opened mines are rich in heavy RE reserve. To reduce the demand of heavy RE elements, alternative magnet technologies that use much less Dy have to be developed. Evidence shows that reducing the grain size of NdFeB magnet may improve its coercivity, making it possible to use an engineering grain-refinement approach to replace the chemistry approach where Dy is used for maintaining NdFeB's coercivity at high temperature [3]. We plan to take advantage of the relationship between grain size and coercivity, and develop a new type of NdFeB magnet with ultrafine grain size.

One viable approach to drastically increase motor power density is to increase motor speed. Although not specified by the DOE 2025 target, 90% efficiency is a key operational limit for electric motors because less efficient motors consume more power, impose extra load on the vehicle battery, and diminish the impact of increasing power density. To maintain such high efficiency at high speed, the magnetic materials need to exhibit exceptionally high electrical resistivity in order to minimize otherwise substantially higher loss caused by the increased eddy currents. These tight constraints on materials are further tightened by the 2025 cost target of \$3.3/kW, which disqualifies most of the existing advanced soft magnetic materials (e.g., amorphous and nanocrystalline) from meeting these requirements. It appears that one of the barriers for meeting the DOE 2025 targets of 50 kW/L power density is the lack of cost-effective magnetic materials that can run at high frequency without excessive eddy current heating. We plan to address these materials challenges by developing the soft magnetic (SM) materials suitable for high speed application. Clearly, a collective effort with the CADET consortium partners on innovative advanced materials and complex system design is needed to meet the aggressive target.

### Objectives

This project will develop the PM and SM materials and their processes for high speed traction drive motors. For PM materials, the objective is to (a) Develop fine-grain RE permanent magnet with high coercivity at high temperature, and (b) Develop graded heavy RE-free magnet with high performance at high temperature. For SM materials, high silicon electric steel is a good candidate to replace the current electric steel with 3.2% Si. High Silicon steel offers relatively high resistivity ( $\rho = 82 \mu\Omega\text{-cm}$ ), high magnetization and low cost, but it suffers from the brittleness problem. Recent research at Iowa State University and Ames Lab shows that such a problem can be mitigated using rapid solidification techniques. The objective is to develop a processing method that can be scaled to mass production of ductile 6.5% Si steel sheet for stator and rotor applications.

### Approach

There are two approach planned for reducing the critical heavy RE (HRE) elements usage in the motor magnet while maintaining their high temperature performance. One is fine grain approach and other is graded magnet approach. Figure I.16.1 shows the effect of grain size on coercivity for the NdFeB magnet [4]. It is possible to push the coercivity to beyond 20 kOe with ultrafine grains. With such high coercivity at room temperature, even with the typical rate of losing coercivity with increasing temperature ( $-0.6\%/K$ ) [1], there will still be enough coercivity at the 400 K, where the high-speed motor may operate. The challenge for the fine grain approach is to obtain fine feedstock

powders with particle size less than  $1 \mu\text{m}$ ; and more importantly, to keep each of the particle size small during the sintering process. This also requires extreme care in handling to avoid oxidation. Specific efforts include investigation of industrial-viable processing methods for synthesize feedstock powder with fine particle size ( $< 1 \mu\text{m}$ ), and methods for sintering the powder into bulk magnets without significant grain growth.

The approach for enabling 6.5% Si steel for high power density motor application focusing on making wide sheet using the planar flow casting method, which is traditionally used for manufacturing amorphous and nanocrystalline materials where rapid cooling rate is essential for preventing grain growth. For 6.5% Si steel, large grain size is preferred. The rapid cooling rate is for controlling phase formation, not for grain size. As such, the principles and parameters for the traditional planar flow casting all need to be modified for casting wide 6.5% Si steel sheet. Specific efforts include investigation of all process parameters and development of equipment for mass production of ductile 6.5% Si steel sheet.

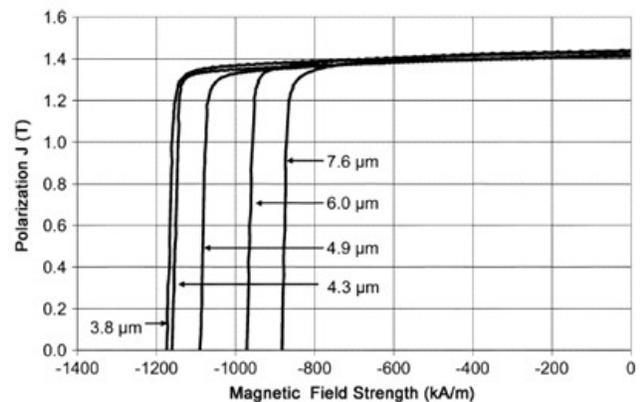


Figure I.16.1 Dependence of coercivity on grain size.

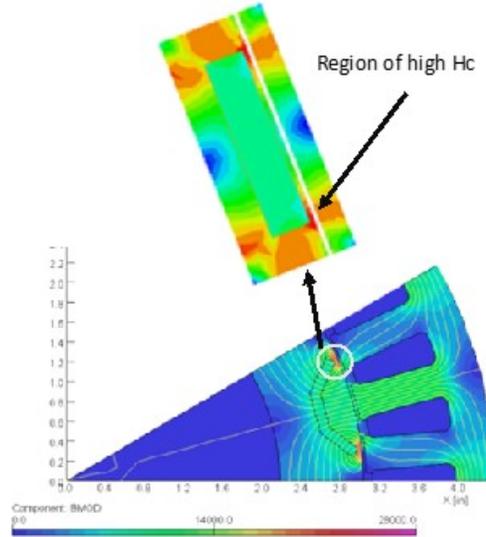


Figure I.16.2 Micromagnetic simulation of the demagnetization field near the permanent magnets in motor.

Synergy with other VTO efforts, especially on system design is needed to take full advantage of the new layered PM and ultrathin highly resistive SM. Internal permanent magnet traction motors are the most compact and efficient electric drive motors. Their optimization is a fine balance between the properties and topology of SM and PM components and the demagnetization fields. Clearly, a new motor topology with complex flux pattern that can take full advantage of new PM and SM is needed. The Ames team will work with ORNL, NREL and an industrial partner (e.g., UTRC) to demonstrate the newly developed magnetics in an electric motor.

**Results**

**Task 1: Develop fine-grain RE permanent magnet with high coercivity at high temperature**

In FY19, several powder size reduction techniques were investigated via literature study. A conclusion has been made that the newest dual head jet-mill is likely the most viable industrial method for fine particle production. Efforts have been made to arrange trial runs with equipment manufacturer (Netzsch Group). While waiting for the trial runs using the jet-mill, Ames team has initiated the study on the effect of finer size powder on magnetic properties and used the conventional ball milling method to obtain finer particles. Longer ball-milling time were used to produce finer powders. The obtained powders were aligned, compacted, and sintered to obtain bulk magnet with different grain sizes. Figure I.16.3 shows the MH curves of the bulk magnets (8 grams each) prepared using the feedstock powder that were ball milled from 3 to 11 hours. It shows longer the milling time, smaller the particle sizes and higher the coercivity. This result validated the overall fine grain approach to improve coercivity. Note that the feedstock coarse powder purchased from Magna-quench is rated at N45 with  $(BH)_{max}$  42-45 MGOe. Ames team was able to obtain 43.6 MGOe after careful processing of

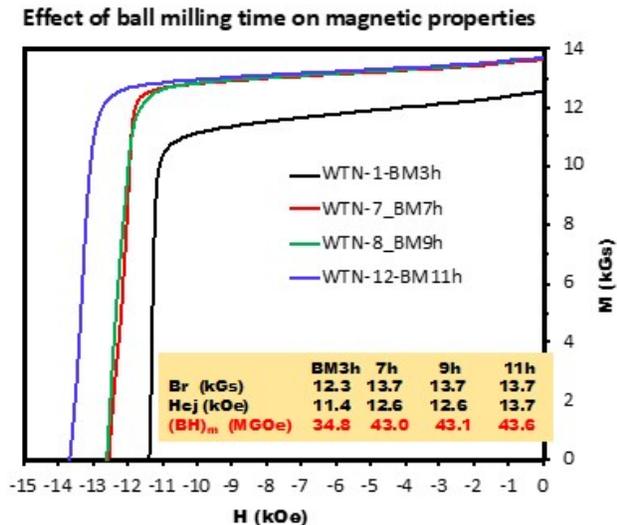


Figure I.16.3 MH curves of the bulk magnet prepared using feedstock powders that were ball-milled for different time. The longer the ball milling hours, the finer the particle size.

this powder. This result qualifies the facility and the processes developed at Ames lab as the state-of-the art and enables the team to carry out frontier research on permanent magnet.

Although starting particle size may be fine, sintering temperature and time can affect the grain size of magnet, resulting in excess grain growth (and decreased coercivity) unless carefully controlled. Ames team has been refining the sintering process for fine grain sizes and protocols for handling these powders to avoid oxidation. With the current feedstock particle size limited to 3  $\mu\text{m}$  and above, the developed process can result in an average grain size about 4  $\mu\text{m}$  in the obtained bulk magnet. This is a significant improvement over the typical 5  $\mu\text{m}$  grain size in the commercial N45 magnet. It is expected that with 1  $\mu\text{m}$  feedstock powder, the bulk magnet grain size may be controlled to be under 2  $\mu\text{m}$ .

**Task 2: Develop graded HRE-free magnet with high performance at high temperature**

In FY19, several assemblies with different combination of NdFeB magnet and pure Fe core were constructed and tested. These models will be used to validate the micromagnetic modeling which will be performed, in part, in collaboration with ORNL. Table I.16.1 shows the configuration and the overall magnetic performance obtained using the Hysteresisgraph Tracer allowing MH loop characterization for the whole assembly. The red curve of the assembly with NdFeB-shell and Fe-core in Figure I.16.4 shows large kink in the second quadrant, indicative of significant magnetic decoupling. Note that with hysteresisgraph tracer, the external magnetic field was applied to the whole assembly, which does not reflect the demagnetization field that the magnet experiences during the motor operation. Although the observed decoupling behavior may not have a large adverse impact on magnet’s performance for motor, it must be corrected through a combined effort of micromagnetic modeling, in-situ testing, and materials combability study. It is expected that through metallurgical bonding between the high coercivity shell and low coercivity core, this decoupling behavior can be reduced. In addition, a proper evaluation tool allowing the application of localized demagnetization field as well as localized magnet response is needed.

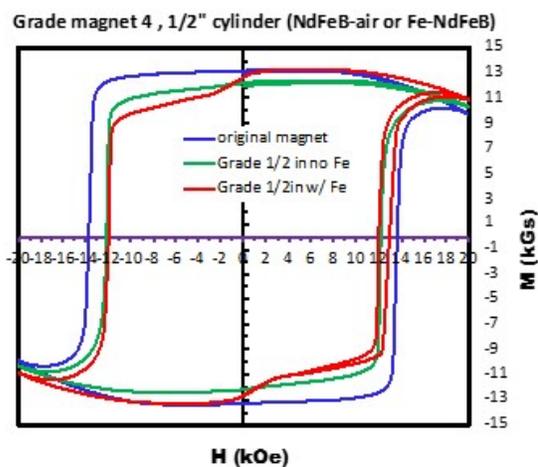


Figure I.16.4 MH curves of the assemblies listed in Table I.1.16.1.

**Table I.16.1 Magnetic Properties of the Magnet Assembly with Different Configuration.**

Magnet Configuration	NdFeB Maget only	air, one NdFeB disc at top and bottom	Fe core, one NdFeB disc at top and bottom	Fe core, two NdFeB discs at top and bottom
Br, kGs	13.2	12.2	12.7	13.2
Hcb, kOe	12.3	10.7	9.8	10.6
Hcj, kOe	13.7	12.2	12.0	12.8
(BH)max, MGOe	42.5	33.7	29.7	34.8

**Task 3: Development of cost-effective manufacturing process for high performance soft magnetic materials in thin sheet form**

The challenge for enabling 6.5%Si steel for mass production of thin sheets lies in the continuous production of wide ribbon using planar flow casting method. Such method has been widely used for producing amorphous and nanocrystalline materials, whose melting point is typically less than 1400 K. In the case of 6.5%Si steel, the melting point is 1750°K. Such high temperature put excessive thermal load to the system. In FY19, Ames team successfully demonstrated the fabrication of 10 mm wide ribbon using the small melt-spinner (as shown in Figure I.16.5). The main challenge in developing this process is the scaling up from 10 mm to 50 mm and the load from 10 gram to kilograms and beyond. The crucible orifice is too large to hold the liquid during prolonged heating; the induction coil is not powerful enough to liquefy the whole steel ingot in time; the induction coil and the cooling water line interconnect is not rigid enough at elevated temperature; the main bus bar overheats due to high heating power. All of these issues have all been addressed. For example, a new crucible with two-body design and multiple small orifice was deployed and tested successfully for holding the melt. New thermal insulation and heat deflector were added to the system to mitigate the overheat problem. Long catching tube extension was installed to allow hot melt-spun ribbon to cool down before they can fuse together. A muffin fan was added to the bus-bar area to cool down the hot bus-bar when the system is at its 90% power output. The cooling line was replaced with new tubed with higher temperature rating. A new charge loading scheme was developed allowing efficient use of the heat power from the induction coil. And a new induction coil geometry was implemented to deliver power to the charge more efficiently. With these modifications, the team expects to produce the first batch 50 mm wide ribbon in November 2019.

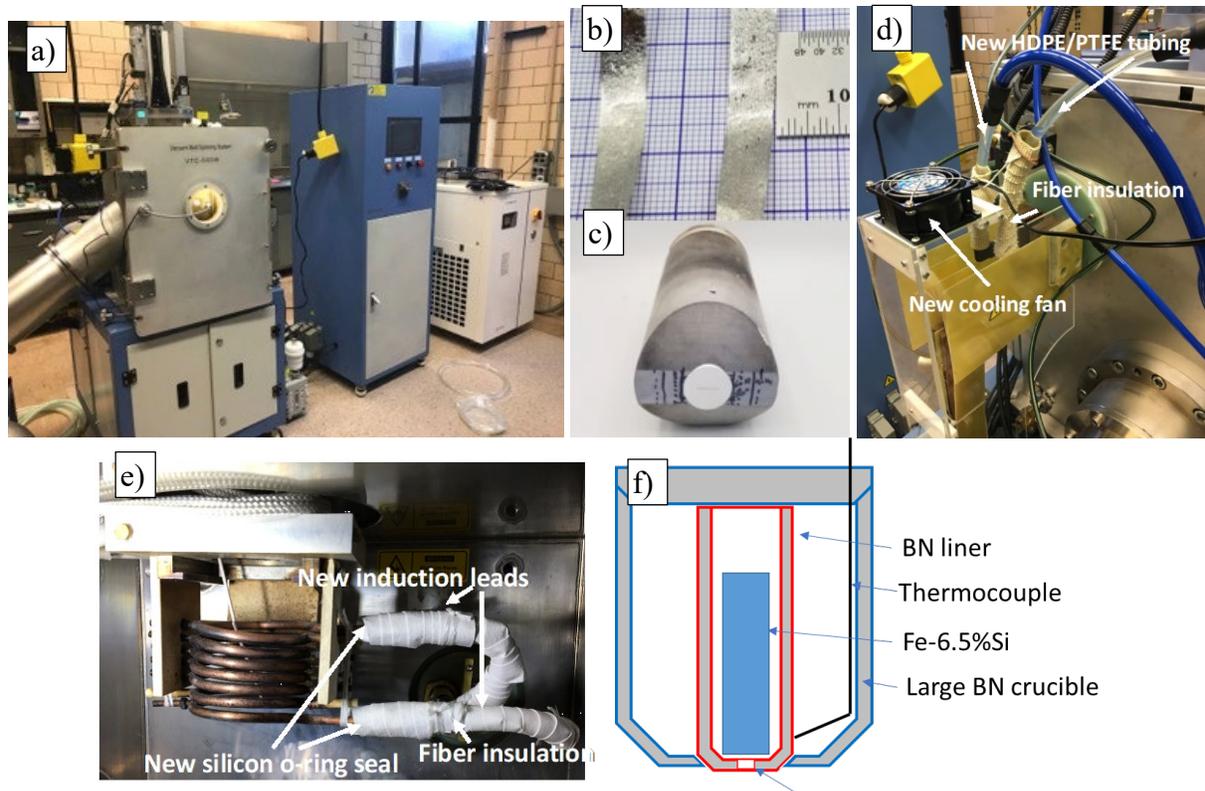


Figure I.16.5 a) the large melt-spinner capable of producing 500 gram thin sheet steel; b) the 10 mm ribbon of 6.5% Si steel prepared using only 10 gram of ingot; c) The new two-body crucible design allowing quick change of orifice; d) new muffin fan for bus-bar and modified cooling lines; e) newly added insulation materials to protect cooling lines from radiation heating by the coil; f) the custom designed BN crucible.

## Conclusions

In FY19, Ames team has been working the magnetic materials for the next generation high power density motor. Three efforts aimed at improving coercivity of PM through grain size refinement, reducing HRE usage through graded architecture, and reducing eddy loss in stator by enable highly resistive 6.5% Si steel were carried out. Direct observation of the desired effect of fine grain on coercivity was achieved; capability for fabricating high performance NdFeB magnet was established; graded magnets were assembled with key issues identified; and significant modification to the melt-spinner allowing fabrication of 50 mm 6.5%Si steel ribbon were completed.

## References

1. Liu, S., and G. E. Kuhl. Development of New High Temperature and High Performance Permanent Magnet Materials. No. UDR-TR-2000-00092. DAYTON UNIV OH RESEARCH INST, 2000.
2. Castilloux, R., Shaping the Outlook for the Rare Earth Market, Adamas Intelligence.
3. Nothnagel, P., K-H. Müller, D. Eckert, and A. Handstein. "The influence of particle size on the coercivity of sintered NdFeB magnets." *Journal of magnetism and magnetic materials* 101, no. 1-3 (1991): 379-381.
4. Uestuener, K., M. Katter, and W. Rodewald. "Dependence of the mean grain size and coercivity of sintered Nd-Fe-B magnets on the initial powder particle size." *IEEE transactions on magnetics* 42, no. 10 (2006): 2897-2899.

## I.17 Integration Methods for High-Density Integrated Electric Drives (University of Arkansas)

### **H. Alan Mantooh, Principal Investigator**

Department of Electrical Engineering  
University of Arkansas  
1475 W Cato Springs Road, Room 211  
Fayetteville, AR 72701  
E-mail: [mantooh@uark.edu](mailto:mantooh@uark.edu)

### **Simon Ang, Co-Principal Investigator**

Department of Electrical Engineering  
University of Arkansas  
3167 Bell Engineering Center  
Fayetteville, AR 72701  
E-mail: [siang@uark.edu](mailto:siang@uark.edu)

### **Fang Luo, Co-Principal Investigator**

Department of Electrical Engineering  
University of Arkansas  
3183 Bell Engineering Center  
Fayetteville, AR 72701  
E-mail: [fangluo@uark.edu](mailto:fangluo@uark.edu)

### **Susan Rogers, DOE Technology Development Manager**

U.S. Department of Energy  
E-mail: [susan.rogers@ee.doe.gov](mailto:susan.rogers@ee.doe.gov)

Start Date: April 1, 2019  
Project Funding: \$300,000

End Date: March 31, 2020  
DOE share: \$300,000

Non-DOE share: \$0

### **Project Introduction**

This project focuses on two key aspects of advancing electric drive technologies: integrated circuits and power electronic packaging. As part of the electronics portion of the team, this project seeks to provide technologies that enable new advances in power density. The first technology effort is integrating gate driving, sensing, and protection functions into the various packaging platforms that will be pursued by the team. Several technologies are possible, but the most advanced is silicon carbide (SiC) based integrated circuitry that can be co-packaged with the SiC power devices. The team will pursue designs that serve the specifications of the target electric drive train, but can survive at junction temperatures expected to enhance power density while maintaining robustness and resiliency.

The second technology effort is in advancing electronic packaging for electric drive train applications. Getting the most out of the advances in wide bandgap power semiconductor devices requires attention to careful packaging to minimize electrical parasitic influences on circuit performance and generated electromagnetic interference. Thermal management of the power devices and the surrounding circuit components must also be carefully managed. This leads to tradeoffs in the layout, arrangement, and interconnection of electronic components to balance these items. This effort will be performed in collaboration with several other organizations to achieve the objectives of power density improvements for electric drives.

## Objectives

The objective of the project is to research, develop, and test a heterogeneously integrated power module platform that will insert into a traction inverter system for power electronics modules capable of the following:

**Table I.17.1 Power Electronics Requirements**

Power Electronics Requirements	
Parameter	Measure
Cost (\$/kW)	$\leq 2.7$
Power Density (kW/L)	$\geq 100$
System Peak Power Rating (kW)	100

During the first budget period, the project focuses on advanced SiC module packaging architectures, performing a trade-off study of these architectures, and performing initial IC designs. Activities to support these investigations include:

- Model-based module architecture study and comparison
- Stacked SiC module and flip-chip module FEA analysis, process preparation, dummy module fabrication
- Selection of decoupling capacitors for integration
- Process/material system preparation and validation
- Integration method study and integrated module design
- High-temperature integrated circuit design in preparation for heterogeneous integration.

## Approach

The approach to the packaging research is to review the literature and propose architectures for tradeoff analysis while also collaborating with ORNL, NREL, and Virginia Tech on materials, thermal management, and layout ideas/constraints as they emerge. The UA team broke down its activities into the following tasks and subtasks for packaging (taken from the Statement of Project Objectives or SOPO):

Task 1.1 – Advanced SiC module architecture study

Subtask 1.1.1 – Literature survey and model-based comparison of potential module architecture

Subtask 1.1.2 – Literature survey and simulation validation to investigate module architecture and its motor drive converter-level impacts

Subtask 1.1.3 – Literature survey and simulation validation of potential integration scheme and justification of benefits/disadvantages for different integration methods

Subtask 1.1.4 – Investigation into best capacitor technologies for in-module integration

Subtask 1.1.5 – Process and material system design and testing/validation for potential advanced module structures

Subtask 1.1.6 – FEA modeling and validation for potential advanced module structures



These activities will promote our efforts in determining weak links in any proposed, tightly packed arrangement of power devices, integrated circuits, passives, and sensors. The primary deliverables from this year's activity will be test coupons and other evaluative structures to determine the efficacy of components, materials, and fabrication steps that have to be arranged in a package fabrication and assembly flow.

The approach to the IC design and sensors research activity is to continue to build momentum from previously funded projects. The UA has pursued SiC integrated circuit design activity for about 8-10 years [1]-[35]. Based on these efforts, the UA will develop new designs specific to the electric drive train requirements. While the world struggles to produce SiC ICs with any high degree of robustness, the UA will simultaneously pursue alternate options in silicon-on-insulator (SOI) technology to mitigate risk. These subtasks were defined for the IC activity:

#### Task 1.2 – High temperature gate drive and protection circuit IC design

Subtask 1.2.1 – Circuit design and simulation for SiC gate drive circuits

Subtask 1.2.2 – Determine protection scheme, and circuit design and simulation for protection circuits

Subtask 1.2.3 – Determine gate driver power supply requirements; investigate on-chip and in-module integrable power supply options

Subtask 1.2.4 – SiC high temperature gate drive, protection, and power supply circuit IC layout design; preliminary design review and layout

#### Task 1.3 – Sensors and interface circuits

Subtask 1.3.1 – Design and layout of sensor interface circuits; Test structures for temperature and current sensors, devices, and on-chip passives; preliminary design review and layout

These research activities will lead to requirements and specifications reviews that ensure that our circuit design team is pursuing the right targets. The subsequent design reviews will ensure that our designs are meeting those targets. The primary deliverables in the first year are the design review documents reflecting the requirements, specifications, and designs as we know them to that point. Of course, in a large project with many moving parts, specifications may change and the IC design team will have to adapt to those changes.

### Results

The UA packaging team has been performing literature reviews on state of the art module architectures. Today, with the advancements in WBG devices, the main limitation for full utilization of the WBG advantages [36] and [37] is the packaging technology that not only should improve but should revolutionize the size, weight, thermal and electrical performance of the power modules.

The integration level, layer structure, the proposed interconnection methods especially suitable for designing compact power modules, stray inductance minimization and the power module system compatibility are the most important topics in power electronic module studies and literature review.

The integration of the gate driver inside the power module is trendy and brings great advantages especially in WBG-based power modules that high switching frequency is one of the main requirements for power density purposes. In [38]-[46], power module structures with this purpose are proposed. For instance, in [38] the gate driver is soldered directly on the DBC of a traditional single-sided power module at the same level with the power circuit, then the parasitic interference between the power circuit and driver circuit that results in false turn-on of the switches is analyzed. Three methods are introduced to prevent this issue: (a) adding capacitance on the control stage which might end up reducing the switching speed, (b) minimizing the capacitance on the DBC layout which will require more advanced soldering equipment for the drivers, and (c) additional shielding layer in which the driver circuit is not at the same level with the power circuit. The last method is the best way

to eliminate the crosstalk. Other than these parasitic issues, however, soldering the surface mount devices (SMD), especially the driver itself on the DBC is cumbersome and can have reliability issues.

To solve this problem, authors in [39] have used a substrate for the power circuit and a separate PCB for the drivers. Both the substrate and PCB sit next to each other inside the power module package and are wire-bonded to each other. Using a PCB for the gate driver inside the power module makes the soldering process much easier. More importantly, the mentioned crosstalk between the driver circuit and power circuit can be totally mitigated. The problem with such a design, however, is that the power module is still single-sided. Conventional wire-bonding method is used in the proposed power module that has reliability issues and increases the stray inductance that prevents full utilization of the features that are only introduced by WBG devices. In [40] and [41], the PCB is molded on the substrate or the devices are placed directly inside the internal layer of the PCBs, respectively.

In [42], a double-sided power module is proposed with the DBC+PCB+DBC structure. IGBTs are used as the power module bare dies; and are stacked at both sides of the PCB which is at the middle of the power module. In this power module structure, the bare dies are soldered on the DBCs from one side, but conductive glues are used for the opposite side to connect their gate and source pads to the PCB. This structure minimizes the stray inductance and has a simple fabrication procedure. Integration of the gate driver with the power module can be done easily thanks to the use of PCBs. The rest of the SMD components used for parasitic mitigation and in gate driver board can be soldered on the same PCB to improve the overall operation of the power module. The structure, however, should deal with the CTE mismatch. The other issue is that, although the power module has a double-sided structure, but the bare dies can cool down only from the DBC side, and in fact may get more heat from the bare die on the other side of the PCB because the bare dies are stacked at the Z-direction. Also, the connection of the bare die to the PCB that is done by a conductive glue needs more investigation. Conductive glue has thermal cycling issues and have high thermal and electrical resistance which will increase the losses and detriment the power module reliability.

In [43], a DBC is used as a power loop and a PCB is used as both power loop and driver loops. In this structure, windows are created inside the PCB such that the DBCs can be placed inside the windows and attached to the PCB. The gate and source pads are wire-bonded to the PCB. By this method, the CTE mismatch problem between the bare dies and PCB will be mitigated. But because of wire-bonding, it is difficult to use it in a double-sided power module structure.

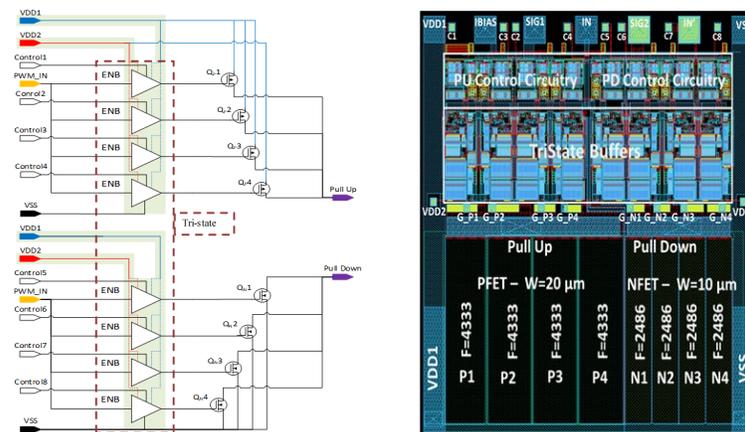


Figure I.17.1 Simplified SiC CMOS gate driver schematic and layout with programmable drive strength.

Based on the on-going literature survey of the previously proposed power modules, two new structures of power electronic modules are proposed up to now. The feasibility of these power module structures is under investigation by fabricating dummy parts for these structures.

The UA IC design team has been actively designing gate drivers and protection circuits in Fraunhofer's 1  $\mu\text{m}$  SiC CMOS process. This process is under development and the UA currently is fabricating its second run. The first run had poor yield, large threshold voltages, and generally poor performance from the p-channel devices. Further, there were some fabrication issues involving ohmic contacts that prevented the devices from having the required current drive capability needed.

As a mitigation step, the IC design group submitted for fabrication a set of SOI chips to determine how well they would perform. These chips were fabricated by XFAB and are now under evaluation.

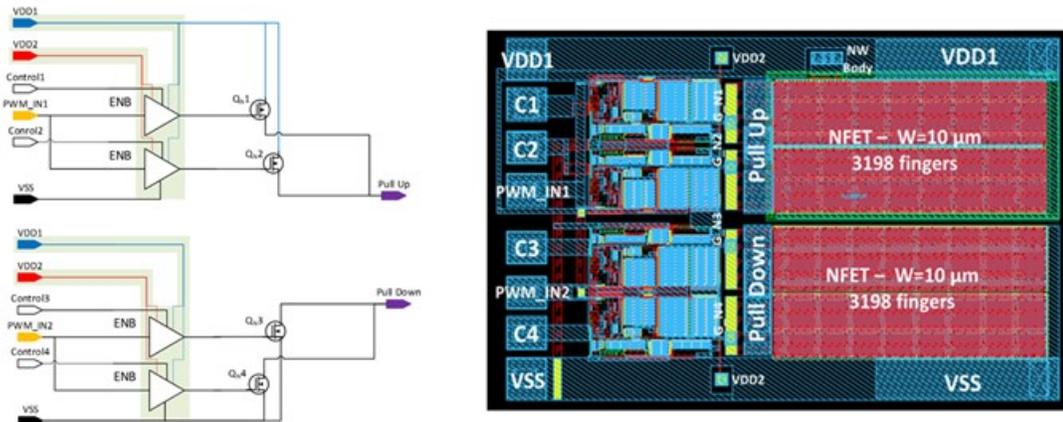


Figure I.17.2 Simplified SiC NMOS gate driver schematic and layout with programmable drive strength.

These fabrication runs were in process before this project started and yet subsequent runs will benefit from the results obtained. Two variants of gate driver circuitry were recently submitted for fabrication. These simplified schematics and layouts are shown in Figure I.17.1 and Figure I.17.2. Figure I.17.1 is a CMOS driver while Figure I.17.2 is an all-NMOS driver. New IC architectures are being formulated based on recent active gate driver research [47],[48].

Sensor development is being leveraged from prior work on GaN/AlGaIn Hall effect devices. This work will be utilized directly as well as migrated into SiC in future runs [49]. This device is able to serve as a simultaneous temperature and current sensor. At present, the IC team is focused on interface electronics to existing sensors that will all be migrated into a single material system during this project.

## Conclusions

UA research is underway on both packaging and IC design. Biweekly meetings are being held with the larger team and UA-only meetings are being held in the intermediate weeks such that a project meeting is held each week. At present, no key findings are available for reporting.

## References

1. M. Shakir, S. Hou, A. Metreveli, A. U. Rashid, H. A. Mantooth, C.-M. Zetterling, "555-timer and comparators operational at 500°C," *IEEE Trans. on Electron Devices*, vol. 66, no. 9, pp. 3734-3739, Sept. 2019.
2. S. Roy, A. Rashid, A. Abbasi, R. Murphree, M. Hossain, A. K. Faruque, A. Met, C.-M. Zetterling, J. Fraley, B. Sparkman, H. A. Mantooth, "Silicon Carbide Bipolar Analog Circuits for Extreme Temperature Signal Conditioning," *IEEE Trans. on Electron Devices*, vol. 66, no. 9, pp. 3764-3770, Sept. 2019.

3. R. Murphree, S. Roy, S. Ahmed, M. Barlow, A. Rahman, A. M. Francis, J. Holmes, H. A. Mantooth, J. Di, "A SiC CMOS linear voltage regulator for high temperature applications," *IEEE Trans. on Power Electronics*, vol. 35, no. 1, pp. 913-923, Jan. 2020, DOI: 10.1109/TPEL.2019.2914169
4. M. W. Hussain, H. Elahipanah, J. E. Zumbro, S. Rodriguez, B. G. Malm, H. A. Mantooth, A. Rusu, "A SiC-BJT Based Negative Resistance Oscillator for High-Temperature Sensors," *IEEE J. Electron Devices*, vol. 7, no. 1, pp. 191-195, Dec. 2018.
5. M. W. Hussain, H. Elahipanah, J. E. Zumbro, S. Schroder, S. Rodriguez, B. G. Malm, H. A. Mantooth, A. Rusu, "A 500 C Active Down-Conversion Mixer in Silicon Carbide Bipolar Technology," *IEEE Electron Device Letters*, vol. 39, no. 6, pp. 855-858, June 2018.
6. M. Barlow, S. Ahmed, A. M. Francis, H. A. Mantooth, "An integrated SiC CMOS gate driver for power module integration," *IEEE Trans. on Power Electronics*, 8 pgs., DOI: 10.1109/TPEL.2019.2900324, Feb. 2019.
7. H. A. Mantooth, T. Evans, C. Farnell, Q. Le, and R. Murphree, "Emerging Trends in Silicon Carbide Power Electronics Design," *CPSS Trans. on Power Electronics and Applications*, vol. 2, no. 3, pp. 161-169, Nov. 2017.
8. S. Roy, R. C. Murphree, A. Abbasi, A. Rahman, A. Gattis, S. Ahmed, A. M. Francis, J. Holmes, H. A. Mantooth, J. Di, "A SiC CMOS Digitally Controlled PWM Generator for High-Temperature Applications," *IEEE Trans. on Industrial Electronics*, vol. 64, no. 10, pp. 8364 - 8372, Oct. 2017.
9. A. Rahman, L. Caley, N. Kuhns, H. A. Mantooth, J. Di, A. M. Francis, J. Holmes, "High Temperature Data Converters in Silicon Carbide CMOS," *IEEE Trans. on Electron Devices*, vol. 64, no. 4, pp. 1426-1432, Apr. 2017.
10. Rahman, S. Roy, R. Murphree, R. Kotecha, K. Addington, A. Abbasi, H. A. Mantooth, A. M. Francis, J. Holmes, J. Di, "High-Temperature SiC CMOS Comparator and op-amp for Protection Circuits in Voltage Regulators and Switch-Mode Converters," *IEEE J. of Emerging and Selected Topics in Power Electronics*, vol. 4, no. 3, pp. 935-945, Sept. 2016.
11. N. Kuhns, L. Caley, A. Rahman, S. Ahmed, J. Di, H. A. Mantooth, A. M. Francis, and J. Holmes, "Complex High-Temperature CMOS Silicon Carbide Digital Circuit Designs," *IEEE Transactions on Device and Materials Reliability*, vol. 16, issue 2, pp. 105-111, February 2016.
12. A. Rahman, A. M. Francis, S. K. Akula, S. Ahmed, J. Holmes, H. A. Mantooth, "High Temperature Voltage and Current References in Silicon Carbide CMOS," *IEEE Trans. on Electron Devices*, vol. 63, no. 6, pp. 2455 - 2461, Jun. 2016.
13. M. Glover, P. Shepherd, M. Francis, M. Mudholkar, H. A. Mantooth, M. Ericson, S. Frank, C. Britton, L. Marlino, T. McNutt, A. Barkley, B. Whitaker, and A. Lostetter, "A UVLO circuit in SiC compatible with power MOSFET integration," *IEEE Journal of Emerging and Selected Topics in Power Electronics*, vol. 2, no. 3, pp. 425-433, Sep. 2014.
14. J. A. Valle-Mayorga, A. Rahman, H. A. Mantooth, "An all-NMOS SiC linear voltage regulator for high temperature applications," *IEEE Transactions on Power Electronics*, vol. 29, no. 5, pp. 2321-2328, May 2014.
15. M. N. Ericson, S. S. Frank, C. L. Britton, L. Marlino, S. H. Ryu, D. Grider, H. A. Mantooth, M. Francis, R. Lamichhane, M. Mudholkar, P. Shepherd, M. Glover, J. Valle-Mayorga, T. R. McNutt, A. Barkley, B. Whitaker, Z. Cole, B. Passmore, A. Lostetter, "A 4H silicon carbide gate buffer for integrated power systems," *IEEE Trans. on Power Electronics*, vol. 29, no. 2, pp. 539-542, Feb. 2014.

16. H. A. Mantooth, M. D. Glover, P. Shepherd, "Wide bandgap technologies and their implications on miniaturizing power electronic systems," *IEEE Journal on Emerging and Selected Topics in Power Electronics*, vol. 2, no. 3, pp. 374-385, Sept. 2014.
17. H. A. Mantooth, "Wide Bandgap Analog and Mixed-Signal IC Design for Advanced Power Electronics," *Electrochemical Society (ECS) Transactions – CSTIC 2011*, 9 pgs., May 2017 (invited paper).
18. M. Barlow, A. M. Francis, N. Chiolino, J. Holmes, A. Abbasi, H. A. Mantooth, "SiC-CMOS digital circuits for high temperature power conversion," *IEEE Workshop on Wide Bandgap Power Devices and Applications (WiPDA)*, pp. 223-227, Fayetteville, AR, Nov. 2016.
19. S. Roy, R.C. Murphee, A. Abbasi, A. Rahman, H. A. Mantooth, J. Di, A. M. Francis, and J. Holmes, "Implementation of a Digitally Controlled SiC CMOS PWM Generator using a Tunable Current-Starved Delay Generator for High-Temperature Switched-Mode Regulators", *IEEE Workshop on Wide Bandgap Power Devices and Applications (WiPDA)*, pg. 210-214, Fayetteville, AR, Nov. 2016.
20. M. R. Benavides, A. N. Castillo, A. Rahman, M. Barlow, D. Abreu, C. Rowlett, H. A. Mantooth, A. M. Francis, and J. A. Holmes, "Low Power Silicon Carbide RS-485 Transceiver," *Proceedings of the International Conference on High Temperature Electronics (HiTEC)*, pp. 257-262, Albuquerque, New Mexico, May 10-12, 2016.
21. M. Barlow, S. Ahmed, H. A. Mantooth, and A. M. Francis, "An Integrated SiC CMOS Gate Driver," *Applied Power Electronics Conference and Exposition (APEC)*, pp. 1646-1649, Long Beach, CA, March 2016.
22. A. Rahman, K. Addington, M. Barlow, S. Ahmed, H. A. Mantooth, and A. M. Francis, "A High Temperature Comparator in SiC CMOS," in *Proc. The 3rd IEEE Workshop on Wide Bandgap Power Devices and Applications (WiPDA)*, pp. 236-240, Blacksburg, Virginia, USA, Nov 2-4, 2015.
23. A. Rahman, S. Roy, R. Murphee, H. A. Mantooth, A. M. Francis, and J. Holmes, "A SiC 8-Bit DAC at 400°C," in *Proc. The 3rd IEEE Workshop on Wide Bandgap Power Devices and Applications (WiPDA)*, pp. 241-246, Blacksburg, Virginia, USA, Nov 2-4, 2015.
24. Rahman, P. D. Shepherd, S. A. Bhuyan, S. Ahmed, S. K. Akula, L. Caley, H. A. Mantooth, J. Di, A. M. Francis, J. Holmes, "A Family of CMOS analog and mixed signal circuits in SiC for high temperature electronics," *IEEE Aerospace Conference*, pp. 1-10, March 2015.
25. J. Brady, A. M. Francis, J. Holmes, J. Di, H. A. Mantooth, "An Asynchronous Cell Library for Operation in Wide-Temperature & Ionizing-Radiation Environments," *IEEE Aerospace Conference*, pp. 1-10, March 2015.
26. N. Kuhns, L. Caley, A. Rahman, S. Ahmed, J. Di, H. A. Mantooth, A. M. Francis, and J. Holmes, "High Temperature Testing Results of Synchronous and Asynchronous Digital Silicon Carbide Integrated Circuits," *Proceedings of the 2015 Government Microcircuit Applications and Critical Technology Conference (GOMAC-Tech)*, 4 pgs., March 2015.
27. A. M. Francis, J. Holmes, H. A. Mantooth, "Towards Standard Component Parts in Silicon Carbide CMOS," *IEEE Aerospace Conference*, pp. 1-9, March 2015.
28. M. N. Ericson, S. S. Frank, C. L. Britton, L. D. Marlino, D. D. Janke, D. B. Ezell, R. R. Lamichhane, A. M. Francis, P. D. Shepherd, M. D. Glover, H. A. Mantooth, S.-H. Ryu, B. Whitaker, Z. Cole, B. Passmore, T. R. McNutt, "An integrated gate driver in 4H-SiC for power converter applications," *2<sup>nd</sup>*

- IEEE Workshop on Wide Bandgap Power Devices and Applications*, 4 pgs., Knoxville, TN, Oct. 13-15, 2014.
29. R. R. Lamichhane, N. Ericsson, S. Frank, C. Britton, L. Marlino, H. A. Mantooth, A. M. Francis, P. Shepherd, M. Glover, S. Perez, T. McNutt, B. Whitaker, Z. Cole, "A wide bandgap silicon carbide (SiC) gate driver for high-temperature and high-voltage applications," *IEEE International Symposium on Power Semiconductor Devices & IC's (ISPSD)*, pp. 414-417, 15-19 June 2014.
  30. R. R. Lamichhane, H. A. Mantooth, A. M. Francis, P. D. Shepherd, M. D. Glover, S. Perez, N. Ericson, S. S. Frank, C. L. Britton, L. D. Marlino, T. R. McNutt, B. Whitaker, Z. Cole, "A wide bandgap silicon carbide gate driver for high-temperature and high-voltage applications," *IEEE Proc. Of International Symposium on Power Semiconductor Devices (ISPSD)*, 4 pgs, Kona, Hawaii, June 2014.
  31. P. Shepherd, D. Kaiser, M. Glover, S. Perez, A. M. Francis, H. A. Mantooth, "Integrated Protection Circuits for an NMOS Silicon Carbide Gate Driver Integrated Circuit," in *2014 Seventh International High Temperature Electronics Conference (HITEC)*, 4 pgs., May 2014.
  32. P. Shepherd, A. Rahman, S. Ahmed, A. M. Francis, J. Holmes, H. A. Mantooth, "500 kHz – 5 MHz Phase-Locked Loops in High-Temperature Silicon Carbide CMOS," in *2014 Seventh International High Temperature Electronics Conference (HITEC)*, 4 pgs., May 2014.
  33. A. M. Francis, A. Rahman, J. Holmes, P. Shepherd, S. Ahmed, M. Barlow, S. Bhuyan, L. Caley, T. Moudy, H. A. Mantooth, J. Di, "Design of Analog and Mixed-Signal Integrated SiC CMOS Circuits with a High Fidelity Process Design Kit," *Proceedings of the 2014 Government Microcircuit Applications and Critical Technology Conference (GOMAC-Tech)*, 4 pgs., March 2014.
  34. L. Caley, N. Kuhns, W. S. Bowden, P. Shepherd, A. Rahman, J. Di, H. A. Mantooth, A. M. Francis and J. Holmes, "Delay-Insensitive Asynchronous Silicon Carbide Integrated Circuit Design for High-Temperature Applications," in *GOMACTech Conference*, Charleston, SC, 4 pgs., March 2014.
  35. J. Valle, A. Rahman, H. A. Mantooth, "Back to the Future: An all-NMOS SiC Linear Voltage Regulator for High Temperature Applications," *IEEE Conf. on Compound Semiconductor Integrated Circuits and Systems*, pp. 1-4, Oct. 17, 2012.
  36. E. Gurpinar, R. Wiles, B. Ozpineci, and T. Raminosa, F. Zhou, Y. Liu, and E.M. Dede "SiC MOSFET-Based Power Module Design and Analysis for EV Traction Systems," [\*IEEE Energy Conversion Congress and Exposition\*](#), Oregon, 2018.
  37. L. Yong, *Power Electronic Packaging: Design, Assembly Process, Reliability and Modeling*, Springer Science & Business Media, 2012.
  38. Z. Dong, X. Wu, and K. Sheng, "Suppressing Methods of Parasitic Capacitance Caused Interference in a SiC MOSFET Integrated Power Module," *IEEE Journal of Emerging and Selected Topics in Power Electronics*, vol. 7, no. 2, pp. 745-752, Jun. 2019.
  39. Q. Hua, Z. Li1, B. Zhang, W. Chen, X. Huang and D. Cheng, "Full-Integrated Power Module for Motor Drive Applications," *International Symposium on Power Semiconductor Devices & IC's*, Japan, 2013.
  40. K. Klein, E. Hoene, R. Reiner, R. Quay, "Study on Packaging and Driver Integration with GaN Switches for Fast Switching," *International Conference on Integrated Power Electronics Systems*, Germany, 2016.

41. C. Buttay, C. Martin, F. Morel, R. Caillaud, J. L. Leslé, R. Mrad, N. Degrenne, S. Mollov, "Application of the PCB-Embedding Technology in Power Electronics – State of the Art and Proposed Development," *Second International Symposium on 3D Power Electronics Integration and Manufacturing*, Maryland, 2018.
42. J.L. Marchesini, P.O. Jeannin, Y. Avenas, J. Delaine, C. Buttay, and R. Riva, "Implementation and Switching Behavior of a PCB-DBC IGBT Module Based on the Power Chip-on-Chip 3-D Concept," *IEEE Trans. on Industry Applications*, vol. 53, no. 1, pp. 362-370, 2017.
43. C. Chen, Y. Chen, Y. Li, Z. Huang, T. Liu, and Y. Kang, "An SiC-Based Half-Bridge Module With an Improved Hybrid Packaging Method for High Power Density Applications," *IEEE Trans. on Ind. Electronics*, vol. 64, no. 11, pp. 8980-8991, Jan./Feb. 2017.
44. H. N. Shah, Y. Xiao, T. P. Chow, R. J. Gutmann, E.R. Olson, S-H. Park, W-K. Lee, J.J. Connors, T.M. Jahns, R.D. Lorenz, "Power Electronics Modules for Inverter Applications using Flip-Chip on Flex-Circuit Technology," [\*IEEE Industry Applications Conference\*](#), Seattle, 2004.
45. Z. Gong, Q. Chen, X. Yang, B. Yuan, W. Feng, And Z. Wang, "Design of High Power Density DC-DC Converter Based on Embedded Passive Substrate," [\*IEEE Power Electronics Specialists Conference\*](#), Greece, 2008.
46. A. B. Jørgensen, S. Beczkowski, C. Uhrenfeldt, N. H. Petersen, S. Jørgensen, and S. Munk-Nielsen, "A Fast-Switching Integrated Full-Bridge Power Module Based on GaN eHEMT Devices," *IEEE Trans. on Power Electronics*, vol. 34, no. 3, pp. 2494-2504, Mar. 2019.
47. S. Zhao, X. Zhao, A. Dearien, Y. Wu, Y. Zhao, and H. A. Mantooth, "An intelligent versatile model-based trajectory optimized active gate driver for SiC devices," *IEEE J. on Emerging and Selected Topics in Power Electronics*, (Early access), June 2019.
48. S. Zhao, A. Dearien, Y. Wu, C. Farnell, A. Rashid, F. Luo, and H. A. Mantooth, "Adaptive multi-level active gate drivers for SiC power devices," *IEEE Trans. on Power Electronics*, vol. 35, no. 2, pp. 1882-1898, Feb. 2020.
49. T. White, S. Shetty, M. Ware, A. Mantooth, G. Salamo, "AlGaIn/GaN Micro-Hall Effect Devices for Simultaneous Current and Temperature Measurements From Line Currents," *IEEE Sensors Journal*, vol. 18, no. 7, pp. 2944 – 2951, April 2018.

## I.18 Design, Optimization, and Control of a 100 kW Electric Traction Motor Meeting or Exceeding DOE 2025 Targets (Illinois Institute of Technology)

### Ian P. Brown, Principal Investigator

Illinois Institute of Technology  
3301 S Dearborn Street  
Chicago, IL 60616  
E-mail: [ibrown1@iit.edu](mailto:ibrown1@iit.edu)

### Susan Rogers, DOE Technology Development Manager

U.S. Department of Energy  
E-mail: [susan.rogers@ee.doe.gov](mailto:susan.rogers@ee.doe.gov)

Start Date: April 4, 2019

End Date: September 30, 2019

Project Funding (FY19): \$300,000

DOE share: \$300,000

Non-DOE share: \$17,595

### Project Introduction

The Illinois Institute of Technology (IIT) is a member of the Department of Energy Electric Drives Technologies (EDT) Consortium. IIT's role in the consortium focuses on developing electric traction motors for electric vehicles with 8x the power density and half the cost of state-of-the-art traction motors.

### Objectives

The overall objective of the electric motor portion of the Electric Drives Technology consortium is to research, develop, and test electric motors for use in electric vehicle applications capable of the specifications in Table I.18.1. Reduced scale physical prototypes in future budget periods for testing developed technologies and full-scale design studies are planned at regular intervals to ensure progress towards the targets.

**Table I.18.1 EDT Consortium Electric Motor Targets**

Parameter	Target Value
Peak Power Rating (kW)	100
Power Density (kW/l)	≥50
Cost	≤3.3

### Approach

The volumetric power density of electric machines can be related to a number of key variables, many of which are fundamentally linked to material properties and limitations, ( $\eta$  = efficiency,  $B_g$  = airgap flux density,  $A$  = total electric loading), to the design/layout of the winding and magnetic circuit, ( $m$  = phases,  $K_e$  = EMF factor,  $K_i$  = current factor,  $K_p$  = electrical power waveform factor,  $\lambda_o^2$  = airgap to stator outer diameter ratio), and the fundamental output frequency of the exciting power electronics, ( $f$  = fundamental excitation frequency).

$$\text{Volumetric Power Density} = \frac{\text{Power}}{\frac{\pi}{4} D_o^2 L_t} \sim 2 \frac{m}{m_i} K_e K_i K_p \lambda_o^2 \eta B_g A \frac{f}{p} \sim K_{\text{machine design}} \eta \frac{f}{p} B_g A$$

To meet the electric traction motor power density and cost targets a number of approaches are being pursued simultaneously throughout the course of this project which address all of the major volumetric power density variables. Many of the approaches are synergistic and complementary with the approaches being taken by partner Electric Drive Technology Consortium member National Laboratories and universities.

- Multiphysics design for increased power density through maximum utilization of active materials.



- Improved dimensional or shape optimization techniques which simultaneously address electromagnetic, thermal, and structural design in a computationally efficient manner.
- Topological optimization techniques to distribute materials in an optimal manner without a geometric template subject to magnetic and structural objectives and constraints.
- Synthesis of electric machine windings and PM flux barriers with controlled space harmonics.
  - Develop windings and PM flux barrier optimization tools which eliminate or reduce unwanted space harmonics while maximizing the working winding factor. Ideally synthesize a feasible winding or flux barrier from a target harmonic spectrum.
- Develop high slot fill windings for increased current loadings or efficiency. Potential options that will be investigated include low proximity loss bar/hairpin windings, cast windings, and die compressed windings.
- Investigate aggressive cooling strategies and support the thermal management research of other National Laboratories and universities in the Electric Drives Technology Consortium.
  - Calibrate thermal models including oil spray cooling in prototype reduced scale motors.
  - Research high slot fill windings with through conductor cooling with the optimum tradeoff of copper area to heat extraction.
- Explore multiple motor topologies for increased power density.
  - Initial machine topologies targeted include high speed interior permanent magnet synchronous machines (IPMSMs) and a transverse flux machine using a low core loss material.
- Apply new technologies, concepts, materials, and learnings from the Illinois Institute of Technology research group and other Electric Drives Technology Consortium members in reduced scale electric traction motors.
  - Design, construct, and dynamometer test a reduced scale motor prototypes in budget period 2 and subsequent budget periods to calibrate progress towards motor targets.
  - Design studies of a 100 kW machine including electromagnetic and structural finite element simulations and lumped parameter thermal modeling to calibrate progress towards motor targets.

For this budget period, work on the first two approaches was completed.

To identify the gap between the project motor power density targets and state-of-the-art machine designs large scale optimization studies using realistic constraints and state of the art materials were completed. Modification and improvements to Professor Brown's in lab developed electric machine design optimization suite were made for improved modelling of IPMSMs. The highest performance electric traction motors in wide use commercially are interior permanent magnet synchronous machines with V-shaped magnet slots. This rotor topology was selected to identify the gap with the project motor targets. Two stator winding types were considered: 48 slot 8 pole bar/hairpin distributed winding and 12 slot 10 pole high slot fill fractional slot concentrated winding with Wye-Delta connection to reduce the space harmonics. Representative cross-sections of the machines are shown in Figure I.18.1. The target specifications and constraints for the optimizations are listed in Table I.18.2. The design studies utilized state of the art materials including high performance grade NdFeB magnets without heavy rare earths (Hitachi S49FSH) and M15-29 Ga and JFE 10JNEX900 6.5% silicon steel. The geometric optimization involved 16 dimensions including the machines aspect ratio. End turns length was accounted for in the machines' overall volume and loss calculations.

State of the art electric machine design procedures utilize a geometric template with dimensional variables coupled to an optimization algorithm. The geometric dimensions are varied to optimize the machines electromagnetic power conversion performance. The machines thermal and structural response is then checked to determine if the machine is within material property limits. Creation of the geometric template is time consuming and to avoid restricting the range of the dimensional variables and the design space, great care must be taken to avoid unfeasible geometries. Small features that have an impact on torque ripple, core losses, etc. are often not included in the geometric template.



(a) 48 Slot 8 Pole Bar/Hairpin Winding IPMSM

(b) 12 Slot 10 Pole Fractional Slot Concentrated Winding IPMSM

Figure I.18.1 Representative interior permanent magnet synchronous machines from optimization Pareto front.

**Table I.18.2 Optimization Target Specifications and Constraints**

<b>Optimization Target Specifications</b>	
Shaft Output Power (kW)	100
Base Speed (RPM)	8000
Maximum Speed (RPM)	24,000
Envelope Power Density (kW/l)	50
<b>Optimization Constraints</b>	
Electromagnet Torque (Nm)	>120
Torque Ripple (%)	< 5
Envelope Volume Including End Turns (l)	2
Total Loss	< 5.26 kW

An alternative approach is to use a topology optimization technique where material is optimally distributed in a free-form manner. Topology optimization was originally developed in mechanical engineering domains. There have been limited investigations of its use for the magnetic design of electrical machines. Magnetic only topology optimization results in designs which are unfeasible or uneconomic to build. As part of this project we have developed a combined magneto-structural topology optimization approach which helps to ensure that designs are structurally sound. One of the primary ways that electric machines can gain power density is by increasing the rotor's rotational speed as power is proportional to the product of torque and speed. However, there is an inherent trade-off between speed and torque production because of second order effects. For instance, in interior permanent magnet synchronous machines as the rotor speeds increase, the thickness of the electrical steel bridges used to support the permanent magnet must increase in size to resist centripetal forces. As the thickness of the bridges increases, the leakage flux from the permanent magnet increases, reducing the airgap flux density and magnetic torque. The combined magneto-structural topology optimization technique is targeted at determining the optimal material distribution to satisfy the tradeoff between magnetic and structural objectives and constraints.

For high power density machines, all aspects of the machine design must be considered. For the stator winding, a high working harmonic winding factor,  $k_w$ , is needed to maximize torque production for a given current. The rotor must also be capable of producing a high airgap flux density,  $B_g$ . The space harmonic content of the magneto-motive force and flux density produced by the stator winding and rotor needs to be low for reduced torque ripple and core losses. A number of candidate stator windings for high power density prototypes have been identified, and a technique for the design of interior permanent magnet rotor flux barriers and magnets have been developed during this budget period.

## Results

### *Pareto Front Identification of Performance Gaps*

Multiple large-scale optimizations were performed with hairpin/bar wound distributed windings or high slot fill fractional slot concentrated windings in order to approach the target specifications, listed in Table I.18.2. The Pareto fronts resulting from these optimizations are shown in Figure I.18.2. Only the Pareto fronts of the 8,000 designs generated for each optimization are shown. Only two designs are capable of meeting the 120 Nm torque requirement at 8,000 RPM to achieve the power density target. If a lower base speed was specified the gap between the torque target and the Pareto fronts would even be larger. Also, note that the state-of-the-art 6.5% silicon steel while it does reduce losses in most cases can result in slightly lower power conversion performance.

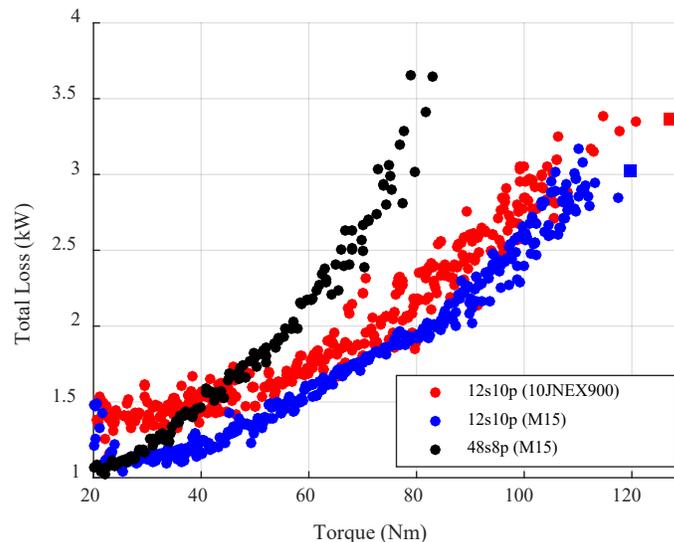


Figure I.18.2 Pareto fronts to identify target performance gaps using state of the art motor topologies and materials.

### *Magneto-Structural Topology Optimization of Synchronous Machine Rotors*

Magneto-structural topology optimization of synchronous reluctance (SynRel) and IPMSM rotors has been developed. The initial development was for SynRel rotors as they are the simplest case with only electrical steel or air in the design domain. The design of the flux barriers and guides in SynRel rotors has a large impact on the performance of the machine in terms of average torque, power factor, and torque ripple.

Magnetic only topology optimization of the SynRel rotor is first considered. The rotor design region is shown in Figure I.18.3(a). In each of the finite elements in the upper rotor mesh highlighted in blue, the density,  $\rho$ , of the electrical steel is allowed to vary between  $0 < \epsilon < \rho < 1$  where  $\epsilon$  is a very small number. The densities in the upper rotor half are mirrored to the lower rotor half to form a symmetric machine. The material properties in each element are made proportional to the density raised to an exponent to penalize the density and force the convergence of the density in each element to  $\epsilon$  or 1. For example, in a magnetic only topology optimization,

the nonlinear relative permeability in each element can be expressed as the following. Material properties are handled in a similar way for structural problems.

$$\mu_{r,k} = \left( \mu_{Fe,k}(B) - \mu_{air,k}(B) \right) \rho_{Fe,k}^p + \mu_{air,k}$$

Objective functions and constraints which express global machine performance criteria can be written. For the example magnetic only topology optimization, the following optimization problem is written to maximize the average torque subject to a constraint on torque ripple.

$$\begin{aligned} \text{minimize} \quad & f = -T_{avg} = -\frac{1}{N \sum_{\theta=0}^N T_{\theta}} \\ \text{s.t.} \quad & g = T_{ripple} = T_{max} - T_{min} \leq K_{ripple} T_{avg} \end{aligned}$$

The sensitivities of the objective function and constraints with respect to changes in the element densities,  $\rho$ , are computed using an adjoint variable method for computational efficiency. The optimization problem is solved using the Method of Moving Asymptotes (MMA) algorithm where sensitivities and updated densities are passed to and from the finite element model. An example magnetic only design of a SynRel rotor is shown in Figure I.18.3(b). The same overall procedure maybe used with a fixed PM in the design domain, Figure I.18.3(c). Both the magnetic only SynRel and PM topology optimization designed rotors are not manufacturable with iron pieces that are not structurally supported. Magneto-structural topology optimization is needed to simultaneously optimize for magnetic and structural optimization objectives and constraints.

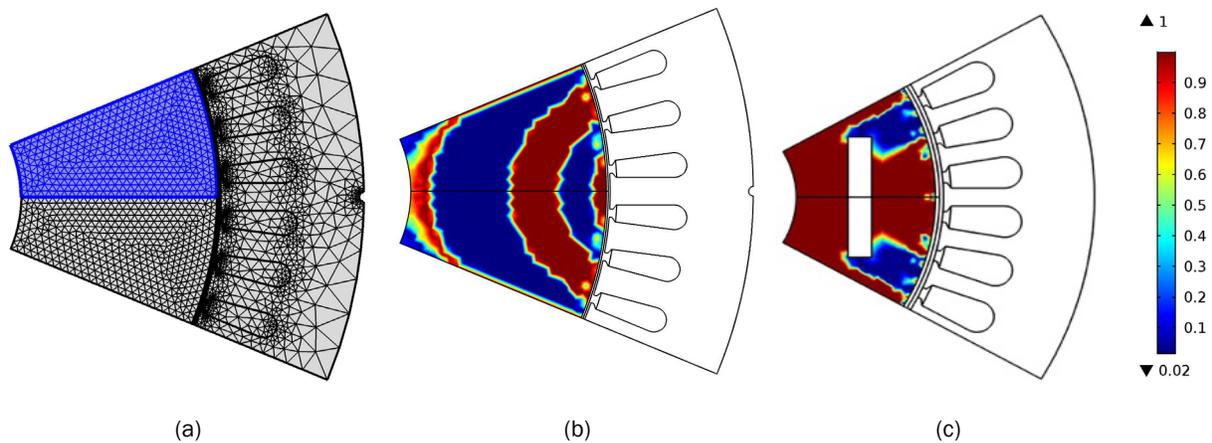


Figure I.18.3 Magnetic only topology optimization, (a) design domain, (b) synchronous reluctance rotor, (c) interior permanent magnet rotor with fixed permanent magnet.

The structural load considered in the technique developed is the design dependent centripetal force arising from the rotation of the rotor. Ideally, we would like to constrain the stress in each element below some fraction of the material yield stress. A stress constraint on each element requires a large number of sensitivity evaluations and depending on how the constraint is expressed, a discontinuous function. Instead, a global approximation of the maximum stress in the design domain is used. This is called P-norm aggregation

$$\sigma_{PN} = c \left( \sum_{n=0}^k \frac{1}{a} \sigma^P \right)^{\frac{1}{P}} \leq k_{sf} \sigma_{yeild}$$

where  $c$  is the normalization factor,  $a$  is the element area of the electrical steel, and  $P$  is the aggregation parameter. With only a stress constraint, the optimized rotor may still be over deformed in the radial direction. An additional compliance constraint or objective can be used to control the displacement of the rotor. The total compliance,  $C$ , is found by integrating the strain energy of each element,  $W_s$ , in the design domain,  $\Omega$ .

$$C = \int W_s ds \leq C_0$$

If structural objectives and constraints are simply used the same way as in the magnetic only topology optimization, an intermediate material issue will occur where the density in some of the elements does not fully converge to  $\varepsilon$  or 1. The intermediate material density issue is solved by switching to a globally convergent MMA optimization algorithm which is able to handle the non-monotonous nature of the compliance term and a thresholding mass filter where  $M_{Fe}$  is the actual mass of the electrical steel and  $\rho_c$  is the density threshold.

$$M = \begin{cases} M_{Fe}, & \rho > \rho_c \\ 0, & \rho \leq \rho_c \end{cases}$$

Many different magneto-structural optimization problems can be formulated. Two examples are presented below. The first formulation (I) has a single term in the objective function, average torque maximization. The second formulation finds the optimum tradeoff between average torque and compliance using adaptive weighting factors in the objective function.

Formulation I	Formulation II
minimize $f = -T_{avg} = -\frac{1}{N} \sum_{\theta=0}^N T_{\theta}$	minimize $f = -w_1 \frac{1}{N} \sum_{\theta=0}^N \frac{T_{\theta}}{T_0} + w_2 \frac{C}{C_0}$
s.t. $g_1 = T_{ripple} = T_{max} - T_{min} \leq k_{ripple} T_{avg}$	s.t. $g_1 = T_{ripple} = T_{max} - T_{min} \leq k_{ripple} T_{avg}$
$g_2 = \sigma_{PN} = \left( c \sum_{n=0}^k \frac{1}{a} \sigma^n \right) \leq k_{sf} \sigma_{yeild}$	$g_2 = \sigma_{PN} = \left( c \sum_{n=0}^k \frac{1}{a} \sigma^n \right) \leq k_{sf} \sigma_{yeild}$
$g_3 = C \leq C_0$	

Examples of SynRel rotors designed with Formulations I and II are shown in Figure I.18.4 for design speeds of 4,000 and 12,000 RPM. In all cases the torque ripple structural constraints are satisfied. It should be noted that at the higher design speed, the magnetic bridges thicken to hold the electrical steel flux guides in place.

The same magneto-structural topology optimization approach has been used for the design of an interior permanent magnet synchronous machine rotor with a fixed permanent magnet position and size, Figure I.18.5. Future work is planned to combine shape and topology optimization to allow the permanent magnet to change orientation and size in the rotor design domain while still allowing for topology optimization of the electrical steel.

### ***Stator Winding and Interior Permanent Magnet Rotor Flux Barrier Design***

To maximize the working harmonic and minimize space harmonics, a number of distributed and fractional slot concentrated windings have been identified to investigate for incorporation into machine prototypes. Two candidate distributed windings are a 12 slot 2 pole mixed layer winding and 12 slot 2 pole single layer dual three phase winding with 30 degree phase shift between phase groups. The pole number can be increased with a proportional scaling of the number of stator slots. A 12 slot 10 pole double layer fractional slot concentrated winding with 2 layers and 30 degree phase shift between subsets will also be investigated for prototyping.

For the high-power density specification of the Project, a low rotor created airgap flux density,  $B_g$ , is most likely to result in very high stator current density and pose a serious thermal management challenge. To make the motor operate at an acceptable stator current density, as a first consideration the rotor has to produce a high airgap flux density  $B_g$  at no load. Besides the use of high-performance PM material, a “flux concentration” structure is also necessary. Some IPM rotors designed for EV/HEV applications produce  $B_g \approx 0.7$  T with neodymium iron boron (NdFeB) magnets of remanence,  $B_r \approx 1.2$  T. With similar PM material, for the Project, it is expected to achieve airgap flux densities,  $B_g$  up to 1.3 T, or slightly higher with an unchanged or reduced remanence.

As a second consideration, the harmonic content of both stator and rotor must be designed in a coordinated manner to minimize harmonic interactions between the rotor and stator. The benefits include reduced eddy current losses and torque ripple. Ideally, the harmonic orders of 5, 7, 11, 13, will not be simultaneously present

in the stator and rotor. The low harmonic content will help to reduce losses caused by MMF space harmonics. A third consideration is the maintenance of a working point for the PM material that is safe from demagnetization. This usually requires that the magnets not be too thin. From the cost perspective, however, the total volume of PM needs to be minimized, which usually results in thin magnets that have lower working points and are more vulnerable to demagnetization.

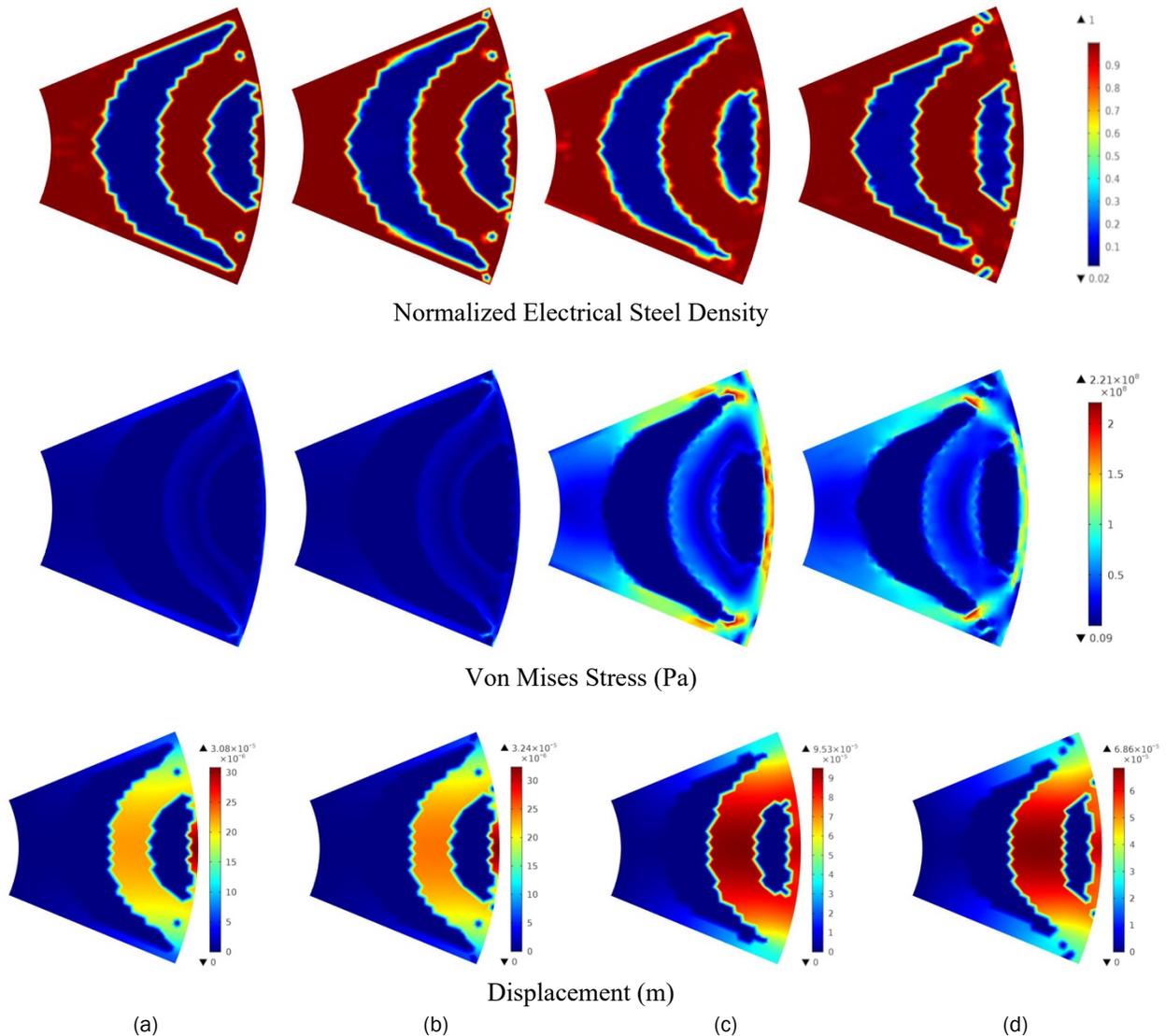


Figure I.18.4 Synchronous reluctance rotor magneto-structural topology optimization results for (a) formulation I 4,000 RPM, (b) formulation II 4,000 RPM, (c) formulation I 12,000 RPM, and (d) formulation II 12,000 RPM.

A design procedure for multi-layer IPM rotors has been developed which considers all three considerations. This design procedure allows for the synthesis of magnet and barrier dimensions to minimize the magnet volume. An example of a multi-layer IPM rotor optimization is shown in Figure I.18.6. Work is continuing to make finer adjustments to the desired harmonic content and account for the effects of stator slotting and magnetic saturation.

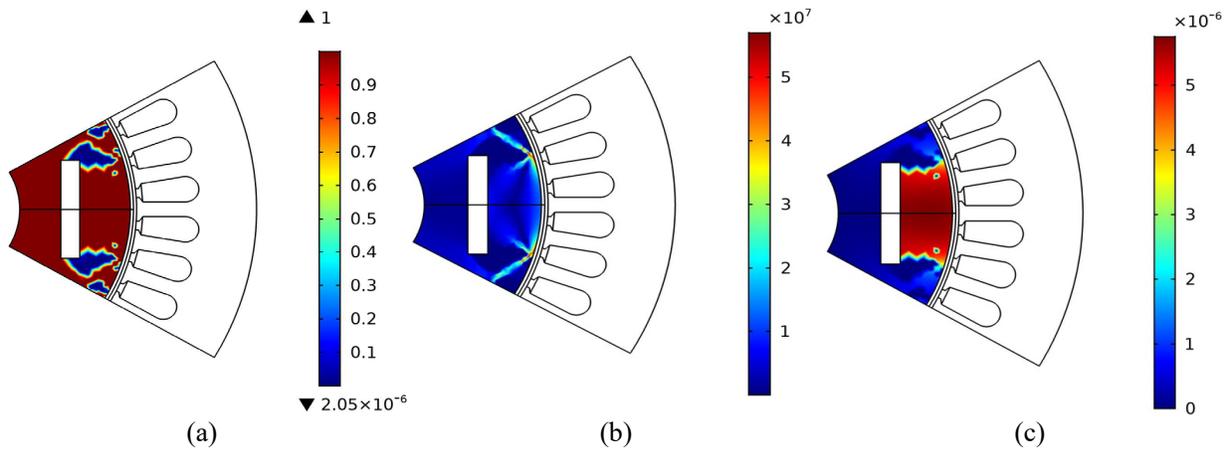


Figure I.18.5 Interior permanent magnet synchronous machine rotor magneto-structural topology optimization with fixed position and size permanent magnet, (a) normalized electrical steel density, (b) Von Mises stress, (c) displacement.

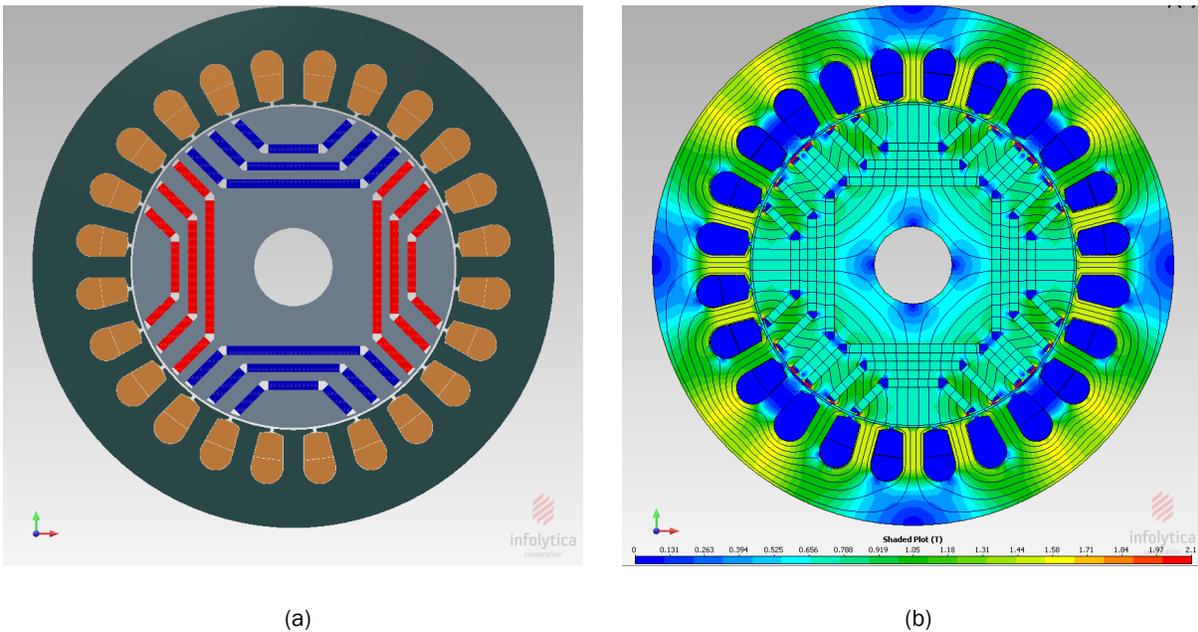


Figure I.18.6 Multi-layer IPM rotor verification of the proposed design approach, (a) cross-section of barriers and magnets, (b) flux density distribution at no-load.

### Conclusions

Two new design techniques have been developed to design high performance interior permanent magnet synchronous machine rotors. The first based on magneto-structural topology optimization optimally distributes electrical steel in the rotor design domain without a geometric template. The second technique adjust the size of flux barriers and permanent magnets to control the rotors no-load airgap flux density, magneto-motive force spectrum, and magnet working point. Stator windings with low harmonic content and high fundamental winding factor have been identified to pair with the rotor designs. The new design techniques greatly aid the design of electric traction motors which meet Dept. of Energy EDT Consortium targets.

## I.19 Cost Competitive, High-Performance, Highly Reliable (CPR) Power Devices on SiC (SUNY Polytechnic Institute)

### Woongje Sung, Principal Investigator

Research Foundation for SUNY Polytechnic Institute  
257 Fuller Road  
Albany, NY 12203  
E-mail: [wsung@sunypoly.edu](mailto:wsung@sunypoly.edu)

### Susan Rogers, DOE Technology Development Manager

U.S. Department of Energy  
E-mail: [susan.rogers@ee.doe.gov](mailto:susan.rogers@ee.doe.gov)

Start Date: April 16, 2019

End Date: April 15, 2024

Project Funding (FY19): \$333,278

DOE share: \$300,000

Non-DOE share: \$33,278

### Project Introduction

The primary objective of this project is to ensure that the next-generation of wide-bandgap devices sufficiently meets performance, reliability, and price targets to achieve DoE system-level goals. In this project, superior 1200V SiC MOSFETs are developed when compared with Silicon counterparts (i.e., IGBT) in all aspects, such as cost, performance, and reliability. To accomplish this goal many different variations in device/process design will be pursued, and the proposed 1200V SiC MOSFETs will be fabricated at a 6-inch, production-grade cleanroom facility.

### Objectives

- Cost competitive (\$4.96/die)
- High-performance ( $BV=1700$  V,  $R_{on,sp}=3.5$  m $\Omega$ -cm<sup>2</sup>, and  $V_{th}=2$  V)
- High reliability (SCSOA=8  $\mu$ s, HTRB=1620 V, TDDB=15 C/cm<sup>2</sup>, and avalanche energy=10 J/cm<sup>2</sup>)

### Approach

#### Cost

A dramatic reduction in chip price will be achieved by conducting ion implantations at room temperature (RT). Process flow will be significantly simplified by RT implants. Appropriate analyses due to RT implants will be conducted. An innovative approach for the gate oxide formation will further reduce the chip size and thus chip price. Unipolar diode integration within the MOSFET structure will be demonstrated.

#### Performance

Cell optimization will be carried out using Sentaurus TCAD 2-D simulation, such as reducing cell pitch and optimization of JFET region. Various edge termination structures such as FFRs, RA-JTE, and Hybrid-JTE will be designed. Process split, such as gate oxide using ALD, self-alignment channel, and JFET implant, will be conducted.

#### Reliability

Short-circuit and avalanche characteristics will be evaluated by mixed-mode device simulations in Sentaurus TCAD. Process split such as p-well implant and thin gate oxide will be carried out.



**Results**

**Device design – MOSFET cell optimization**

Figure I.19.1 shows the proposed 1.2kV SiC MOSFET structure. Drift layer was designed to be  $8 \times 10^{15} \text{ cm}^{-3}$  doped and  $10 \mu\text{m}$  thick to achieve approximately 1.7kV breakdown with a parallel-plane PN junction. On-resistance can be reduced through reduced cell pitch, higher channel mobility, and optimization of JFET region. The cell pitch was largely reduced by putting P+ source in orthogonal direction, intermittently. An accumulation channel was designed for higher channel mobility. For lower  $R_{on}$  and reduced electric field in the gate oxide, JFET width and doping concentration were optimized using Sentaurus TCAD 2-D device simulation [1]. Figure I.19.2 shows specific on-resistance and electric field as a function of JFET doping concentration. When considering both of them, JFET doping concentration of  $3 \times 10^{16} \text{ cm}^{-3}$  was determined as an optimum doping concentration. In the same way, half JFET width was optimized in Figure I.19.3. From these results, JFET width of  $0.8 \mu\text{m}$  became the nominal design value in our fabrication for the 1<sup>st</sup> lot.

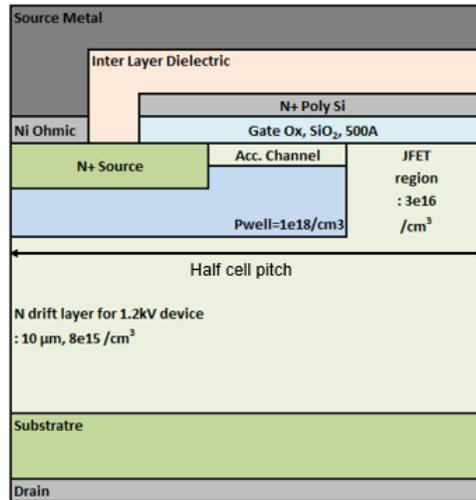


Figure I.19.1 Cross-sectional view of proposed 1.2kV 4H-SiC MOSFETs.

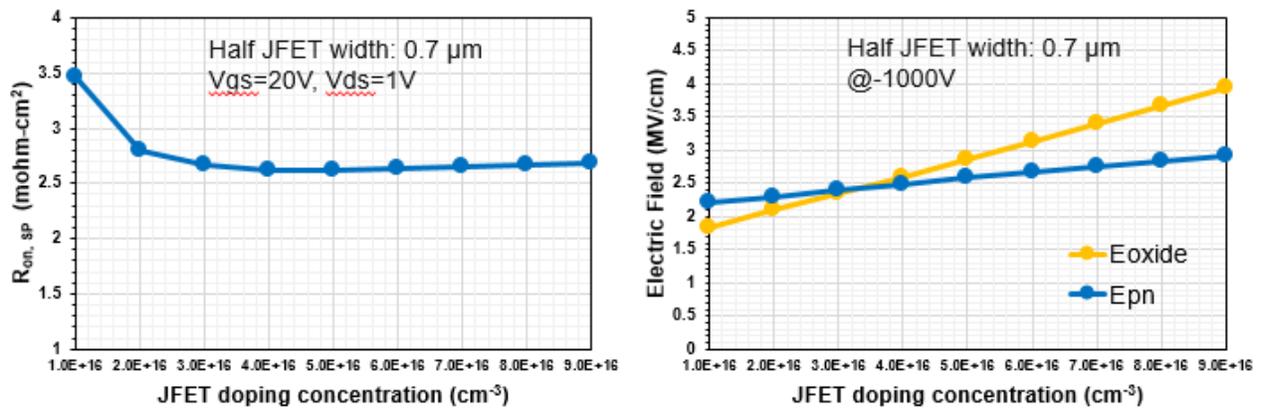


Figure I.19.2 Optimization of the JFET doping concentration to minimize the on-resistance and electric field in gate oxide and PN junction.

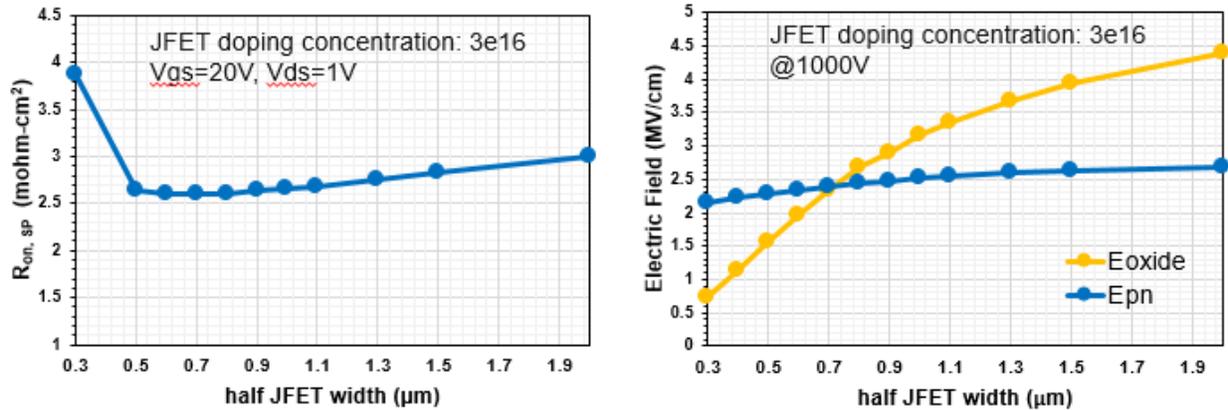


Figure I.19.3 Optimization of the JFET width to minimize the on-resistance and electric field in gate oxide and PN junction.

**Mask generation for 1<sup>st</sup> lot**

The mask for the 1<sup>st</sup> lot, shown in Figure I.19.4, included 42 different devices, which included PiN diodes, JBS diodes, MOSFETs, and JBSFETs. Reduced cell pitch and channel length was designed to decrease on-resistance of MOSFETs and JBSFETs. For improving MOSFET reliability, especially high temperature reverse bias (HTRB), a narrow JFET width was used. Hexagonal topology types, which have higher channel density for MOSFETs and JBSFETs, were added. SZ-JTE, RA-JTE, MFZ-JTE, Hybrid-JTE, and FFRs are also proposed to examine the effect of dV/dt in the edge termination. Moreover, the mask included large size, split gate, process split for Schottky opening, and the number of different P+ sources.

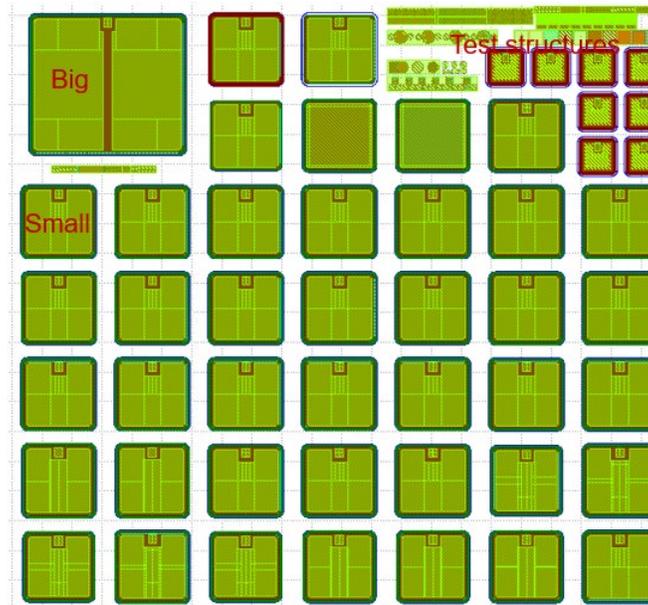


Figure I.19.4 Top view for Mask

**Fabrication for 1<sup>st</sup> lot**

Table I.19.1 shows summary of process flow for 1<sup>st</sup> lot. There are 12 photolithography processes, including 5 implant processes. Activation anneal, oxidation, and RTA process will be applied during the fabrication process. Fabrication for 1<sup>st</sup> lot is in progress and currently is at JTE implant step, which is the final implant step. The scheduled date for completion of 1<sup>st</sup> lot fabrication is Jan. 13, 2020 and the process is on time shown in Figure I.19.4.

Table I.19.1 Summary of Process flow for 1<sup>st</sup> lot

Mask	Process steps	Description	Specifications	Comments
	Wafer	N-/N+ substrate		6ea per run
1	Alignment Mark	SiC Etch	~0.5um	
2	JFET implant P-well implant	Oxide dep. (USG)	Oxide thickness 1.5um	Oxide Thickness depends on the implant schedule
3		Photo, Oxide etch		
		N or Al implant, HT		
4,5,6	N+, P+, JTE implant process	N, Al imp. For N+, P+&JTE	Similar to JFET or P-well process	standard
	Activation Anneal			>1650C, 10min, Ar, Capping process
	Sacrificial Oxidation	Oxidation/Removal	20nm	1175C, 20nm/BOE
	Gate Oxide, N <sub>2</sub> O anneal	Oxidation	50nm	50nm, <b>Process split</b>
7	Gate Poly dep., Photo, Etch	Std Process	Poly, 5000A	Poly Etch, stop at Gate oxide
8	Oxide dep., Photo, Etch	Std process	Oxide ~0.5um	USG
	Ohmic metal	Ohmic, Anneal		Ni, 100nm, RTP:1000C, 2min
9	Schottky opening	Pattern, Etch		
10	Poly Contact open	Std process	Oxide ~0.5um	
11	Top Metal, B/S Metal	Std process	4um	Std Metal process
12	Passivation	Std process	Nitride, Polyimide	Pad open

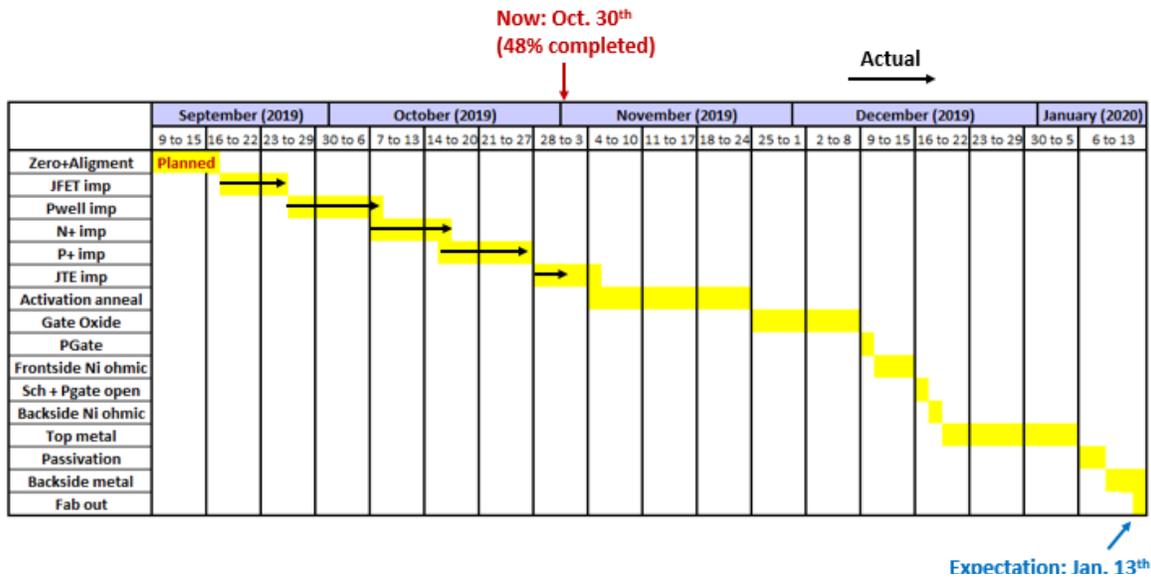


Figure I.19.5 1<sup>st</sup> lot fabrication status

**Simulation models**

One of the main goals is improving reliability of devices. In order to improve reliability, device simulation is required. In particular, mixed-mode simulation with thermode is needed to predict the electrical characteristics of the device in high-temperatures and look into vulnerable regions. For exact simulation results, simulation models are required to reflect the actual material properties that are known for 4H-SiC. Therefore, simulation results are aimed at matching corresponding experimental results.

Table I.19.2 shows summary of simulation models. Heat capacity, thermal conductivity, bulk mobility, channel mobility, channel mobility degradation, and SRH lifetime were developed. In order to obtain similar threshold voltage characteristic captured from experimental measurements, interface traps were added between 4H-SiC and SiO<sub>2</sub> within the simulation models. Furthermore, Fowler-Nordheim model is applied to investigate gate failure.

**Table I.19.2 Summary of Simulation Models**

	Parameter model	Values	Reference
Heat capacity	$C_V = 4.10 \times 10^{-9}T^3 - 1.22 \times 10^{-5}T^2 + 1.29 \times 10^{-2}T - 0.685$		[2]
Thermal conductivity	$K = (0.00105 \cdot T - 0.03)^{-1}$		[3]
Bulk electron mobility	$\mu_{Bulk}(SiC) = \frac{\mu_{max}(T/300)^{-\alpha}}{1 + [(N_D + N_A)/N_{ref}]^\gamma}$	$\alpha=2.8$ $\mu_{max}=950$ $N_{ref}=1.94e17$ $\text{Gamma}=0.61$	[4]
Bulk hole mobility	$\mu_{Bulk}(SiC) = \frac{\mu_{max}(T/300)^{-\alpha}}{1 + [(N_D + N_A)/N_{ref}]^\gamma}$	$\alpha=2.8$ $\mu_{max}=124$ $N_{ref}=1.76e17$ $\text{Gamma}=0.34$	[4]
Channel electron mobility	$\mu_{ch}(SiC) = \frac{\mu_{max}(T/300)^{-\alpha}}{1 + [(N_D + N_A)/N_{ref}]^\gamma}$	$\alpha=-0.2$ $\mu_{max}=28.5$ $N_{ref}=1.94e17$ $\text{Gamma}=0.61$	[5]
Channel mobility degradation	$\mu_{ph,3D} = \mu_{max} \left( \frac{T}{300K} \right)^{-\theta}$	$\mu_{max}=950$ $\theta=3.2$	[5]
SRH lifetime	$\tau_{n,p} = \frac{\tau_{max}(T/300)^\beta}{1 + [(N_D + N_A)/N_{ref}]^\gamma}$	$\beta=1.72$ $N_{ref}=3e17$ $\text{Gamma}=0.3$	[4,5]

## Conclusions

- 1.2kV SiC MOSFET with reduced cell pitch and accumulation channel was designed to improve on-resistance.
- JFET regions in SiC MOSFET were optimized by using Sentaurus TCAD 2-D simulation for lower on-resistance and reduced electric field in gate oxide.
- Mask for 1<sup>st</sup> lot was generated. Mask included many different types of structure, such as reduced cell pitch, hexagonal topology types, and process split to improve yield, performance, and reliability.
- Process flow of 1.2kV MOSFET contains 5 implants, Activation anneal, Oxidation, Gate poly, Ohmic, Metal, and Passivation. Fabrication for 1<sup>st</sup> lot is in last implantation step.
- Thermal simulation models were optimized to obtain exact simulation results. Heat capacity, thermal conductivity, bulk mobility, channel mobility, and SRH lifetime were developed. In addition, interface trap model for V<sub>th</sub> and FN tunneling model were also included in the simulation.

**References**

1. Woongje Sung, Kijeong Han, B. J. Baliga, “Optimization of the JFET region of 1.2kV SiC MOSFETs for improved high frequency figure of merit (HF-FOM),” 2017 IEEE 5th Workshop on Wide Bandgap Power Devices and Applications (WiPDA)
  2. L. Hitova,<sup>a</sup> R. Yakimova,<sup>b,z</sup> E. P. Trifonova,<sup>c</sup> A. Lenchev,<sup>d</sup> and E. Janzenb, “Heat Capacity of 4H-SiC Determined by Differential Scanning Calorimetry”, Journal of The Electrochemical Society, 147 (9) 3546-3547 (2000)
  3. Lance L. Snead, Takashi Nozawa, Yutai Katoh, Thak-Sang Byun, Sosuke Kondo, David A. Petti, “Handbook of SiC properties for fuel performance modeling,” Journal of Nuclear Materials 371 (2007) 329–377
  4. Woongje Sung, “Design and Fabrication of 4H-SiC High Voltage Devices”, Diss. North Carolina State University, 2012
  5. Synopsys Inc., Sentaurus<sup>TM</sup> Device User Guide, ver. K-2015.06, June 2015
- 50.

**Acknowledgements**

Duy-son Nguyen, Igal Deckman, and Jin-ho Seo at Analog Devices (ADI) have been contributing to the fabrication of SiC MOSFETs in this project.

## I.20 Cost Competitive, High-Performance, Highly Reliable (CPR) Power Devices on GaN (SUNY Polytechnic Institute)

### Shadi Shahedipour-Sandvik, Principal Investigator

SUNY Polytechnic Institute  
257 Fuller Road  
Albany, NY 12203  
E-mail: [sshahedipour-sandvik@sunypoly.edu](mailto:sshahedipour-sandvik@sunypoly.edu)

### Susan Rogers, DOE Technology Development Manager

U.S. Department of Energy  
E-mail: [susan.rogers@ee.doe.gov](mailto:susan.rogers@ee.doe.gov)

Start Date: October 1, 2018	End Date: September 30, 2019	
Project Funding (FY19): \$150,000	DOE share: \$150,000	Non-DOE share: \$0

### Project Introduction

The primary objective of this project is to demonstrate highly reliable wide bandgap AlGaIn/GaN HEMT power devices. In this project, we will demonstrate AlGaIn/GaN HEMT power devices with superior performance and reliability. To accomplish this goal, growth conditions and processing will be optimized for HEMT devices on foreign substrates as well as on bulk GaN to reduce the effect of defects in the bulk and at interfaces. Additionally, we investigate the processing of gate dielectric materials to improve the performance and reliability of HEMT devices.

### Objectives

- AlGaIn/GaN growth on foreign substrates (sapphire, Si)
- AlGaIn/GaN growth on GaN substrate
- Fabrication and characterization of AlGaIn/GaN HEMT devices
- Investigation of gate dielectrics and their impact on device reliability

### Approach

#### *AlGaIn/GaN Growth on Foreign Substrates*

Growth of GaN and AlGaIn is often done on foreign substrates such as sapphire, Si, or SiC due to the high cost of bulk GaN substrates. While use of these foreign substrates can reduce cost, epitaxial growth of (Al)GaN requires buffer layers to overcome the lattice mismatch with the substrate. Table I.20.1 shows a comparison of common substrates for GaN growth. Growth on Si presents additional difficulty because the lattice constant of the (111) Si face is 17 % larger than the GaN, and the large mismatch between the coefficients of thermal expansion (CTE) of Si and GaN causes excessive tensile stress in the GaN layer upon cooldown which results in increased dislocation density and higher probability of cracking [1]. One way to overcome the large lattice mismatch between GaN and Si is through the use of a compliant AlN buffer layer to separate the GaN from the Si. The lattice constant of GaN is 3.189 Å and AlN is 3.112 Å. To bridge the lattice mismatch between AlN and GaN, Al<sub>x</sub>Ga<sub>1-x</sub>N inter-layers can be grown with Al fractions ranging from 0.0 to 1.0. The lattice constant follows a linear trend between the two values of GaN and AlN, according to Vegard's Law. As the lattice constant of GaN is greater than that of AlN, Al<sub>x</sub>Ga<sub>1-x</sub>N will have a larger lattice constant than AlN and thus will grow under compression on an AlN buffer.

**Table I.20.1 A Comparison of the Most Commonly Used Substrates for GaN Epitaxy [4]**

Substrate Property	Si (111)	Al <sub>2</sub> O <sub>3</sub> (0001)	6H-SiC	GaN (0001)
Lattice Constant (Å)	3.846	4.758	3.081	3.189
Lattice Mismatch (%)	17	13	3.5	-
Thermal Expansion (10 <sup>-6</sup> K <sup>-1</sup> )	2.6	7.3	4.5	5.6
Thermal Mismatch (%)	116	-23	24	1.3
Thermal Conductivity (W cm <sup>-1</sup> K <sup>-1</sup> )	1.5	0.5	4.5	1.3
Relative Cost	Low	Medium	Very High	Extremely High

Using this technique, an initial high Al% Al<sub>x</sub>Ga<sub>1-x</sub>N layer is grown on AlN followed by Al<sub>x</sub>Ga<sub>1-x</sub>N layer with a lower Al% than the one below it. Multiple layers of AlGa<sub>x</sub>N are grown, with a decreasing Al% ultimately ending with a GaN layer. Because each layer grows under compression the total thickness should have enough compressive stress to counteract the thermal stress created upon cooling. This method has been extensively used by multiple researchers including Shahedipour-Sandvik group. Using our k-Space ICE in situ stress monitoring system, we are able to monitor the stress during growth and precisely control the thickness of each stress mitigation layer for maximum benefit [2].

#### ***AlGa<sub>x</sub>N/GaN Growth on GaN Substrate***

Because there is no lattice or thermal mismatch between substrate and epitaxy during growth on a native substrate, GaN can be grown directly on the bulk substrate. Before purchasing and using the more expensive semi-insulating GaN substrates, growth conditions were determined on n-type HVPE GaN. These growth conditions will be applied to the growth of full AlGa<sub>x</sub>N/GaN device structure on bulk GaN, and once the quality of the growth is confirmed, we will proceed with growth and fabrication of HEMT devices on semi-insulating GaN.

#### ***Investigation of Gate Dielectrics and their Impact on HEMT Reliability***

One issue with conventional Schottky-gated HEMT devices is high gate leakage current, particularly in forward biasing. Reduction of gate leakage has been achieved by adding a dielectric layer between the gate metal and the semiconductor to create a metal-insulator-semiconductor HEMT (MISHEMT) [3]. However, device reliability issues associated with the dielectric, namely, threshold voltage (V<sub>T</sub>) instability, have yet to be fully resolved [4]–[7]. The V<sub>T</sub> instability in these devices is due to the high density of interface states (D<sub>it</sub>) that act as electron traps with a wide distribution of time constants [8]. Reduction of this D<sub>it</sub> is the subject of ongoing research and is essential for the commercialization of MIS- (Al)Ga<sub>x</sub>N devices.

The ideal dielectric would have a high dielectric constant as well as a bandgap much greater than that of GaN (3.4 eV) with large valence and conduction band offsets in order to prevent leakage through the gate [9]. Al<sub>2</sub>O<sub>3</sub> has both a large band offsets relative to GaN, and a high dielectric constant (~9 for amorphous material), making Al<sub>2</sub>O<sub>3</sub> an attractive choice for GaN-based devices [10].

To study the effects of post-deposition processing on Al<sub>2</sub>O<sub>3</sub>, GaN MIS capacitors were formed using 20 nm ALD Al<sub>2</sub>O<sub>3</sub> as the dielectric layer. Annealing of the Al<sub>2</sub>O<sub>3</sub> layer is studied, ranging in temperature from 350°C to 600°C for times ranging between 1 min and 20 min. The impact of the annealing condition on the density of charge traps at the interface of GaN and Al<sub>2</sub>O<sub>3</sub> is studied through capacitance-voltage (C-V) measurements. Further, we studied the impact of the annealing condition on the structure of the Al<sub>2</sub>O<sub>3</sub> and its interface with the underlying GaN.

## Results

### *AlGaIn/GaN Growth on Foreign Substrates*

Crack-free AlGaIn/GaN growth was achieved on sapphire and Si substrates. The surface roughness of AlGaIn/GaN on sapphire was similar to that of AlGaIn/GaN on Si, though the atomic step edges are more clearly visible on sapphire. Figure I.20.1 shows AFM scans of AlGaIn/GaN grown on sapphire and Si. For growth on Si, Al<sub>x</sub>Ga<sub>1-x</sub>N stress mitigation layers were employed and stress was monitored in situ. Figure I.20.2 shows a plot of the in situ curvature measurement used to determine stress.

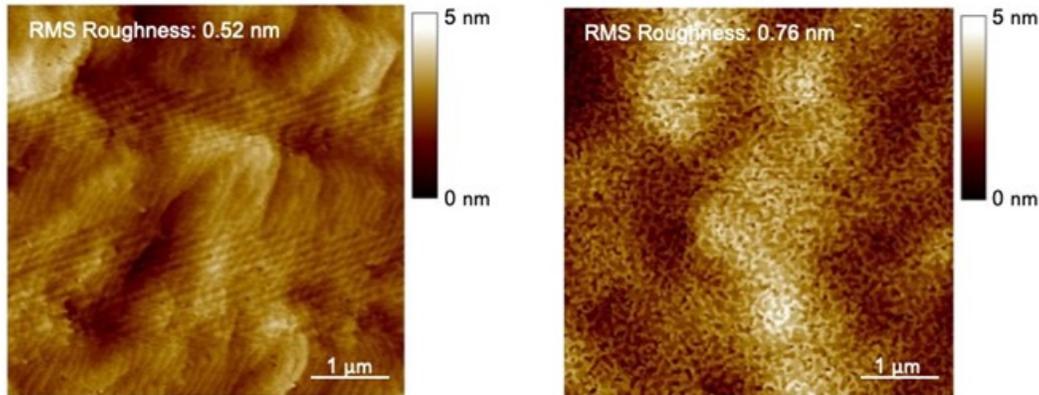


Figure I.20.1 AFM scans of (a) AlGaIn/GaN on sapphire and (b) AlGaIn/GaN on Si

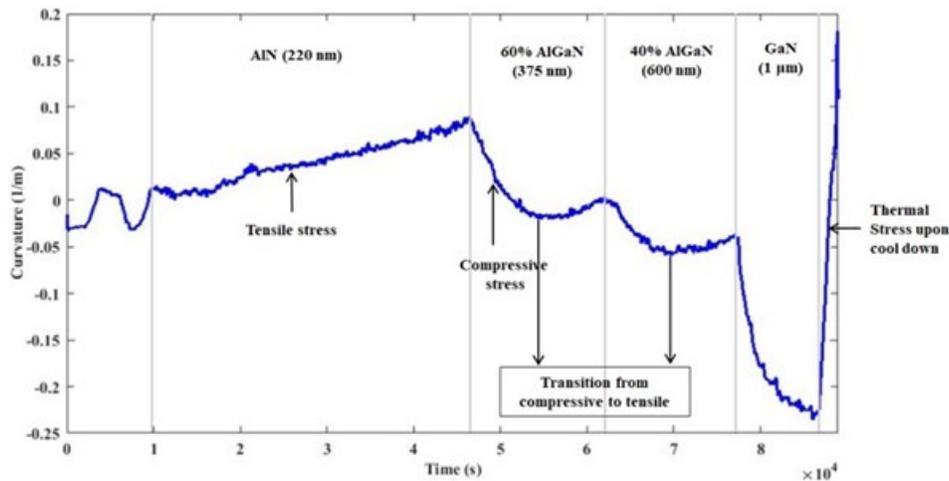


Figure I.20.2 in situ curvature measurement during growth

### *Fabrication and Characterization of HEMT on Foreign Substrate*

HEMT devices were fabricated on sapphire and Si substrates. The DC output characteristics are shown in Figure I.20.3 and Figure I.20.4.



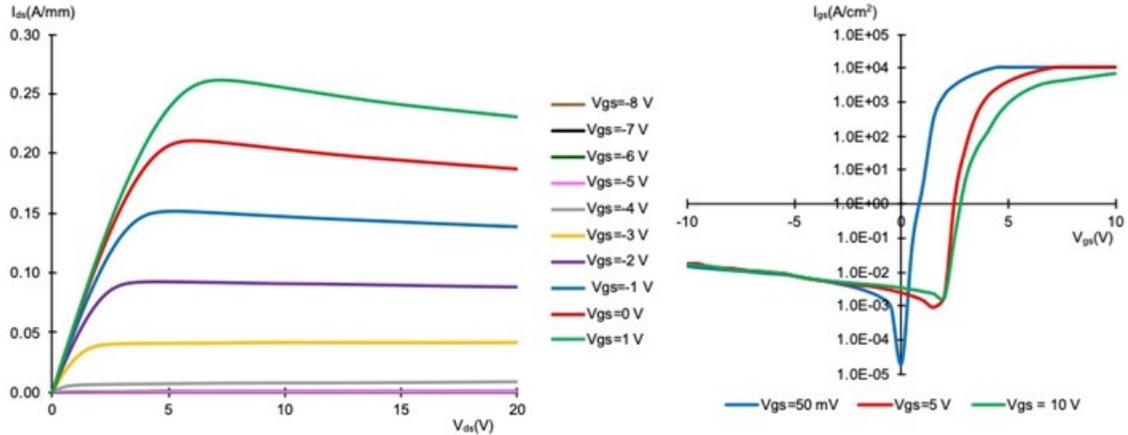


Figure I.20.3 Output and gate leakage characteristics for HEMT on sapphire. Device Dimensions:  $W_g=150 \mu\text{m}$ ;  $L_g=7 \mu\text{m}$ ;  $L_{gs}=4 \mu\text{m}$ ;  $L_{dg}=10 \mu\text{m}$ ;  $L_{ds}=21 \mu\text{m}$ .

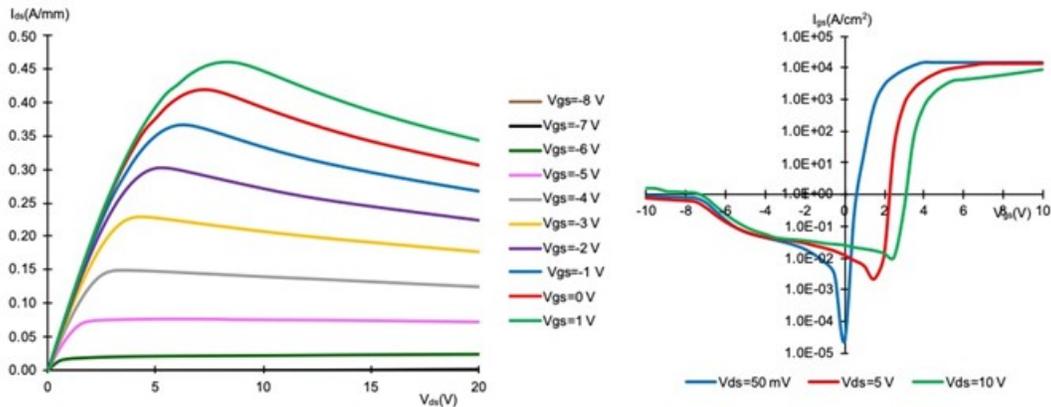


Figure I.20.4 Output and gate leakage characteristics for HEMT on sapphire. Device Dimensions:  $W_g=150 \mu\text{m}$ ;  $L_g=7 \mu\text{m}$ ;  $L_{gs}=4 \mu\text{m}$ ;  $L_{dg}=10 \mu\text{m}$ ;  $L_{ds}=21 \mu\text{m}$ .

Although the maximum output of the HEMT on sapphire is higher than the HEMT on Si, there is a smaller decrease in  $I_{dsat}$  at high drain voltages on the Si substrate due to superior heat dissipation.

**Investigation of Gate Dielectric and its impact on HEMT Reliability**

The frequency-dependent C-V and C-V hysteresis characteristics of  $\text{Al}_2\text{O}_3/\text{GaN}$  MIS capacitors are shown in Figure I.20.5 and Figure I.20.6.

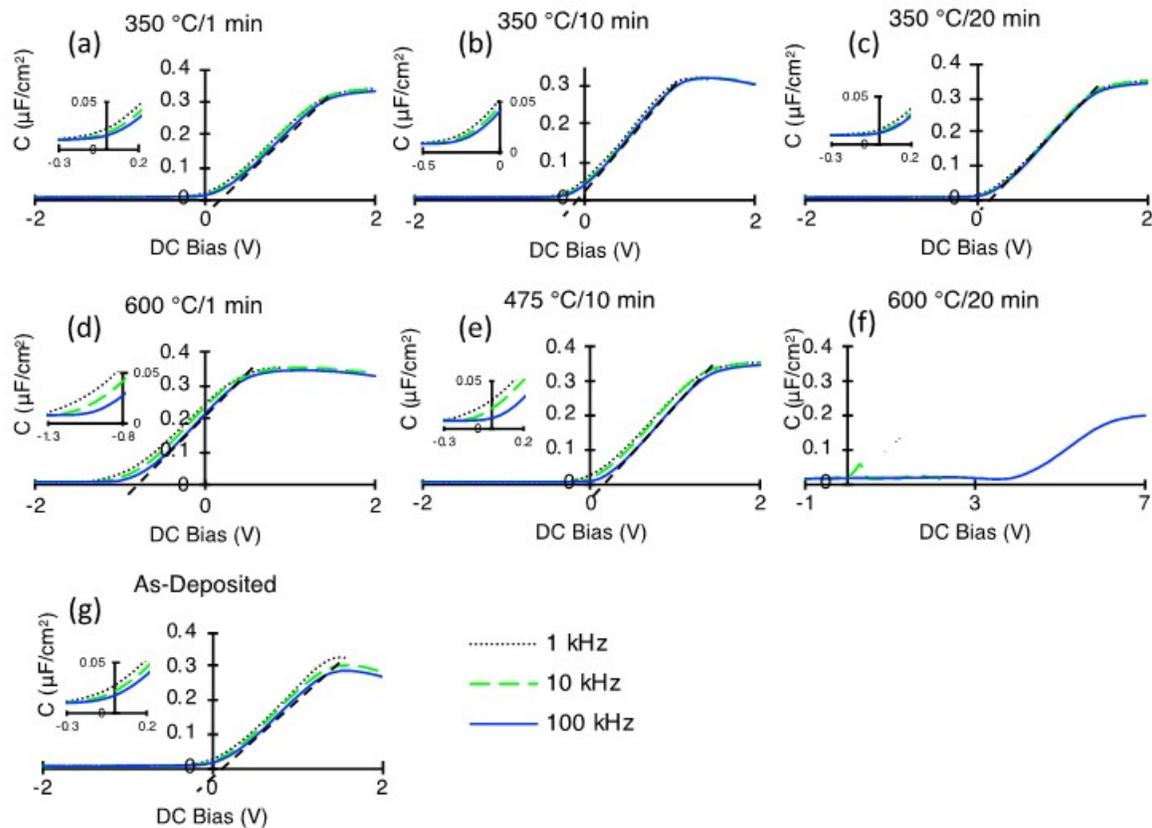


Figure I.20.5 Frequency-dependent C-V measurements for samples annealed at (a) 350 °C for 1 min, (b) 350 °C for 10 min, (c) 350 °C for 20 min, (d) 600 °C for 1 min, (e) 475 °C for 10 min, (f) 600 °C for 20 min, and (g) as-deposited. Threshold voltage is indicated by a dashed line. The insets show frequency dispersion close to threshold voltage. A large negative shift in threshold voltage is observed in the sample annealed at 600 °C for 1 min relative to the other curves, and the effect observed after annealing at 600 °C for 20 min indicate poor oxide and/or interface quality.

Annealing at low temperature (350 °C) decreased frequency dispersion; high temperature annealing increased frequency dispersion and shifted threshold voltage negative by  $\sim 0.8$  V. High temperature for extended time (600 °C 20 min) caused extensive degradation. Even brief periods of time at high temperature caused increase in frequency dispersion and large negative shift in  $V_T$ .

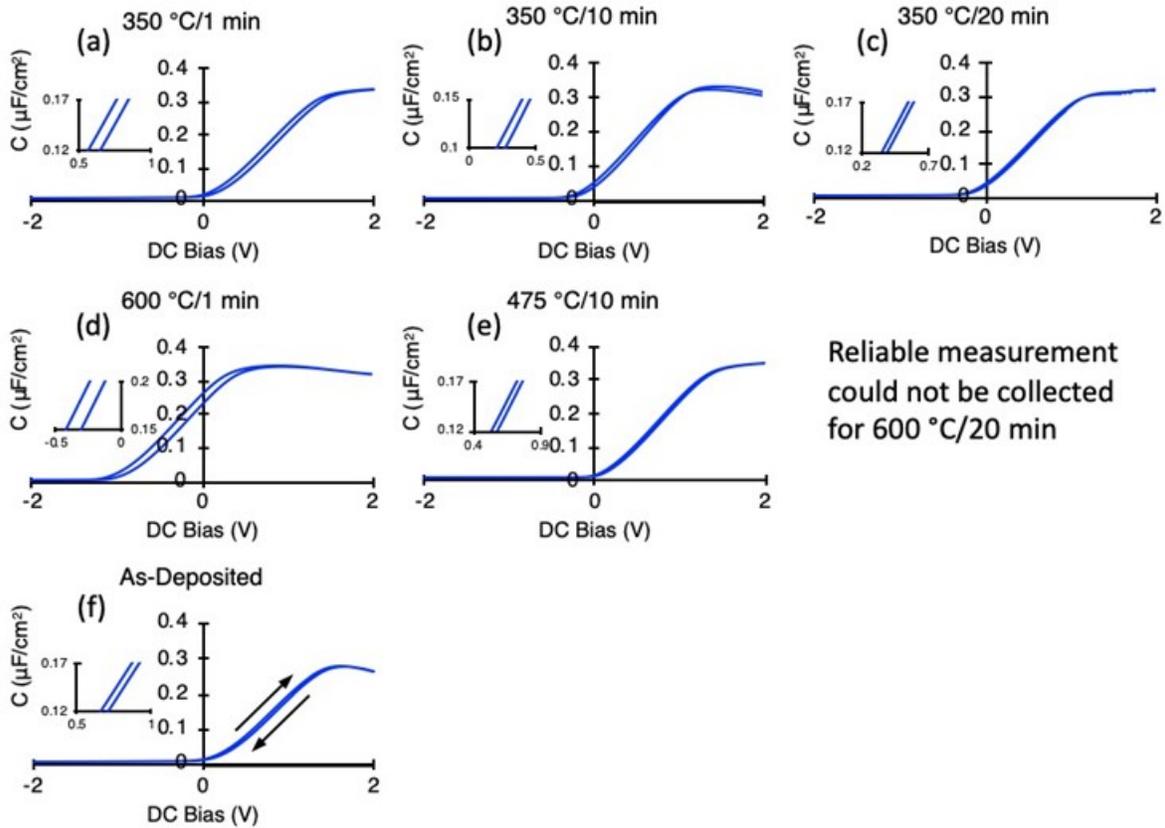


Figure I.20.6 C-V measurement data collected at 100 kHz AC signal. The arrows indicate the direction of the DC bias sweep. Insets show zoomed in area of hysteresis to show changes in  $\Delta V$  from sweep up to sweep down. The largest reduction in hysteresis is observed after annealing at 350 °C for 20 min.

Similar trend to frequency-dependent C-V: Annealing at low temperature decreased hysteresis; high temperature increased hysteresis. High temperature for extended time (600 °C 20 min) caused extensive degradation such that hysteresis measurements could not be collected.

To investigate whether there is a correlation between dielectric annealing conditions, electrical performance of the MIS devices and the structural characteristics of the MIS structures, Scanning Transmission Electron Microscopy/Energy Dispersive Spectroscopy (STEM/EDS) was performed. The results of STEM/EDS is shown in Figure I.20.7. As shown, O and Al did not diffuse into the GaN, but remained confined within the  $\text{Al}_2\text{O}_3$  layer. Further, the O and Al remained evenly distributed throughout the layer after the annealing. This is seen in the EDS maps of O and Al taken from the as-deposited, 350 °C/10 min, and 600 °C/20 min samples. These results show that annealing at various temperatures and times does not adversely impact the oxide or its interface with GaN.

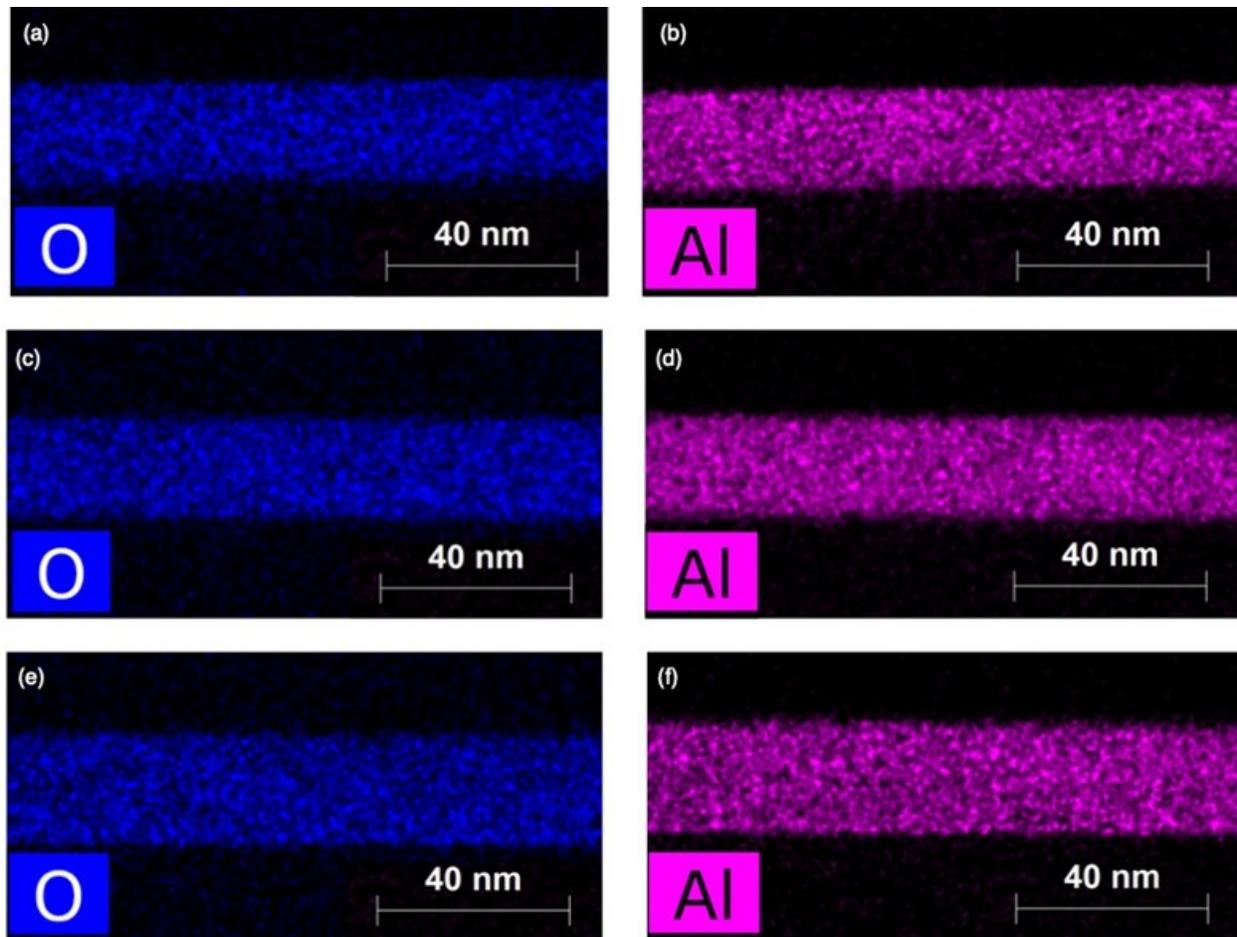


Figure I.20.7 EDS elemental maps showing the spatial distribution of (a) O in the as-deposited sample, (b) Al in the as-deposited sample, (c) O in the sample annealed at 350 °C for 10 min, (d) Al in the sample annealed at 350 °C for 10 min, (e) O in the sample annealed at 600 °C for 20 min, and (f) Al in the sample annealed at 600 °C for 20 min. No diffusion of Al or O is observed.

## Conclusions

Crack-free AlGaIn/GaN structures were successfully grown on foreign substrates, and HEMT devices were fabricated and characterized. Although DC output current density was higher for HEMT on sapphire, superior heat dissipation is observed in HEMT on Si.

High quality homoepitaxy of GaN on GaN was achieved. The growth conditions from these studies will be used for deposition of AlGaIn/GaN HEMT on (conducting and less expensive) HVPE GaN substrate before moving on to semi-insulating substrates to fabricate devices.

MIS capacitors were fabricated to characterize ALD deposited Al<sub>2</sub>O<sub>3</sub> after annealing under various conditions. It was found that while the electrical parameters of the devices vary widely with different annealing conditions, no large-scale structural changes occurred. The optimum conditions that results in lowest  $D_{it}$  were 350 °C for 20 min. These results suggest that longer annealing times at relatively low temperatures in forming gas are an effective method to passivate defect states at the Al<sub>2</sub>O<sub>3</sub>/GaN interface without generating new defects.

## Key Publications

1. B. McEwen, I. Mahaboob, E. Rocco, K. Hogan, V. Meyers, R. Green, F. Nouketcha, T. Murray, V. Kaushik, A. Lelis, F. Shahedipour-Sandvik, "Investigation of the Effects of Forming Gas Annealing

on Al<sub>2</sub>O<sub>3</sub>/GaN Interface,” submitted for publication to the Journal of Electronic Materials, October, 2019.

## References

1. D. Visalli, “Visalli, Domenica. Optimization of GaN-on-Si HEMTs for High Voltage Applications. Diss. KATHOLIEKE UNIVERSITEIT LEUVEN, 2011.,” no. December 2011, 2011.
2. B. J. Leathersich, “Rational Design and Development of Stress Engineering Techniques for III-Nitride Epitaxy on Si,” no. August, 2015.
3. G. Meneghesso *et al.*, “Reliability and parasitic issues in GaN-based power HEMTs: A review,” *Semicond. Sci. Technol.*, vol. 31, no. 9, 2016.
4. N. Szabó *et al.*, “High-k/GaN interface engineering toward AlGaN/GaN MIS-HEMT with improved V<sub>th</sub> stability,” *J. Vac. Sci. Technol. B, Nanotechnol. Microelectron. Mater. Process. Meas. Phenom.*, vol. 35, no. 1, p. 01A102, 2017.
5. P. Lagger, C. Ostermaier, G. Pobegen, and D. Pogany, “Towards Understanding the Origin of Threshold Voltage Instability of AlGaN / GaN MIS-HEMTs,” *2012 Int. Electron Devices Meet.*, p. 13.1.1-13.1.4, 2012.
6. A. Winzer *et al.*, “Analysis of threshold voltage instability in AlGaN / GaN MISHEMTs by forward gate voltage stress pulses,” 2016.
7. H. Huang, F. Li, Z. Sun, and Y. Cao, “Model Development for Threshold Voltage Stability Dependent on High Temperature Operations in Wide-Bandgap GaN-Based HEMT Power Devices,” *Micromachines*, vol. 9, no. 658, 2018.
8. C. Ostermaier, P. Lagger, M. Reiner, and D. Pogany, “Review of bias-temperature instabilities at the III-N/dielectric interface,” *Microelectron. Reliab.*, vol. 82, no. December 2017, pp. 62–83, 2018.
9. J. Robertson and B. Falabretti, “Band offsets of high semiconductors gate oxides on III-V,” *J. Appl. Phys.*, vol. 100, no. 014111, 2006.
10. Y. C. Chang *et al.*, “Atomic-layer-deposited Al<sub>2</sub>O<sub>3</sub> and HfO<sub>2</sub> on GaN: A comparative study on interfaces and electrical characteristics,” *Microelectron. Eng.*, vol. 88, no. 7, pp. 1207–1210, 2011

## Acknowledgements

B. McEwen, I. Mahaboob, E. Rocco, K. Hogan, V. Meyers, R. Green, F. Nouketcha, T. Murray, V. Kaushik, A. Lelis, and M. Yakimov substantially contributed to the work presented here. A large portion of this work was jointly supported by an award from Army Research Lab under Award#W911NF-18-2-0019. This work was performed in part at the Cornell NanoScale Facility, a member of the National Nanotechnology Coordinated Infrastructure (NNCI), which is supported by the National Science Foundation (Grant NNCI-1542081).

## I.21 Device- and System-Level Thermal Packaging for Electric-Drive Technologies (Georgia Institute of Technology)

### **Yogendra Joshi, Principal Investigator**

Georgia Institute of Technology  
771 Ferst Drive NW  
Atlanta, GA 30332  
E-mail: [yogendra.joshi@me.gatech.edu](mailto:yogendra.joshi@me.gatech.edu)

### **Samuel Graham, Co-Principal Investigator**

Georgia Institute of Technology  
771 Ferst Drive NW  
Atlanta, GA 30332  
E-mail: [sgraham@gatech.edu](mailto:sgraham@gatech.edu)

### **Satish Kumar Co-Principal Investigator**

Georgia Institute of Technology  
771 Ferst Drive NW  
Atlanta, GA 30332  
E-mail: [satish.kumar@me.gatech.edu](mailto:satish.kumar@me.gatech.edu)

### **Susan Rogers, DOE Technology Development Manager**

U.S. Department of Energy  
E-mail: [susan.rogers@ee.doe.gov](mailto:susan.rogers@ee.doe.gov)

Start Date: April 1, 2019	End Date: March 31, 2020	
Project Funding (FY19): \$300,000	DOE share: \$300,000	Non-DOE share: \$0

### **Project Introduction**

Wide-bandgap (WBG) devices can have higher breakdown voltages, higher efficiencies, thermal conductivities, operating temperatures, and switching speeds than silicon devices. However, using them as a drop-in solution for silicon-based power modules rather than designing specifically for WBG devices does not fully utilize their potential, particularly in regard to system-miniaturization and high-temperature operation. The objective of this project is to research, develop, and test Electric Drive Technology (EDT) for use in emerging WBG based vehicle applications capable of meeting the targets set by the Department of Energy Vehicle Technologies Office (VTO).

### **Objectives: Bonding Interfaces for Electronic Packages**

The overall objective of this project is to investigate the thermal management solutions for WBG EVs. Specifically, this work focuses on: (i) single-phase and boiling flows in additive manufactured metal foams for system-level cooling of WBG device-based traction inverters, (ii) a new transient liquid phase bonding technique to directly bond Aluminum foam with AlSiC to create a combined AlN – AlSiC – Al foam stack, and alternative bonding techniques to join Cu – invar, invar – invar, Cu – Cu to improve the durability of EDT packages, and (iii) Permanent magnet electric motor modeling for optimization of the thermal management system, and reduction of copper in the windings and rare earth materials.

### **Approach**

*Additively Manufactured (AM) Metal Foams for Thermal Management:* AM metal foams will be investigated as a cold plate based thermal management solution. A combination of experimentation and computational methodology will be used to compute the performance of the metal foam structures. For the experimental portion, a flow loop was constructed with appropriate instrumentation (i.e., pressure transducers, flowmeters,

and thermocouples) to measure relevant thermohydraulic information. Coupled computational fluid dynamics / heat transfer (CFD-HT) models will be used for additional investigation.

*Transient Liquid Phase (TLP) Bonding Technique:* This technique developed for bonding AlSiC with Al-foam involves the use of a Cu foil and an Al foil between the two layers. The AlSiC coupon is stacked with AlN and Al-foam for bonding. The TLP bonding technique of using Cu- Al hypoeutectic alloy for joining AlN with AlSiC has been described in detail by Pahinkar et al. (2018)<sup>1</sup>. For bonding the AlSiC and Al foam, a mass fraction of 45% of Cu is chosen for the interlayer between the two, because of abundance of Al in both, AlSiC and Al foam. The effectiveness of the bonding technique is further evaluated by varying the component materials bonded. Implementing the procedure detailed above, a series of Cu and Invar coupons are tested in different combinations: Cu-Invar, Invar-Invar and Cu-Cu. Invar, a nickel-iron alloy, is chosen for its relatively low coefficient of thermal expansion of about  $1.2 \times 10^{-6} \text{ K}^{-1}$  between 20°C and 100°C.

*Electric Motor Modeling:* The modeling has been performed with Motor-CAD software. Subsequently, we may use ANSYS Maxwell for more detailed modeling. Simulations of motor performance with respect to the cooling system and other thermal parameters have been performed. For different cooling systems, coolant properties, flow rates and insulation materials, and a specified temperature limit we will obtain the maximum torque, power, current density and efficiency of the motor with respect to the motor rotational speed. We will identify the cause of the performance threshold limit: electromagnetic saturation, and/or thermal resistances and heat transfer coefficients within the motor. Considering optimal thermal management of the motor, we will estimate to what extent the amount of copper and rare earth materials in magnets can be reduced, while keeping acceptable performance. Eventually, we will assess the cost reduction that can be achieved from these thermal performance improvements.

## Results

*AM Metal Foams for Thermal Management:* The recent work compared single-phase convection in AM versus traditional metal foams. A commercial, aluminum foam (5 pores per inch, 86.5% porosity) was purchased from ERG Aerospace, and the sample was analyzed using x-ray microcomputed tomography. A metal foam was based on the cell diameter and porosity of this sample. Reduced domain CFD-HT models were made for both samples. A flow loop with DI water was assembled for experimental testing, and the data was used for model validation. Then, flow behavior, the effect of thermal attachment method, and thermal performance of both models were further investigated.

The commercial aluminum foam was 5 PPI, 6101 T-6 aluminum alloy. A Zeiss Metrotom 800 was used for the x-ray scanning, with the resulting 2D images being imported to ImageJ. A series of ImageJ and BoneJ<sup>2</sup> commands were used for property (porosity, pore diameter, ligament diameter, ligament length, cell diameter, and specific surface area) analysis. The steps for characterization can be seen in Figure I.21.1. A rhombic dodecahedron unit cell was used for the additive manufactured foam, as it forms a 3D honeycomb structure, can be manufactured, and imitates the foaming process. Table I.21.1 shows the geometric properties obtained from said analysis, as well as the properties of the rhombic dodecahedron unit cell. This unit cell was generated by matching the cell size and porosity of the analyzed ERG sample.

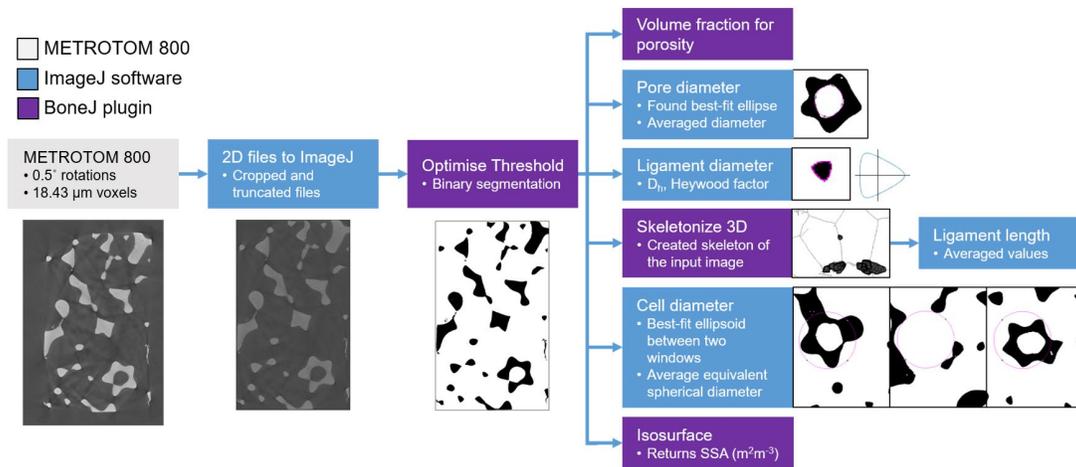


Figure I.21.1 Illustration of steps for commercial stochastic foam characterization

Table I.21.1 Comparison of Foam Properties for Analysis, Literature<sup>3</sup>, and AM Unit Cell

Parameter	Result	Literature	AM Unit Cell
PPI	5	5	5
Porosity	86.5%	92%	86.5%
Ligament diameter (mm)	0.508	0.505	0.548
Ligament length (mm)	1.94	1.72	2.014
Pore diameter (mm)	2.58	2.61	1.35
Cell diameter (mm)	4.65	4.60	4.65
Surface area (m <sup>2</sup> m <sup>-3</sup> )	571.1	510	927.35

Figure I.21.2 illustrates the experimental and reduced computational domains. The ERG foam sample was cut using electrical discharge machining to 100 mm x 40 mm x 9.3 mm, and then attached to an aluminum substrate with Omegabond 200 Epoxy Adhesive. The epoxy layer was 0.3 mm thick, and the adhesive’s thermal conductivity was given as 1.38 W/m-K. The AM file was outsourced to an external vendor, who used AlSi10Mg direct metal laser sintering to manufacture the AM foam. The base plate was cut and machined to the correct size and then heat treated to relieve stresses created during machining. The 3D geometries were used for pore-scale models, which will allow for increased understanding and visualization of intra-foam phenomena.

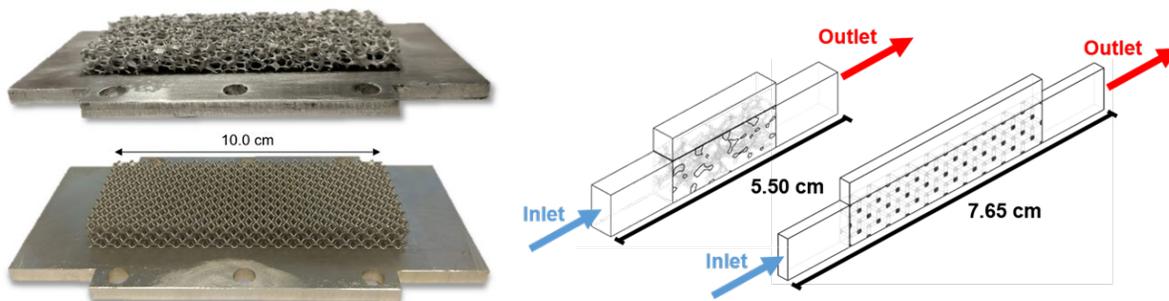


Figure I.21.2 Comparison of ERG foam versus AM foam (left) and reduced computational domains (right)



The computational models were validated using experimental data so that they could be further analyzed. The experimental and numerical total pressure drop and Nusselt number for varying Reynolds numbers were compared for the ERG and AM samples. The pressure drop results were fit to a second-order polynomial, which is common for laminar flow through a porous medium. A power law curve was used for curve-fitting the Nusselt number. Figure I.21.3 demonstrates that the computational model agrees with the experimental data over the ranges studied, ensuring model validity and allowing for further studies. The figure also shows a higher pressure drop for AM structure (~66%), likely due to the pores' rhombic as opposed to circular shape.

While the AM sample's thermal performance is shown to be superior, the reason behind the performance increase can be attributed to both structural differences in the foam as well as elimination of the thermal interface material between the foam and substrate. A 1D thermal resistance network was used to calculate the effective Nusselt number when adjusting the thermal conductivity of the interface material from  $k = 1.38 \text{ W/m-K}$  to 4.0, 40, and  $\infty \text{ W/m-K}$ . A simulation was run to show that using the thermal resistance network approach was valid. The values calculated using the semi-analytical resistance network were denoted with an (N) in Figure I.21.4. It can be seen that the effect of a small improvement in thermal conductivities significantly improves the thermal performance, but further increasing or eliminating the TIM layer causes only nominal improvements.

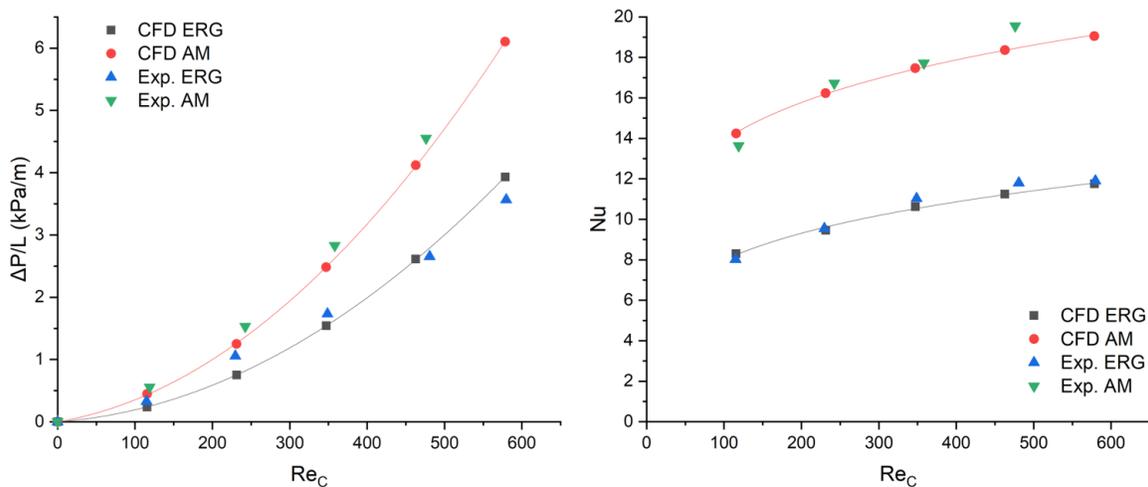


Figure I.21.3 Pressure drop per unit length (left) and Nusselt number (right) for the ERG and AM samples.

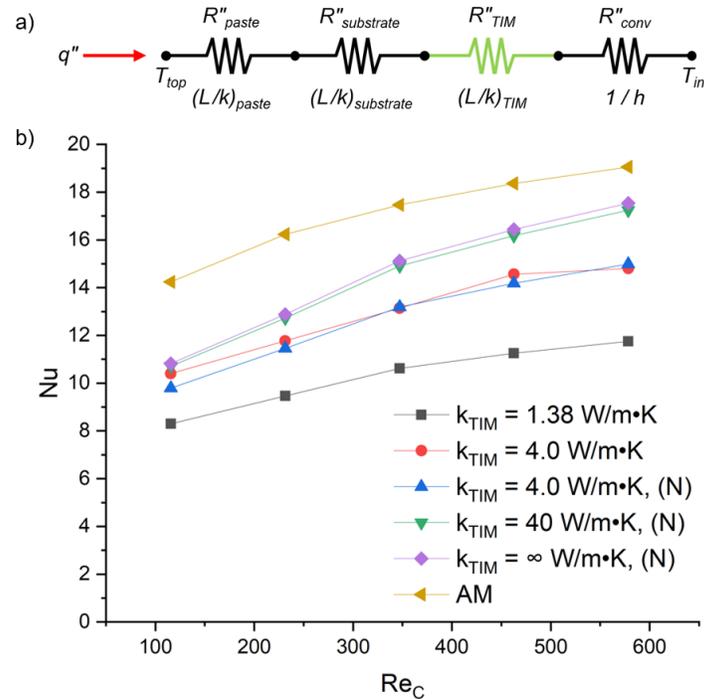


Figure I.21.4 Nusselt numbers recalculated with varying TIM thermal conductivities.

**TLP Bonding Technique:** The combined AlN – AlSiC – Al foam samples examined during the past few months were found to have high strength against shearing and tension (pending quantitative shear tests). Further analysis of the AlSiC – Al foam bond using SEM analysis is in progress. Meanwhile a liquid coolant loop has been constructed to measure the pressure drop across the foam cooling feature, temperature rise in the liquid coolant and the device temperature rise for a given mass flow rate. For this test set-up, a 50 mm × 50 mm AlSiC base plate with bolt holes was fabricated and bonded with 25 mm × 25 mm AlN and Al foam samples (Figure I.21.5). Additionally, a liquid coolant header was also designed and fabricated to house the Al foam and inlet and outlet of the liquid coolant. A thin film resistance heater was attached to the AlN layer. The resultant electronic package is shown in Figure I.21.6(a). The liquid coolant loop includes pressure and temperature sensors at the inlet and the outlet of the header, mass flow rate through the coolant loop and an infrared camera to capture the hot spot location and its maximum temperature as shown in Figure I.21.6 (b).

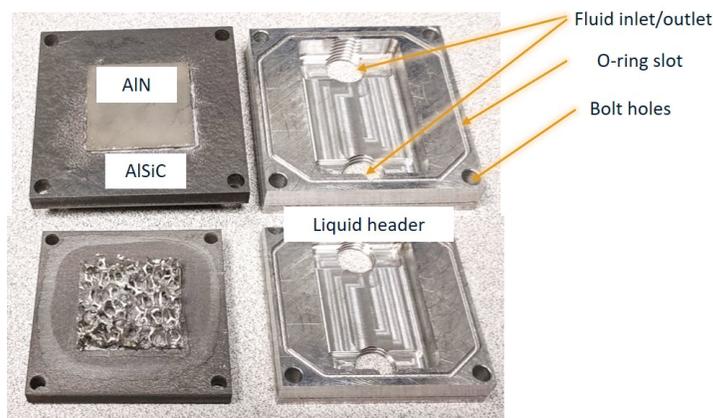


Figure I.21.5 50 mm × 50 mm prototype of AlSiC heat sink bonded to AlN and Al foam with liquid header

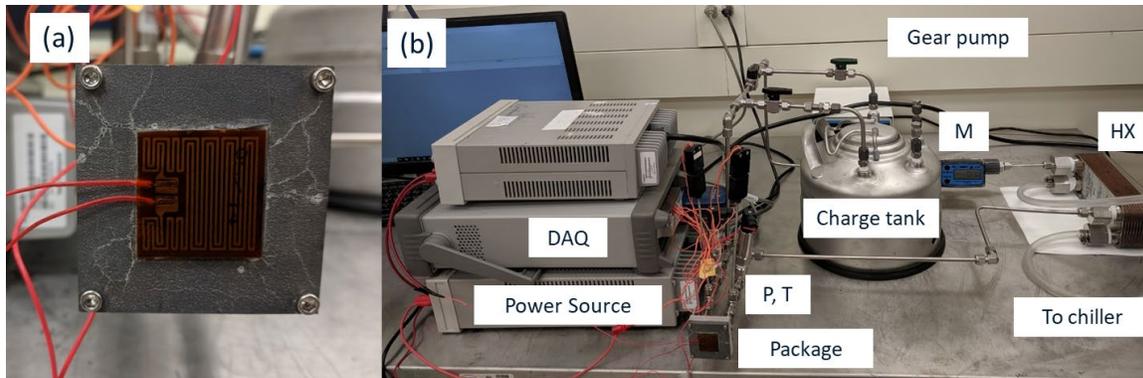


Figure I.21.6 (a) Assemble packaged prototype (b) Liquid coolant loop setup showing essential sensors and DAQ

The Al foam samples with three different porosities, 5, 10, 20 PPI were bonded to the 50 mm × 50 mm AlSiC to analyze the effect of foam density on the device temperature and extrapolating the effect of AlSiC – Al foam bond thermal conductivity on the cooling feature effectiveness. Cooling tests on these samples are ongoing.

Copper and Invar coupons measuring 25.4mm in diameter, 2mm in thickness and polished to 5 $\mu$ m were bonded using Cu-Al foils in a 1:3 ratio. An Energy Dispersive X-ray Spectroscopy test revealed the chemical composition of the invar coupon to be 37% nickel and 63% iron, while the copper coupon contained 99% Cu and about 0.7% nickel impurity. A Cu-Al TLP bond using the specified temperature profile resulted in uniform bonds between Cu-Cu coupons, while bonds between Copper-Invar and Invar-Invar coupons were unsuccessful. SEM results of the Cu-Invar bond show that the Cu foil as well as adjacent layers of the pure copper coupon were effective in melting over 2/3 of the Aluminum foils. However, the Invar coupon remained undisturbed in the bonding process. This could be a result of its high melting temperature of 1427°C compared to the bond temperature of less than 570°C. The Cu-Invar bonds delaminated along lines of uneven melting of Aluminum foils as illustrated in the figure below. Invar-Invar bonds showed less promise, as SEM results revealed cracks within the bond structure, depicted below.

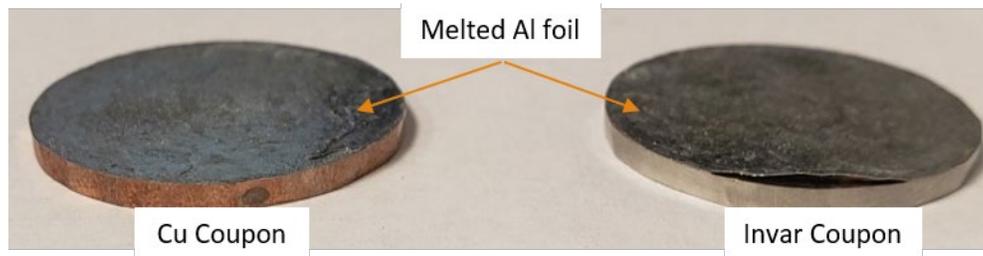


Figure I.21.7 Failed Cu-invar bond

Conversely, the Cu-Al bond was notably successful in combinations of pure Copper – Copper coupons. The SEM image below shows a uniform diffusion of copper into layers of Aluminum foils resulting in a cohesive bond. Further testing on the conceived bond to evaluate its physical and elastic properties are underway. Both instances of bonds involving Invar samples showed no interaction of elements within the Invar coupons with the bond, and lacked the reinforcing properties of Silicon particles from AlSiC which typically migrate into and help to solidify the bonds. Alternative combinations will involve bonding Copper to AlSiC coupons.

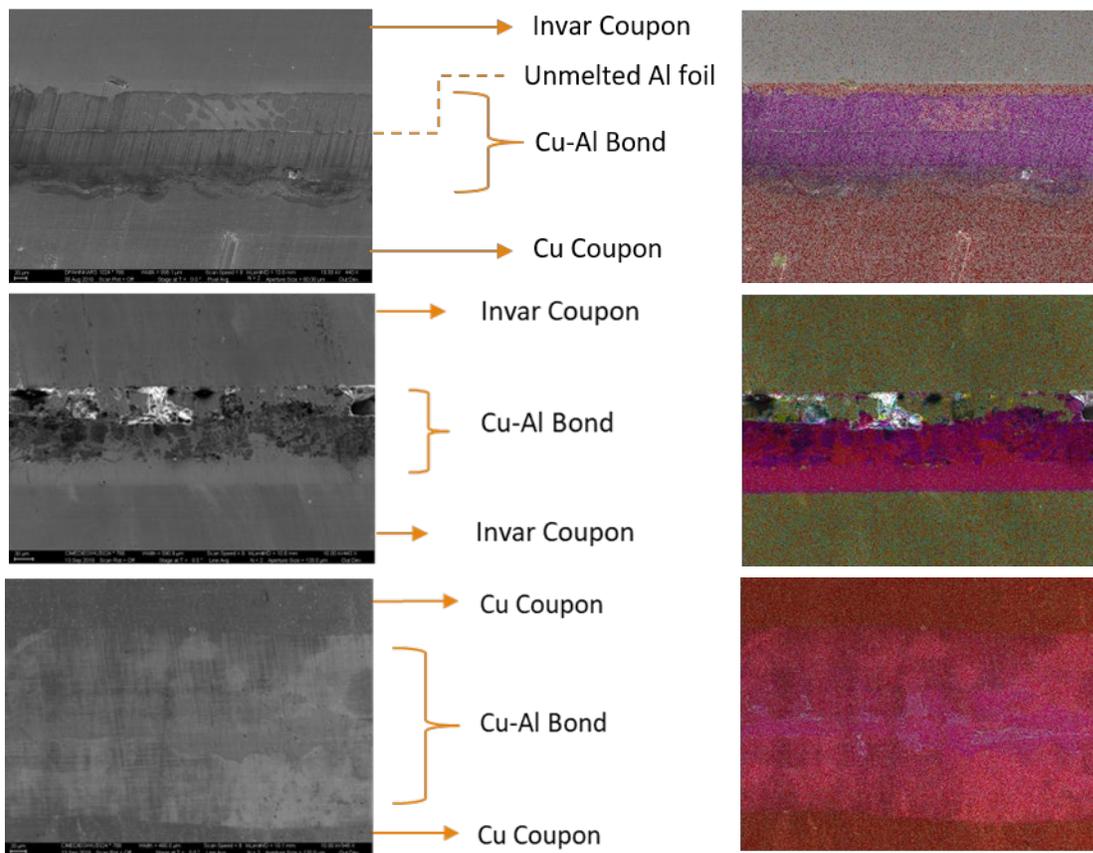


Figure I.21.8 SEM and EDS results of Cu-Al bond between a) Cu-Invar coupons b) Invar-Invar coupons c) Cu-Cu coupons

*Electric Model Thermal Modeling:* Results have been obtained from Motor-CAD simulations for the Nissan Leaf Electric Motor. Motor data for the geometry, winding properties, water jacket cooling system features and all materials within the motor are available. Therefore, as a first approach we used this data to come up with a first performance assessment. The thermal model used is a lumped parameter network, whose resistances are automatically implemented by Motor-CAD with respect to input materials. The electromagnetic model is a finite element analysis (FEA) model. We have used Electromagnetic and Thermal coupling models with a set temperature limit of  $200^{\circ}\text{C}$ . Therefore, we have been able to get the performances of the motor with respect to the flow rate of the coolant inside the water jacket: on Figure I.21.9, graph (a) shows the maximum shaft torque of the motor, (b) the maximum shaft power, (c) the maximum stator winding current and (d) the maximum efficiency with respect to shaft speed and with the temperature threshold of  $200^{\circ}\text{C}$  (inlet temperature of the coolant is fixed to  $65^{\circ}\text{C}$ ). We have also simulated the performances of the motor using different coolants for a fixed flow rate of 9 Lpm and an inlet temperature of  $40^{\circ}\text{C}$ . The results are available on Figure I.21.10. The calculated metrics are the same as that of Figure I.21.9. Before interpreting these results, we need to be sure the models are validated by experimental data. This is the next step.

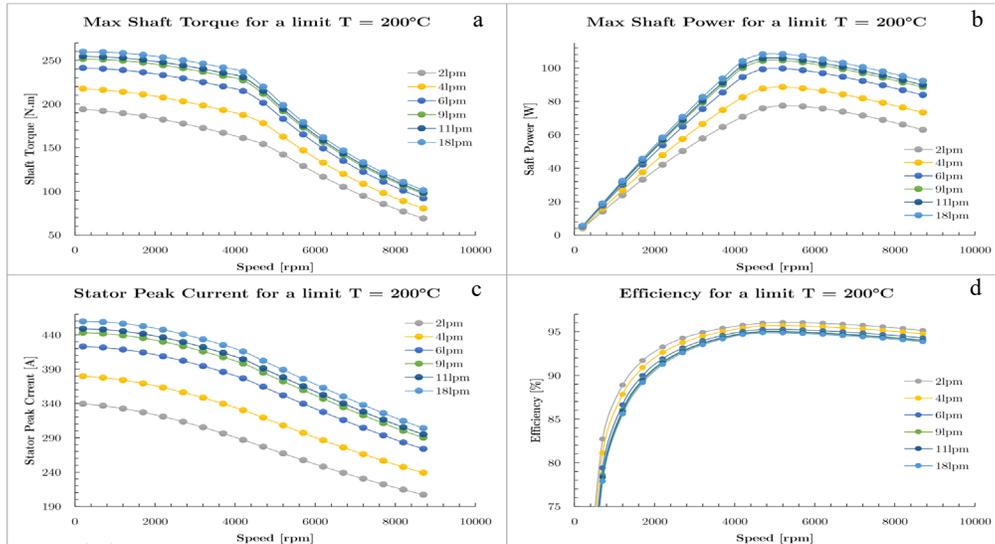


Figure I.21.9 (a) Maximum Shaft Torque, (b) Maximum Shaft Power, (c) Maximum Stator Winding Current and (d) Maximum Efficiency, with a temperature threshold of 200°C and for six different flow rates. These results have been extracted from Motor-CAD simulation.

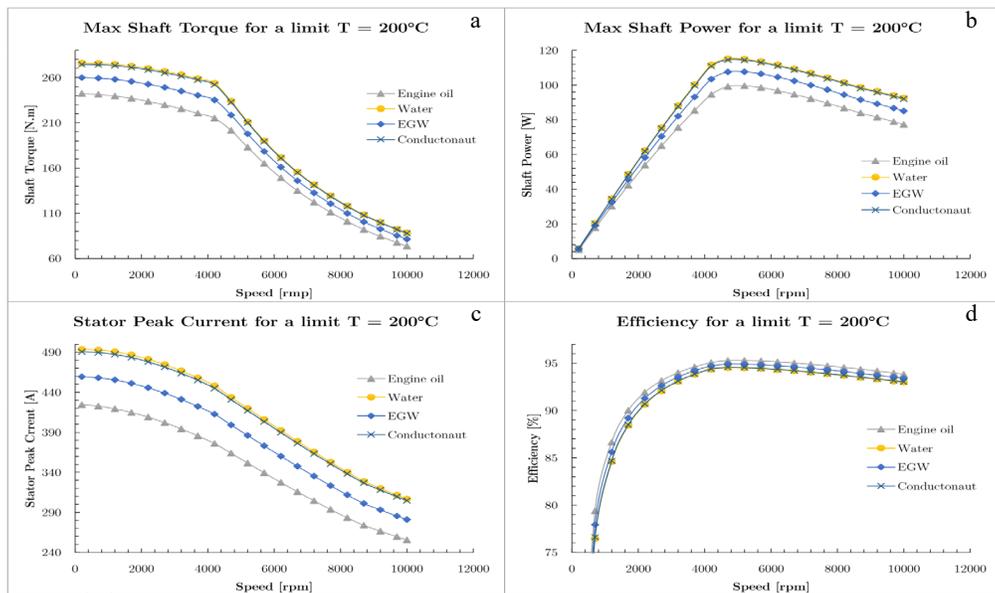


Figure I.21.10 (a) Maximum Shaft Torque, (b) Maximum Shaft Power, (c) Maximum Stator Winding Current and (d) Maximum Efficiency, with a temperature threshold of 200°C, a fixed 9 Lpm flow rate and for four different liquid coolant materials. These results have been extracted from Motor-CAD simulation.

## Conclusions

*AM Foams:* The above work shows the potential of using both traditionally manufactured and AM foam for power electronics thermal management. Simulations for the reduced geometries were shown to agree with the experimental data. The numerical simulations also indicated that commercial foams would be viable if the interface material’s thermal conductivity was increased significantly, and eliminating the attachment layer would increase the ERG foam to close to that of the AM foam.

*TLP Bonding:* Cu – Al TLP bonds have been demonstrated to be successful for AlN – AlSiC. Lifetime improvement over 16 times has been reported along with improvement in heat dissipated. AlSiC is difficult to machine, hence introducing cooling features within AlSiC is costly. Therefore, Al foam can be integrated in the bonding process of AlN – AlSiC resulting in reduction in cost of fabrication. Cu-Al bonds proven successful for Cu-Cu. Subsequent tests will focus on determining properties of bond, including hardness and elastic modulus. TLP bonding to determine effectiveness of Cu-Al bond between Cu and AlSiC coupons is in progress.

*Motor Thermal Modeling:* The first results show a significant influence of the coolant flow rate over the maximum current allowed for a 200°C temperature threshold. Indeed, from a 4 Lpm flow rate to a 9 Lpm flow rate, a current increase of 16% is possible for shaft speeds under 5,000 rpm. This is not negligible especially if we have copper amount reduction in mind. Moving forward, we need to validate our models, so that we can go further with more simulations.

### Key Publications

1. J. Broughton and Y. Joshi, “Thermal Management of Power Electronics Using Stochastic, Open-Cell Metal Foams,” in *2019 25th International Workshop on Thermal Investigations of ICs and Systems (THERMINIC)*, Lecco, Italy, 2019, pp. 1-5.
2. J. Broughton and Y. Joshi, “A Numerical Investigation of Additive Manufactured Foam Structures For Single Phase Hotspot Thermal Management,” in *ASME InterPACK*, Anaheim, California, 2019.
3. J. Broughton and Y. Joshi, “Comparison of Single-Phase Convection in Additive Manufactured versus Traditional Metal Foams,” *Journal of Heat Transfer*, 2019 (submitted).
4. D. Pahinkar, C. Imediegwu, J. Hoyer, B. Kelly, S. Graham, Direct Bonding of Aluminum Foam with AlSiC for Rapid Fabrication of Power Electronic Packages, ASME InterPack, 2019, Anaheim, CA (Presentation Only)

### References

1. Pahinkar, D. G., Puckett, W., Graham, S., Boteler, L., Ibitayo, D., Narumanchi, S., Paret, P., DeVoto, D. and Major, J. (2018), Transient Liquid Phase Bonding of AlN to AlSiC for Durable Power Electronic Packages. *Adv. Eng. Mater.*, 20: 1800039. <https://dx.doi.org/10.1002/adem.201800039>
2. Doube, Michael, Michał M. Kłosowski, Ignacio Arganda-Carreras, Fabrice P. Cordelières, Robert P. Dougherty, Jonathan S. Jackson, Benjamin Schmid, John R. Hutchinson, and Sandra J. Shefelbine. “Bonej: Free and Extensible Bone Image Analysis in Imagej.” *Bone* 47, no. 6 (09/15 2010): 1076-79.
3. Schmierer, Eric N., and Arsalan Razani. “Self-Consistent Open-Celled Metal Foam Model for Thermal Applications.” *Journal of Heat Transfer* 128, no. 11 (2006): 1194-203.
4. A. Boglietti, C. Andrea, S. David, S. Martin, M. Markus and M. Carlos, “Evolution and Modern Approaches for Thermal Analysis of Electrical Machine,” *IEEE TRANSACTIONS ON INDUSTRIAL ELECTRONICS*, 2019.
5. D. G. Dorrell, D. A. Statont, J. Kahout, D. Hawkins and M. I. McGilp, “Linked Electromagnetic and Thermal Modelling of a Permanent Magnet Motor,” University of Glasgow.

### Acknowledgements

We would like to acknowledge the Georgia Tech Machine shop for the help in fabricating the liquid header. The assistance from Haipeng Qiao and Prof. Christopher Saldana in the tomographic imaging is acknowledged.

## I.22 Next-Generation, High-temperature, High-frequency, High-efficiency, High-power-density Traction System (University of California, Berkeley)

### **Prof. Robert Pilawa-Podgurski, Principal Investigator**

University of California, Berkeley  
253 Cory Hall  
Berkeley, CA 94720  
E-mail: [pilawa@berkeley.edu](mailto:pilawa@berkeley.edu)

### **Susan Rogers, DOE Technology Development Manager**

U.S. Department of Energy  
E-mail: [susan.rogers@ee.doe.gov](mailto:susan.rogers@ee.doe.gov)

Start Date: October 1, 2019	End Date: September 30, 2020	
Project Funding (FY19): \$302,342	DOE share: \$302,342	Non-DOE share: \$0

### **Project Introduction**

To meet performance and reliability requirements necessary for broader adoption of electric drive vehicles, the Electrical and Electronics Technical Team of the U.S. Drive partnership has established aggressive design goals for next-generation electric vehicle drivetrains. Specifically, the 2025 roadmap stipulates a 100 kW/L power density target and a \$2.7/kW cost target for power electronics, in addition to high-voltage operation (i.e., greater than 800 VDC). The additional targets for traction motor and the overall system performance impose further challenges on the power electronics design. For example, many high specific power machines have reduced iron content, and therefore reduced intrinsic filtering, thus requiring the inverter to supply a low-distortion drive current. These machines also typically have a high pole count, thus requiring drive current at a higher electrical frequency. Other motors, such as brush-less dc and switch reluctance machines, require a carefully-shaped, non-sinusoidal drive current.

Two- and three-level inverter topologies are the conventional framework for the power electronics design of the drivetrain, and some demonstrations have shown recent progress towards addressing cost, power density and efficiency goals [1]. However, an unconventional approach may be necessary to take the dramatic leap in power density necessitated by the roadmap—while simultaneously addressing the other system needs. Therefore, this project leverages the flying capacitor multilevel (FCML) topology, together with a scalable, modular approach, to address these needs. This type of hybrid converter has several advantages: lower voltage (i.e., less than 300 V) transistors can be used, energy-dense capacitors process most of the power, and the output current waveform is multilevel and exhibits a frequency multiplying effect—in other words, the output has reduced dv/dt and filtering requirements for the same high voltage dc bus. For example, in an electric vehicle with an 800 V bus, a 10-level FCML could leverage 100 V, commercially available GaN devices switching at 115 kHz to produce a ~1 MHz switching waveform (modulated according to the motor drive requirements) with one ninth of the dv/dt of a two-level converter.

Prior work has already demonstrated promising performance and gravimetric power density figures for more electric aircraft applications [2]. This project leverages lessons learned to achieve the volumetric power density of 100 kW/L by employing advanced liquid cooling, address the 300,000 mile reliability challenge with redundant design, topology failure studies and online health monitoring, and reduce costs to \$2.7/kW through the use of low-cost GaN devices, modular converter assemblies, and modest modifications to traditional manufacturing methods.

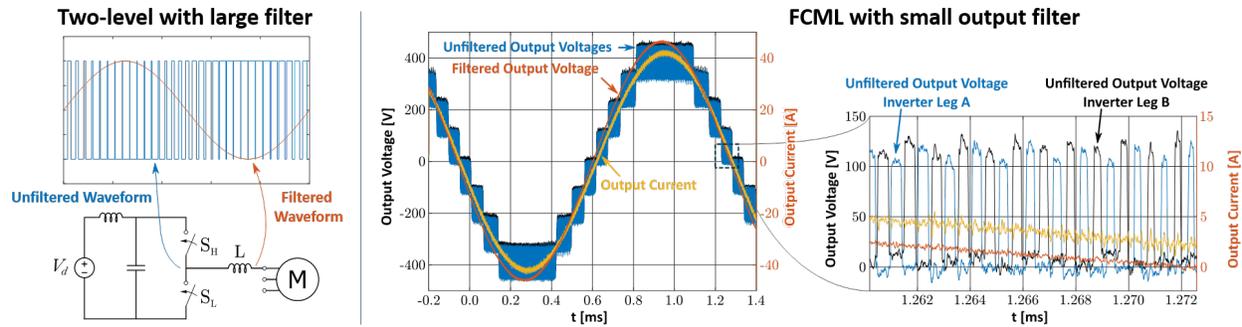


Figure I.22.1 Comparison in output waveforms of a conventional two-level design (left), and a 9-level, dual-interleaved FCML design (right). The latter are from results in [2], and illustrate reduced  $dv/dt$ , interleaving and high effective frequency.

## Objectives

The main objective of this project is to develop a 100 kW/L traction power inverter, compatible with next-generation, low-weight (and low inductance) electric machines. The efficiency, size, and cost targets will be demonstrated through the development of several hardware prototypes, including electrical and thermal systems. This overall goal is comprised of several key tasks, including:

- Establishing the high-level traction inverter specifications
- Evaluating state-of-the-art semiconductor and passive components (e.g., inductors and capacitors)
- Performing a multi-objective optimization to establish circuit topology and operating conditions
- Prototyping designs to verify performance and implement digital control and online health monitoring
- Codesigning a liquid-cooled hardware revision
- Validating the cooling approach with finite-element analysis
- Manufacturing, assembling and experimentally validating the full hardware prototype.

Additionally, this work will address several key barriers in the 2025 roadmap:

- WBG device power and voltage levels and availability
- WBG multi-physics integration designs to enable optimal use
- Component optimization for miniaturization and cost reduction.
- Low inductance requirements for WBG multi-physics integration.

## Approach

The fundamental approach for achieving the power density and performance requirements is to develop new circuit topologies and control method to enable FCML inverters in harsh automotive environments and under dynamic loads. The key benefits of this type of converter design illustrated in comparison to the conventional two-level design in Figure I.22.2., with relevant considerations as follows:

- Energy-dense capacitors process most of the converter energy
- Multilevel operation and high effective frequency reduce the output  $dv/dt$  and filter requirements



- High-switching frequency facilitated by GaN transistors reduces the required flying capacitance
- Dual-interleaved design to further mitigate switching ripple at the input and output.

Designs are informed through both theoretically and empirically derived loss modelling, wherein an optimal solution is chosen from the design space using Monte-Carlo simulations and possibly informed by topology agnostic theoretical analysis. This aspect of the approach provides:

- Large-signal loss models, derived from calorimetric testing of passive components, that are of higher value to the broader power electronics community than small-signal datasheet parameters [3]
- Experience in a common design toolbox, allowing for faster iterations when adding new design considerations (e.g., dynamic  $R_{ds,on}$ , coupled inductances), or newly available components.

Furthermore, to support output power beyond the 2025 roadmap—while also providing converter redundancy—this project leverages a scalable and modular (or segmented) architecture; a lower power module design is first optimized, and multiple of the resulting design are paralleled in and across phases and coil sets to achieve the full system target power. This strategy, exemplified in Figure I.22.2, both simplifies the scope of initial design, manufacturing and experimental testing. Additional benefits of this approach include:

- Shedding redundant modules when operating at low power to achieve higher light-load efficiency
- Supporting continued system operation at a reduced rating in the event of a module or winding failure
- Reducing filter requirements on the dc bus if switching signals across modules are also interleaved.

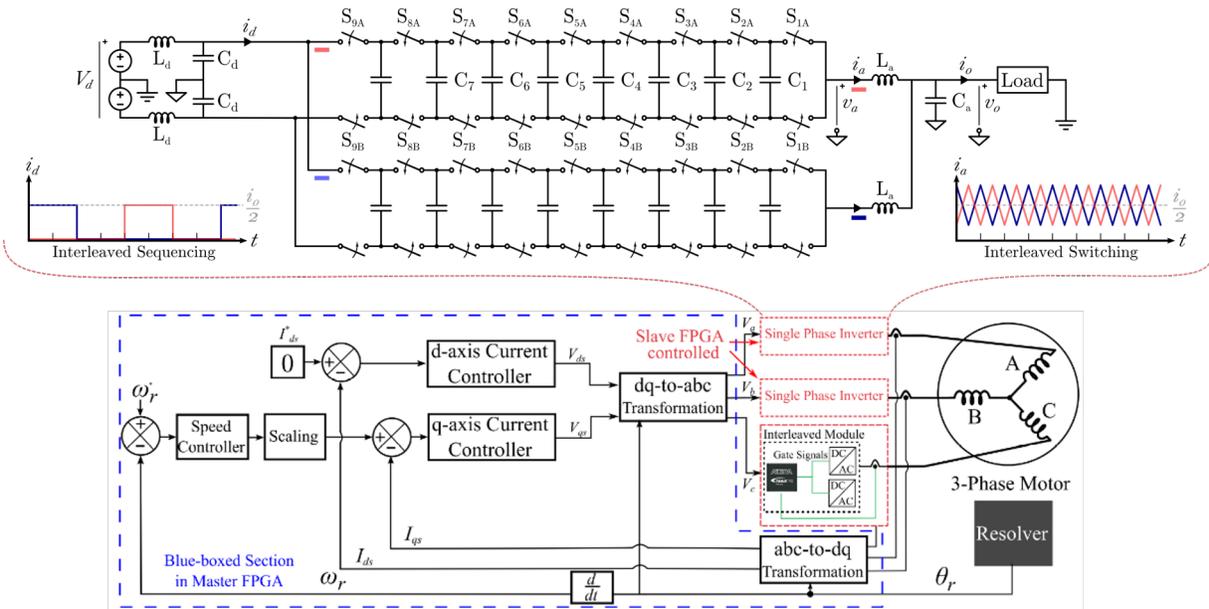


Figure I.22.2 Top: schematic and current waveforms for a dual-interleaved, 10-level FCML inverter. Bottom: hierarchical control strategy and system diagram of paralleled converters of the modular (i.e., segmented) approach.

Additionally, to address high-voltage module packaging challenges outlined in the 2025 roadmap, the approach of this project will often differ from conventional two- and three-level designs in that it will:

- Allow for the use lower-cost, low-voltage GaN devices, in addition to higher-voltage, wide-bandgap semiconductor modules in custom, specialized packaging

- Manufacture with conventional assembly and printed circuit board technologies to facilitate extreme cost reductions compared to high power semiconductor modules.

This plan is, however, is complemented by including some advanced manufacturing techniques, such as:

- Blind and buried vias and internal layers in circuit board fabrication to reduce parasitics
- Additive manufacturing for rapid prototyping of thermal management and mechanical assemblies.

## Results

Several aspects of the project have yielded experimental or simulated results demonstrating progress towards the ambitious goals set forth in the introduction. These are broken down into four categories:

- Design, contract manufacture, and successful experimental testing of a batch of 10-level, dual-interleaved FCML inverter module prototypes
- Proof-of-concept demonstration of paralleled converter operation (9 modules, 3 phases) under hierarchical control and current feedback to spin a permanent magnet synchronous machine
- CFD validation of system level thermal performance for this air-cooled iteration
- Simulation and analysis of balancing behavior during startup transient (i.e., dc supply power on)
- Calorimetric characterization of capacitors under high-power conditions that will be useful for future optimization iterations, and are much anticipated in the broader power electronics community.

A hardware prototype was designed and a batch of printed circuit assemblies were manufactured, both according to the methodology outlined in the previous section. This design leveraged both modular cooling and electrically thin design practices, and took advantage of recent work characterizing dynamic  $r_{ds,on}$  of GaN devices when deciding on the appropriate level count. Unlike previous FCML designs, the hardware in this project does not use switching cell daughter boards; instead, all flying capacitors and transistors are populated on the main converter circuit board. This drastically reduced commutation overshoot, as illustrated by the experimental measurements in the left plot of Figure I.22.3. The converter was successfully tested at high-voltage and high-power, shown in the right plot of, with results summarized in Table I.22.1.

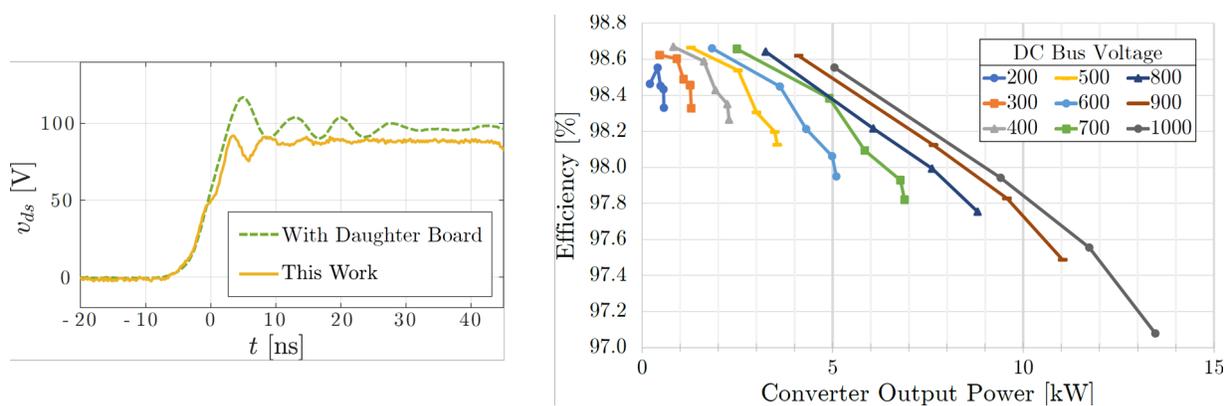


Figure I.22.3 Left: measured overshoot of the commutation loop in this design. Right: measured experimental performance of the prototype inverter module across various load impedances and dc bus voltages.

**Table I.22.1 Key Inverter Prototype Experimental Results**

DC Bus Voltage	Peak Efficiency	Peak Power	Assembled Mass	Assembled Volume	Gravimetric Power Density	Volumetric Power Density
1000 V	98.6%	13.46 kW	505 g	775 cm <sup>3</sup>	26.7 kW/kg	17.4 kW/L

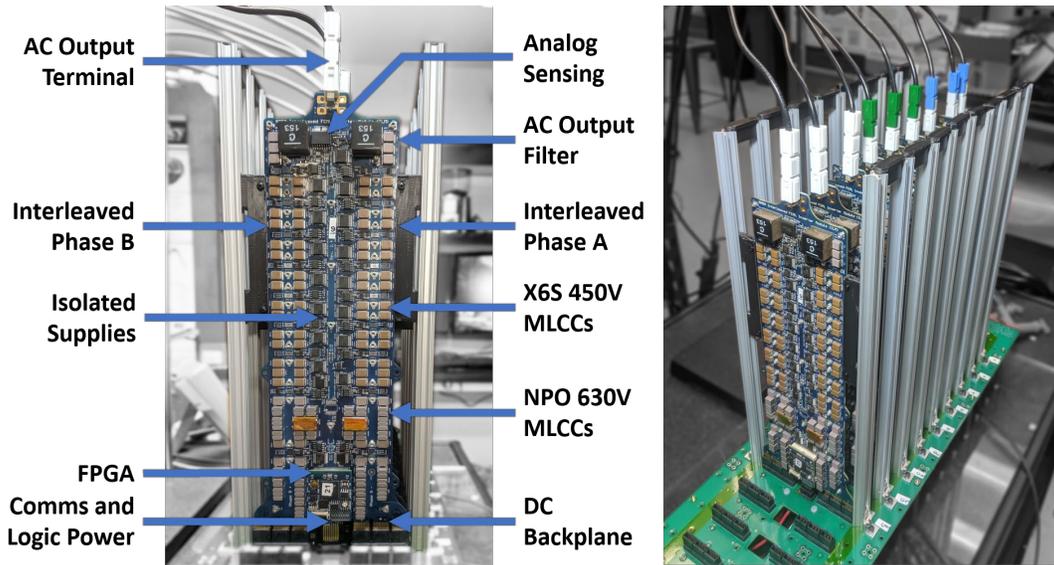


Figure I.22.4 Left: an annotated hardware prototype of the 10-level, dual-interleaved inverter module for this project. Right: a 9-module, segmented inverter paralleled across three winding phases assembled for initial motor testing.

In addition to benchmarking individual module performance, this project achieved a major milestone by demonstrating parallel operation of multiple modules to spin an off-the-shelf high-performance TG7150 motor from ThinGap. Individual modules were paralleled in a dc backplane, with the annotated interleaved module and 9-module inverter assembly both shown in Figure I.22.4. This demonstration retires several risks, including:

- Assembly and testing repeatability across a lot of the low-power interleaved modules
- Operation of multiple interleaved modules in parallel at partial power
- Integrity of communication between master controller delegating motor commands and module controllers generating the corresponding gate signals
- Integrity of the current feedback on each module—from the analog signal chain, through the master controller, to a host computer reading telemetry data over a serial link.

Since the dc backplane in Figure I.22.4 was designed for easy access to signals and components during the initial control debugging and spin testing, an assembly variant focusing on integrated thermal management was simultaneously designed to facilitate the cooling needed for higher power testing. This design was simulated and prototyped as shown in Figure I.22.5, and is facilitating the next stages of experimental benchmarking.

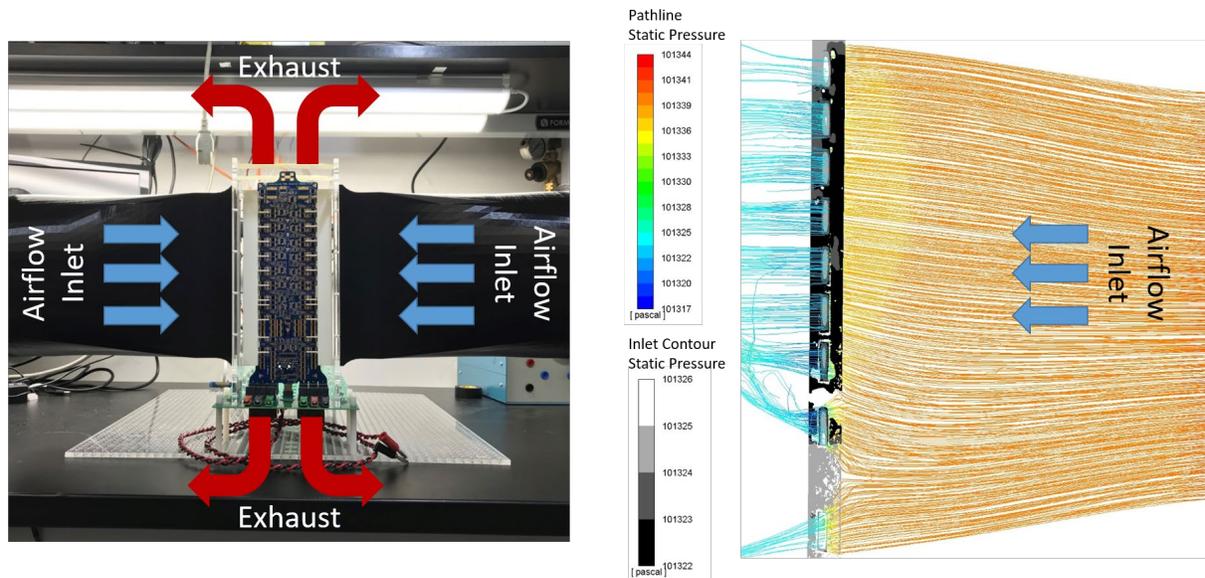
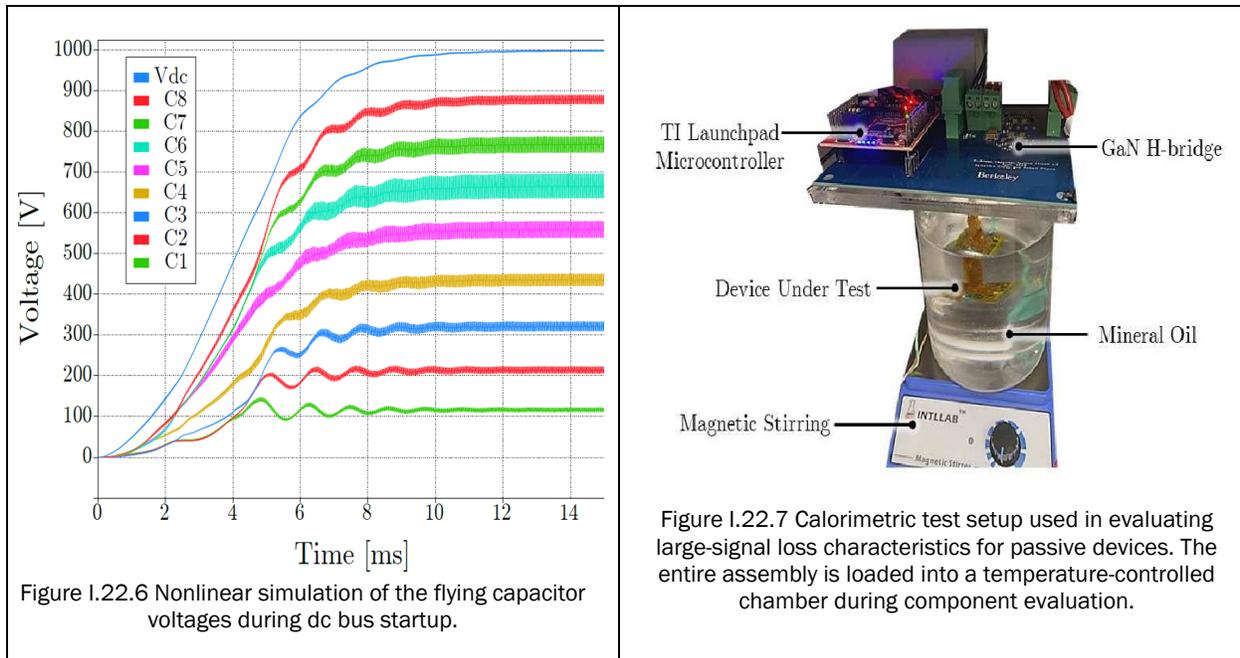


Figure I.22.5 Left: experimental setup showing the thermal test assembly for this air-cooled inverter iteration. Right: CFD results showing a relatively uniform pressure front across the inlet window of each modular heat sink.

While the FCML topology implemented clearly shows promise from a power density and efficiency perspective, investigating issues of stability of flying capacitor voltages during transients—and specifically during startup—is also an ongoing facet of this project. Fortunately, prior work provides analytical methods for capturing dynamics of capacitor voltages, as well as some suggestions on the appropriate control directions to be employed. These were explored using PLECS simulation software that included modeling of the bias-dependent nonlinearities of the X6S flying capacitors, with results presented in Figure I.22.6. The simulation indicates balancing can be rapidly achieved during startup when the correct control is implemented, and experimental validation of this approach is forthcoming.

Finally, to support better understanding of how best to choose capacitors for high-power, high-performance inverter designs, extensive testing has been underway to establish better large-signal loss parameters. Specifically, calorimetric tests have been performed on several type I and type II MLCCs, varying both in temperature rating, capacitance and manufacturer. In addition, newly introduced Ceralink capacitors were also evaluated. Calorimetric tests using the fixture in Figure I.22.7 were performed under a wide range of voltage biases (0 V – 400 V), frequencies (75 kHz – 500 kHz), and current square wave excitation amplitudes (1 A – 6 A pk-pk). These testing conditions were chosen to replicate hybrid switched capacitor operating conditions. Results show that the DC bias and frequency have a great effect on the losses of the device. Current work is being done to condense these results into an easy-to-use model which will be beneficial to the power electronics community.



## Conclusions

Through an innovative circuit topology and advanced digital control, a high density, low-costs inverter prototype suitable for lightweight electric vehicle motors has been demonstrated. The high performance already demonstrated is likely to increase dramatically with the use of the new air-cooling test setup. Furthermore, the excellent results for the air-cooled indicates the move towards liquid cooling in the next phase of the project will provide the dramatic increase in volumetric power density required to meet or exceed the goals of the 2025 roadmap.

## Key Publications

Two publications resulting from this project, one on capacitor characterization and another on the inverter prototype presented above, were accepted for presentation at the IEEE Applied Power Electronics Conference in March of 2020. The associated manuscripts will be published in the subsequent conference proceedings.

## References

1. E. Gurpinar and B. Ozpineci, "Loss Analysis and Mapping of a SiC MOSFET Based Segmented Two-Level Three-Phase Inverter for EV Traction Systems," in 2018 IEEE Transportation Electrification Conference and Expo (ITEC), 2018.
2. N. Pallo, T. Foulkes, T. Modeer, S. Coday and R. C. N. Pilawa-Podgurski, "Power-dense multilevel inverter module using interleaved GaN-based phases for electric aircraft propulsion," in 2018 IEEE Applied Power Electronics Conference and Exposition (APEC), 2018.
3. S. Coday, C. B. Barth and R. C. N. Pilawa-Podgurski, "Characterization and Modeling of Ceramic Capacitor Losses under Large Signal Operating Conditions," in 2018 IEEE 19th Workshop on Control and Modeling for Power Electronics (COMPEL), 2018.
4. T. Foulkes, T. Modeer and R. C. N. Pilawa-Podgurski, "Developing a standardized method for measuring and quantifying dynamic on-state resistance via a survey of low voltage GaN HEMTs," in 2018 IEEE Applied Power Electronics Conference and Exposition (APEC), 2018.

## **Acknowledgements**

The following graduate students at the University of California, Berkeley contributed to the content of this report: Nathan Pallo, Samantha Coday, Logan Horowitz and Joseph Schaadt. Christopher Barth, formerly a graduate student at the University of Illinois, Urbana-Champaign and now with the NASA Glenn Research Center, contributed to the motor testing and hierarchical control. TDK Corporation provided applications and logistics support for the capacitors used in the demonstration hardware. Support for development of some of the hardware used in this project was also provided by the NASA Fixed Wing research program through the NASA cooperative agreement: NASA NNX14AL79A.

### I.23 Heterogeneous Integration Technologies for High-temperature, High-density, Low-profile Power Modules of Wide Bandgap Devices in Electric Drive Applications (Virginia Tech)

**Guo-Quan Lu, Principal Investigator**

Virginia Tech  
 Department of MSE and ECE – 0111  
 Blacksburg, VA 24060  
 E-mail: [gqlu@vt.edu](mailto:gqlu@vt.edu)

**Rolando Burgos, Co-Principal Investigator**

Virginia Tech  
 Department of ECE, CPES – 0179  
 Blacksburg, VA 24060  
 E-mail: [rolando@vt.edu](mailto:rolando@vt.edu)

**Khai D.T. Ngo, Co-Principal Investigator**

Virginia Tech  
 Department of ECE, CPES – 0179  
 Blacksburg, VA 24060  
 E-mail: [kdtm@vt.edu](mailto:kdtm@vt.edu)

**Susan Rogers, DOE Technology Development Manager**

U.S. Department of Energy  
 E-mail: [susan.rogers@ee.doe.gov](mailto:susan.rogers@ee.doe.gov)

Start Date: April 1, 2019                      End Date: March 31, 2020  
 Project Funding: \$300,000                      DOE share: \$300,000                      Non-DOE share: \$0

**Project Introduction**

The goal of this project is to research, develop, and evaluate the integration and packaging technologies for making high-temperature, high-density, and low-profile wide-bandgap (WBG) power electronics modules. These modules are aimed at enabling the DOE VTO Electrification Technologies’ University Consortium to reach its 2025 targets (listed below) for the cost, power density, and system peak power rating of automotive electric drive systems.

**Table I.23.1 Power Electronics Requirements**

Parameters	Measure
Cost (\$/Kw)	≤ 2.7
Power Density (kW/L)	≥ 100
System Peak Power Rating (kW)	100

**Objectives**

The overall objectives of this project are to:

- develop a low-cost sintered-metal (copper or silver) interconnect technology for packaging power modules and gate drivers capable of working over 200°C;

- develop designs and fabrication processes of 3D, planar power modules with parasitic inductances  $< 5$  nH, heat flux density  $> 400$  W/cm<sup>2</sup>, and working junction temperature  $> 200^{\circ}\text{C}$ ; and
- design and prototype intelligent gate drivers with integrated current sensor and protection for  $200^{\circ}\text{C}$  module.

A schematic of the hardware to be developed in this project is shown below in Figure I.23.1. Phase-leg modules capable of working at  $200^{\circ}\text{C}$  or  $250^{\circ}\text{C}$  ambient will be designed and fabricated. Three of the phase-leg modules will be assembled on cooling plates (with or without double-side cooling) and interfaced to a bus bar and gate-driver boards. The gate driver boards will have integrated current sensors, power supplies, and other components that are capable of working at  $200^{\circ}\text{C}$  or  $250^{\circ}\text{C}$  ambient.

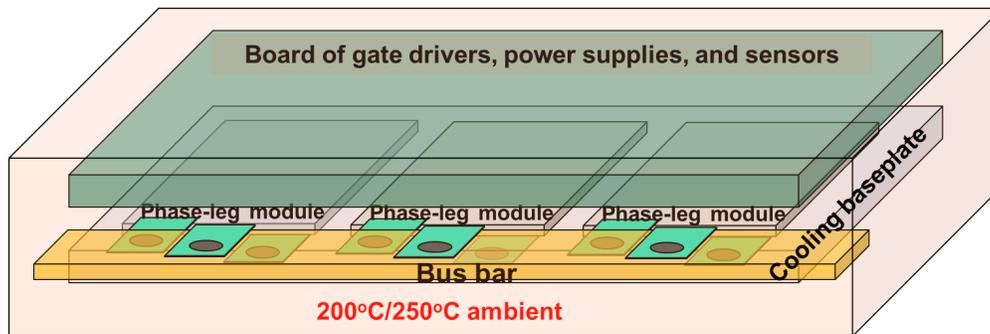


Figure I.23.1. A schematic of the hardware to be developed in this project.

For this reporting period, we focused on achieving the following specific objectives:

- acquiring extensive knowledge on the state-of-the-art packaging materials and components for making high-temperature power modules, gate drivers, and current sensors;
- designing and processing planar SiC phase-leg power-stage packages for making segmented three-phase inverters; and
- designing integrated phase current sensors with short-circuit protection and current reconstruction based on power module parasitics. Verify theoretical analysis with simulation results.

## Approach

To achieve the objectives of this report period, we surveyed the literature on the state-of-the-art high temperature materials, components, and packaging technologies for power switching cells, gate drivers and their power supplies, passive components, and current sensors. The module packaging survey led to recommendations for the design and selection of packaging materials and assembly processes for a phase-leg power stage module of 1200 V SiC MOSFET devices. The other studies led to a comparison of various designs for current sensors with short-circuit protection and current reconstruction that are based on power module parasitics. Theoretical analyses of the current sensor were then conducted and compared with simulated results.

## Results

### 1. Findings from literature surveys

#### 1.1. High-temperature WBG module packaging materials

Findings of the module packaging survey are summarized in Figure I.23.2. This survey included substrates, interconnects, and encapsulants for working at high temperature ( $>200^{\circ}\text{C}$ ). As for the substrates,  $\text{Si}_3\text{N}_4$  AMB and AlN DBA are recommended as they can survive temperature cycles between  $-55$  to  $250^{\circ}\text{C}$  for over 1000



cycles [11],[2] while Al<sub>2</sub>O<sub>3</sub> or AlN DBC can only survive tens of cycles under the same condition [3]. To further improve the high-temperature reliability of substrates, adding dimples or using stepped edges to substrates can improve thermal cycling reliability by 10 and 65 times, respectively [4]. As for the interconnect (die-attach), sintered Ag is recommended since it can be processed at low-temperature (<250°C) while working at high temperature (<714°C). Sintered Ag also has higher electrical and thermal conductivity compared to conventional interconnect materials like solder. The sintered Ag with Ag finish on both die and substrate showed good reliability (>2000 hours aging at 300°C and >1000 cycles at -55 to 250°C) [5]. Al bond wire is widely used as interconnects for gate or power loop. [6] showed 40 um Al wire on Ag metallization did not lift off until 6000 hours at 200°C and 400 um Al wire on Al metallization did not lift off after 3000 cycles at -40°C to 250°C [7]. Reliability can be further improved by using larger wire (~20 mil) or using ribbon bond [8]. 3D packages can also be used to eliminate bond wires to reduce the parasitics and improve reliability of power modules. As for encapsulant, polymeric materials (soft and hard) are commonly used. The soft polymer encapsulant (silicone gel and silicone elastomer) can survive several hundred aging hours at 250°C [9]. Adding fillers to soft polymer is an effective way to improve thermal stability of soft polymer. For example, adding 30 wt% alumina fiber into silicone elastomer can improve thermal aging reliability at 250°C from 200 hours to 1300 hours [10]. As for hard polymer encapsulant, bismaleimide, polyimide, cyanate esters are promising but their CTE has to be reduced by adding fillers to match the CTE of substrate and device [9]. Some inorganic materials like lead glass can also be used as encapsulant because of their high temperature stability, but the processing parameters have not been extensively reported in the literature.

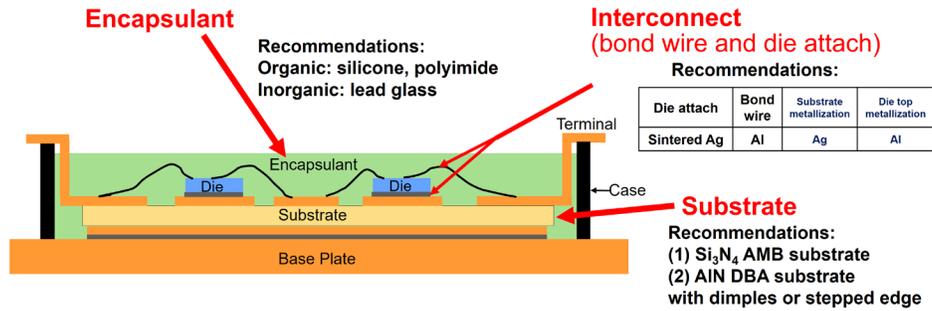


Figure I.23.2. Summary of recommended high temperature packaging materials for power modules.

### 1.2. High-temperature gate driver

Most integrated gate drivers available on the market can only operate to 125°C; nevertheless, three ways exist in the literature for higher temperature. The first way is to use integrated SiC transistors [11],[12]. The second solution is by commercial-off-the-shelf (COTS) discrete transistors and diodes for 200°C. A COTS-based IC has been designed with short-circuit protection and under-voltage lockout (UVLO) [13]. These two methods have shown good performance, but there are no commercial products available. The third solution is to use silicon-on-insulator (SOI) [14],[15] at 225°C. XREL Semiconductor and CISSOID have designed products with large output current to satisfy the demand for SiC MOSFETs. An example of the ICs is shown as Figure I.23.3.



Figure I.23.3. High temperature gate driver IC from Cissoid.

### 1.3. High-temperature power supply for the gate driver

To fit with the small footprint of the targeted power module, the power supply needs to operate at high switching frequency to reduce the size of passive components. Although flyback converters are most commonly used [16], they suffer from high switching loss at high frequency due to hard switching. In order to

solve this problem, new topologies have been proposed to realize soft switching, including active-clamp flyback converters and other resonant converters [17],[18]. Normal transformers with core are usually used in the literature. Since most magnetic cores perform poorly under high temperature, air-core transformers need to be considered.

Air-core transformers have already been used in high-frequency converters to further reduce the profile and increase efficiency with the elimination of magnetic cores [19]. At very high frequency, resonant capacitors can also be integrated with low-dielectric-loss laminates [15]. Figure I.23.4 shows an air-core inductor with PCB winding [20].

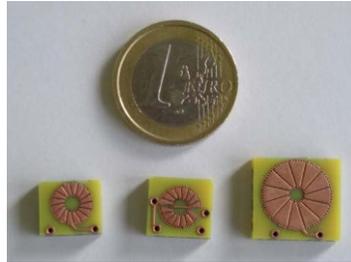


Figure I.23.4. Air-core inductors.

## 1.4. High-temperature passive components

### 1.4.1 High-temperature resistors

Table I.23.2 summarizes available resistors for high-temperature applications [21]. Metal foil resistor is a good candidate because it offers high precision and stability. Vishay offers products at 225°C.

Table I.23.2 Commercially Available High Temperature Resistors

Resistor type	Packaging	Max. Temperature
Metal foil	Through-hole, surface-mount-device (SMD)-chip, flip-chip	240°C
Metal oxide	Through-hole	275°C
Thin film	SMD-chip, flip-chip	275°C
Thick film	SMD-chip, flip-chip	300°C
Wire-wound	Through-hole	350°C

### 1.4.2 High-temperature capacitors

Capacitors are widely used in gate drivers mainly for filter purposes. Several dielectric materials are suitable for high-temperature applications, such as tantalum and ceramic. The tantalum capacitor can reliably work to 230°C; however, it has relatively low voltage rating which also degrades at high temperature. For ceramic capacitors, X7R and C0G are widely used. X7R is a cheap option under 250°C but the capacitance decreases about 70% at 250°C. C0G can operate to 250°C with stable capacitance over the entire temperature range. The capacitance of C0G is also constant at different voltage bias. Companies like AVX and KEMET offer C0G capacitors with temperature rated at 250°C. The company Presidio components, Inc. offers high performance dielectric materials at high temperature at and above 250°C, such as NPO and XHT. Table I.23.3 summarizes available capacitors with brief comments.

**Table I.23.3 Commercially Available High Temperature Capacitors**

Capacitor type	Max. Temperature	Comments
Tantalum	230 °C	High capacitance value; voltage rating degradation at high temperature
X7R	250 °C	High capacitance value; degraded capacitance above 175 °C
COG	250 °C	Stable capacitance; Lower capacitance value
XHT	250 °C	Smaller capacitance degradation than X7R; High capacitance value
NPO	500 °C	Stable capacitance; Lower capacitance value

### 1.5. Current sensors

Current and voltage sensors play important roles in electric drive systems. Switching current sensors help protect the power MOSFET module from short-circuit event [22]-[26]; and common-mode current sensors help identify correctly the common-mode current, which is a useful information for designing compensating circuits to mitigate its effect [27]. Good sensor design, thus, increases the reliability of the overall electric drive system.

In recent years, some advanced techniques, which are suitable for high power MOSFET modules, have been developed [22]-[26]. In [22], a current sensing circuit for short-circuit protection based on parasitic inductances of the power MOSFET module has been presented. The concept has been applied and extended for both short-circuit and overload protection in [25]. For both works [22],[25], although good protection can be achieved, the current waveforms cannot be recovered due to the high-pass filter characteristic that rejects all low frequency components in the measured current. In [26], switch current sensor for 1.7 kV power MOSFET model based on Rogowski coil is developed. The work [24] further extends the design for both switching current sensing and phase current reconstruction under both continuous and discontinuous modulations. One of the main disadvantages of current sensors based on Rogowski coil [24],[26] is the complexity in PCB design.

An additional drawback of all aforementioned designs is the limit in operating temperature. For example, the stated maximum operating temperature of [25] is 105°C.

Based on pros and cons of existing current sensors, there is a need for an enhanced design that has the following features:

- based on module parasitics, which is much simpler than Rogowski coil, while still enables switching current sensing and protection, and phase current reconstruction;
- overcome limit of previous designs in terms of temperature. Operating temperature is expected to be up to 200°C.

Besides switching current sensors and construction, common-mode current sensors based on parasitics and DC-bus voltage sensor for high temperature will also be developed.

## 2. Designs of Phase-leg Power-stage Packages and Gate Drivers

### 2.1. SiC Power-stage Package design

We chose to start the high-temperature power-stage packaging effort by designing and fabricating packages of SiC MOSFET (1200 V, 13 mΩ, 149 A) from CREE. We have been in communication with Dr. Gui-Jia Su at Oak Ridge National Lab to ensure that the designed switching cells once packaged can be inserted into his testbed for evaluation. Figure I.23.5 shows the layout of the half-bridge power stage. The overall dimensions are 17.5 mm\*17.3 mm\*3.6 mm. Two SiC MOSFETs were placed on the bottom substrate and six metal posts were used to interconnect top substrate. All the terminals were designed on one side and the connectors for gate drivers and protections were on the other side as shown in Figure I.23.6. The parasitic inductance of this power module was simulated by ANSYS Q3D. The parasitic inductances of power loop and drive loop were 4.67 and 3.44 nH, respectively. Electrical, thermal, and thermos-mechanical field analysis of this module will be conducted and the module will be fabricated and tested in the on-going work.

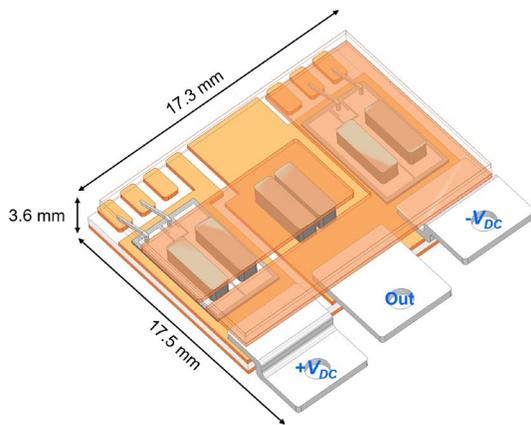


Figure I.23.5. The layout design of a 1.2kV, 149 A SiC MOSFET planar module with double-side cooling.

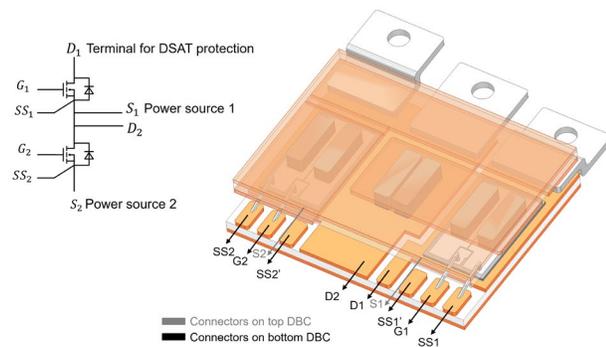


Figure I.23.6. Terminals of the power module for gate driver and current sensor.

## 2.2. Gate driver and power supply

The gate driver circuit board will utilize the SOI gate driver IC from Cissoid. Peripheral circuits using high temperature components will be designed for the IC and a PCB will be made with compact design to fit with the design of the single-phase module. High-temperature test setup will be investigated. Air-core transformer for the power supply will be designed and optimized.

## 2.3. Current sensor

Figure I.23.7 shows the equivalent circuit of one power MOSFET model and circuit for current sensing with short-circuit protection and current reconstruction.

It is seen from Figure I.23.7 (a) that there is a stray inductance, denoted as  $L_d$ , between the  $(+V_{dc})$  terminal and  $(D_1)$  terminal of the power module. Assume the inductor current is  $i_d$ . If its voltage is input to the integral circuit in Figure I.23.7 (b), the obtained output voltage after the first Op-amp is as follows:

$$v_{o1} = L_d i_d / RC \quad (1)$$

where R and C are the resistance and inductance, respectively, of the integral circuit.

The second Op-amp is utilized as a voltage follower circuit, which created large input impedance so that variation in impedance caused by the processing circuit after it does not affect the output voltage.  $v_{o1}$  is then input to a low-pass filter to attenuate the ringing in its waveform. Using the third Op-amp, the signal is then compared with a threshold voltage for short-circuit protection. The current sensor for the lower MOSFET is similar to that of the upper MOSFET, except that the input to the first Op-amp is the voltage from Kelvin source terminal ( $SS_2$ ) to Power source terminal ( $-V_{dc}$ ). In order to create the same ground for outputs of upper and lower sensors, it is necessary to use isolation amplifiers. The signals after the isolation amplifiers are input to a subtractor to reconstruct the phase current.

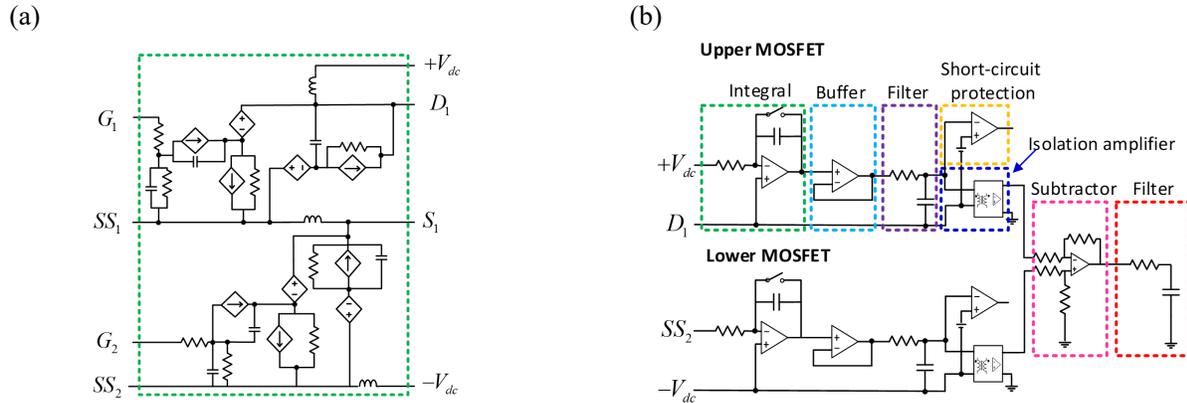


Figure I.23.7. (a) Equivalent circuit of power MOSFET model, and (b) Current sensing with short-circuit protection and current reconstruction.

The common-mode current can be obtained by using information of current sensors in three phases. Assume the upper MOSFET currents and lower MOSFET currents of three phase are  $(i_{d1}, i_{d2}, i_{d3})$  and  $(i_{s1}, i_{s2}, i_{s3})$ . Then the common-mode current can be obtained as follows:

$$i_{cm} = (i_{d1} + i_{d2} + i_{d3}) - (i_{s1} + i_{s2} + i_{s3}) \quad (2)$$

Based on theoretical analysis of the sensors described above, experimental circuits can be built. In order to verify the working principle, the circuit will be firstly designed for commercial power MOSFET modules with low-temperature operation. After that, the designs will be further modified for high temperature.

A simulation model of a two-level inverter with  $RL$  load is built on SIMPLIS to verify the operating principle of the current sensor circuit. The simulation parameters are as follows:  $V_{dc} = 1 \text{ kV}$ , switching frequency  $f_s = 20 \text{ kHz}$ , load resistance and inductance:  $R_{load} = 2.5 \Omega$ ,  $L_{load} = 0.5 \text{ mH}$ . The inductances from  $(+V_{dc})$  to  $(D_1)$  terminal of the power MOSFET module is  $7.34 \text{ nH}$ , while one from  $(SS_2)$  to  $(-V_{dc})$  is  $2.36 \text{ nH}$ .

With negligible resistances of stray inductors, good switching currents and reconstructed current are obtained as in Figure I.23.8, Figure I.23.9, and. Figure I.23.10 shows the output signal that triggers the system to shut down when there is a short circuit event caused by switching on both upper and lower MOSFETs of the power module. In a real circuit implementation, in order to have fast response time of the trigger signal, high bandwidth commercial Op-amps should be selected.

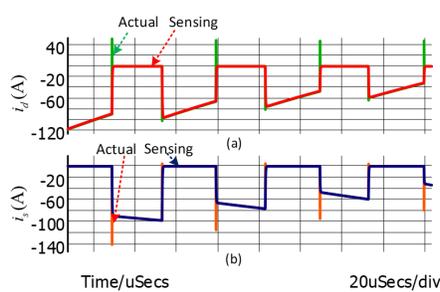


Figure I.23.8. Sensor waveforms (scaled) in comparison to the actual current waveforms.

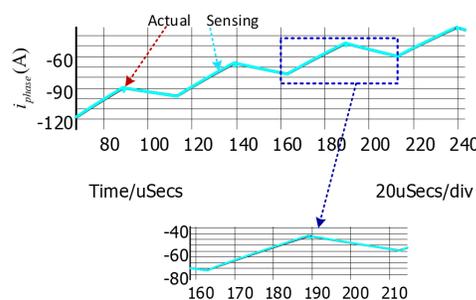


Figure I.23.9. Reconstructed current waveform.

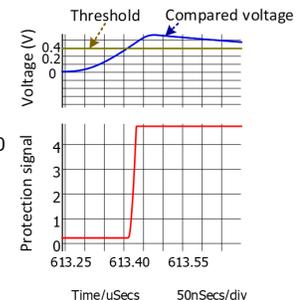


Figure I.23.10. Short-circuit protection.

## Conclusions

Literature surveys were conducted to gain knowledge on the state-of-the-art technologies of high temperature packaging materials, gate driver and power supply, passive components, and current sensor with protection and reconstruction. A half-bridge SiC planar power stage module was designed and analyzed for parasitic

inductances. The high temperature gate driver IC has been selected and passive components of the peripheral circuits have been compared. The operating principle of switching current sensor and common-mode current sensor based on model parasitics have been investigated. Theoretical analysis has been verified by simulation results.

## References

1. Fukumoto, Akihisa, David Berry, Khai D. T. Ngo, and Guo-Quan Lu. "Effects of Extreme Temperature Swings on Silicon Nitride Active Metal Brazing Substrates." *IEEE transactions on device and materials reliability* 14, no. 2 (2014): 751-56.
2. Lei, Thomas Guangyin, Jesus Noel Calata, Khai D. T. Ngo, and Guo-Quan Lu. "Effects of Large-Temperature Cycling Range on Direct Bond Aluminum Substrate." *IEEE Transactions on Device and Materials Reliability* 9, no. 4 (2009): 563-68.
3. Dong, Guangcheng, Guangyin Lei, Xu Chen, Khai Ngo, and Guo-Quan Lu. "Edge Tail Length Effect on Reliability of Dbc Substrates under Thermal Cycling." *Soldering & Surface Mount Technology* 21, no. 3 (2009): 10-15.
4. Schulz-Harder, Juergen, and Karl Exel. "Recent Developments of Direct Bonded Copper (Dbc) Substrates for Power Modules." 2003.
5. Yu, Fang, Jinzi Cui, Zhangming Zhou, Kun Fang, R. Wayne Johnson, and Michael C. Hamilton. "Reliability of Ag Sintering for Power Semiconductor Die Attach in High-Temperature Applications." *IEEE Transactions on Power Electronics* 32, no. 9 (2016): 7083-95.
6. Schneider-Ramelow, Martin, and Christian Ehrhardt. "The Reliability of Wire Bonding Using Ag and Al." *Microelectronics Reliability* 63 (2016): 336-41.
7. Yamada, Yasushi, Yoshikazu Takaku, Yuji Yagi, I. Nakagawa, T. Atsumi, M. Shirai, I. Ohnuma, and K. Ishida. "Reliability of Wire-Bonding and Solder Joint for High Temperature Operation of Power Semiconductor Device." *Microelectronics Reliability* 47, no. 12 (2007): 2147-51.
8. Jacques, Sebastien, René Leroy, and Marc Lethiecq. "Impact of Aluminum Wire and Ribbon Bonding Technologies on D2pak Package Reliability During Thermal Cycling Applications." *Microelectronics reliability* 55, no. 9-10 (2015): 1821-25.
9. Yao, Yiying, Guo-Quan Lu, Dushan Boroyevich, and Khai D. T. Ngo. "Survey of High-Temperature Polymeric Encapsulants for Power Electronics Packaging." *IEEE Transactions on Components, Packaging and Manufacturing Technology* 5, no. 2 (2015): 168-81.
10. Yao, Yiying. "Thermal Stability of Al<sub>2</sub>O<sub>3</sub>/Silicone Composites as High-Temperature Encapsulants." Virginia Tech, 2014.
11. Barlow, Matthew, Shamim Ahmed, Anthony Matthew Francis, and Alan Homer Mantooth. "An Integrated Sic Cmos Gate Driver for Power Module Integration." *IEEE Transactions on Power Electronics* (2019).
12. Whitaker, Bret, Zach Cole, Brandon Passmore, Daniel Martin, Ty McNutt, Alex Lostetter, M. Nance Ericson, et al. "High-Temperature Sic Power Module with Integrated Sic Gate Drivers for Future High-Density Power Electronics Applications." 2014.
13. Nayak, Parthasarathy, Sumit Kumar Pramanick, and Kaushik Rajashekara. "A High-Temperature Gate Driver for Silicon Carbide Mosfet." *IEEE Transactions on Industrial Electronics* 65, no. 3 (2017): 1955-64.

14. Huque, M. A., S. K. Islam, B. J. Blalock, C. Su, R. Vijayaraghavan, and L. M. Tolbert. "Silicon-on-Insulator Based High-Temperature Electronics for Automotive Applications." 2008.
15. Huque, Mohammad A., Syed K. Islam, Leon M. Tolbert, and Benjamin J. Blalock. "A 200 C Universal Gate Driver Integrated Circuit for Extreme Environment Applications." *IEEE Transactions on Power Electronics* 27, no. 9 (2012): 4153-62.
16. Pressman, Abraham. *Switching Power Supply Design*. McGraw-Hill, Inc., 1997.
17. Ponzo, G. M., G. Capponi, P. Scalia, and V. Boscaino. "An Improved Flyback Converter." 2009.
18. Sun, Bingyao, Rolando Burgos, and Dushan Boroyevich. "Ultralow Input–Output Capacitance Pcb-Embedded Dual-Output Gate-Drive Power Supply for 650 V Gan-Based Half-Bridges." *IEEE Transactions on Power Electronics* 34, no. 2 (2018): 1382-93.
19. Zhang, Zhiliang, Ke Xu, Zhi-Wei Xu, Jiahua Xu, Xiaoyong Ren, and Qianhong Chen. "Gan Vhf Converters with Integrated Air-Core Transformers." *IEEE Transactions on Power Electronics* 34, no. 4 (2018): 3504-15.
20. Orlandi, Stefano, Bruno Andre Allongue, Georges Blanchot, Simone Buso, Federico Faccio, Cristian Alejandro Fuentes, Maher Kayal, Stefano Michelis, and Giorgio Spiazzi. "Optimization of Shielded Pcb Air-Core Toroids for High-Efficiency Dc–Dc Converters." *IEEE Transactions on Power Electronics* 26, no. 7 (2010): 1837-46.
21. Liang, Wei, Luke Raymond, Lei Gu, and Juan Rivas. "27.12 Mhz Gan Resonant Power Converter with Pcb Embedded Resonant Air Core Inductors and Capacitors." 2015.
22. Awwad, Abdullah Eial, and Sibylle Dieckerhoff. "Short-Circuit Evaluation and Overcurrent Protection for Sic Power Mosfets." 2015.
23. John, Vinod, Bum-Seok Suh, and Thomas A. Lipo. "Fast-Clamped Short-Circuit Protection of Igbt's." *IEEE Transactions on Industry Applications* 35, no. 2 (1999): 477-86.
24. Mocevic, Slavko, Jun Wang, Rolando Burgos, Dushan Boroyevich, Marko Jaksic, Mehrdad Teimor, and Brian Peaslee. "Phase Current Reconstruction Based on Rogowski Coils Integrated on Gate Driver of Sic Mosfet Half-Bridge Module for Continuous and Discontinuous Pwm Inverter Applications." 2019.
25. Sun, Keyao, Jun Wang, Rolando Burgos, and Dushan Boroyevich. "Design, Analysis, and Discussion of Shortcircuit and Overload Gate-Driver Dual-Protection Scheme for 1.2 Kv, 400 a Sic Mosfet Modules." *IEEE Transactions on Power Electronics* (2019).
26. Wang, Jun, Zhiyu Shen, Rolando Burgos, and Dushan Boroyevich. "Integrated Switch Current Sensor for Shortcircuit Protection and Current Control of 1.7-Kv Sic Mosfet Modules." 2016.
27. Wang, Shuo, Yoann Yorrick Maillet, Fei Wang, Dushan Boroyevich, and Rolando Burgos. "Investigation of Hybrid Emi Filters for Common-Mode Emi Suppression in a Motor Drive System." *IEEE Transactions on Power Electronics* 25, no. 4 (2009): 1034-45.

### Acknowledgements

We are grateful to Dr. Gui-Jia Su of Oak Ridge National Laboratory (ORNL) for introducing us to his segmented three-phase inverter technology and working with us to better design our SiC power modules. He will also support us with the testing of our power modules in his testbed at ORNL.

## I.24 Integrated Motor and Drive for Traction Application (University of Wisconsin – Madison)

### Bulent Sarlioglu

University of Wisconsin – Madison  
1415 Engineering Drive  
Madison, WI 53706  
E-mail: [sarlioglu@wisc.edu](mailto:sarlioglu@wisc.edu)

### Susan Rogers, DOE Technology Development Manager

U.S. Department of Energy  
E-mail: [susan.rogers@ee.doe.gov](mailto:susan.rogers@ee.doe.gov)

Start Date: April 1, 2019

End Date: April 1, 2024

Project Funding (FY19): \$300,000

DOE share: \$300,000

Non-DOE share: \$0

### Project Introduction

The objective of the project is to research, design, develop, and test a high-performance traction motor and a high-efficiency traction inverter, and then to combine them into a state-of-the-art integrated motor drive (IMD) that requires only a single housing for use in vehicle applications.

The new IMD system will significantly increase the motor and inverter power density values to meet the aggressive DOE targets while simultaneously reducing their cost. The high-power-density, reduced-cost prototype IMD will become a valuable source of technical data that can be used by automakers and their suppliers to improve the performance of future EV traction drive systems.

### Objectives

This project has two separate sets of performance targets for the power electronics and motor in Table I.24.1.

**Table I.24.1 Power Electronics and Motor Requirements**

Power Electronics Requirement	
Parameter	Measure
Cost (\$/kW)	$\leq 2.7$
Peak Power Density (kW/L)	$\geq 100$
System Peak Power Rating (kW)	100
Electric Motor Requirement	
Parameter	Measure
Cost (\$/kW)	$\leq 3.3$
Peak Power Density (kW/L)	$\geq 50$
System Peak Power Rating (kW)	100



## Approach

This project begins with an evaluation of several types of electric motors and inverters that are candidates for future land-based vehicle traction applications. The evaluation results will lead to selection of the most desirable machine plus inverter topology that will then be developed into a working state-of-the-art prototype integrated motor drive (IMD) during the remainder of the project.

During Budget Period #1, a literature review is being carried out that sets the stage for trade-off studies to evaluate several alternative motors and inverters that are candidates for adoption in the target integrated motor drive system. The motor configurations as well as the power inverter topologies are being compared, leading to selection of the most promising motor and power electronic inverter candidates for further development.

During Budget Period #2, a preliminary motor electromagnetic design and power electronics electrical design will be carried out for the selected motor and power inverter topologies. A bench-top inverter will be designed, fabricated, and tested to verify key IMD concepts and reduce technical risks. In addition, we will also carry out thermal and mechanical designs of the motor and inverter, including their physical integration into an IMD.

During Budget Period #3, the IMD design will be finalized in preparation for prototype component construction. The final design of the IMD will be carried out, leading to a final design review. The prototype machine and inverter will be fabricated and tested individually. A dynamometer test-stand will be designed and assembled, including instrumentation for testing the motor and power inverter.

During Budget Period #4, the motor and power inverter will be integrated into the same IMD enclosure and made operational. Initial tests will then be carried out to demonstrate functionality of the prototype IMD.

During Budget Period #5, the combined prototype IMD system will be tested. The IMD performance will be measured to verify the ability of the prototype IMD to meet its performance targets.

## Results

### *1. Investigation of Various Traction Drive System Peak Power Densities*

The objective of this project is to achieve high-power-density traction drive systems ( $\geq 100$  kW/L for power electronics,  $\geq 50$  kW/L for motors). However, when the power density of power electronics and motors are considered separately, it is possible to maximize the power density of either the motor or power electronics individually by sacrificing the power density of the other. In Table I.24.2, the 2017 Toyota Prius exhibits the highest inverter peak power density when the volume of the dc/dc boost converter is excluded. Nevertheless, the calculated peak power density of the combined motor plus inverter for the 2017 Toyota Prius is lower than that of the 2014 Honda Accord. Therefore, to increase the total power density of the traction drive system, both the power electronics and motor should be considered in an integrated manner. The last column includes a 2025 peak power density target value for the integrated motor drive (33.3 kW/L) which is derived by combining the separate peak power density target values of the inverter and motor that are also provided in the last column.

**Table I.24.2 Production Electric Vehicle Power Density Metrics [1]-[3]**

	2012 Nissan Leaf	2014 Honda Accord	2016 BMW i3	2017 Toyota Prius	2025 DOE Target
Inverter Peak Power Density [kW/L]	5.7	12.1 (18.5)	18.5	11.5 (21.7)	$\geq 100$
Motor Peak Power Density [kW/L]	4.2	8.5	9.1	5.7	$\geq 50$

Combined Motor+Inverter Peak Power Density [kW/L]	2.42	4.99 (5.82)	6.10	3.81 (4.51)	≥ 33.3
Values in parenthesis mean the power density when the volume of dc/dc boost converter is excluded					

### Identified Benefits of Integrated Motor Drive for Traction Applications

There are several valuable benefits provided by IMDs that are motivating the automotive industry to favor this configuration for their future hybrid- and battery-electric vehicles, summarized as follows [4]:

- **Enclosure mass/volume/cost reduction:** All power electronics and machine are combined into a single enclosure, providing the basis for a substantial reduction in traction drive system volume, mass, and cost.
- **Motor cable elimination:** IMD technology eliminates the bulky high-voltage cables connecting the inverter output terminals to the motor terminals. This approach not only reduces the cost of the system by eliminating the expensive cables and connectors, but also helps to suppresses motor terminal overvoltage and EMI problems associated with long cables excited by inverters that use wide-bandgap (WBG) power switches.
- **Compatibility with motors with high phase/terminal numbers:** Motor configurations with high phase or terminal numbers require additional cables and connectors to connect the motor to a conventional inverter in a separate enclosure. The IMD eliminates this disadvantage, making it more practical to consider these special motor topologies as candidates for minimizing torque ripple and raising the drive's fault tolerance.
- **Compatibility with motor/inverter modularization:** A special type of IMD known as an *integrated modular motor drive* (IMMD) is shown in Figure I.24.1. This high level of inverter and motor modularization offers benefits for manufacturing scalability as well as enhanced fault tolerance of the traction drive system.
- **Integrated cooling systems:** The IMD is compatible with integrated cooling systems that combine the thermal dissipation path that cools both the motor and the inverter, reducing its volume, mass, and cost.

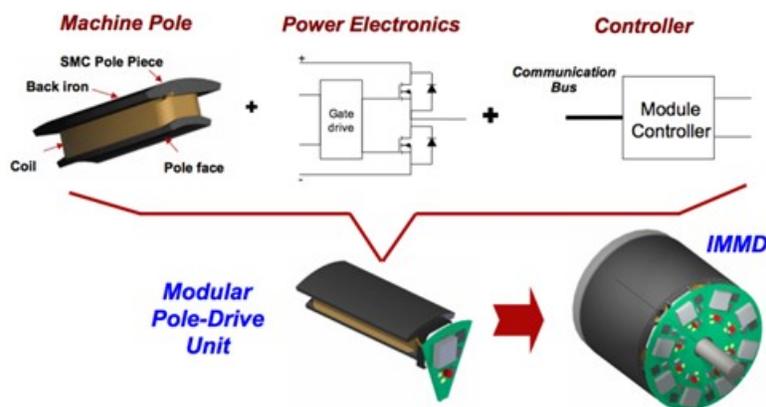


Figure I.24.1 Integrated Modular Motor Drive (IMMD) concept [4]

### Identified Challenges of Integrated Motor Drives

However, integrating motor drive system to motor imposes new technical challenges which must then be resolved throughout this project. Following lists are the major issues of IMD that we identified. [5]

- Thermal management:** The IMD configuration imposes higher thermal challenges for cooling the power electronics when it is integrated with the motor into a single enclosure. Hot spots in traction motors can reach 180°C which is higher than the maximum temperature that can be tolerated by most of the inverter components. Shielding the inverter from unacceptably high motor temperatures under all operating conditions requires innovative design of the IMD cooling system, aided by the adoption of advanced heatsink materials and manufacturing technology.
- Vibration:** The IMD configuration exposes the drive electronics to a more demanding mechanical stress environment due to motor vibration and thermal excursions. Special care is required to isolate the power electronics from the peak mechanical and thermal stresses generated by the motor, as well as to adopt mechanical design techniques and materials that ruggedize the inverter to better suit its environment.
- EMI:** Placement of the inverter so close to the motor exposes it to high-amplitude, high-frequency electromagnetic fields that create threats of damaging interference with the power electronics operation. Here again, special design techniques for shielding and ruggedizing the power electronics is required to protect it from the impact of these high-intensity magnetic fields.

**Classifications of Integrated Motor Drive Topologies**

While there are a near-infinite number of ways to design integrated motor drives, IMDs can be categorized into four major physical topologies which are: 1) radial housing mount (RHM); 2) axial housing mount (AHM); axial stator mount (ASM); and radial stator mount (RSM) as illustrated in Figure I.24.2 (a), (b), (c), and (d), respectively. The power electronics is more intimately integrated with the machine in the two stator-mount topologies. While stator mounting of the power electronics helps to minimize the IMD mass and volume, it increases the thermal, mechanical, and EMI challenges by bringing the power electronics into closer proximity with the motor. Advantages and challenges associated with the IMD topologies are summarized in Table I.24.3.

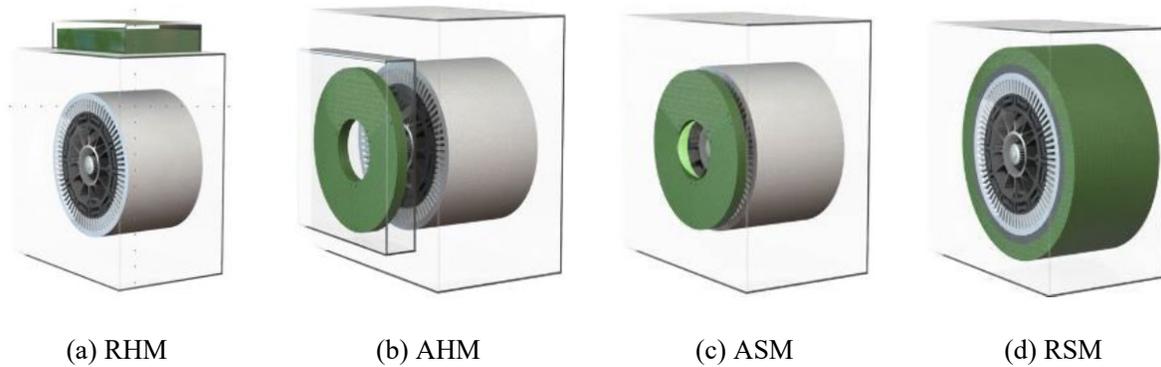


Figure I.24.2 IMD Topologies [6],[7]

**Table I.24.3 Key Advantages/Disadvantages of Major IMD Topologies [6],[7]**

	Advantages	Challenges
<b>RHM</b>	Thermal isolation between motor and inverter Low implementation risks	Separate enclosures for motor and inverter Higher mass and volume
<b>AHM</b>	Thermal isolation between motor and inverter Low implementation risks	Separate enclosures for motor and inverter Higher mass and volume
<b>ASM</b>	Lower mass and volume	Inverter exposed to heat & EMI from end windings

	Convenient access of inverter to windings	Generally smaller inverter footprint than RSM
<b>RSM</b>	Lower mass and volume Convenient access to stator cooling jacket	Peripheral configuration requires special mounting Access to windings less convenient than ASM

## 2. Comparison Analysis between VSI and CSI

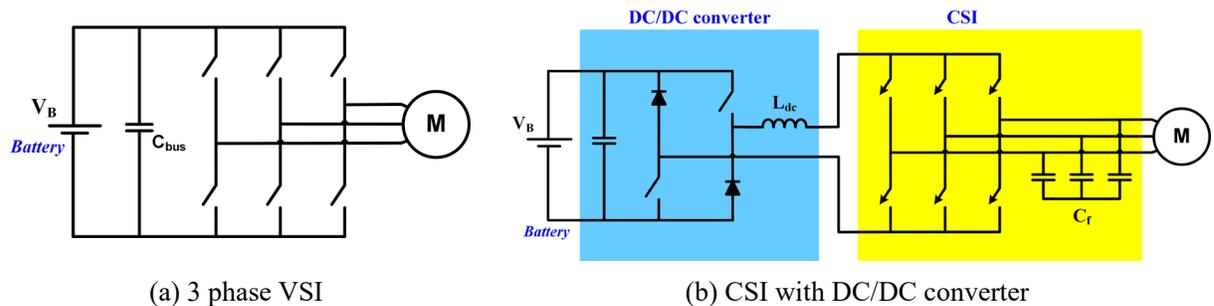


Figure I.24.3 Alternative traction inverter drive configurations: a) VSI excitation; and b) CSI excitation

The three-phase voltage source inverter (VSI) shown in Figure I.24.3 (a) is the dominant inverter configuration used in electric traction drives today. However, the three-phase current source inverter (CSI) shown in Figure I.24.3 (b) offers some advantages over the VSI for integrated motor drive applications. The CSI replaces the VSI's thermally-limited dc-link capacitor ( $<150^{\circ}\text{C}$ ) with a higher-temperature inductor ( $>200^{\circ}\text{C}$ ) as an energy storage element, improving the inverter's compatibility with the IMD's high-temperature limits. The three small capacitors connected to the CSI's output terminals function naturally as a low-pass filter in combination with the dc bus inductors, resulting in much more sinusoidal output voltage waveforms and lower common-mode EMI compared to the VSI, as shown in the simulated waveforms provided in Figure I.24.4. The built-in lower-pass filter helps to reduce the motor's PWM core losses and common-mode EMI, its overvoltage risks at the motor terminals, and potential bearing failures caused by  $dv/dt$ -induced bearing currents.

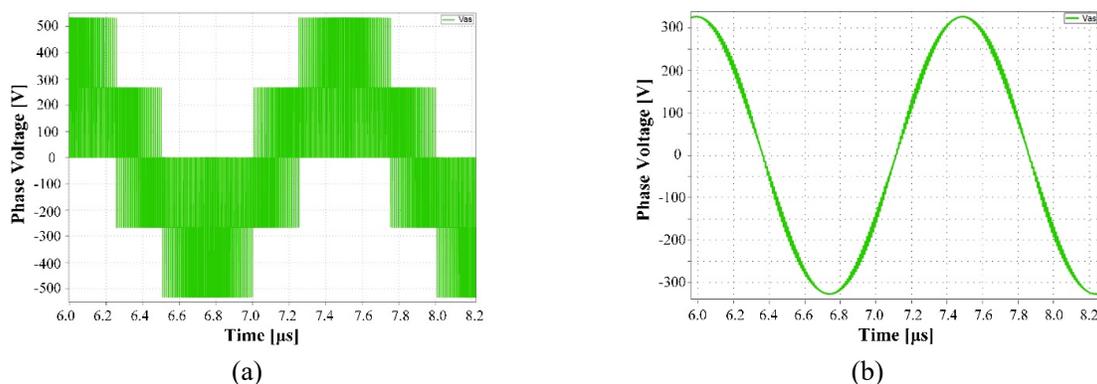


Figure I.24.4 Typical line-to-neutral voltage waveforms for (a) VSI and (b) CSI

Another notable advantage of the CSI over VSI in traction drive applications is the CSI's natural output voltage boost function. While the theoretical peak phase-neutral voltage of the VSI is limited to  $0.637 V_{dc}$ , the CSI can deliver higher output voltage due to its boosting characteristics. This voltage-boosting feature of the CSI offers multiple advantages for traction drive application: (1) When the battery voltage drops, the CSI can boost the output voltage to maintain the same output power, while the VSI needs a front-end boost converter (as Toyota uses); (2) the voltage boost function of the CSI can be used to extend the constant power operation region to achieve a higher CPSR than the VSI; and (3) voltage boosting can be used to control the motor's power factor at high speed to help maximize its efficiency while reducing the CSI's current rating.

**Table I.24.4 Calculated Efficiency Comparison of VSI and CSI Power Converters**

RPM	Output Power (kW)	Efficiency of VSI (%)	Efficiency of CSI (%)	Efficiency of CSI + DC/DC (%)
3200	55	99.09	99.13	98.87
3200	100	98.58	98.56	98.17
20000	100	98.71	98.68	98.22

Assumptions: The “MOSFET+Diode” hybrid RB switch is used for CSI, and the inductor and capacitor losses are ignored for this comparison

To investigate the value of this CSI voltage boosting feature, a new traction motor with higher rated voltage and lower rated current compared to the VSI machine has been designed to take fuller advantage of the CSI’s capabilities. Note that the efficiency comparison between VSI and CSI in Table I.24.4 is based on different motors because of the different voltage limits. The CSI-based motor is designed with higher number of turns per slot than the VSI-based motor to obtain a higher back-EMF. The current density between the two motors are also kept same for fair thermal constraints. The third and fourth columns of this table show that the predicted efficiencies of the VSI and CSI power stages are nearly identical.

However, a controlled front-end dc/dc converter is required in the CSI to convert a voltage source (battery) to a current source as shown in Figure I.24.3 (b). The presence of this additional power conversion stage slightly decreases the overall CSI efficiency by 0.5% or less as shown in the Table I.24.4. However, the net impact of this change on the IMD efficiency requires a more detailed system level efficiency analysis because the CSI-connected motor will operate more efficiently than its VSI counterpart due to lower PWM-based core losses. When these PWM losses are incorporated into the total IMD loss calculations, it is expected that total IMD losses will be comparable for the VSI- and CSI-based cases.

One of the challenges posed by the CSI is that it requires switches that can block reverse voltage, a feature not provided by standard silicon power switches (e.g., IGBTs, MOSFETs). Typical voltage and current waveforms for switches in the CSI and VSI are shown in Figure I.24.5. when the switching frequency is 100 kHz. As expected, the switch in the VSI must be able to conduct current in both directions while it is required to block the voltage in only one direction. In comparison, the switch in CSI is required to conduct current in one direction while it must be capable of blocking voltage in both directions. Several power device manufacturers are in the process of developing monolithic WBG power switches that provide reverse voltage blocking (RB) capability. Until these devices become commercially available, high-performance hybrid WBG power switches that consist of two WBG switches connected in anti-series [9] are being used in CSI development programs to provide the required RB switches.

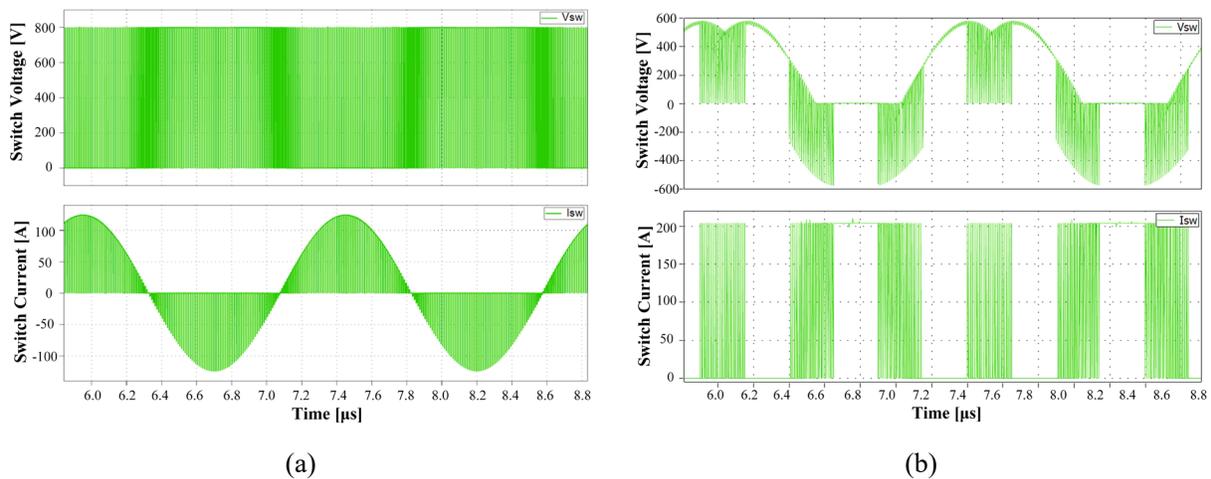


Figure I.24.5 Typical switch voltage and current waveforms for (a) VSI and (b) CSI

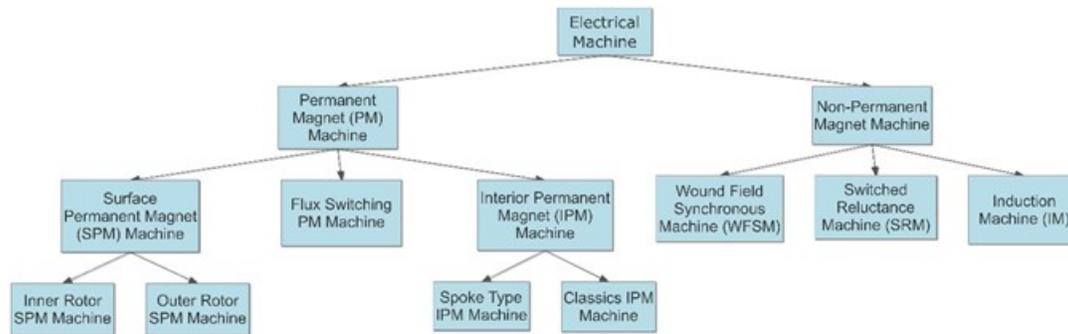


Figure I.24.6 Electric machine categorization segregating machine types with and without permanent magnets

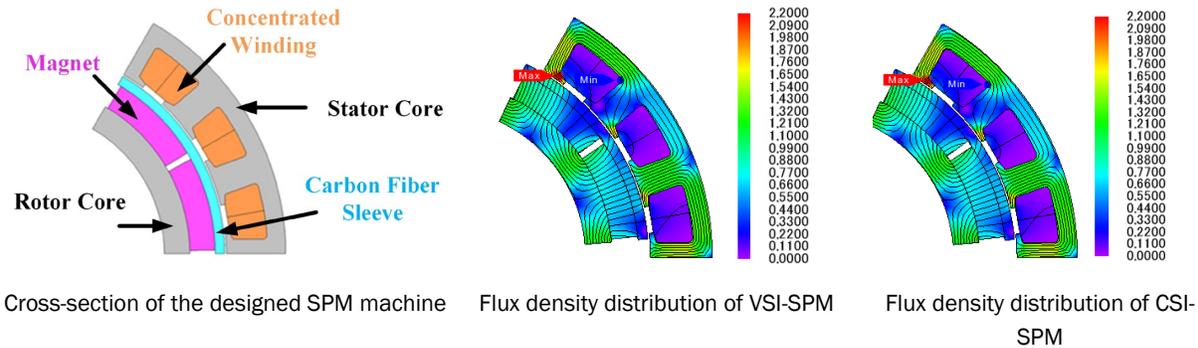
### 3. Candidate Machine Evaluation and CSI/VSI Flux-Weakening Performance Comparison

There are many ways to categorize electric machines. One metric is whether there a machine type includes permanent magnets or not. Figure I.24.6 shows a categorization tree for electric machines that focuses on the incorporation of permanent magnets. The surface permanent magnet (SPM) machine is known for high power density. Therefore, an SPM machine with 100 kW peak output power and 55 kW continuous power has been designed during the first-year reporting period. In addition to high power density, this design achieves a constant power speed ratio (CPSR) of 6.25 for 55 kW power delivery that is desired as part of the 2025 traction drive targets. To achieve this performance, the thickness of the surface mount magnets is 12 mm and airgap thickness is 0.8 mm. In order to contain the magnets on the spinning rotor, a carbon sleeve was selected for this motor. The minimum thickness for retaining the magnets has been calculated to be 4.5 mm. The corner speed of the motor design is 3,200 rpm while the maximum speed is 20,000 rpm.

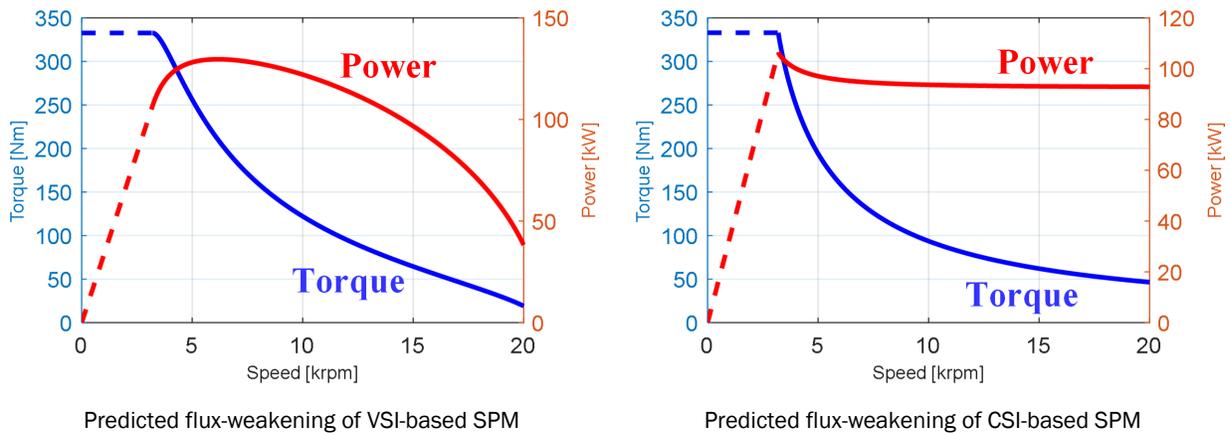
The flux-weakening performance of this SPM machine under both VSI and CSI excitation with the capability of achieving the desired CPSR value of 6.25 are compared in Figure I.24.7. The CSI-based SPM machine has the identical stator and rotor geometry as the VSI-based SPM machine except for a larger number of turns that raise its back-EMF and lower its rated current. For the VSI-based motor large negative d-axis current needs to be applied to the motor during flux weakening operation in order to keep the motor output voltage below the VSI inverter voltage limit. This operating mode decreases its power factor and limits the CPSR.

In contrast, the CSI motor voltage is designed to be higher than that of the VSI motor because the CSI operates as a boost-type inverter, freeing it from the dc bus voltage limit imposed by the naturally buck-type VSI. As a result, the CSI can raise the motor terminal voltage above the dc link voltage during flux weakening operation,

enabling it to achieve an extended constant-power speed range. Operating the machine at a higher terminal voltage makes it possible to reduce the negative  $d$ -axis current amplitude during flux-weakening operation. Lowering the required current in the CSI reduces the motor conduction losses, improving the efficiency of the CSI-based traction motor drive. As a result of this feature, the CSI-based drive is predicted to be capable of delivering more than twice as much power at 20,000 rpm as the VSI-based drive (i.e., 92 kW vs. 40 kW), a highly-significant advantage for this traction drive application that is being explored in more detail.



Cross-section of the designed SPM machine    Flux density distribution of VSI-SPM    Flux density distribution of CSI-SPM



Predicted flux-weakening of VSI-based SPM    Predicted flux-weakening of CSI-based SPM

Figure I.24.7 Flux-weakening performance comparison of the CSI-excited and VSI-excited SPM machines for CPSR=6.25

### Conclusions

This report has provided a summary of key findings developed to date during the first year of the project. The topics addressed in this report include literature review and key traction drive requirements, benefits and challenges of integrated motor drives, and an initial assessment of attainable motor drive performance and its dependence on the design of both the motor and power electronics. It is important to emphasize that this project is squarely focused on advancing the integrated motor drive (IMD) concept, making it critical to simultaneously address the motor and the inverter as a system that is being optimized. The appealing advantages of the IMD concept have been highlighted together with the significant technical challenges that must be overcome in order to achieve IMD designs that are suitable for adoption in future production electric vehicles.

Several machine types with and without permanent magnets are being considered as candidates for the advanced traction drive system. This report highlighted preliminary results from the design of a surface permanent magnet (SPM) motor that can deliver the desired constant-power speed ratio (CPSR) value of 6.25. An important observation that emerged from this work is that CSI excitation of this SPM motor can achieve significantly enhanced CPSR capability compared to VSI excitation because of the inherent voltage-boost

feature of CSIs. The implications of this comparison will be evaluated more thoroughly during the next phase of this project. In addition, other machine types beyond the SPM topology will be evaluated to set the stage for choosing the best motor-inverter combination for upcoming IMD design activities planned for Year 2.

## References

1. Burress, Tim. “Electrical Performance, Reliability Analysis, and Characterization.” Oak Ridge National Laboratory, 2017. [https://www.energy.gov/sites/prod/files/2017/06/f34/edt087\\_burress\\_2017\\_o.pdf](https://www.energy.gov/sites/prod/files/2017/06/f34/edt087_burress_2017_o.pdf).
2. Burress, Tim. “Benchmarking State-of-the-Art Technologies”, Oak Ridge National Laboratory, 2013. [https://www.energy.gov/sites/prod/files/2014/03/f13/ape006\\_burress\\_2013\\_o.pdf](https://www.energy.gov/sites/prod/files/2014/03/f13/ape006_burress_2013_o.pdf).
3. Burress, Tim. “*Benchmarking EV and HEV Technologies*,” Oak Ridge National Laboratory, 2016. [https://energy.gov/sites/prod/files/2016/06/f32/edt006\\_burress\\_2016\\_o\\_web.pdf](https://energy.gov/sites/prod/files/2016/06/f32/edt006_burress_2016_o_web.pdf).
4. Jahns, Thomas M., and Hang Dai. “The Past, Present, and Future of Power Electronics Integration Technology in Motor Drives.” CPSS Transactions on Power Electronics and Applications 2, no. 3 (2017): 197–216. <https://doi.org/10.24295/cpsstpea.2017.00019>.
5. Shea, Adam M., and T. M. Jahns. “Hardware Integration for an Integrated Modular Motor Drive Including Distributed Control.” 2014 IEEE Energy Conversion Congress and Exposition (ECCE), 2014. <https://doi.org/10.1109/ecce.2014.6954070>.
6. Lee, Woongkul, Silong Li, Di Han, Bulent Sarlioglu, Tatiana A. Minav, and Matti Pietola. “A Review of Integrated Motor Drive and Wide-Bandgap Power Electronics for High-Performance Electro-Hydrostatic Actuators.” IEEE Transactions on Transportation Electrification 4, no. 3 (2018): 684–93. <https://doi.org/10.1109/tte.2018.2853994>.
7. Chowdhury, Shajjad, Emre Gurpinar, Gui-Jia Su, Tsarafidy Raminosa, Timothy A. Burress, and Burak Ozpineci. “Enabling Technologies for Compact Integrated Electric Drives for Automotive Traction Applications.” 2019 IEEE Transportation Electrification Conference and Expo (ITEC), 2019. <https://doi.org/10.1109/itec.2019.8790594>.
8. Tang, Lixin, and Gui-Jia Su. “Boost Mode Test of a Current-Source-Inverter-Fed Permanent Magnet Synchronous Motor Drive for Automotive Applications.” 2010 IEEE 12th Workshop on Control and Modeling for Power Electronics (COMPEL), 2010. <https://doi.org/10.1109/compel.2010.5562430>.
9. Dai, Hang, Renato A. Torres, Thomas M. Jahns, and Bulent Sarlioglu. “Characterization and Implementation of Hybrid Reverse-Voltage-Blocking and Bidirectional Switches Using WBG Devices in Emerging Motor Drive Applications.” 2019 IEEE Applied Power Electronics Conference and Exposition (APEC), 2019. <https://doi.org/10.1109/apec.2019.8721910>.



## I.25 Multi-Objective Design Optimization of 100 kW Non-Rare-Earth or Reduced-Rare Earth Machines (Purdue University)

### Scott Sudhoff, Principal Investigator

Purdue University  
1285 Northwestern Avenue  
West Lafayette, IN 47906  
E-mail: [sudhoff@purdue.edu](mailto:sudhoff@purdue.edu)

### Steve Pekarek, Co-Principal Investigator

Purdue University  
1285 Northwestern Avenue  
West Lafayette, IN 47906  
E-mail: [spekarek@purdue.edu](mailto:spekarek@purdue.edu)

### Susan Rogers, DOE Technology Development Manager

U.S. Department of Energy  
E-mail: [susan.rogers@ee.doe.gov](mailto:susan.rogers@ee.doe.gov)

Start Date: May 15, 2019	End Date: May 14, 2020	
Project Funding (FY19): \$300,000	DOE share: \$300,000	Non-DOE share: \$0

### Project Introduction

The goal of this project is to reduce the size, weight, cost, and losses associated with rotating electric machinery and its associated power electronics for electric and hybrid vehicle applications. In particular, the goal of this effort is to facilitate electric machinery that will meet the requirements set forth in the USDRIVE *Electrical and Electronics Technical Team Roadmap* of October 2017. This document calls for an electric machine with a peak power of 100 kW, a continuous rated power of 55 kW, a peak speed of less than 20,000 rpm, a volume of no more than 2 liters, a mass of less than 20 kg, and a useful life of 15 years or 300,000 miles of vehicle service. This will be achieved through a combination of (i) new materials, (ii) new electric machine topologies, (iii) advances in power electronics, and (iv) superior design through the use of formal and rigorous multi-objective optimization-based design based on advanced analysis techniques. This effort is being conducted by a large consortium comprised of National Laboratories (Sandia National Laboratories, Oak Ridge National Laboratories, Ames Laboratory, and the National Renewable Energy Laboratory) and universities (Virginia Tech, Georgia Tech, SUNY, Arkansas, Ohio State, IIT, Purdue, University of Wisconsin – Madison, University of California Berkeley, and North Carolina State). Purdue’s role in this effort will focus on (ii) and (iv).

### Objectives

The objective of this effort is to explore the use of new materials and develop new design paradigms to enable unprecedented propulsion motor power densities at a reduced cost. In order to achieve this objective, Purdue’s goals will be to investigate new machine topologies such as the homopolar ac machine, and to develop new improved design codes which (i) incorporate high switching frequency performance analysis, (ii) thermal performance, (iii) high-speed rotor structural analysis, and (iv) advanced magnetic analysis techniques into its existing design paradigm based on rigorous multi-objective optimization in order to take best advantage of new materials and machine topologies developed by Purdue and other team members. An additional objective will be to build and test a prototype machine whose design is based on the enhanced design paradigm developed under this effort.

## Approach

In order to achieve the objectives described in the previous section, Task 1.1 described below is being carried out during the first year of the program.

### ***Task 1.1 – Electric Machinery Design Paradigm Enhancements***

This task consists of 3 related subtasks. In particular,

Subtask 1.1.1 – Homopolar machines have long been considered for high-speed applications. Their attributes include a simple rotor structure well-suited for high-speeds and which is ideally electrically lossless, no permanent magnet materials, suitability to high-temperature operation, and the ability to operate over a very wide speed range. One of their chief disadvantages is that, like a switched reluctance machine, the flux density in the stator varies from a zero to the saturated value rather than from a negatively saturated value to a positive saturated value. Purdue has developed a new type of homopolar machines that has advantages over its traditional counterpart and may prove to be ideal for traction applications. A basic design code is being developed under this task to see if this arrangement is in fact competitive.

Subtask 1.1.2 – High Frequency Switching Losses. Presently, the design code formulation developed at Purdue include dc resistive, skin effect, and proximity effect losses at the fundamental frequency. Core losses are determined using an enhanced version of the Modified Steinmetz Approach. Semiconductor conduction and switching losses are also included in existing design codes. In this task, this aspect of the code development is being improved. Of particular interest will be including switching frequency losses in the machine and permanent magnet losses at both the switching frequency and the slot passing frequency. The goal here is to support the co-optimization of the machine with the power electronic converter so that the impact of switching frequency on the machine is captured.

Subtask 1.1.3 – In the multi-objective optimization-based design of electric machine, one of the key analyses is the magnetic performance. While analytical magnetic equivalent circuit methods have been used with considerable success, they can require significant insight on the part of the user; and can be inaccurate for some conditions.

As an alternative, numerical methods of field analysis have been used, and in particular Finite Element Analysis (FEA) is a common approach. Indeed, commercial FEA packages often include some optimization capability. However, these are invariably restricted to ‘small’ problems in the sense that there are only a few degrees of freedom and the optimization is restricted to the machine itself and does not include the converter, system, and other factors which takes the number of unknowns into the twenties, thirties, or more, whereupon the FEA approach becomes intractable. This is particularly the case when the speed/torque required by the machine is in the set of unknowns.

The Method of Moments (MOM) is a numerical method used to solve fields-based integral equations. In contrast to finite-element analysis (FEA) that is based upon solving differential equations, MOM has an advantage that only the active material is meshed. In modeling electric machinery, this means there is no mesh in the airgap nor outside the machine. As a result, the number of unknowns can be greatly reduced compared to FEA.

In the past, a disadvantage of MOM is that numerical integration had to be used to populate the corresponding MOM matrices, which in many cases eliminated its advantage over FEA. Recently, Purdue developed analytical expressions for the MOM matrices that eliminates the numerical integration step. As a result, there is a strong likelihood that MOM can be much more computationally efficient compared to FEA for low frequency magnetic modeling. Thus, it is likely MOM can be used within rigorous multi-objective design of electric machinery (and passives) in which potentially millions of candidates are evaluated. In this effort, Purdue is developing an open-source MOM toolbox intended for electric machine optimization. The toolbox will include the data structures utilized by Purdue in their widely published machine design formulations for surface mount PMSMs, interior PMSMS, and wound rotor synchronous machines. Thus the toolbox will be

compatible with the geometric, material, and winding constructs that have been already developed over decades of effort. In Year 1 the toolbox will be formulated to solve magneto-static 2D problems. The toolbox will then be applied to PMSM and WRSM machines and the computational performance compared to FEA.

**Results**

The progress on the three subtasks thus far this year are as follows:

***Subtask 1.1.1 – Homopolar machines***

Figure I.25.1 illustrated one instantiation of a Homopolar AC Machine (HAM) which is being investigated in this effort. This machine topology has several attractive characteristics including low rotor losses, no permanent magnets, no rotating field connections, no slots, a mechanically robust rotor, capability for high temperature operation, an inherently segmented stator to reduce manufacturing cost, it is easily wound with a high packing factor, it has a high surface area per unit volume facilitating heat transfer, and it has a stationary field winding so that electrical connections to a rotating field. A disadvantage is that the flux in a given leg alternates between zero and some peak value rather than some value and the negation of that value.

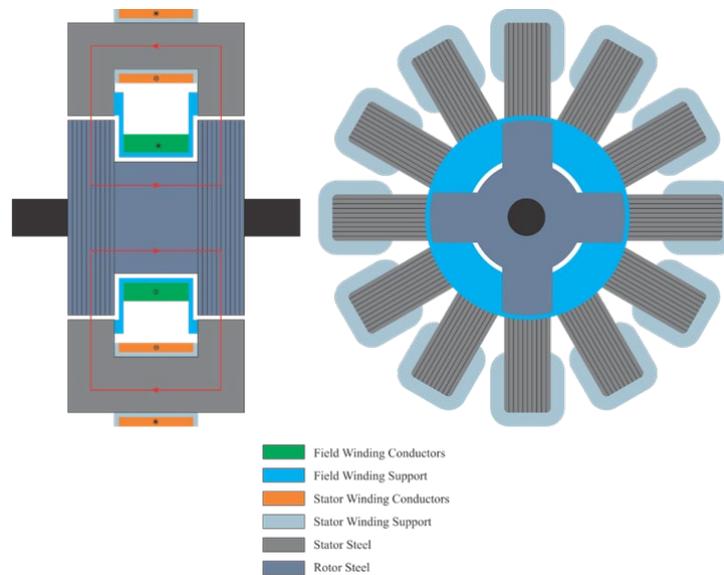


Figure I.25.1 Homopolar AC Machine

Prior to developing a full design model, the first activity to investigate the HAM topology was to investigate the excitation of the device. To this end, a crude magnetic equivalent circuit was first developed. This is shown in Figure I.25.2.

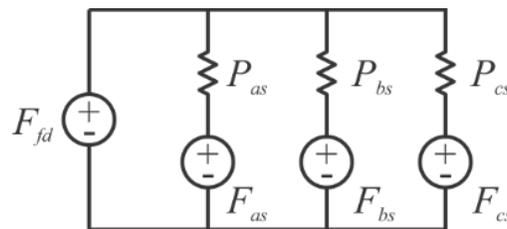


Figure I.25.2 HAM magnetic equivalent circuit.

In this model, the permeances may be expressed

$$P_{as} = P_A - P_B \cos(2\theta_r)$$

$$P_{bs} = P_A - P_B \cos(2\theta_r + 2\pi/3)$$

$$P_{cs} = P_A - P_B \cos(2\theta_r - 2\pi/3)$$

where  $\theta_r$  is the electrical rotor position. The machine can be excited several different ways. One approach is using sinusoidal excitation, which will be referred to as Excitation Strategy 1. A second excitation strategy was derived wherein the field and phase winding MMFs are assigned as

$$F_{fd} = \frac{2}{\pi} F_2$$

$$F_{as} = F_{fd} - \frac{1}{\sqrt{2}} F_2 \sqrt{1 + \sin(2\theta_r + 2\phi_c)}$$

$$F_{bs} = F_{fd} - \frac{1}{\sqrt{2}} F_2 \sqrt{1 + \sin(2\theta_r + 2\phi_c - 2\pi/3)}$$

$$F_{cs} = F_{fd} - \frac{1}{\sqrt{2}} F_2 \sqrt{1 + \sin(2\theta_r + 2\phi_c + 2\pi/3)}$$

This will be referred to as Excitation Strategy 2. In this strategy, the field winding will see a dc current, whereas the phase currents will have the shape of a half-wave rectified signal less the dc offset. Figure I.25.3 compares the two strategies for waveforms that will produce identical torque. It was found that this strategy produces 5.3 times torque for a given current that a strategy in which the phase currents were pure sinusoids. A generalization of this strategy was also explored to further increase torque production, but that strategy is not yet fully mature.

Based on the basic strategy, a preliminary design model of the HAM was developed. This design model considers the detailed design geometry. The heart of the design model is a magnetic equivalent circuit. The MEC used is somewhat similar to the elementary model set forth in Figure I.25.2, but includes nonidealities such as the saturation of the stator legs, the rotor, and the rotor field post.

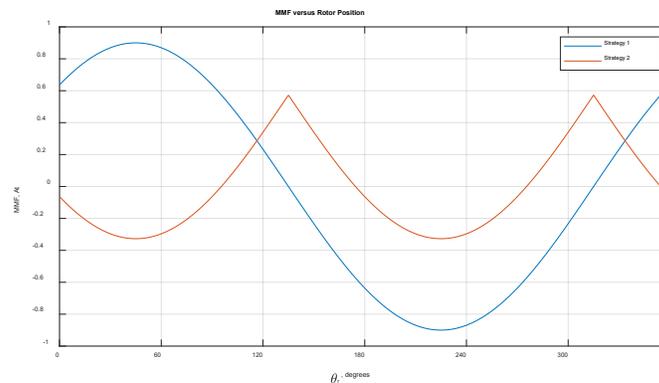


Figure I.25.3 HAM phase MMF waveforms.

Figure I.25.4 illustrates an initial Pareto-optimal front in which mass and loss are minimized. It must be emphasized that this is a highly preliminary result given to demonstrate progress rather than to assess the performance of the machine in any way. It is based on the initial MEC developed under this effort. In this study, a single operating point of 100 Nm at 1000 rad/s is considered for a power of 100 kW. It is assumed that the stator windings are copper, the field winding is aluminum, and that a cobalt steel is used magnetic components. The winding temperature was assumed to be 150°C. In this very preliminary model, ac losses are not considered, and there are issues with local (spot) saturation that have not been addressed. Also, in this figure is the Pareto-optimal front of a surface mounted PM machine, with copper windings at 150°C, also using cobalt steel. In this case, ac losses are included. If the results are correct, one can see that the PM machine is superior to the HAM in torque density. However, if the HAM can be operated at higher speed, the HAM may compare more favorably in terms in power density. Since the HAM does not have permanent magnets, it may also compare more favorably in terms of cost. However, drawing such conclusions is at this point premature. The inclusion of multiple operating points may significantly change the comparison.

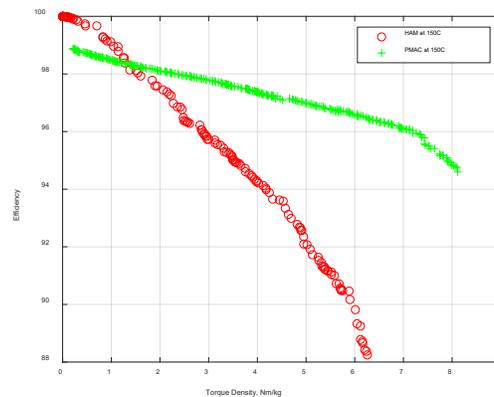


Figure I.25.4 Preliminary HAM Pareto-optimal front.

Before concluding the description of this subtask, it is interesting to look at a rendering of the HAM design. In particular, Figure I.25.5 illustrates a rendering of the most torque dense design from Figure I.25.4.

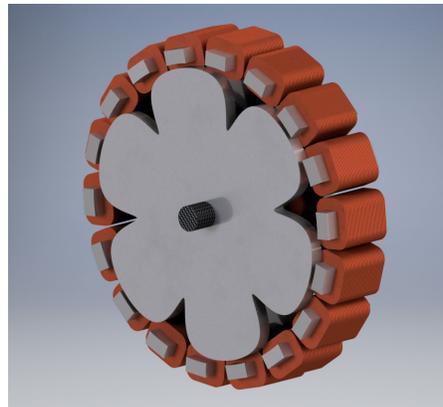


Figure I.25.5 Preliminary HAM design.

### Subtask 1.1.2 – High Frequency Switching Losses

Presently, the design code formulation developed at Purdue include dc resistive, skin effect, and proximity effect losses at the fundamental frequency. Core losses are determined using an enhanced version of the Modified Steinmetz Approach. Semiconductor conduction and switching losses are also

included in existing design codes. In this task, this aspect of the code development will be improved. Of particular interest will be including switching frequency losses in the machine and permanent magnet losses at both the switching frequency and the slot passing frequency. The goal here is to support the co-optimization of the machine with the power electronic converter so that the impact of switching frequency on the machine is captured. Work on this task hasn't yet been initiated but will begin next quarter.

### Subtask 1.1.3 – Method of Moments

The Method of Moments is a numerical method that can be used for solving fields-based integral equations. In contrast to methods used to solve differential equations, such as Finite Element Analysis (FEA), MoM has an advantage that only the active material is meshed. As a result, the number of unknowns can be greatly reduced compared to FEA. Additional advantages include that any combination of polygons can be used to establish the mesh, and the nodes are not required to be coincident. Thus for machine design one can use pre-meshed building blocks and readily assemble them to generate candidate designs. Furthermore, only a surface mesh is required when the materials are magnetically linear.

Within this research, a 2D MoM formulation has been adopted to model electric machinery. The mesh discretization used is shown in Figure I.25.6. Specifically, in the case in which a machine is modeled using nonlinear magnetic materials, the resulting system of equations that are solved are expressed:

$$\mathbf{f}_{\text{B}_{\text{tot}}\mathbf{M}}(\mathbf{M}) = \mathbf{f}_{\text{B}_M}\mathbf{M} + \mathbf{f}_{\text{B}_f}\mathbf{I}_f + \mathbf{f}_{\text{B}_{PM}}\mathbf{I}_{PM}$$

For the case in which the machine is modeled using only linear magnetic materials are expressed:

$$[\mathbf{f}_{\text{B}_{\text{tot}}\mathbf{M}} - \mathbf{f}_{\text{B}_M}]\mathbf{M}_{\text{tan}} = \mathbf{f}_{\text{B}_f}\mathbf{I}_f + \mathbf{f}_{\text{B}_{PM}}\mathbf{I}_{PM}$$

In both formulations, the magnetization field  $\mathcal{M}$  represent the unknowns. In the case of nonlinear materials, the number of unknowns is  $2N$ , where  $N$  is the number of elements. The unknowns are the  $M_x$  and  $M_y$  components at the center of each element. In the case of linear materials, the unknowns are the magnetization tangential to the respective element,  $M_{\text{tan}}$ . The inputs to both MoM formulations are the free currents  $\mathbf{I}_f$  (i.e., currents due to conductors in the stator or rotor) and the currents used to represent the magnetization of permanent magnet materials,  $\mathbf{I}_{PM}$ . The  $\mathbf{f}$  terms in the above formulations are matrices used to relate the inputs to the unknowns. The elements of all matrices have been derived analytically, thus enabling faster computation.

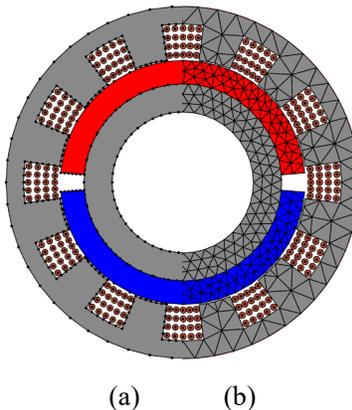


Figure I.25.6 (a) Surface meshed linear materials and (b) volume-meshed nonlinear materials for a PMSM model.

Within this research, it has been found that the axial periodicity inherent in the geometry of electric machinery can be exploited to decrease the computational complexity of the MoM formulation. Specifically, the primary computational bottleneck in MoM field analyses is the population of the dense system matrix

$[\mathbf{f}_{B_{tot}} - \mathbf{f}_{BM}]$ , thus it is desired to avoid computing it in its entirety. A method to limit the number of components that need to be computed has been derived and implemented for the case in which linear materials are used. A method of doing so for the nonlinear formulation is in the process of being derived.

Finally as part of this research, a method of efficiently computing the torque based upon a Lorentz formulation has been derived and implemented. In FEA formulations, torque is often computed using a Maxwell stress tensor approach. Such an approach can be applied in the MoM formulation. However, since the airgap is not meshed, this requires one to place additional elements within the airgap and numerically integrate the corresponding force densities to calculate torque. In the method that has been derived, one uses the bound currents at the edge of all meshed materials to calculate the flux density present at all bound and free currents on the rotor. The cross product of the vector from the center of the machine to the element then provides torque. It has been found that the approach derived is much more efficient numerically compared to a Maxwell stress tensor approach.

A goal of the MoM is to utilize it within population-based design (PBD) of electric machinery and indeed have it adopted within the consortium. Toward this goal, the approach has been tested for the PBD of surface mount PM machines operated in the linear magnetic region. The goal was to design a machine with a peak torque of 20 Nm and a rated speed of 5000 rpm. It was assumed the dc voltage supplying the machine was 400 V. Although such a machine would not be applied to a propulsion drive, similar design specs have been utilized in the literature and a goal was to ensure that the results obtained were similar to those found by other researchers. Indeed they were.

Within the optimization Purdue's Matlab-based toolbox for multi-objective optimization, GOSSET, was utilized with a population size of 500 individuals applied over 500 generations. Each machine was evaluated at 4 rotor positions, over which the mean torque was evaluated. The Pareto-Optimal front of the optimization run is shown in Figure I.25.7. The computation time required to complete the design study was 11.4 hours on a simulation workstation with an Intel Xeon E5-2687W v2 3.4 GHz processor and 32 GB of RAM. On average 0.164 s was required for an evaluation of a candidate machine. The computed flux density in the tooth and back-iron calculated using the MoM was found to be identical to that obtained using FEA. The FEA was performed using the commercial package ANSYS Electronics Desktop, which required more than 10,000 elements per pole on average, whereas the MoM required only 190 unknowns per pole. An approximate FEA unknown count is given since the geometry is re-meshed at each rotor position. While it is not precise to compare computation times for codes written by different authors, it is informative of the potential offered by the MoM. Specifically, the commercial FEA solver required several minutes to perform the same machine evaluation on the same workstation used to perform the 0.164 s MoM solve.

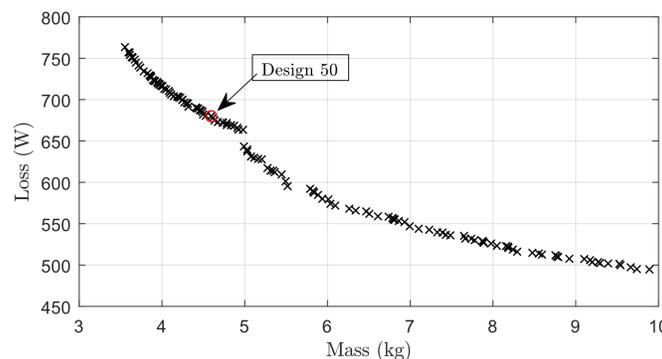


Figure I.25.7 Pareto-optimal front from an MoM-based optimization.

Ongoing research is now focused on utilizing the nonlinear MoM solver within the PBDs. The results will be presented in the next quarterly report. In addition, the team is working on structuring the MoM code into a toolbox that is readily transferred and useable by the entire team.

## Conclusions

Thus far, a crude preliminary design model of the HAM has been constructed, and the performance of the HAM has been compared to a permanent magnet ac (PMAC) machine. It is not yet clear if the results are correct, but if they are then for the single operating point study it would appear that the torque density (Nm/kg) of the HAM is lower than the PMAC machine, if both machines operate at the same current density. This may be a vexed comparison however since the HAM could mostly likely operate at higher current densities, higher speeds, and be less expensive than the PMAC machine. In addition to the work on the HAM a Method of Moments formulation for 2D magnetostatic machine design was derived. Initial evaluation of the tool and its utility for the analysis and design of a PMSM where the magnetic materials were assumed linear has been demonstrated. Ongoing research is focused on evaluating the formulation in cases of high-levels of magnetic saturation.

## Key Publications

1. D. C. Horvath, S. D. Pekarek and R. A. Howard, "Analysis and Design of Electric Machines Using 2D Method of Moments," *2019 IEEE International Electric Machines & Drives Conference (IEMDC)*, San Diego, CA, USA, 2019, pp. 476-483.

## Acknowledgements

Although Purdue is collaborating with the entire consortium, the relationship with Sandia National Laboratories has been particularly helpful. Thus the help and contributions by Jason Neely, Lee Rashkin, Todd Monson, and Vipin Gupta are particularly recognized.



## I.26 Implementation of WBG devices in circuits, circuit topology, system integration as well as SiC devices (The Ohio State University)

### Dr. Anant Agarwal, Principal Investigator

The Ohio State University  
 2015 Neil Avenue  
 Columbus, OH 43210  
 E-mail: [agarwal.334@osu.edu](mailto:agarwal.334@osu.edu)

### Dr. Jin Wang, CO-Principal Investigator

The Ohio State University  
 2015 Neil Avenue  
 Columbus, OH 43210  
 E-mail: [wang.1248@osu.edu](mailto:wang.1248@osu.edu)

### Susan Rogers, DOE Technology Development Manager

U.S. Department of Energy  
 E-mail: [susan.rogers@ee.doe.gov](mailto:susan.rogers@ee.doe.gov)

Start Date: April 1, 2019                      End Date: March 31, 2020  
 Project Funding (FY19): \$300,000              DOE share: \$300,000              Non-DOE share: \$0

### Project Introduction

All device vendors have sacrificed reliability/ruggedness to reduce cost. Short channel length is an example which reduces device size and cost but at the expense of reduced short-circuit time of 2-3 $\mu$ s. Another example is the gate oxide thickness which has been thinned to 30 – 40 nm without reducing the gate voltage in order to reduce device size/cost. This leads to gate oxide leakage issues and susceptibility to rupture during extreme events such as short-circuit and exposure to static electricity. Hence, commercial devices, available to-date, are not suitable for insertion into a vehicle power train for long operational life. A comprehensive reliability study will be undertaken for commercially available devices both as discrete devices and in an inverter to uncover failures such as threshold voltage instability, inadequate short circuit time, gate oxide failures due to gate voltage overshoot and high junction temperature, as well as body diode instability.

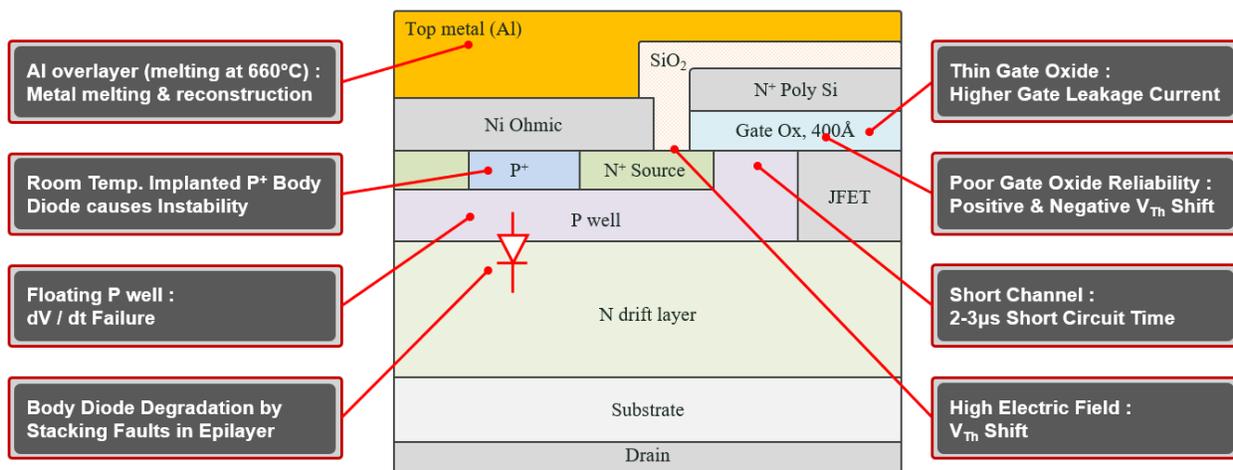


Figure I.26.1 SiC MOSFET Reliability Issues

OSU will share the findings with SUNY Poly and collaborate with them to strengthen the existing device designs to overcome the given weakness in the device. These devices will be fabricated by SUNY Polytechnic in a state of the art commercial 150 mm SiC Foundry. The new designs will be improved every year through extensive testing by OSU, re-design (in collaboration between OSU and SUNY Poly) and fabrication by SUNY Polytechnic. The ultimate goal is to demonstrate that SiC devices can be designed to be suitable for automotive applications such as 100 kW Inverter with reliability to last 300,000 hours and publish findings so that commercial vendors can follow suit.

### Objectives

The objective of the project is to ensure that SiC devices are reliable and rugged as required in automotive applications for operational life of 300,000 hrs and create new device designs to address various weaknesses in currently available commercial devices. OSU will work closely with SUNY Polytechnic. OSU will carry out the reliability and ruggedness evaluations of commercial devices as well as those fabricated by SUNY Polytechnic, discuss the results with SUNY Poly, collaborate with the PI at SUNY Poly to improve the designs with respect to reliability/ruggedness. SUNY Poly will fabricate the devices and perform routine DC and dynamic tests. This cycle will continue for 5 years to ensure that new devices meet the standards of automotive industry. OSU work will focus on reliability/ruggedness evaluation of SiC devices by individually testing them and then evaluate them in a 10 kW, 3 phase inverter system built with a specific purpose of stressing devices using realistic drive cycles such as a 10-minute hill climb. It should be noted that the primary purpose of the 10 kW inverter is to provide a platform for stressing the SiC devices under accelerated but realistic drive conditions and NOT to meet the 100 kW power and power density goals. The 100 kW inverter will be built by other team members.

### Approach

#### *Collaboration with National Laboratory:*

Achievement of overall project objectives is dependent upon tasks performed by a National Laboratory under a separately funded DOE contract. The Recipient will coordinate and collaboratively conduct work with the selected national laboratory on selected tasks integral to the completion of the project. The results of this collaborative effort with the national laboratory will be included in all project reporting. Sandia National Laboratories (SNL) will participate in the design reviews of the SiC MOSFETs and inverters and coordinate efforts between the SUNY Poly and OSU team and other project teams within the consortium.

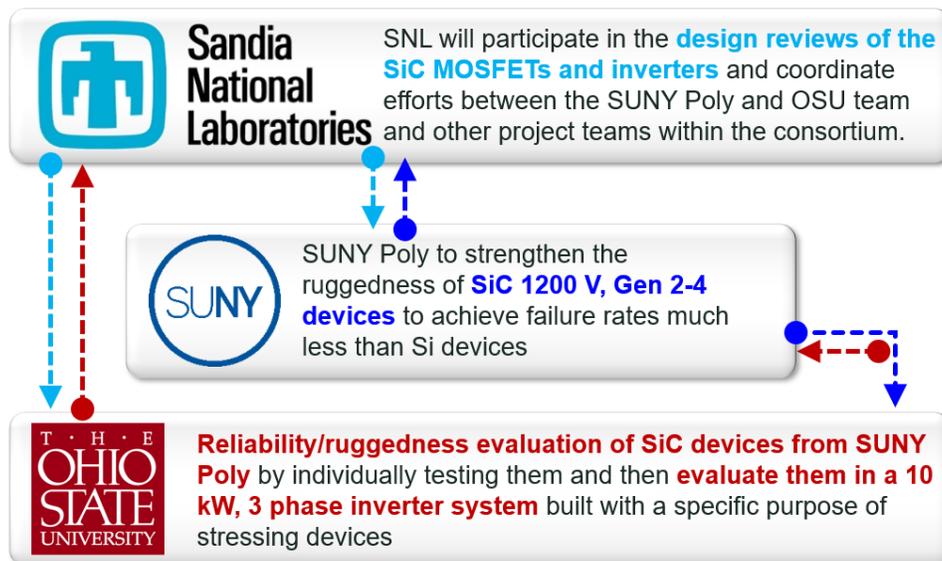


Figure I.26.2 Key Partnerships

**Stand-alone evaluation of commercial devices and Inverter-1 build**

**Task 1.1** – Ruggedness of Commercial SiC MOSFETs: SiC MOSFETs from several commercial vendors will be obtained and following tests will be performed to identify the failure mechanism. A control sample of commercial Si MOSFET and/or IGBT will also be tested for comparison.

**Subtask 1.1.1** – Gate oxide leakage current vs. gate voltage will be evaluated from 0 V to breakdown voltage at temperatures up to 280°C to accelerate the failure process. The gate current at various gate voltages vs. Temperature will be plotted as an Arrhenius plot to find the activation energy of Fowler Nordhiem (F-N) tunneling current.

**Subtask 1.1.2** – Body diode stability will be evaluated by stressing the body diode in DC mode up to 100% of the rated current for various time intervals. The on and off characteristics such as on-resistance, leakage current and threshold voltage will be measured after each stress. Gate bias will be kept at -5.0 V to completely shut-off the MOSFET channel.

**Subtask 1.1.3** – Threshold voltage stability will be evaluated by applying DC gate voltage of +20 V at various temperatures up to 300°C for various time intervals. The above experiment will be repeated at a gate voltage of -10 V.

**Subtask 1.1.4** – Short circuit time of commercial SiC MOSFETs will be measured as a function of drain and gate voltages. Based on this information, appropriate de-rating can be applied for a given product based on the requirements for short-circuit time.

**Subtask 1.1.5** – Avalanche energy will be measured for various commercial SiC and Si MOSFETs and IGBTs.

**Task 1.2** – Inverter Development as a vehicle to assess reliability of SiC MOSFETs in realistic and accelerated operation of the Inverter:

**Subtask 1.2.1** – A gate drive with comprehensive protection functions will be designed based on the device evaluation results from Task 1.1.

**Subtask 1.2.2** – Thermal and mechanical designs of the Inverter-1 will be accomplished. The system layout not only will have high power density but also will enable multiple approaches to apply thermal stresses to either selected areas (components) or the overall inverter.

**Subtask 1.2.3** – Inverter-1 will be built and de-bugged using commercial devices.

**Results**

The main objective in this report is the reliability and ruggedness evaluations in commercial 1200 V and 1700 V SiC MOSFETs from various vendors in Table I.26.1.

**Table I.26.1 Tested Commercial SiC Power Mosfets**

Device	Gate Structure	Voltage Rating	Current Rating
Device C	Planar	1200 V	12 A
Device D	Trench	1200 V	17 A
Device E'	Planar	1200 V	10 A
Device D''	Trench	1700 V	3.5 A
Device E''	Planar	1700 V	5 A
Device G	Planar	1700 V	5 A

### Subtask 1.1.1 : Gate Oxide Leakage current

#### A. Gate Leakage Measurement Results

show the gate leakage current measurements at 28°C, 175°C and 280°C for all three vendors. It can be observed in (a) that for vendor E', the leakage current maintained the same level from 28°C to 175°C and then increased from 175°C to 280°C. The breakdown voltage decreases as temperature is increased. These can be explained by reduction of effective barrier height and re-emission of electrons that are trapped at the interface at elevated temperatures. Due to electron emission from the interface, threshold of the device under test (DUT) will decrease. Therefore, for a constant gate bias, the voltage drop across the gate oxide will increase and enhance F-N tunneling. Assuming that the critical electric field for dielectric breakdown stays constant at different temperatures, reduced gate voltage is needed to reach dielectric breakdown. Therefore, the breakdown voltage reduced from 28°C to 280°C. Vendors C and D exhibit different gate leakage current behaviors as shown in (b) and (c). When the gate bias approached a certain voltage (crossover point), the leakage current at higher temperature decreased and became less than the leakage current at lower temperature. The behavior before the crossover point are similar to vendor E'. So, the reduction of effective barrier height and electron re-emission from the interface traps are still taking place. However, with the presence of near interface oxide traps, more electrons can be injected into these oxide traps at elevated temperatures. This process can relax the oxide electric field near the interface thus increase the barrier width and suppress F-N tunneling [1]. Furthermore, with the injected electrons into the oxide traps, the threshold voltages of the DUTs will increase. Therefore, in contrast to vendor E', the breakdown voltages of vendors C and D increased with elevated temperatures. These measurements show that the leakage current behavior at elevated temperatures is strongly related to interface traps and near interface oxide traps and it can be used as an indication of the quality of gate oxide.

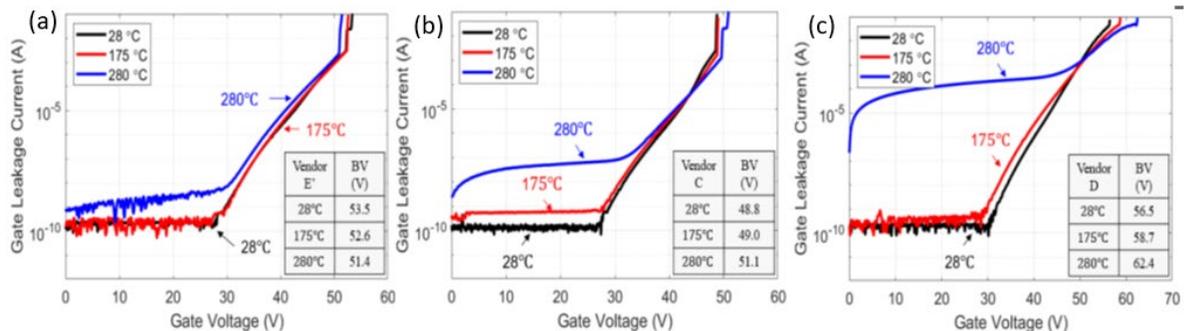


Figure I.26.3 Gate leakage current-voltage characteristics at three different temperatures

#### B. TDDB Measurement Results

A total of 80 commercial devices from vendor E' were characterized with constant-voltage TDDB measurements at 28°C and 175°C. At each temperature, four different gate voltages were applied. These gate voltages were selected so that the failure times are of the order of 10 minutes, 1 hour, 10 hours and 100 hours, respectively at 28°C. The Weibull distributions for both temperatures are shown in Figure I.26.4 (a) and (b). When approximating the linear regression lines for the Weibull distribution, data points that fall significantly outside of the rest of the distribution were ignored. Despite the effort, variations of the slope parameter can still be observed for both 28°C and 175°C. According to the percolation theory of dielectric breakdown, the slope parameter is proportional to the oxide thickness and inverse of active area [2]. Therefore, the mismatch of oxide thickness might contribute to the variations of  $\beta$ . Percolation theory assumes that there is no pre-existing gate oxide defects. In practice, gate oxide defects exist before the stress is applied. These defects can introduce different failure modes and modify values. Another potential cause for variation is the threshold voltage difference for the commercial devices. For a given gate bias, with different threshold voltages, the gate oxide electric field will vary thus resulting in different failure times. Threshold voltage variations also indicate

potentially different interface states and oxide defects distributions. This might cause the failure mode to change between devices and thus creating variations of the values. From the two distributions presented in Figure I.26.4 (a) and (b), the 63% failure times ( $t_{63\%}$ ) and slope parameter at different gate voltages can be extracted.  $t_{63\%}$  as a function of applied gate voltages at both 28°C and 175°C are plotted in Figure I.26.4 (c). Assume that  $\log(t_{63\%})$  is linearly proportional to  $V_G$  as predicted by thermal-chemical E-model [3], the failure time at  $V_G = 20$  V can be extracted by extrapolating back to the normal condition with a linear regression line. Failure times for other cumulative percentage of failures such as 1ppm ( $t_{1ppm}$ ) are often used in automotive industry.  $t_{1ppm}$  at 175°C as a function of applied gate bias are also calculated and shown by the blue up-word triangles in Figure I.26.4 (c). Extrapolation back to  $V_G = 20$  V, predicts  $t_{1ppm}$  at 175°C to be larger than 173 years. It is concluded that gate oxide for vendor E' have adequate qualify for automotive applications.

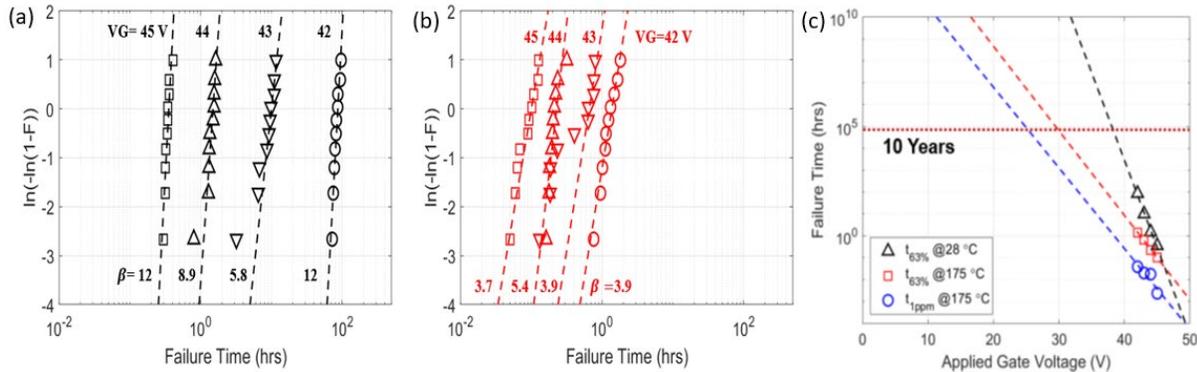


Figure I.26.4 Weibull distribution of vendor E' for four different gate voltages at 28°C and 175°C.

### Subtask 1.1.2 : Body Diode Stability

#### A. 3<sup>rd</sup> Quadrant Body Diode Characteristics

The 3<sup>rd</sup> quadrant  $I_D$ - $V_D$  characteristics of the body diode are shown in Figure I.26.5 for devices from the vendors listed in Table I.26.1. The devices from all vendors show a built-in voltage of approximately -3 V with a gate voltage of -5 V. There was no current degradation in the body diode after forward stress on device E". This indicates that the devices have been fabricated in sufficiently low Basal Plane Dislocation (BPD) epitaxial layer or body diode has been somehow been prevented from getting forward biased. In the case of device G, two of the 10 devices show an increased forward voltage with increasing stress time. After 100 hours of forward bias stress, the forward voltage shift is found to be about 9% in device G. When the MOS channel is turned off and the body diode is forward biased, the holes in the p-well region are injected to the drift layer. The electron-hole recombination in the drift layer provides the energy to activate Stacking Faults (SFs). The recombination-induced SFs cause reduction of both the carrier lifetime and the mobility. Moreover, the spatial size of the SFs depends on the thickness of the drift layer. For example, the thickness of the drift layer of 1.7 kV 4H-SiC MOSFET is about 20  $\mu\text{m}$  grown on a 4° off-axis substrate. Thus, the projection length of SF on the top surface will be about  $20 \mu\text{m} / \tan 4^\circ = 286 \mu\text{m}$  [4]. All tested devices D" were degraded after forward stress as shown in Figure I.26.5 (c). The forward voltage is checked at 3.5 A, which is the current rating of these devices. The forward voltage was measured as 6 V before the forward stress test. It increased to approximately 9 V after inducing forward stress for 100 hours. The forward voltage shift of the device D" is found to be ~6 times higher than that of the device G. Therefore, these results imply one of four reasons may be responsible for such a high degree of degradation. First, that device D" may be using room temperature ion implantation of Al to form  $p^+$  contacts which can create many BPDs. Second, some other process may result in the creation of BPDs. Third, the starting epi-layer has many BPDs. Lastly, BPDs can be introduced from the Al implanted region and glide through the epitaxial layer during the annealing [5].

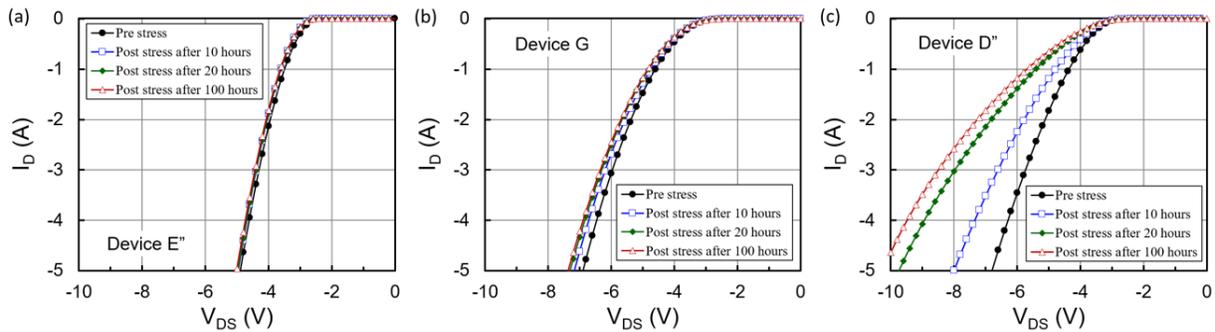


Figure I.26.5 Degradation of the 3<sup>rd</sup> quadrant  $I_D$ - $V_{DS}$  characteristics for built-in body diode of one selected 1.7 kV SiC DMOSFET from each vendor.

### B. Forward Leakage Current in Forward Blocking Mode

The leakage current in forward blocking mode at room temperature before and after stress is shown in Figure I.26.6. The forward leakage current has a gradual increase in device G with increasing stress on the body diode. Furthermore, the decrease in breakdown voltage is attributed to the increase in leakage current. Also, breakdown seems to happen in active area, caused by recombination-induced SFs. However, device D'' and E'' show no significant change in leakage current. Results from device E'' are expected since this vendor might be using sufficiently low BPD epitaxial layer. However, device D'' does not show higher leakage current or reduced blocking after stress even though devices have a lot of SFs in active area. Therefore, it could be due to the fact that breakdown occurs in the edge termination region where there are no SFs. These results have significant impact for the design and processing of SiC MOSFETs less than 1.7 kV. Some vendors may be using a heavy dose of Al implants at room temperature to form  $p^+$  contacts in the SiC MOSFETs. Although this process could reduce the device cost, it creates new BPDs [6]. If SiC MOSFETs are used without separate freewheeling diode chips in high frequency switching applications, the body diode will conduct during some portion of the switching cycle. These results indicate that built-in body diode cannot be relied upon. Integral Schottky barrier diodes are needed.

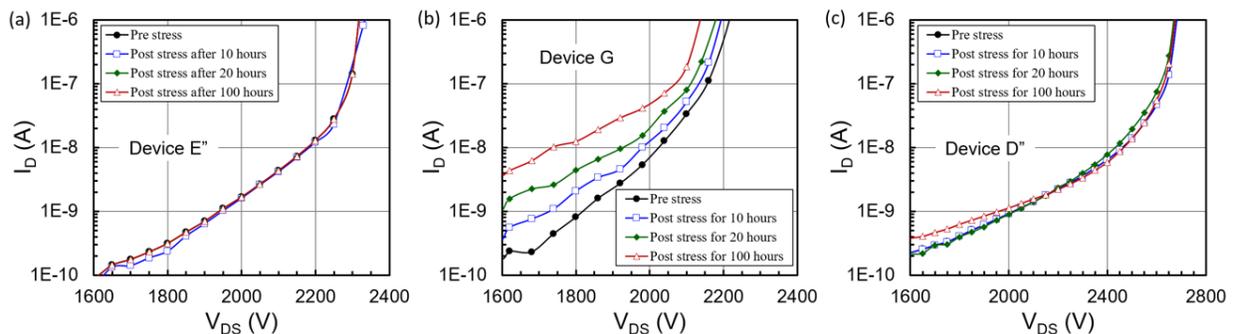


Figure I.26.6 Reverse bias characteristics at gate voltage of  $V_{GS} = 0$  V of one selected 1.7 kV SiC DMOSFET from each vendor at room temperature before and after stress of the body diode

#### Subtask 1.1.3: Threshold Voltage Stability

Threshold voltages are measured as a function of temperature. The temperature was ramped up from 25°C to 200°C where the devices were placed on a hot plate. Transfer characteristics ( $I_D$ - $V_G$ ) is measured with the constant drain voltage of 0.1 V using an Agilent 4145 parameter analyzer to determine the threshold voltage. Threshold voltage is extracted by the linear extrapolation (LE) method where the intercept of gate voltage is obtained by extrapolating from the maximum transconductance,  $g_m$ , point in that linear region [7].

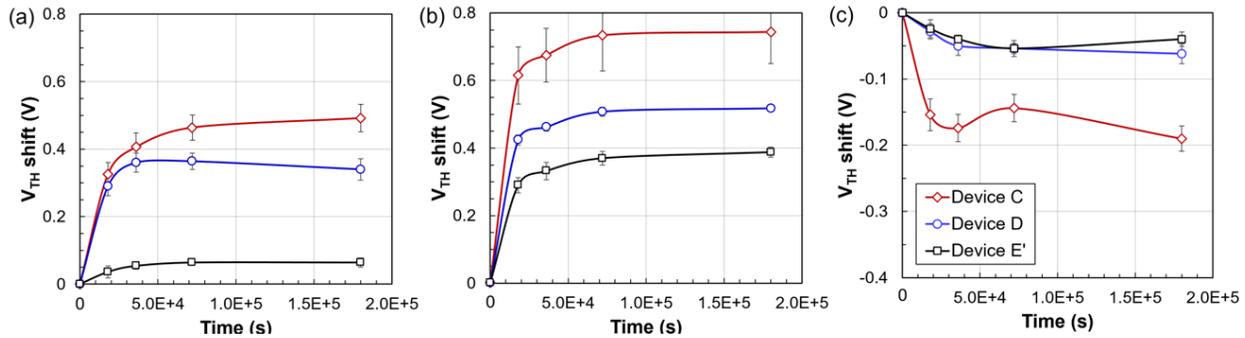


Figure I.26.7 Time-dependent threshold voltage shifts for (a) positive bias-stress of +20 V, (b) +30 V, and (c) negative bias-stress of -10 V for 50 hours.

As temperature increases, threshold voltages of all devices decrease. Device C shows the maximum threshold voltage reduction of about 2.5 V in negative direction whereas device D and E' show a reduction about 1 V at 200°C. The subthreshold characteristics for various devices are shown in Figure I.26.7 (b). It is clearly seen that the slope of curves in subthreshold region for device E' is much steeper than that of device C indicating device E' has lower interface state density than device C where the slope is gradual [8]. Device D is not shown in the figure but is located between the other two. In a virgin device, there are a lot of positive charges in the oxide which are balanced by the negative charges in the interface states. When the device gets into strong inversion, these negative charges define the threshold voltage of the device. As temperature increases, electrons in the interface states get enough energy to emit out of the interface traps into the conduction band reducing the negative charge at the interface [9]. This contributes to the reduction in threshold voltage. Therefore, since device C has higher interface states density, it shows larger shift in threshold voltage.

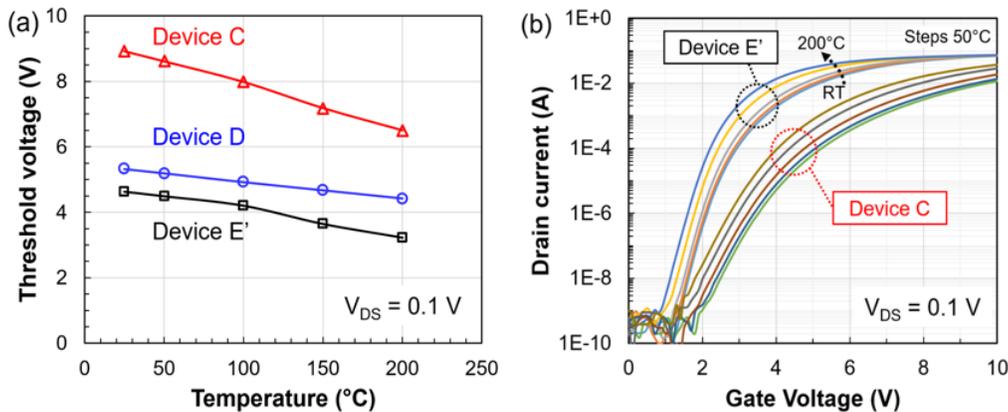


Figure I.26.8 Temperature-dependent (a) threshold voltage values and (b)  $I_D$ - $V_G$  transfer characteristics of device E' and C.

### Subtask 1.2.1 : A gate drive with comprehensive protection functions

The gate driver design is shown in Figure I.26.9. This design is a compact, dual-channel, gate-driver solution for driving SiC MOSFETs in half bridge or two high sides configuration. This design provides 20 V and -5 V output voltage and 6 W output power for each channel. The current booster is capable of providing 14 A source and sink peak current and up to 500 kHz switching frequency. The galvanic isolation is good enough to support 5.7 kV RMS isolation voltage. Active miller clamp is integrated for better switching performance. Desaturation protection and UVLO function protects the MOSFETs from unexpected faults. Its footprint and 12 V supply voltage make it a plug-in replacement for existing SiC MOSFET gate drive solutions.

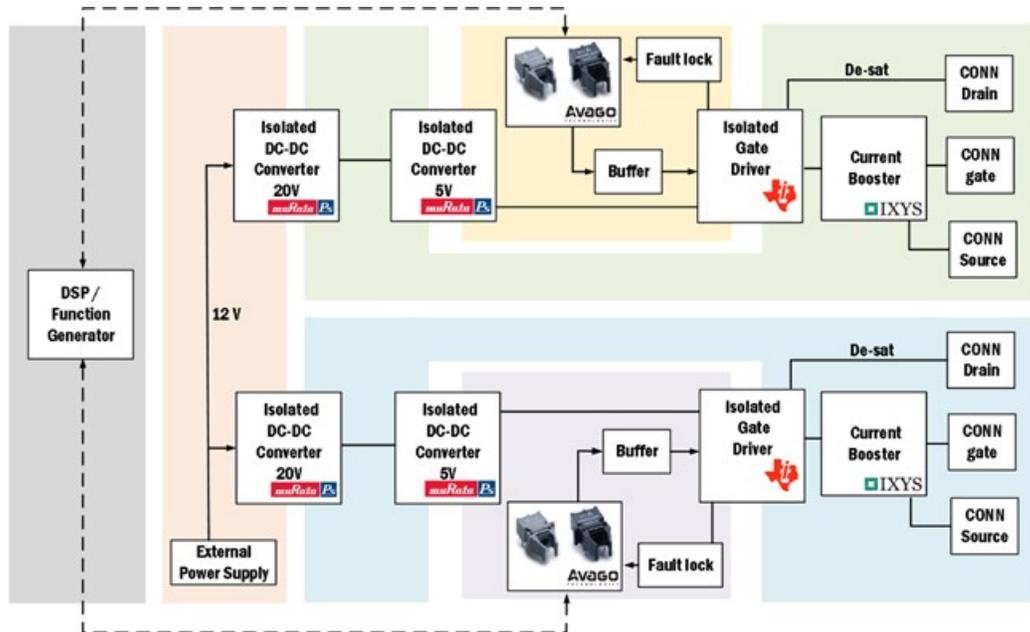


Figure I.26.9 Block diagram of gate drive circuit

All was designed on a four-layer PCB board with a 109 mm x 95 mm size. This design consists of three main parts for each channel. These two DC/DC converters provides 20 V, 5 V, -5 V for the whole board, the 12 V to 20 V/-5 V provides 5.7 kV voltage isolation capability with a small barrier capacitance. Isolated gate driver and the current booster provide the 14 A sink and source capability and ensure the circuit can operate up to 500 kHz switching frequency. The input side is isolated from the current booster by the 5.7 kV PMS reinforced isolation barrier, with a minimum 100 kV/ $\mu$ s CMTI. The interface functional element is isolated with the main power circuit. This part contains both optical receivers/transmitters and normal electrical terminals for PWM signal and fault feedback. A test with 20 nF capacitive load, 500 kHz switching frequency operation is chosen as the worst case. Figure I.26.10 (a) presents the output voltage waveform of the current booster in the worst operating condition. Figure I.26.10 (b) shows the PWM switching waveforms at the input of the buffer and output of the current booster, IXDD614. Propagation delay:  $t_{PLH} = 168$  ns,  $t_{PHL} = 207$  ns. The output voltage levels of the PWM signals follow the bias supply voltages. When the switching frequency is higher, the switching loss also increases. Heavier load influences the output voltage of the 6 W DC/DC converter. The output voltage levels of the PWM signals drops a little bit while load gets heavier.

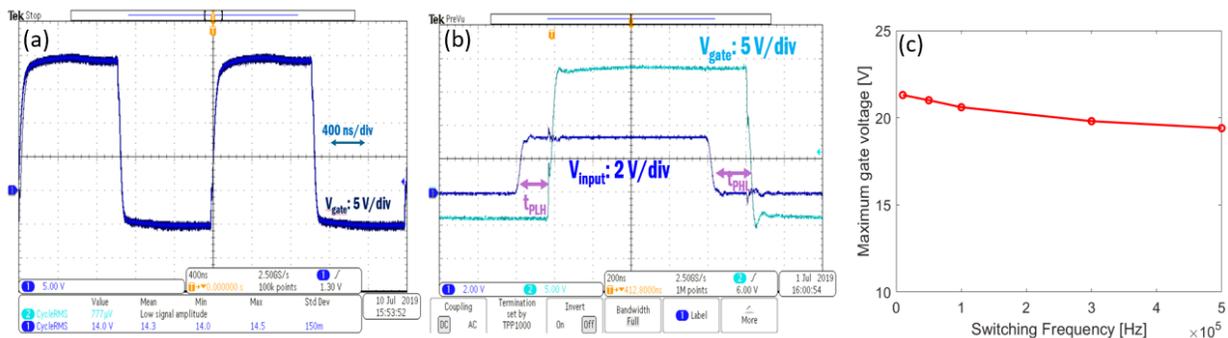


Figure I.26.10 Load transient response, Propagation delay waveform, Relationship between the output voltage levels of outputs and switching frequency



## Conclusions

This study, so far, has shown that gate oxide is reliable for vendor E'. However, the study for other vendors is in progress. Some vendors such as C and D have with density of interface traps as border traps in the gate oxide. Therefore, vendor C and D should not be used for automotive application unless they improve the gate oxide.

## Key Publications

1. Susanna Yu, Minseok Kang, Tianshi Liu, Diang Xing, Arash Salemi, Marvin H. White, Anant K. Agarwal, Bias-induced Threshold Voltage Instability and Interface Trap Density Extraction of 4H-SiC MOSFETs, Proc. on 7th IEEE Workshop on Wide Bandgap Power Devices and Applications, 2019
2. Minseok Kang, Susanna Yu, Diang Xing, Tianshi Liu, Arash Salemi, Kristen Booth, Shengnan Zhu, Marvin H. White, Anant K. Agarwal, Body Diode Reliability of Commercial SiC Power MOSFETs, Proc. on 7th IEEE Workshop on Wide Bandgap Power Devices and Applications, 2019
3. Tianshi Liu, Shengnan Zhu, Susanna Yu, Diang Xing, Arash Salemi, Minseok Kang, Kristen Booth, Marvin H. White, Anant K. Agarwal, Gate Leakage Current and Time-Dependent Dielectric Breakdown Measurements of Commercial 1.2 kV 4H-SiC Power MOSFETs, Proc. on 7th IEEE Workshop on Wide Bandgap Power Devices and Applications, 2019

## References

1. S. J. Oh, Y. T. Yeow, "Voltage shifts of Fowler-Nordheim tunneling J-V plots in thin gate oxide MOS structures due to trapped charges", *Microelectronics Reliability*, vol. 30, no. 3, p. 626, 1990.
2. J. H. Stathis, "Percolation models for gate oxide breakdown", *Journal of applied physics*, 86(10), pp.5757-5766, 1999.
3. J. W. McPherson, H. C. Mogul, "Underlying physics of the thermochemical E model in describing low-field time-dependent dielectric breakdown in SiO<sub>2</sub> thin films", *Journal of Applied Physics* 84, no. 3, pp. 1513-1523, 1998.
4. Agarwal, H. Fatima, S. Haney, and S.H. Ryu, "A New Degradation Mechanism in High-Voltage SiC Power MOSFETs" *IEEE Electron Device Lett.* vol. 28, no. 7, pp. 587–589, 2007.
5. R. E. Stahlbush, K. N. A. Mahakik, A. J. Lelis, R. Green, "Effects of Basal Plane Dislocations on SiC Power Device Reliability", in Proc. 2018 IEEE International Electron Devices Meeting (IEDM), pp. 448-449, 2018.
6. T. Ohno, H. Yamaguchi, S. Kuroda, K. Kojima, T. Suzuki, K. Arai, "Influence of growth conditions on basal plane dislocation in 4H-SiC epitaxial layer", *J. of Crystal Growth*, vol. 271, issues 1–2, pp. 1-7, 2004.
7. Ortiz-Conde, F. J. Garcia-Sanchez, J. Muci, A. T. Barrios, J. J. Liou, and C. S. Ho, "Revisiting MOSFET threshold voltage extraction methods", *Microelectron. Reliab.*, vol. 53, no. 1, pp. 90-104, 2013.
8. R. Schörner, P. Friendriches, and D. Peters, "Detailed investigation of N-channel enhancement 6H-SiC MOSFETs", *IEEE Trans. on Electron Devices*, vol. 46, no. 3, pp. 533-541, 1999.
9. S. Potbhare, N. Goldsman, G. Pennington, A.J. Lelis, and J. McGarrity, "Numerical and experimental characterization of 4H-silicon carbide lateral metal–oxide–semiconductor field-effect transistor", *J. Appl. Phys.*, vol. 100, no. 4, pp. 044515, 2006.

## I.27 Rugged WBG Devices and Advanced Electric Machines for High Power Density Automotive Electric Drives (North Carolina State University)

### Victor Veliadas, Principal Investigator

North Carolina State University  
Main Campus Drive, Suite 200  
Raleigh, NC 27606  
E-mail: [jvveliad@ncsu.edu](mailto:jvveliad@ncsu.edu)

### Susan Rogers, DOE Technology Development Manager

U.S. Department of Energy  
E-mail: [susan.rogers@ee.doe.gov](mailto:susan.rogers@ee.doe.gov)

Start Date: April 1, 2019

End Date: March 31, 2020

Project Funding (FY19): \$300,000

DOE share: \$300,000

Non-DOE share: \$0

### Introduction

The Department Of Energy's Electric Drive Technologies Area Goals for 2025 have set an aggressive target for traction electric motors. The targets are to increase power density (kW/L), and to reduce cost (\$/kW) using Heavy Rare Earth (HRE) free permanent magnets. The target for power density, efficiency, and cost are 50 kW/L, 97%, and 3.3 \$/kW, respectively. These targets have to be met within 2025 through design innovations, new manufacturing process, material innovations, and thermal innovations. Generally, the power density of the motor increases as the machine speed increases. However, the major challenges for high-speed machines (> 20,000 rpm) are the frequency dependent losses (resulting in poor efficiency), structural integrity (due to material limitations), poor performance of HRE-free permanent magnets at elevated temperature (> 140°C) or demagnetization during high temperature. Therefore, the motivation of this work is to design, modeling, and control of a 50 kW/L, and 97% efficient traction motor for the next generation electric drive using HRE-free permanent magnets.

### Objective

The objective of this project is to investigate, and design two alternative high-speed electric machines optimized for high power density (kW/L) and ultra-high efficiency with HRE-free permanent magnet materials and keeping practical limitations of manufacturability in context while addressing DOE EDT 2025 targets. One of the machines is based on a high pole count slotless stator and Halbach rotor with the combination of novel magnetic wedge in teeth, thermal plastic (silicone rubber) non-conventional winding material (Cu-CNT), and emerging Dy free magnet (to reduce cost). The second machine is based on conventional IPM structure using HRE-free magnets but with innovations in winding, rotor, pole shaping, and high pole count. A candidate machine will be down selected from the two and the DOE EDT 2025 targets of efficiency, cost, specific power (kW/kg), power density (kW/L) will be met.

### Approach

The design approach increases the operating speed while using non-conventional winding material (Cu-CNT), HRE-free permanent magnet, shaped teeth design, optimum slot/pole combination, and enhanced cooling techniques. In the first phase of work in BP1, three 100 kW permanent magnet machines have been designed to select the optimum design that can achieve the target performance of DOE ELD 2025.

#### ***Design-01: High-power Density (> 50 kW/L) Electric Traction Motor using Stranded Conductor in Stator and HRE-free Permanent Magnet in Rotor***

- Single V-shape rotor
- NEOREC45MHF HRE-free permanent magnet

- 72-slot/12-pole combination
- Cu-CNT conductors

**Design-02: High-power Density (> 50 kW/L) Electric Traction Motor using Bar/Hairpin Conductor in Stator and HRE-free Permanent Magnet in Rotor.**

- Single V-shape rotor
- NEOREC45MHF HRE-free permanent magnet
- 72-slot/12-pole combination
- Shaped teeth
- Asymmetric Bar/Hairpin Conductor in stator

**Design-03: High-power Density (> 50 kW/L) Electric Traction Motor using Slotless Stator and HRE-free Permanent Magnet Halbach Rotor.**

- Halbach rotor
- NEOREC45MHF HRE-free permanent magnet
- 24-slot/14-pole combination
- Slotless stator
- Space-shifted wye-delta winding,4,5
- Thermal plastic (conductivity > 2 )6
- Cu-CNT conductor

## Results

The electromagnetic design results for the three machines are summarized in the Table I.27.1 below:

**Table I.27.1 Summarized Electromagnetic Results**

Parameters	Design-I	Design-II	Design-III
Topology	Slotted	Slotted	Slotless
Outer Diameter (mm)	204	204	215
Active length (mm)	61	61	55
Corner (rpm)	5,700	6,200	9,000
<b>Power (kW)</b>	<b>&gt; 100</b>	<b>&gt; 100</b>	<b>&gt; 100</b>
Torque (Nm)	175	155	108
Voltage, $V_{LL}$ (V)	360	330	440
Current ( $I_m$ ) (A)	564	564	300
Current Density ( $A/mm^2$ )	28	24	27
<b>Maximum speed (rpm)</b>	<b>18,000</b>	<b>18,000</b>	<b>20,000</b>
Conductor loss (W)	3,350	2,600	3300
$\eta$ (%)	96.00	96.80	97.00
<b>Power Density (kW/L)</b>	<b>&gt;53</b>	<b>&gt;51</b>	<b>&gt;51</b>

<b>Ripple (%)</b>	<b>6%</b>	<b>5%</b>	<b>0.1%</b>
<b>Magnet (kg)</b>	0.7	0.6	2.3
<b>Topology</b>	Fig. 1	Fig. 3	Fig. 5
<b>Short circuit current at 18,000 rpm</b>	Fig. 2	Fig. 4	Fig. 6
<b>Comment</b>	Achieved the target density	Achieved the target density	Very high short circuit current
	Working on Demagnetization	Working on Demagnetization	Working on Demagnetization

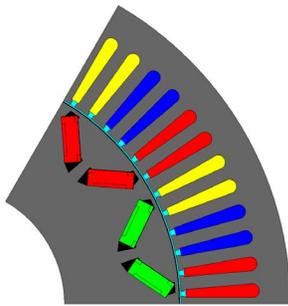


Figure I.27.1 Design-I

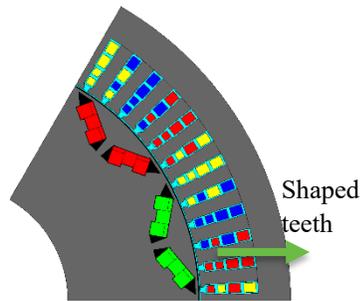


Figure I.27.2 Design-II

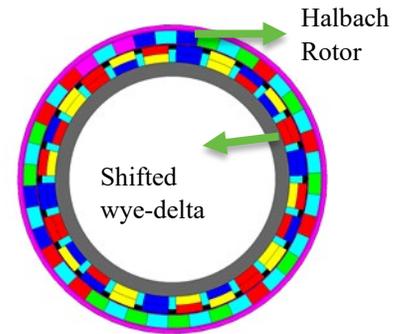


Figure I.27.3 Design-III

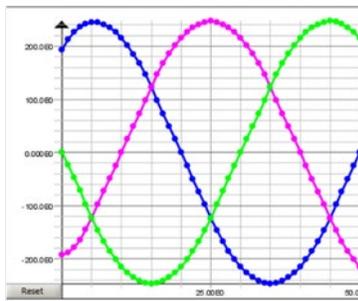


Figure I.27.4 Short circuit at 18,000 rpm

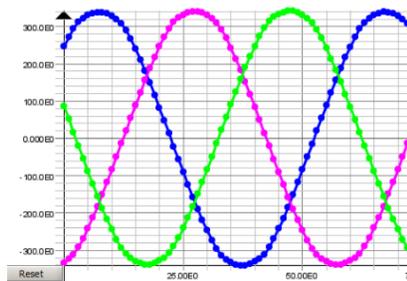


Figure I.27.5 Short circuit at 18,000 rpm

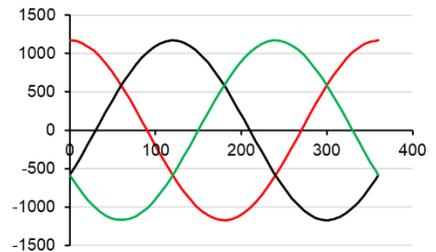
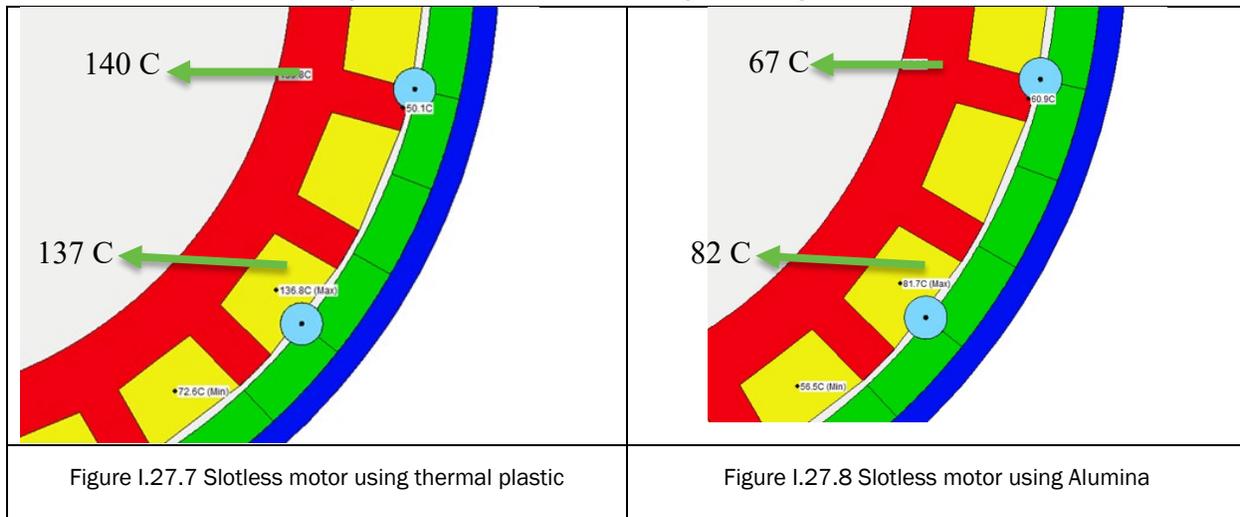


Figure I.27.6 Short circuit at 18,000 rpm

### Thermal Performance Investigation of Slotless Motor using Non-magnetic Alumina Teeth



### Conclusion

All three designs can achieve the target power density of 50 kW/L, and peak efficiency of 97% validated by electromagnetic analysis. Design-I and Design-II have the advantage of low short circuit current and low magnet material usage compared to the Design-III. Therefore, all three designs are feasible candidates to meet the DOE EDT 2025 targets. However, the major problem is the demagnetization issue during high-temperature (>150C) and short circuit conditions. Therefore, we are focusing on design innovation in rotor pole shaping or rotor design to achieve the target demagnetization performance during high-temperature (150 C) operation of HRE-free permanent magnets.

### References

1. T. Raminosa and T. Aytug, "Impact of Ultra-Conducting Winding on the Power Density and Performance of Non-Heavy Rare Earth Traction Motors," 2019 IEEE International Electric Machines & Drives Conference (IEMDC), San Diego, CA, USA, 2019, pp. 2107-2114.
2. [https://product.tdk.com/info/en/catalog/datasheets/magnet\\_neo\\_neorec45mhf\\_en.pdf](https://product.tdk.com/info/en/catalog/datasheets/magnet_neo_neorec45mhf_en.pdf)
3. M. S. Islam, I. Husain, Adeeb Ahmed and Anand Sathyan, "Asymmetric Bar Winding for High Speed Electric Machines," IEEE Transaction on Transportation Electrifications, 2019 (In R-2).
4. M. S. Islam, M. A. Kabir, R. Mikail and I. Husain, "A New Space Harmonics Minimization Strategy for Fractional Slot Concentrated Windings," 2018 IEEE Transportation Electrification Conference and Expo (ITEC), Long Beach, CA, 2018, pp. 412-417.
5. M. S. Islam, M. A. Kabir, R. Mikail and I. Husain, "Space-shifted Wye-Delta Winding to Minimize Space Harmonics of Fractional Slot Concentrated Winding," IEEE Transaction on Industry Applications, 2019 (In R-2).
6. M. S. Islam, R. Mikail and I. Husain, "Slotless Lightweight Motor for Aerial Applications," in IEEE Transactions on Industry Applications, 2019.

## II Electric Drive Technologies Development

### II.1 High Speed Hybrid Reluctance Motor Utilizing Anisotropic Materials (General Motors LLC)

#### Edwin Chang, Principal Investigator

General Motors Global Propulsion Systems  
777 Joslyn Avenue  
Pontiac, MI 48360  
E-mail: [edwin.chang@gm.com](mailto:edwin.chang@gm.com)

#### Steven Boyd, DOE Program Manager

U.S. Department of Energy  
E-mail: [steven.boyd@ee.doe.gov](mailto:steven.boyd@ee.doe.gov)

Start Date: October 2016

End Date: April 2020

Total Project Cost: \$7,081,060

DOE share: \$4,637,060

Non-DOE share: \$2,444,000

#### Project Introduction

The objective of this project is to design and verify motor designs without heavy rare earth (HRE) content capable of achieving DoE Motor Year 2020 performance and cost targets. These three motor variants are Variant 1: Heavy Rare Earth-free Permanent Magnet Motor (HRE-free PM motor), Variant 2: Synchronous Reluctance Motor (SyRM) with Small HRE-free Magnet Assist, and Variant 3: Hybrid Induction Motor with Insert Copper Bars and Cast Aluminum End-rings.

#### Objectives

The objective of the project is to research, develop, and demonstrate 3 new motor types for traction applications. Each design should be capable of achieving or exceeding the following technical targets, set by the DoE to be achieved by 2020:

- Cost (\$/kW) less than \$4.7
- Specific Power (kW/kg) greater than 1.6
- Power density (kW/L) greater than 5.7

These motors are enabled by the following technologies, which are evaluated through the course of this project:

- HRE-free magnets must be developed to meet stringent coercivity and remanence performance criteria
- Copper – aluminum interfaces must be developed to be robust in a traction motor environment
- Motor electromagnetic and mechanical design techniques must be developed to ensure that these enabling technologies can be incorporated to meet motor performance requirements.

Each design should demonstrate advantages over conventional baseline designs in one or more of the following categories: cost, efficiency, and power density. Each design is also expected to have proven manufacturability and to undergo typical durability and performance testing by GM to ensure they meet market requirements.

## Approach

Three motor design types will be studied to determine the feasibility of each approach. These three motor variants will be selected based on their expected ability to meet the technical targets. These design approaches will take advantage of material advancements which will allow these motors to meet the performance requirements without heavy rare earth elements or rare earth elements altogether.

The project will concentrate on four major tasks:

Task 1: Material Evaluation and Selection

Task 2: Electromagnetic and Mechanical Machine Design

Task 3: Electric Motor Prototype Manufacturing

Task 4: Verification Testing and Performance Evaluation

### ***Task 1: Material Evaluation and Selection***

- Development of the requirements for Grain Oriented Electrical Steel (GOES)
- Survey of available grades of GOES
- Industry survey of GOES available grades and Selection for Electromagnetic Design Studies
- Execution of FEA-based design studies for Synchronous Reluctance Motor using GOES, and Hybrid Synchronous Reluctance Motor using Anisotropic HRE-free magnets and GOES
- Development of, working with suppliers, HRE-free anisotropic magnet material
- Evaluation of the developed anisotropic HRE-free magnets and Non-Oriented Electrical Steel (NOES) for use in the motor laminations.

### ***Task 2: Electromagnetic and Mechanical Design of 3 Machines***

- Detailed structural, thermal, and electromagnetic analysis of the machine concepts to ensure that the motors meet both the performance and reliability objectives required for use in General Motor's electrified vehicle portfolio
- Generation of an Indentured Bill of Materials (BoM).

### ***Task 3: Electric Motor Prototype Manufacturing***

- Prototype motors will be built to ensure that those meet all GM Production Bill of Process (BoP) requirements
- Production Manufacturing Equipment will be identified and its associated costs will be documented
- Comprehensive test plan for machine verification will be defined and durability test plan for demonstration will be developed.

### ***Task 4: Verification Testing and Performance Evaluation***

- All three motor designs will be calibrated for peak torque and efficiency
- Machines will be tested for performance and efficiency verification
- Torque and power vs. speed curves will be generated

- Complete efficiency maps for both motoring and generating will be generated for operations at different voltage levels
- Measured performance maps will be compared to the predicted results for data correlation purposes
- Rotor durability testing will be executed on two variants (Synchronous Reluctance motor with HRE-free Magnet Assist and High Performance Hybrid Induction Motor using Inserted Copper Bars and Aluminum Die Cast End-rings) and will include rotor speed cycling at various RPM to induce fatigue failures in the rotor laminations
- HRE-free PM motor variant will be excluded from rotor durability testing due to its similarity to other production designs that have previously demonstrated superior reliability.

Oak Ridge National Laboratory, ORNL, a co-recipient of this project, is responsible for aspects of materials testing. The objectives are to characterize material properties of electrical steels and cast Al to Cu bar interfaces.

## Results

### Motor Design

Table II.1.1 summarizes the motor designs. The designs exceed the DoE Motor Year 2020 power density and specific power targets.

**Table II.1.1 Summary of motor performance results for all three variants**

	HRE-free PM Motor	Synchronous Reluctance Motor with HRE-free PM Assist	Hybrid Induction Motor with Insert Cu Bars and Cast Al End-rings
Stator Outer Diameter (mm)	208	190	190
Rotor Outer Diameter (mm)	139.5	139.1	139.1
Stator Core Length (mm)	200	100	100
Power (kW)	148	86	84
Torque (N-m)	372	255	310
Max RPM	12000	16500	14000

### Motor Manufacturing

General Motors worked with key suppliers to produce all subcomponents for the stators and rotors. All rotors and stators were constructed, as show in Figure II.1.1 and Figure II.1.2.



Figure II.1.1 Variant 1, 2, and 3 rotors shown from left to right





Figure II.1.2 Variant 1, 2, and 3 stators shown from left to right

Significant development was performed to improve the casting results of Variant 3. Simulations were performed as shown in Figure II.1.3 to aid in tooling design. A design of experiment was created varying bar length, casting parameters, and flux, leading to a 33% improvement in bar retentions over the baseline design, as shown in Figure II.1.4.

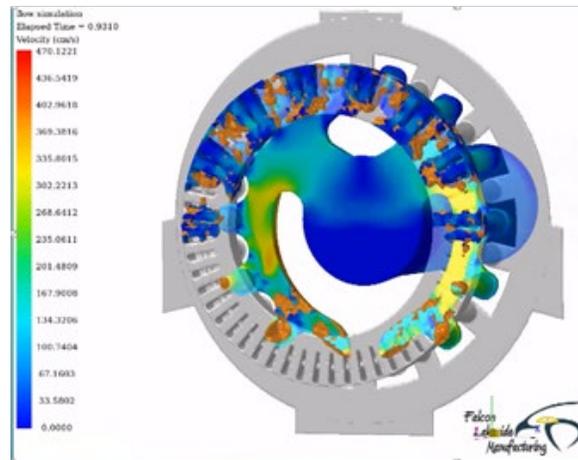


Figure II.1.3 Rotor casting simulations for improved Al-Cu interface strength

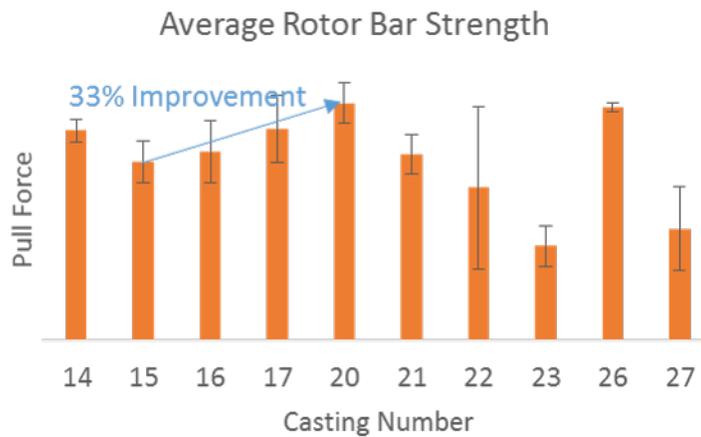


Figure II.1.4 Average rotor bar improvement from baseline (Casting #15) based on pull force. Casting numbers represent different parameters in the design of experiment

### Cost analysis

GM completed initial cost analysis showing that while the DoE cost target of \$4.7/kW was met for the Variant 1, significant challenges were still found to meeting the DoE 2020 cost target with Variant 2 and Variant 3. The cost estimate is shown below in Figure II.1.5. Manufacturing analysis, including floor plans, tooling estimates, and required headcount were completed.

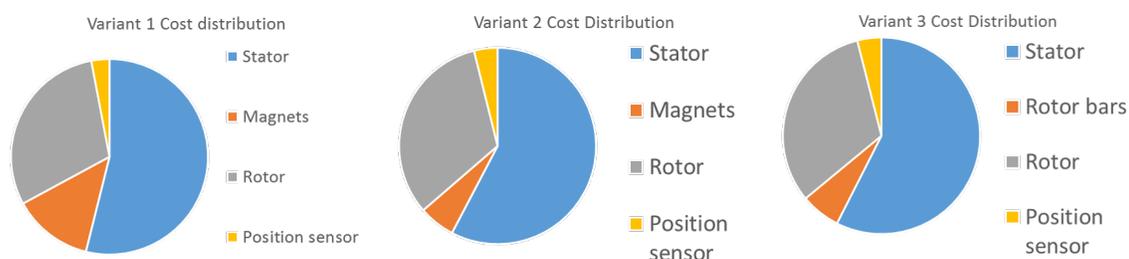


Figure II.1.5 Cost analysis of Variants 1, 2, and 3. Variant 1 only was estimated to be below the DoE cost target of \$4.7/kW.

### Motor Testing

All rotors were tested at high speeds to ensure rotor strength. The testing results are shown in Table II.1.2. All rotors demonstrated capability beyond the rated speed and were tested until failure. In addition, two of the three variants were calibrated for low speed operation and efficiency and performance testing were completed, with correlation with analytical data underway. This testing is expected to complete in the first quarter of 2020.

Table II.1.2 Rotor overspeed testing

Test unit	Type	Speed 1	CMM	Speed 2	CMM	Speed 3	CMM	Ramp Speed to Failure
1	Variant 1 HRE-free PM							*
2				*				
1	Variant 2 (SyRM w PMA)							*
2								*
1	Variant 3 (IM)							*
2						*		

\* indicates test step at which rotor rub occurred

### Oakridge National Lab (ORNL) testing

#### Background and Ongoing Efforts

ORNL continued working with steel samples and copper/aluminum bars that were provided by GM for materials analysis. GM previously provided various sample sizes and shapes for three steel products for metallography, mechanical testing, and electromagnetic testing. Earlier in the project, tensile tests were performed on a single sample of each of the three candidate materials. Five additional samples for each material (15 total) underwent tensile testing at room temperature. Fatigue testing of 20 samples per material (60 total) were completed. These tests were performed with load control at 50 Hz with a sinusoidal waveform and are discontinued after 10,000,000 cycles. Upon failure, each sample is inspected with SEM to show crack initiation location and any grain orientation at the crack initiation site. The resulting stress live curves are shown in Figure II.1.6, showing

that the fatigue life of material “C” is generally greater than that of material “B”, and the fatigue life of material “B” is generally greater than that of material “A” for all tested stress levels.

Upon failure, each sample was inspected with SEM to analyze crack initiation location and any grain orientation at the crack initiation site. Furthermore, microscopy and microhardness measurements are being performed on the edge of the samples to inspect for cleaved grains, various deformation patterns, and to determine a distribution hardness and investigate residual stress as a result lamination stamping action. Compositional analysis of the bulk material of the sample, as well as the coating is also underway. Coating thickness and overall sample density are being determined.

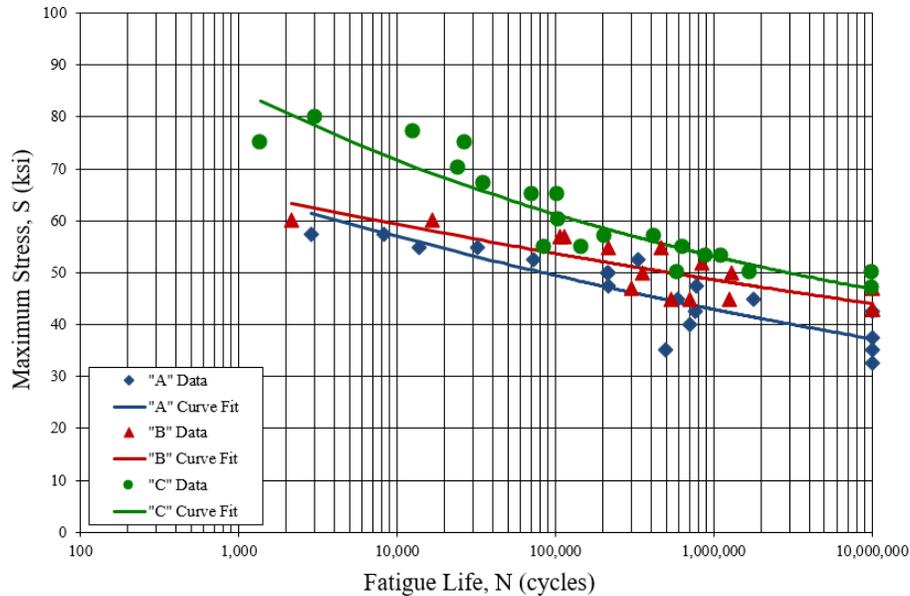


Figure II.1.6 Stress life curves for materials “A”, “B”, and “C”.

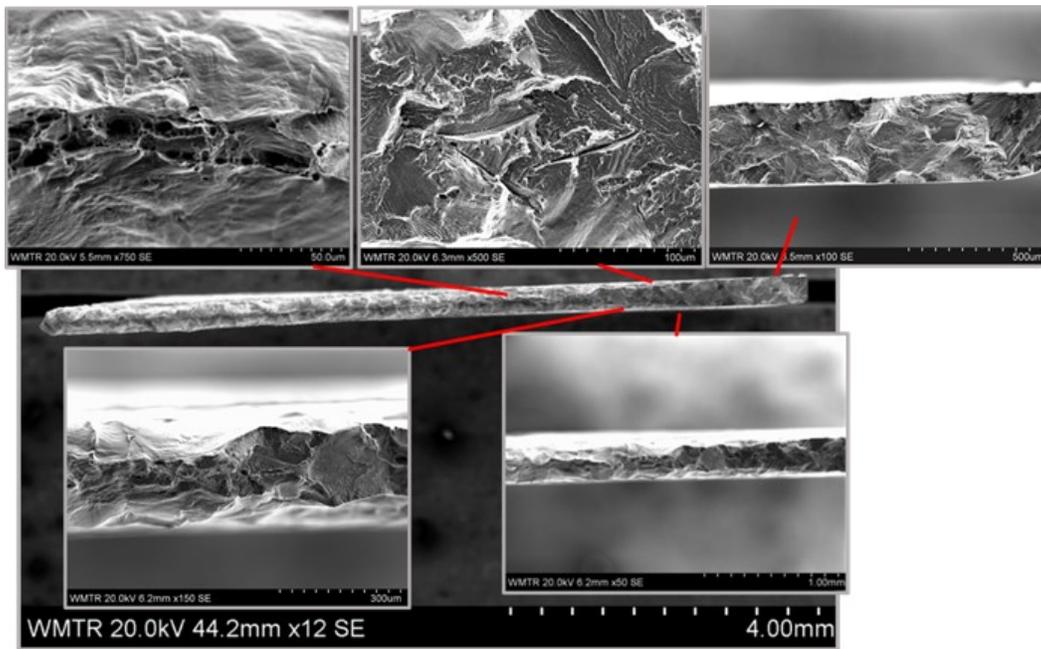


Figure II.1.7 Example of fracture analysis with SEM for material A, sample #2.

### 3D Analysis of Single Bar Samples with X-Ray CT Scanning

GM provided ORNL with single bar samples (shown in Figure II.1.8) that were prepared for porosity analysis. X-Ray CT scanning faces the similar issue as CT scanning with neutrons. In this case, the sample is small enough not to sufficiently attenuate the X-Ray beam during analysis. Scanning of one bar has been completed, and a reconstructed 3D rendering is shown in Figure II.1.9. Both left and right images are 3D renderings at the same angle, with the left image having no object (Al and Cu) opacity and the right image with higher opacity to distinguish the orientation of the sample. This data is being analyzed to determine pore size and distribution throughout the sample. A visual inspection shows that while large voids are present near the tab-like features of sample, there are very few and small voids at the Cu-Al interface, the critical area of interest.

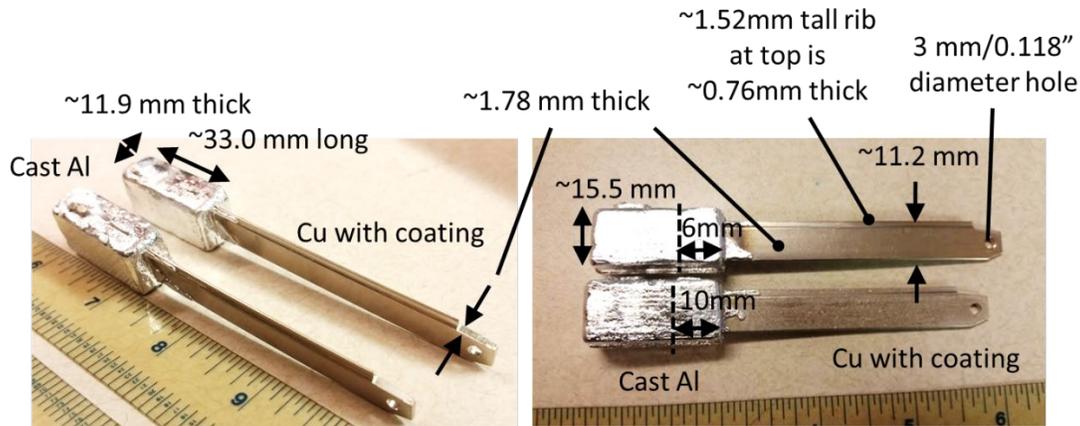


Figure II.1.8 Rotor bar casting sample.

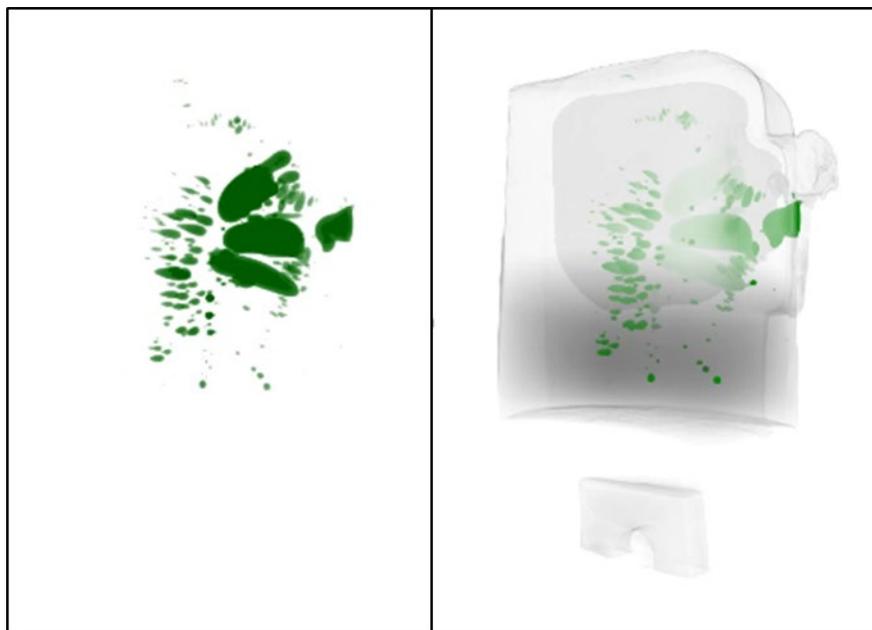


Figure II.1.9 X-ray CT scanning results from rotor bar sample.

### Conclusions

GM completed manufacturing of the three rotor variants. The motor designs showed promise in exceeding the DoE 2020 motor targets for power density and specific power. Variant 1 cost estimates beat the DoE 2020 motor targets, but Variants 2 and 3 show some challenges to meeting the targets, largely due to the lower

power density of the two variants. The three motor variants were tested at high rotational speeds to confirm rotor strength. Motor calibration and performance were completed at low speeds for two of the three variants, with plans to complete the testing activity, including rotor fatigue, in the upcoming year, with expected completion in the first quarter of 2020. The test results will be compared and correlated with the analytical predictions.

## **Key Publications**

### ***Patent Applications***

1. “Rotor for an Electric Machine”

## **Acknowledgements**

ORNL testing managed by Tim Burrell, who also contributed text for the Oak Ridge National Lab testing portion of this report. Motor designs completed by Jorge Cintron-Rivera, Jihyun Kim, and Jingchuan Li. Testing and calibration activity coordinated by Antonio Aviles. GM electric drive engineering, research and development, motor manufacturing, and development/validation teams contributed design, manufacturing, and testing expertise to this project. GM contract management performed by Sean Campbell.

## II.2 Dual Phase Soft Magnetic Laminates for Low-cost, Non/Reduced-Rare-Earth Containing Electrical Machines (GE Global Research)

### **PR Subramanian, Principal Investigator**

GE Research  
One Research Circle  
Niskayuna, NY 12309  
E-mail: [subrampr@ge.com](mailto:subrampr@ge.com)

### **Steven Boyd, DOE Program Manager**

U.S. Department of Energy  
E-mail: [steven.boyd@ee.doe.gov](mailto:steven.boyd@ee.doe.gov)

Start Date: October 1, 2016  
Project Funding: \$6,148,355

End Date: December 31, 2019  
DOE share: \$4,299,285

Non-DOE share: \$1,849,050

### **Project Introduction**

In this project, GE is scaling-up the processing of an innovative dual phase soft magnetic material which will enable electric traction drive manufacturers to achieve the cost target of \$4.7/kW peak power. Cost reduction is driven by enabling non-rare earth materials containing machine designs with over 40% reduction in active material cost due to the elimination of rare earth magnets. A full-scale prototype motor with 55 kW peak power and 30 kW continuous power capability will be manufactured with the dual phase material to prove both performance and manufacturability.

The dual phase magnetic material is a uniquely programmable material with the capability of having its magnetic permeability being locally controlled at the millimeter scale. The magnetization can be programmed to have values between zero and full saturation to meet the machine design requirements without having to remove the material in these regions to reduce the flux leakage. This capability enables rotor and/or stator poles to be magnetically decoupled, while maintaining mechanical integrity of the laminations. As shown in Figure II.2.1, bridges and center posts used to define flux barriers in SynRel and IPM machines can be made non-magnetic, improving the effectiveness of the barrier. The magnetic decoupling of the poles reduces the flux leakage from pole to pole on the rotor, while improving the flux linkage between the rotor and stator. Maintaining the mechanical integrity enhances the mechanical strength for high speed operation, thus enhancing the machine power capacity, power factor, power density, and efficiency. The ability of the non-magnetic regions to act as retaining elements shows the greatest advantage in machines with high tip speeds. Thus, dual phase materials are particularly well suited to the high-power density, high-efficiency designs used in the transportation market sector.

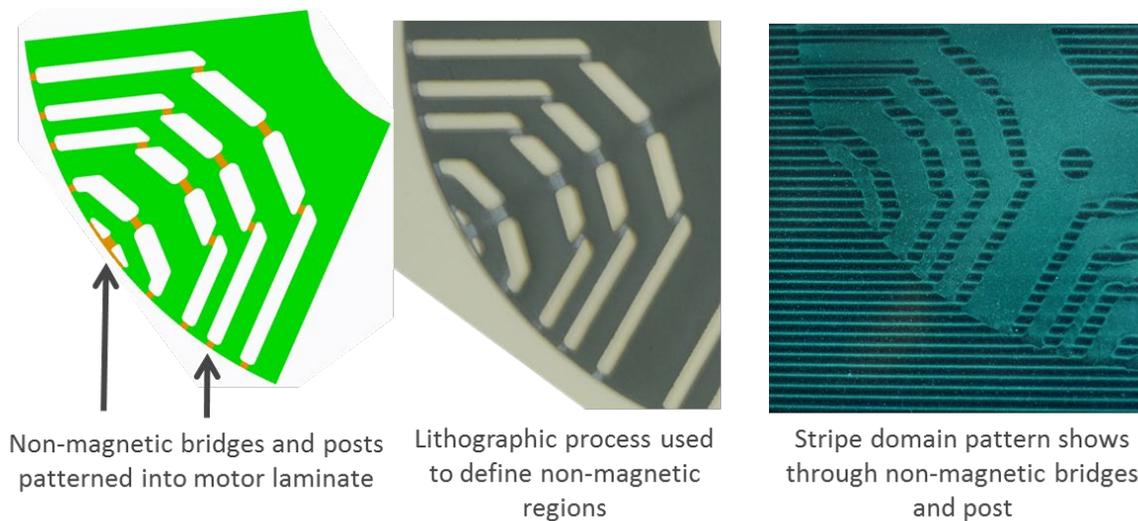


Figure II.2.1. Illustration of the dual phase structure in a laminate used to manufacture a SynRel machine. The left image shows where the non-magnetic (orange) regions are patterned into the magnetic (green) laminate. The middle image shows an actual laminate in which a ceramic mask has been applied. The exposed regions will become non-magnetic after nitrogenation. The right image shows a laminate after nitrogenation, placed underneath a magnetic indicator film. The stripe domains shine through the regions which have been made non-magnetic.

## Objectives

GE Global Research leads a team comprised of Carpenter Technology Corp. and Oak Ridge National Lab to advance unique and innovative dual phase soft magnetic material technology to Technology Readiness Level (TRL) 7 and demonstrate the material in a 30 kW electric motor for electric vehicles. Dual phase laminate materials will revolutionize the design of electric machines by opening the design space for new cost-effective and sustainable topologies. Dual phase laminates have the potential to be the first, completely new class of soft magnetic materials to be introduced in over a quarter of a century. Their introduction will lead to a step change in system performance and could dramatically accelerate the penetration of electric vehicles into the global automotive market. Dual phase magnetic materials offer the electric motor designer the ability to locally control the magnetic saturation level in a motor laminate at the millimeter scale, while at the same time enhancing the mechanical strength of the laminate material, resulting in an enhancement in motor performance and efficiency.

The project goal is to demonstrate scaled-up manufacturing of the dual phase magnetic materials and demonstrate a full-scale traction motor manufactured with this material. Two motor prototypes are fabricated using the dual phase material: 1) A subscale prototype with a continuous power rating of  $\approx 3.7$  kW (5 hp) has been fabricated in the second year to demonstrate dual phase alloy process improvement; and 2) a full-scale prototype with a continuous power rating of  $\approx 30$  kW (40 hp) will be fabricated in the third year of the effort to demonstrate a manufacturable machine that can be tested in an operational environment, thus achieving TRL 7.

## Approach

The team is comprised of GE Global Research, Carpenter Technology Corporation, and Oak Ridge National Lab. GE is responsible for selecting the motor topology, writing performance specifications, and performing detailed design activities for the two prototypes. GE performs in depth testing of each prototype on test facilities located in the Electric Machines Laboratory. Existing motor drive electronics are used to validate performance over the envelope of speed, power and torque conditions defined for electric vehicle motors.

Figure II.2.2 shows the manufacturing method for the prototypes with dual phase magnetic laminate rotors. Carpenter has responsibility for producing the 0.010" rolled sheet of the dual phase magnetic material needed

for the prototypes. This requires developing the melt practice, heat treatment sequences, and rolling schedules customized for this alloy. This amount of material is sufficient for producing both prototypes. The rotor design for each prototype is laser cut from the rolled sheet. GE applies the ceramic mask needed to modulate the uptake of nitrogen into the laminates and create the specified pattern of magnetic and non-magnetic regions. The coated laminates are nitrogenated at high temperature, which austenitizes the regions to be made non-magnetic. GE then removes the ceramic mask prior to assembly of the rotor stack. A prototype manufacturer, Applinetics Engineering LLC, shrink fits the rotor stack onto a shaft prior to integration into the prototypes.

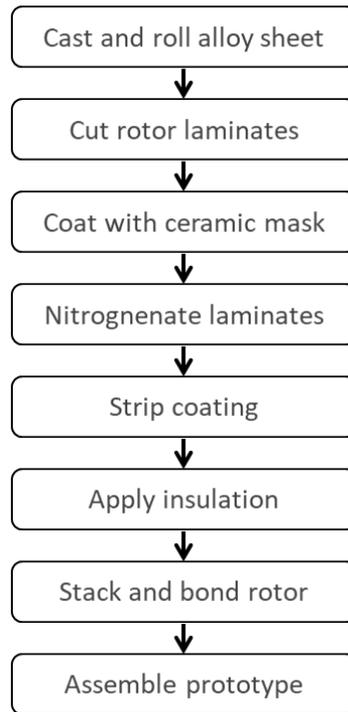


Figure II.2.2 Manufacturing sequence for prototypes containing dual phase magnetic laminates.

In parallel, GE and ORNL perform an in-depth study of the nitrogenation kinetics of the dual phase alloy material. The studies are performed on coated coupons and laminates prepared by GE. ORNL explores the effect of nitrogenating conditions on the austenitization of the alloy. Residual stress analysis is performed to verify finite element calculations of the stress states caused by differential thermal expansion between the magnetic and non-magnetic regions. The results of the coupon tests are used to optimize gas nitrogenation furnace parameters to minimize total cycle time and cost. Further, the residual stress analysis is used to set design rules that will avoid warpage and minimize distortion in the nitrogenation processing of the rotor laminates.

The first annual performance period focused on 1) scale-up of alloy production at Carpenter, 2) optimization of nitriding furnace parameters at ORNL, and 3) detailed subscale prototype design at GE. The first annual Go/NoGo condition is the creation of a subscale motor design that shows a calculated level of performance in excess of a best in class design using conventional materials. The second annual performance period focused on 1) scaled-up processing of the subscale dual phase rotor laminates, 2) assembly and test of the subscale prototype, and 3) detailed design of the full-scale prototype. The second annual Go/NoGo condition is a demonstration of the subscale prototype and measured power output of 3.7 kW. The third annual performance period will focus on 1) scaled processing of the full-scale dual phase rotor laminates for the full-scale prototype, 2) and assembly and test of the full-scale prototype.



## Results

Scaled production of the full-scale dual phase rotor laminates was explored in FY2019. 275 pieces of 20 cm diameter dual phase laminates with a stack length of 7 cm were manufactured at a sheet metal manufacturer (Carpenter Technology Inc.) and several engineering and heat treatment service suppliers. All processing steps are conventional and scalable. A full-scale synchronous reluctance prototype motor has been fabricated using the dual phase laminate rotor manufactured following the sequence shown in Figure II.2.2.

Besides the dual phase laminate rotor, other components of the full-scale prototype motor were procured, custom made, machined and manufactured in Q2 FY2019. The motor assembly was initiated by the successful installation of the dual phase rotor core onto the rotor shaft using a shrink fit. The rotor assembly was then balanced to an ISO G1 balance, which is typical of electric motors with this size. Following the rotor assembly and balance, the armature assembly including the assembly of the cooling sleeve onto the stator core, the stator core into the housing, and the motor endplates was carried out. The fully assembled motor was shipped to GE Research in Q3 FY2019, as shown in Figure II.2.3a. The mass and volume of the active components including rotor core, stator core and windings are 30 kg and 4 L, respectively. The mass and volume of the motor including rotor shaft and bearings, based on the overall stator outside diameter and overall length, are 44 kg and 12.7 L, respectively. The exterior dimensions of the prototype motor are shown in Figure II.2.3b.

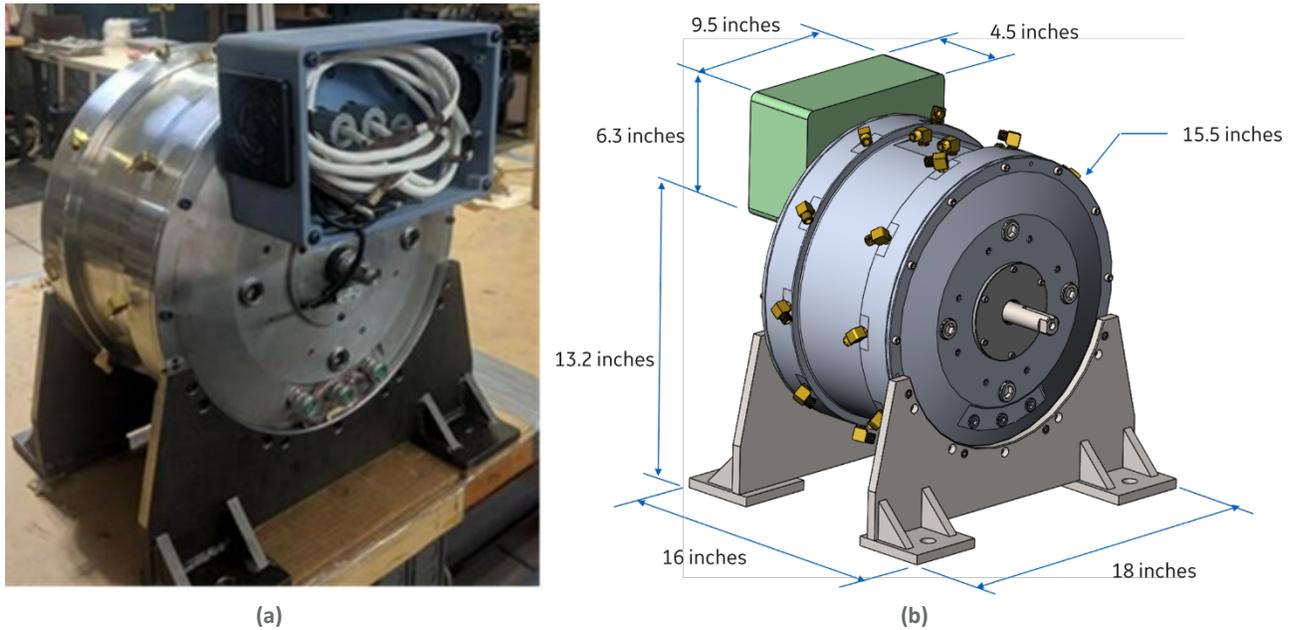


Figure II.2.3 a) Fully assembled full-scale prototype motor. b) exterior dimensions of the prototype motor.

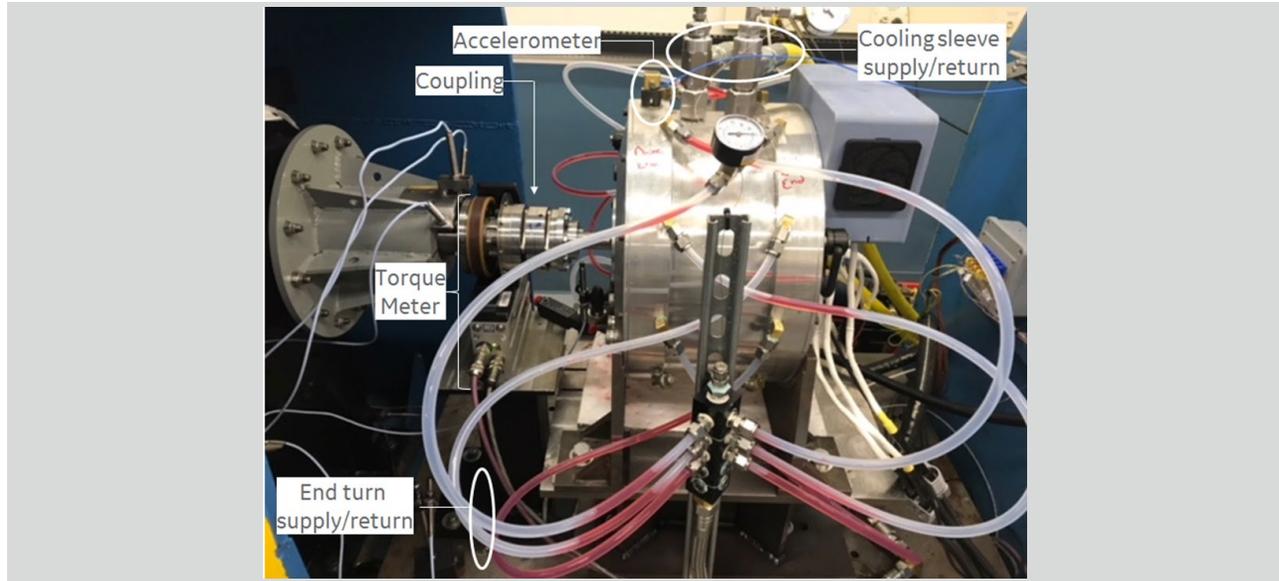


Figure II.2.4 Full-scale prototype motor on a dynamometer test stand.

The prototype was loaded to the dynamometer test stand, as shown in Figure II.2.4, and tested in the GE Research Electric Power Lab. The motor was driven by the dyno dc motor in a constant speed mode. The ac current excitation was applied to the test motor at a constant torque mode. The measurements were conducted over an operating voltage range between 300 and 450 Vdc and a speed range between 500 and 12000 rpm with a maximum per-phase current of 400 A rms. A current angle ( $\gamma$ ) sweep was conducted at  $\pm 1$  to 2 degrees (electrical) around the predicted  $\gamma$  values to locate the maximum torque per ampere (MTPA) point at each speed. The shaft torque output was measured by a torque meter. The 3-phase input voltage, current, and temperatures were measured at each operating speed. The power output, power factor, and efficiency were then derived accordingly. Heat run tests were conducted for 30 minutes at 2800, 5000, and 7000 rpm at the 30kW power output points.

The coolant flowrate, inlet pressure, coolant pressure drop, and temperature were measured at continuous power operating points. The results are summarized in Table II.2.1.

**Table II.2.1 The coolant flowrate, inlet pressure, coolant pressure drop, and temperature at continuous power.**

Location	Flow rate (liter/min)	Inlet Temp ( °C)	Inlet Pressure	Outlet Pressure
End turn spray	12 (total for 12 nozzles)	50-60	40 psig	0 psig (Cavity at atmospheric pressure)
Cooling Sleeve	10.6	50-60	20 psig	8 psig

The measured continuous power output meets the FreedomCAR 2020 advanced traction motor target [1] of 30 kW at the speed range between 2800 and 8000 rpm (20% and 60% of designed maximum speed of 14000 rpm), as shown in Figure II.2.5. The shaft torque also meets the target at speeds up to 8000 rpm. The origin of the decreased torque and power at the speed range between 9000 and 12000 rpm is under investigation.

The maximum measured efficiency is 94%, which meets the FreedomCAR 2020 advanced traction motor target [1] of 94-96%, as shown in Figure II.2.6. The efficiency at 20% of rated torque of 105 Nm as a function of speed is also shown in Figure II.2.6. The measured maximum efficiency is 1.3% lower than the predicted value of 95.3%, the origin of which is also under investigation.

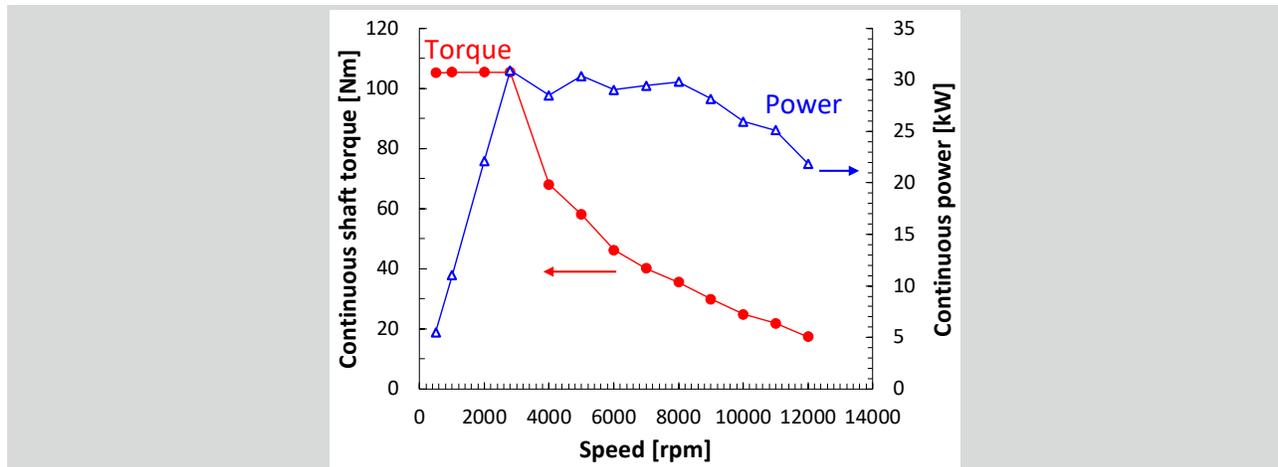


Figure II.2.5 Measured continuous shaft torque and power output of the full-scale dual phase synchronous reluctance prototype made from the dual phase laminate rotor.

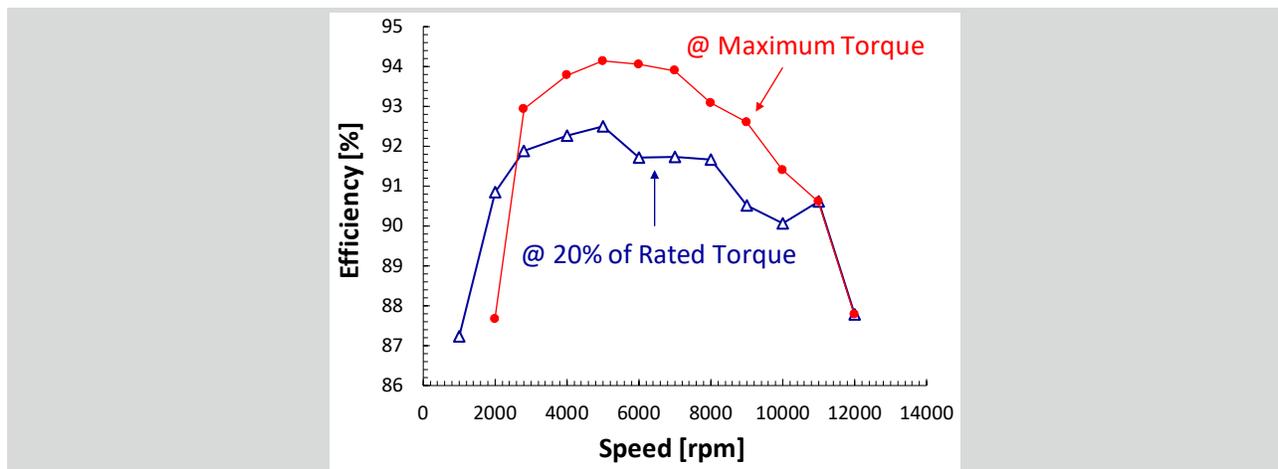


Figure II.2.6 Measured efficiency of the full-scale dual phase synchronous reluctance prototype made from the dual phase laminate rotor.

The peak power at 20% of designed maximum speed of 14000 rpm was measured at 2800 rpm and 400 A<sub>rms</sub> with a time duration of 25 seconds. The measured peak power of 41.7 kW is 26% lower than the 55 kW target [1]. As a consequence, the specific power and power density calculated based on the measured peak power have not met the targets [1].

It is worth noting that the motor was tested up to 12000 rpm, instead of the designed maximum speed of 14000 rpm. A detailed mechanical analysis indicates that the mechanical strength of the dual phase laminate rotor with the original design is strong enough to operate up to 14000 rpm. However, at the beginning of the laminate manufacturing, to mitigate the risk on stacking and bonding the laminates due to the laminate warpage, several holes were added on each laminate so that bolts and nuts through these holes could be used to apply axial force to overcome the warpage when needed. The outer peripheries of these holes become highly stress concentrated regions, thus exposing the rotor to the risk of operating beyond 12000 rpm. The holes could be removed in future for laminates with reduced warpage by improved control of the manufacturing process.

The comparison of the calculated and measured full-scale dual phase synchronous reluctance motor prototype and FreedomCAR 2020 advanced traction motor target is shown in Table II.2.2.

**Table II.2.2 Target vs. calculated and measured performance of the full-scale dual phase synchronous reluctance motor prototype.**

Parameter	Target	Calculated	Measure
Peak Power (kW)	≥55	56.2	41.7
Continuous Power (kW)	≥30	34	30
Specific Power (kW/kg)	≥1.6	1.93 (1.28) <sup>a</sup>	1.38 (0.95) <sup>a</sup>
Power Density (kW/l)	≥5.7	5.86 (4.47) <sup>b</sup>	4.53 (3.31) <sup>b</sup>
Maximum Speed (rpm)	14,000	14,000	12,000
Maximum Efficiency (%)	≥94-96	95.3	94.1
Cost (\$/kW)	≤4.7	Tbd	Tbd

<sup>a</sup> The values inside and outside of the parentheses were calculated based on the weight of active machine materials including and excluding rotor shaft and bearings, respectively.

<sup>b</sup> The values inside and outside of the parentheses were calculated based on overall stator outside diameter and overall length, and an initial estimate of the volume without the exact coil dimensions, respectively.

### Conclusions

The full-scale synchronous reluctance dual phase motor prototype was fabricated and tested in FY2019. The 20 cm-diameter and 7 cm-stacking length dual phase laminate rotor was manufactured in collaboration with US industry suppliers from sheet metal manufacture, to laminate cutting, surface treating, heat treating, and laminate stacking and bonding engineering service suppliers using scalable approaches.

The measured prototype motor performance met the FreedomCAR 2020 advanced traction motor targets [1] of continuous power of 30 kW and maximum efficiency of 94% over the speed range of 2800 to 8000 rpm. The peak power was measured as 41.7 kW at 2800 rpm with 400 A<sub>rms</sub>. The causes for the lower than predicted continuous power over the speed range of 9000 and 12000 rpm and the peak power at 2800 rpm are under investigation.

### Key Publications

1. Lawrence Bernard Kool, Min Zou, Wanming Zhang, Susan Corah, Christopher Klapper, Francis Johnson, Steve Buresh, “Method for forming a nitrogenation barrier and machine formed using a body having the nitrogenation barrier”, US Patent Application Publication 20180183279A1, published June 28, 2018.

### References

1. Patel B. Reddy, Ayman M. EL-Refaie, Steven Galioto, and James P. Alexander, “Design of Synchronous Reluctance Motor Utilizing Dual-Phase Material for Traction Applications”, *IEEE Transactions on Industry Applications*, vol. 53, No.3, pp. 1948-1957, May/June 2017

### Acknowledgements

The project team would like to acknowledge all the research members who performed different portions of the material development, motor design, motor fabrication & testing tasks. In particular, we would like to thank Steve Buresh, Sue Corah, James Graham, Shenyan Huang, Christopher Klapper, Lawrence Kool, Di Pan, Robert Pietrocola, Changjie Sun, Vandana Rallabandi, Yongxiang Wang, Wanming Zhang, Yichao Zhang, Joseph Zierer, Min Zou (from GE Research), and Karthik Bodla, Anoop Jassal, Frank Johnson (formerly of GE Research). We would also like to thank our external partners from Oak Ridge National Laboratory – Michael Brady, Craig Bridges, Hunter Henderson, and Orlando Rios.

## II.3 Cost Effective 6.5% Silicon Steel Laminate for Electric Machines (Iowa State University)

### Jun Cui, Principal Investigator

Iowa State University  
2220 Hoover Hall  
Materials Science and Engineering Department  
Ames, IA 50011  
E-mail: [cuijun@iastate.edu](mailto:cuijun@iastate.edu)

### Steven Boyd, DOE Program Manager

U.S. Department of Energy  
E-mail: [steven.boyd@ee.doe.gov](mailto:steven.boyd@ee.doe.gov)

Start Date: October 1, 2016                      End Date: September 30, 2019  
Project Funding (FY19): \$4,268,002      DOE share: \$3,835,152              Non-DOE share: \$432,850

### Project Introduction

Rare Earth magnet is the most expensive component in permanent magnet motor. Since 2000, the price of the rare earth NdFeB-Dy magnet has gone through a series of volatile rises and falls. The price of Nd oxide increased from ~\$10/kg in 2000 to ~\$80/kg in 2010, then jumped to an historical high of \$244/kg in 2011. It fell sharply to \$37/kg in 2016, then back up to \$51/kg in 2017, and stayed in this range in 2018 and 2019. As Europe and China are aggressively pursuing electric vehicle with higher efficiency, the demand for rare earth magnet is expected to be doubled by 2025. The rising demand and manufacturing cost make it difficult to meet the DOE 2025 cost target of \$6/kW for the 100 kW electric drive system.

MnBi permanent magnet is the only non-rare earth magnet holds a viable potential to meet the DOE cost target. The cost is expected be ~\$26/kg when mass produced. This cost estimation is based on the same methodology used by IMARC group (ID: 2818708, 2014) to study the economic feasibility of a rare earth magnets manufacturing plant. The price of MnBi magnet is expected to be stable over the next few decades due to the world-wide availability of the elements Mn and Bi. It is important to understand that criticality is defined by availability, not by abundance. Rare earth elements Nd and Dy are critical elements not because they are rare, but because the major reserves are concentrated in a few countries. These elements may not be available to the rest of the world due to the political and economic conflict of interests. According to 2016 US Geological Survey, there are 181 producers of Bi in 22 countries around the world.

Unfortunately, non-rare earth permanent magnets are not as powerful as the rare earth magnets. The highest energy product that bulk MnBi permanent magnet can achieve using the current technology for mass production is about 8 MGOe at room temperature, albeit 20 MGOe is the theoretical limit and 12 MGOe has been demonstrated with a small magnet weighing about 0.1 gram. The current energy product of 8 MGOe is about 20% of that of the NdFeB magnet. In order to meet the DOE 2022 power density targets of 1.6 kW/kg and 5.7 kW/L, the motor has to be operated at much higher excitation frequency, which in turn, demands advanced soft magnetic materials to make up the efficiency loss due to the rising eddy current.

Electrical steel with 3.2% Si is the most common soft magnetic material used by motor and power electronics industries. While the excellent performance/cost ratio justifies the popularity of the 3.2 wt.% Si steel, its limited physical properties are hindering the further improvement of motor efficiency, power density and cost. The current trend in the motor and power electronics industry is to increase the excitation frequency because it leads to higher power density with lower \$/kW. However, higher excitation frequency also results in higher eddy current and lower efficiency. For example, a 100 kW motor at 50 Hz with 90% efficiency would deliver 200 kW when running at 100 Hz, but efficiency would decrease to 80%.

Thinner laminate reduces eddy current loss, but very thin laminate has a poor stacking factor and increases assembly cost. With lamination thickness at its practical limit, mitigating increased eddy current requires increasing electrical resistivity. Advanced soft magnetic materials, such as nanocrystalline and amorphous soft magnetic materials, possess higher electric resistivity but the cost is high and the thickness is limited to <0.03 mm. With such thin thickness, the stacking factor can only reach 0.687, about 28% less active magnetic volume than that of the 0.4 mm laminate. High Si electrical steel has the potential to be both efficient and cost effective. Increasing Si content improves magnetic and electrical properties, with ~6.5 wt.% being optimum. Compared to the 3.2 wt.% Si steel, saturation magnetization decreases by 10% (to 1.7 T) but permeability improves by 27% (to 19,000 at 1 kHz), while electric resistivity improves by 44% (to 82  $\mu\Omega\text{-cm}$ ) and magnetostriction reduces from 7.8 ppm to 0.1 ppm. However, with increasing Si content, Si atoms start to pair and form ordered phases. The emerging B2 and D0<sub>3</sub> phases embrittle the A2 matrix. At 6.5 wt.% Si, the steel is too brittle to be cold rolled or stamped. The current manufacturing method diffuses Si into the thin gauge 3.2 wt.% Si steel after chemical deposition. It is an elegant engineering solution. Unfortunately, the method has notable shortcomings. Manufacturing cost is high (~5X of the price of 3.2 wt.% Si steel), productivity is limited, sheet thickness (0.1 mm) is thinner than the one for common motor lamination, the final product is brittle and difficult to stamp. Even with these shortcomings, the 6.5 wt.% Si steel 0.1 mm sheet made by JFE is still steadily gaining market share.

This project develops a near net shape molding process that could enable the application of 6.5 wt.% Si steel for electric motors at a cost competitive with the cost effective 3.2 wt.% Si steel. The anticipated breakthrough material could reduce motor cost by enabling higher excitation frequency and higher power density without sacrificing efficiency; or for a given power density, it could lead to 35% reduction in core loss and 3% increase in motor efficiency. In addition to the materials effort, the project designs, constructs and evaluates a non-rare earth motor that integrates the novel MnBi magnet for rotor and the advanced Fe-6.5%Si steel laminate for stator.

### Objectives

The objective is to demonstrate a cost effective non-rare earth PM motor. The new motor uses MnBi magnet as the permanent magnet in rotor and Fe-6.5%Si as the stator laminate material. It operates at 400 Hz and has 10 kW power. The target cost is 2/3 of the rare earth motor with same power.

### Approach

Our approach for lowering PM motor cost is three folds: 1) use non-rare earth magnet to control magnet cost, 2) increase motor excitation frequency to improve motor power density, and 3) use advanced soft magnetic materials to improve motor efficiency at high frequency. The project team comprises two universities (Iowa State University and Delaware University) specialized in magnetic materials and alloy development; one national lab (Ames Lab) specialized in predictive materials science, mid-scale (10 kg) alloy casting and processing, and magnetic materials development; and one company (United Technologies Research Center) specialized in motor design, construction and testing.

- For MnBi magnet, the demonstrated energy density of a bulk MnBi magnet (9 gram) is about 8.5 MGOe at room temperature. It was fabricated using a lab-scale warm compaction process that was developed by a previous DOE supported project. Unfortunately, large warm press is not commonly used by the magnet industry. Our approach is to study and understand the thermodynamics of the demonstrated warm compaction process and apply the understanding to develop a robust process without using any special equipment.
- High excitation frequency (400 Hz) is used to make up the loss in power density caused by weaker magnet. Our approach to improve the torque/power density of the motor is to use advanced flux switching topologies that would enable focused flux and improve average airgap flux density.

- Fe-6.5%Si steel is used for stator lamination to mitigate the efficiency loss at high frequency. The challenge is how to cost-effectively fabricate the brittle 6.5%Si steel laminate. Our approach is based on the observation that rapid solidified Fe-6.5%Si flakes is ductile. This unique property is possible because the heterogeneous formation of  $\alpha 2$ -FeSi (B2) and  $\alpha 1$ -FeSi (D03) ordered phases are suppressed. These ductile flakes can be pressed to near-net-shape in high green density, then sintered for full density and desired magnetic properties. The approach is simpler than the cold roll, stamping and lamination process.

**Results**

**MnBi Permanent Magnet**

The efforts on developing MnBi permanent magnet technology are divided into two directions: (1) develop an economic and industry-friendly bulk magnet fabrication method and demonstrate it by making a large number of bulk magnets; (2) develop new chemistry and new processing to push MnBi-based magnet  $(BH)_{max}$  over 12 MGOe.

In 2019, an economical bulk magnet fabrication method was successfully developed. The procedure includes: a) Align the loose powder in magnetic field to obtain high degree of texture; b) Press the loose powder into a green compact in the magnetic field. The force is moderate (<12 MPa) and the compact is <70% dense; c) compress the green compact with 500 MPa hydrostatic pressure. The obtained bulk magnet is >90% dense. d) magnetic anneal at 260°C for 2 hr. e) silver spray coating for corrosion protection.

The fabricated magnets consistently exhibit the desired physical properties, meeting or exceeding the target energy production of 8 MGOe. Figure II.3.1 depicts the M-H-T data of a typical MnBi magnet fabricated using the newly developed process. The significance of this achievement is that the hot-compaction step in the previous fabrication procedure was replaced with cold-iso-press (CIP) compaction. This replacement not only cuts the need for the expensive vacuum hot-press system, but also drastically increase the productivity. This replacement is enabled by a newly designed powerful CIP system capable of 500 MPa. This achievement lays the foundation for economic manufacturing of non-rare earth magnet. In FY19, 80 magnets (9 gram/each) have been manufactured using this process (Figure II.3.1).

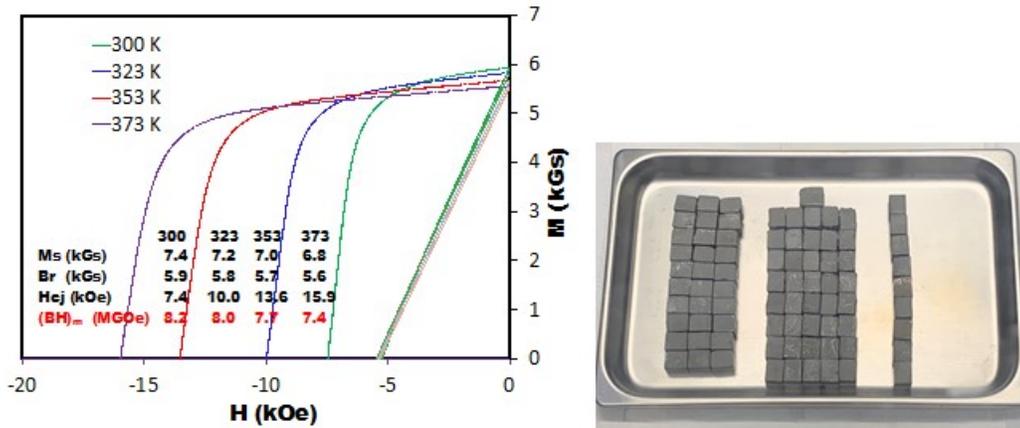


Figure II.3.1 Magnetization vs. applied field at different temperature of the bulk magnet fabricated using the newly developed CIP process. Note that the coercivity increases with increasing temperature, resulting in a series of B-H curves that are overlaid on top of each other. This is the most desired magnet feature for motor design.

In 2019, extensive MnBi chemistry refinement was carried out. Table II.3.1. lists the investigated compositions. Each of these compositions were prepared using melt-spin method. The obtained ribbons were compacted and magnetically annealed. The findings can be briefly summarized as follows. Alloying with Mg is essential for manufacturing of the textured MnBi magnets exhibiting a reasonable coercivity. Additional alloying with 0.5 at.% In improves both the coercivity and the remanence, whereas additional alloying with Co

or Sb increases the coercivity, but decreases the remanence. The optimal alloying with Mg, In and Sb allowed for a  $(BH)_{\max}$  of 12 MGOe in the magnet with a nominal composition  $Mn_{50}Bi_{46}Mg_3In_{0.5}Sb_{0.5}$ , but even without the costly indium additive, the  $(BH)_{\max}$  can reach 11.5 MGOe. Although most of the magnets in the study were compacted at the elevated temperatures of 80°C or 150°C, the more affordable *cold compaction* (e.g., 340 MPa for 60 min) has also been shown to produce fully dense magnets with the excellent properties.

**Table II.3.1 Properties of magnets prepared by compacting melt-spun MnBi-based alloys at  $T_{\text{comp}}$  and subsequently annealing them in magnetic field of 30 kOe.**

Composition	$T_{\text{comp}}$ (°C)	$B_r$ (kG)	$H_{ci}$ (kOe)	$(BH)_{\max}$ (MGOe)
$Mn_{50}Bi_{50}$	150	5.4	0.6	2.1
$Mn_{50}Bi_{48.5}In_{1.5}$	150	5.8	1.0	3.8
$Mn_{50}Bi_{47}Sn_3$	150	6.0	0.5	2.2
$Mn_{50}Bi_{48.5}Sb_{1.5}$	150	4.7	7.4	5.1
	80	4.9	7.2	5.4
$Mn_{50}Bi_{47}Mg_3$	150	6.8	3.4	9.8
	80	7.0	2.9	8.9
$Mn_{50}Bi_{46}Mg_3Ca$	150	6.5	1.1	4.8
$Mn_{50}Bi_{46.5}Mg_3Co_{0.5}$	150	6.3	5.2	9.2
$Mn_{50}Bi_{46.5}Mg_3Cu_{0.5}$	150	7.0	1.8	7.8
$Mn_{50}Bi_{46.5}Mg_3Zn_{0.5}$	150	7.6	1.8	6.7
$Mn_{50}Bi_{46.5}Mg_3Ga_{0.5}$	150	6.5	4.8	9.9
$Mn_{50}Bi_{46.5}Mg_3Zr_{0.5}$	150	6.4	3.7	8.6
$Mn_{50}Bi_{46.5}Mg_3Ce_{0.5}$	150	6.2	4.2	7.6
$Mn_{50}Bi_{46.5}Mg_3In_{0.5}$	150	7.1	4.7	11.6
	80	7.3	3.7	11.3
$Mn_{50}Bi_{46}Mg_3In$	150	7.2	4.4	11.4
$Mn_{50}Bi_{46.5}Mg_3Sn_{0.5}$	150	6.7	2.9	9.6
$Mn_{50}Bi_{46.5}Mg_3Sb_{0.5}$	150	7.0	5.6	11.5
$Mn_{50}Bi_{46.25}Mg_3Sb_{0.75}$	150	6.5	6.4	9.9
$Mn_{50}Bi_{46}Mg_3Sb$	150	6.4	8.2	9.5
$Mn_{50}Bi_{45.5}Mg_3Sb_{1.5}$	150	5.9	9.3	8.1
	80	6.5	6.9	9.5
$Mn_{50}Bi_{46}Mg_3Co_{0.5}Zn_{0.5}$	150	6.3	5.1	9.0
$Mn_{50}Bi_{46}Mg_3Cu_{0.5}Sb_{0.5}$	150	5.7	6.3	7.4
$Mn_{50}Bi_{46}Mg_3Ga_{0.5}Sb_{0.5}$	150	6.5	5.0	9.9
$Mn_{50}Bi_{46}Mg_3In_{0.5}Sb_{0.5}$	80	7.1	7.1	12.0
$Mn_{50}Bi_{45}Mg_3In_{0.5}Sb_{1.5}$	150	6.7	9.4	10.6
	80	6.9	8.5	11.6
	22	6.8	8.3	11.3



### ***Near net shape molding of Fe-6.5%Si laminate***

In 2018, the team was able to reliably produce Fe-6.5%Si flakes for physical properties characterizations and for near-net-shape molding. In 2019, the W10/400 iron losses for Fe-6.5%Si samples have been further lowered using polymer coating and MgO lamination techniques.

Experiments to coat the flakes with both phenolic resin and epoxy resin have been conducted. Epoxy resin was found to be superior to phenolic resin in achieving a thinner and more uniform coating with enhanced structural integrity. The resin was dissolved into acetone and then mixed with the flakes until the solution dried out. The coated flakes were then loaded into a ring-shaped steel mold and cold-pressed using 4 tons of force (103 MPa applied to ring surface). The pressed ring samples were removed from the die and cured in oven at 150°C for 1 hour. The polymer effectively isolates the flakes as there is no electric continuity between the flakes as tested by digital multimeter. Figure II.3.2 shows a photo of a typical ring sample.



Figure II.3.2 Photo of 5 wt% epoxy bonded core after curing. The surface epoxy coat has not been applied.

The AC iron loss for 5 wt% and 3 wt% epoxy bonded, 5 mm thick cores are shown in Figure II.3.3. It shows that samples prepared with lower polymer content have lower iron losses. The W10/400 is ~100 W/kg for the 5 wt% epoxy bonded sample, and ~80 W/kg for the 3 wt% epoxy bonded sample. The low iron loss is achieved by minimizing eddy current losses with effective lamination. The epoxy bonded cores also display low DC coercivity (~80 A/m) which minimizes the hysteresis loss. However, the DC permeability is quite low. The permeability for 5 wt% epoxy bonded flake core is only 87. Such low permeability material may find application in power electronic applications, but it may not be suitable for motor application as it can lead to significant copper loss (winding loss) as a large current is needed for the desired flux density. The epoxy used to isolate the flakes also serves as air gaps, which are responsible for the low permeability of the epoxy bonded ring sample. Currently, the density of the 5 wt% epoxy bonded core and 3 wt% epoxy bonded core are 3.56 g/cc and 3.61 g/cc, respectively, much less than the Fe-6.5wt%Si theoretical density of 7.48 g/cc. The sample density has to be improved in order to improve permeability, possibly by using a thinner coating, lower polymer loading, and better flake compaction.

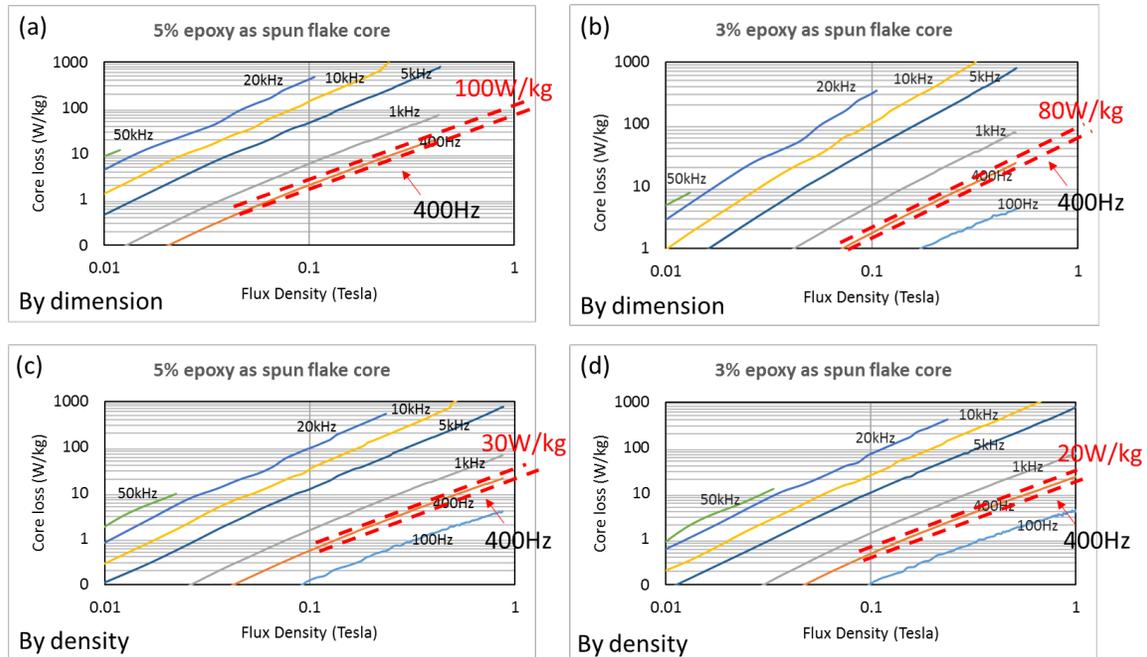


Figure II.3.3 Iron loss of epoxy bonded, flake core ring samples as a function of flux density for a number of frequencies (a) 5 wt% epoxy, flux area by dimension; (b) 3 wt% epoxy, flux area by dimension; (c) 5 wt% epoxy, flux area by density; (d) 3 wt% epoxy, flux area by density.

As a means to create a continuous pathway for magnetic field and minimize the air gap for each layer, coating/flake inter-laminated bulk samples have been prepared. MgO has been chosen as a coating due to its high resistivity and excellent thermal stability. For the initial study, 10 layers of flakes, 0.1 mm thick each, and 9 layers of MgO or mica powder, 0.01 mm thick each, were prepared. The flakes and insulating powders were then filled into a ring shape mold in alternating layers. The pack was consolidated using the hot press at 850°C with a pressure of ~50 MPa. After hot pressing, the ring samples height is about 4 mm.

The densification of the MgO laminated ring is 85.8%. For the mica laminated sample, a piece of graphite foil that was used for mold isolation and lubrication was loaded into the pack by operator error, and resulted in a dent in the ring sample. Depending on the thickness chosen, the densification of the mica laminated ring varies from 84% to 90%. Figure II.3.4(a) shows a photo of the MgO laminated ring sample after hot pressing. It shows that the MgO has been successfully embedded into the sample, but its distribution is rather poor.

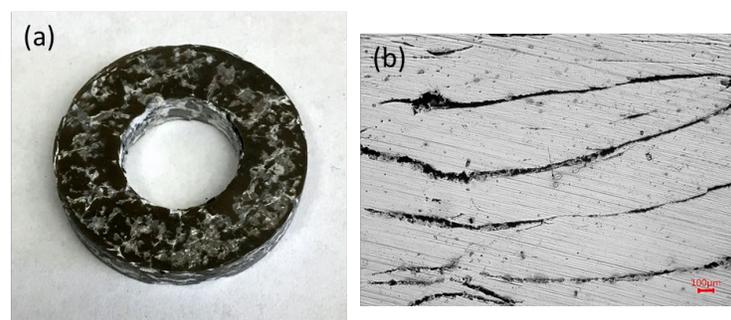


Figure II.3.4 (a) MgO laminated ring, the bright features are MgO agglomerations. (b) Cross-section optical image of the MgO laminated ring sample, the dark strips are MgO layers, while the gray bands are FeSi.

The magnetic properties of the MgO laminated hot pressed ring sample are shown in Figure II.3.5. Compared to the polymer bonded flake core sample, the permeability of this sample is significantly higher, i.e.,  $\mu_{\text{Max}} \sim$

16,700 by dimension method and  $\mu_{\text{Max}} \sim 28,600$  by density method. The sample is quickly magnetized by a small magnetic field. The W10/400 iron loss of the sample is around 130 W/kg. The W10/400 is significantly lower than that of previously prepared CaF<sub>2</sub> coated and uncoated samples which were  $\sim 300$  W/kg and  $\sim 600$  W/kg, respectively. The MgO laminated sample benefits from reduced eddy current losses as can be seen in Figure II.3.5(a) and (b). The coercivities for AC400Hz was around 500 A/m, respectively. In comparison, the AC400Hz coercivity is  $\sim 3,300$  A/m for the uncoated sample and  $\sim 1,300$  A/m for the CaF<sub>2</sub> coated sample at its best.

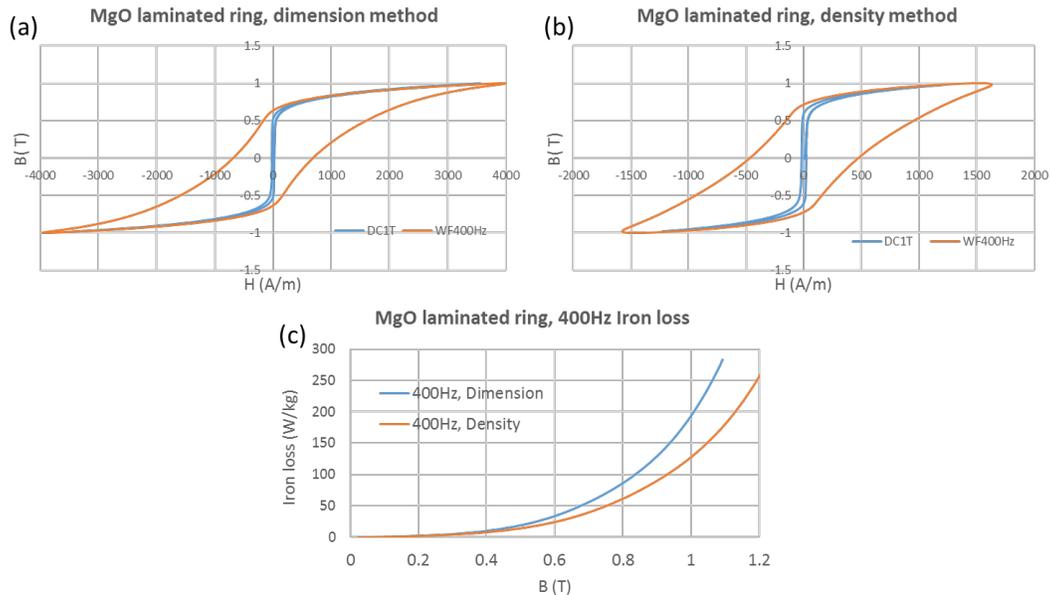


Figure II.3.5 Magnetic properties of MgO laminated rings. (a) Flux density as a function of magnetic field for both the DC and AC400Hz condition using dimension method; (b) flux density as a function of magnetic field for both the DC and AC400Hz condition using density method; (c) AC400Hz iron loss as a function of flux density.

However, the MgO laminated sample is only 85.8% dense, which limits the magnetic saturation. Increasing the flux density to 1 Tesla relies heavily on increasing the current in the induction coil, which inevitably results in higher losses. The field required for 1 Tesla flux density is  $\sim 1,600$  A/m. Future work is needed to increase the densification of the sample. Better distribution of the insulating material also needs further attention.

### Motor design

UTRC has received first motor prototype from the motor manufacturer as per UTRC's design specifications and drawings. This motor topology includes a Fractional Slot Concentrated Winding (FSCW) Surface Permanent Magnet (SPM) machine with a 10 poles and 12 slots combination using the equivalent MnBi magnets (SmCo) and the high silicon JFE steels (10JNEX900). Figure II.3.6 shows the rotor, stator and full assembly of the prototype.



Figure II.3.6 Picture of the prototype rotor (left) and stator (middle), and fully assembled motor.

UTRC team has finished constructing the test-setup (Figure II.3.7). The prototype motor was mechanically aligned to the dyne motor via a flexible coupler. Two blocks of aluminum spacers were trimmed to fit underneath the prototype motor. The dyne motor is an inductor motor driven by a Siemens commercial drive operating under the speed mode; whereas the prototype motor is driven by a Phase-Motion drive operating at torque mode. Many RTD wiring connections and thermal couples were in place to monitor the winding temperature. In addition, cooling refrigerant, delivered by a cooler, is fed to the inlet and outlet of the cooling jacket. The torque meter is sitting between two motors in order to provide the actual speed and torque readings in real time during testing. A new encoder was attached to the end of the prototype machine. The encoder pulse readings are fed to the phase-motion drive as a source of the feedback signal for current regulation. Serial connection was established between the human interface, i.e., a Phase-Motion software program running on a computer, and the actual Phase-motion drive.

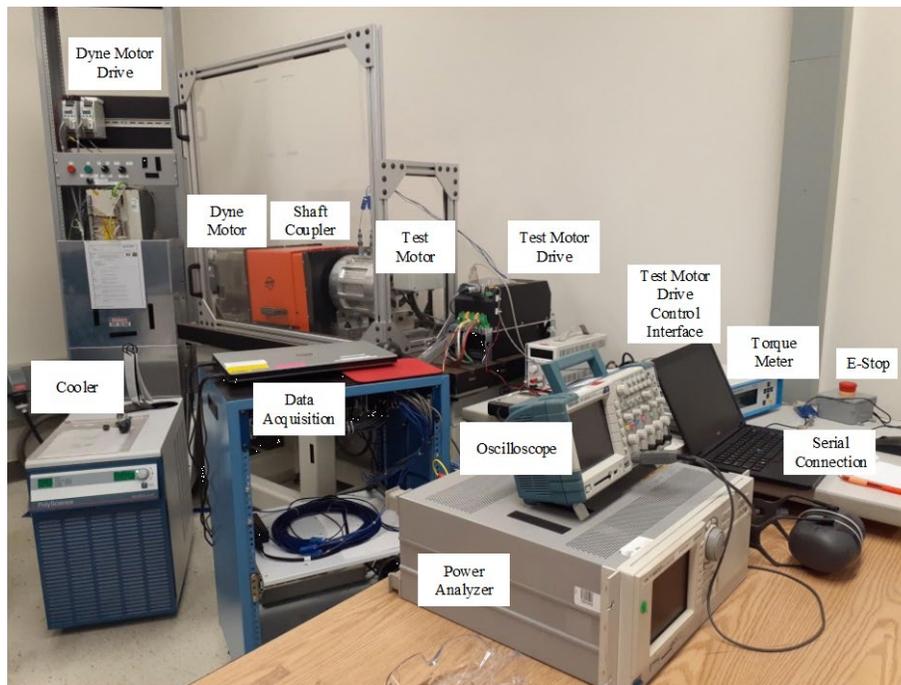


Figure II.3.7 Motor test setup at UTRC.

The motor per phase resistance can be accurately measured using a micro-ohm meter. The phase inductance was measured using a sensitive multimeter. The resistance and the inductance measurements are given in Table II.3.2. against the predicted results. It can be seen that the measurements aligned to the prediction with minor discrepancy. This discrepancy in resistance is due to the connector as connector resistance is not included in the model predictions.

**Table II.3.2 Per-phase resistance and inductance measurements**

	Predicted	Measured	Difference [%]
Ra [mW]	102	111.0	8.1
Rb [mW]	102	111.5	8.5
Rc [mW]	102	111.1	8.1
La [mH]	2.2	2.25	2.2

The back EMF was conducted in the next test. The rotor can be commanded to different rotor speeds. The per-phase back EMF was measured using three differential probes tapped between the neutral point of the machine and each motor winding input. The predicted back EMF waves were obtained using a transient solver in finite

element analysis. The comparison between the predicted back EMF and the measurement of phase-A are overlaid in Figure II.3.8. It is seen that the predicted waveform is very close to the measurement. The very small discrepancy comes from the variation of the actual strength produced by the purchased magnets.

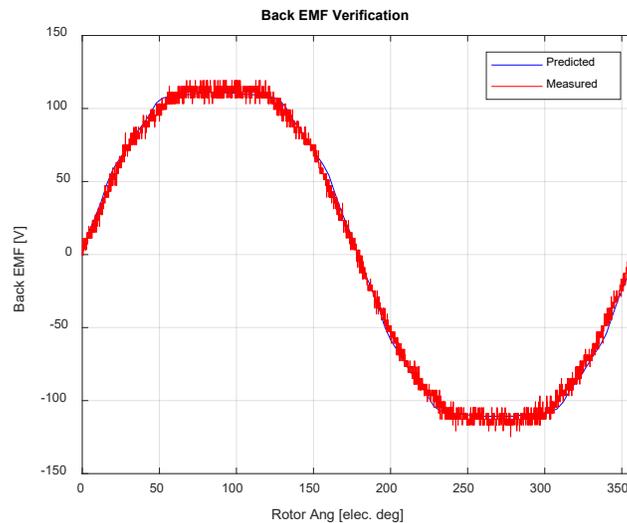


Figure II.3.8 Comparison between the predicted back EMF results and the actual measurements.

## Conclusions

A robust and cost-effective process was developed to fabricate bulk MnBi permanent magnet. The process uses the common cold-iso-press process to densify the magnet while keeping the powder aligned. The newly developed process not only improves the squareness of the demagnetization curve, but also reduce the capital cost of the large-scale warm compression system. A significant progress was made toward near-net shape molding of thick 6.5%Si steel laminate. Ductile flakes with desired size and shape can be routinely produced; the obtained flakes can be consolidated into rings with excellent mechanical and magnetic properties. While our recent results proved the concept of near-net shape molding of 6.5%Si steel, they also showed that high quality flake coating and lamination are critical for overall iron loss and motor efficiency. Lastly, our first 400 Hz prototype motor (1.3 kW/kg and 4.5 kW/L) has been constructed and tested. The prototype delivered 11 kW power at 400 Hz with 91% efficiency, exceeded the designed specification.

## Key Publications

1. Ouyang, Gaoyuan, Brandt Jensen, Chad R. Macziewski, Tao Ma, Fangqiang Meng, Qishen Lin, Lin Zhou, Matt Kramer, and Jun Cui. "Characterization of ordering in Fe-6.5% Si alloy using X-ray, TEM, and magnetic TGA methods." *Materials Characterization* (2019): 109973
2. Gabay A, Cui, J, and G. Hadjipanayis, "Effect of Sb substitution on crystal structure, texture and hard magnetic properties of melt-spun MnBi alloys", *J. Alloy and Compound*, 2019, July 5; 792:77-86.
3. Ouyang G, Liang Y, Chen X, Cui J, "A review of Fe-6.5wt%Si high silicon steel—a promising soft magnetic material for sub-kHz application", *Journal of Magnetism and Magnetic Materials*, 2019, Feb 26;481:234-250.
4. Cui, Senlin, Gaoyuan Ouyang, Tao Ma, Chad R. Macziewski, Valery I. Levitas, Lin Zhou, Matthew J. Kramer, and Jun Cui. "Thermodynamic and kinetic analysis of the melt spinning process of Fe-6.5 wt.% Si alloy." *Journal of Alloys and Compounds* 771 (2019): 643-648.

5. Tangudu, Jagadeesh, Gaoyuan Ouyang, and Jun Cui. "Trade Studies for a Manganese Bismuth based Surface Permanent Magnet Machine." In *2018 IEEE Transportation Electrification Conference and Expo (ITEC)*, pp. 600-605. IEEE, 2018.
6. Ouyang, Gaoyuan, Brandt Jensen, Wei Tang, Kevin Dennis, Chad Macziewski, Srinivasa Thimmaiah, Yongfeng Liang, and Jun Cui. "Effect of wheel speed on magnetic and mechanical properties of melt spun Fe-6.5 wt.% Si high silicon steel." *AIP Advances* 8, no. 5 (2018): 056111.
7. Gabay, A. M., G. C. Hadjipanayis, and J. Cui. "Preparation of highly pure  $\alpha$ -MnBi phase via melt-spinning." *AIP Advances* 8, no. 5 (2018): 056702.
8. Cui, Jun, Matt Kramer, Lin Zhou, Fei Liu, Alexander Gabay, George Hadjipanayis, Balamurugan Balasubramanian, and David Sellmyer. "Current progress and future challenges in rare-earth-free permanent magnets." *Acta Materialia* (2018).
9. Ouyang, Gaoyuan, Dennis, Kevin, Jensen, Brendt and Cui, Jun. "Near net shape BULK laminated silicon iron electric steel for improved electric resistance and low high frequency loss", Provisional patent filed (2018)

## II.4 Mapping the North American Light Duty Electric Vehicle (LDEV) Charging Market and Supply Chain: Assessment of Suppliers, Technology Developments and Gaps. (Synthesis Partners, LLC)

### **Christopher L. Whaling, Principal Investigator**

Synthesis Partners, LLC  
 11250 Roger Bacon Drive, Suite 2  
 Reston, VA 20190  
 E-mail: [cwhaling@synthesispartners.com](mailto:cwhaling@synthesispartners.com)

### **Steven Boyd, DOE Program Manager**

U.S. Department of Energy  
 E-mail: [steven.boyd@ee.doe.gov](mailto:steven.boyd@ee.doe.gov)

Start Date: October 1, 2018	End Date: September 30, 2019	
Project Funding (FY19): \$219,958	DOE share: \$219,958	Non-DOE share: \$0

### **Project Introduction**

This project covers original research on the supply chain for the North American (NA) Light Duty Electric Vehicle (LDEV) charging market, including an assessment of companies, technologies, suppliers, business model issues and technology trends and gaps. This work addresses the need for an up-to-date, independent assessment of the state-of-NA EV Supplier Equipment (EVSE) players and their equipment, revenue rankings, technology developments, business model issues and VTO-relevant gaps (e.g., expert sources' views on power level issues, siting issues, installation costs, electricity rates and other technical or business model issues). The collection cut-off date was July 31, 2019. More information is available in a forthcoming public report on the NA EVSE supply chain to be provided by Synthesis Partners ("SP").

### **Objectives**

The objective of this work is to provide EERE with quantitative and qualitative information on markets, trends and technologies relevant to the mission of increasing energy affordability, efficiency and resiliency – and in particular with regard to EV charging networks in NA. This work also identified and characterized R&D gaps and capabilities in the NA EVSE market that can impede the transition of R&D into NA EVSE entities, and by extension impede transition of R&D into high-quality US-based jobs. By collecting, analyzing and reporting on vetted, multi-sourced data regarding the NA EVSE market, this project provides EERE with actionable intelligence relevant to R&D and technology transition planning.

### **Approach**

This research is based on a 2018-2019 assessment of thousands of secondary sources alongside hundreds of anonymized, primary industry sources that exchanged information with SP directly. Quantitative data is ordered, ranked and analyzed according to an EVSE domain model developed by SP. Qualitative information is assessed through multi-source vetting, which includes running insights through quantitative information filters, secondary sources and confidential information secured from primary sources. Each primary source is hereby acknowledged by SP and thanked for their time and contributions to this effort. All errors and omissions remain the sole responsibility of SP. The project produced an independent assessment of EVSE players, suppliers and their plans, revenues, regional impacts, technologies or other key characteristics, and made assessments regarding gaps and trends extending to five years out.

### **Results**

SP identified 170 companies and organization as active in the NA EVSE supply chain. These companies are characterized in an internal database according to the EVSE products or services they provide, their size (by

revenue and employees), their JV and partnership relationships, their business model type and links to technical product specification information. The following provides an overview of selected data collected and analyzed in FY19.

**Table II.4.1 NA EVSE Supply Chain Overview**

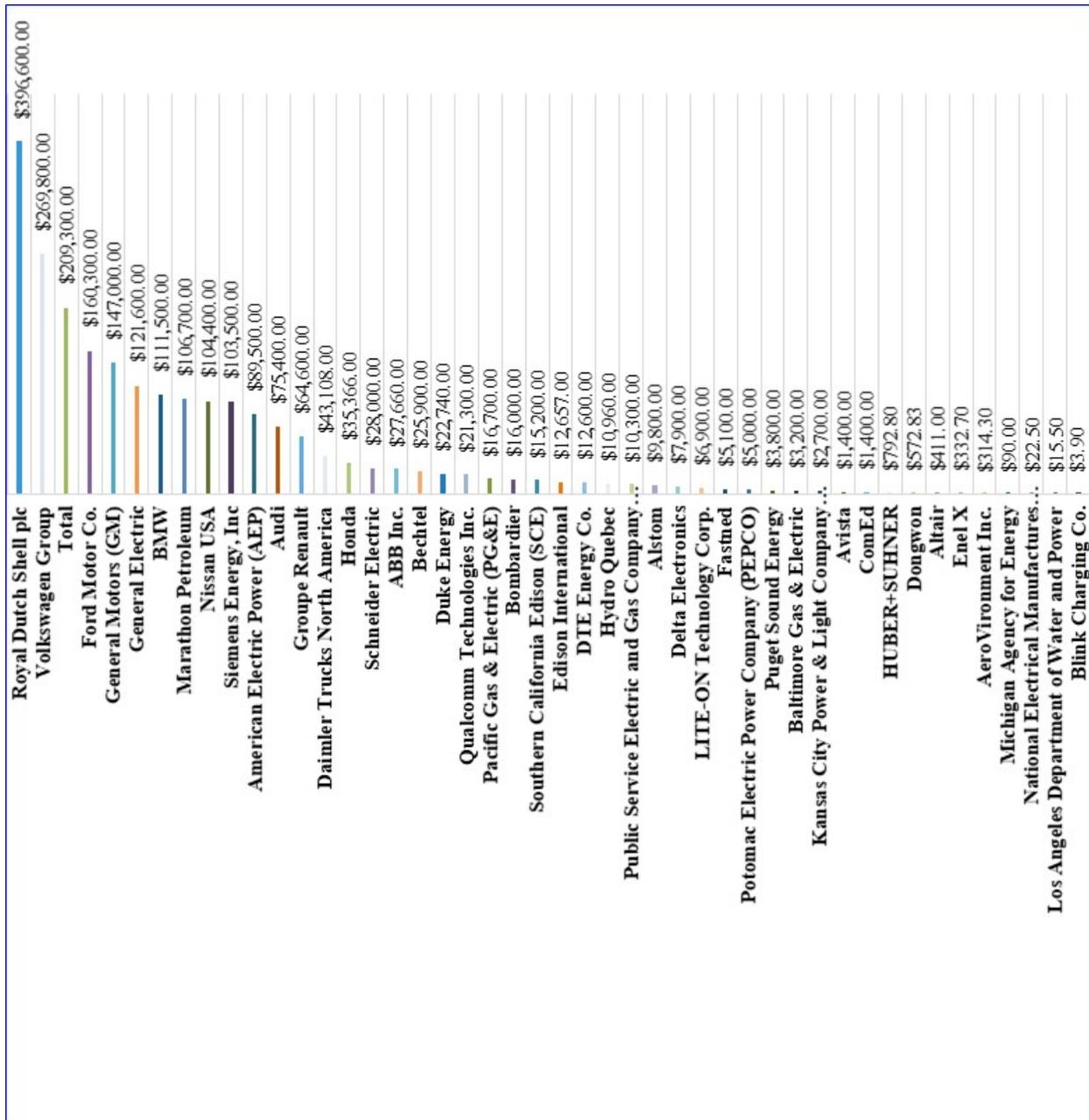
NA EVSE Supply Chain Companies, By Ownership Type	Number	Percent of Total Revenue of For-Profit Companies	Percent of All Entities, Incl. For-Profit and Non-Profit.
Private Cos. > \$100M Annual Revenues	16	3.75%	10%
Private Cos. < \$100M Annual Revenues	52	0.03%	31%
Public Cos. > \$100M Annual Revenues	42	96.22%	25%
Public Cos. < \$100M Annual Revenues	4	0.01%	2%
Total Other Orgs. (State, Local & Federal Government, Non-Profits, Associations)	56	N/A	34%
<b>Sub Total: For-Profit Cos.</b>	<b>114</b>	<b>100%</b>	<b>68%</b>
<b>Total</b>	<b>170</b>	<b>N/A</b>	<b>100%</b>

The following key points are drawn from the NA EVSE database and SP’s analysis of associated primary and secondary source data, with a collection cut-off date of July 31<sup>st</sup>, 2019.

- The revenue distribution in the NA EVSE market is skewed towards public companies that earn more than \$100M in annual revenues, which is understandable because these large public companies represent 96% of total revenue of all for-profit companies in the NA EVSE supply chain, and their range of products and services is large and extends well beyond EVSE products only.
- In terms of numbers, the distribution is weighted towards privately owned, for-profit companies that make less than \$100M (at 31% of the total number of entities), which is six percent more than the share (in terms of numbers of entities) of public companies that earn more than \$100M in revenues.
- In total, private for-profit entities make up 41% of entities in the NA EVSE market-space, whereas public companies make up 27% of the total number of entities. This points again to the significant role that private entrepreneurs are now playing in this market place based on their number.
- Private for-profit companies make up just 4% of the total annual revenue of all for-profit entities identified in the NA EVSE market. However, our research shows that private companies earning less than \$25 million in annual revenue are building the majority of new EV charging networks in NA. These companies are characterized and highlighted in the Charts that follow.
- The significance of small private companies underscores the significance of team building among bigger public and smaller for-profit companies, and with utilities, for the purpose of transitioning EV charging research and technologies.
- Technical and business model interactions between private companies earning less than \$25 million and large, regulated utilities represent a key market growth factor. The transition of new technologies into the NA EVSE market will depend on very different types and sizes of organizations working together with utilities, in new and complex ways.

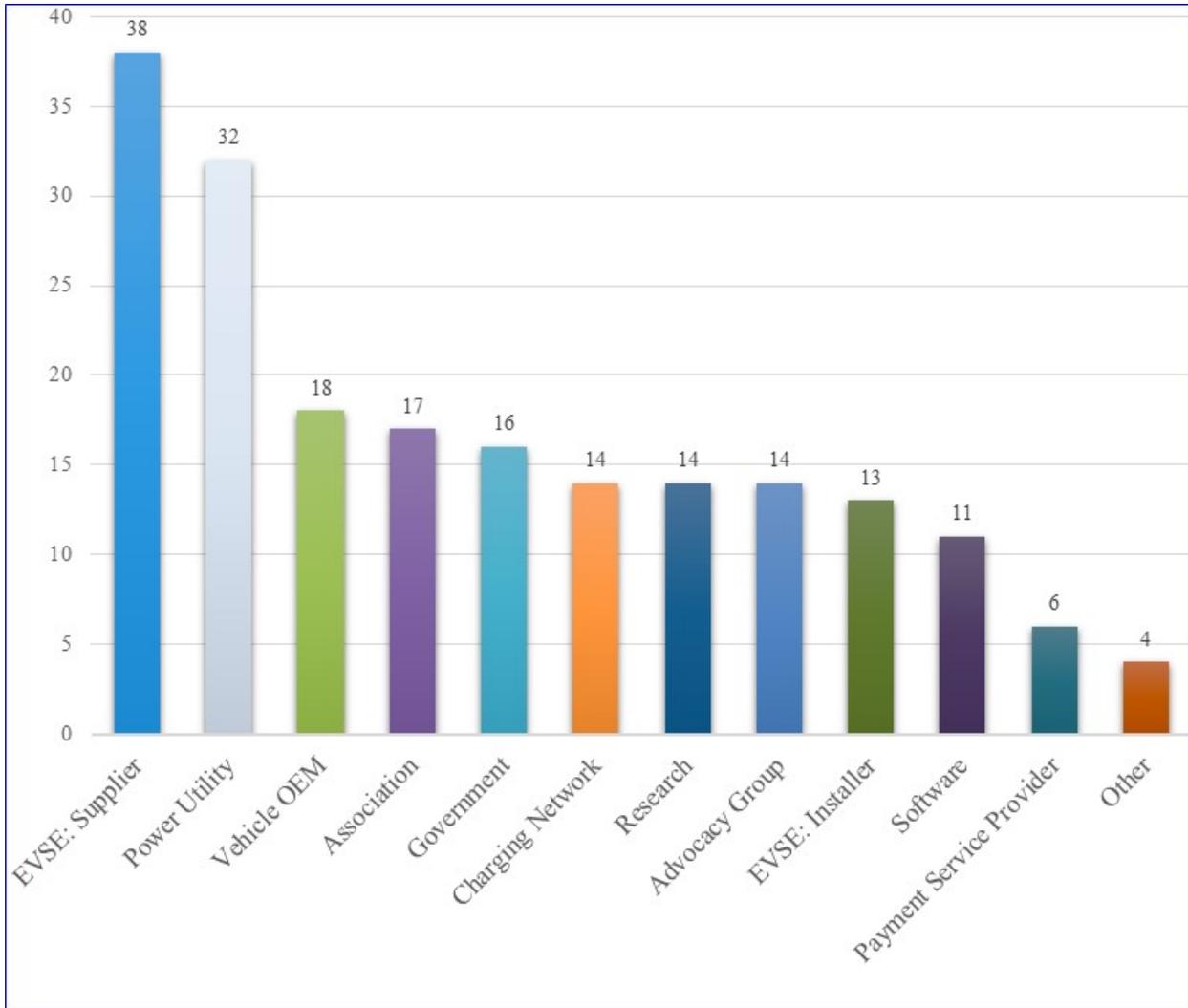


- A lack of consolidation among smaller companies within the growing NA EV marketplace can translate into potential delays as utilities manage complex regulatory paths to identify and define optimal investments.
- Other organizations, including government and non-profit organizations, comprise 34% of the market in terms of numbers of entities. This is a large share and shows the significant role that policy-driven organizations play in the NA EVSE market today.
- Of the 120 companies in the NA EVSE supply chain with US HQs, the top locations are: California (42 companies); Washington, DC (17 companies); Virginia (10 companies); Michigan (7 companies); and New York (6 companies).
- States with a small footprint (1-4 companies with US HQs) to-date, include: Arizona, Colorado, Connecticut, Florida, Georgia, Illinois, Kansas, Massachusetts, Missouri, New Jersey, Ohio, Oregon, Pennsylvania, Tennessee, Texas, Utah and Washington.
- The total annual revenue of the 114 for-profit companies identified, is approximately \$2.4 trillion. Notably, this is not to say that EVSE products and services add up to \$2.4 trillion, but rather that the total revenue of all for-profit (private and public) companies that have been identified as being involved in the NA EVSE market is \$2.4 trillion. In other words, this is a market with significant vitality and business interests.



Source: Synthesis Partners, EVSE Supply Chain Database (August 2019).

Figure II.4.1 Organizations That Are Publicly Held and Actively Engaged in the NA EVSE Supply Chain, Ranked by Annual Revenues (Dollar Millions, Calendar Year 2018).



Source: Synthesis Partners, EVSE Supply Chain Database (August 2019).

\* Includes companies that are double-counted due to having capabilities across categories.

Figure II.4.2 NA EVSE Supply Chain Organizations, By Product or Service Category (Represents 170 organizations, both public and private.\*) As of July 2019.

**Table II.4.2 Priority Gap Areas, by Frequency of Gap Statements**

Main Gap Statement Categories	Number of Gap Statements	Percent of Gap Statements
Business Model Issues	59	24%
Technology Hardware Issues	34	14%
Standards Issues	32	13%
Data Gap Issues	32	13%
Network Systems Eng. Issues	22	9%
Technical Coordination Issues	21	8%

VTO Feedback Points	21	8%
Cybersecurity Issues	10	4%
Software Issues	10	4%
Metrology Issues	5	2%
Grid Infrastructure Issues	2	1%
Material Supply Issues	2	1%
Safety Issues	1	0%

The top gap category of gap statements is Business Model Issues, which underscores the current ambiguity among EVSE suppliers and related companies about how to build an effective business model in EV charging.

The next tier of gaps includes Technology Hardware Issues [14%], Standards Issues [13%], and Data Gap Issues [13%]. These are equally important in terms of frequency count, and reflect the need for research and market development work to focus on building better hardware (esp. for batteries and V2G applications), addressing related standards issues, and improving independent data collection and market research on the evolution of the fast-changing EV charging market. The third tier include Network Systems Engineering Issues [9%], Technical Coordination [8%], and VTO Feedback Points [8%]; each of which comes in at just above 5% of total number of gap statements.

## Conclusions

This project's FY19 research on the current state and gaps in the NA EVSE supply chain provides the basis for the following selected conclusions and recommendations.

- Business Model Issue gap statements are paramount, including calls for increased collaboration, standards development and design thinking among all EVSE market participants. These gaps are followed by technology hardware and then system design-related issues where government involvement can be especially useful, such as in standards development, data-gap filling, network systems and technical coordination needs.
- The gap of top interest among sources, when they are discussing government involvement, is the need for assistance with the process of setting EVSE standards in NA. The need for assistance with standards comes across in many ways, across several gap categories. The second gap category of most interest among sources discussing government involvement is a call for support in facilitating coordination among municipals, states and federal agencies in the delivery of EV charging nationwide. Lastly, a call for assistance in coordination with utilities follows in the next spot.
- Across all gaps statements analyzed, the main challenge to suppliers in the NA EVSE market is less about technology and more about the need for targeted, practical design thinking and system design improvements. Improved design thinking is needed in order to deliver better, faster, cheaper outputs (fully charged vehicles on-demand) in a better, faster, cheaper way (that is, more efficiently, flexibly and cheaply for vehicle or fleet owners). Fully 67% of gap statements among the top six gap categories analyzed are about the general need for improved design thinking that can help market participants to accelerate and implement more efficient and effective EV charging infrastructure systems. This is even though the EVSE marketplace has numerous players and is generally meeting expressed market needs.
- Technical Coordination gaps include concrete recommendations by sources for activities to improve design thinking through private-public sector projects. These activities can deliver technical learning

and potentially significant system design improvements through sharing of independently developed, expert guided, technical challenges and solutions in pilot projects. Several examples follow:

- V2G Infrastructure Pilot Projects and Assessments: “The focus of the pilots needs to be to demonstrate the economic viability of a vehicle-to-grid infrastructure. In particular, the pilots need to test and ensure that charging transactions can be resolved, e.g., initiated and completed.”
- Fleet Charging at Scale: “It would be beneficial to have research done on how the infrastructure will handle the charging of thousands of EVs at once. This type of research would quantify the resources available/needed in relation to a given population of EVs and could help determine the ideal ratio of vehicles-to-grid. Pilot projects have been done using hundreds of vehicles, but a larger pilot program is needed that would cover thousands of vehicles.”
- Off-Board Bi-Directional Charging Pilots: “A small-scale V2G pilot project utilizing off-board bidirectional inverter/chargers was completed by the Los Angeles Air Force Base beginning in 2013, but was too small to demonstrate the commercial viability of V2G. Now, a larger pilot program is needed to encourage broader support and engagement.”
- More Engagement with Utilities, Especially with Regard to V2G: “It might be helpful for the VTO to initiate a pilot project that would assess the best means for communication between utilities, EVs, chargers and charging networks. There are a variety of solutions currently available and an assessment needs to be done to determine which solution offers the means to serve the largest percentage of the market.”
- Within the context of the above findings, this research also identified support among sources for concrete technology development activities, and specifically in the following areas:
  - reduce battery (energy storage) costs;
  - improve battery cycle time and capability;
  - focus on V2G technology integration;
  - reduce costs: commoditize core EVSE technology;
  - deliver lower-cost, more effective on-board chargers; and
  - accelerate mobile charger scale and technology development.
- Last, selected sources seek support with technology developments that accelerate the delivery of better V2G or V2H connectivity to faster chargers, at lower cost, at home or at work where EV owners spend most of their time charging their vehicles. At-home Level 2 units is a key focus among companies in the EVSE field and sources note these units will clearly benefit from increased V2G and V2H capabilities.

### Key Publications

Most recent publications or presentations by SP based on EERE sponsored work:

1. Synthesis Partners, LLC, Class 3-8 Hybrid and Electric Vehicles Operating on North American Roads: Supply Chain Assessment of Vehicles, Drive-Train Motors, Inverters, Converters and Batteries, May 2019.

2. Synthesis Partners, LLC, Assessing the North American Supply Chain for Traction Drive Inverters, Motors and Batteries for Class 3-8 Hybrid and Plug-In Electric Commercial Vehicles, Presentation by C. Whaling on June 11, 2019 to Annual Merit Review (AMR) meeting.

## References

For a list of references, please see the public report.

## Acknowledgements

Special thanks to Mr. Steven Boyd, Program Manager, Batteries and Electrification for his technical guidance and management, and to Ms. Adrienne Riggi, Contracting Officer at the National Energy Technology Laboratory (NETL) for her ongoing oversight of this effort. Synthesis acknowledges the entire EERE-VTO team and all stakeholders for their active interest and support of this work. Synthesis team members are:

- Richard Holcomb, Managing Partner.
- Steve Johnson, Senior Researcher.
- Ryan Bunch, Researcher.

## II.5 Highly Integrated Wide Bandgap Power Module for Next Generation Plug-In Vehicles (General Motors LLC)

### Marko Jaksic, Principal Investigator

General Motors, Global Propulsion Systems  
 777 Joslyn Avenue  
 Pontiac, MI 48340  
 Phone: (248) 860-9099  
 E-mail: [marko.jakisc@gm.com](mailto:marko.jakisc@gm.com)

### Steven Boyd, DOE Program Manager

U.S. Department of Energy  
 E-mail: [steven.boyd@ee.doe.gov](mailto:steven.boyd@ee.doe.gov)

Start Date: January 1, 2016	End Date: September 30, 2020	
Project Funding (FY19): \$682,756	DOE share: \$454,032	Non-DOE share: \$228,723

### Project Introduction

This project aims to develop a highly integrated wide bandgap (WBG) power module for traction automotive applications. The developed power module will be used to design a traction inverter for the next generation plug-in hybrid and electric vehicles. The goal is to develop an improved power module package that will enable operation of WBG devices at higher switching speeds. Standard IGBT power modules do not provide satisfactory fast-switching performance. The main target is to use a new generation of SiC devices and package an optimum number of devices in parallel that will increase efficiency of the traction inverter.

### Objectives

The objective of the project is to research, develop, and demonstrate a new WBG power module design and package that targets GM's next generation plug-in and electric vehicles. Requirements for the proposed power module will be derived from the projected specifications of vehicles launching over the next few years. The power module proposed herein will be functionally, electrically and mechanically optimized for GM's traction inverter architecture. The resulting voltage source inverter will achieve or exceed DOE's specific targets of

- power density above 14.1 kW/kg
- power volumetric density above 13.4 kW/L
- cost below \$3.3/kW

In addition to achieving DoE targets, the inverter shall operate more efficiently, providing increased power throughput, and increased electric vehicle range. Each design should demonstrate technical advantages over conventional Si traction inverter baseline designs in one or more of the following categories: cost, efficiency, and power density. Each traction inverter design with WBG power devices is also expected to have proven manufacturability and to undergo typical durability and electric drive performance testing by GM to ensure meeting market requirements for the next generation of electric vehicles.

### Approach

In order to achieve DoE targets, new SiC devices are selected to be used in the new generation of automotive traction drives. Critical to implementing fast switching WBG devices is optimization of module layout and reduction of DC loop inductance, as well as effective control and protection of the SiC MOSFETs.

GM is exploring improvement of the following components and features: gate drive circuitry, high bandwidth phase leg current measurement, fast and reliable over current protection, gate drive IC's with high common-mode transient immunity (CMTI), ideally greater than 100V/ns, distributed DC link capacitors with a portion of DC link capacitors integrated with the power module; low inductance gate control interface, and potential for on-die sensing.

The targeted maximum junction temperature of the power module is 200C. To achieve this goal, GM will evaluate new technologies for bonding and joining. GM will also investigate new thermal management technologies that can further reduce overall thermal impedance of the power module and improve high temperature reliability. Efficiency of the traction drive is an important design target and a trade-off study is being conducted to determine if it is better to set maximum temperature below 175°C to achieve larger vehicle range. Operating at high temperatures results in high conduction losses in SiC MOSFETs, reducing overall drive efficiency. Therefore, it is desired to set maximum temperature limit that will not severely affect drive efficiency.

To achieve the aggressive power density targets for the power module with high reliability requires:

- Minimize the number of paralleled SiC die to reduce module cost
- Evaluate performance of SiC die to eliminate parallel Schottky SiC die
- Use 900V and 1200V SiC MOSFET die that are being developed by our partners
- Customize die topside metallization to provide manufacturability and good thermal and electrical conductivity
- Use double side sintering and copper wirebonding
- Design power module with low thermal resistance
- Evaluate die characteristics at high junction temperatures (>150°C) to properly design power module protection.

SiC MOSFET's body diode can be used for commutation with other side SiC MOSFET, thereby reducing or eliminating the need for separate anti-parallel Schottky Barrier Diodes (SBD). GM studied the effects of SBD elimination on switching characteristics, losses, and thermal management without the anti-parallel Schottky Diodes and concluded that newly developed 900V and 1200V SiC die have body diodes that meets inverter specifications. Hence the SBD are not necessary to be used in the power module, simplifying module design, reducing cost, and saving space. Internal body diode has low reverse recovery losses and can commute fast with the SiC switch. It has higher conduction losses, but the body diode will conduct only during dead-time, increasing the overall switch losses by only few tens of watts.

Finally, GM will verify the performance of the resulting power module and fully packaged inverter prototypes using a selected set of GM production validation tests, including inverter level testing with inductive loads and active load emulators.

## Results

Power modules for automotive applications should have several important characteristics such as operation at increased temperatures, high efficiency power conversion and compliance with electro-magnetic interference (EMI) standards. Additionally, it is desired to design an automotive power module, and other inverter components, using materials that will reduce overall size and weight. Obviously, SiC switches, as an emerging technology, are excellent candidates for this application. However, in order to achieve the aforementioned optimization goals, several new concepts need to be implemented.



In order to improve switching performance of SiC MOSFETs, a flexible PCB circuit is soldered on the power module which is shown below in Figure II.5.1. It should be noted that the flex PCB is perpendicular to the power loop, achieving strong decoupling between the control and power loops. Finally, wirebonds connect gate and source pads of die to the flex PCB. Bottom of the flex PCB is soldered to the substrate. In this way PCB flex is easily integrated into the power module and can be used to control switch, protect SiC MOSFETs, and also for the characterization purposes.

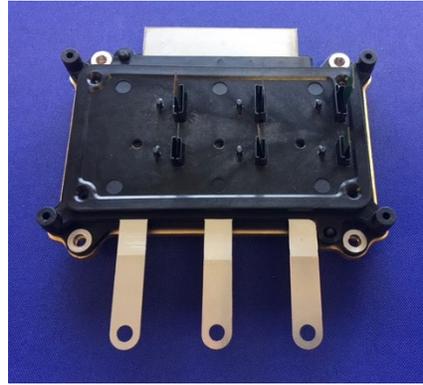


Figure II.5.1 Automotive SiC power module with 900V SiC die

Furthermore, Figure II.5.2 shows  $R_{dson}$  switch resistance for different temperatures. As expected, switch resistance increases when higher gate voltage is used. Very low switch resistance design is achieved for a wide current and temperature range. It can be concluded that if a gate driver board is designed to drive switches with 16V bias, equivalent switch resistance is reduced by approximately 10%. Furthermore, when switch conducts in the reverse direction, on state resistance drops close to 2.0 mΩ and 2.75 mΩ, at room and high temperatures, respectively. Standard property of JFET devices is that channel gets narrower as current is increased, due to the associated voltage drop. The switch resistance increases as switch current is increased. Similarly, in the reverse

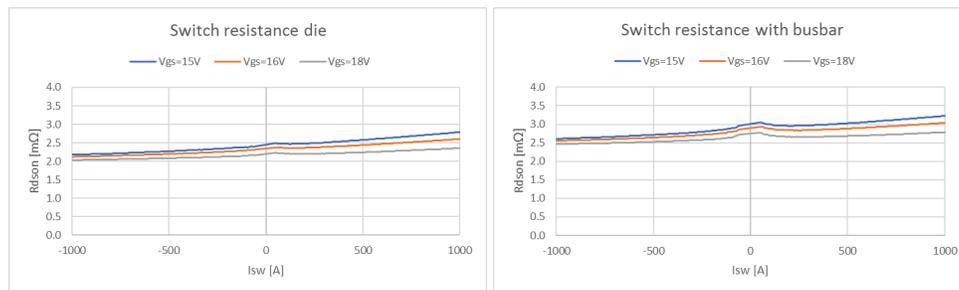


Figure II.5.2 Switch resistance: (left) measured through pcb flex circuit (right) measured through module terminals

direction, large currents increase the width of MOSFET channel and switch resistance decreases. Flex PCB provides low resistance and low inductance interface that enables precise switch control and characterization. As expected, switch resistance measured through terminals is higher as it includes parasitic resistances of the power module package, including resistance of wire bonds, terminals, substrate, and terminal-substrate connections. Summary of the power module resistances is shown in Table II.5.1. Undesired parasitic resistance of the power module range from 0.44mΩ to 0.61mΩ.

**Table II.5.1 SiC power module switch resistances,  $T=25^{\circ}\text{C}$ ,  $V_{gs}=15\text{V}$** 

<b>Rdson [mΩ]</b>	<b>PHS U Low Side</b>	<b>PHS U High Side</b>	<b>PHS V Low Side</b>	<b>PHS V High Side</b>	<b>PHS W Low Side</b>	<b>PHS W High Side</b>
<b>Die</b>	2.49 [mΩ]	2.53 [mΩ]	2.60 [mΩ]	2.47 [mΩ]	2.51 [mΩ]	2.56 [mΩ]
<b>Busbar</b>	2.94 [mΩ]	2.97 [mΩ]	3.03 [mΩ]	3.08 [mΩ]	3.09 [mΩ]	3.14 [mΩ]
<b>Power module</b>	0.45 [mΩ]	0.44 [mΩ]	0.43 [mΩ]	0.61 [mΩ]	0.58 [mΩ]	0.58 [mΩ]

Additionally, the built power module, which utilizes 900V SiC MOSFET die, was tested in the power module lab and thermal impedance curves were measured using Mentor Graphics equipment. Setup for the characterization of the thermal impedance is shown below in Figure II.5.3. Power module is placed inside the inverter housing, with coolant flowing through the designed heatsink structure and housing. Device under the test dissipates heat through the heatsink directly to the coolant and precise thermal impedance characterization is performed with the instrument.

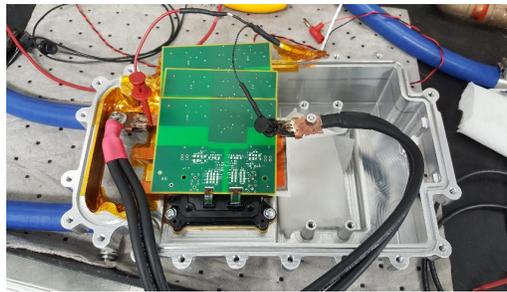
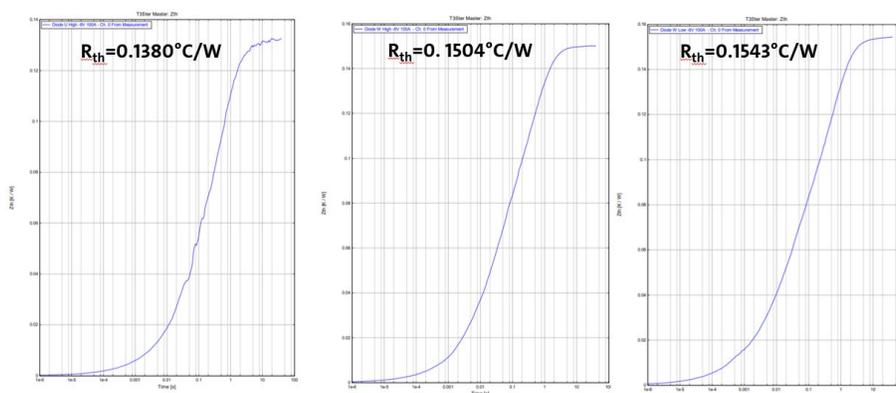


Figure II.5.3 Hardware set-up for the thermal impedance measurements

In order to accurately estimate thermal impedance of the power module, several different tests are conducted, and different gate voltages are used to turn off the MOSFET channel completely. It is worth noting that the standard procedure for measuring thermal impedance of Si IGBT modules cannot be directly applied to SiC power modules. Thus, thermal impedance is measured through the body diode using several different gate voltages ( $V_{gs}=0\text{V}$ ,  $V_{gs}=-5\text{V}$  and  $V_{gs}=-8\text{V}$ ). The explanation is that by applying negative bias voltage on gate source, the MOSFET channel is pinched off accurately and no trapped charge exists in MOSFET. In this way, accurate electrical measurements can be performed and correlated to the temperature curve values. Heating of the body diode is performed with 100A and 200A current. Transient response is recorded through the instrument and plotted in Figure II.5.4.


 Figure II.5.4 Thermal impedance curves for  $V_{gs}=-8\text{V}$ : (left)  $Z_{th}$  for switch UHI, (middle)  $Z_{th}$  for switch VHI, (right)  $Z_{th}$  for switch WHI

Initial thermal impedance values that are measured when gate source voltage is shorted appear smaller than expected. It has been found that both applied negative voltages accurately measure thermal impedance values. The substrate used inside the power module consists of three conductive Al layers and two dielectric AlN layers, which have very high thermal conductivity. Therefore, the designed power module has very low thermal impedance, which provides better thermal heat extraction. This is an important power module feature as it means it is possible to deliver higher power to the electric motors, which directly impacts the performance of the electric vehicle.

Equivalent thermal impedance for the power module, as shown in Figure II.5.5, is extracted from the measured curves. It is based on the 6th order Cauer network and corresponding Cauer network parameters are listed in Table II.5.2. Detailed thermal impedance curve is used to model rise of the junction temperature and to capture device temperature ripple.

**Table II.5.2 Thermal impedance parameters for equivalent Cauer Network**

Parameter	1	2	3	4	5	6
Rith [K/W]	0.0115	0.0201	0.0392	0.0483	0.0111	0.0078
Cith [Ws/K]	0.003786	0.008822	0.029542	0.142142	2.560142	24.67014

Finally, based on the power module loss data, several inverter operating points are evaluated for power, efficiency and temperature rise. Complete table with key parameters for four different operating points is shown in Table II.5.3. SiC inverter can deliver peak power of approximately 280kW and still operate at extremely high efficiency of 99%. It can be noted that SiC inverter losses are relatively low, while SiC inverter operates at efficiencies above 99% for all four operating points. Technically, SiC inverter tends to operate at even higher efficiencies for the low output currents because conduction loss drop at quadratic function rate.

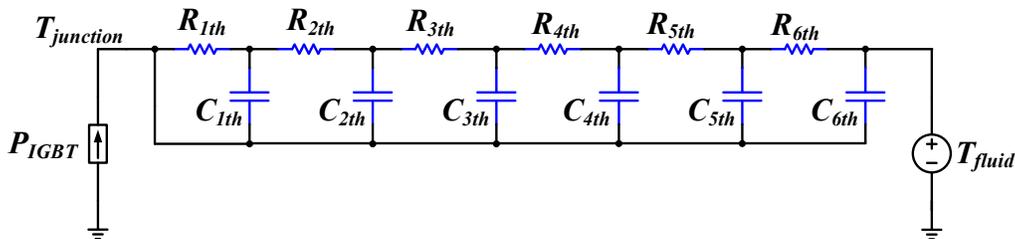


Figure II.5.5 Equivalent 6<sup>th</sup> order Cauer impedance network to represent thermal impedances

The developed solution is cost effective as it utilizes four 900V 10mOhm SiC die from CREE. By using Dowa substrate that utilizes highly conductive materials, the designed power module thermal resistance is 0.15°C/W. The achieved thermal resistance number is very low as it represents total resistance for four paralleled die.

**Table II.5.3 Thermal impedance parameters for equivalent Cauer Network**

Parameters	Operating point 1	Operating point 2	Operating point 3	Operating point 4
DC bus voltage	600V	600V	600V	600V
Phase current	300Arms	350Arms	400Arms	500Arms
Conduction loss	135W	184W	241W	380W
Switching loss (f <sub>sw</sub> =10kHz)	63W	75W	87.5W	114W
Thermal resistance	0.15°C/W	0.15°C/W	0.15°C/W	0.15°C/W
<b>Total inverter loss</b>	<b>1.14kW</b>	<b>1.37kW</b>	<b>1.75kW</b>	<b>2.67kW</b>

<b>Inverter power</b>	<b>168kW</b>	<b>196kW</b>	<b>225kW</b>	<b>281kW</b>
<b>Efficiency</b>	<b>99.32%</b>	<b>99.30%</b>	<b>99.22%</b>	<b>99.05%</b>
<b>Temperature rise</b>	<b>27 °C</b>	<b>32 °C</b>	<b>41 °C</b>	<b>62 °C</b>

### Conclusions

Project goal of “operate more efficiently” has been quantified through detailed characterization of SiC power module. Only four SiC die are used per switch to design 280kW traction inverter, reducing the size and weight of the power module. In the next phase of the project, more power module samples with 1200V SiC die will be built and evaluated. 900V 10mOhm die modeling was successfully refined to have good agreement to experimental results. Key performance parameters of package inductances have been estimated to be below 5nH for the power module and 10nH for the complete power stage (power module and dc bulk capacitor). Although initial concepts were unable to keep the maximum die temperature below requirements, revised concepts have improved thermal performance.

Project will move forward with plans to implement production ready traction inverter with the designed SiC power module and to evaluate its performance on dyno testing in phase three.

### Key Publications

1. G. Watt et al., “Design of a Compact, Low Inductance 1200 V, 6.5 mΩ SiC Half-Bridge Power Module with Flexible PCB Gate Loop Connection,” 2019 IEEE Applied Power Electronics Conference and Exposition (APEC), Anaheim, CA, USA, 2019, pp. 2786-2793.
2. Mocevic et al., “Phase Current Reconstruction based on Rogowski Coils Integrated on Gate Driver of SiC MOSFET Half-Bridge Module for Continuous and Discontinuous PWM Inverter Applications,” 2019 IEEE Applied Power Electronics Conference and Exposition (APEC), Anaheim, CA, USA, 2019, pp. 1029-1036.
3. G. Watt, S. Mocevic, R. Burgos, A. Romero, M. Jaksic, and M. Teimor, “Current Sharing Behavior and Characterization of a 1200 V, 6.5 mΩ SiC Half-Bridge Power Module with Flexible PCB Gate Loop Connection”, ECCE 2019, Baltimore, MD.
4. M. Jaksic et al., “Novel SiC Power Module for Traction Power Inverters with Low Parasitic Inductances”, ECCE 2019, Baltimore, MD
5. M. Jaksic, M. Teimorzadeh, “High Density WBG Traction Inverter for Automotive Applications”, presentation at PowerAmerica special session at ECCE 2019, Baltimore, MD.
6. Invention “Low Inductance Package for Traction Power Modules” (P045682), was reviewed internally in GM and decided to proceed with filing.
7. Invention “High frequency dc bulk capacitor design with interleaved busbar structure” (P044918), was reviewed internally in GM and decided to proceed with filing.

## II.6 V2G Electric School Bus Commercialization Project (Blue Bird Corporation)

### **Brandi Abram, Principal Investigator**

Blue Bird Corporation  
 402 Blue Bird Boulevard  
 Fort Valley, GA 31030  
 E-mail: [andy.moore@blue-bird.com](mailto:andy.moore@blue-bird.com)

### **Steven Boyd, DOE Program Manager**

U.S. Department of Energy  
 E-mail: [steven.boyd@ee.doe.gov](mailto:steven.boyd@ee.doe.gov)

Start Date: February 1, 2017  
 Project Funding: \$9,389,350

End Date: August 31, 2021  
 DOE share: \$4,487,059

Non-DOE share: \$4,902,291

### **Project Introduction**

Two key contributors to the sustainable energy economy of the future are now in view. One is the exploitation of intermittent resources such as solar photovoltaics and wind for electricity generation. The other is the transportation sector's transition from direct use of fossil fuels to electricity. The potential exists to integrate these two elements in a strongly synergistic relationship. The batteries in electric vehicles can store energy and stabilize grid conditions in a way that offsets the intermittency of renewable generation resources. The income generated through this dual use of vehicle batteries can reduce the total cost of ownership of electric vehicles and hasten their displacement of fossil-powered incumbents.

The problem addressed by the V2G Electric School Bus Commercialization Project is that no guidebook exists for this process of mutually beneficial integration. While all of the technological elements are in place and have been demonstrated in various settings, the challenges on commercial and regulatory dimensions remain substantially unaddressed. Heavy-duty vehicles lend themselves most readily to vehicle-to-grid (V2G) use cases in that they have large batteries, are often grouped in fleets, and often have predictable and limited working hours. Yet as of today, purchasers of trucks or buses cannot readily deploy a V2G fleet and reap the benefits of grid integration for themselves or the electric grid.

### **Objectives**

At the highest level, the goal of the V2G Electric School Bus Commercialization Project is to help blaze a trail for the V2G concept through pertinent commercialization and regulatory landscapes via the development and real-world deployment of a fleet of grid-integrated school buses. If successful, the Project will be a catalyst for the creation of policies and precedents that will allow subsequent V2G fleets to interconnect and operate as distributed energy resources in their respective service territories.

At a practical level, Project objectives include development of a V2G electric school bus model that has a short path to total-cost-ownership parity with fossil-powered buses; and a replicable template for both financing school-district uptake of V2G buses and making the physical and commercial arrangements for deploying the buses as distributed energy resources. The specifications originally targeted by the Project to support these objectives were an energy efficiency of 1.1 kWh per mile or better, and a standards-compliant on-board bidirectional inverter. Considerations detailed in the Results section below led to changes in both of these dimensions, to a number likely to be in the 1.20-1.30 kWh/mile in the first case and an off-board (curbside) inverter in the second. Project objectives will be tangibly realized via a fleet of eight type-C original-equipment V2G electric school buses that will be transferred to and operated by the Rialto Unified School District (Rialto USD) in California.

## Approach

The Project is structured into three budget periods, the first two of which culminate in go/no-go decision points. In each budget period, vehicle-oriented and charging-system-oriented activities run in parallel.

The vehicle-oriented focus of budget period 1 (BP1) was technology advancement and prototype vehicle development. The scope in this area included a range of energy efficiency concepts including thermal management of batteries and other assemblies; drivetrain gearing; the adjustment of energy management parameters based on real-time conditions and inputs; and the conservation of energy via regenerative braking. The scope also included development and certification of an on-board inverter with bidirectional charge-discharge functionality and grid-forming capability.

The charging system focus of BP1 was the design of the charging system at Rialto USD's pupil transportation facility and initiation of the interconnection application process with host utility Southern California Edison (SCE). The scope at this stage also included the design of the charging interface immediately up- and downstream of the charging port on the bus.

The go/no-go point at the end of BP1 called for energy efficiency testing of one of the prototype vehicles on the REFUEL dynamometer at the National Renewable Energy Laboratory (NREL) to verify that a stipulated intermediate target for energy efficiency had been achieved.

The vehicle-oriented focus of budget period 2 (BP2) will be prototype vehicle refinement, and construction of the production buses for the Rialto USD. One of the four prototype vehicles will be used for safety and durability testing to ensure compliance with Blue Bird's corporate standards and all applicable Federal Motor Vehicle Safety Standards. Another prototype will serve as the model for the production buses that will be deployed at Rialto USD.

Much of the work on the charging system side of BP2 will flow from the decision, made at the end of BP1, to shift from a charging architecture based on an on-board inverter to one where the inverter is incorporated in a curbside charging station. An additional focus in BP2 will be completion of the interconnection application process with SCE. Once this is done, it will be possible to develop terms and conditions for the Rialto USD fleet to participate in California's wholesale power market. This will involve negotiation with SCE and the California Independent System Operator (CAISO).

The go/no-go point at the end of BP2 was originally to have been achievement of the 1.1 kWh per mile energy efficiency target. Given that the nature and scope of changes for the project's energy efficiency and charging system modules are still pending, a new definition of go/no-go point #2 has not been established.

The parallel vehicle and charging system tracks of BP1 and BP2 will converge with the deployment of the buses in budget period 3 (BP3). Key phases of performance of the Rialto USD fleet will be tracked and documented, including the buses' real-world energy efficiency and their generation of explicit and/or implicit revenues in a range of value-added activities. Another focus of BP3 will be completion of a Market Transformation Plan through which Blue Bird will develop measures to overcome commercial hurdles to EV school bus adoption. An important aspect of this work will be exploration of financing expedients, such as leasing of batteries, to bring the up-front price of the vehicles to parity with conventional school buses, and to achieve total-cost-of-ownership parity via offset of lease payments with V2G revenues and savings on fuel and maintenance expenses.

## Results

The main accomplishment during FY2019 was the partial attainment of the energy efficiency benchmark set for go/no-go point #1. The Project team made the decision during the year to work with prototype bus P1 for this purpose, instead of starting with the "blank slate" of a new prototype vehicle. This decision was predicated on the desire to measure the impact of improvements that could be made on an "upfit" basis before starting to engineer an efficiency-optimized prototype.

Efficiency improvements were made in four areas: regenerative braking; rotational mass and inertia reduction; friction reduction; and thermal management.

The approach taken so far to regenerative braking involves two key elements. The first is an increase in regenerative torque when neither brake nor accelerator pedal is being applied (“coasting regen”). Maximum deceleration allowed with this system is that deemed by the Project team (in the absence of a guiding standard) to be safe without the illumination of brake lights. The second is the automatic adjustment of regeneration parameters to ensure that maximum energy recovery is achieved under all loading conditions on all road grades (“closed-loop regen”).

The primary measures applied under rotational mass and inertia reduction were reduced-circumference aluminum wheels, and lightweight seats, windows, and side skirts. These efforts yielded a decrease in vehicle weight of 620 pounds.

The primary measures applied under friction reduction were low-rolling-resistance tires and bearings; and a variety of aerodynamic enhancements.

Thermal management improvements centered on rigorous thermal isolation of the battery modules and development of an innovative approach to system control. One result of the improvements is a reduction in the amount of time the coolant pump and AC compressor for the battery loop spend in operation. Another is enhanced responsiveness to real-time conditions by the pumps used in other cooling loops.

Exploration of another possible source of efficiency improvement was discontinued in FY2019. The animating concept was to endow the vehicle telematics system with “bidirectional” functionality, so that data could flow from the vehicle and electronic instructions could flow back, all in real time. This would have allowed energy management parameters to be “pre-optimized” based on conditions foreseeable on the route ahead. The idea was abandoned after it became clear that the potential benefits would be minor and not commensurate with the amount of development effort that would be required.

The Project team hoped that the upfitting of bus P1 to bus P1’ would allow attainment of the go/no-go point #1 energy efficiency benchmark of 1.32 kWh per mile. In the event, as shown in Table II.6.1, the result measured by the NREL REFUEL dynamometer was 1.39 kWh per mile.

**Table II.6.1 Results of P1’ Dynamometer Testing**

Test	Start Time	End Time	Net Energy (kWh)	Distance (miles)	Consumption (kWh/mile)
002	2019-05-29 11:25:40:000	2019-05-29 11:52:39:000	8.090	5.970	1.355
004	2019-05-29 12:22:50:000	2019-05-29 12:49:50:000	8.408	5.970	1.408
005	2019-05-29 13:06:43:000	2019-05-29 13:33:43:000	8.390	5.957	1.409
006	2019-05-29 13:50:05:000	2019-05-29 14:17:05:000	8.184	5.956	1.374
007	2019-05-29 14:43:26:000	2019-05-29 15:10:26:000	8.395	5.959	1.409
<b>Average</b>					1.391

The Sankey diagrams prepared by NREL for the original version of bus P1 and the upfitted P1’ (see Figure II.6.1) quantify the effects of the implemented improvements. Energy recovered by the regenerative braking system went from 0.301 kWh per mile to 0.345, while energy dissipated by the friction brakes went from 0.349

kWh per mile to 0.294. Although rolling and drag losses during constant-speed vehicle operation were slightly higher for P1' (by 0.002 kWh per mile), rolling and drag during acceleration went from 0.170 kWh per mile to 0.159 (a reduction of 0.011). Finally, auxiliary loads and motor losses not specifically associated with braking (the category that includes auxiliaries associated with thermal management systems) went from 0.296 kWh per mile to 0.281. The final result is that the improvements delivered the impacts that were anticipated, just not in the amounts that were hoped for.

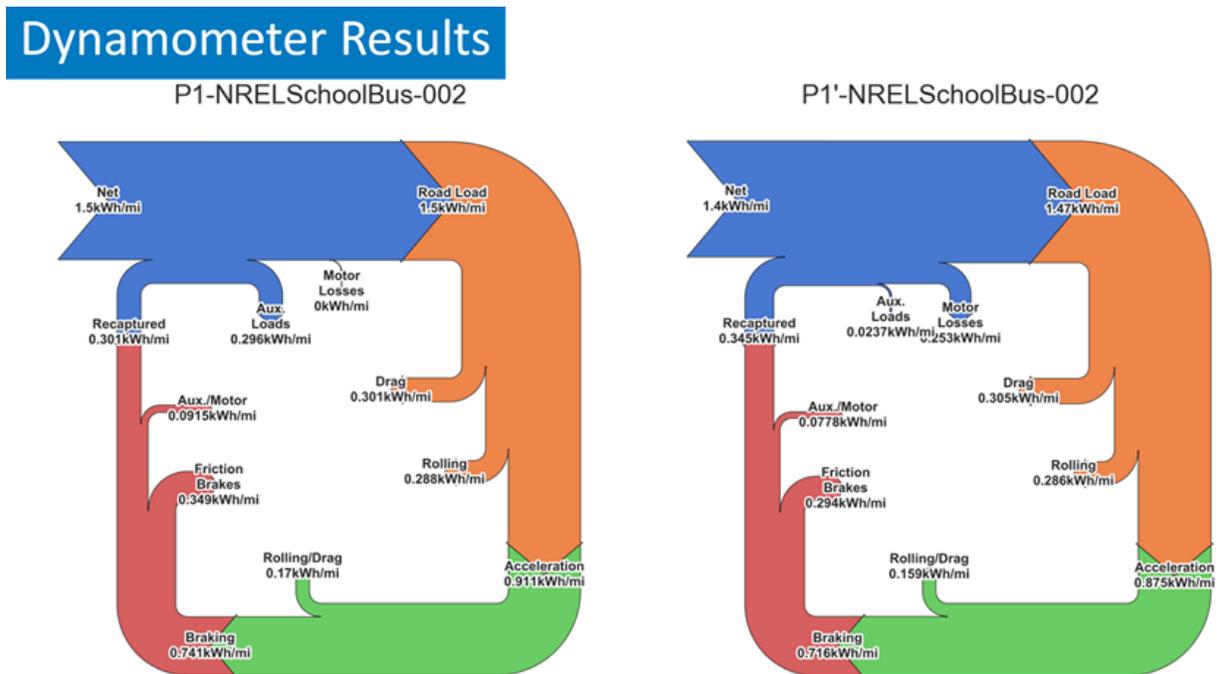


Figure II.6.1 Dynamometer results for bus P1' vs. bus P1. Provided by NREL based on P1' dynamometer testing on May 29, 2019.

The Project team's results were mixed on the charging systems side as well. On the one hand, progress was made in developing a 150 kW bidirectional inverter that could be installed in an on-board configuration. On the other hand, the number of massive components associated with the device would have driven its weight above 500 pounds. This gave the Project team pause, given the hard-won nature of the gains from the weight-reduction initiative detailed above.

A reconsideration of the on-board inverter concept ensued. Although there are arguments in favor of both on-board and off-board configurations, the Project team recognized that every other original equipment manufacturer (OEM) of heavy-duty electric vehicles—most of whom have entered the space since the Project team submitted its proposal to the Department of Energy in August 2016—has chosen the off-board option. Lacking a strong rationale to become the industry outlier—with the alienation from accumulating technical knowledge and shared production volumes that that would imply—the Project team elected to switch from on-board to off-board inverter architecture.

## Conclusions

The Project team concluded, based on serious, sustained investigation of potential energy efficiency expedients, that the economic proposition of an EV school bus capable of achieving the Project's original target of 1.10 kWh/mile would not be viable. The incremental cost of the more extreme measures needed to deliver that level of energy efficiency (example: chemically strengthened lightweight glass for windows) would not be recoverable from operating savings over the useful life of the bus. While an analysis of the economic viability of the most promising heretofore unimplemented measures is pending, the Project team



anticipates that only a high-yield version of a regenerative braking system will have a favorable economic profile. The expectation in this regard is based on the insight that 21% of the energy consumed by bus P1' over the course of the NREL School Bus duty cycle was lost to the use of friction brakes. The Project team believes that a substantial increment of this energy could be recovered through the implementation of a braking system with two-stage activation. (Stage-one deceleration would be realized through energy regeneration, stage-two through activation of the friction brakes.) As a consequence, the Project team expects to propose a new target for energy efficiency in the range of 1.20-1.30 kWh/mile.

The Project team also concludes that the need and opportunity for leadership in the heavy-duty vehicle-to-grid field remains compelling. In spite of the growing number of OEMs in the heavy-duty EV market, the Project team is not aware of any other programs with strong V2G orientations. (Such an orientation would be manifested by the capability for high-power (e.g., >100 kW) bidirectional charging). The practical implication of this conclusion is that development of certain elements of the charging system, including the electric vehicle supply equipment, will be a key focus in the next phase of the Project.

### Key Publications

1. Whitaker, D., Blue Bird [V2G Electric School Bus Commercialization Project](#). U.S. Department of Energy Vehicle Technologies Office 2019 Annual Merit Review, June 12, 2019, Washington, D.C. Project ID: EE0007995.

## III Grid and Infrastructure Industry Awards

### III.1 Emission Drayage Trucks Demonstration (ZECT I)

#### **Matt Miyasato, Principal Investigator**

South Coast Air Quality Management District  
21865 Copley Drive  
Diamond Bar, CA 91765  
E-mail: [mmiyasato@aqmd.gov](mailto:mmiyasato@aqmd.gov)

#### **Phil Barroca, Co-Principal Investigator**

South Coast Air Quality Management District  
E-mail: [pbarroca@aqmd.gov](mailto:pbarroca@aqmd.gov)

#### **Lee Slezak, DOE Program Manager**

U.S. Department of Energy  
E-mail: [lee.slezak@ee.doe.gov](mailto:lee.slezak@ee.doe.gov)

Start Date: October 1, 2012

End Date: March 31, 2020

Total Project Cost: \$9,374,641

DOE share: \$4,169,000

Non-DOE share: \$5,205,641

#### **Project Introduction**

On-road heavy-duty diesel trucks are one of the largest sources of diesel particulate matter and NO<sub>x</sub> emissions in the South Coast Air Basin. The large number and extensive operation of conventionally powered higher emitting mobile sources continue to have an adverse impact on air quality and public health in this region, particularly on communities adjacent or in proximity to the various transportation corridors that facilitate the significant volume of goods movements from the San Pedro Bay Ports - Ports of Los Angeles and Long Beach. As a measure to reduce the impact and to meet federal ambient air quality standards, the South Coast Air Quality Management District (SCAQMD) has been working with regional stakeholders, including the Ports of Los Angeles and Long Beach, to promote and support the development and deployment of advanced zero emission cargo transport technologies. In 2012, SCAQMD applied for and received a \$4.17 million grant from the DOE under the Zero Emission Cargo Transport Demonstration Program to develop and demonstrate Class 8 electric drayage trucks with zero emission operation capability in real world drayage service.

#### **Objectives**

This project is to develop and demonstrate zero emission capable electric truck technologies in real world drayage operations to assess its technical feasibility to support demanding drayage duty cycles. The project is also to promote and accelerate market adoption of electric truck technologies in cargo transport operations, by engaging trucking fleets, the end users, in demonstrations to experience the technologies first hand.

#### **Approach**

SCAQMD, as the award recipient, will provide overall project management in this project. TransPower and US Hybrid, locally based EV system developers and vehicle integrators in Southern California, are to develop a total of eleven Class 8 zero emission capable drayage trucks for demonstration, based on four different architectures, consisting of two types of battery electric vehicles (BEVs) and two types of plug-in hybrid electric vehicles (PHEVs) with all-electric range capability as summarized in Table III.1.1. Initial portfolio of demonstration technologies included a fuel cell truck by Vision Motors and another battery electric truck from

Balqon. However, with these two technology providers dropping out due to financial hardship, the portfolio was amended to the current mix by adding two PHEV technologies in 2015.

Upon completion, demonstration vehicles are deployed in real world drayage service for up to two years of demonstration with fleet partners at the San Pedro Bay Ports. During the demonstration, vehicle performance and O&M data will be collected and analyzed by National Renewable Energy Laboratory (NREL) to assess technical feasibility and market viability of the technologies in drayage truck applications. In addition, at least one truck from each technology is tested on chassis dynamometer at the University of California, Riverside (UCR) for performance validation and optimization.

**Table III.1.1 2012 Zero Emission Cargo Transport Demonstration Portfolio**

	Battery Electric Trucks		Plug-In Hybrid Electric Trucks	
<b>Developer</b>	TransPower	US Hybrid	TransPower	US Hybrid
<b>No. of Trucks</b>	4	2	2	3
<b>Hybrid Architecture</b>	N/A	N/A	Series	Parallel
<b>Chassis</b>	International Prostar	International Prostar	International Prostar	Peterbilt 384
<b>Traction Motor</b>	Dual PM Motor 300 kW	Induction Motor 320 kW	Dual PM Motor 300 kW	223 kW PM Motor (403 kW combined)
<b>Transmission</b>	Automated Manual	Direct Drive	Automated Manual	Automatic
<b>Auxiliary Power Unit</b>	N/A	N/A	3.7L CNG	8.9L LNG
<b>Battery/Storage Capacity</b>	215 kWh-311 kWh	240 kWh	138 kWh/60 DGE	80 kWh/72 DGE
<b>Charger</b>	On-Board ICU 70 kW	On-Board 60 kW	On-Board ICU 70 kW	On-Board 20 kW
<b>Refuel Time</b>	2.5-4 hrs	3-4 hrs	2 hrs/15 min	3-4 hrs/15 min
<b>Drayage Range</b>	75-150 miles	70-100 miles	200 miles/ 30-40 AER miles	250+ miles/ 30 AER miles

## Results

### *Battery Electric Trucks (BETs)*

#### *TransPower*

TransPower completed the development and demonstration of four BETs funded under this project. Three of the four BETs, EDD-2, -3 and -4, continued operation in drayage service through 2017, with EDD-3 and EDD-4 being deployed in service for almost two years, and EDD-2 in service for nearly three years since January 2015. Three additional EDD trucks were deployed under separate funding. The EDDs under ZECT 1 accumulated approximately 26,000 drayage miles as recorded by NREL and all seven EDDs accrued more than 43,000 miles. Table III.1.2 summarizes daily average use and performance characteristics for EDD trucks 2-4, in comparison to baseline diesel trucks in comparable duty cycles running short-haul drayage operations. As shown in the table, EDD trucks averaged 5.08 hours and 43.69 miles of operation per day, similar to the baseline diesel trucks that operated 6 hours per day, averaging 52.26 miles in drayage service. What is notable is that both EDD trucks and diesel trucks spent well over 50% of their operating hours idling, mostly while waiting in queues to load and unload cargo containers at the port terminals. This is typical for short-haul drayage trucks operating at the San Pedro Bay Ports and such duty cycles are an ideal match for electric trucks which, unlike conventional diesel trucks that keep its engine running for A/C and other amenities during such operations, can use battery power for hoteling loads with zero tailpipe emissions, thus providing significant fuel savings as well as considerable benefits in air quality and public health. Also noted is that the EDD trucks

demonstrated much higher fuel efficiency, averaging 2.13 kWh/mi or 17.68 MPG<sub>de</sub>, which is three times better than the 5.67 MPG for the baseline diesel trucks, providing significant savings in fuel costs.

**Table III.1.2 Average Daily Use – TransPower BETs**

	EDDs (EDD2 – EDD4)	Baseline Diesel Filtered <sup>1</sup>
Operational Time (hr)	5.08	6.02
Idle/Stationary Time (hr)	2.86	3.67
Daily Distance (mile)	43.69	52.26
Average Driving Speed (mph)	19.79	22.45
Regen Energy (%)	17.20	N/A
A/C Energy Use (kWh)	3.07	N/A
Remaining SOC (%)	54.74	N/A
Energy Efficiency (kWh/mi)	2.13	6.64 <sup>2</sup>
Fuel Economy (MPG <sub>de</sub> )	17.68 <sup>2</sup>	5.67

1. Filtered out days with distance >100 mi and Ave. driving speed >40 mph
2. kWh/mi and MPG<sub>de</sub> calculated using 37.656 kWh/gallon of diesel fuel

EDD truck demonstration started with two fleets, namely TTSI and SA Recycling in January 2015, and expanded to include Cal Cartage, National Retail Transportation, Knight Transportation, PASHA, and 3 Rivers Trucking. Feedback from fleet operators and drivers was generally positive, describing the trucks as quiet, clean and easy to drive, especially in the stop-and-go traffic at the Ports. However, range limitation was the main challenge to overcome for the fleets to readily adopt and deploy the trucks in drayage service without any limitations. To address this challenge, TransPower explored several high-density battery chemistries, including the Nissan Leaf nickel manganese cobalt (NMC) batteries that have greater energy capacity compared to lithium iron phosphate (LFP) batteries deployed in the EDD trucks demonstrated. Also, as battery technology is expected to improve in energy density, TransPower expects the operating range of EDD trucks to increase from the current fully-loaded range of 70 miles to perhaps 200 miles, considered by many fleets as the minimum range for drayage trucks. EDD trucks 1, 3, and 4 are in the process of being retrofitted with the NMC battery technology as well as being up-fitted with Fuel Cell range extender technology under CARB’s Fast Track Fuel Cell Program.

Testing of one of the EDD trucks on a chassis dynamometer at the University of California, Riverside (UCR) in 2014 showed the ElecTruck™ technology to be nearly twice as efficient than an all-electric HDV tested at UCR in 2011 over the same cycles. This suggests the current all-electric HDV is a significant improvement in the state-of-the-art of all electric HDVs. This testing, along with in-service demonstrations, showed the practicality of zero-emission operation of Class 8 trucks. The UCR report also concluded “the all-electric HDV performed well on all the cycles and showed a very reliable operation from full to 20% SOC



Figure III.1.1 TransPower EDD Battery Electric Trucks

load,” while concluding that the energy cost of operating the TransPower electric truck compared favorably with the costs of operating diesel trucks or competing electric trucks.

### US Hybrid

US Hybrid completed and delivered the first of two BETs to drayage operator TTSI in late 2016, however, due to unexpected delays in permitting and installation of EVSEs at TTSI’s new location in San Pedro, BET-1 was not deployed in drayage service until July 2017. This truck was deployed through the end of 2018 and recorded 61 days of service and 1,798 drayage miles according to NREL data. The NREL data shows that BET-1 resulted on a median daily use of 7.32 hours and 21.7 miles of operation, and a daily average efficiency of 2.17 kWh/mi in electrical energy. US Hybrid conducted additional testing for validation and optimization. The testing included medium and long-distance excursions on surface streets and highways, as well as pulling a fully loaded trailer over the Vincent Thomas Bridge, a suspension bridge located in the San Pedro Bay Port complex with a 7% grade. The truck demonstrated sufficient power to manage the bridge with a full load while maintaining posted speed limits.



Figure III.1.2 US Hybrid Battery Electric Truck No. 1



Figure III.1.3 US Hybrid Battery Electric Truck No. 2

In Q1-2019 US Hybrid commenced the building of BET-2. After having experienced more than the usual share of glitches and reliability issues with batteries and suppliers, US Hybrid elected to switch from its former battery supplier and LFP batteries used in BET-1 to A123 battery supplier and the use higher energy density NMC battery technology, which US Hybrid claims has 30% higher energy density relative to the LFP batteries it was using. BET-2 was completed at the end of May 2019 and was subsequently delivered to the demonstration fleet, TTSI, in early June 2019. The vehicle was expected to be deployed with high frequency to begin amassing data collection in the short time remaining under this project. The vehicle experienced a problem with its air conditioning system which incapacitated the vehicle for 4 weeks. Subsequently, the vehicle was

involved in a minor accident that kept in out-of-use for another 5 weeks. During this extensive period of inactivity TTSI reported that the auxiliary battery (12 Volt) was discharged and that the vehicle would shut down soon after the 12 Volt jumper cable was removed. After some investigation, it was determined that there was an imbalance issue with the traction battery cells. The batteries did not balance on their own because the battery management system (BMS) did not have 12 Volts power from the low Voltage master switch when it was switched off. The reason for that was that if the master switch was left on, the 12-volt battery would discharge over a few days.

BET – 2 is equipped with six strings of batteries connected in parallel. When there is a large voltage difference between the cells and the strings the contactors will not close in order to protect the batteries. One Engineer and one Technician spent two entire days at the site with limited resources, manually balancing strings such that three sets of contactors close allowing the truck to be driven to US Hybrid’s facility in Torrance, CA. US Hybrid manually balanced the cells on all six strings of batteries to ensure their health. Once this process was completed the traction batteries were recharged to their maximum capacity.

US Hybrid also made a change to the truck wiring so the power for the BMS will not be switched off by the master disconnect switch and allow the cells to balance as needed. If the cells are allowed to balance after every charge it will require less time to balance and not result in a major drain on the auxiliary battery. If the truck is not to be used for more than 5 days, a 12 V battery charger should be connected to keep the auxiliary battery charged. Following the repairs on BET-2 it was delivered back to TTSI on 10/30/2019. Data is being collected on this vehicle and will be reported in a Final Report.

### ***Plug-In Hybrid Electric Trucks (PHETs)***

#### ***TransPower***

TransPower continues to demonstrate its small (3.7-liter) CNG-powered APU, series-hybrid battery electric truck (CNGHs). Under this project, TransPower was to develop and demonstrate two vehicles, the first of which was completed in 2017. The first CNGH completed a series of testing for validation and optimization, including local and highway driving, in-field operation of the auxiliary power unit (APU) for extended range, and initial load pulling exercises. TransPower also concluded research to characterize variable valve control signals for higher RPM and power on its test dyno cell, which has been constructed using all of the parts and features of the production article generator sets to run calibration testing of custom engine control software. The original design included converting the APU from a limited stationary-trim power mode to the APU’s full power potential in automotive-trim mode. This effort did not prove successful due to TransPower’s inability to obtain the engine codes necessary to operate the engine at the higher power levels and output, about 110 kW. As a result, the APU is restricted to a power output level approximately 55% of full design capability (automotive-trim) or about 60kW. This limited power output affects range extension and on-highway performance under load, restricting its deployment to near-dock and near domicile operations.



Figure III.1.4 TransPower CNGH-1

In October 2018 TransPower deployed CNGH-1 into drayage operation with TTSI. The vehicle was used for two days out of 20 working days in that month. On the first day of deployment the truck experienced an ESS failure while being driven by a TTSI driver. It was reported that the CNG supply valve was not opened prior to departure, and it appears that heavy loads borne solely by the battery without APU assist, may have been at least partially responsible for the cell failure.

Subsequent to this occurrence, TP initiated a request for a review of driver training procedures to help prevent a recurrence. TP also discussed developing additional software changes to protect against this type of failure. The second day the vehicle was deployed the APU experienced overheating and required the vehicle to be turned off to allow the vehicle to be returned to base. CNGH-1 exhibited a series of battery cell failures and overheating events in deployment with partner TTSI. As a result, TP moved to address these overheating issues in the development of CNGH-2 and, after consulting with all parties, sidelined CNGH-1 to focus on CNGH-2. Since CNGH-2 employs the higher energy density and better balanced NMC battery energy system, some immediate relief and dependence on the limited power APU could be expected. In addition, TP devoted more focus on addressing engine overheating including cooling enhancements such as better baffles and seals,

air scoops, and exhaust wrapping; software changes such as idle-down control features, and output reduction based on effective engine temperature.

Significant on-road testing of CNGH-2 was accomplished during Q4 2018. In Q1 2019 additional on-road testing was performed including dispatching the truck on warmer days, subjecting the vehicle to hill climbs to add load and increase temperature, followed by stop and dwell periods with the APU engaged and generating power. Key temperatures and power levels were recorded. These tests were repeated a total of three times in a single day and TP reported no overheating issues.

The further improvements that were made to CNGH-2 in this period included: better sealing in key areas, new air control plenum, APU power controlled by coolant temperature feedback, APU ramps with vehicle speed to account for increased convective heat transfer, and higher radiator fan speed at all power levels.

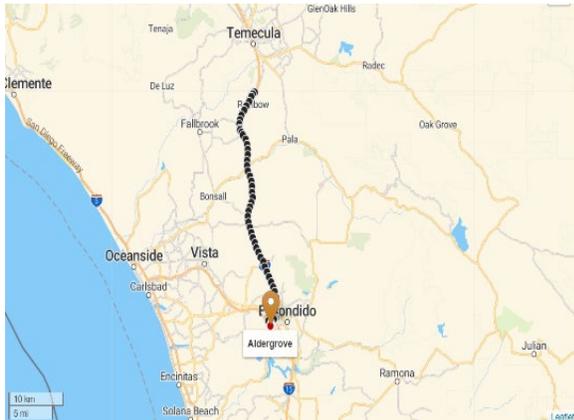


Figure III.1.5 Route containing hills during Q4 2018 tests



Figure III.1.6 TransPower - CNGH-2 (APU view)



Figure III.1.7



Figure III.1.8 TransPower - CNGH-2 with trailer

CNGH-2 continues to be demonstrated with TTSI and is being deployed on 40-mile routes. The vehicle is demonstrating satisfactory power and reliability under these near-dock conditions. Data collection efforts are being hampered by the datalogging system that TP has been using since its EDD trucks. TP is seeking to resolve the issues with the supplier of this system.

Chassis dyno testing completed in Q1-2019 has been analyzed and a final report released by UC Riverside. The report indicates that fuel consumption rates based on carbon balance indicate that significant range extension is achievable with the serial hybrid configuration. Table III.1.3 shares the dyno testing schedule actually implemented. Further analysis is anticipated by TransPower to examine cost effectiveness of range

extension when compared to diesel ICE. Preliminary indication is that there is cost parity. Also, as anticipated, the early exit of Ford from this partnership, and the related loss of certified engine control software and hardware, led to unacceptable emissions from the engine while operated under the control of stationary generator control hardware and software. Table III.1.3 illustrates the emissions outcomes of the testing.

**Table III.1.3 Summary Across All Cycles for Chassis Dyno Testing of CNGH-2**

Cycle	Ave Speed	Duration	Distance	Net Total Energy	Net Generator Energy	Net Battery Energy	Total Energy usage	Generator energy usage	Battery Energy usage	SOC usage
n/a	mi/hr	sec	mi/cycle	kWhr	kWhr	kWhr	kWhr/mi	kWhr/mi	kWhr/mi	%
SG1 Hill	40.79	448	5.07	22.95	4.37	18.58	4.53	0.86	3.66	11
UDDS	18.39	1061	5.42	15.02	12.34	2.67	2.77	2.28	0.49	2
UDDS	18.48	1061	5.45	14.97	12.83	2.14	2.75	2.36	0.39	1
DTP 3	23.98	4229	26.65	56.52	50.20	6.32	2.12	1.88	0.24	5
UDDS (No APU)	18.31	1061	5.40	17.15	0.00	17.15	3.18	0.00	3.18	10
SG1 (No APU)	33.15	427	3.93	19.04	0.00	19.04	4.85	0.00	4.85	12
UDDS	18.46	1061	5.44	15.49	11.87	3.62	2.85	2.18	0.67	2
UDDS	18.59	1061	5.48	14.65	12.09	2.56	2.67	2.21	0.47	2

**US Hybrid**

US Hybrid is demonstrating a hybrid system that converts an existing 8.9L LNG-powered ISL-G engine, which is considered underpowered for heavy-duty drayage operations, to a plug-in parallel hybrid truck capable of providing sufficient power and torque, comparable to a larger 12L engine, that can support a full range of demanding drayage duty cycles. Although this LNG parallel hybrid technology was added in midstream in late 2015, US Hybrid made considerable progress, having completed and delivered two of the three contracted LNGHs to TTSI in 2017. After completing necessary paperwork and vehicle inspections, the trucks were deployed in drayage service in July 2017. Based on preliminary data, as provided by NREL, the two trucks have collectively operated 269 days and logged more than 13,840 miles in drayage service, with each vehicle contributing nearly equal miles. The two trucks have produced a daily mean average of 3.83 hours of daily usage and 40.43 travel miles. Individually, US Hybrid’s LNGH-1 and 2 experienced different operation. LNGH-1 saw 51 fewer days of operation, experienced longer median operating times and distances per event, significantly longer idle time, twice as much regeneration energy and lower energy efficiency than LNGH-2. The net average fuel economy for each vehicle as calculated by NREL is: 8.9 mpg<sub>deq</sub> (LNGH-1) and 12.8 mpg<sub>deq</sub> (LNGH-2).

The third LNGH was delivered to UCR for chassis dyno testing to improve engine control and SOC control strategies to further reduce NOx emissions and enhance fuel economy.



Figure III.1.9 US Hybrid LNGH



Figure III.1.10 US Hybrid LNGH pulling a container for TTSI



## Conclusions

Despite many challenges, including withdrawal of two technology providers in 2015, this project has been largely successful. As of June 2019, all eleven electric trucks funded under this project were constructed with two trucks continuing demonstration efforts until March 2020. NREL has received various data from these trucks including more than 34,000 miles of collective reported activity with drayage operators. Additional miles have been accrued on these trucks that have not been included in the NREL report that includes transportation to and from the technology integrator, or for vehicle trials and testing. Overall, the trucks that have completed demonstration have proven successful in demonstrating their feasibility in various drayage operations and handling daily loads and many routine schedules. The trucks have generated significant interest from trucking companies, which is helping promote and accelerate market adoption of electric truck technologies in cargo transport operations including the development of fuel cell-electric trucks.

Based on available data collected from demonstration vehicles and feedback from fleet operators and drivers, these electric trucks have demonstrated sufficient power and torque to support real world drayage operations, while providing superior fuel economy over conventional diesel trucks in short-haul drayage duty cycles. The feedback from drivers was generally positive, with comments on its quiet and easy operations as well as smooth accelerations during take offs. These trucks also demonstrated sufficient capability to manage steep grades, even with a full load, including the Vincent Thomas Bridge, a suspension bridge located in the San Pedro Bay Port complex with sections reaching a 7% grade. As expected, fleets expressed concerns over limited operating range for battery electric trucks. Fleets cited the range limitation as a significant barrier for them to fully adopt and deploy these trucks in more range-extensive drayage operations. To address this barrier, both TransPower and US Hybrid have explored alternative high-density battery chemistries, including nickel manganese cobalt which has greater energy capacity relative to lithium iron phosphate used in both company's trucks. In addition, both companies are exploring electric range extending features such as hydrogen fuel cell technologies as well as the ongoing research into high energy density batteries.

TransPower expects to increase the operating range of all electric trucks from the current 70 miles to over 200 miles, even with a full load, supporting a wider range of drayage operations.

US Hybrid has successfully demonstrated the feasibility and superior load hauling performance of a parallel hybrid electric Class 8 truck utilizing a Cummins 8.9-liter natural gas engine. This parallel hybrid system provides seamless and sufficient power and torque in routine drayage operations, that many operators found favor with and compared its performance and capabilities to trucks equipped with larger displacement internal combustion engines such as the Cummins 12- and 13-liter engines. The combined power systems also produced a fuel economy benefit of better than 60% relative to the conventionally fueled baseline trucks. Two of the three US Hybrid hybrid-electric trucks have been deployed in drayage service since July 2017 and have received positive feedback from drivers and operators alike, especially on its exceptional power and torque. Upon successful demonstration in this project, US Hybrid is developing the next generation of a parallel CNG hybrid system employing Cummins L9N ultra low-NOx engine. This upgraded version is expected to retain the power and torque performance of the existing system, produce very low emissions based on Cummins' engine and exhaust treatment systems, and be designed to operate in all-electric mode in highly sensitive areas.

### III.2 Zero Emission Cargo Transport II San Pedro Bay Ports Hybrid & Fuel Cell Electric Vehicle Project (South Coast Air Quality Management District)

#### **Seungbum Ha, Principal Investigator**

South Coast Air Quality Management District  
21865 Copley Drive  
Diamond Bar, CA 91765  
Email: [sha@aqmd.gov](mailto:sha@aqmd.gov)

#### **Lee Slezak, DOE Program Manager**

U.S. Department of Energy  
E-mail: [Lee.Slezak@ee.doe.gov](mailto:Lee.Slezak@ee.doe.gov)

Start Date: October 1, 2014                      End Date: September 30, 2021  
Project Funding (FY18): October 1, 2014    DOE share: \$9,725,000                      Non-DOE share: \$10,685,075

#### **Project Introduction**

The proposed project area is known as the Los Angeles Goods Movement and Industrial Corridor. This area is adjacent to the Ports of Long Beach and Los Angeles, the busiest port complex in North America. The area is in an industrial setting with diesel truck activity mingled with a variety of uses including residences, schools, daycares and senior centers. The area is also a known Environmental Justice Community made up of predominantly low-income and minority populations that are adversely impacted by vehicle emissions.

The proposed technologies, fuel cell range extenders and hybrid electric trucks, face many challenges in the process of commercialization: proper sizing of the fuel cell stack, battery and fueling system; system integration and packaging of power train components and systems for safe, efficient and economical deployment of the technologies are just a few of the challenges. Many options exist in sizing the energy systems for these type of vehicle architectures—making the battery, engine or fuel cell dominate in size; plug in charging versus operation in charge sustaining mode and sizing of the energy storage system. Considerations for the power requirements of vehicle under load and providing enough onboard energy to attain the range requirements for the drayage operation and duty cycles all come into play in the design of the energy storage and power systems. Another challenge is to design the energy and power train systems described above and then integrate them into a vehicle for safe and efficient operation that can be made economical in volume and series production.

#### **Objectives**

- Reduce criteria pollutants and GHG's in South Coast Air Basin by reducing diesel emissions from transportation and movement of goods
- Accelerate introduction and penetration of zero and near-zero emission fuel cell and hybrid technologies in cargo transport sector
- Execute a joint project with the Port of Los Angeles and Long Beach consisting of demonstration, data collection and analysis of seven fuel cell and hybrid trucks on five different vehicle architectures.

#### **Approach**

Our approach to implementing the proposed technology is to address some of the challenges of developing the fuel cell range extended and hybrid truck platforms with the cost and time constraints of this FOA. By bringing together small to medium sized vehicle integrator contractors along with global manufactures and developers our strategy is to obtain the best partners with innovation and experience for this project. Vehicle integrators

Transportation Power, Hydrogenics and U.S. Hybrid, are extremely cost effective in demonstrating proof of concept and exploring design variants in a timely fashion; OEM’s BAE Systems a global defense and security company, Kenworth Trucks a major truck OEM and Ballard Power Systems an international fuel cell manufacturer have engineering and manufacturing capabilities and experience; both BAE and Ballard have experience in developing fuel cell transit buses. Together our project contractors offer the opportunity to explore design variations concurrently and address many of the challenges developing new technologies in a timely and cost effective manner. Some of the metrics that will be used to evaluate the design variants of the five fuel cell range extended and hybrid architectures are: operational capabilities (range), energy usage and efficiency, fueling/charging requirements and costs compared to diesel powered trucks.

**ZECT 2 Projects:**



Figure III.2.1 CTE/Kenworth Fuel Cell Truck



Figure III.2.2 TransPower Fuel Cell Truck in Foreground & CNG Truck in Background

**CTE/BAE Systems and Kenworth** have developed a battery electric truck with a hydrogen fuel cell range extender. The vehicle will operate in electric mode at all times and all speeds until the battery energy system reaches a lower operating state of charge level, at which point the hydrogen range extender would be activated to supplement power.

**TransPower** has developed two battery electric trucks with hydrogen fuel cell range extenders. These trucks will employ a small fuel cell and stored hydrogen. One truck will be equipped with a 30 kW fuel cell and one with a 60 kW fuel cell, enabling a direct comparison of both variants

**U.S. Hybrid** has developed two equivalent battery electric trucks with an on-board hydrogen fuel cell generator. Each truck is estimated to have 20 kg of hydrogen storage at 350 BAR with an estimated fueling time under 10 minutes.



Figure III.2.3 U.S. Hybrid Truck: Design to Fabrication

**GTI/BAE Systems and Kenworth** have developed one hybrid battery electric truck with CNG range extender. The proposed technical concept provides an all-electric mode, and in a conventional hybrid mode using CNG. The truck will have an on-board battery charger to fully charge the batteries in daily use.

**Hydrogenics** has replaced International Rectifier in the ZECT 2 San Pedro Bay project and they will be developing and demonstrating a fuel cell range extended Class 8 truck. Hydrogenics working with Daimler’s VVG dealership group developing a fuel cell range extended truck under a California Energy Commission (CEC) project.



Figure III.2.4 Kenworth/BAE - CNG Hybrid System Architecture

**Table III.2.1 Hydrogenics Vehicle Systems Specifications**

Item	Target Specification
Chassis	Daimler Freightliner Cascadia Day Cab
GVWR	80,000 lbs
Fuel Cell Power System	Hydrogenics CelerityPlus
Electric Drive	Siemens ELFA PM Motor
Battery	ACTIA100 kWh
System Voltage	650 V
Hydrogen Storage	30 kg @ 350 bar
Refuel Time	10-15 minutes
Expected Range	150-200 mi

## Results

### *TransPower*

***Fourth Quarter 2018:*** The first fuel cell truck was taken out of service since there have been two faults which have interrupted operation, one reported as a drive train fault and one as a fuel cell overheating fault.

The second fuel cell truck (FC2) is in a slow and thorough commissioning process:

- Isolation fault issues have been studied and substantially eliminated
- Faulting due to sudden stops and driving over rail tracks have led to ordering a replacement to the DC-DC converter (24VDC source), which will have higher voltage capability
- The fuel storage pressure gauge is suspected of leaking, a new gauge will replace the old
- The truck has been driven with full trailer (80,000 pound GVW), leading to revealing some drivability issues to be addressed in January
- The end of December mileage of FC2=1621 miles

**First Quarter 2019:** FC1 has been returned to the TransPower integration facility, for evaluation and recommissioning, including at minimum 500 miles of drive testing. During four months of not being used and in particular, of not being periodically connected for charging, the battery system had been discharged and hence damaged. Thus the battery was rebuilt with several cells being replaced with undamaged cells. To assure that the prototype FC1 could be charged from the same EVSE as the newer trucks, its charger connection was upgraded to the new design. Re-commissioning was initiated following software upgrades which are intended to remedy intermittent issues experienced on the road in September.

FC2 has completed commissioning process. Isolation fault issues were studied and substantially eliminated. It was found that one of the fuel cells had developed coolant leakage, so both fuel cells were replaced with new fuel cells. Following this replacement it has been observed that the isolation impedance has substantially increased, and one can now expect no further isolation fault issues. Faulting due to sudden stops and driving over rail tracks have been eliminated by replacing high voltage cables which had developed intermittent hvil connections. The DC-DC converter (24VDC source) was thought to have possibly been the source of overvoltage faults, it has been replaced with a unit rated for higher voltage capability. Software improvements have addressed the fuel cell current control. New software addressed the rollback issue, improved to limit the movement. The truck was driven with fully loaded trailer (80,000 lb.) on the routes with repeated climbs to the Temecula ridge. The most severe result in battery heating to the extent of limiting performance, but the truck repeatedly completed these routes without interruption or stopping.

**Second Quarter 2019:** The first truck was commissioned in 2017 and was stationed at TTSI starting late 2017. In limited service over the summer and into September there were occasional drivetrain failures interrupting service, resulting in the truck being sidelined. It was returned to the TransPower facilities in February 2019 for further testing and software upgrades. Early commissioning driving of the FC1 (prototype) truck, first in bobtail configuration and later as tractor trailer loaded to approximately 55,000 pound GVW. The results have been encouraging. It has been observed that the fuel cell system has power variability which detracts from average power. Hence the validation process has been expanded to include improving the stability of the power system control software.

The FC2 was commissioned and was driven to TTSI in April, 2019 and is presently in service.

FC2, now in service at TTSI, has been reliable. The end of June mileage of FC2 was 3335 miles, with 646 miles added in Q2.

**Third Quarter 2019:** For FC1, the battery system was rebuilt, and further commissioning driving was done to evaluate reliability. It has been observed that the fuel cell system has power variability which detracts from average power. Hence the validation process has been expanded to include software improvement and validation. In the process of this one of the fuel cell engines developed a leak, and was removed and returned to the manufacturer. After repairing the leak they noted several cells were below expected voltage, and insisted on again rebuilding with new cells, which is being discussed to find best solution to repair.

FC2, now in service at TTSI, has been reliable and has seen limited service. The end of September mileage of FC2 was 4791 miles, with 1456 miles added in Q3. On or about August 20 driving was suspended at request of TransPower management, inasmuch as there was concern about the truck paperwork legality. These issues have been resolved and the truck returned to service at the end of the quarter. Hence the accumulation of 1456 miles indicates it was being used at a rate of about 1000 miles per month

### ***US Hybrid***

**Fourth Quarter 2018:** US Hybrid deployed fuel cell truck #1 and began operation at TTSI from the past quarter. Following deployment of the first vehicle, a problem was encountered. During in-house life testing, US Hybrid detected that the vehicle's manifolds showed evidence of corrosion that penetrated the coating, which was due to the supplier's Q/A. In order to solve this issue as quickly as possible, the FCE80 power plant was sent to our South Windsor, Connecticut facility for manifold upgrades. Also, during the FC engine

removal, it was noticed that the WEG cooling system has evidence of rust and debris particulates. These debris may be due to not fully flushing or aging of the old radiator (this is a repowered 2012 truck). The cooling lines have been changed and re-flushing the system has been done to ensure that there are no debris/containment in WEG.

**First Quarter 2019:** US Hybrid worked on designing and installing a new battery box for liquid cooling for the second fuel cell truck. This was done in order to re-build the truck cooling system with complete flushing and change of cooling lines. It was recommended to increase the FC engine power to 100kW based on TTSI/ operator demand for higher highway speed at 80,000 GVWR.

Procurement of the liquid cooling cold plate and fabricating the new liquid cooled battery boxes have been completed followed completed installation. Motor mount bracket, traction motor and power electronics have been integrated in the second fuel cell truck.

**Second Quarter 2019:** US Hybrid completed the high voltage and low voltage wire harness integration, completed the battery integration (A123, NMC modules, with liquid cooling) in the vehicle, as well as completed the integration of power electronics (drive and auxiliaries) in the truck.

The vehicle integration was completed, US Hybrid delivered Truck #2 to TTSI on May 29, 2019 and this truck is in service at TTSI. US Hybrid continues operation support for both trucks.

**Third Quarter 2019:** US Hybrid has completed upgrading and installing liquid cooling system for the first fuel cell truck. The truck has been delivered to TTSI and back to service. Daily operation mileage is up to 50miles and hydrogen consumption is 7kg/day average.

After being deployed in May 2019, Truck #2 experienced an issue with its hydrogen valves and had to return to our facility in Torrance. US Hybrid is currently waiting for the GFI incoming shipment in order to repair the hydrogen valves and redeploy the vehicle. Due to delay of replacement part delivery, US Hybrid is looking at removing valves from tanks from other developed vehicle (bus/shuttle bus) to replace failed part with it as a back-up solution.

#### ***CTE/BAE and Kenworth Fuel Cell Truck***

**Fourth Quarter 2018:** Kenworth continued conducting track testing, road trials, and system tuning during this reporting period. Initial vehicle data packets have been created and reviewed by NREL. Extended range testing is underway, and testing indicates that the vehicle meets or exceeds all contractually required performance. The emphasis of track testing is rapid mileage accumulation testing to accumulate as many miles as possible and under multiple loads, full range of vehicle speeds and varying operational characteristics that replicate real world applications. The vehicle, to date, has accumulated more than 15,000 miles of track testing and some operations on the open road. The chassis continues to accumulate test track miles but also continues to fault out before hitting minimum reliability targets.

The transmission speed sensor caused multiple propulsion system faults. The causes of the failures varied, but hardware and software fixes have been implemented. These same changes were made to another Kenworth hybrid truck which subsequently showed improved reliability.

**First Quarter 2019:** Kenworth completed track testing, road trials, and system tuning during the reporting period and assigned the VIN. The vehicle was shipped on February 1st, 2019 and delivered to the operator, TTSI, at the Port of LA on February 4th, 2019. Kenworth submitted vehicle performance parameters that were measured during the test and validation phase. Software updates were implemented into the vehicle which are aimed to mitigate faults during transmission shifting. These updates were validated on the test track at the Kenworth R&D center. During this validation phase, Ballard discovered that the fuel cell power output was derated from 85kW to 55-70kW. Ballard technicians were on-site at the Kenworth dealership in Carson, CA to complete diagnostics in February, and root cause determination is ongoing.

The project team finalized planning for pre-demonstration activities such as training for the vehicle operators, maintenance teams, and local First Responders. Kenworth conducted training for TTSI operators and maintenance staff as well as local First Responders. Internal maintenance and safety training were also conducted at the Kenworth dealership in Carson, CA.

During routine inspection, a TTSI maintenance staff member mistakenly put diesel coolant into the fuel cell coolant reservoir. Ballard was on-site to flush the coolant lines and fill them with appropriate coolant. Ballard was on-site at the Kenworth dealership to conduct fuel cell diagnostics and repair activity related to de-rated fuel cell power. Ballard performed a dry out and leak test of the fuel cell and then conducted stationary testing with no issues.

**Second Quarter 2019:** The vehicle made several commercial runs for TTSI but experienced minor issues: oil leaks, fluid leaks, an inability to refuel with hydrogen, and HV and LV fuse failures. All these issues have been resolved. BAE and Ballard discovered that current draw was higher than what was allowable by the fuel cell. This occurred during the end of the previous reporting period and caused the fuel cell to shut down outside of demonstration service. The primary focus for the April and May reporting periods was investigating root cause, developing and testing a solution, and implementing that into the vehicle propulsion system software. This effort was conducted in close collaboration with the full project team and was resolved.

Transmission controls issue which has the vehicle locked between gears and reporting an impossible gear condition occurred in late June. BAE and EATON (transmission supplier) were notified of the issue and are actively attempting to find the root cause and develop a fix. In total, the vehicle has been driven 196 miles in service with TTSI.

**Third Quarter 2019:** Early in this reporting period, the truck experienced failures in the transmission system resulting in missed shifts and faulty operation. Kenworth returned the vehicle to their facility in Renton, WA for further investigation. The original set screw was determined to be inappropriate for this application, and a more robust set screw was procured and tapered as a preventative measure. The motor was replaced with an upgraded motor that ensures stability against issues observed in the HECT truck which has experienced failures related to the connection of the motor shaft and rotor. This motor upgrade is a proactive step to ensure better vehicle reliability during demonstration. While preparing to bring the truck back into service, the hybrid drive system was brought online, but the vehicle was power de-rated with fuel cell output at approximately 45 kW. The vehicle is still capable of starting and stopping on its own. TTSI will operate the vehicle in limited service during the next reporting period, and the Project Team will continue working toward issue resolution.

#### ***GTI/BAE and Kenworth CNG Hybrid Truck***

**Fourth Quarter 2018:** The truck completed approximately 12 hours of local Rapid Mile Accumulation (RMA) testing with overall positive results. Although drivers reported solid operation, there was an incident with a failed shift that did not require the truck to be shut down, but did require the driver to stop, switch to neutral, then back to drive before continuing. This minor incident is a known issue that will not cause a slowdown in the final testing. HECT continues to operate as designed and is performing as predicted. The truck will be released to the Kenworth PTC in Renton for final range tests and for a thermal evaluation test. Overall, Chassis 176832 has completed almost 2,000 miles of track and road testing to date. Local runs are pulling a loaded trailer yielding a GVW: 66-68k lbs. The team is focused on completing documentation of vehicle build as final phase of chassis commissioning. Project goal is to complete the remaining RMA testing in January.

**First Quarter 2019:** During the RMA (Rapid Mileage Accumulation) testing in January the vehicle suffered a failure of one of the BDUs (Battery Disconnect Units). The failure was caused by a loose cable terminal and required replacement of the BDU. The troubleshooting and repair process required moving the truck to a facility with appropriate staff and equipment to handle the high-voltage components of the vehicle. The troubleshooting and repair process revealed several secondary component failures resulting from the loose cable connector and required extensive time and resources.

The problems are related to the failure of components stemming from a loose HV cable connection in one of two BDUs. This failure mode required a replacement of both BDU's, a number of fuses, and HV cables. The team is investigating the root cause and developing corrective measures moving forward.

**Second Quarter 2019:** Following the string of failures and downtime encountered in Jan through March, and after the replacement of both BDU units, PIM fuse, and software upgrades, the team managed to address the issues and return the truck to operation.

In early May, HECT was driven approximately 60 miles, at which time the transmission failed to shift from second to third gear. The motor was removed from the chassis and replaced with a Gen2 motor, which has the shaft attached via heat-shrink vs bolted in place. HECT was driven locally, which resulted in no missed shifts and no resolver movement. On 5/29, HECT was driven to PTC, without issue.

In early June, during testing at PTC two issues were found: 1) transmission failed to change gear, which was deemed as a corner case and observed in production vehicles as well; 2) the power steering failed due to the controller dropping off, and is now mitigated by a software update.

On June 28, during the grade test, it was found that the CNG engine continues to run at full output even at a complete stop, regardless of SOC. BAE team has assigned their experts to investigate the root cause and provide a fix as soon as possible.

The reliability testing was a positive addition to the commissioning process as it has identified multiple issues that would have been difficult to resolve and would have pulled the chassis from revenue service. The delivery of the truck to TTSI has been delayed due to the issues described above.

**Third Quarter 2019:** The vehicle has been retrofitted with updated exhaust components and performed range test, which was determined to meet the project objective.

The software was updated in early August to fix the CNG controls and regenerative braking issue. After the update, the truck was driven on a circuit in Renton to verify the software. The software update overall works as anticipated.

Based on the lesson learned from the Fuel-Cell ZECT2 truck transmission failure, the HECT transmission was removed in order to upgrade it for robustness. The transmission upgrade was completed mid-September and upon the return to testing, the vehicle reported a ground fault. The repair was confirmed through a fault-free test drive and truck was prepared for off-campus testing with load prior to shipment.

PACCAR and CalStart have developed a data exchange mechanism via a secure online storage and CalStart began analyzing the data from captive tests performed by PACCAR.

R&D was still able to perform a range test where the truck was driven over Snoqualmie pass to Easton and returned to Renton. The truck traveled 155 miles with 80,000lb load, surpassing the required 150 mile range. At the end of the test, the CNG tank still had approximately 25% fuel remaining.

### ***Hydrogenics***

**Fourth Quarter 2018:** Hydrogenics accomplishments for the identical truck funded by CEC include the following:

- Fuel Cell System & Cradle:

Celerity system was reinstalled in truck with successful fit check of all components with hood closed, including final air intake and filter mounting to Celerity and external hydrogen sensors mounted on top of Celerity.



- Battery System:
  - i.) Extension harnesses and coolant hoses between components mounted on the truck and components mounted off truck were built to allow complete system checks and tests before the Siemens cradle and battery packs are installed on the truck. The battery pack mounting process takes place after installation and mounting of the Siemens cradle in the truck during the assembly process.
  - ii.) The battery packs are mounted on the truck, and connected electrically to the EVCU and Siemens cradle along with the coolant plumbing lines.
  - iii.) ACTIA sent engineer to Hydrogenics Mississauga to perform post-delivery power on check of the battery pack communications and proved out all systems checked out ok.

ACTIA will continue support integration of battery packs and chiller into the vehicle as needed.
- Electric Drive:
  - i.) Buildup of Siemens cradle with installation of major components complete. Mechanical plumbing and electrical wiring and routing of Siemens cradle complete.
  - ii.) Siemens cradle installation on the truck complete.
  - iii.) Hydrogenics and Siemens continue with regular review meetings to review all aspects of the project. System and sub system test plan has been revised for the entire project including drive cycle testing. Overall systems testing continued with Siemens support with weekly remote sessions.

***First Quarter 2019:*** The ZECT II Truck project design review work scope has commenced in tandem with documentation of as-built detail for the CEC truck, already identified optimizations to improve performance of the DOE truck. Ordering of long lead items for ZECT II truck has commenced. Hydrogenics has hired one US based controls/electrical engineer and one field support engineer to support this project, and is underway to hire two more engineers to support this ZECT II truck project in our California facility.

Hydrogenics team met with NREL on Tuesday January 22, 2019 to discuss and review data collection plan for ZECT II truck. Data collection design plan commenced.

Build of CEC vehicle is completed as of January 2019 with all major subsystems installed, and final electrical and communication connections completed. Commissioning completed in February.

***Second Quarter 2019:*** Ordering of long lead items for ZECT II truck has commenced with preparation of purchase orders and is expected to complete early Q3 2019. Design optimizations and build drawing package for ZECT II truck in process. Reviewed and streamlined the Base Truck specification including listing items to add and remove with specific part numbers. All long lead items expected to arrive by October 30, 2019.

As at end of this reporting period, Hydrogenics has already hired one US based controls/electrical engineer and one field support engineer, and one mechanical engineer expected to join in the next reporting period to support this project. Currently underway to hire one more electrical engineer to join our California facility to support this ZECT II truck project.

During this reporting period, CEC truck was in preparation to be delivered to Carlsbad office and for demonstration. Test drive validation started in last reporting period was substantially complete. As of the date of this report submission, CEC Truck has arrived at Hydrogenics Carlsbad facility on July 22, 2019.

**Third Quarter 2019:** All long lead items expected to arrive by October 30, 2019.

Hydrogenics is underway to hire one more electrical engineer to join our California facility to support this ZECT II truck project meeting the US labor requirement of DOE.

Hydrogenics has qualified several local machine and fabrication shops for the fabrication of metal subassembly structure components. Evaluation and qualification process involved development of requirements and score criteria matrix, vendor research, interviews/phone consultations to understand specialty, capabilities such as CNC machining, milling, punch/laser cutting, sheet metal forming, polishing/deburring, powder coating and other finishes, sheet metal fabrications to name a few. Engagement of top suppliers currently underway.

Data collection plan in process with data logging and data processing scripts in development for data collection plan. The CEC base truck is currently in process of plating and registration for demonstration, requiring several trips to the California DMV offices and preparation of registration fees and highway use tax fees. Demonstration of CEC base truck scheduled to commence Q4 2019.

### III.3 Medium-Duty Urban Range Extended Connected Powertrain (MURECP), (Robert Bosch LLC)

#### **Matt Thorington, Principal Investigator**

38000 Hills Tech Drive  
Farmington Hills, MI 48331  
E-mail: [Matt.Thorington@us.bosch.com](mailto:Matt.Thorington@us.bosch.com)

#### **Lee Slezak, DOE Program Manager**

U.S. Department of Energy  
E-mail: [Lee.Slezak@ee.doe.gov](mailto:Lee.Slezak@ee.doe.gov)

Start Date: August 16, 2016	End Date: June 30, 2020	
Original Project Cost: \$6,716,791	DOE share: \$4,318,834	Non-DOE share: \$2,682,138

#### **Project Introduction**

The purpose of this project is to develop and demonstrate a commercially viable PHEV powertrain for MD vehicles that reduces fuel consumption by 50% on a real-world drive cycle by utilizing an advanced dual-planetary gear transmission with multiple clutches, coupled with cost-optimized electric machines. Such an improved powertrain efficiency will translate to a reduced fuel consumption of approximately 26 million diesel gallons per year, based on an average use of 22,000 miles per year at 8.3 mpg and a 30% market penetration for Class 4 delivery trucks.

The proposed design approach optimizes the usage of all powertrain components, particularly the internal combustion engine [ICE], the electric powertrain, and the battery pack to result in an incremental price and economic payback required for widespread commercial fleets' purchase without requiring financial incentives. Future developments are planned to explore the suitability of the MURECP powertrain for Class 2b – 8a delivery trucks.

#### **Objectives**

Key objectives:

- Dual Planetary Gear Transmission with multiple clutches, enabling the use of cost-optimized electric motors (PC/LD separated motor generators, high speed/ power dense design).
- Development of a multi-mode control strategy that ensures system optimal efficiency under a wide range of operating conditions, especially with the flexibility of powersplit operation.
- Efficient downsizing of the ICE for further reductions in fuel consumption.
- Electronic Horizon forward-looking input to HEV and EV driving modes, maximizing real-world fuel consumption reduction.
- Provide a >35 mile all-electric range, achievable with existing battery packs on the CSHVC cycle.

#### **Approach**

The project will be conducted in 3 budget periods:

Budget Period 1 (Aug '16 – Nov '17): Powertrain Development: Hybrid-electric vehicle topologies will be investigated through simulation and evaluation of each configuration on a real-world drive cycle to define the technical requirements and most promising architecture for the powertrain system.

Budget Period 2 (Dec '17 – Oct '19): Powertrain Integration: The supervisory control algorithms, battery management system, thermal energy management, and vehicle control strategy will be integrated with the conventional powertrain controller and further refined. The mechanical design and assembly of the hybrid drive system will also be completed along with the manufacturing of the prototype transmission. All PHEV solution components and a downsized diesel engine will be integrated onto the prototype vehicle.

Budget Period 3 (Oct '19 – Jun '20): Powertrain Demonstration: The prototype vehicle will be tested and deployed, including chassis dynamometer testing and demonstrations on closed courses to quantify the achievable benefits and help finalize the control algorithms.

## Results

### Task 6 – Validate Supervisory Control Algorithms

Simulation results will be updated for the final design throughout the project, as we continue to refine the models or the control strategy. Updated comparisons for powertrain dyno results against GT-SUITE simulations during City Suburban Heavy Vehicle Cycle (CSHVC) show very good alignment (Figure III.3.1) following the implementation of a closed-loop pedal control in the dyno with improved PID settings in the test cell to better match dynamic content. Both consumption and regenerative (negative) energy follow simulation results. Initial MATLAB fuel consumption simulations between Rule-based control and Equivalent Consumption Minimization Strategy (ECMS) showed favorable results with ECMS for both charge sustaining and for linear SOC ramp decline conditions. Further investigations are postponed because of other higher prioritized project tasks.

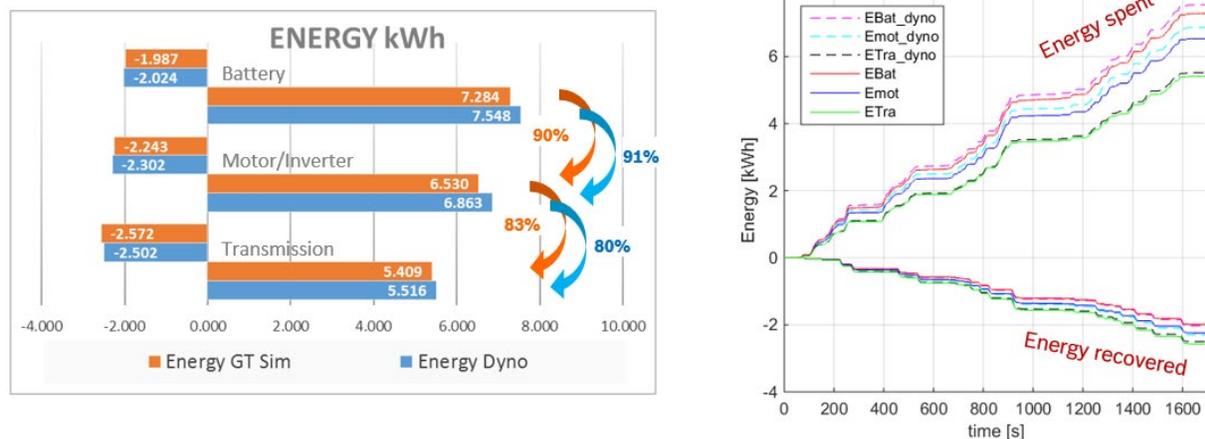


Figure III.3.1 Mutual verification of simulation and powertrain dyno measurements

### Subtask 7.1 – Develop Power Prediction Algorithm

This item has been rescoped. Multi-pack coordinator software will evaluate current state of each pack (SOC, voltage, current limits, temperature, cell balancing, etc.) and provide the battery ‘system’ state to the VCU.

### Subtask 7.2 – Develop Charging Algorithm

Item is no longer required, as production packs without fast charging capabilities will be used.

### Task 8 – Hybrid Drive System Design

Powertrain layout, assembly and installation on chassis of completed. A dual 24V power pack system installed to support electro-hydraulic power steering and braking with the ICE off. Thermal management system layout defined. Detailed 1D thermal system model in GT-suite constructed with results showing that thermal system strategy is able to control battery pack and power electronic temperatures within the target limits (35° and 65°C respectively) for the three steady-state operating points considered. VOSS integrated the majority of the thermal system into a “Fluids Box” including new thermally controlled valves that will ease integration onto the chassis. The fluids box layout was consolidated, reducing the space consumed by approximately ½ as shown in Figure III.3.2. VOSS fluids box was installed onto the chassis and electrically connected. Electrical/Electronic Architecture system designs have been frozen. The EE Architecture layout is finalized. HVIL (high voltage interlock) system integrated into a redesigned 12V/24V Power Distribution Unit. Through the redesign, three separate boxes were combined into one housing all the low voltage fuses and relays added for the system as shown in Figure III.3.3. All 12V/24V systems communications check including the thermal system components were completed. System design component layouts for both thermal system and HVIL were completed.

### Redesign of FLUIDS BOX Layout

- ▶ 1- BRUSA 24V/HV DC/DC Converter
  - ▶ 1A: Inlet from 4A-MECP Y1
  - ▶ 1B: Outlet to QC1 (To inverter1)
- ▶ 2- BRUSA 24V/HV DC/DC Converter
  - ▶ 2A: Inlet from 4A-MECP Y1
  - ▶ 2B: Outlet to QC2 (To inverter2)
- ▶ 3- VOSS Thermo-Mech. Cl. Valve
  - ▶ 3A: From QC7 (Low-Temp Radiator)
  - ▶ 3B: From QC8 (From LTR Bypass)
  - ▶ 3C: To 4B- MECP Inlet
  - ▶ 3D: To 5B- TBCP Inlet
  - ▶ 3E: From 6B- CHSWV
  - ▶ 3F: Outlet to QC6 (to engine, bleed port)
- ▶ 4- Motor Electric Coolant Pump
  - ▶ 4A: Outlet to Y1 (DC/DC converter inlets)
  - ▶ 4B: Inlet from 3C (TMCV)
- ▶ 5- Traction Battery (Electric) Coolant Pump
  - ▶ 5A: Outlet to 7-T\_B inlet (Battery Temp Sensor)
  - ▶ 5B: Inlet from 3D-TMCV
- ▶ 6- Chiller Switch-over Valve
  - ▶ 6A: Inlet from QC4
  - ▶ 6B: Outlet to 3E-TMCV
  - ▶ 6C: Outlet to QC5 (Chiller inlet)
- ▶ 7- Battery Temperature Sensor (Inlet)
  - ▶ 7A: Inlet from 5A-TBCP
  - ▶ 7B: Outlet to QC3 (to battery inlet)
- ▶ 8- Engine Waste-heat Shut-Off Valve
  - ▶ 8A: Inlet from QC9 (from engine)
  - ▶ 8B: Outlet to Y2\_4B-MECP (pump inlet)

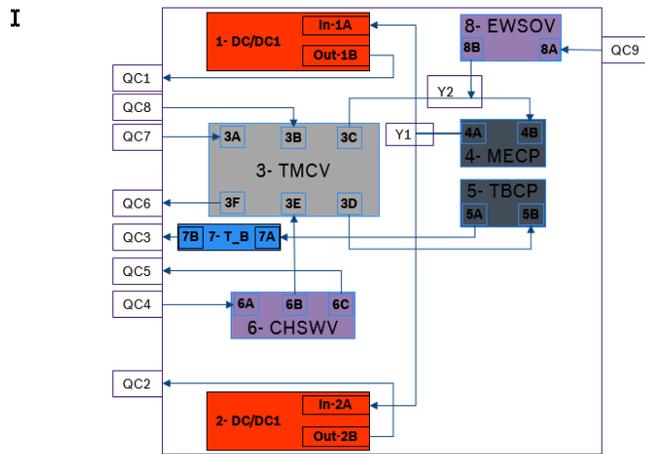


Figure III.3.2 Fluids box redesign to improve space utilization, ease assembly on truck chassis

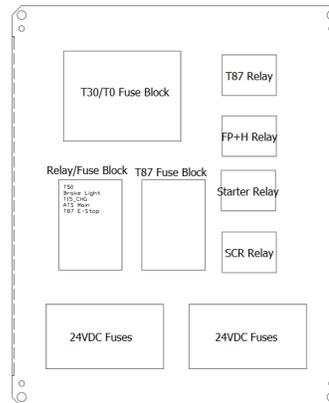


Figure III.3.3 Consolidation of separate 12V 24V and HVIL fuse relay boxes into one

### ***Task 9 – Electronic Horizon Controls Integration***

This task represents the development of a control strategy that uses real-time data based on vehicle location and environmental variables. The system will use the Advanced Driver Assistant System Interface Specification (version 2) in order to assist the control strategy with making determinations for the desired mode of the hybrid drive system, the limits it should operate within before triggering a mode transition due to driver input, and setting trajectories for state of charge based on the route.

#### ***Subtask 9.1 – Input Study***

At the start of the project, an electronic horizon provider device was acquired that can provide map based data per the ADASIS V2.0 specification. The vehicle control unit can use this information to create a ‘horizon’ based view of the coming road characteristics that may affect the control of the vehicle. During our software development we implemented the electronic horizon ‘reconstructor’, an algorithm that takes the ADASIS messages and merges the information into a format that the supervisory and powertrain control algorithms can use to ‘look ahead’ and make better determinations in terms of the desired mode or trajectory of the state of charge. We can collect electronic horizon data from the vehicle when it is ready. This data can be used for future predictive control simulation studies.

#### ***Subtask 9.2 – Electronic Horizon Controls Integration Interface/Interaction***

The interaction of the electronic horizon system with the supervisory control is an open topic that will require further development. Considering the higher priority of other tasks (vehicle buildup, mode switch investigation), it is rather unlikely that the full predictive control algorithm will be implemented in the vehicle.

### ***Task 10 – Powertrain and Aftertreatment System Development***

The ICE will be downsized to target peak efficiency operation. The hybrid powertrain will also be utilized to shift the load point of the engine, targeting lower fuel consumption. Initial focus is set on fuel efficiency. A production ATS will be introduced making only basic modifications to ensure functionality in the application. Optimization will not be pursued.

#### ***Subtask 10.1 – Downsized Engine Calibration***

The torque path in the engine controller software will be updated and calibrated with a hybrid specific torque structure for the MD delivery truck application utilizing a baseline from the light-duty passenger car segment.

Move completion of this subtask to BP3 due to availability of calibration time on the demo vehicle, however, due to the production calibration of the engine, only minor modifications are expected.

#### ***Subtask 10.2 – Aftertreatment System Verification***

Basic diesel particulate filter regeneration calibration investigation will be performed to enable vehicle driving. A production ATS will be introduced making only basic modifications to ensure functionality in the application. Optimization will not be pursued.

Move completion of this subtask to BP3 due to availability of calibration time on the demo vehicle, however, due to the production calibration of the aftertreatment system, only minor modifications are expected to provide functional results.

#### ***Subtask 10.3 – VCU & ECU Software Implementation***

Hybrid torque structure will be implemented into the VCU/ECU to enable power-split driving operation.

The ECU torque structure has been updated to work within the hybrid environment. ICE and electric machine torque requests are now being coordinated by the VCU via CAN. This communication has been established and tested on the engine dyno. Successful mode switch testing of all operating modes were completed on the powertrain dyno, including Powersplit with hybrid start (Figure III.3.5 and Figure III.3.6). Improvements during mode switch transitions while driver demand varies incorporated into the software by updating the

component driving command during clutch engagement. Further, the mode switch torque behavior transient was smoothed as well. On-board charger module integration and power steering integration completed.

**Subtask 10.4 – Integrated Powertrain Calibration Optimization**

Powertrain calibration on the engine dynamometer will be performed, enabling additional fuel consumption reduction when integrating the downsized engine with the 2PG transmission. ICE shifting strategies identified in task 2 above will be validated with measurements.

Based upon initial powertrain transient measurements performed on the engine dyno, updated spin loss calculations were completed with the results shown in Figure III.3.4. The revised calculations indicate that while there is no impact at low vehicle speeds (drive-off and curb climb), high-speed EV output torques are reduced while vehicle drag is increased. This results in a maximum 2MEV speed of 111 kph and a 1MEV speed of 87 kph. EV-only range is also reduced by approximately 7 miles.

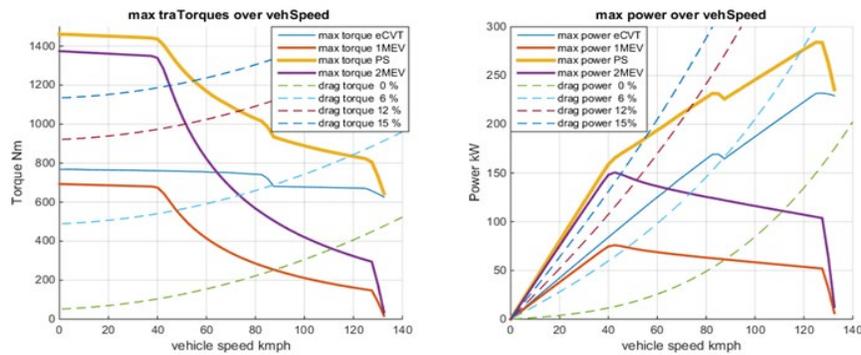


Figure III.3.4 Performance vs. Speed simulation results in different modes including transmission spin losses

PHEV transmission clutch calibration completed on the engine dyno. One motor and two motor EV mode along with Powersplit mode testing and calibration ongoing. Mode switch was validated transitioning from 1MEV to 2MEV and back. Current status provides output shaft speed variation of 1% and an output torque variation of 5% during a mode switch and is most likely negligible in terms of drivability and comfort. Switch timing from 1MEV to 2MEV is 3.5 sec while switching back is 1.5 sec. Target of 1.5 sec switch time will be achieved by further optimizing the speed sync PID control, the clutch control (e.g., kiss-point control in preparation of an actuation), and the torque handover. Other mode switches, 1MEV to Powersplit and back and 2MEV to Powersplit and back have also been tested successfully on the engine dyno.



Figure III.3.5 1MEV to Powersplit Transient including Hybrid Start

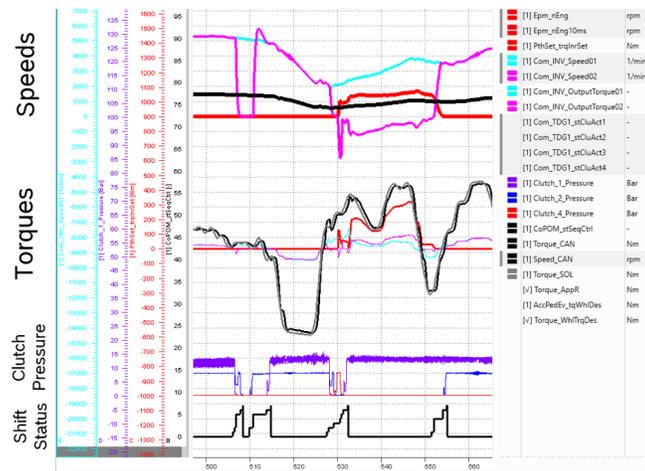


Figure III.3.6 1MEV to Powersplit Transient including Hybrid Start

### Subtask 11.2 – Sub-System Integration

The downsized engine and hybrid transmission tested on engine dyno during 4Q 2018 installed on truck chassis. Exhaust system and new transmission drive shaft installed on chassis. Electric power steering pumps installed with cooling circuit included. Completed low voltage wire harness routing and termination at the 12V/24V Power Distribution Unit, wire harness functional verification and CAN communication checks with the vehicle's controllers (VCU, ECU, TDG1, inverters), fluids box mounting, electrical and hydraulic line termination. The truck body was reattached to the chassis, the DEF tank and fuel tanks were reinstalled to the chassis. The high voltage battery packs, multi-pack coordinator and on-board charger were installed in the cargo area (will be covered by a false floor in the future). The thermal system was filled, commissioned, and initially calibrated for basic testing in the chassis dyno. The electric fans are set to operate at 85% of capacity while the electric motor and high voltage battery cooling pumps operate at 95% capacity. Full thermal system calibration for improved efficiency operation will take place during BP3.

### Conclusions

The integration phase of the PHEV powertrain continued throughout the year. A dual 24V power pack was installed for electro-hydraulic power steering and braking while the ICE is not running. Thermal management is accomplished using an integrated fluids box from VOSS including new thermally controlled valves. Fluids box installed on the chassis, filled and commissioned for initial chassis dyno testing. E/E Architecture was frozen and the 12V 24V and HVIL (High Voltage InterLock) systems were integrated into a single Power Distribution Unit for convenient access and space considerations. In parallel, engine dyno test results with a downsized diesel engine assembled to a hybrid transmission successfully demonstrated mode switches between one and two motor EV as well as Powersplit during transient cycles.

### Key Publications

1. Thorington, Matt, U.S. Department of Energy Vehicle Technologies Office 2019 Annual Merit Review and Peer Evaluation Meeting, June 12, 2019, Arlington, VA. Project ID-elt190, MURECP: Medium-duty Urban Range Extended Connected Powertrain
2. Thorington, Matt, CTI Symposium, May 16, 2019, Novi, MI. Hybrid Powersplit Transmission For Commercial Vehicles: Design, integration, and demonstration of an innovative transmission, enabling >50% fuel consumption reduction
3. Thorington, Matt, Electric & Hybrid Vehicle Technology Expo 2019, September 11, 2019, Novi, MI. Hybrid Powersplit Transmission For Commercial Vehicles: Design, integration, and demonstration of an innovative transmission, enabling >50% fuel consumption reduction



### III.4 Medium Duty Vehicle Powertrain Electrification and Demonstration (McLaren Engineering)

#### Mr. Wiley McCoy, Principal Investigator

McLaren Engineering division of Linamar  
32233 W Eight Mile Road  
Livonia, MI 48152  
E-mail: [Wiley.Mccoy@Linamar.com](mailto:Wiley.Mccoy@Linamar.com)

#### Lee Slezak, DOE Program Manager

U.S. Department of Energy  
E-mail: [lee.slezak@ee.doe.gov](mailto:lee.slezak@ee.doe.gov)

Start Date: June 1, 2016

End Date: March 30, 2021

Awarded Project Cost: \$3,650,000

DOE share: \$2,640,000

Non-DOE share: \$2,559,000

#### Project Introduction

This project is intended to address a number of technical barriers regarding use of electric / hybrid drive systems in the medium duty marketplace as described in the Vehicle Technologies Multi-Year Program Plan. Specifically, the technical barriers are:

- Acceptance of electric drive as Medium Duty vehicle choice.
- Reduce the carbon footprint of transportation (FE Improvement)
- Cost of hybridization (medium duty TCO)

A team consisting of industry leading engineering, production and user companies was formed to specify, design, build and test a commercially viable medium duty drive system that would reduce fossil fuel use by a minimum of 50% in real world drive cycles. McLaren Linamar, AVL, & UPS were partnered to achieve the program objectives.

#### Objectives

Project Objective / Expected Outcome – to attain a 100% improvement in Fuel Economy over real world drive cycles for medium duty package delivery vehicles & achieve a system at project conclusion that can be commercialized at a reasonable Total Cost of Ownership.

#### Approach

Project Approach – Team has developed the hybrid system specifications in simulation and completed the first milestone by showing a 100% fuel economy improvement over real world drive cycles measured over UPS delivery routes. This completed the first phase of the program. The second phase, which is still in progress, is to design and develop a plug-in hybrid powertrain, incorporating a novel medium duty electric drive axle. The team is in the process of building and commissioning 4 demonstration vehicles and will conduct a demonstration of performance, cost and reliability for a period of up to 12 months.

Future work will include a third phase of system demonstration. This demonstration will commence in the 2020 CY. At present, the team is in the process of final build and commissioning of the demonstration vehicles. McLaren / Linamar is responsible for design and build of the eAxle; AVL has simulated the system & design, built and installed in one vehicle the energy storage and range extender systems. McLaren contracted N-Fab to take over the final build and commissioning responsibilities to complete the vehicles for

the demonstration. UPS will conduct the demonstration on real world package delivery routes and transmit data back to the McLaren team for ongoing analysis of performance, durability and reliability. This project is intended to support commercialization of the system. An analysis of the system cost and complexity, as well as a calculation of total cost of ownership will also be completed with the support of UPS. At the end of or during the demonstration phase a decision will be made regarding commercialization of the systems on a broader group of package delivery vehicles.

## Results

In the 2019 FY, the entire time was used to progress the build of initial units, test both sub-systems and the full eAxle system and complete the physical build of vehicles for calibration work. The 4 units are in various states of completion.

Large challenges arose during this FY. The first major challenge was that testing of the subsystems revealed the need for updates to create a reliable and durable system for the demonstration. It was agreed by all stakeholders that delays should be minimized but not at the expense of achieving a highly reliable product. At the end of FY19, a fully commissioned and reliable eAxle system had not been achieved. It has become apparent that the system design technology has been succeeded by more efficient and less complex ones due to component technology improvements. It is now being contemplated that a change to a more technically advanced eAxle system that is being developed for another demonstration program may be the preferred hardware choice. As FY20 begins discussions with DoE Program Office and the demonstration stakeholder are in process. When a decision is agreed a new plan will be developed and enacted by McLaren.

The technical results achieved in this FY were to attempt to resolve all of the challenges in commissioning the eAxle system. Many challenges were overcome with component upgrades and some reconfiguration of the cooling system. The most significant challenge, to deliver vehicles that are reliable enough to complete the demonstration cycles with little or no issues, has yet to be achieved.

- Phase 3 Technical Milestones In Progress
  - The eAxles were upgraded and tested on McLaren Test rigs
  - The vehicle builds were progressed and are close to completion
  - Vehicle 1 & 2 powertrains were installed and tested for adequate reliability as per the requirements of the demonstration partner
  - Reliability issues remain unresolved and an alternative eAxle system is being proposed with upgraded technology.

Below are a series of photos showing the eAxle sub-systems in test conditions as well as vehicles in build and/or on routes to test function and/or reliability.



Figure III.4.1 Hybrid System vehicles in Build Shop

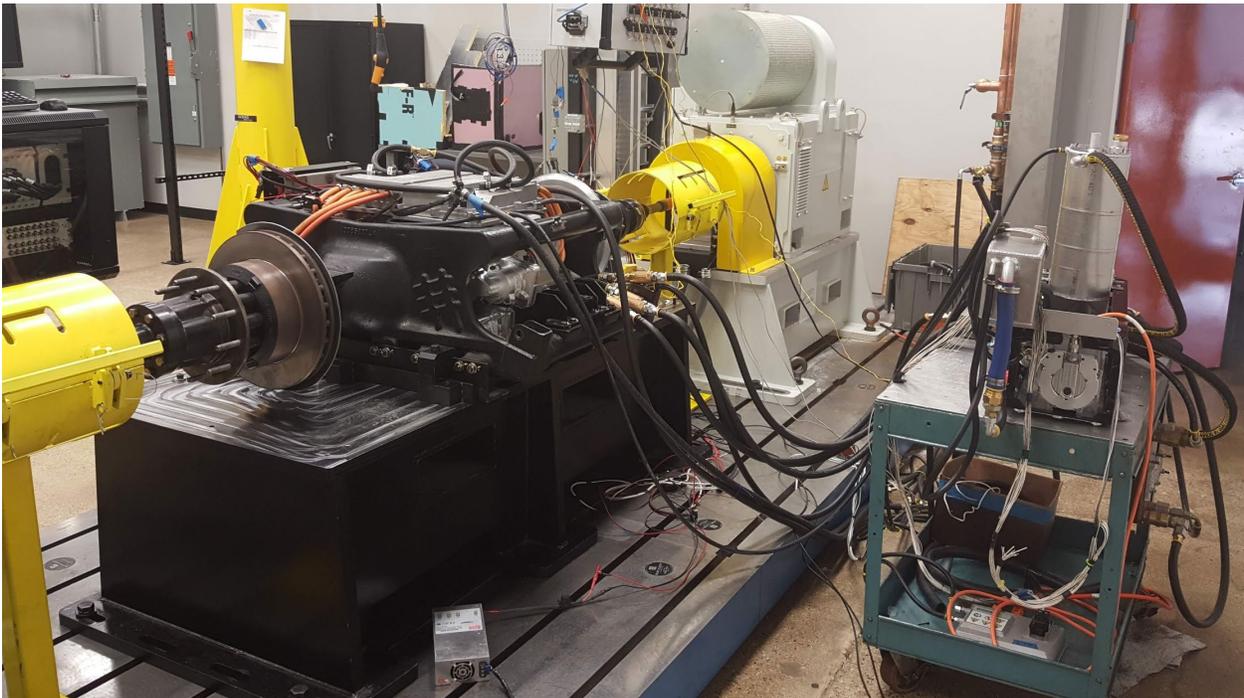


Figure III.4.2 Complete eAxle System on McLaren Test Rig



Figure III.4.3 1st Design Demonstrator On Real World Commissioning Drive



Figure III.4.4 Vehicle, Being Returned to Shop for Adjustments/Updates

## Conclusions

As of the end of FY19, the conclusions of this program to date are:

1. A system can be designed and built using advanced modeling and simulation tools that will demonstrate an electrified vehicle powertrain system that will achieve the overall program objectives.
2. A novel eAxle system, energy storage & range extender systems have been built and tested for installation and final calibration in 4 demonstration vehicles. There have been continued challenges to achieve the desired reliability for demonstration routes. The current system with the 2-speed transmission feature will continue to be developed.
3. The development of a real world package delivery system has taken more time than originally anticipated primarily due to subsystem development issues. The demonstration can commence in Q2 of CY 2020 after decision has been taken to replace the eAxle system with a more advanced, lower complexity design.
4. Commercial interest continues to be confirmed.
5. The results of the demonstration will determine the magnitude of full volume production that could be attained through by providing data for an accurate TCO. (Total Cost of Ownership)

### III.5 Wireless Extreme Fast Charging for Electric Trucks

#### Michael Masqueller, Principal Investigator

WAVE  
4752 W California Avenue, Suite B400  
Salt Lake City, UT 84104  
E-mail: [michael@waveipt.com](mailto:michael@waveipt.com)

#### Steven Boyd, DOE Program Manager

U.S. Department of Energy  
E-mail: [Steven.Boyd@ee.doe.gov](mailto:Steven.Boyd@ee.doe.gov)

Start Date: August 1, 2018	End Date: October 31, 2021	
Project Funding (FY19): \$643,243	DOE share: \$246,240	Non-DOE share: \$397,002

#### Project Introduction

The purpose of the wireless extreme fast charging (WXFC) truck project is to significantly accelerate electrification of heavy-duty trucks, starting with shipping ports and expanding to regional delivery operations across the US. Charging time and range anxiety are major barriers to electric vehicle adoption, particularly for truck applications. Therefore, the major goal of this project is to demonstrate high efficiency, WXFC as applied to Class-8 trucks that have a typically higher gap and lower available space than, for example, transit buses.

#### Objectives

The objective of this project is to develop and integrate a new 500kW WXFC system developed by WAVE into a Class 8 electric drayage truck developed by Cummins so that it can automatically and wirelessly charge at a high charging rate (c-rate) during their dwell times. The proposed wireless charger features a direct connection to the Medium Voltage (MV) 3-phase grid developed by Utah State University and Schneider Electric and the final prototype will be deployed at Total Transportation Services Inc. (TTSI), which is a truck operator at the Port of Los Angeles (POLA).

#### Approach

WAVE has assembled a strong and diverse team to develop, deploy, and operate two all-electric Class-8 drayage trucks with WXFC at the Port of Los Angeles

(POLA). The WXFC truck project leverages active involvement of key partners on six major project tasks, as shown in Figure III.5.1. Project tasks include:

- Early deployment and evaluation of a 250 kW wireless fast charging system using a baseline truck provided by TTSI at POLA and state-of-the-art WAVE wireless charger
- New development of 500 kW wireless power transmitter and receiver modules
- New battery pack and Class 8 truck powertrain development to support high C-rate charging
- New development of an MV grid-tied converter to improve safety and simplify grid integration of WXFC stations
- WXFC grid and vehicle side system integration

- WXFC system deployment and evaluation at POLA.

WXFC for electric trucks is a WAVE-led project with assistant from the following partners:

- The Port of Los Angeles – Deployment partner
- Los Angeles Department of Water and Power – Deployment partner
- Total Transportation Services Inc. – Port trucks partner
- Cummins – Truck integration and electric drivetrain partner
- Utah State University – Research partner
- Schneider Electric – Electrical supplier, industrialization partner.

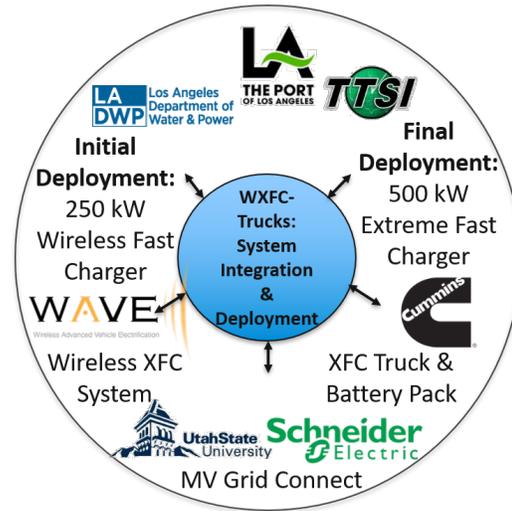


Figure III.5.1 WXFC project activities.

The general project approach for the MV AC-DC Converter, wireless charger, and the high c-rate Class 8 drayage truck development is outlined in Figure III.5.2.



Figure III.5.2 Project design and implementation approach.

The USU approach to the MV, grid connected, AC/DC supply is:

- 3-phase unloader with a soft DC bus two-level output
- Develop the 3-phase unloader to achieve direct MV grid connection with switches commutating at the line frequency
- Design the series stacked isolated DC/DC converters to achieve the voltage step down function from MV naturally with near unity conversion ratio to obtain high efficiency.

The WAVE approach to the 500kW wireless charger is:

- Deploy 250kW charger with initial truck integration to demonstrate appropriate charging gap and form factor
- Develop and simulate new magnetics design for the higher power density required at 500kW

- Leverage deployment experience with 250kW charger to feed into design updates of the 500kW charger.

The Cummins approach to the extreme fast charging capable electric truck is:

- Investigate appropriate battery chemistry (LTO cells or NMC cells)
- Design custom thermal management for the cell to facilitate charging at 3C
- Select appropriate battery pack capacity and cell chemistry to integrate with electric powertrain applicable to Class 8 drayage applications.

## Results

The project team has worked together to define the requirements for the MV AC/DC supply, wireless charger, and Class 8 truck to deliver a solution that meets the needs of TTSI. A block diagram for the system is shown in Figure III.5.3.

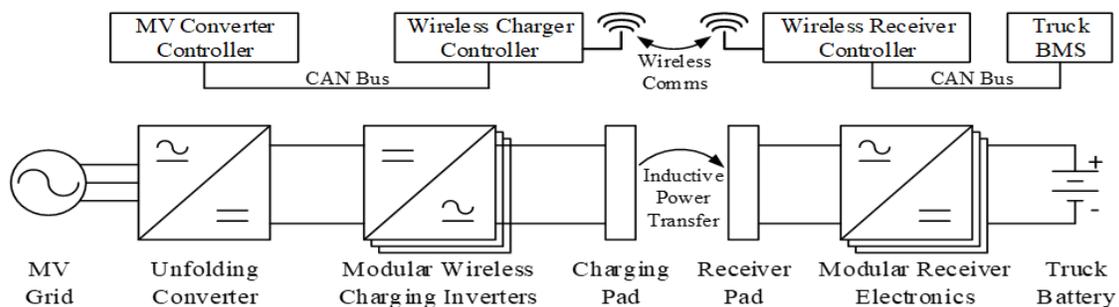


Figure III.5.3 System block diagram.

Key results from each project section are outlined below:

- 250kW Wireless Charger
  - Initiated contact with five class-8 truck vendors and enlisted TTSI to assist in the approval of a truck to be the recipient of the 250kW installation
  - Determined site for the 250kW charger and primary equipment location
- MV AC/DC Supply
  - Built 2kW triple active bridge series resonant converter (TABSRC) prototype
    - Tested up to 1.5kW output at 600V
  - Built 2kW unfolder prototype
    - Currently under open-loop testing
  - Selected and ordered power devices for full-power unfolder and full power TABSRC module
  - Assembled MV test area in the lab with 480V to 4.16kV step up transformer from Schneider
- 500kW Wireless Charger
  - Power requirements and communication interface with MV supply defined



- Rough space claim and location defined for vehicle side equipment
- Pad Design
  - New concepts developed for much higher power density compared to 250kW system
  - Magnetic simulation used to evaluate merits of multiple design options and iterate toward optimal solution
- Class 8 Electric Truck
  - Determined work day duty cycle that will meet TTSI operational needs
    - 45 mile range requirement
    - 5-6% grade on Vincent Thomas bridge
  - Selected Kenworth T680 Chassis
  - Battery selected to achieve useable energy and charge power requirements.

### Conclusions

It is important to consider the entire work day duty cycle based on customer requirements and to have a good understanding of port operations. Initial discussions indicated a 30-mile range requirement which did not account for 10-15 miles of trailer movement in addition to the typical drayage route. Based on this information the truck battery requirements were adjusted accordingly to provide a 45 mile range needed for TTSI operation.

This project is well positioned with the correct technical requirements to address the range anxiety and charging time restrictions, which are the key barriers to electric vehicle operation at the Port of Los Angeles. Designs that meet these requirements are well underway with prototype testing ongoing and some final solution parts on order.

### Key Publications

1. M. Masquelier, "Wireless Extreme Fast Charging for Electric Trucks." 2019 DOE VTO Annual Merit Review, Washington, DC, June 2019.

### III.6 Bidirectional Wireless Power Flow for Medium-Duty Vehicle-to-Grid Connectivity

#### **Steven Sokolsky, Principal Investigator**

CALSTART  
1509 Wendy Lane  
Madison, WI 53716  
E-mail: [ssokolsky@calstart.org](mailto:ssokolsky@calstart.org)

#### **Omer C. Onar, Principal Investigator**

Oak Ridge National Laboratory, Power Electronics and Electric Machinery Group  
National Transportation Research Center, 2360 Cherahala Boulevard  
Knoxville, TN 37932  
E-mail: [onaroc@ornl.gov](mailto:onaroc@ornl.gov)

#### **Lee Slezak, DOE Program Manager**

U.S. Department of Energy  
E-mail: [Lee.Slezak@ee.doe.gov](mailto:Lee.Slezak@ee.doe.gov)

Start Date: October 1, 2016  
Project Funding: \$2,631,321

End Date: September 30, 2020  
DOE share: \$1,949,007

Non-DOE share: \$712,314

#### **Project Introduction**

Wireless power transfer (WPT) is a paradigm shift in electric-vehicle (EV) charging that offers the consumer an autonomous, safe, and convenient option to conductive charging and its attendant need for cables. With WPT, charging process can be fully automated due to the vehicle and grid-side wireless communication systems, and is non-contacting and inherently isolated; therefore, issues with leakage currents, ground faults, and touch potentials do not exist. It also eliminates the need for touching the heavy, bulky, dirty cables and plugs. It eliminates the fear of forgetting to plug-in and running out of charge the following day and eliminates the tripping hazards in public parking lots and in highly populated areas such as shopping malls, warehouse loading areas, recreational areas, parking buildings, etc. Furthermore, the high-frequency (HF) magnetic fields employed in power transfer across a large air gap are focused and shielded, so that fringe fields (i.e., magnetic leakage/stray fields) attenuate rapidly over a transition region to levels well below limits set by international guidelines for the public zone. With the bidirectional wireless power transfer, not only vehicles can be wirelessly charged, but also the vehicles can wirelessly provide power back to the grid or the facility. With bidirectional power flow, vehicles can be enabled to provide microgrid or grid support or ancillary services. Grid support may include peak shaving, renewable energy firming/integration, time of use energy management, power quality improvement, voltage regulation, reactive power compensation, etc. Grid ancillary services to be provided might include spinning and non-spinning reserves, area/frequency regulation, load following, scheduling and dispatch, etc. if a number of vehicles are aggregated to provide such services. In the case of an outage, vehicle batteries can also serve as an emergency backup power for a period of time.

In this project, CALSTART, ORNL, UPS, Workhorse Group, and Cisco Systems proposed to model, research, analyze, design, develop, integrate, and demonstrate a bi-directional wireless power transfer system (BWPT) suitable for Class 5 and Class 6 medium-duty plug-in hybrid delivery trucks. The project team designs, develops, integrates, and tests a bi-directional wireless charging system capable of meeting the 11-inch ground clearance needed for UPS delivery trucks. After integrating to a Workhorse manufactured plug-in hybrid electric vehicle (PHEV), the system performance will be demonstrated at the deployment site. Within the first budget period of the project (May 2017-May 2018), team has completed the modeling, simulations, design, and analysis of the system power conversion stages including the 3-phase active front-end rectifier with power

factor correction (also grid interface inverter), primary-side HF inverter (also primary-side rectifier), primary and secondary-side resonant tuning components, primary and secondary-side electromagnetic coupling coils, vehicle-side HF rectifier (also the vehicle-side HF inverter). As of submission time of this report, hardware both the primary and secondary sides have been completed and the power conversions stages have been successfully tested. All of the subsystems and components have been validated based on their parameters and performance metrics. Now the team is starting the vehicle integrations and system will be deployed with full vehicle integrations for the testing, demonstrations, and data collection purposes.

## Objectives

The overall project objectives can be summarized as follows:

1. Provide an automated, high power, interoperable, high-efficiency wireless charging for a plug-in hybrid electric medium duty delivery truck with a nominal ground clearance of approximately 11 inches
2. Optimize the add-on vehicle-side wireless charging components through integration and utilization of already existing vehicle-side components while implementing grid-side controls and regulations to reduce the vehicle-side cost, size, volume, and complexity
3. Utilize bi-directional wireless charging systems when trucks are parked in the yard for staging to provide grid support applications or ancillary or grid support services such as frequency regulation, load leveling/peak shaving/load factor improvement/reactive power support/demand charge management, and spinning/non-spinning reserves
4. Provide an integrated > 20kW wireless charging system (grid to vehicle) with high efficiency (85%) while meeting the international guidelines on electromagnetic and electric field emissions during charging and include all other appropriate safety features
5. In vehicle-to-grid mode, achieve 6.6kW wireless power transfer to building or grid loads.

## Approach

Starting from the AC grid to the vehicle battery terminals, the system power converters must be well-designed and operated in order to achieve high efficiency. In addition, power flow control to the pick-up system should be resolved where the control parameters (DC link voltage, frequency, duty cycle, phase-shift, etc.) are actively controlled to improve efficiency while meeting the vehicle-side target voltage, current, and/or power. Simultaneously, vehicle-side DC link or battery voltage, current, temperature, and the state-of-charge (SOC) should be carefully monitored and fed-back to the primary side for controls. Moreover, the battery management system (BMS) or other vehicle-side functions (i.e., contactors and liquid cooling system) should be monitored for safety. The bidirectional wireless charging system that will be used in this project is shown in Figure III.6.1. This is the overall system architecture that is determined and agreed upon by the technical team. For this architecture, the baseline performance metrics have been defined, system specifications have been determined, and the hardware including the power stages and passive components have been designed and developed in ORNL PEEM laboratory. As shown in Figure III.6.1, system utilizes a three-phase rectifier/inverter system that interfaces the wireless charging system to the grid. During charging, the active-front end rectifier with power factor correction (PFC), delivers power from the grid with high power factor to the HF power inverter's input. The input (grid) current is controlled in order to regulate the inverter input voltage, depending on the amount of power to be transferred to the vehicle-side battery. The HF power inverter generates the HF current for the primary coupling coil. On both primary and secondary, LCC type resonant tuning configuration was utilized for operational symmetry since the bidirectional power flow is needed. Additionally, LCC type resonant tuning circuitry provides load and coupling factor independent constant current on primary coil which simplifies the communication requirements and the control systems. On the vehicle side, there is a receive coil with a rectifier/inverter, and a filter capacitor. During discharging or vehicle battery powering the AC grid/building loads, the vehicle-side converter is operated in an inverter mode and

delivers HF current to the vehicle coil. The vehicle-side coil generates a magnetic field that is linked to the ground coil. The ground coil induces a high frequency voltage that is rectified and inverted to 60Hz to power

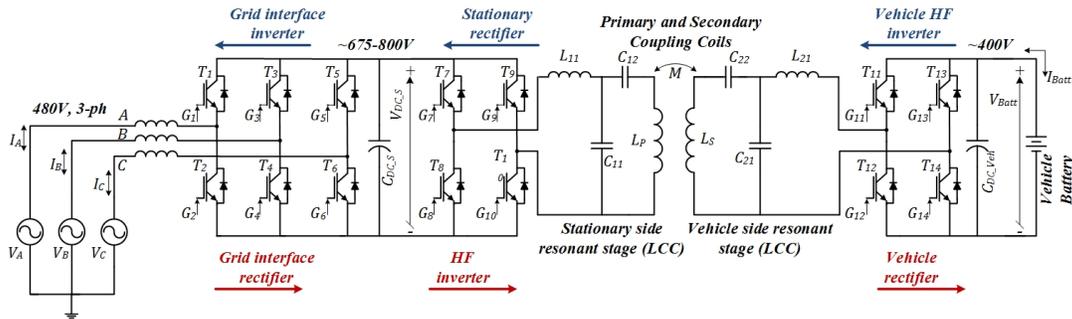


Figure III.6.1 System level diagram of the proposed architecture for the bidirectional wireless charging system.

the building loads or to the AC grid.

The first step in the design process was to determine the architecture of the active front-end rectifier/inverter which is a bidirectional grid interface converter. Technical team performed a very comprehensive literature review on three-phase bidirectional grid-connected power electronics interfaces. Among other candidate interface topologies, team determined to use the two-level voltage source converter (VSC) due to the advantages over the other topologies. For the primary-side HF inverter/rectifier as well as the vehicle-side HF rectifier/inverter, the converter topology is designed to be a full-bridge converter with two phase-leg modules per converter. The developmental evolution of the primary and secondary-side power stages is given in Figure III.6.2.

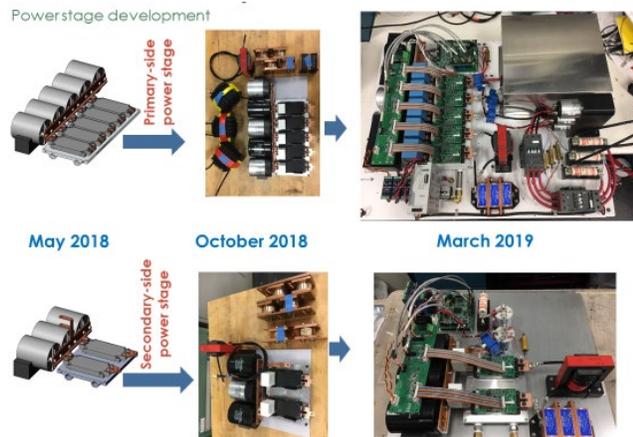


Figure III.6.2 System level diagram of the proposed architecture for the bidirectional wireless charging system.

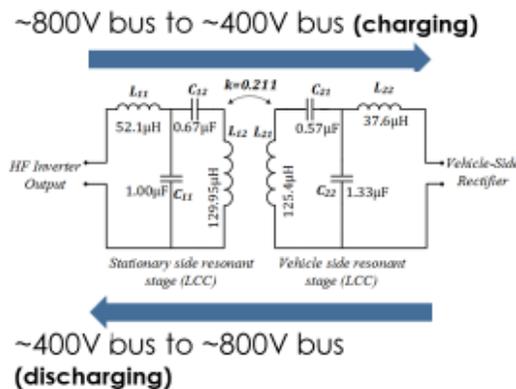


Figure III.6.3 System level diagram of the proposed architecture for the bidirectional wireless charging system.

During the system design, one of the approaches taken was to achieve the required voltage gain in the resonant stage of the system. Since the input is 480V, 3-phase AC, the rectified voltage would be around 678V. Since some boost factor is required for power factor correction, primary-side DC bus should be regulated to around ~750–800V. Since the vehicle-side battery nominal voltage is around 400V, we need to have a resonant voltage gain of 0.5 when charging the vehicle and the resonant voltage gain should be around 2 when the power flow direction is reversed (from vehicle to grid).

Once the team completed the fabrication of all the components and subsystems, these were validated for their parameters and functionalities. In order to verify the voltage gain characteristics of the resonant stage, a Bode

100 frequency response analyzer was connected to the coupling coils and their resonant tuning circuitries as shown in Figure III.6.4. On the analytical model of the system, the voltage gain of the resonant tank was analyzed and compared and validated with the frequency response analyzer’s gain results. In both cases, the voltage gain is about 0.5 at the resonant frequency. When power flow direction is reversed, the ~400V battery needs to transfer power to the ~750–800V DC bus on the primary-side. Again, this is accomplished by having a voltage gain of 2 from vehicle-side to the primary which is verified in the model and experiment.

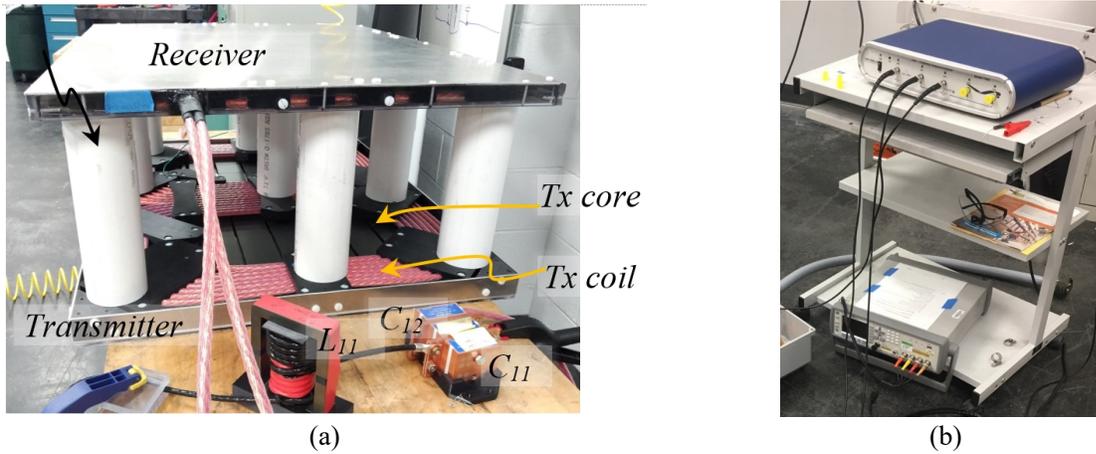


Figure III.6.4 Primary and secondary coils with their resonant tuning components (a) and Bode 100 frequency response analyzer used for voltage gain characterization of the system.

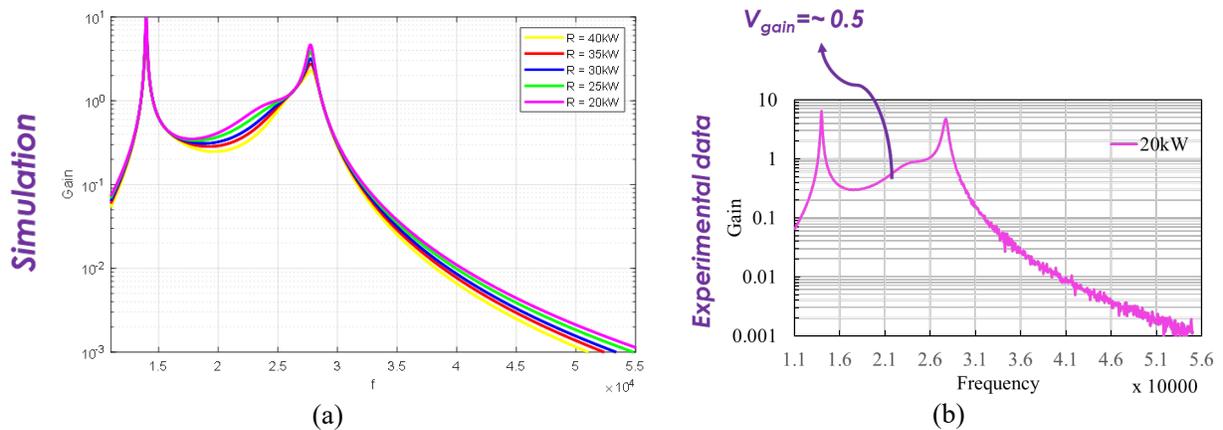


Figure III.6.5 Resonant voltage gain of the system using the analytical model (a) and the experimental validation (b).

**Results**

Once all the hardware was completed and parameters validated and the resonant stage characteristics have been tested, functionality tests of individual subsystems have been performed. Team has completed several tests including testing the resonant stage in loaded condition while transferring 20 kW power with 11 inches airgap separation (dc-to-dc test), HF inverter tests feeding a resistive load, grid-interface converter feeding a resistive load, grid-interface converter feeding the HF inverter with a resistive load, secondary-side power converter rectifier mode tests, and reverse power flow with repeated functionality tests. Figure III.6.6 shows the laboratory test setup with the primary-side inverter/rectifier, secondary-side rectifier/inverter, electromagnetic coupling coils with 11” airgap, and their LCC-LCC resonant tuning components.

This setup was first tested with grid-to-vehicle (G2V) power flow and then with vehicle-to-grid (V2G) power flow test cases. In this mode of operation, 20 kW was delivered to the battery emulator that is connected to the output of the secondary-side rectifier. At the primary-side, ~737V dc voltage was applied to the inverter input. Vehicle-side battery voltage was set to 402V. This operation resulted in 96.05% dc-to-dc efficiency which includes the efficiency of the inverter, coil-to-coil efficiency, and the efficiency of the rectifier.

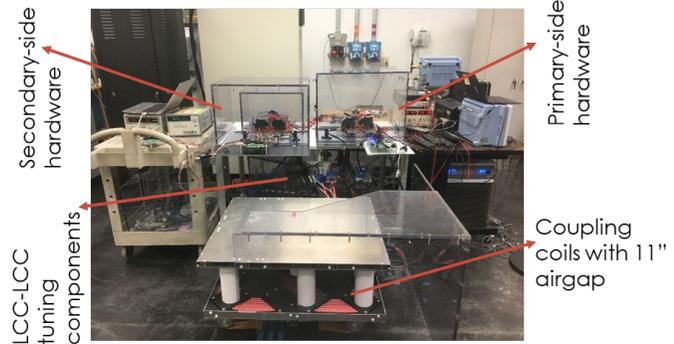


Figure III.6.6 Resonant voltage gain of the system using the analytical model (a) and the experimental validation (b).

Figure III.6.7 (a) shows the operational waveforms of the system in G2V 20 kW power transfer mode where the first quadrant indicates the inverter output voltage and current, second quadrant shows the primary coil voltage and current, third quadrant shows the secondary coil voltage and current, and the fourth quadrant shows the rectifier input voltage and current waveforms. Figure III.6.7 (b) shows the power analyzer measured stage-by-stage voltage, current, active and reactive power, power factor, and the dc-to-dc efficiency. According to the power flow show in Figure III.6.7(b), the primary-side inverter efficiency is 99.5%, coil-to-coil efficiency is 96.86%, and the secondary-side rectifier efficiency is 99.64%.

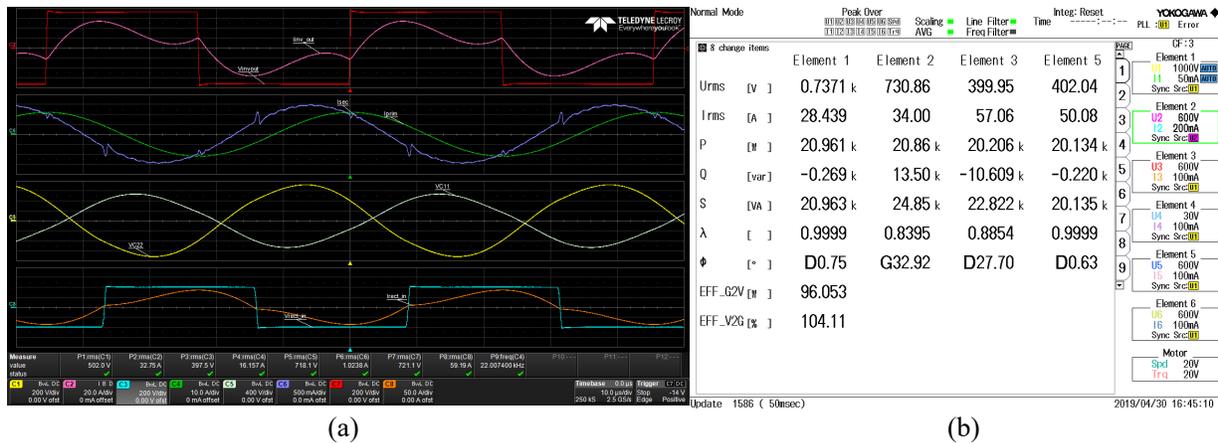


Figure III.6.7 Experimental test results for G2V mode with 20 kW power transfer to the vehicles-side battery emulator: Operational waveforms (a) and power analyzer measurements (b).

G2V operation test results are shown in Figure III.6.8 where ~20 kW of power is delivered from secondary-side battery emulator to the primary-side DC bus. The primary-side DC bus voltage is 700V while the vehicle-side battery voltage is set to 382V. In this case, the dc-to-dc efficiency from vehicle battery to the primary DC bus is 96.21%. In Figure III.6.8 (a) the operational waveforms of the system in V2G 20 kW power transfer mode are shown where the first quadrant indicates the primary-side rectifier input voltage and current, second quadrant shows the primary coil voltage and current, third quadrant shows the secondary coil voltage and current, and the fourth quadrant shows the vehicle-side inverter output voltage and current waveforms. Figure III.6.8 (b) shows the power analyzer measured stage-by-stage voltage, current, active and reactive power, power factor, and the dc-to-dc efficiency. According to Figure III.6.8 (b), the vehicle-side inverter, from vehicle-side coil to ground-side coil, and the primary-side rectifier efficiencies are 99.47%, 97.67%, and 99%, 98.99%, respectively.

An additional test was performed to test the functionality of the 3-phase grid-side inverter and the HF inverter simultaneously. The primary-side DC bus was powered with a DC voltage of 758V. While the grid-interface converter was operated in inverter mode feeding a 3-phase resistive load with 60 Hz output, the HF inverter was operated with 22 kHz output feeding another resistive load. In this case, DC bus total power was 44.613 kW. HF inverter output was 20.414 kW while the 3-phase inverter delivers 23.65 kW to the output. This corresponds to a combined efficiency of the 3-phase inverter and HF inverter of 98.867% on the primary-side.

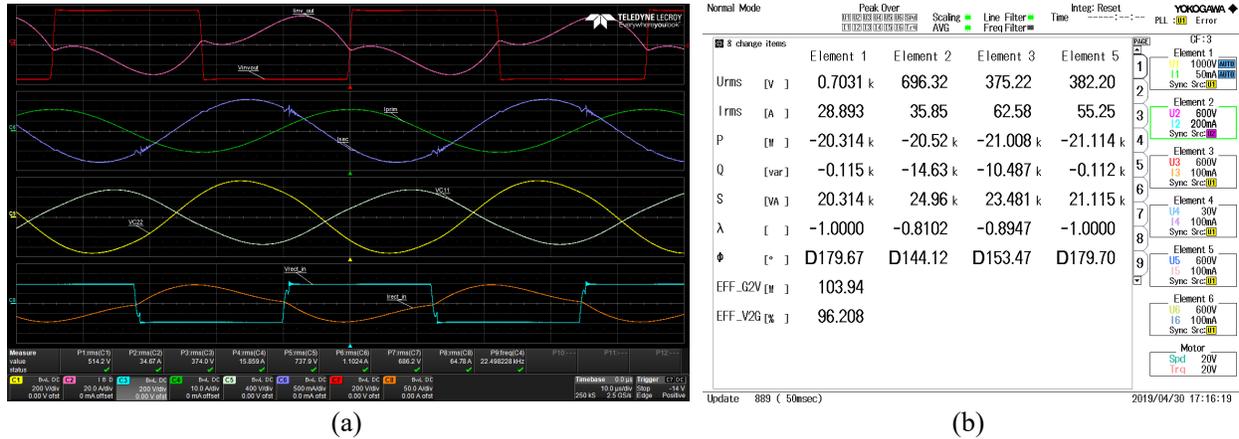


Figure III.6.8 Experimental test results for V2G mode with 20 kW power transfer to the primary-side DC link.

### Conclusions

During the first budget period of the project, the team worked on modeling, simulations, analysis, and design of the system power conversion stages and control systems. Upon the successful design review meeting in May 2018 which concluded the first budget period of the project, team started building the hardware of all the system power conversion stages along with the control systems. During the second budget period, team built all the power electronic converter hardware and fabricated all the passive components including the 3-phase grid-connected inductors, capacitor systems, resonant tuning circuit components, coupling coils, and the vehicle-side filter components. Team also designed and developed two DSP interface boards for the primary and secondary sides. Team has successfully tested the operation of the power conversion stages. The bidirectional power flow tests demonstrated more than 95% dc-to-dc efficiency at 20 kW power delivery in both power directions. Team also completed the tests of the 3-phase grid-interface converter in both power factor correction boost rectifier and inverter operating modes. The challenges experienced include the change in the vehicle battery nominal voltage from 650V to 420V. This change in the battery voltage required to modify the resonant stage of the system to optimize the operation with 420V nominal secondary-side voltage. Team modified the resonant stage components and verified the resonant voltage gains that would optimize the power transfer between the ~750–800V primary dc bus voltage and the ~308–429V. After confirming the successful operation in simulations, hardware modifications are done in the resonant stage components and tests validated the achieving the proposed functionalities. As of the submission time of this report, team is working on vehicle integrations and preparations to demonstrate the operation of the technology on the UPS research truck.

### Key Publications

1. “Secondary Active Rectifier Control Scheme for a Wireless Power Transfer System with Double-Sided LCC Compensation Topology,” in Proc., 44<sup>th</sup> Annual Conference of the IEEE Industrial Electronics Society (IECON), October 2018, Washington, D.C.
2. “Sensitivity of an LCC-LCC Compensated 20-kW Bidirectional Wireless Charging System for Medium-Duty Vehicles,” in Proc., IEEE Transportation Electrification Conference and Expo (ITEC), June 2019, Novi, MI.

## **Acknowledgements**

Project team would like to thank Mr. John Jason Conley of the National Energy Technology Laboratory for his continuous support and guidance on this project.



### III.7 Development and Demonstration of Medium-Heavy Duty PHEV Work Trucks (Odyne Systems)

**John R. Petras, Principal Investigator**

Odyne Systems LLC  
W237 N2878 Woodgate Road, Suite 2  
Pewaukee, WI 53072  
E-mail: [John.Petras@Odyne.com](mailto:John.Petras@Odyne.com)

**Ken Kelly, Principal Investigator**

National Renewable Energy Laboratory (NREL)  
15013 Denver West Parkway  
Golden, CO 80401  
E-mail: [Kennith.Kelly@nrel.gov](mailto:Kennith.Kelly@nrel.gov)

**David Smith, Principal Investigator**

Oak Ridge National Laboratory (ORNL)  
2370 Cherahala Boulevard  
Knoxville, TN 37932  
E-mail: [Smithde@ornl.gov](mailto:Smithde@ornl.gov)

**Steven Boyd, DOE Program Manager**

U.S. Department of Energy  
E-mail: [Steven.Boyd@ee.doe.gov](mailto:Steven.Boyd@ee.doe.gov)

Start Date: January 19, 2017  
Project Funding: \$6,172,732

End Date: January 31, 2021  
DOE share: \$2,149,644

Non-DOE share: \$4,023,088

#### Project Introduction

The heavy-duty vehicle market (Class 6-8) has been a difficult segment for the introduction of plug-in vehicles due to the large energy storage requirement (with corresponding cost), challenging duty cycles, and the diversity of vehicle configurations. The Work Truck market represents a significant opportunity for Heavy-Duty PHEV adoption. Odyne proposes development of a new class of PHEV Work Truck which will be modularized and customized to provide optimal ROI across multiple customers and applications. The proposed project will first demonstrate this technology as a Utility Work Truck variant:

- The usage cycle includes driving and stationary/worksite power requirements, ensuring full daily usage of the grid-charged battery (battery size: 25–40kWhr). Though daily driving can often be short (an average of 26 miles per day), worksite power includes substantial demand (hydraulics, exportable 110/220V power, 12V support, HVAC)
- Worksite power demands for conventional vehicles require continuous loaded engine operation, resulting in significant emissions, fuel consumption and noise impacts
- These trucks serve an industry that is strongly incentivized to promote vehicle electrification, and which has publicly committed to spending a portion of their annual vehicle purchase budget on electrified vehicles (EEI press release of 11/18/14).

This project will develop and demonstrate a medium/heavy duty plug-in hybrid solution capable of meeting the needs of the work truck market while delivering fuel and emissions reductions of 50% when evaluated against the full-day work truck duty cycle.

### Objectives

The project goal is to design, develop, and demonstrate a new generation of medium/heavy-duty plug-in hybrid electric work truck that achieves a 50% reduction in fuel consumption versus a conventional vehicle baseline when evaluated across a full day work cycle representative of the vocational work truck. The primary objectives are:

- To simulate, design and develop unique and innovative integrated powertrain, software, and calibrations which will optimize the complete diesel/transmission/hybrid powertrain and demonstrate the potential for driving fuel efficiency improvements greater than 40% with commensurate reductions in GHG emissions
- To develop and validate a modular Lithium Ion battery system based on high volume lower cost cells and modules that are utilized in the light-duty sector which will meet the power, energy, and duty cycle requirements of the MD-HD vocational truck market at a cost approaching half that of currently available low volume solutions
- To integrate fully electrified worksite functions and a daily duty cycle optimization function with the powertrain and battery solutions on an OEM class 6-7 chassis and demonstrate the capability of 50% reduction in total fuel used when measured against a full day duty cycle's and real world performance
- To demonstrate ten optimized PHEV work trucks and validate the vehicle's operating performance, emissions and full work cycle fuel reduction capability in excess of 50%.

### Approach

The proposed solution incorporates a simple, parallel hybrid system that allows the torque of the electric motor to augment the torque output of the diesel engine, thus saving fuel. The motor speed is synchronized with the engine speed through the existing power take-off (PTO) unit. The traction motor drives the PTO, adding torque to the rear axle, or converts torque from the PTO into power to charge the PHEV batteries (see Figure III.7.1). Six patents have been granted, and other patents are pending prior to initiation of this project.

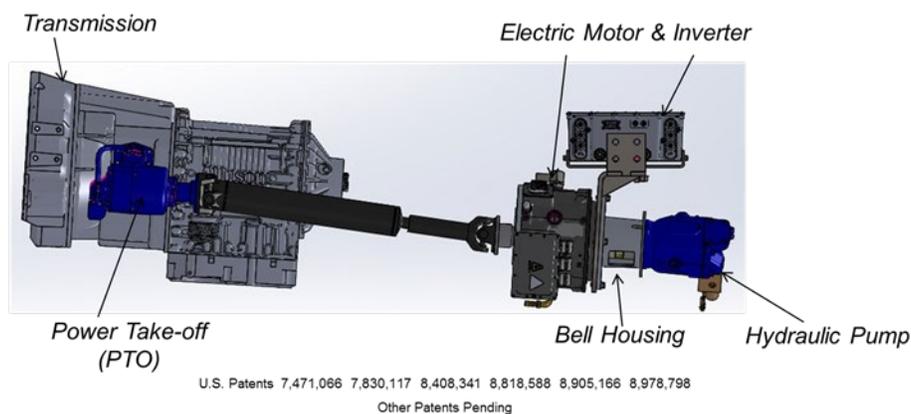


Figure III.7.1 Odyne powertrain configuration

The system is also designed to provide full jobsite engine off electrification utilizing power from the lithium ion battery system to provide 120/240 V exportable power, 12V chassis systems support, high efficiency electric heating and air conditioning along with the power to drive the primary work equipment (Figure III.7.2).

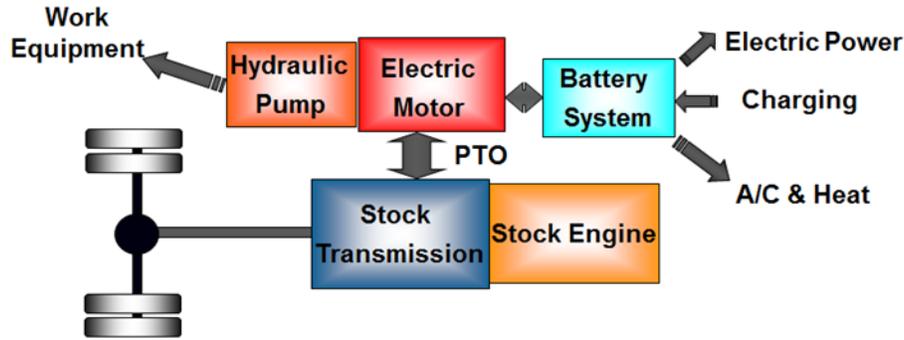


Figure III.7.2 Odyne hybrid architecture

The project will be conducted in three periods:

**Period 1: System Design and Analysis:** Analysis of existing fleet data will be performed and will be used for the establishment of baseline driving and full day usages cycles and current vehicle performance for system simulation, development and test. The project will create designs and systems which, when integrated, will produce a Medium-Heavy duty work truck capable of achieving requirements under real world conditions. The period will conclude with an analytical simulation verifying this performance improvement.

**Period 2: System and Vehicle Verification:** The subsystems will be verified and refined using prototype hardware and the full vehicle will undergo final development, functional and performance test. The prototype phase will conclude with test results confirming that the final design will provide a  $\geq 50\%$  reduction in fuel use under real world conditions. Approximately ten vehicles will be built to support field test and evaluation.

**Period 3: Prototype Vehicle Demonstration:** Ten vehicles will be put in regular service with telematics to measure performance. The Recipient will analyze the data along with customer feedback and will report the calculated real-world reduction in fuel use and customer acceptance of the technology.

The three-year period of the project will integrate three development streams into a final Prototype vehicle solution and 10 vehicle field demonstrations:

#### Powertrain Development and Optimization

- Odyne – Lead, Hybrid Powertrain development and design, Hybrid optimization and control strategies
- NREL – Duty cycle analysis, Dynamometer test, Full-year fuel use simulation and analysis
- Oak Ridge National Laboratory – Powertrain simulation and optimization, HIL Test
- Allison Transmission – Transmission control and optimization strategies.

#### Battery Development

- Odyne – System Specifications and integration requirements, system integration test
- Odyne, Ricardo Strategic Consulting – Battery System supply chain evaluation
- Supplier TBD – Lithium Ion Module and BMS Supplier, Component System integration requirements.

#### Chassis Development & Integration

- Odyne – System design, control, cost, and integration lead, Systems Efficiency & Sizing, System build
- Freightliner – OEM Chassis Integration improvements, Prototype and demonstration chassis supplier.

**Results**

In FY19, the project completed the final analytical drive optimization, selection of the primary path battery system, and build of the prototype test chassis and Oak Ridge National Laboratory Hardware-in-Loop (HIL) powertrain dynamometer test system fixturing and assembly. The year ended with both the HIL and prototype chassis undergoing final debugging in preparation for powertrain system and vehicle development and verification activities which will be performed in FY20.

**Powertrain Development and Optimization**

Odyne worked with Oak Ridge National Laboratory (ORNL) to complete the analysis of hybrid strategies to assess best possible means of employing hybrid driving strategy with an aim towards maximizing fuel economy benefits with efficient use of available plug-in battery energy utilization. After iterative development, 2 primary strategies were chosen to move to Hardware-in-Loop (HIL) powertrain dynamometer development: A Charge Depleting (CD) strategy which, when combined with Neutral Idle (NI), provided 29 – 57 % improvement in fuel economy. The second strategy is a Charge Sustaining (CS) strategy which, when combined with NI provided 8 – 17% improvement in fuel economy with no net use of battery energy. These strategies will be verified and refined during HIL testing in CY4Q19. The results of the analysis are summarized in Table III.7.1

**Table III.7.1 Oak Ridge Driving Simulation Fuel Economy Improvement Summary**

Cycle	CS	CS NI	CD	CD NI
UDDS	5%	8%	20%	29%
HHDDT	4%	6%	44%	48%
NREL Med	8%	11%	39%	39%
NREL Low	11%	17%	46%	57%

Procurement of parts for HIL testing, including Engine, Transmission and Hybrid System were completed and delivered to Oak Ridge in May–July, 2019. During June, Oak Ridge personnel began construction of test fixtures and preparation for assembly of the test components for HIL testing. Figure III.7.3 shows the Engine, Transmission and Hybrid Drive configuration assembled for system debug—September, 2019.

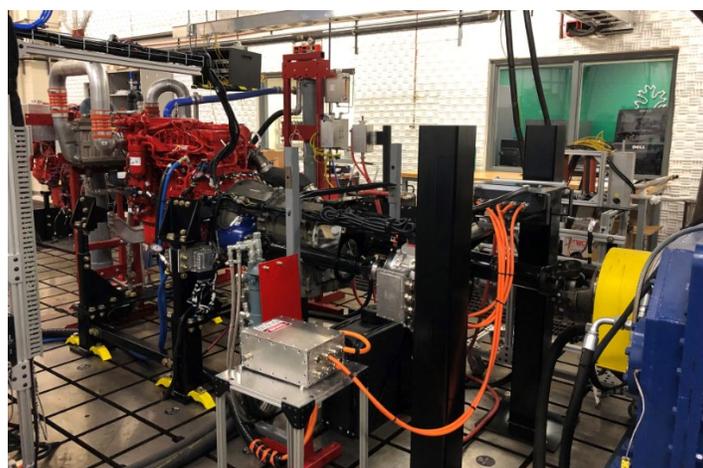


Figure III.7.3 Odyne / Oak Ridge HIL powertrain test stand

Remaining tasks in powertrain development are the completion of HIL testing, final refinement of the hybrid drive strategies and verification of the driving strategies and full day duty cycles fuel savings on a full test chassis at the National Renewable Energy Laboratory (NREL) chassis dynamometer Scheduled for CY20.

**Battery Development**

Early in CY19, Odyne selected 2 potential suppliers for battery systems. During late 2018, technical and commercial concerns caused the primary, and lowest cost supplier to be dropped from consideration and the second supplier, Octillion, missed several delivery milestones, at which point Odyne began the search for an alternate supplier of battery systems. In January, 2019, Torqeedo provided an 11.6 kWh battery pack based on a system used in light duty regular production (Figure III.7.4). In May, 2019, the Torqeedo pack passed test vehicle evaluations and was selected as the primary project battery system.

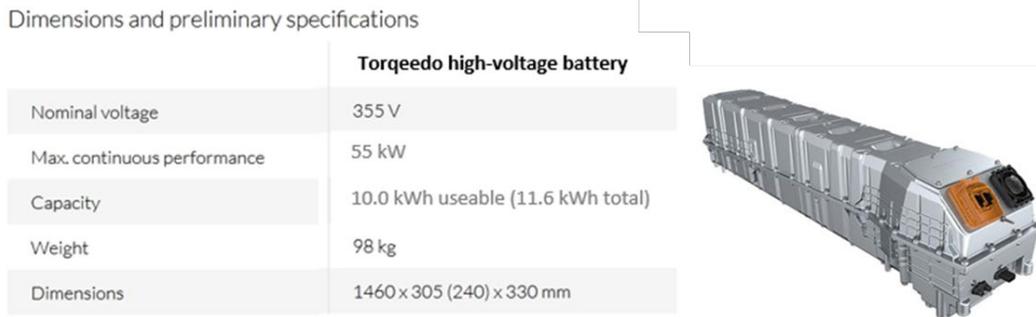


Figure III.7.4 Torqeedo 11.6 kWh battery pack

**Chassis Development & Integration**

Component selection was completed and the test chassis design was updated to include the Torqeedo battery pack (Figure III.7.5). Once build began, wiring harness design and build became the pacing item for completion of the test chassis.

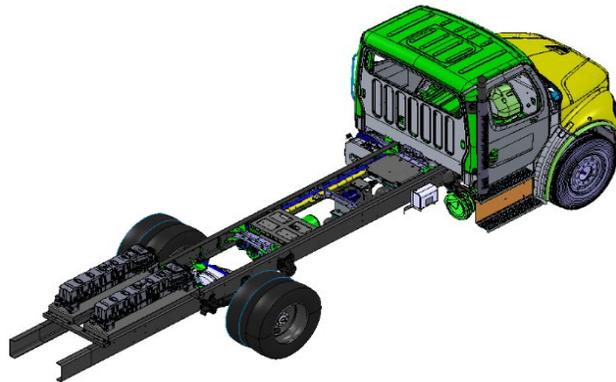


Figure III.7.5 Test chassis design layout

The test truck build was completed in July, 2019. Testing is in process and expected to be completed in October, 2019 (Figure III.7.6). Remaining tasks include delivery of the validated test chassis with the final driving strategies for vehicle performance testing and NREL and the detailed design and build of the 10 demonstration vehicles which will be used for field evaluation in Period 3.



Figure III.7.6 Completed test chassis and hydraulic test stand

### Conclusions

In FY19, the project completed the final analytical drive optimization, selection of the primary path battery system, and build of the prototype test chassis and Oak Ridge National Laboratory Hardware-in-Loop (HIL) powertrain dynamometer test system fixturing and assembly. The year ended with both the HIL and prototype chassis undergoing final debugging in preparation for powertrain system and vehicle development and verification activities which will be performed in FY20.

### Acknowledgements

Odyne wishes to acknowledge the substantial contributions of John (Jason) Conley (NETL), Kevin Walkowicz (NREL), Adian Cook, Dean Deter (Oak Ridge National Laboratory), Greg Mann, Brent Maurer (Allison Transmission), Dan Purdy (Freightliner Trucks), and Mark Kuhn, Alan Munday (Ricardo Strategic Consulting)

### III.8 Cummins Electric Truck with Range-Extending Engine (ETREE) (Cummins, Inc.)

#### **Jesse Dalton, Principal Investigator**

Cummins, Inc.  
1900 McKinley Avenue  
Columbus, IN 47201  
E-mail: [jesse.dalton@cummins.com](mailto:jesse.dalton@cummins.com)

#### **John Jason Conley, NETL Program Manager**

U.S. Department of Energy  
E-mail: [john.conley@netl.doe.gov](mailto:john.conley@netl.doe.gov)

#### **Lee Slezak, DOE Program Manager**

U.S. Department of Energy  
E-mail: [lee.slezak@ee.doe.gov](mailto:lee.slezak@ee.doe.gov)

Start Date: July 1, 2016	End Date: June 30, 2020	
Project Funding: \$6,295,281	DOE share: \$4,126,570	Non-DOE share: \$2,168,711

#### **Project Introduction**

Many medium duty commercial vehicles (classes 5 – 7) have daily duty cycles with energy requirements that may lend themselves to the use of a plug-in electrified powertrain. However, often the duty cycle energy requirements are near, or over, the limits that can be served by a pure battery electric vehicle (BEV). A range extending electric vehicle (REEV) architecture may enable the fleet operator's needs to be met using a substantial amount of grid energy, while also allowing the vehicle to complete any number of more challenging duty cycles typically completed by conventionally powered vehicles.

The Cummins Electric Truck with Range Extending Engine (ETREE) project makes use of grid energy to offset fuel consumption used by medium duty commercial vehicles and, specifically, those that are used for class 6 urban/suburban pickup and delivery.

The ETREE project aims to develop a class 6 (GVW 26k lb.) box truck, with equivalent performance to conventional diesel-powered trucks, that reduces fuel consumption by at least 50% over a wide range of urban/suburban pickup and delivery applications.

#### **Objectives**

In the target vehicle (a Kenworth K270 equipped with a 24' van body), the electrified powertrain will achieve at least a 50% fuel consumption reduction for a wide range of pickup and delivery work day drive cycles compared to the baseline powertrain (a Cummins 6.7L ISB diesel engine and automatic transmission).

The Kenworth K270 with the ETREE powertrain will be demonstrated in simulation, in a powertrain test cell, on a test track (SAE J1526 testing), and in fleet operation.

#### **Approach**

ETREE is a Cummins-led project with assistance from the following partners:

- PACCAR, Inc.,
- Argonne National Laboratory (ANL),

- National Renewable Energy Laboratory (NREL), and
- The Ohio State University (OSU).

The project will:

- Develop target entire work day duty cycles by employing NREL's FleetDNA and DRIVE Analysis Tools
- Rely on simulation (by ANL, Cummins and OSU) to determine component requirements for a plug-in series hybrid
- Build test vehicles which include:
  - The use of applicable electrified vehicle accessories,
  - Appropriate thermal management systems, and
  - An electric braking system (EBS) to promote kinetic energy recovery while maintaining conventional vehicle drivability
- Employ a “test heavy” project schedule (simulation, powertrain test cell located at Cummins Technical Center, test tracks, and fleet operators) to confirm predicted results
- Identify & deploy test vehicle(s) to fleet operators that would likely use these vehicles in production.

## Results

Previously, the ETREE project developed the target work day duty cycles which are used to measure the project against its objectives. These work day duty cycles, denoted NREL 80 and NREL 100, are 80 and 100-mile duty cycles, respectively, applicable for use for class 6 pickup and delivery. Their required duty cycle energies are in the 80th and 95th percentile of all measured duty cycles available in NREL’s FleetDNA database. In the past year, these work day duty cycles were shared with the industry by Adam Duran at the 2018 SAE World Congress.

In FY2017, simulation against the work day duty cycles, and against typical class 6 performance metrics, ANL, Cummins and OSU identified the components as summarized in Table III.8.1. This component selection assured the fuel consumption reduction targets will be met on the work day duty cycles.

**Table III.8.1 Summary of ETREE Powertrain Components**

Component	Description
Traction Motor	160 kW permanent magnet traction motor
Transmission	Allison 3000 ETREE transmission with transmission input stop-start system
Nominal DC bus voltage	700 VDC
Energy Storage	112 kW-h NMC Li-ion battery
Range Extender – Generator	130 kW permanent magnet generator
Range Extender – Engine	155 kW ISB4.5 w/ full complement of aftertreatment components (diesel particular filter, selective catalytic reduction, diesel oxidation catalyst)
Final Drive Ratio	5.29



Also in FY2017, the simulation results were validated in a powertrain test cell, equipped with a battery emulator at the Cummins Technical Center as shown in Figure III.8.1.

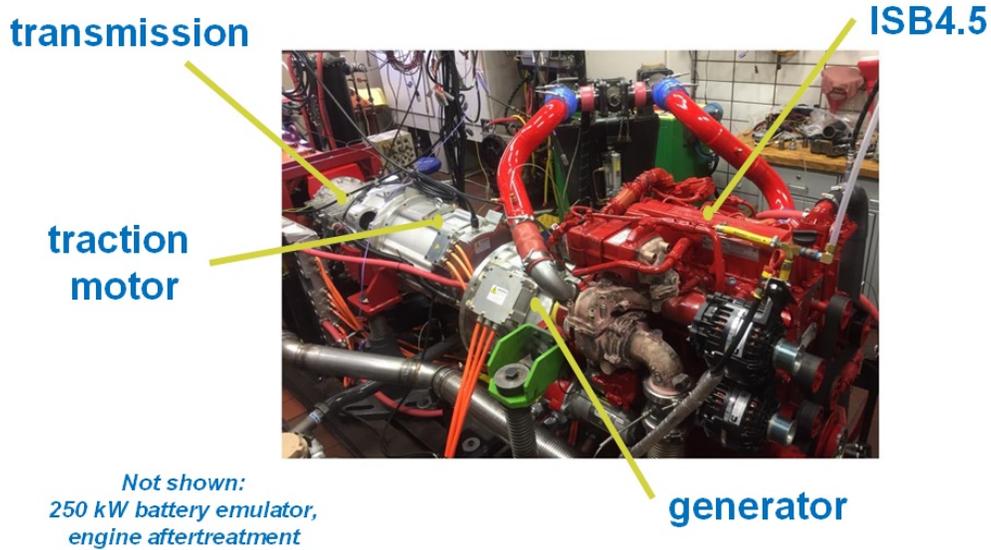


Figure III.8.1 ETREE powertrain test cell located at Cummins Technical Center, Columbus, Indiana

In FY2018, two test trucks were built based on the Kenworth K270 / Peterbilt Model 220 chassis. These trucks underwent validation testing where it was found that the original 112 kw-h NMC li-ion batteries did not exhibit the desired robustness for a demonstration project to be used at a customer location. Due to this reliability concern, the decision was made to create alternate batteries (see Figure III.8.2).

An alternate battery (drivers side enclosure shown in Figure III.8.2), consisting of a nominal total energy capacity of 123 kw-h, was designed to fit the space-claim of the original batteries. This battery, consisting of 14 44V/200A-h production Li-ion battery modules—or 7 on each vehicle side—connected in series, was developed in less than four months. After construction, the battery underwent extensive testing at the Battery Innovation Center (BIC) in Newberry, Indiana. The full suite of tests was completed as scheduled, and the batteries were put into use on both ETREE trucks.

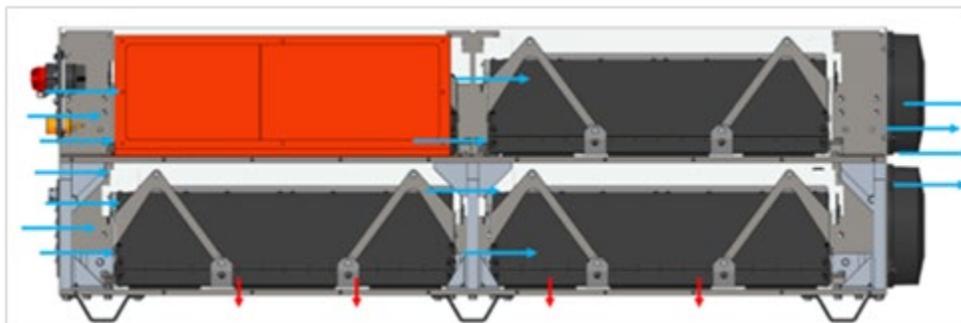


Figure III.8.2 ETREE alternate battery— drivers side enclosure (shown without cover)

Also in FY2018, working with WABCO (a supplier of commercial vehicle braking systems), controls software was developed to integrate an electronic braking system (EBS) with the traction motor’s negative torque capability (typically used to recover vehicle kinetic energy during vehicle deceleration events). The objective

of this “brake blending feature” is to enable a commercial electric vehicle to drive similarly to a conventional diesel truck under all driving conditions and battery state-of-charge.

In FY2019, the two test trucks were subjected to an extensive verification and validation plan to ensure they meet performance, reliability, and robustness expectations necessary to operate in a public fleet. This included static tests, dynamic tests, closed course testing, and accumulated mileage on public roads. Additionally, one truck will be deployed into fleet service in Q4 of FY2019. This will expose the end fleet user to the ETREE architecture and provide a platform for industry feedback.

Also in FY2019, a key technical objective of the project was to demonstrate on a test track, during a J1526 test (employing a baseline and ETREE truck), the project fuel consumption targets are met. This included the modification of the target NREL 80 drive cycle, by NREL and Cummins, so that it is more appropriate to operation on a test track while still containing similar energy requirements and drive cycle metrics. This testing was conducted in conjunction with Southwest Research Institute, who administered the testing at a test track in Uvalde, Texas. An autonomous drive system consisting of accelerator position and brake control was installed on both the ETREE and baseline trucks to ensure cycle to cycle repeatability during each run of testing. As well as the ETREE truck and the baseline vehicle were operated simultaneous for each of 3 runs of the cycle, spaced 5 minutes apart. The ETREE truck demonstrated 65% fuel reduction with 1.8% confidence interval over the modified NREL80 cycle, which was better than the project goal of 50% and in line with simulation prediction. Testing results for the 3 NREL80 test runs are summarized in Table III.8.2 below.

**Table III.8.2 Summary J1526 Testing Results**

ETREE Compared to Baseline Truck on Modified NREL80 Cycle	
Average Difference in Fuel Quantity (lbs.)	46.46 ± 1.27
% Less Fuel Consumed by ETREE	65.3% ± 1.8%

### Conclusions

The ETREE program team has developed an EV powertrain and related systems to meet the project goals. The team has validated the powertrain in a powertrain test cell. The ETREE architecture installed in vehicle was put through a verification and validation process to demonstrate robustness in line with expectations from a fleet operator. Subsequently, 1 ETREE truck will be deployed in daily fleet use in Q4 of 2019.

The ETREE team completed J1526 fuel consumption testing operated by Southwest Research Institute at a test track located in Uvalde, Texas. This testing demonstrated 65% reduction in fuel consumption on a modified NREL80 cycle over a baseline vehicle, which exceeded the project goal of 50%.

### Key Publications

1. The following technical paper, based on ETREE project work, was presented at the 2019 Innovations in Mobility Conference: Title: Opportunities and Challenges of Internal Combustion Engine Range Extenders in Commercial Vehicles, Primary Author: Ke Li
2. The following technical paper, based on ETREE project work, was presented at the 2018 SAE World Congress: Title: Development of 80 and 100 Mile Work Day Cycles Representative of Commercial Pickup and Delivery Operation, Primary Author: Adam Duran of NREL, Additional Authors: Ke Li and John Kresse of Cummins, Ram Vijayagopal of ANL
3. The following technical paper, also based on ETREE project work, was presented at the 2018 ASME Dynamic Systems and Controls conference: Title: Battery Discharge Strategies for Energy Management in Electrified Truck for Pick-up and Delivery Application, Primary Author: Mukilan Arasu, Additional Authors: Qadeer Ahmed and Giorgio Rizzoni.

### III.9 Comprehensive Assessment of On-and Off-Board Vehicle-to-Grid Technology Performance and Impacts on Battery and the Grid (EPRI)

#### **Sunil Chhaya, Principal Investigator**

Electric Power Research Institute (EPRI)  
3420 Hillview Avenue  
Palo Alto, CA 94304  
E-mail: [schhaya@epri.com](mailto:schhaya@epri.com)

#### **Lee Slezak, DOE Program Manager**

U.S. Department of Energy  
E-mail: [Lee.Slezak@ee.doe.gov](mailto:Lee.Slezak@ee.doe.gov)

Start Date: October 1, 2016

End Date: June 30, 2020

Total Project Funding: \$2,786,278

DOE share: \$1,547,678

Non-DOE share: \$1,238,600

#### **Project Introduction**

There is heightened interest in the value for Vehicle-to-Grid (V2G) applications to provide energy management services to support grid reliability and resiliency. The research community is seeking to maximize the total value of a vehicle by exploring other services beyond transportation, but the automotive manufacturing and transportation battery communities remain reluctant to embrace V2G applications because of uncertainties associated with the exposure to grid applications and concerns about potential degradation of the transportation battery. Also, there are the challenges for enabling V2G technology development of bidirectional power electronics with the functionality, communications, and controls that are compliant with applicable regulatory and safety requirements, and standards. This proposal is to address the automotive industry concerns and the regulatory challenges to V2G technology.

The requirements for grid interconnected bidirectional inverters impose significant challenges to the automakers for on-vehicle inverter V2G functionality. Automakers self-certify their vehicles to Society of Automotive Engineers (SAE) and Federal Motor Vehicle Safety Standards (FMVSS) requirements, and do not submit vehicles to National Recognized Test Laboratories (NRTL) such as UL. SAE is addressing this by developing SAE J3072 “Interconnection Requirements for On Board Utility Interactive Inverter Systems” providing communications and process requirements for validating the on-vehicle inverter certification. It incorporates the test certifications required by UL 1741 and requirements of IEEE1547. Acceptance by utilities of a J3072 compliant vehicle inverter certification is an open issue. As a part of a collaborative California Energy Commission program the team evaluated and verified these requirements for on-vehicle bidirectional inverters.

In contrast, off-vehicle inverter enabled V2G using DC charging avoids the issues and challenges relative to on-vehicle V2G inverters. DC chargers contain the charge control electronics and are a location fixed asset that is hard wire connected to the grid. Because DC chargers are a fixed standalone product, they can easily be UL tested, certified, and site permitted. No vehicle UL certification would be required. The vehicle is only required to be DC charge capable with embedded J2847/2 communications software and J2931/1 power line communications (PLC) compliant connectivity with the DC charger which is standard with all DC charge capable Electric Vehicles.

The DC charger integrated off-vehicle bidirectional inverter is the most viable strategy and less challenging method for automakers to engage in commercialization of V2G as a distributed resource. However, there are still the automaker concerns with battery capacity degradation from V2G cycling and impacts on warranty

services. This DOE project is to address the development, implementation, and verification of DC charging integrated off-vehicle bidirectional inverter enabled V2G; and to assess the impact of V2G cycling on battery durability. Also, will be working with the SAE J2847/2 task force in the development and testing of the control messaging requirements and protocol for V2G communications that is presently ongoing.

### Objectives

The objective of the program is to test and evaluate grid DER management / integration use cases using V2G bidirectional power flow (charging and discharging) integrated with solar and stationary energy distributed resources in the AC (on-vehicle) and DC (off-vehicle) domains. The outcome is data to be analyzed and evaluated for performance, durability, and usage characteristics of the V2G technology, and impacts on battery life and vehicle components. As such, the proposal involves evaluation of Vehicle to Grid (V2G) technologies for on-vehicle (AC) and off vehicle (DC) bi-directional inverters thereby providing the best research value for the DOE.

The project goals are:

- Provide experimental and analytical basis to V2G technology as a key enabler in improving the value of owning a Plug-in Electric Vehicle
- Demonstrate the usefulness of off-vehicle Smart Power Integrated Node (SPIN) system to further enhance the value of V2G by enabling increased renewable generation on the grid and providing Vehicle to Home type services in conjunction with on-vehicle and off-vehicle storage
- Provide experimental and analytical basis for assessing effect on EV batteries from their application to grid services
- Provide key metrics for evaluation of performance and value of an off-vehicle V2G system in comparison to an on-vehicle V2G system
- Assess the effect of transformer constraints on grid service implementation
- Provide analytical framework and research results on the valuation of V2G services for high-impact (high-stress) regions of the distribution grid.

### Approach

The project is the comprehensive development, testing, and evaluation of Vehicle to Grid (V2G) and energy management technologies for on-vehicle bidirectional inverters, through a companion cost share project and for off-vehicle bidirectional inverters, through this DOE funding request. Figure III.9.1 provides a representative overview of the two V2G projects. The cost share funded project focuses on the effects of V2G energy management on the distribution system using on-vehicle inverter enabled bi-directional power flow to balance solar output for improved grid reliability and stability, including an economic evaluation of V2G services.

The focus of this DOE project is to develop, test, and demonstrate off-vehicle inverter enabled bidirectional power flow (V2G) utilizing a DC charging bi-directional converter integrated into a Smart Power Integrated Node (SPIN) system. The communications, control, and interface functionality for the SPIN system will be based on SAE standards (SAE J2847/2, J2931/1, J2931/4). The intent is to demonstrate a fully functional, grid-compatible DC charging based V2G end-to-end system that provides secure, interoperable communications and information processing.

The uniqueness is the SPIN system capability to control and process power flow between PEVs (charging/discharging), the grid, local solar and backup energy storage with a single multifunctional modular unit. The SPIN system will synchronize these energy sources to act as dispatchable DER. Innovation lies

within the development of V2G with DC bi-directional charging, and support of local Distributed Energy Resource (DER) integration use cases that will accelerate the deployment of V2G as a part of an integrated DER ecosystem.

The project is to achieve the objectives through accomplishment of the following activities:

- Development/fabrication of the Smart Power Integrated Node System hardware integrating a bidirectional dual active bridge converter using Wide Band Gap SiC power module technology with DC charging functionality (6.7kW to 10kW).
- Development/integration of the system control and communications software utilizing standards based protocols with interoperability between the SPIN system, utility or Energy Service Provider, and the PEV. This includes the development/integration of Energy Management System (EMS) control algorithms and functionality in the SPIN hardware for integrating V2G with solar and back up energy storage as coordinated distributed energy resources. Expectation is to extrapolate data on customer value and utility benefits for V2G DER integration.
- Develop/test determined cycle plan based on selected grid service use cases in both a lab environment and subsequently in a vehicle field demonstration. Evaluate battery life and conduct battery durability impact testing and analyses
- Conduct a field or in-lab demonstration of the V2G grid service use cases utilizing 3 to 5 Fiat Chrysler Pacifica PHEVs fully developed SPIN systems. The systems will be connected to a single transformer to allow evaluation of the grid impact from clustered EV charging and discharging.

The design, component technical specification, and simulation of the SPIN bidirectional converter has been completed by Flex Power Control (FPC) under a Technology Innovation contract from EPRI. ORNL has had specific experience in the development and integration of Wide Band Gap Silicon Carbide (SiC) power module devices in inverter systems for electric drive propulsion systems, and will provide engineering expertise to evaluate, test and verify the SPIN system design. Hardware fabricator Current Ways has established expertise and knowledge in power electronics manufacturing engineering and in UL certification processes. FPC, ORNL, and Current Ways have an established interaction on the design for the SPIN system and are collaborating on the design and fabrication of the FPC-designed SPIN technology.

The SAE J2847/2 and J2847/3 standards incorporating the required PEV/charger communications for PEV reverse power flow are in progress. EPRI is a working member of the SAE Task Force and is engaged in the development of these standards. This project will correlate with the development of the standards and provide a basis for verification of the determined communications requirements.

Kitu Systems is presently developing the IEEE 2030.5 software into the AeroVironment EVSE for the CEC V2G project, which will be leveraged to successfully implement the software for the SPIN system. Additionally, EPRI will work with Fiat Chrysler to implement the required J2847/2 communications for V2G, which are based on the DIN 70121 protocol, into the Pacifica Mini Van PHEVs for the field demonstration.

EPRI has been working to develop and deploy DER management control algorithms in another project in Southern California around a community of Zero Net Energy homes, and these control algorithms will utilize the underlying stack developed by Kitu Systems that creates open standards-based communications. This experience integrating DER as well as the code-base will be leveraged to develop and implement the SPIN EMS control algorithms for coordinated DER management of V2G, solar, and back up energy storage, establishing the capability for micro grid operations at the local facility or residential level. EPRI's ongoing work with NREL on the INTEGRATE projects will inform the open DERMS and DRMS integration. In addition, EPRI will develop the grid models and provide the simulated utility DR and ISO regulation command/request signals for activating V2G during the lab testing and field demonstration phases.

LG Chem are the world leaders in electric mobility and grid-scale Lithium-ion batteries and will be an active participant in this project to lend both battery application, testing and data interpretation expertise, with battery hardware and test services to create data sets that can be analyzed.

Fiat Chrysler Group is making available Model Year 2017 Pacifica PHEVs for this pilot which will be modified to add V2G services related hardware and control algorithms. The on-vehicle V2G communications module utilizing J2847/3 standard application based on IEEE2030.5 protocol will be developed by EPRI and Kitu Systems. EPRI is developing the IEEE2030.5 translation to the vehicle CAN to ensure interoperability of the protocols for V2G functionality and control.

Special facilities access and planned utilization:

- ORNL: Characterization and system integration testing of the Spin System will be accomplished at the ORNL Power Electronics and Electric Machinery Laboratory is in the National Transportation Research Center (NTRC), which has more than 9,000 square feet of space for developing, fabricating, and testing the next-generation power electronics and electric machine technologies. Lab testing of the complete V2G system with the SPIN system and LG battery packs will be accomplished at the Distributed Energy Communications and Control (DECC) Laboratory at ORNL which focuses on distribution system control and operation, grid interconnection and control of distributed energy resources including energy storage and electric vehicles, as well as smart grid, and communication applications.
- The University of California, San Diego, also known as UCSD, is a public research university located in the La Jolla neighborhood of San Diego California in the United States. The university occupies 2,141 acres near the coast of the Pacific Ocean with the main campus resting on approximately 1,152 acres. UC San Diego is the seventh oldest of the 10 University of California campuses. UCSD is the host and testing site for multiple California Energy Commission funded EV Infrastructure projects with a comprehensive installation of DC Fast Chargers and AC Level 2 EVSEs from multiple manufacturers and EV service providers.
- Fiat Chrysler Automobiles Group: Fiat Chrysler group's Auburn Hills engineering center has world-class facilities and engineering staff that will be leveraged to do vehicle software and CAN bus integration of the grid communications hardware and software, as well as system commissioning and integration with SPIN module available for functional testing and performance assessment. One Pacifica PHEV will remain with Chrysler to validate any software or hardware changes in the lab before making them in the field.

## Results

### *Hardware Development / Readiness / Acceptance Testing*

SPIN rack hardware, after delays in the component supplier deliveries, was finally assembled, tested and delivered to ORNL NTRC in December 2018. Following Figure III.9.1 shows the hardware and test setup that was utilized to do power mode testing for all the SPIN operating modes. SPIN rack is on the right half inside the yellow oval. This was after the supplier completed the upgrade of the SPIN Proof of Concept Rack System to the latest Version 5 OBCMs (On Board Charge Module). Upgrade was necessary to resolve reliability and software issues with the original Version 3 OBCMs. The upgraded SPIN Rack System was then transitioned to Oak Ridge National Laboratory (ORNL) National Research Technical Center (NRTC) for continued DER/V2G functional integration and testing. The supplier also completed production and shipment of one spare set of OBCMs (Two Each). These units were tested within the SPIN rack system prior to shipment.



Figure III.9.1 NRTC Lab Equipment Set Up with SPIN Rack System

**Summary of Testing Results:**

- Ran all DC Switching modes to full power (AC-DC, DC-AC) – demonstrated 11kW with both OBCs operating
- Temperature faults on DC Switch transitions is a known issue – automatically cleared with applied reset/restart software patch
- Switching mode 9 (reduce RESS charging/discharging) not functional due to unknown software supplier issue—FPC work around—will not limit SPIN operation.

Following Figure III.9.2 shows the results of the testing across multiple modes and transitions through power analyzer test data trace.

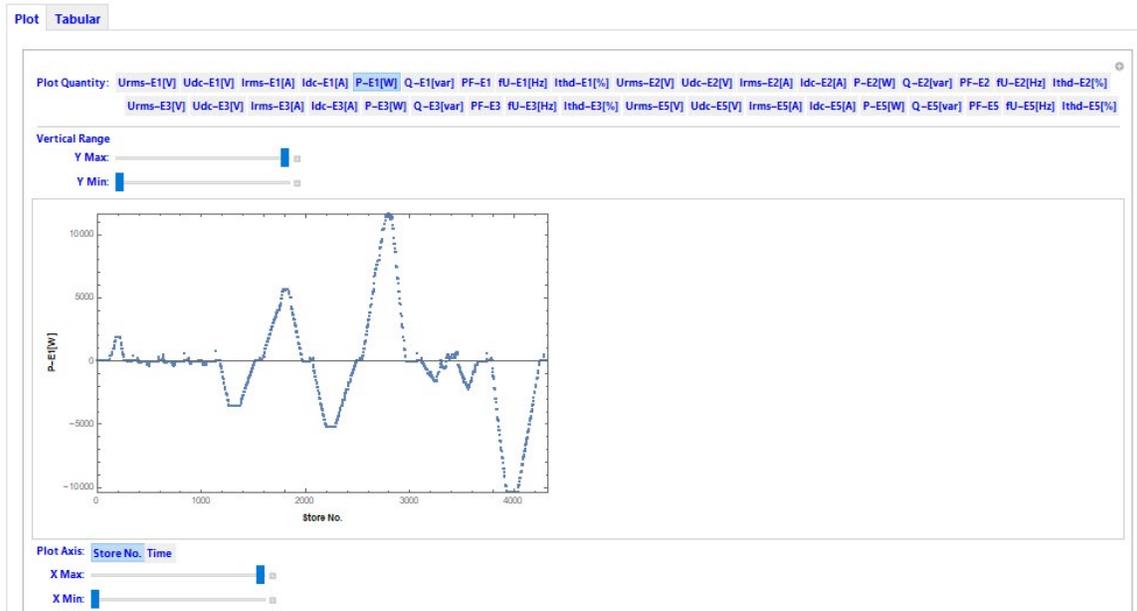


Figure III.9.2 Power Analyzer Test Trace Showing Sequential Execution of All of the SPIN Operating Modes (Source: ORNL NTRC)

### ***DC Convenience Charge Module***

DC Convenience Charge Module (CCM) is the key component of a DC V2G system and essentially functions as a DC charger (AC/DC rectifier) with bidirectional power flow capability (Essentially capable of acting as a four-quadrant smart inverter, through its Dual-Active Bridge (DAB) topology). DC CCM is coupled with the DC-connected DERs (EV, PV, storage) powered by SPIN through the switching matrix also via the same DC bus. CCM specification was created and provided to the supplier. The supplier then delivered the hardware and control electronics as seen in Figure III.9.3. The CCM connects to the vehicle through CCS (Combo) charging connector. The hardware and firmware allowing the bidirectional power capability was delivered and tested to be functional. This will be part of a setup that will be tested at ORNL NTRC as an integrated system.

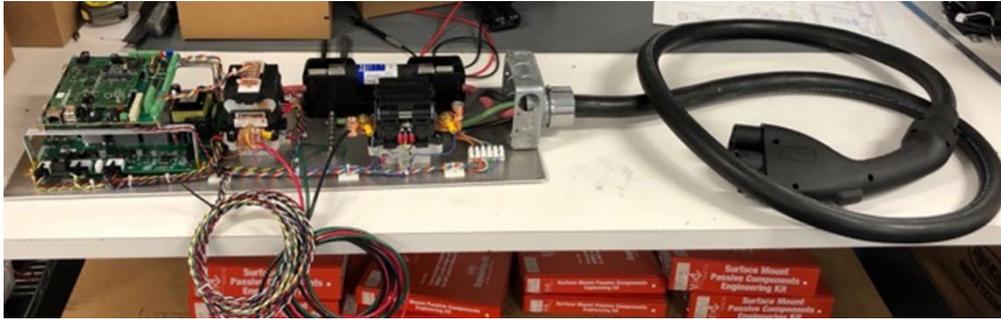


Figure III.9.3 SPIN DC Communications Control Module (CCM) with J1772 Combo Coupler Assembly

### ***On-Vehicle Hardware Modifications:***

On Chrysler Pacifica PHEVs, the only modification that is being done (as compared to on-vehicle V2G project), is replacing the on-vehicle V2G power electronics (bidirectional inverter) with a new V2G communications controller, from IoTecha (EV Communications Controller or EVCC). This includes an STMicroelectronics PLC link to facilitate the physical layer for SPIN – EV communications. The firmware includes an implementation of DIN 70121 specification that allows the DC charging messaging communications per SAE J2847/2 between SPIN and Pacifica PHEV, with an on-vehicle CAN link connecting the EVCC to the vehicle BMS (battery management system). Figure III.9.4 shows a picture of the IoTecha control card (EVCC and SECC (Supply Equipment Communications Controller) are physically almost identical).



Figure III.9.4 IoTecha EVCC and SECC Card Facilitates SPIN to PHEV DC Charging Communications (Source: IoTecha, Inc)



***SPIN System Hardware Layout in Productized Concept:***

Flex Power Controls-led team won yet another DoE SETO award (DE-EE-0008352) to productize the SPIN technology, under FOA 1740. This project is underway currently and will embody all of the learnings from the various contributing projects to-date, to create an integrated DC-coupled multi-port DER ecosystem that is grid-interactive and resiliency-enabling, replete with the necessary customer interface, open standards-based communications and an ability to operate standalone or in a legacy environment with existing smart inverters with PV and storage while allowing EVs to provide V2G services. Figure III.9.5 below shows a conceptual layout of this integrated SPIN system.

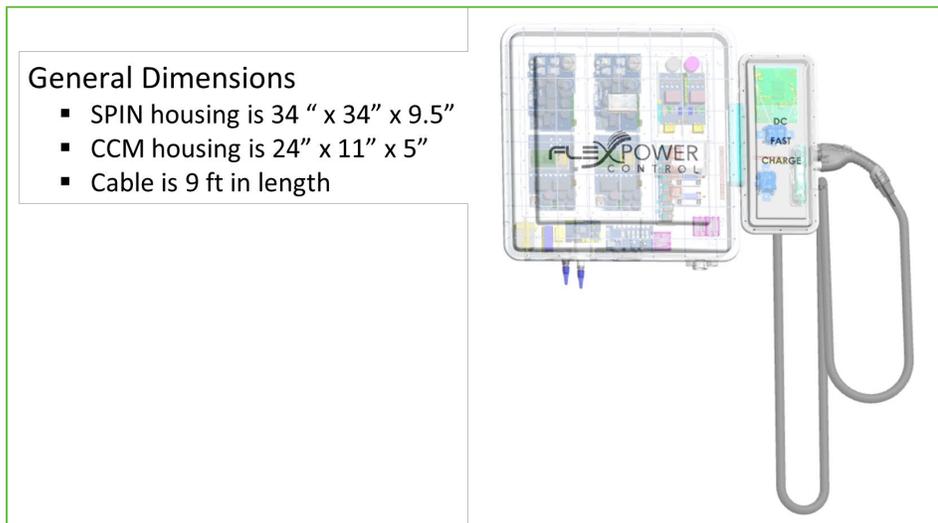


Figure III.9.5 SPIN Product Concept 3D-Layout including DC CCM and Charging Cable

***SPIN System Software: Use Cases, Architecture, Design:***

Through a companion CEC project, the team is implementing applying SPIN module to three distinct scenarios:

1. Standalone, managing residential DERs including V2G capable EV
2. In a grid-interactive building environment, interfacing with the Building Management System (in this case, the BMS resides inside the SPIN itself)
3. In a microgrid interfacing with the DERMS and integrating V2G capable EV.



A description of the key software components is as follows:

***In-Cloud:***

- DSO Server – this server is DSO-resident wide-area DERMS that dispatches DERs across the DSO or in specific segments. The communications to these DERs are over IEEE2030.5-2018 version. A server resides in the cloud

***On SPIN:***

- IEEE 2030.5 client resides on the SPIN. An App wrapper translates the IEEE2030.5 signals to local parameters (and vice versa). This IEEE2030.5 client has a mirror image IEEE2030.5 server that communicates to the IEEE2030.5 client residing in the EV over PLC link facilitated by the IoTecha control card
- SPIN Master Controller: This is the central, orchestration piece that coordinates operation of each of the DERs (PV, EV, Storage) according to the real-time and forecasted conditions while complying with the grid and local energy needs using the information from the vehicle, the DERs and the grid
- SECC – this is the Supply Equipment Communications Controller that enables J2847/2 DIN 70121 communications to enable DC charging and acts as a pass-through for the IEEE2030.5 messages. Figure III.9.8 shows the sequence diagram that explains the coordinated communications between SECC and EVCC and orchestration of DER messages via IEEE2030.5 and DC charging comms via the DIN spec. The reverse power flow is facilitated simply by reversing the current sign (positive to negative)

***On-Vehicle:***

- IEEE2030.5 Client communicates with the IEEE2030.5 server residing on SPIN. Here, On-vehicle V2G project based IEEE2030.5-2013 version client/server pair is leveraged as-is. IEEE2030.5 provides the smart inverter related messages
- DIN70121 client – this enables the vehicle to request negative or positive current from the SPIN, allowing the batteries to either send or receive power from the grid. DIN 70121 client resides on the EV Communications Controller (EVCC) that facilitates the IEEE2030.5 and DIN message communications over PLC link and these messages are locally translated to CAN messages that the vehicle can process.

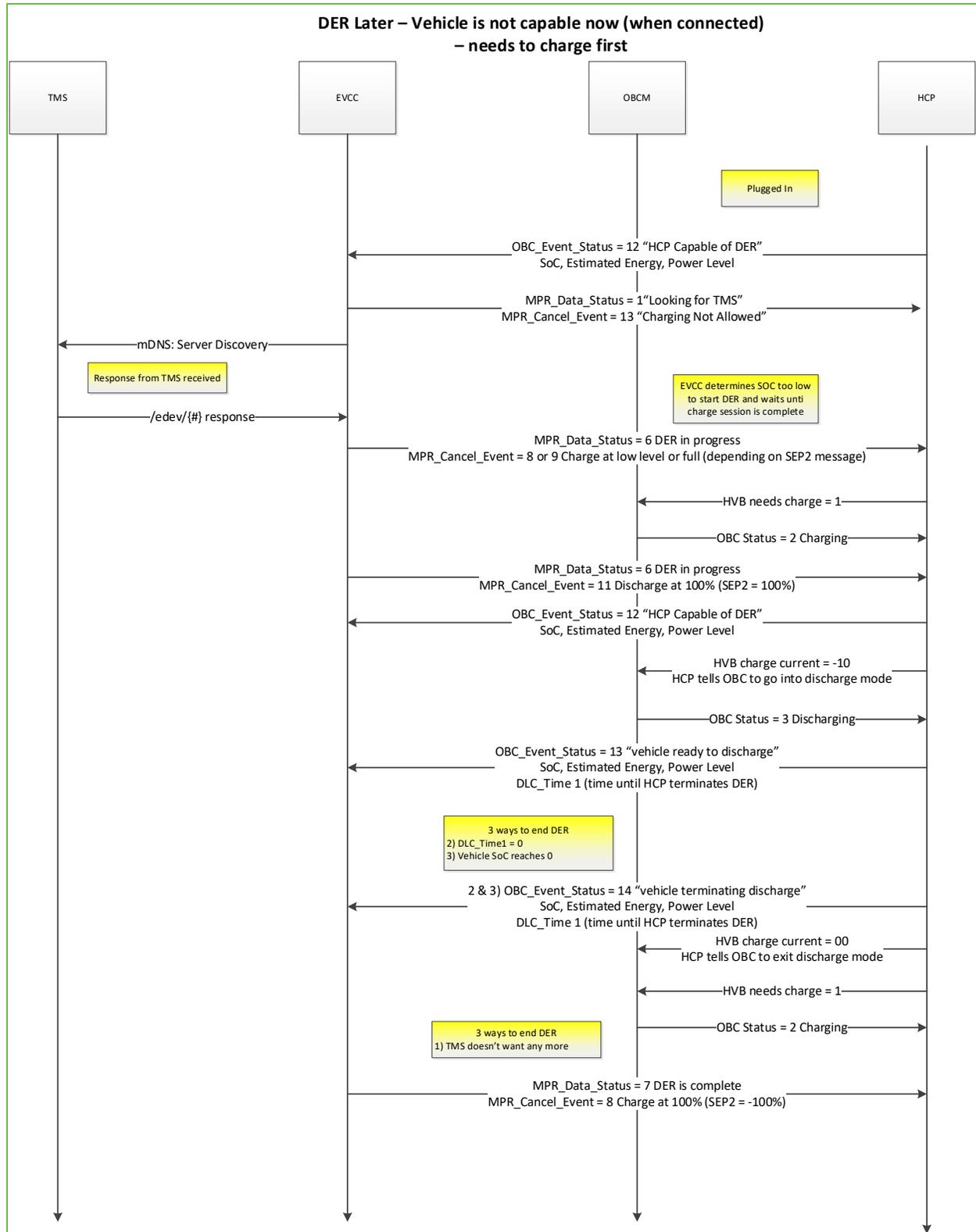


Figure III.9.8 Combined IEEE2030.5 and DIN 70121 Communications Sequence Diagram

**Battery Impact Assessment:**

Planning: FCA has shipped two Chrysler Pacifica PHEV battery packs to NREL ESIF for performance and impact evaluation. NREL is tasked with testing the two battery packs—one on the regular PHEV mobility-only duty cycle and another on a mobility and grid services combined duty cycle, to assess the impact of grid services on the battery life and performance. FCA and NREL agreed to a test protocol that is considered reasonable and more realistic. Table III.9.1 below shows the energy consumption estimates related to this protocol.

**Table III.9.1 Pacifica PHEV Battery Impact Energy Consumption for Test Protocol (Source: FCA, NREL)**

Cycle Discharge ~ 15 mi.					
	Cycle	Time (hr)	Distance (mi)	Energy Throughput (kWh)	Net Energy (kWh)
CD	CD1 City	0.3811	7.44	3.96	2.24
	CD US06	0.1667	8.01	5.27	2.81
CD total		0.5478	15.45	9.22	5.05
Total pack kW					11.8
Usable energy after both drive cycles (kW)					6.75
Proposed discharge power (kW) - available for DER					2
DER Duration (Hrs)					3.375

Table III.9.2 below shows how each of the two packs will be tested. The plan is to exercise the batteries with two cycles run per day, so as to assess one year-worth of battery impacts in six month testing window. In addition, there will be one full deep-discharge cycle at C/3 rate + HPPC (High Power Pulse Characterization) Cycle.

**Table III.9.2 Battery Test Cycle for Grid Services Impact Evaluation**

	Cycle Time (Hours)	
	Pack 1 (Reference)	Pack 2 (Test Pack)
At work		
Drive home	0.5	0.5
discharge at home (10kW)	1	0
charge to 100%	2	1
Wait (key cycle – Contactor open)	1	3
drive to work	0.5	0.5
Charge (50% to 100%)	1	1
Total time/cycle	6	6

The battery cycling has commenced in August 2019 as planned, at NREL ESIF, and will continue until February 2020. The results will be published in the final report.

## Conclusions

Significant progress has been made toward accomplishing the overarching goals of the project during the time period of this annual report. These include the following:

- Delivery of the fully functional SPIN unit and acceptance testing at NREL NTRC of its operational modes
- Definition of DC DER software and communications strategy—an industry first, that will inform both the IEC/ISO and SAE standards
- Definition of the control and communications architecture for information exchange between the grid and SPIN as well as the SPIN and PEV
- Development of SPIN master controller and integration of the IoTecha EVCC and SECC cards on Pacifica PHEV and SPIN, with hardware and firmware updates in progress
- End to end communications bench is being set up to verify system-level communications and control functions before implementing them on the hardware for easy troubleshooting and upgrades
- Pacifica PHEVs from the on-board V2G program have been refreshed to have off-board V2G functionality
- Battery test cycle has been defined and the battery has been provided by FCA to NREL where the test set up has been completed and the battery testing has commenced.

The entire process was not without necessary learnings, which included revising the scope as well as delivery timeline for the fully functional hardware as well as end of Budget Period 2 milestone, as follows:

- Early supplier of SPIN V2G systems turned out to be sub-optimal and resulted in significant (over 8-10 months) delay as well as cost overrun to get them to deliver first functional SPIN hardware. This has since been addressed and the supplier for DC CCM now has been exceptional to work with.
- The SPIN hardware remains at an early stage of maturity (it's a functional breadboard). As such, it was deemed unwise to put this level of hardware through UL certification. So, the UL certification requirement was set aside for the scope of this project (this will be addressed in a follow-on project being conducted by FlexPower (SETO, EE0008352).
- Also, full implementation of CSIP (California Smart Inverter Profile) was deemed out of scope to focus exclusively on integrating the DC V2G functionality, the highest-value outcome of this project.
- Interim deliverable date for the IoTecha control hardware had to be delayed owing to extended NDA negotiations between FCA and IoTecha. This has delayed the project timeline by about 4 months.

## Key Publications

On-Board V2G part of the project resulted in the following publications:

1. [https://www.academia.edu/38676029/Distribution\\_System\\_Constrained\\_Vehicle-to-Grid\\_Services\\_for\\_Improved\\_Grid\\_Stability\\_and\\_Reliability](https://www.academia.edu/38676029/Distribution_System_Constrained_Vehicle-to-Grid_Services_for_Improved_Grid_Stability_and_Reliability)
2. Open Standards-Based Vehicle-to-Grid: Technology Development, EPRI, 3002014770, 2018, <https://membercenter.epri.com/abstracts/Pages/ProductAbstract.aspx?ProductId=00000003002014770>

3. Open Standards-Based Vehicle-to-Grid: Integrated Resource Planning Considerations, EPRI, 3002014801, <https://membercenter.epri.com/abstracts/Pages/ProductAbstract.aspx?ProductId=000000003002014801>
4. Open Standards-Based Vehicle-to-Grid: Value Assessment, EPRI, 3002014771, 2019, <https://membercenter.epri.com/abstracts/Pages/ProductAbstract.aspx?ProductId=000000003002014771>

### **Acknowledgements**

The project team would like to recognize and memorialize exceptional contributions of Late George Bellino, who served as the lead technical coordinator of the multitude of moving parts in a constantly challenging set of circumstances. George passed away on 11/1/2019, and left an indelible mark on the outcome of this project.

The project team would also like to recognize continued encouragement, support and understanding of DoE VTO program managers, John Conley and Lee Slezak, without whose patient guidance, this project would have failed after Budget Period 1!

The Principal Investigator would also like to express his profound gratitude to the entire team including EPRI staff, Flex Power Controls, Fiat Chrysler Automobiles Group, NREL and ORNL scientists and engineers, who formed the backbone of this project. The project success belongs to the team.

### III.10 Enabling Extreme Fast Charging with Energy Storage (Missouri University of Science and Technology)

#### Jonathan W. Kimball, Principal Investigator

Missouri University of Science and Technology  
301 W 16<sup>th</sup> Street  
Rolla, MO 65409  
E-mail: [kimballjw@mst.edu](mailto:kimballjw@mst.edu)

#### Samuel Gillard, DOE Technology Manager

U.S. Department of Energy  
E-mail: [samuel.gillard@ee.doe.gov](mailto:samuel.gillard@ee.doe.gov)

Start Date: October 1, 2018	End Date: December 31, 2019	
Project Funding (FY19): \$1,636,038	DOE share: \$816,826	Non-DOE share: \$819,212

#### Project Introduction

This project aims to advance electric vehicle (EV) adoption by enabling widespread deployment of charging stations that can re-charge an EV in a time similar to refueling a conventional vehicle. The proposed work will create and demonstrate an extreme fast charging (XFC) station that operates at a combined scale exceeding 1 MW while mitigating grid impact with smart charging algorithms and local energy storage. An active front-end (AFE) will connect directly to a distribution feeder and provide reactive power support and harmonic compensation.

The station will incorporate high-frequency transformers instead of conventional low-frequency transformers for isolation, thereby reducing size. A stationary battery will be used to buffer power transients due to charge initiation and termination. The complete station will be coordinated by a high-level controller that uses information gleaned from distribution network analysis to ensure grid compatibility.

There are three basic challenges: power conversion at 1 MW from a medium-voltage (12.47 kV) source; grid compatibility between this large, dynamic load and a wide range of possible distribution networks; and battery charging at high rates (beyond 5C) with minimal degradation. Battery charging algorithm development must account for the internal construction of the cells, modules, and pack, and also requires innovation in the pack design.

#### Objectives

The high-level objective of this project is to demonstrate a complete XFC station, capable of charging three vehicles at 350 kW each, with local energy storage to mitigate active power transients and station control to ensure grid compatibility. The station will connect to a 15-kV-class network (e.g., 12.47 kV three-phase). The objective for the budget period that began in FY 2019 is to develop a sub-scale version of the station.

For the power conversion aspect, the objectives are to develop a laboratory-scale power converter, with 1/10<sup>th</sup> voltage, 1/10<sup>th</sup> current, and 1/100<sup>th</sup> power ratings (1247 V input, 10 kW); to develop a converter control system that coordinates the grid input (AFE) and high-frequency isolated dc-dc converter; and to explore alternative topologies, components, and construction methods.

For the grid compatibility aspect, the objectives are to obtain network data for the demonstration site; to analyze static and transient requirements considering only local impacts; to construct a simulation of the distribution network; and to derive specifications for the XFC station, considering grid compatibility.



For the battery aspect, the objectives are to create a single-particle model of the target lithium-ion cells that incorporates degradation models; to derive optimal charging algorithms; to validate the algorithms experimentally; and to design and document a complete vehicle pack for later testing.

In future budget periods, these separate aspects will be integrated and ultimately demonstrated at a field site.

**Approach**

The overall XFC station architecture is illustrated in Figure III.10.1. The station comprises a multi-level AFE, a multi-phase dc-dc converter with isolation, multiple non-isolated dc-dc converters to provide charging ports, and a bidirectional dc-dc converter that connects to a fixed battery (energy storage system, or ESS).

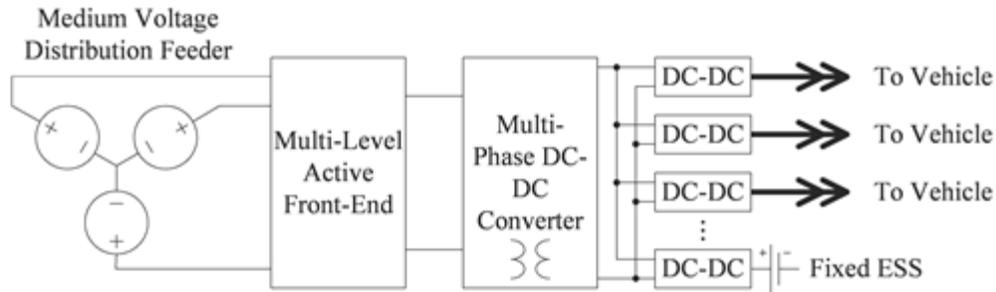


Figure III.10.1 Block-diagram schematic of the XFC station.

The AFE provides a variety of grid service capabilities. As compared to a passive rectifier, an AFE can control active and reactive power, unbalanced current, and harmonics. An AFE is also inherently bidirectional, so that the station can provide peak shaving—storing energy in the ESS when electric rates are low, providing it back when rates are high. Here, the AFE is multi-level so that the station may connect directly to a medium-voltage feeder (e.g., 12.47 kV) with existing, commercially-available power semiconductor devices.

The multi-phase dc-dc converter provides isolation for safety. Rather than conventional low-frequency transformers, the dc-dc converter uses high-frequency transformers for reduced size. As for the AFE, the multiple phases are necessary to enable construction with commercially-available devices. The system will be composed of several modules, each of which incorporates one level of one phase of the AFE and one phase of the isolated dc-dc converter.

The fixed ESS provides active power buffering capabilities. To mitigate the impact of charging transients on the grid, the ESS may provide charging power during transients. In addition, the ESS may be used for arbitrage of time-of-use electric rates.

Other grid compatibility features will be incorporated in various levels of control. The system control architecture has several nested layers, illustrated in Figure III.10.2. Each layer uses input from the layer above and provides output to the layer below and/or the actual power conversion hardware. The exception is the system management layer (startup, shutdown, fault handling), which cuts across all of the others.

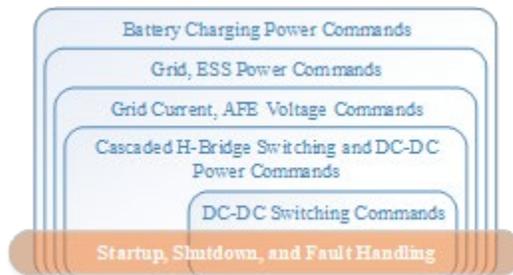


Figure III.10.2 Hierarchical control architecture.

Advanced battery charging algorithms will be derived to minimize degradation. The new algorithms will be based on advanced single-particle models of the cells, incorporating the side reactions expected at any charging rate (SEI layer formation, crack propagation, etc.) as well as those specific to high rates (such as lithium plating). The proposed algorithm replaces the constant-current (CC) portion of a typical algorithm with constant solid-phase concentration gradient at the anode surface (constant gradient, CG). Such an algorithm relies on accurate models that incorporate variable diffusivity.

## Results

### Battery Modeling and Charging Algorithm Development

When the local anode potential becomes negative (vs. Li/Li<sup>+</sup>), deposition of lithium onto the surface of graphite particles will take place. During XFC, ions tend to accumulate on the surface of anode locally, leading to an overpotential that exceeds equilibrium potential. Plated Li metal is hazardous to both the electrochemical performance and safety of cells.

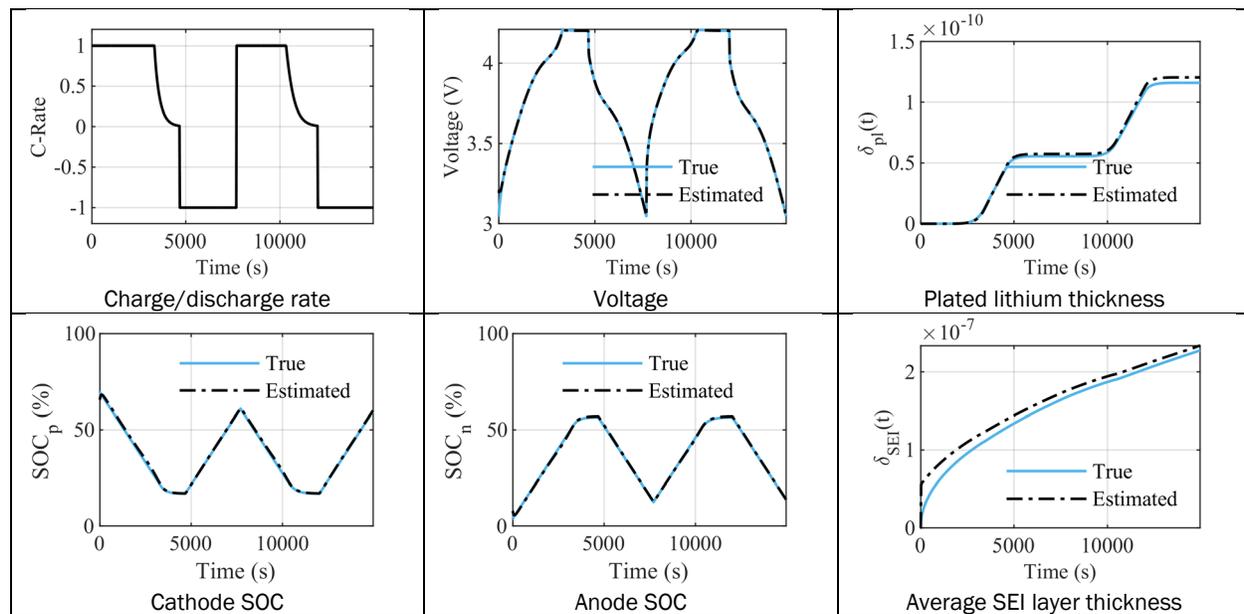


Figure III.10.3 Comparison between full model and estimator for two CCCV cycles at 1C with constant diffusivities.

The Single Particle Model (SPM) is commonly used to describe lithium-ion batteries in place of full electrochemical models since it is more computationally efficient and requires fewer parameters. In addition to SOC and SOH estimation, control-oriented battery models are used to design, test, and implement fast charging algorithms. However, most SPM implementations are inaccurate at high C-rates where the electrolyte-phase dynamics become more important, and do not incorporate degradation effects such as SEI layer formation/growth, crack propagation, lithium plating, and metal dissolution.

The present approach replaces constant electrolyte-phase concentrations with two linear ordinary differential equations (ODEs). A modified form of Fick's law that describes diffusion-induced stress was also approximated by assuming a 4th order spatial distribution. This results in four ODEs, two linear and two nonlinear. SEI layer growth/formation and lithium plating were incorporated at the anode surface. As a result, the model is more accurate, so a more accurate estimator is possible. Results for constant current, constant voltage (CCCV) charge/discharge cycles at 1C are shown in Figure III.10.3.

The SPM is also designed to develop and implement an optimal charging algorithm. The solid-phase concentration gradient at the anode surface is known to be a useful indicator of battery degradation. Thus, in this project, we have proposed that CGCV (constant gradient, constant voltage) will lead to less degradation

than conventional CCCV profiles in the same amount of time. However, CGCV and CCCV charging are equivalent if the solid-phase diffusivities of each electrode are assumed to be constants, but solid-phase diffusivities are functions of SOC. The Galvanostatic Intermittent Titration Technique (GITT) was used to experimentally obtain the diffusivities of anode and cathode half cells as functions of voltage. Results of the open-circuit potentials (OCP) and diffusivity are given in Figure III.10.4.

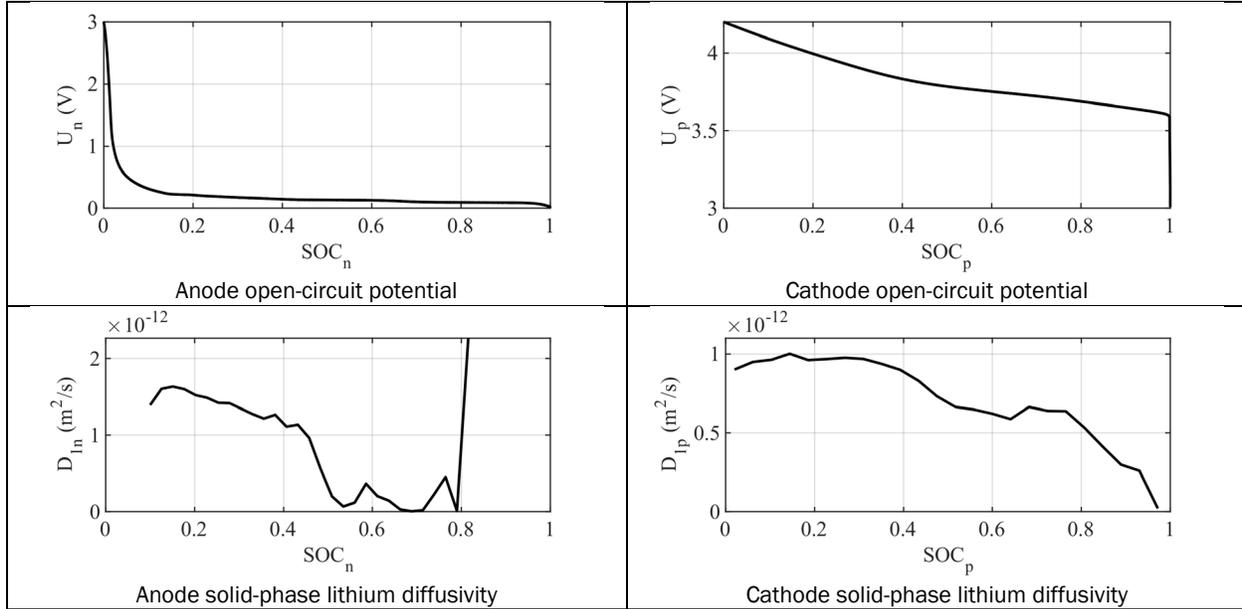


Figure III.10.4 Experimental results for open-circuit potential and solid-phase lithium diffusivity of half-cells.

**Power Converter Development**

In this phase of the project, a lab-scale prototype is being constructed, at 1/10<sup>th</sup> the voltage, 1/10<sup>th</sup> the current, and 1/100<sup>th</sup> the power of the eventual field prototype. This will enable topology exploration, control development, and component optimization before scaling to full size. A module is shown in Figure III.10.5. The complete lab prototype will consist of seven modules per phase, three phases. Each module has two H-bridges, one for the active front-end (AFE) and one for the high-frequency dc-dc converter. Not shown is the high-frequency transformer and the low-voltage side of the converter.



Figure III.10.5 Prototype module to construct cascaded H-bridge.

The AFE will be controlled to have virtual inertia, to mimic the behavior of a synchronous motor and improve frequency and voltage stability of the local grid. Whereas typical AFE controllers assume that the grid impedance is predominantly inductive, distribution systems have significant resistance. Therefore, the proposed approach will use a neural network to adapt to the true impedance of the local grid. Then a model-

predictive controller will issue the optimal voltage command based on both active and reactive power injections. The complete system is illustrated in Figure III.10.6. Figure III.10.6(a) is the loop used to train the model in Figure III.10.6(b). A comparison to conventional and well-tuned classical controllers is shown in Figure III.10.7.

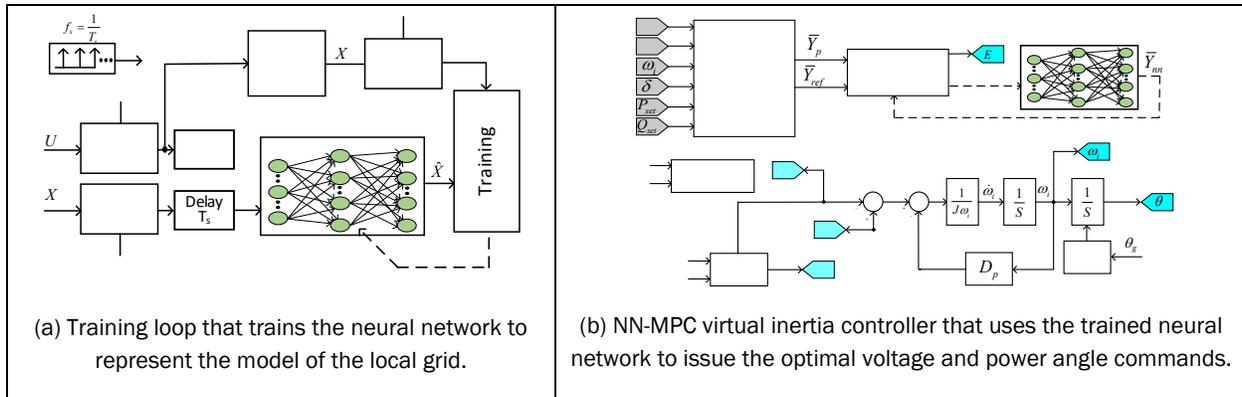


Figure III.10.6 Virtual inertia control scheme.

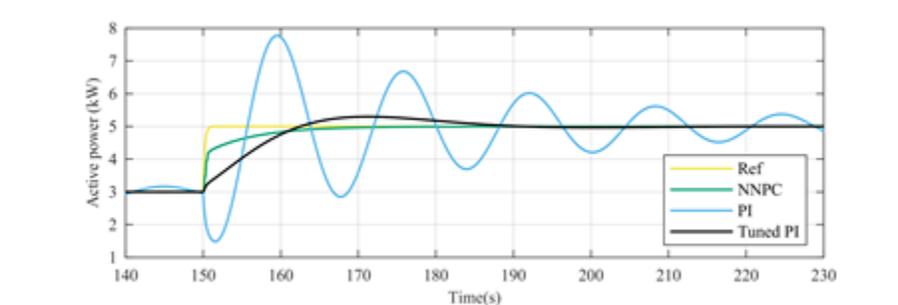
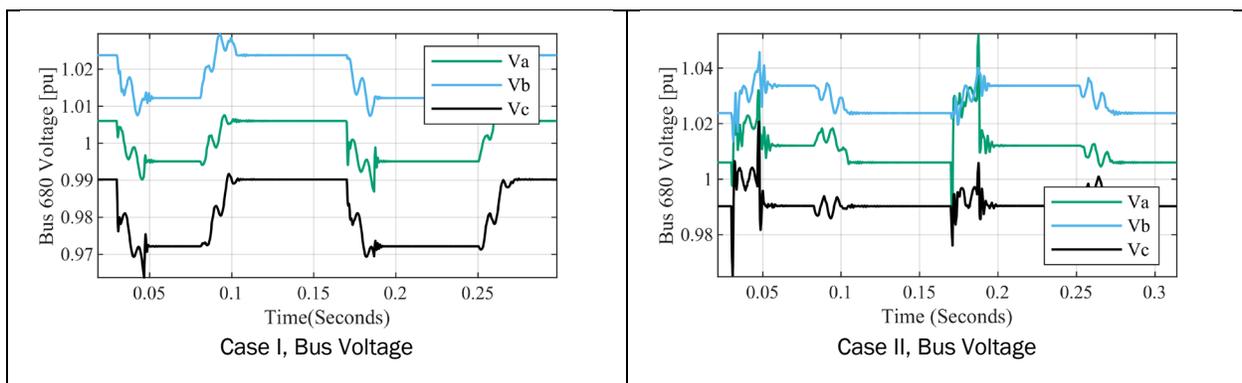


Figure III.10.7. Improved performance of the NN-MPC virtual inertia compared to PI controllers.

### Grid Interface and Compatibility

To prepare for analysis of a specific case, an IEEE standard 13-bus distribution network is being analyzed. An active/reactive power source/sink is modeled and connected to bus #680 (furthest from the substation). Two cases have been studied to demonstrate the transient impact of XFC station load: Case I with 1MW active power consumption only, Case II with 1MW active power consumption and 0.5MVAR reactive power injection. In both cases, the source/sink was switched on, off, on, off at 0.03 s, 0.08 s, 0.17 s, and 0.25 s respectively. Resulting currents and voltages are shown in Figure III.10.8. The reactive power injection stabilizes the grid voltage.



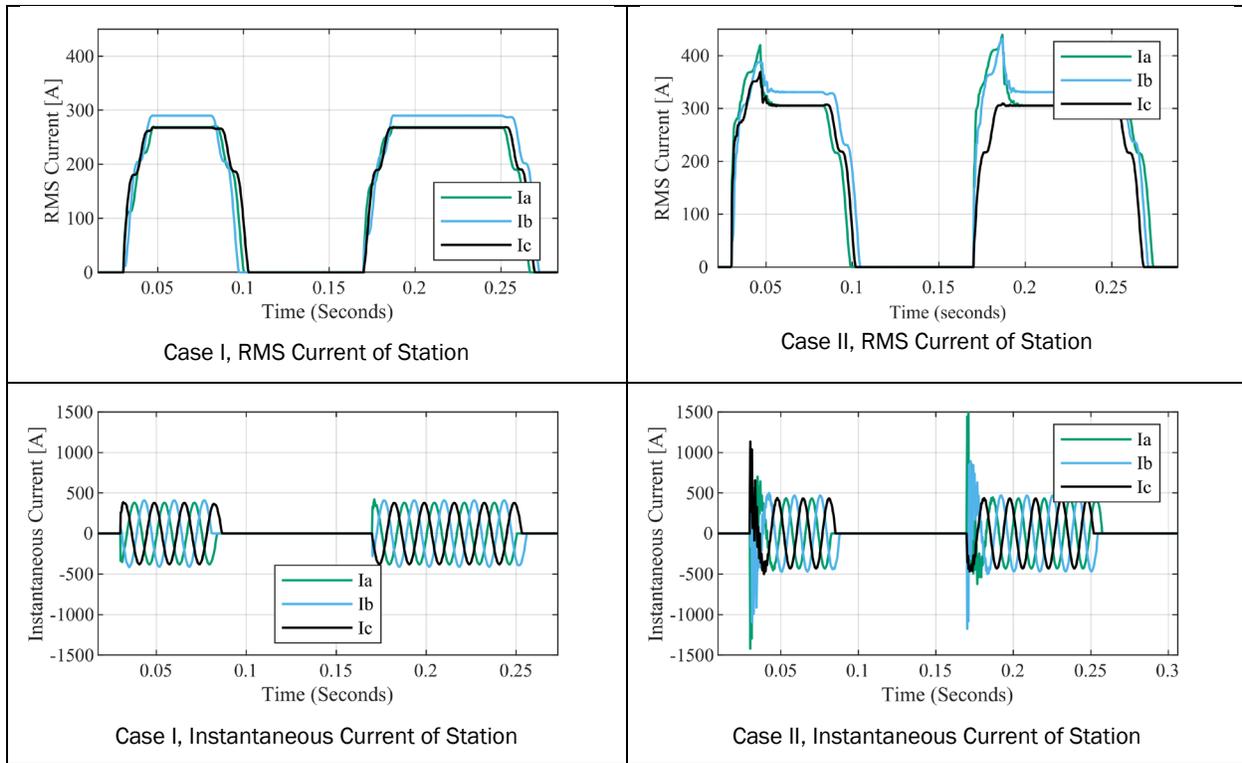


Figure III.10.8 Bus voltage and current without (Case I) and with (Case II) reactive power injection.

**Conclusions**

This project will advance the state of the art in electric vehicle charging by addressing three key challenges: battery charging algorithms for minimal damage during extreme fast charging, medium-voltage power conversion for rapid, inexpensive deployment, and grid compatibility to mitigate the impact of charging transients on the grid. The project began in FY 2019 and has produced some preliminary results on sub-scale analysis, design, and construction, to be completed in FY 2020 and scaled up in future years.

**Acknowledgements**

At Missouri S&T, other faculty on the project are Rui Bo, Mehdi Ferdowsi, Robert Landers, Jonghyun Park, and Pourya Shamsi. Subawardees are Ameren (Jason Wibbenmeyer, Technology Transfer Manager); Bitrode Corporation (Mike Hill, Engineering Director); and LG Chem Michigan (Mohamed Alamgir, Director of Research).

### III.11 Intelligent, Grid-Friendly, Modular Extreme Fast Charging System with Solid-State DC Protection (NCSU)

#### **Srdjan Lukic, Principal Investigator**

North Carolina State University  
1791 Varsity Drive  
Raleigh, NC 27695  
E-mail: [smlukic@ncsu.edu](mailto:smlukic@ncsu.edu)

#### **Steven Boyd, DOE Program Manager**

U.S. Department of Energy  
E-mail: [steven.boyd@ee.doe.gov](mailto:steven.boyd@ee.doe.gov)

Start Date: October 1, 2018	End Date: December 31, 2021	
Project Funding (FY19): \$2,435,511	DOE share: \$1,099,164	Non-DOE share: \$1,336,347

#### **Project Introduction**

With the wider adoption of electric vehicles, there is an urgent need for an electric vehicle (EV) charging infrastructure that will parallel the refueling capabilities of existing gasoline stations, particularly in regions where long-distance trips are common. However, designing and deploying such an EV charging infrastructure is complex, and must consider competing industry standards, available technologies, grid impacts, and other technical and policy issues. With higher penetration of the EVs in the near future, the EV charging infrastructure will present itself as a substantial load and its impact on the power grid could be significant. Specifically, the additional load at a single point can lead to feeder overload and voltage variations beyond the allowable limits along the feeder. Thus, any large extreme fast charger (XFC) installations should control their power factor to help mitigate the voltage deviations, and should be able to curtail their loads in case of a contingency on the grid. Further, if significant generation resources are available at the charging station, the XFC station should allow for bi-directional power flow. Another issue is the availability of utility service at a selected XFC installation location. Feeding loads at hundreds of kilowatts requires new electrical service and significant infrastructure for the grid tie capacity, including step down transformers and metering. Co-locating multiple chargers at the same location allows for the costs associated with new service to be spread over multiple stalls, and allows the station owners to take advantage of lower energy rates that may be available from the utility for large power consumers. This project aims to develop a framework for designing compact and efficient medium voltage (MV) XFC stations for electric vehicles that minimize the negative effect on the power grid, while also minimizing installation and operating costs of the system, and providing design flexibility for the installers and system integrators.

#### **Objectives**

Our proposed solution is to design a novel XFC that addresses many of the challenges associated with high-power charging requirements. The team will design a 1 MVA charger that connects directly to the MV distribution line. The system will consist of a solid-state transformer (SST) that delivers power to a shared DC bus, to which multiple vehicles and storage units connect (see Figure III.11.1). The system will be protected using novel intelligent solid-state DC circuit breakers. Each vehicle will interface to the DC bus through a DC/DC converter, allowing charging in the 50 kW to 350 kW range at the vehicle battery voltage. The innovations of the proposed concept includes an SST that connects directly to the MV line, a dc distribution network feeding multiple DC nodes, and an integrated energy management platform. Each component is described in detail below.

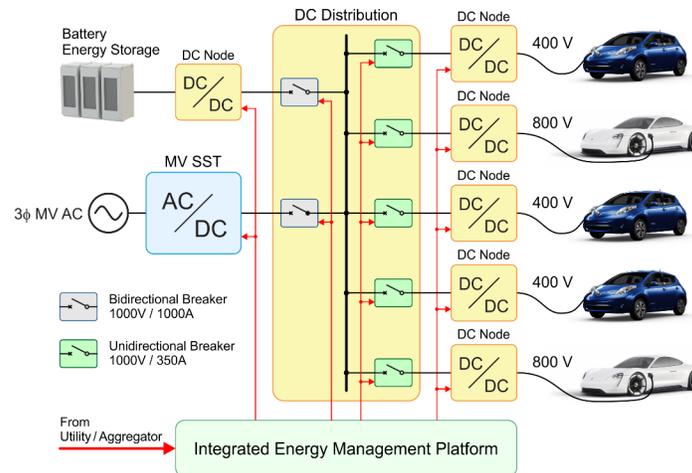


Figure III.11.1 System Layout showing the key components: MV SST, DC distribution network, and DC node that contains the DC/DC converter and vehicle interface

**An SST that connects directly to the medium voltage (MV) line**, without use of a step-down transformer, significantly reduces the system footprint and power conversion losses compared to the state of the art. The smaller footprint allows system installation in space-constrained areas, while significantly reducing installation costs. Higher power conversion efficiency reduces operating costs by delivering more of the input power to the vehicle. The MV SST allows bidirectional power flow and connects directly to the MV distribution grid, eliminating the need for a bulky and inefficient step-down transformer. The MV SST provides ancillary services to the grid to help mitigate power quality issues on its feeder. Key capabilities of the SST are its ability to control the power factor and provide for bi-directional power flow in response to a command from the utility. By controlling the power factor of the station, the MV fast charger not only compensates for its effect on the feeder, but also can help maintain a flat voltage profile along the feeder, resembling a capacitor bank's characteristics.

A DC distribution network allows for efficient, low-cost integration of storage with minimal number of conversion stages between the storage system and the vehicle battery. A key innovation of the proposed approach is the use of a shared DC bus and solid-state protection to supply multiple chargers from a single MV SST. Conventional solutions do not have the ability to share the same power electronics and route the power processing capacity to different stalls. A shared DC bus, on the other hand, naturally allows power sharing between all nodes. Furthermore, the shared DC bus allows for simple integration of storage or renewables directly to the DC bus, thus eliminating the costs and losses associated with the AC/DC conversion stage and simplifying the interconnection to the utility, since no separate utility-grade metering infrastructure is necessary.

DC Nodes using DC/DC converters enable optimal sharing of the available 1 MVA power between multiple vehicles, while reducing the number of power conversion stages. The system will efficiently serve state-of-the-art EVs at voltages below 500 V, at power levels up to 175 kW, while also delivering power to next-generation vehicles following emerging standards, where the vehicle battery operates at voltages up to 1,000 V, at power levels up to 350 kW.

The integrated energy management platform will allow the utility to take control actions including (1) curtailing power delivered to the station; (2) controlling the power ramp rates; and (3) controlling the XFC power factor or the reactive power injection into the grid. Further, the platform will optimally dispatch the available storage resources to satisfy vehicle-charging requirements. The team will deliver a centralized, integrated energy management platform that will communicate with the local storage, EVs, and the utility substation. The integrated solution will use commercial off-the-shelf products and microgrid controller

platforms that communicate with the utility substations. The integrated solution will allow for the optimal use of the available resources, dispatched by the charging station operator or directly by the utility.

## Approach

The scope of this project is to demonstrate operation of the proposed MV fast charger in the field. The system will consist of a medium voltage (MV) solid-state transformer (SST) that delivers power to a shared DC bus, to which multiple vehicles and storage units are connected through DC/DC converters. The DC bus will be protected using novel intelligent solid-state circuit breakers. Each vehicle will interface to the DC bus through a DC node, which contains a correctly sized DC/DC converter, allowing charging at the vehicle battery voltage. The project will be conducted in three budget periods:

**Budget Period 1 – Sub-system Development:** This effort will evaluate the SST, DC node, and DC distribution network designs to optimize for reliability and maintenance simplicity, while keeping system initial cost low. The team will design, prototype and individually test the SST and the DC nodes that make up the 1 MVA XFC station. The team will prototype the DC circuit breaker and demonstrate its operation in the laboratory. The team will select a site and complete engineering drawings for the system deployment. The team will also develop a detailed use case and fault case test plan.

**Budget Period 2 – System Integration:** The team will finalize, package, and test the SST, DC node, DC distribution network and protection, and integrated energy management system. The systems will be fully tested in the lab prior to deployment to ensure that the system operates as expected. The site preparations will be completed to prepare the site for system deployment.

**Budget Period 3 – System Deployment and Demonstration:** The integrated 1 MVA XFC will be shipped to the site and commissioned. The team will demonstrate the use case scenarios and fault scenarios outlined in the test plan and develop a comprehensive operations and maintenance manual.

## Results

The focus in the first year has been on identifying the XFC deployment site; development of the sub-systems that will make up the XFC; and on producing the engineering drawings for the XFC installation. The team has identified a deployment site at NYPA, and has generated the preliminary engineering drawings for the XFC installation. The team has also made progress in designing the SST stage of the converter. So far, the team has identified the SST topology, and has built a small-scale prototype for initial proof of concept. The team demonstrated the system-level control for the SST using the small-scale prototype. Further, we have identified a vendor and the design for the SST high frequency isolation transformers—a critical component of the SST design. The team has determined that using a single DC bus operating at 750V is the lowest risk path for delivering a shared DC distribution bus to the DC nodes. This will allow using near-commercial DC/DC converters as DC nodes. The team also worked on specifying the protection system requirements and on the initial solid-state switchgear prototyping.

### *Deployment Site Selection and Engineering Drawings*

Working with NYPA, the team identified the feeder that will supply the proposed charging station at a location at the Clark Energy Center in Marcy, New York. The selected deployment site meets the project requirements, since the location has a dedicated space for the installation of the medium voltage extreme fast charger and medium voltage service to the location. The team has drafted preliminary single line diagram of EV charging station system, and shared it with NYPA engineers located at the deployment site, who will be responsible for the actual system installation and commissioning. This diagram identifies the key components that will make up the extreme fast charger system including the SST cabinet, the switchgear cabinet, and multiple DC node cabinets that will serve the individual vehicle chargers.



### SST Design and Testing

A key deliverable in the first year of the project is to demonstrate the operation of the MV SST. The team has made significant steps toward reaching this goal. The team finalized the SST topology that will be used to construct the system prototype and has selected the suppliers for all key long-lead-time components, including the isolation transformer and the silicon carbide switching devices.

The selected SST topology is modular, and consists of six “Levels” which are stacked in input-series output-parallel (ISOP) configuration (see Figure III.11.2). The series connection on the input allows for the connection of the system directly to the medium voltage line, which supplies 13.8kV ac line-to-line. Each Level is made up of three identical modules, where each module connects to one of the lines of the three-phase system. Due to this configuration, the instantaneous power pulsation in single phase modules is canceled out within each three-phase Level. Thus, the capacitor voltage variations due to single-phase pulsating power is minimal, and the semiconductor devices and the transformer handle the power pulsations. Each module consists of an active front end (AFE) and an isolated DC/DC stage. The MV ac side forms the well-known cascaded H-bridge topology, while the isolation stage uses the dual active bridge topology (DAB). To minimize the number of modules on the high voltage side, we use the full-bridge neutral-point clamped (NPC) topology for the DAB on the high-voltage side of the DC/DC converter. A centralized controller coordinates the AFEs in all modules. Decentralized control of DAB stage uses only local measurements, thus simplifying the overall system control and coordination. Input line filter and output capacitor size is significantly reduced by using an interleaved modulation of AFEs (six interleaved AFEs in each phase of U, V, and W), and interleaved modulation of low-voltage side bridges of DABs. As mentioned earlier, the DABs are designed to for sinusoidal power flow: three DAB outputs (phases U, V, W) in each level generate DC power. This results in minimal energy storage requirement on MVDC (2kV) bus reducing the size of the medium voltage capacitors.

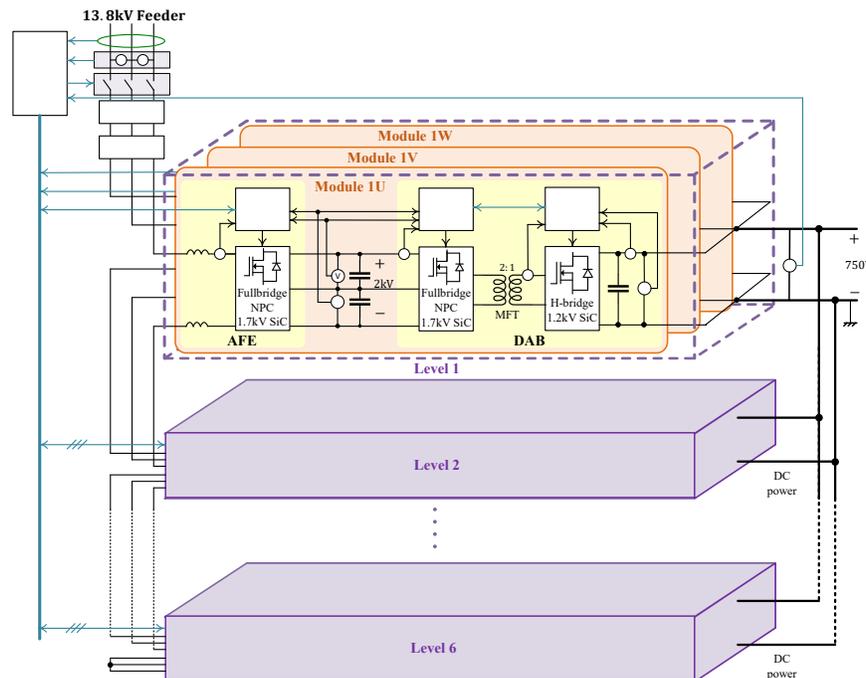


Figure III.11.2 MV SST Converter topology. The SST is made up of 6 Levels connected in input-series output-parallel configuration

To support the development of the SST, the team has designed a low-power prototype of three modules that will make up one Level of the SST. The prototype serves as the initial proof of concept, and allows for system testing and controller design and validation. The small-scale prototype has three 10kW modules that consist of

the AFE stage and the DC/DC converter. Having three stages for testing allows for the development and validation of system and sub-system control algorithms. The team completed the construction of the modules, and has verified the system level control on the scaled down prototype. This includes the verification of the operation of the front end and the isolated DC/DC stage; system level control; and system startup. Figure III.11.3 shows the converter prototype and the experimental results for a single module connected to the ac grid on the input and a variable resistive load on the output. The experimental results show the system response during a load variation. The grid current increases in response to the load variation, while the input grid voltage remains unaffected. Importantly, the MV DC bus voltage remains constant, while the DAB transformer low voltage side current increases in response to the load change, proving experimentally that the DAB is able to control the power pulsations in the single-phase module. The scaled-down system will be in continuous use for system-level control optimization, while the team continues the development of the full-scale prototype.

In addition to the work on the scaled down prototype, the team has been actively looking for a supplier of the

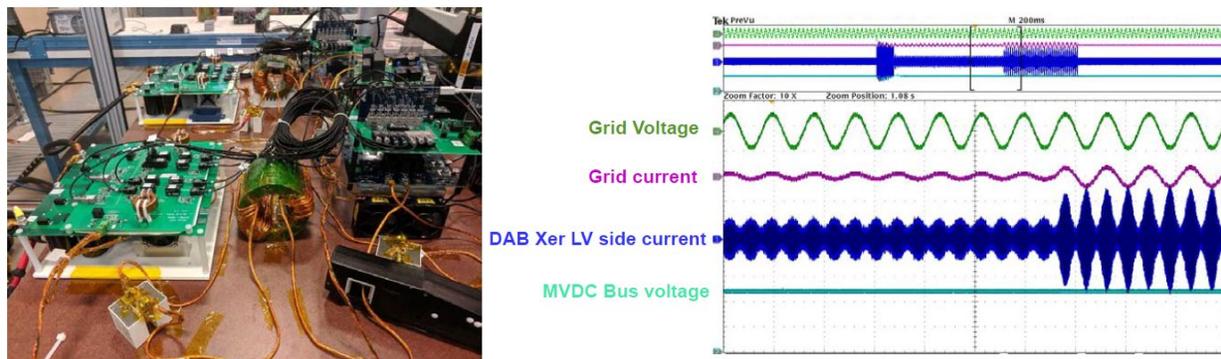


Figure III.11.3. [Left] Small-scale prototype of the SST stage used for control validation [Right] Experimental results showing the behavior of the single module connected to an ac source and a variable DC load. The controller response shows the ability of the DAB stage to handle the power pulsations present in the single phase system

high-voltage, high-frequency transformer. This component is not readily available and must be custom-designed for the application. The team has identified a potential supplier of the high-voltage transformer, and has obtained a quote for this component. Further, the team is developing the high-frequency transformer at NCSU as a contingency plan.

The team has made the strategic decision to use near-commercial DC/DC converters for the needs of the project. These isolated DC/DC converters connect to a 750V DC bus, and deliver voltage between 200V-1000V to the vehicle. Using these near-commercial prototypes will help minimize the project risk, and will simplify the system deployment, since these converters support the existing vehicle communication protocols, thus allowing the XFC station to easily interact with the vehicle battery management systems.

#### ***Solid State DC Protection Circuit Design and Implementation***

The team started developing the DC switchgear and two Solid State DC Circuit Breaker (SS DCCB) sizes (one rated at a nominal current of 1500 A and one rated at 500 A). The 1500 A class SS DCCB will be used as main circuit breakers, one connecting the power from the main power source (SST) and another connecting the battery energy storage system. The 500 A class SS DCCB is a unidirectional breaker that will be used as branch circuit breaker for the protection of the cables transferring power to the SST to the DC/DC converters and protect against short circuit and grounding faults.

The team has identified the system-level requirements, and has defined the technical requirements for the two types of circuit breakers to be designed. Further, the team completed the initial system protection and

coordination simulation; made progress on designing the control board platform for the detection of high di/dt short circuit faults and protection coordination.

Fault scenarios under investigation listed below, and correspond to locations in Figure III.11.4:

1. Fault at the output of the SST
2. Fault at the output of the BESS DC-DC converter
3. Fault at the DC bus (within the switchgear cabinet)
4. Fault on one of the charger branch, just after B2 breaker (high di/dt fault)
5. Fault on one of the charger branch, near the input of the charger DC-DC converter (lower di/dt fault compared to 4).

The fault cases will consider system variances to include different output/input filter capacitances, unidirectional vs bidirectional B2 breakers and (3) different cable impedances.

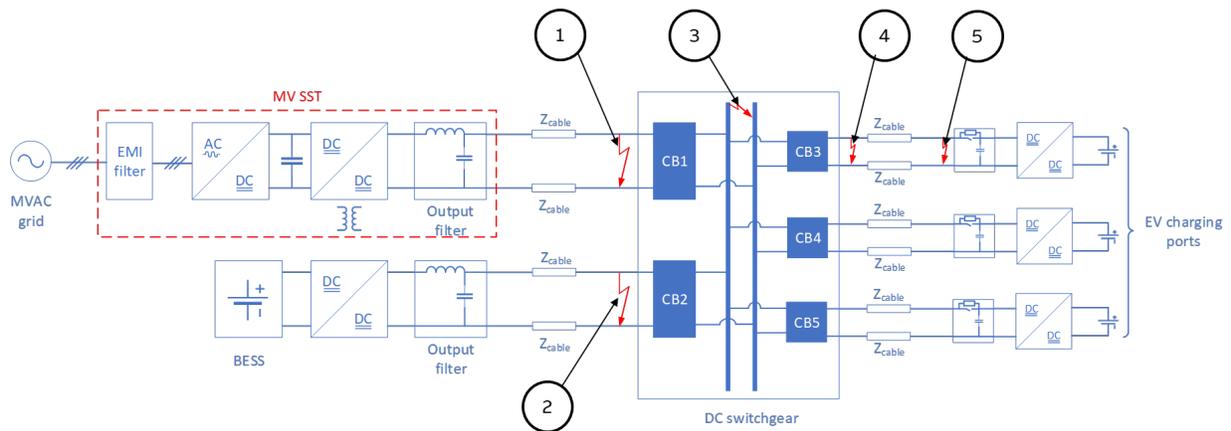


Figure III.11.4 Fault scenarios under investigation

The team developed two types of cooling systems that were optimized for the two circuit breaker classes. One of the cooling systems is based on an advanced thermosyphon, a two phase cooling method dissipates large amounts of heat making it well-suited for the 1500 A class and enables high power density. The main benefits of the advanced thermosyphon design include (1) High Power Density (-60% volume reduction, -50% weight reduction compared to air heatsink) (2) Simplicity of Air cooled solution and (3) Performance similar to liquid cooling but with less auxiliaries and maintenance. The cooling elements were designed for following requirements (1) Thermal loads up to 750 W per cooler, design target  $R_{th} = 0.067$  K/W, with  $\Delta T < 50$  K, at 40 °C intake temperature and (2) Heat flux up to 20 W/cm<sup>2</sup>. Figure III.11.5 illustrates the design of the advanced thermosyphon, its operating principle, and the first batch of manufactured cooling element under thermal test and validation.

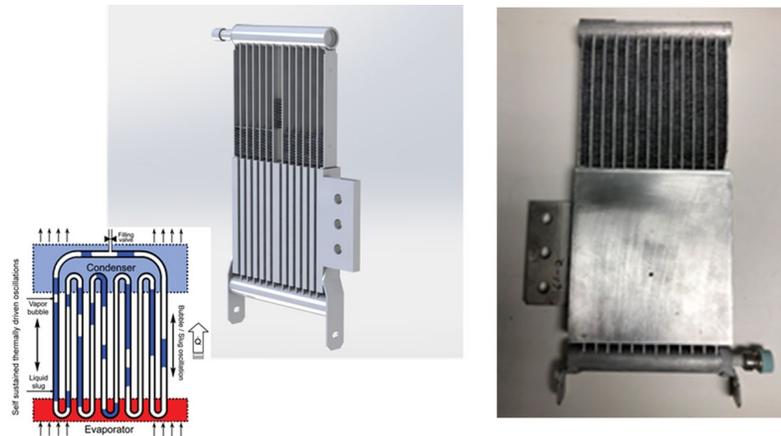


Figure III.11.5. [Left] Advanced thermosyphon design and operating principle [Right] First batch of manufactured advanced thermosyphon for breaker B1

The other cooling system is based on forced-air heat sinks designed for double side cooling of the power semiconductors. This cooling system is easy and economical and it fits well the requirements of the 500 A class SS DCCB. Advantages of forced air-cooling for 500 A include the simplicity and low cost of air-cooled solution and the ability to reduce the footprint for 500 A breaker (<50% volume compared to 1500A breaker). The cooling elements were designed for following requirements: (1) air flow validation for 500 A and overload conditions; (2) Thermal loads up to 250 W per heat sink, design target  $R_{th} = 0.2 \text{ K/W}$ , with  $\Delta T < 50 \text{ K}$ , at  $40^\circ\text{C}$  intake temperature; and (3) Heat flux up to  $10 \text{ W/cm}^2$ . Figure III.11.6 shows the design of the air cooling system.

The team designed, simulated, and manufactured a mixed signal electronic circuit for fast detection circuit of high di/dt faults and for protection coordination. The control circuit was designed for fault detection in less

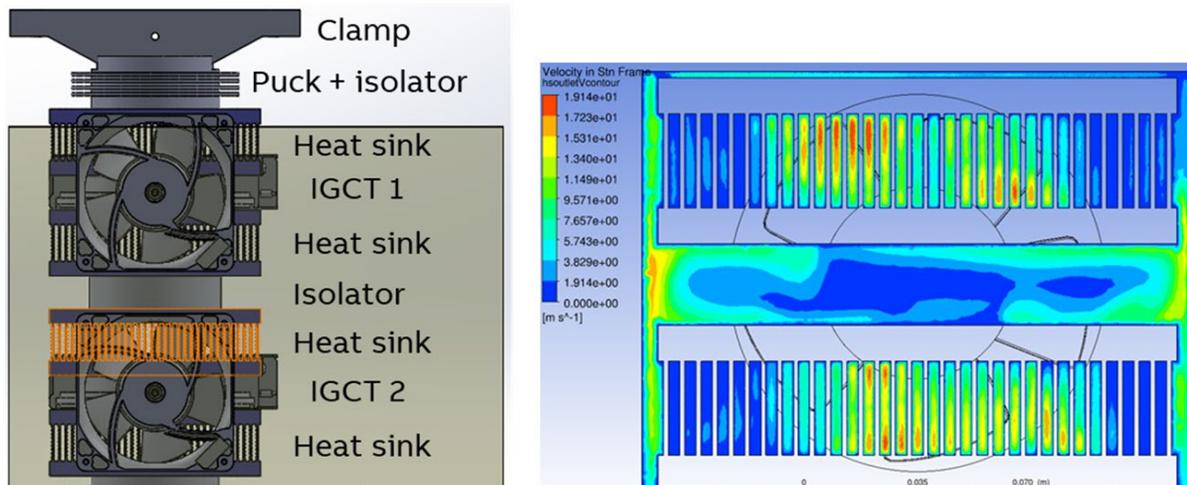


Figure III.11.6 [Left] IGCT stack for 500 A class breaker B2 with forced air cooling system [Right] Air flow analysis for design validation of cooling system for 500 A class breaker B2

than  $10 \mu\text{s}$  for up to  $500\text{A}/\mu\text{s}$ . The mixed signal solution has the robustness of digital filters and logic and the speed of analogue circuits. The fast short circuit detection will enable protection coordination for systems with high power converters penetration, like EV charging infrastructures. Figure III.11.7 illustrates an example of high di/dt current transient during a short circuit event.

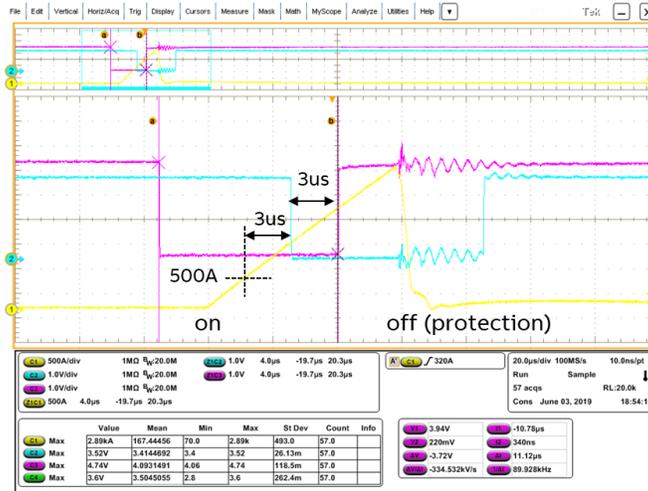


Figure III.11.7 Example of high di/dt current transient during a short circuit event

The team manufactured the cooling system for SS DCCB B1 and the mechanical design of the internal bus bar connections, the custom 40kN mechanical clamp for the bidirectional stack, and the mechanical support structures. The team also designed and manufactured the samples of power stack for the SS DCCB B2 based on the selected and validated cooling elements. The team designed the mechanical support structures and bus bar connections for the galvanic isolation switch and the metal oxide varistors for SS DCCB B2. Figure III.11.8 shows the mechanical designs of SS DCCB B1 and B2. The team also proposed the initial mechanical and thermal design of outdoor rated enclosure for the DC switchgear that will house the SS DCCBs. Input on the high level design and footprint of the DC switchgear was provided for the first assessment of the demo site identified by the team.

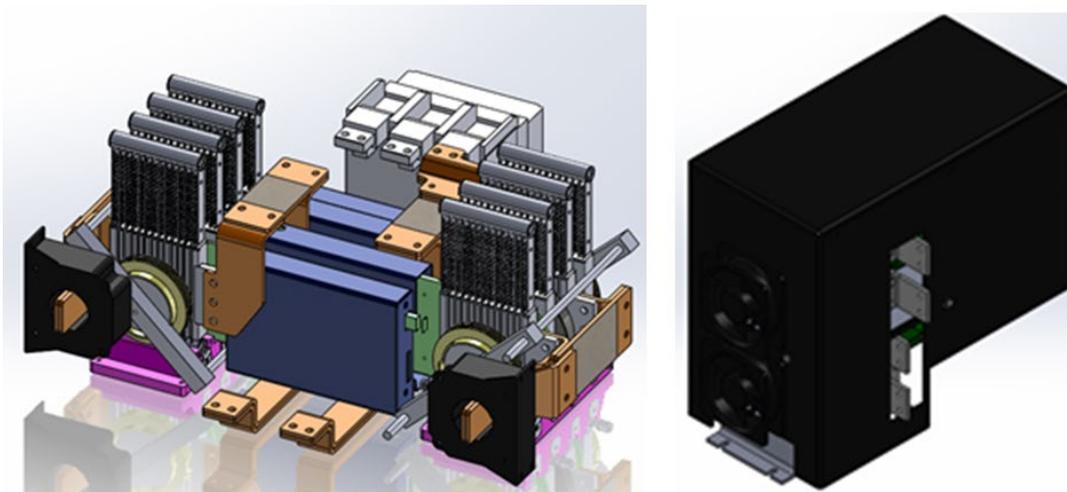


Figure III.11.8 [Left] Mechanical design of SS DCCB B1; [Right] Mechanical design of power stack for unidirectional SS DCCB B2

### Conclusions

In FY19, the project team has made significant progress in all key aspects of the XFC station design. The team has selected the MV SST topology; completed the system-level control simulations, and has constructed a small proof-of-concept prototype to validate the system control. In addition, the team has made significant progress in designing the full-scale SST module and has identified a vendor for the DC/DC stage that will

make up the DC node for the system. The team has made significant progress in developing the DC solid-state breaker and has completed a number of system-level protection coordination studies, which will drive the design of the DC distribution system. Finally, the team has selected the deployment site for the system and is making progress on completing the detailed engineering drawings for the system site.

### **Key Publications**

1. Dakai Wang and Wensong Yu, “Series Connection of SiC MOSFETs with Hybrid Active and Passive Clamping for Solid State Transformer Applications,” to be presented at 2019 IEEE 7th Workshop on Wide Bandgap Power Devices and Applications (WiPDA), Raleigh, NC, October 2019.
2. S. Chen, M. Bipu, D. Wang and W. Yu, “Analysis and Solution of the Unbalanced Device Voltage Issue for SiC MOSFET Based Diode Neutral Point Clamped Converter,” to be presented at 2020 IEEE Applied Power Electronics Conference and Exposition (APEC), New Orleans, LA, USA, March 2020

### III.12 Direct Current Conversion Equipment Connected to the Medium-Voltage Grid for XFC Utilizing a Modular and Interoperable Architecture (EPRI)

#### Watson Collins, Principal Investigator

Electric Power Research Institute, Inc.  
3420 Hillview Avenue  
Palo Alto, CA 94304  
E-mail: [wcollins@epri.com](mailto:wcollins@epri.com)

#### Lee Slezak, DOE Program Manager

U.S. Department of Energy  
E-mail: [Lee.Slezak@ee.doe.gov](mailto:Lee.Slezak@ee.doe.gov)

Start Date: October 1, 2018  
Project Funding: \$5,803,000

End Date: December 31, 2021  
DOE share: \$2,601,500

Non-DOE share: \$3,201,500

#### Project Introduction

With the rapid development of power electronic devices, it is becoming possible to use high frequency pulse width modulated converters as distribution transformers. A power electronics-based solid state medium voltage AC-to-DC converter provides an attractive alternative to a conventional 60Hz magnetic transformer. The system architecture for XFC (Extreme Fast Charging) charging proposed in this project consists of an AC-to-DC converter operating directly from the medium voltage grid without the use of a low-frequency step-down transformer. These converters including a small high-frequency isolation transformer provide the required galvanic isolation, and supply a regulated voltage in the 950-1000V DC range to the other components in the system. This DC voltage is then processed with a non-isolated DC-to-DC converter contained in the “head unit” adjacent to the vehicle, to convert it down to the regulated voltage and current requested by the vehicle. This non-isolated DC-to-DC converter in the head unit, can achieve efficiency levels above 99%. This efficiency exceeds the efficiency of isolated DC-to-DC converters. This combination will achieve efficiency levels well above other system configurations which enable DC micro grids.

Compared to current commercial charger system architectures, the proposed project has the potential to provide several benefits:

- **Reduced Equipment Footprint** – By eliminating the use of medium voltage low-frequency transformers, the site footprint of the XFC is expected to be dramatically smaller, allowing XFC installations in a much wider choice of sites
- **Increased Efficiency** – There is a single galvanic isolation barrier, improving size and efficiency of the conversions. The voltage distributed the long distance between the power cabinets and the vehicles is at the highest voltage possible (950-1000V), minimizing any cabling losses, and giving the highest possible total system throughput efficiency
- **Enables DC Microgrids** – The presence of this regulated DC link also provides for a simple method of connection for Distributed Energy Resources (DER) that may be directly interfaced into the DC system without the size, expense, and efficiency losses of DC-to-AC conversion
- **Equipment Sizing** – The power electronics in the medium voltage AC-to-DC converter can be sized to the diversified load of the downstream equipment

- Grid Integration – The capabilities of a converter connected to the medium voltage grid can be utilized to enable the integration of XFC to the utility grid.

The MV AC/DC converter not only decreases in volume and weight compared with conventional transformer, but it can also behave like smart transformer with the advantage of power flow control, reactive power compensation capability and potential fault current limitation. In addition, with this approach, the regulated low voltage DC bus could be used as an interface to renewable resources and storage devices, such as wind, solar, charging stations and DC Microgrid.

Since the power electronics are directly connected to the grid, they are a promising solution that provides voltage regulation, reactive power compensation, DC-sourced renewable integration, and communication capabilities in addition to the traditional step-up/step-down functionality of a transformer. In addition, medium-voltage distributed directly to the point-of-use (XFC head units) simplifies power distribution by eliminating numerous conversion stages to reduce cost and improve efficiency. The full benefits of high voltage distribution, simplified conversion and high efficiency and power density enabled by wide bandgap semiconductors (SiC), has the potential to produce a disruptive impact by reducing energy consumption and cost of operation. The proposed application of power electronics for XFC addresses grid impact, redundancy and scalability, a primary barrier to adoption of higher voltage chargers.

Promising applications beyond ultra-fast charging that can benefit from this technology are: solid-state transformers (SSTs), traction applications, DC Microgrids and data-centers.

### Objectives

The Electric Power Research Institute (“EPRI”), along with Eaton Corporation, National Renewable Energy Laboratory (“NREL”), Tritium, and Argonne National Laboratory will develop and validate a system of plug-in electric vehicle (PEV) XFC equipment with a direct connection to the medium-voltage utility grid with a novel, modular, and interoperable approach. The objective of the project is to develop and demonstrate medium voltage SiC-based AC-DC conversion equipment and the DC-to-DC head unit for use in XFC equipment capable of simultaneously charging multiple light duty PEVs at rates of  $\geq 350$  kW and a combined power level of  $\geq 1$  MW while minimizing the impact on the grid and operational costs.

The project goals are to:

- Develop medium-voltage (“MV”) AC-to-DC conversion equipment and the XFC DC-to-DC head unit for light duty vehicles charging at 350 kW
- Accelerate the development and implementation of DC system architectures that can serve vehicle DC fast charging applications in a modular, interoperable and scalable manner
- Advance technologies that can reduce the grid impacts from XFC and enable the integration of storage and other distributed energy resources with DC fast charging equipment
- Assess the technical, performance and cost implications of the proposed system in serving DC fast charging opportunities.

### Approach

The team will develop a MV solid-state converter-based system employing a novel architecture and a DC-to-DC charging head for XFC of the EVs. Multilevel converter based on cascaded cells has been selected as a preferred topology for medium voltage AC-to-DC converter stage since it is well suited for high power applications due to good control performance, extensive modularity and reduced harmonic distortion. Moreover, a modular converter system can be easily scaled up/down for different voltage and power levels. To decrease system downtime in case of a failure, a modular approach offers built-in redundancy which can be



embedded in the converter and control design process. Additionally, by using standard components in each module manufacturing costs are decreased significantly due to economy of scale.

The team will develop a MV solid-state converter-based system employing a novel architecture and a DC-to-DC charging head for XFC of the EVs. Multilevel converter based on cascaded cells has been selected as a preferred topology for medium voltage AC-to-DC converter stage since it is well suited for high power applications due to good control performance, extensive modularity and reduced harmonic distortion. Moreover, a modular converter system can be easily scaled up/down for different voltage and power levels. To decrease system downtime in case of a failure, a modular approach offers built-in redundancy which can be embedded in the converter and control design process. Additionally, by using standard components in each module manufacturing costs are decreased significantly due to economy of scale.

The proposed topology consists of a cascaded multilevel AC-to-DC rectifiers and a dual-active-bridge (DAB) converters with high-frequency transformers. The AC-to-DC rectifiers act as active front ends that manage the grid and regulate intermediate VDC that serves as the input to DAB converters. The DAB converter consists of a primary and a secondary full-bridge. The two full-bridges are connected to the windings of a two-winding transformer and generate high-frequency/medium frequency (HF/MF) square-wave voltages with amplitudes of the DC port voltages (input and output). The converter is operated by phase shift control where the control variables are the clamping intervals and the phase shifts of the HF/MF voltages. DAB converter is controlled by phase-shift modulation (PSM). The amount of power transferred is controlled by the phase shift angle between the two bridges and the input/output voltages  $V_i$  and  $V_o$ . Active power flows from the leading bridge to the lagging bridge. Two operating modes, corresponding to positive and negative power flow respectively, are possible with this power topology. The symmetry of the circuit configuration enables seamless bidirectional power control.

The team will design and build a MV converter at TRL-5 to validate the concept architecture. The input voltage will be at or above 7.2kV, the power, at 350kW and the MV AC/DC converter will be matched for a charging head from Tritium. The medium voltage AC-to-DC converter will make it possible to extend the industry trend of safely moving medium-voltage close to the application and directly to the charging head units at the charging stations. The DC-to-DC XFC head topology is comprised of six interleaved half-bridges switching into two three-phase cyclic-cascade coupled inductors.

System testing will occur first at the Energy Systems Integration Facility (ESIF) at NREL. NREL will support the evaluation of the XFC system developed under this proposal. This will occur at the Medium-voltage Outdoor Test Area (MVOTA) which is designed to support systems up to 13.2 kV. The MVOTA is arranged with reclosing breakers to simulate two utility distribution feeders at the medium-voltage range. The MVOTA contains two 20-ft by 40-ft and three 10-ft by 10-ft test pads that facilitate easy configuration and connection of a test article to the ESIF AC Research Electrical Distribution Bus (REDB) at either 13.2 kV or 480 V or to the DC REDB at 1000V DC. The AC REDB connection is used to connect the MVOTA to other fixed equipment at ESIF such as the grid simulators (2x 1 MW), utility-scale PV and battery inverters (2x 500 kW, 100 kW), diesel gen. sets (125 kW, 80 kW), and AC load banks (1.1 MW). The grid simulators and AC load banks will be used in this effort to assess the conformance of the equipment to IEEE 1547 and other grid integration requirements of the XFC system.

Testing at NREL will be followed by deployment of the XFC system at a yet-to-be determined demonstration site. The demonstration site will be selected among the sites identified by the participating utilities.

### III.13 High-Efficiency, Medium-Voltage-Input, Solid-State-Transformer-Based 400-kW/1000-V/400-A Extreme Fast Charger for Electric Vehicles (Delta Electronics (Americas) Ltd)

#### Charles Zhu, Principal Investigator

Delta Electronics (Americas) Ltd  
46101 Fremont Boulevard  
Fremont, CA 94538  
Email: [charles.zhu@deltaww.com](mailto:charles.zhu@deltaww.com)

#### Steven Boyd, DOE Program Manager

U.S. Department of Energy  
E-mail: [steven.boyd@ee.doe.gov](mailto:steven.boyd@ee.doe.gov)

Start Date: July 20, 2018

End Date: November 30, 2021

Project Funding: \$7,000,086

DOE share: \$3,499,961

Non-DOE share: \$3,500,124

#### Project Introduction

Range anxiety and long battery charging time continue to be critical challenges to mass adaptation of EVs. A major identified gap to wider adoption of BEVs is the ability and availability to refuel quickly or to fast charge. Studies have shown that in areas where drivers have access to 50-kW or 120-kW fast charge stations, annual electric vehicle (EV) miles traveled (i.e., eVMT) increased by over 25%, even in cases where fast charging was used for 1% to 5% of total charging events [1]. Charge stations of higher power not only alleviate the “range anxiety” and reduce the driver’s waiting time, but also requires less investment. Michigan Energy Office completed a study in early 2019 titled “Electric Vehicle Charger Placement Optimization in Michigan: Phase I – Highways”. This study finds a system with 150kW chargers, though more expensive individually, actually has lower total system cost when compared to a 50kW charging system when serving the same battery size EV [2]. To be truly competitive to the ICEV refueling experience, even higher power stations are necessary. However, high power charge stations would create large power draws from the grid. If this occurs during peak demand periods, grid capacity could be overloaded. This problem needs to be addressed to reduce the impact on the electric utility infrastructure.

The main goal of this project is to develop a 400-kW/400-A XFC system targeting total efficiency of 96.5 percent from the MVAC grid to a vehicle. The novel SST power cell topology, combined with a new silicon carbide (SiC) MOSFET device, enables a 3.5 percent improvement in system efficiency, a 50-percent smaller equipment footprint, and four times less weight than today’s DCFC systems. The SST technology would directly utilize MVAC at 4.8-kV or 13.2-kV. This would eliminate the line frequency transformer (LFT), which steps down medium-voltage AC to 3-Phase 480-V line-to-line voltage in current DCFC systems. Activities in this fiscal year includes specification development, advanced circuit development and 1-phase series SST and Buck cell Integrated test.

#### Objectives

The objectives of the program are:

- To design and test a high-efficiency, medium-voltage-input, solid-state-transformer-based 400-kW Extreme Fast Charger (XFC) for electric vehicles, achieving better than 96.5 percent efficiency
- To demonstrate extreme fast charging with a retrofitted General Motors’ light-duty battery electric vehicle at 3C or higher charging rate for at least 50 percent increase of SOC

- To achieve a 180-mile charge within 10 minutes.

**Approach**

The team first developed the XFC system specification and module specifications. It includes the System architecture, SST specification, DC charger specification, charge interface specification, communication architecture, fault protection specification, and installation specification. The system block diagram is illustrated in Figure III.13.1.

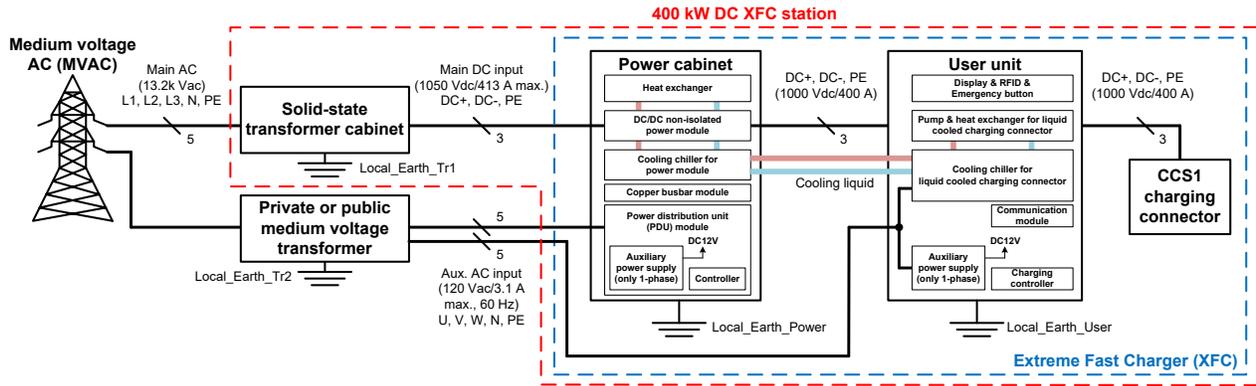


Figure III.13.1 XFC System Architecture

The XFC system consists of a Solid-State Transformer (SST), a Charge Controller (in power cabinet), a Charge Dispenser (A.K.A. User Unit) and an optional Energy Storage System (ESS).

The SST is the key component in the whole system because it has multiple functions such as voltage step-down, AC/DC conversion, MV insulation, and grid interface. Of all the possibilities of medium voltage levels, the standard voltages most often used in the United States are 4.16-KV, 4.8-KV, 12.47-KV, 13.2-KV, 13.8-KV, etc. The team selected modularized architecture to accommodate the various voltages. For the 4.8-kV AC medium-voltage applications, each phase has twelve modules connected in a four-series and three-parallel configurations. Alternatively, for a 13.2-kV medium-voltage application, nine power cells in each phase are connected in series for the higher voltage. For both voltage levels, the outputs of all the power cells are connected in parallel to provide total 400-kW power to the 1-kV intermediate DC bus. Each SST module is rated at 15-kW, which is optimized for the transformer thermal dissipation. Cascaded H-bridge (CHB) topology is used in system level, which lowers the voltage stress on semiconductor devices, reduces the filter size with more voltage level, and improves the power quality and electromagnetic interference (EMI) performance on grid side. The power module's circuit diagram is illustrated in Figure III.13.2.

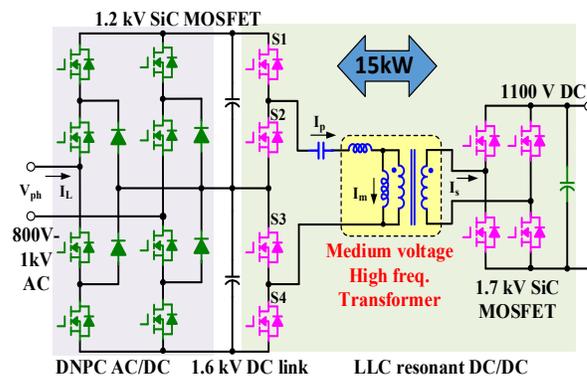


Figure III.13.2 Circuit Diagram of Power Module

Silicon Carbide (SiC) power switches are more suitable for high voltage, high frequencies and high-temperature operation compared to the Si counterparts due to the superior properties [3],[4],[5]. For the SST and charge controller in the XFC system, high-efficiency and high-power density design is expected while the system operates at high voltage and high-switching frequency. As a result, SiC switches are the key technology to achieve the challenging design target.

The transformer winding structure design with medium voltage insulation capability was analyzed in the context of SST converter topology to assess the best system performance. Different insulation material were compared. The transformer loss was simulated to achieve the best balance between winding loss and core loss.

Electrical circuit, mechanical package and control software were developed around the power switch circuit and the isolation transformer. Two sets of version 1.5 SST cells have been built and tested. The picture of SST module is shown in the left half of Figure III.13.3.

The 400-kW charging controller has a modularized design as well. The power modules, each capable of outputting 200-A, are connected in parallel. The maximum output power of each module is determined by the power dissipation and thermal design. Based on the original design target of 120-kW, four charge controller modules will be needed to provide 400-kW. Detailed analysis and simulation shows that the module has potential to output 135kW through design optimization. The charging controller module is based on Buck topology, thus also called Buck module. The buck converter runs at continuous conduction mode (CCM) with 50-kHz switching frequency. A full-bridge SiC MOSFET module with 1.2-kV, 50-A rating is used as the switching device. Two sets of version charging controller modules were built and tested. The picture of charging controller module is shown in the right half of Figure III.13.3.



Figure III.13.3 Picture of an SST Module at left, and Charging Controller (Buck) Module at right

The SST module, the charging controller module and the SST controller were integrated into a 15-kW charge system and tested.

Each SST module is capable of handling 1-kV AC input voltage. Four SST modules were connected in series for single phase of 4.8-kV system, which has 2.77-kV phase voltage. The output of the SST modules are connected in parallel. The output voltage of the SST modules is 1050V, to allow the charging controller to further step down to 1000V or less.

In parallel to the XFC development, General Motor has been developing the vehicle Rechargeable Energy Storage System (RESS), Charge Inlet, and Vehicle Integration Control Module (VICM). The team tested RESS candidate battery cell and verified the cells can take 3C charge and even higher rate for short time. The battery package is configured to receive 400-kW charge power, supporting the program objectives.

## Results

### *SST Module Test*

The SST module was tested on bench. The test result matches the design calculation very well and meets the specification. The peak efficiency is 97.8%. Figure III.13.4 shows one of the operation waveforms of the SST's AC/DC stage and Figure III.13.5 shows the operation waveforms of the SST's DC/DC stage.

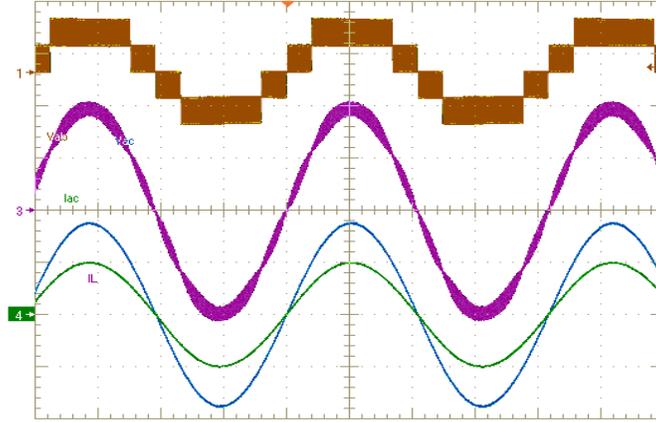


Figure III.13.4 SST's AC/DC Stage Waveforms (CH1 brown:  $V_{ph}$ , CH2 blue:  $V_{AC}$ , CH3 purple:  $I_L$ , CH4 green:  $I_{AC}$ )

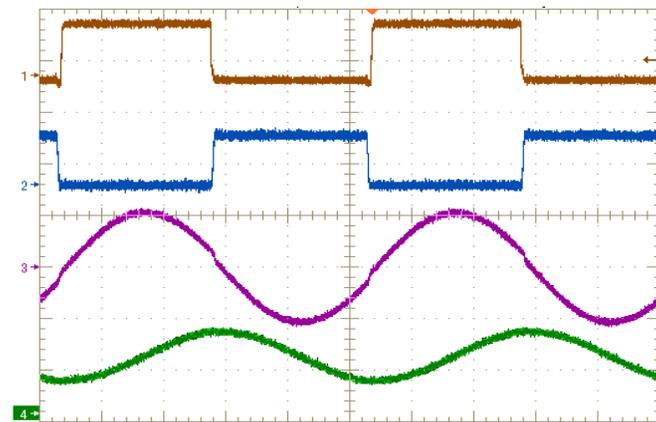


Figure III.13.5 SST's DC/DC Stage Waveforms (CH1 brown:  $V_{GS}$ , CH2 blue:  $V_{DS}$ , CH3 purple:  $I_L$ , CH4 green:  $V_{Cr}$ )

### *Buck Module*

The Buck module was tested on bench. The result matches the design calculation and meets the specification. The peak efficiency is 99.2%.

### *1-Phase Series SST and Buck Module Integrated Test*

The four SST modules are integrated into the SST cabinet at center. The cabinet at left contains the line filter inductors, line voltage sensors and current sensors. The cabinet at right contains the SST controller and output filter. Figure III.13.6 shows the test system.



Figure III.13.6 1-Phase Series SST and Buck Module Test Setup (up to 45-kW)

This system was tested from 4.5kW to 45-kW and in a wide range of input voltage and output voltage. Figure III.13.7 shows the efficiency test result.

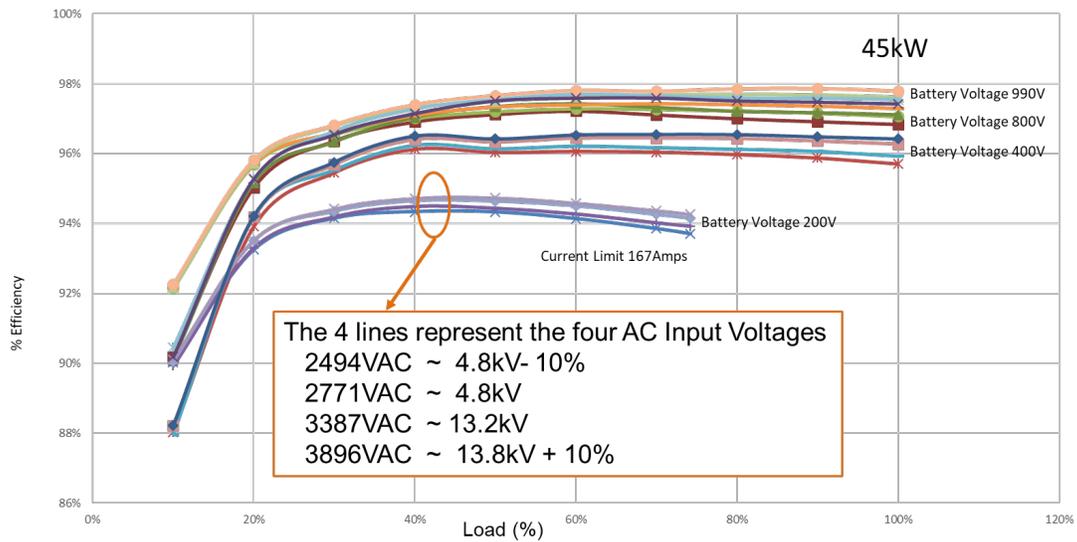


Figure III.13.7 1-Phase Series SST and Buck Module Efficiency Test Result (up to 45-kW)

## Conclusions

The test result shows that the SST module and the Buck module meet the specification. The integration of the series SST and Buck module is successful. The program objects of FY 2019 is completely met. The next step is to integrate three 1-phase series SST modules into a 3-phase SST and do integration test with the Buck module.

1. J. Pries, V. Galigekere, O.C. Onar, and G. -J. Su, "Coil power density optimization and trade-off study for a 100 kW electric vehicle IPT wireless charging system," in *Proc., IEEE Energy Conversion Congress and Exposition (ECCE)*, September 2018, Portland, OR.
2. V. Galigekere, J. Pries, O.C. Onar, and G. -J. Su, "Design and implementation of an optimized 100 kW stationary wireless charging system for EV battery recharging," in *Proc., IEEE Energy*

## Key Publications

1. Charles Zhu, "180-Mile Charge in 10 Minutes: Utilizing Solid-State-Transformer Technology for Micro-Grid-Capable Extreme Fast Chargers," presentation in SAE Hybrid and Electric Vehicle Technologies Symposium, February 2019, Anaheim Garden Grove, CA.

## References

1. D. Howell, S. Boyd, B. Cunningham, S. Gillard, and L. Slezak, "Enabling Fast Charging: A Technology Gap Assessment," U.S. Department of Energy, October 2017. [Online]. Available: <https://energy.gov/sites/prod/files/2017/10/f38/XFCn%20Technologyn%20Gapn%20Assessmentn%20Reportn%20FINALn%2010202017.pdf>
2. Mehrnaz Ghamami, Ali Zockaie, Joy Wang, Steven Miller, "Electric Vehicle Charger Placement Optimization in Michigan: Phase I – Highways", Michigan Energy Office, February 2019. [Online]. Available: [https://www.michigan.gov/documents/energy/EV-Charger-Placement-Opt-PhaseI-Final-Report-021319\\_646220\\_7.pdf](https://www.michigan.gov/documents/energy/EV-Charger-Placement-Opt-PhaseI-Final-Report-021319_646220_7.pdf)
3. L. D. Stevanovic, K. S. Matocha, P. A. Losee, J. S. Glaser, J. J. Nasadoski, and S. D. Arthur, "Recent Advances in Silicon Carbide MOSFET Power Devices," 2010 Twenty-Fifth Annual IEEE Applied Power Electronics Conference and Exposition (APEC), Palm Springs, CA, 2010, pp. 401-407.
4. J. S. Glaser, J. J. Nasadoski, P. A. Losee, A. S. Kashyap, K. S. Matocha, J. L. Garrett, and L. D. Stevanovic, "Direct Comparison of Silicon and Silicon Carbide Power Transistors in High-frequency Hard-switched Applications," 2011 Twenty-Sixth Annual IEEE Applied Power Electronics Conference and Exposition (APEC), Fort Worth, TX, 2011, pp. 1049-1056.
5. T. Daranagama, N. Udugampola, R. McMahon, and F. Udrea, "Comparative Analysis of Static and Switching Performance of 1.2 kV Commercial SiC Transistors for High Power Density Applications," The 1st IEEE Workshop on Wide Bandgap Power Devices and Applications, Columbus, OH, 2013, pp. 48-51.

## Acknowledgements

This work is supported by the DOE Office of Energy Efficiency and Renewable Energy, Vehicle Technologies Office, and administrated by National Energy Technology Laboratory, under contract number DE-EE0008361. The author wishes to thank project team members:

Steven Boyd and Lee Slezak VTO and John Jason Conley of NETL for their contributions.

## IV Grid and Infrastructure Grid Interoperability and Control

### IV.1 Smart Vehicle-Grid Integration (ANL)

#### Keith Hardy, Principal Investigator

Argonne National Laboratory  
9700 S Cass Avenue  
Lemont, IL 60439  
E-mail: [khardy@anl.gov](mailto:khardy@anl.gov)

#### Lee Slezak, DOE Program Manager

U.S. Department of Energy  
E-mail: [Lee.Slezak@ee.doe.gov](mailto:Lee.Slezak@ee.doe.gov)

Start Date: October 1, 2018

End Date: September 30, 2021

Project Funding (FY19): \$1,700,000

DOE share: \$1,700,000

Non-DOE share: \$0

#### Project Introduction

**Problem Statement** – The charging of grid connected vehicles must be managed and controlled or else the impacts of EVs at scale on the grid will be extremely disruptive, expensive, and will lead to the need for increased generating capacity. EVs at scale can contribute to grid resilience and reliability if charged intelligently. This will require controlled charge management that is coordinated with building and distribution network loads and requirements. Grid services previously identified in VTO-sponsored projects must be integrated into Smart Charge Management to maximize the potential benefit of EVs at scale to vehicle owners, building managers, charging network operators, grid services aggregators, and utilities.

Benefits of plug-in vehicles will be fully realized when the automotive, EVSE and utility industries cooperate, technically and programmatically, to ensure an integrated grid perspective and an implementation approach that supports sustainable business. This project takes a step in that direction by partnering with the Global Grid Integration Program, whose members are from US and European automotive, utilities, energy companies and research organizations. The intent is to collaborate on use cases/requirements for vehicle-grid integration and interim technology demonstrations, leading to a ‘public’ demonstration of smart energy management, where vehicles, buildings, renewable energy sources and energy storage are linked to meet the needs of customers as well as the electric power grid. This project will result in a managed network of devices at Argonne’s Smart Energy Plaza capable of demonstrating the use cases/grid services specified by the GMLC and our industry partners.

#### Objectives

**Primary goals** – Demonstrate how smart charge management can be integrated with a network of building systems, renewables and energy storage; using an open source approach to:

- Respond to grid conditions/signals with minimal impact on local operations
- Identify potential benefits/impacts of EVs @ scale (controlled v. uncontrolled charging)
- Maximize the benefits of VGI on the customer-side of the meter
- Develop monetization scenarios of VGI for owners, utilities and aggregators



Achieving this goal necessitates several technical achievements: incorporating protocols for High-Level Communication (HLC) to enable ‘smart’ charging; control strategies that balance the needs on the customer-side of the meter with grid conditions; and enabling technologies (i.e., digital communication, tools to verify interoperability and perform diagnostics). This project’s yearly objectives:

**Year 1** – Establish expectations and requirements for vehicle integration in the home and workplace (with automotive and utility industry partners); demonstrate GMLC use cases using Smart Charge Management. Demonstrate key enabling technologies (e.g., sub-meter system and beta version of DEVA). Define HIL methodology and design of experiments.

**Year 2** – Demonstrate use cases to meet utility/grid demands (e.g., price signals; grid services or emergency power); integrate enabling technologies in the Smart Energy Plaza and develop field test plan with industry partners.

**Year 3** – Demonstrate a fully integrated ‘Grid of Things’ system concept, illustrating the benefits of controlled versus uncontrolled charging using the energy plaza and a simulated grid. Initiate field testing, technology transfer and commercialization studies; plan public demonstration projects with industry partners.

### Approach

Argonne utilizes its integrated network of devices at the Smart Energy Plaza to develop integrated control strategies for EV charging, building power demands, utilizing solar photovoltaic power and interacting with the Argonne grid. This includes demonstrating the flexibility/agility to manage loads and supply power from the customer side of the meter ... considering actual conditions on the grid side of the meter as well as characteristics of a simulated distribution network.

In addition, the plaza is used to demonstrate enabling technologies that support smart energy management, including the Common Integration Platform (CIP.io), Smart Charge Adapter (SCA), the Diagnostic Electric Vehicle Adapter (DEVA), SpEC communication control modules, sub-metering and test equipment to verify interoperability.

#### ***Task 1: Quantify benefits of smart charging (w/GMLC use cases)***

##### **Barriers:**

- Lack of consensus on ‘smart’ VGI communication protocols (i.e., ISO 15118 or SEP2.0)
- Use cases demonstrated in the GMLC 062 project were implemented without the ‘smart’ protocols due to lack of commercially available compliant hardware (EVs and EVSE).

##### **Solution:**

Collaborate with GGIP to refine use case definitions from an industry perspective, facilitate interim technology demonstrations and help source EVs/EVSE with HLC capability. Acquire EVs and EVSE with HLC, link to CIP.io and demonstrate the GMLC-defined use cases using ‘smart’ communication and control (FY 2019 milestones listed):

- Acquire ISO 15118-compliant EVs and EVSE (Q1)
- Adapt ISO 15118 EVSE to CIP.io (Q1)
- Demonstrate demand response and charge mitigation use cases (Q3)
- Demonstrate frequency regulation and charge capacity deferral use cases (Q4).

***Task 2. Develop and demonstrate control strategies for grid integration (GMLC+)***

**Barrier:**

Lack of use cases with DC charging and grid integration based on economics

**Solution:**

Demonstrate additional uses cases identified by technical advisors to the project “to adequately assess the potential benefits of smart charging and its role in providing grid services”. GMLC use cases were limited to AC conductive charging and did not consider the smart charging capabilities of ISO 15118. All of the recommended use cases require smart communication; the two cases planned for FY 2019 are listed.

- Demonstrate Plug’n Charge (Q4)
- Transactive energy trading with cryptocurrency(Q4).

***Task 3. Optimized control for grid resiliency/reliability; Impact of EVs @ scale***

**Barriers:**

- Unknown ability of Smart Charge Management to respond to grid conditions
- Lack of control strategies that consider the customer and the grid simultaneously
- Unknown impact of EVs @ scale.

**Solutions:**

Characterize the ability of a network of controlled devices on the customer side of the meter to respond to grid conditions utilizing control strategies that support the customer and/or the grid. Translate the network responses to node characteristics (i.e., behaviors) in the distributed network model to allow studies of the impact of EV penetration and use patterns at the distribution level. The knowledge from distribution level studies will be translated to INL grid models to identify potential impacts of controlled versus uncontrolled charging on local, regional and national grids.

Since this task must follow the implementation of smart communication with EVs and EVSE, only one task was defined for FY 2019, ‘Requirements and interfaces of Argonne and INL grid models defined’ (Q4).

***Task 4. Early-stage R&D; Interoperability/grid integration components***

**Barriers:**

- Equipment to verify interoperability and identify communication faults
- Compact sub-meters for multi-unit EVSE installations
- VGI solution for OEMs.

**Solutions:**

- Develop and demonstrate the Diagnostic Electric Vehicle Adapter (DEVA) (Q4) – Based on the refined SCA, this device will enable digital communication for smart charge management, assess EV-EVSE interoperability and identify faults. Note that development of the SCA is separately funded by the Technology Commercialization Fund and its status is reported separately
- Compact, low-cost sub-meters (Q4) – Power panel configuration to monitor and report from multiple EVSE plus PV/battery inverter buffer and net load on the main feed to the load center
- Develop the Smart Inlet (TBD) – This device was proposed as a possible solution to VGI following discussions with an OEM in FY 2018. A derivative of the SCA, it would be designed for the inlet

space of an EV (roughly half the size of the SCA). In contrast to the SCA or DEVA, this component would need to meet the more harsh requirements of a vehicle environment.

## Results

Quantifying the benefits of smart charging (Task 1) and developing control strategies for grid integration (Task 2) depend on integrating EVs and EVSE with HLC capability to implement smart energy management. Few EVs and EVSE are available globally with this capability, and none in the US so far. Though some compliant hardware was acquired from Europe, the EVSE were not ‘open’ to allow direct communication and control via CIP.io. The access issues are being resolved with the EVSE OEMs, but the demonstrations of use cases defined in Tasks 1 and 2 have been shifted to FY 2020. Despite the inability to complete the milestones, preparations have been underway to integrate the compliant hardware when the access issues are resolved.

### ***Task 1. Quantify benefits of smart charging (w/GMLC use cases)***

#### ***Milestone 1.1 – Acquisition of ISO 15118-compliant EVs and EVSE***

- The GMLC use cases have been demonstrated with emulated smart charging using simulated vehicle charging patterns and recharge energy requirements
- One compliant EV and two EVSE were acquired from European manufacturers, however neither had open access to implement smart communication and control
- Argonne is in the process of establishing a non-disclosure agreement (NDA) with one EVSE supplier to gain access to their Application Programming Interface (API) and working with a software supplier (and the EVSE OEM) to acquire an interface to the other EVSE. These issues are expected to be resolved in Q1 FY 2020.

#### ***Milestone 1.2 – Integrate ISO 15118-compliant EVSE in CIP.io (originally Q1 2019).***

- An AC charge session was successfully completed with an ISO 15118-compliant EVSE and the Smart ED4, implying that controlling the charge session will be possible when the EVSE API is integrated
- Developed ISO 15118 EV Charge Scheduler with User Interface in CIP.io. Once EVSE API is integrated, CIP.io will be able to schedule charge sessions at Bldg. 300.

#### ***Milestones 1.3-1.6 – Demonstration of Demand Response, Demand Charge Mitigation, Frequency Regulation and Charge Capacity Deferral (originally Q3/Q4 FY 2019)***

These milestones are delayed until the ISO 15118-compliant EV and EVSE are integrated with CIP.io, expected to be accomplished in Q1/Q2 FY 2020.

### ***Task 2. Develop and demonstrate control strategies for grid integration (GMLC+)***

#### ***Milestone 2.1 – Demonstrate Plug’n Charge (originally Q4 FY 2019)***

One acquired EVSE is supposedly designed for Plug’n Charge, but it will not be accessible via CIP.io until the NDA with the manufacturer is in place.

#### ***Milestone 2.2 – Demonstrate Transactive Energy w/Cryptocurrency (originally Q4 FY 2019)***

In addition to requiring smart control capability of EVSE, this use case requires further clarification of the transaction requirements with our industry partners to develop the communication/control requirements. Argonne has developed a Transactive Simulation Framework [\[1\]](#) that could be applied to this case. This milestone is expected to be accomplished by Q3 FY 2020.

### ***Task 3. Optimized control for grid resiliency/reliability; Impact of EVs @ scale***

No progress was made on this task due to both participating labs (ANL and INL) losing their personnel assigned to this task; steps have been taken to resolve the issue in Q1 FY 2020. This has not greatly impacted

the overall schedule due to the slip in implementing smart connectivity in the plaza; the resulting schedule slip is expected to be approximately six months (Q2 FY 2020).

**Task 4. Early-stage R&D; Interoperability/grid integration components**

**Milestone 4.1 – Diagnostic Electric Vehicle Adapter (originally Q4 FY 2019)**

The beta version of DEVA, which utilizes the same hardware as the SCA (Figure IV.1.1), was demonstrated with CIP.io on schedule. The next milestone is to demonstrate High Level Communication (HLC, e.g., ISO 15118 protocol) via Power Line Communication (PLC) in DEVA in Q3 FY 2020.



Figure IV.1.1 SAE J1772 charge connector w/DEVA

**Smart Grid PEV Communication (SpEC) Module 2.0**

This task is a continuation from FY 2019 due to the subcontractor delays, but five alpha boards have been delivered to ANL for driver/application software development. A custom device tree has been developed, the majority of interfaces and functionality have been tested and debugging of the HomePlug Green PHY (HPGP) interfaces is in process.



Figure IV.1.2 SpEC module 2.0 alpha board

**Milestone 4.3 – Compact, low-cost sub-meters (originally Q4 FY 2019)**

The primary achievement was to combine the meters with the AC/DC logic power supply and Olimex ESP32 gateway/data logger to fit in the volume of a SquareD switch rated 240vac/40A two pole circuit breaker (Figure IV.1.3). Work continues on packaging and configuration of the software to connect the stack of MODBUS connected meters to the Olimex gateway, and to CIP.io via MQTT/Node Red. Installation in the Energy Plaza is expected in FY 2020.



Figure IV.1.3 Multi-unit sub-meter (w/o current sensors)

**Milestone 4.2 – Smart Inlet (Go/No Go FY 2020)**

This device was proposed as a possible solution to VGI following discussions with an OEM in FY 2018. It would be a derivative of the SCA, with a new enclosure designed for the existing inlet space of an EV (roughly half the size of the SCA). In contrast to the SCA or DEVA, this component would need to meet the requirements of a more harsh vehicle environment. The Go/No Go decision will follow the SCA pilot demonstration (Q1/Q2 FY 2020) and will be based on obtaining the commitment of an OEM partner with explicit functional and packaging requirements.

**Conclusions**

Progress has been made toward incorporating EVs and EVSE with ‘smart’ communication capabilities in the network at the Smart Energy Plaza; use cases have been demonstrated for controlled and emulated smart charging, EVs and EVSE have been acquired with high level language (i.e., smart) capability and the common integration platform, CIP.io, has been enhanced to enable charge scheduling using ISO 15118. However the GMLC use cases that depend on smart charging have not been demonstrated on schedule due to delays in overcoming the proprietary interfaces of the EVSE. Resolution of the issue is underway with the device manufacturers, but the deliverables are delayed until Q1/Q2 FY 2020.

Substantial progress has been made in the development of enabling technologies. The beta version of the Diagnostic Electric Vehicle Adapter (DEVA) was demonstrated on schedule. Completion of the sub-meter package has been delayed slightly, but integration in the Smart Energy Plaza is expected in FY 2020. Alpha boards for the SpEC 2.0 communication module have been delivered and driver/application software development is underway.

The issues that cause delays in FY 2019, i.e., limited availability of smart EVs/EVSE and proprietary communication interfaces, have been addressed. The project is expected to be on track within the fiscal year.

**Key Publications**

1. Cao, Chong, Bo Chen and Jason Harper. “Plug-in Electric Vehicle Charging Control Adapting to Limited Power Resources.” Paper presented at the 10th Conference on Innovative Smart Grid Technologies, February 18, 2019 – February 21, 2019.
2. Cao, Chong, Bo Chen and Jason Harper. “The Hardware-in-the-Loop Simulation of Vehicle-Grid Integration in a Distribution Grid.” Paper presented at the 2019 IEEE Power and Energy Society General Meeting, August 4, 2019 – August 8, 2019.

**References**

1. D. Dobrzynski, J. D. Harper, “Transactive Framework Simulation”, Copyright 2018, Argonne National Laboratory, SF-19-053.

**Acknowledgements**

The work in this report was conducted by researchers in the Advanced Mobility and Grid Integration Technology Section of the Energy Systems Division of Argonne National Laboratory: Jason Harper, Dan Dobrzynski, Bryan Nystrom and Nick Lau (grid integration, communication and diagnostic technologies) supported by subcontractors Planet Innovation and Chicago Software Solutions; Ted Bohn (sub-metering) supported by subcontractors 2G Engineering and Amzur Technologies.

## IV.2 Scalable Electric Vehicle Smart Charging Using Collaborative Autonomy (LLNL)

### Steve Chapin, Principal Investigator

Lawrence Livermore National Laboratory  
7000 East Avenue  
Livermore, CA 94550  
E-mail: [chapin8@llnl.gov](mailto:chapin8@llnl.gov)

### Jovana Helms, Principal Investigator

Lawrence Livermore National Laboratory  
7000 East Avenue  
Livermore, CA 94550  
E-mail: [helms7@llnl.gov](mailto:helms7@llnl.gov)

### Lee Slezak, DOE Program Manager

U.S. Department of Energy  
E-mail: [Lee.Slezak@ee.doe.gov](mailto:Lee.Slezak@ee.doe.gov)

Start Date: October 1, 2018

End Date: September 30, 2019

Project Funding (FY19): \$766,000

DOE share: \$766,000

Non-DOE share: \$0

### Project Introduction

Since 2011 the number of plug-in electric vehicles (PEVs) has grown exponentially, both in the U.S. and across the world, and this number is expected to continue to grow [1]. Along with these new vehicles, coupled with increases in vehicle battery sizes, comes a large demand for electric vehicle charging stations. The expected increase in electricity demand from PEV charging presents a challenge to reliable power grid operation, as many PEV owners are likely to plug in their vehicles immediately after the morning and afternoon commutes, times of day that are already high-demand periods for the power grid. In this way, unregulated charging would lead to higher demand peaks, increasing the need for controllable generation and thus making reliable power grid operation more difficult.

To illustrate the scale of the problem imposed by widespread EV adoption, consider the Riverside Public Utilities, which has approximately 110,000 metered customers spread across 14 distribution feeders. At the California average of 4% of households having PEV, that means that approximately 4,400 RPU customers have EVs, which is of a scale handled by traditional centralized mechanisms. California had approximately 500,000 PEV as of November 2018 [2], and is expected to grow to 5,000,000-11,000,000 EV by 2030, a 10-to-22-fold increase<sup>6</sup>, and also representing 33-70% of the total vehicles on the road in California. This means that RPU would be supplying charging for 45,000-97,000 vehicles in 2030.

In contrast, if properly managed, the widespread adoption of PEVs presents a mechanism for demand response through vehicle charging. While today most charging stations simply provide power to connected vehicles until the charge capacity is reached, there has been a great deal of interest in developing “smart charging” technology, that is, charging stations with the ability to respond to market signals to control vehicle charging. Smart charging stations have the potential to communicate with the power grid to implement demand response, i.e., intelligently charge PEVs in order to improve charging economics, and to improve the resilience and

<sup>6</sup> A 25% growth rate, which the state has exceeded in 6 of 8 years since 2011, yields 5,000,000 PEV in CA in mid-2026, and almost 11,000,000 EV by 2030.

reliability of the power grid [3]-[9]. With these methods, typically a PEV owner specifies some willingness to have vehicle charging delayed in exchange for a lower price. Given that flexibility, smart charging can be used to shift demand from peak hours to off-peak hours.

Smart charging could also be used to improve power grid stability and protect equipment such as transformers from overloading. Some prior work has considered using PEVs for voltage and frequency regulation in the power grid. In this application, if there is a disturbance in the power grid, e.g., a failure at a major power plant, the smart charging stations can respond by increasing or decreasing the power draw to help regulate voltage or frequency on the power grid [10],[11]. Due to the strain on batteries, most charging customers are unlikely to agree to have their PEVs discharged regularly, but PEV owners may be incentivized to allow their vehicles to be leveraged in this way on the rare occasion that it is necessary to prevent a power outage event or other grid instability.

To the authors' knowledge, no prior work on voltage and frequency regulation with smart chargers has considered the challenges associated with effectively scaling to hundreds of thousands or even millions of PEVs in the system. Most prior work on this topic requires PEVs "register" with a central control system, which sends charge/discharge commands to the connected charging stations. This approach is problematic when the system scales to large numbers of devices, as the control center often must perform some nontrivial calculation (such as the optimization problem solved in [10]) and communicate the results to many smart chargers. Broadcasting messages to a large number of chargers is in itself a nontrivial communication task that takes enough time to hinder the system's ability to respond to voltage and frequency fluctuations in a timely manner.

One approach to the scalability problem is to develop hierarchical systems, in which clusters of smart chargers are governed by individual control computers; clusters of control computers are, in turn, governed by higher-level control computers, and so on until a central controller is reached. This approach is scalable, but brittle: if any point in the control hierarchy fails, an entire branch of smart chargers will be disabled. Such problems have been observed in hierarchical road networks; in 2016, for instance, the Nipigon River Bridge in Canada sustained a partial failure, completely severing traffic between eastern and western Canada for several days. Because the Nipigon River Bridge was a key component in a road hierarchy, its failure caused a widespread problem.

Having a single or a small number of control centers for such a large system also presents a security vulnerability to the power grid. A malicious actor who gained access to the control center could send malicious control commands to the smart charging stations in order to destabilize the power grid, for example, by commanding all charging stations to immediately draw maximum power.

A solution to these issues arises from the field of *collaborative autonomy* (CA), also called collaborative intelligence. Collaborative autonomy comprises of techniques for distributed, networked, multi-agent systems to work together to solve problems autonomously. One can use collaborative autonomy to enable, for example, a group of autonomous vehicles to work together to travel safely at highway speeds; a group of search-and-rescue drones to collectively search for people trapped after natural disasters; or a group of computers to work together to watch for signs of cyber intrusions. Collaborative autonomy is particularly useful when no central controlling computer exists or communication with the central computer is slow or unreliable.

## Objectives

### *Objective for Year 1: Algorithmic Framework Development*

Develop a decentralized, collaborative algorithm that will enable local groups of charging station controllers to coordinate the load reduction responses required by the centralized grid command center, while meeting technological, policy, and contractual constraints imposed at the level of the smart charging stations and possibly at the level of the individual electric vehicles.

To be successful, this algorithm, or family of algorithms, must optimize constraints for all principals in the charging system: the EV owners, the charging station operators, and the distribution system operator (DSO). EV owners will expect the system to meet specified states-of-charge and deadlines at minimum cost; charging station (and network) operators will want to maximize profits or minimize cost; and the DSO will be primarily concerned with maintaining grid stability. The constraints imposed by the DSO are hard constraints that must not be exceeded; the constraints imposed by the EV and charging station owners are soft constraints that may be violated, but with associated penalties that the algorithm(s) will minimize.

### Approach

Our approach is to apply the Alternating Direction Method of Multipliers (ADMM), a powerful method within the field of collaborative autonomy, which allows groups of distributed computers to jointly solve optimization problems [12],[13],[14]. The technique applies to optimization problems whose objective functions are a sum of functions. The problem is first rewritten in *consensus form*, and then that is rewritten in *augmented Lagrangian* form. As seen in Figure IV.2.1, the augmented Lagrangian form allows one to split the problem into multiple sub-problems that can be solved in parallel. ADMM then alternates between solving the sub-problem in parallel and sharing iterate information between computers to update the other variables. ADMM is powerful because it does not require strong assumptions to guarantee convergence and because it works for a wide range of distributed network topologies. It is often used as a parallelization technique to accelerate expensive optimizations. In our case, ADMM provides a flexible framework for smart charging demand response. Any demand response algorithm that can be cast as an optimization problem within the ADMM framework can be used in this setting.

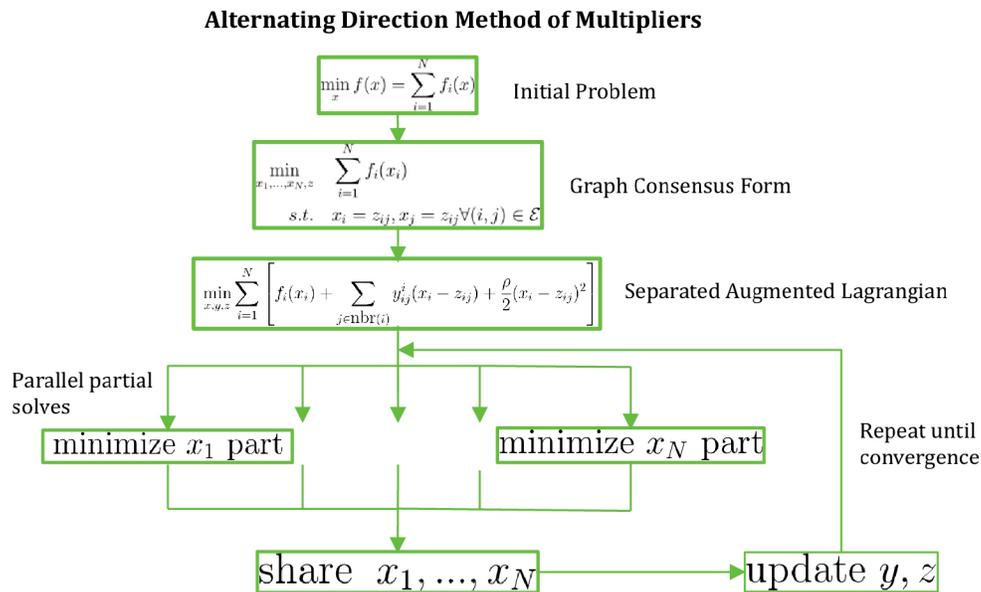


Figure IV.2.1 ADMM allows groups of distributed computers to jointly solve optimization problems

In this project, we are developing a collaborative autonomy-based framework using ADMM to enable a fleet of smart charging stations to implement demand response—as well as possible applications in other ancillary services such as frequency and voltage regulation—in a collective, distributed manner. It is a framework in the sense that we will not develop a single algorithm for demand response; rather, we will develop a means of converting existing demand response techniques into a collaboratively autonomous form, enabling utilities and smart charging companies to employ the effective techniques already in existence, but using our more scalable and more robust platform. The distributed nature of collaborative autonomy enables smart charging stations to respond to events faster than would be possible with a control center in the loop at a scale of hundreds of thousands of charging stations. Furthermore, the flexibility of collaborative autonomy removes single points of



failure so that the loss or compromise of a single machine is never a major problem, making the system as a whole highly robust.

**Results**

**Background Survey**

As part of our initial work, we conducted two literature reviews to survey the existing work in charge management algorithms and to understand the constraints placed on decentralized charge management by deployed charging hardware. The first survey, C. Applegate, “Requirements and Capabilities Needed for Scalable Electric Vehicle Charging Using Collaborative Autonomy,” reviewed communications technologies used by charging stations and looked at the computation capabilities of a typical charging station; the results are summarized in Table IV.2.1 and Table IV.2.2. These limits, particularly the communication limits, require parsimonious resource usage to achieve algorithm scalability. Measuring the performance of our algorithms is a key milestone in year 2.

**Table IV.2.1 Performance characteristics of widely-used charging station communications media**

Media	WiFi	LTE 4G	5G ULL	Wired
Maximum Messages per Period	15 minutes	450,000	4,500	450,000
	4 seconds	2,000	20	2,000
	1 second	500	5	500
Bandwidth	1.3 Gbps	100 Mbps	10 Gbps	1 Gbps

**Table IV.2.2: ChargePoint CT4000 specifications**

Manufacturer	Processor ISA	Clock Speed (GHz)	Storage	Network Interface
ChargePoint CT4000	ARMv5 (32-bit), single core	800 MHz	<ul style="list-style-type: none"> <li>RAM: 512 MB</li> <li>Long-Term: 512 MB</li> </ul>	<ul style="list-style-type: none"> <li>2.4/5 GHz Wi-Fi LAN</li> <li>3G GSM, 3G CDMA WAN</li> </ul>

**Initial Formulations**

The second survey, J. Donadee and A. Musselman, “Electric Vehicle Charging Control Models and Algorithms,” reviewed existing algorithms, and proposed two formulations of charging models that would be suitable to decentralized implementation. We call the two Price Taker and Price Maker. Price Taker accepts a new aggregate load constraint in the form of a price signal, and the utility function minimizes the aggregate billing cost for the customers. Price Maker uses the demand response activities of the vehicles as a factor in determining the price, and seeks to minimize the average price over the time span. To implement the two algorithms, we applied the basic collaborative autonomy framework to the problem of PEV charging control. We modified and extended existing algorithms for PEV charging control to adapt them to use collaborative autonomy.

Preliminary results from the Price Maker model are shown in Figure IV.2.2 and Figure IV.2.3. Figure IV.2.2 shows the net load (base load – solar PV production) based on CAISO data, scaled to a distribution grid with a load cap of 8,000 kVA. In this case, the black line shows a fairly shallow duck curve, and the other lines represent the additional load that would be placed on the distribution grid by adding 1 (red line), 10 (green line), 100 (blue dotted line), or 1,000 (blue dashed line) charging stations, when each charging station draws 18

kW and serve up to three PEV simultaneously. These curves are the result of the Price Maker attempting to average out the charging load over the course of a day. Figure IV.2.3 shows the same data, but with the PEV charging load added to the net load. Note that the red line (1 charging station) is indistinguishable from the net

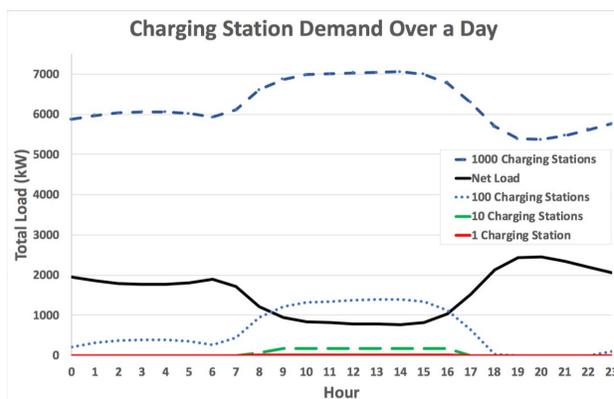


Figure IV.2.2: Charging station demand and net load for an 8,000 kVA distribution grid based on CAISO data

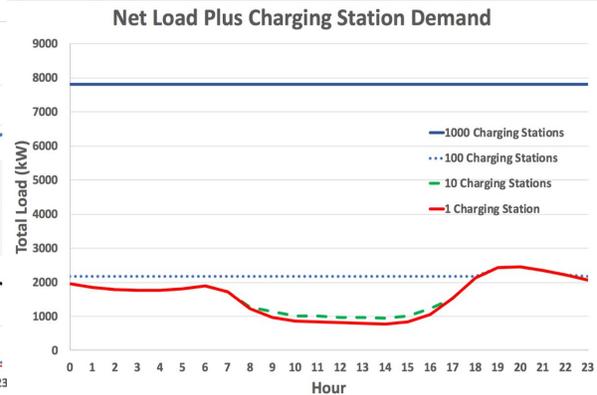


Figure IV.2.3: 100 CS show valley filling; net load from 6-10 pm cannot be flattened by reducing charging load.

load. The green (10 station) line can be discerned, but only during the trough of the day. In both cases, all of the charging is done during peak solar production, but the aggregate load of the PEV is not sufficient to fill the valley, and thus these cases are not interesting. The 1,000 charging station (solid blue line) case is uninteresting for the opposite reason: the aggregate charging demand dominates the net load, and causes the distribution system to run at near capacity for the entire day. The 100 charging station (dotted blue) case is the most interesting. It shows how the model fills in the trough of the duck curve, and does all of its charging before the evening peak at 6pm. Our initial models assume that we know about future vehicle arrivals; to handle arbitrary vehicle arrivals, we will set discrete time periods, and recalculate a new schedule if any vehicles arrive or depart within the window. We will start with a 15-minute window to test feasibility of the approach, and explore the parameter space to understand the tradeoff between window and fleet sizes for scalability.

## Conclusions

Our work developing charge management algorithms in the first year of the project has laid the foundation for future testing in the areas of scale and algorithm enrichment. We will test scale to understand the maximum number of charging stations we can include in time frames suitable for multiple applications, including demand response and frequency and voltage regulation. We will also add loads based on charging session data from our industrial partner, ChargePoint, and accommodate dynamic arrivals and departures. The final topic of investigation for year two will be to extend the framework to manage multiple self-interested parties while preserving grid stability using game theory [15].

## Key Publications

1. J. Donadee and A. Musselman, “Electric Vehicle Charging Control Models and Algorithms,” 2019.
2. C. Applegate, “Requirements and Capabilities Needed for Scalable Electric Vehicle Charging Using Collaborative Autonomy,” 2019.

## References

1. Agency, International Energy, “Global EV Outlook,” 2017. [Online]. Available: <https://www.iea.org/publications/freepublications/publication/GlobalEVOutlook2017.pdf>. [Accessed 8 May 2018].

2. J. Szczesny, "Sales of Electric Vehicles Growing Steadily in California," The Detroit Bureau, 11 Dec 2018. [Online]. Available: <https://www.thedetroitbureau.com/2018/12/sales-of-electric-vehicles-growing-steadily-in-california/>. [Accessed 23 Oct 2019].
3. S. Deilami, A. S. Masoum, P. S. Moses and M. A. S. Masoum, "Real-Time Coordination of Plug-In Electric Vehicle Charging in Smart Grids to Minimize Power Losses and Improve Voltage Profile," *Transactions on Smart Grid*, vol. 2, no. 3, pp. 456-467, Sep 2011.
4. Z. Fan, "A Distributed Demand Response Algorithm and Its Application to PHEV Smart Charging in Smart Grids," *Transactions on Smart Grids*, vol. 3, no. 3, pp. 1280-1290, Sep 2012.
5. P. Zhang, K. Qian, C. Zhou, B. G. Stewart and D. M. Hepburn, "A Methodology for Optimization of Power Systems Demand Due to Electric Vehicle Charging Load," *Transactions on Power Systems*, vol. 27, no. 3, pp. 1628-1636, Aug 2012.
6. S. Shao, M. Pipattanasomporn and S. Rahman, "Demand Response as a Load Shaping Tool in an Intelligent Grid with Electric Vehicles," *Transactions on Smart Grid*, vol. 2, no. 4, pp. 624-631, Dec 2011.
7. P. Finn, C. Fitzpatrick and D. Conolly, "Demand-side Management of Electric Car Charging: Benefits for Consumer and Grid," *Energy*, vol. 42, no. 1, pp. 358-363, 2012.
8. L. Gan, U. Topcu and S. Low, "Optimal Decentralized Protocol for Electric Vehicle Charging," in *50th IEEE Conference on Decision and Control*, Orlando, FL, 2011.
9. R. Abousleiman and R. Scholer, "Smart Charging: System Design and Implementation for Interaction Between Plug-In Electric Vehicles and the Power Grid," *Transactions on Transportation*, vol. 1, no. 1, pp. 18-25, Jun 2015.
10. C. Wu, H. Mohsenian-Rad, J. Huang and J. Jatskevich, "PEV-Based Combined Frequency and Voltage Regulation for Smart Grid," in *PES Innovative Smart Grid Technologies (ISGT)*, Washington, DC, 2012.
11. A. Y. S. Lam, K. C. Leung and V. O. K. Li, "Capacity Estimation for Vehicle-to-Grid Frequency Regulation Services with Smart Charging Mechanism," *Transactions on Smart Grid*, vol. 7, no. 1, pp. 156-166, Jan 2016.
12. S. Boyd, N. Parikh, E. Chu, B. Peleato and J. Eckstein, "Distributed Optimization and Statistical Learning via the Alternating Direction Method of Multipliers," *Foundations and Trends in Machine Learning*, vol. 3, no. 1, pp. 1-122, 2011.
13. N. Parikh and S. Boyd, "Proximal Algorithms," *Foundations and Trends in Optimization*, vol. 1, no. 3, pp. 123-231, 2014.
14. B. Kailkhura, P. Ray, D. Rajan and A. Yen, "Byzantine-Resilient Collaborative Autonomous Detection," in *International Workshop on Computational Advances in Multi-Sensor Adaptive Processing*, Curacao, Netherlands, 2017.
15. F. Munoz-Garcia and D. Toro-Gonzalez, "Pure Strategy Nash Equilibrium and Simultaneous-Move Games with Complete Information," in *Strategy and Game Theory*, Springer, ISBN 978-3-030-11902-7.

### Acknowledgements

We wish to acknowledge the work done by the Stargazer team members: Chloe Applegate, Jonathan Donadee, and Amy Musselman

## V Grid and Infrastructure Fast Charging Enabling Technologies

### V.1 Fast Charging: Interoperability and Integration Technologies (ANL)

#### **Daniel Dobrzynski, Principal Investigator**

Argonne National Laboratory  
9700 S Cass Avenue  
Lemont, IL 60439  
E-mail: [ddobrzynski@anl.gov](mailto:ddobrzynski@anl.gov)

#### **Lee Slezak, DOE Program Manager**

U.S. Department of Energy  
E-mail: [Lee.Slezak@ee.doe.gov](mailto:Lee.Slezak@ee.doe.gov)

Start Date: October 1, 2018	End Date: September 30, 2020	
Project Funding (FY19): \$800,000	DOE share: \$800,000	Non-DOE share:

#### **Project Introduction**

This project addresses key enablers for fast charging, i.e., DC EVSE capable of delivering 150-350 kW, often referred to as extreme fast charging, or xFC. Argonne's areas of interest are testing and evaluation, focusing on EV-EVSE-network connectivity, interoperability and backward compatibility (i.e., the requirement to charge vehicles with a lower battery voltage and 50 kW maximum charge rate).

This is a cooperative project with industry; participation ranges from providing technical support for purchased EVSE to providing complete EVSE system(s) and supporting the testing. Argonne provides infrastructure modifications, hardware installation and testing at the Smart Energy Plaza. The project will provide data and insight to support standards and technology development for xFC implementation in the public domain and enable studies related to grid impacts, energy management and mitigation of peak power demands.

As part of the cooperative agreement between DoE and the European Commission's Joint Research Center (JRC) xFC EVSE systems are being tested at JRC and Argonne, utilizing specific capabilities of each lab, e.g., electromagnetic compatibility and network connectivity/communication, respectively.

#### **Objectives**

The objective is to identify issues associated with EV-EVSE-network connectivity, interoperability and backward compatibility. The project will also develop/verify interoperability test procedures for xFC in cooperation with JRC. Since xFC will be deployed in the public domain in support of DOE's objectives for vehicle fleet electrification, it is necessary to develop procedures to evaluate the functionality and interoperability of the systems.

ANL, in cooperation with industry, developed the requirements, procedures and test equipment for AC interoperability testing (i.e., the SAE J2953 standard). That knowledge was transferred to the joint activity with the Global InterOP team (the precursor of the Global Grid Integration Program) to develop a set of universal AC/DC requirements for verification testing in the US and Europe. This program will utilize that equipment and develop any new procedures deemed necessary.

#### **Approach**

The primary issue is to understand the ramifications of implementing xFC, with peak charging rates of 5 to 50 times current Level 2 AC EVSE. Considerations include the requirements of and implications for the

infrastructure, communication/control requirements and standards for the EV-EVSE connection as well as the grid interface. In addition, xFC must be incorporated in energy management strategies and integrated control schemes with other grid-connected devices (e.g., building energy management systems and battery storage).

The primary technical challenge is to assemble test hardware and implement a test program that covers the range of the vehicles that will utilize xFC systems, i.e., ranging from 50 kW @ ~400Vdc to 350 kW @ ~1000Vdc. Vehicles with 800-900 volt systems (i.e., due to battery charge current limitations) will not be readily available until at least MY 2020, necessitating the use of vehicle emulators for testing.

Argonne proposes a phased testing program that aligns with the expected capabilities of vehicles over the next 2-3 years. Prior to high voltage EVs being available, Argonne will utilize its in-house emulator, a programmable source/sink that is capable of 170 kW and explore the benefits of incorporating available vehicles with 800-900 Vdc batteries (e.g., medium-duty trucks or buses).

The development and adoption of DC interoperability standards are still in process. However, since Argonne and its automotive partners participated in Global InterOP, which led the development of requirements for an AC/DC interoperability test tools for the US and Europe, the requirements and tools will be incorporated in this program.

## Results

### *200kW Charge System*

Installation and commissioning of the EVSE system, including power and user units, was completed in Q1 FY2019. Commissioning included two ad-hoc charging tests and a manufacturer diagnostic evaluation. The results indicated no apparent charging issues. Further testing by Argonne is outlined below.

**Connectivity and Control:** The initial installation of the 200kW charge system included connectivity via OCPP1.5 SOAP. In Q3 FY2019 the system was upgraded to OCPP1.6 JSON. The charge system was integrated in CIP.io seamlessly. The implementation of OCPP was found to be complete and proper.

**Interoperability:** The 200kW station underwent testing using the Comemso Electric Vehicle Charging Analyzer (EVCA). The testing included analysis of the EVSE communication via Power Line Communication (PLC). The EVSE was tested with the EVCA in both EV-simulation mode and man-in-the-middle mode. In both test cases the EVCA showed that both Signal Level Attenuation Characterization (SLAC) and non-SLAC communication from the EVSE followed the HomePlug Green PHY and DIN 70121 standards, respectively. Results are shown in the timing diagrams on the next page.



Figure V.1.1 200 kW DC EVSE Interoperability Testing

Figure V.1.2 depicts the timing diagram and message set for the SLAC matching process. Within this process the EV and EVSE go from un-matched broadcasting mode to develop a unicast closed network where further PLC messaging can be private and direct. The EVCA assessed the EVSE SLAC implementation as technically correct, meaning that EV messages were interpreted and responded to correctly within specified timing thresholds. This should be taken as an indication that the EVSE should not have problems establishing a closed PLC network with any other DIN 70121-capable EV.

After a closed network is established PLC messaging between an EVSE and EV related to charging the EV can begin. This messaging will establish available and preferred protocols, session requests, charge parameter limitations, safety and isolation checks, and charge parameter requests. The messaging between EVSE and EV

is expected to be sequential and within certain timing limits. Figure V.1.3 depicts Comemso EVCA analysis of the EVSE charge-related PLC messaging. The EVCA shows that EVSE messages are properly formatted, in correct sequence and within timing limits. Not shown in the figure are the messages related to EV and EVSE initiated charging shutdown, but the results show the EVSE following protocol properly.

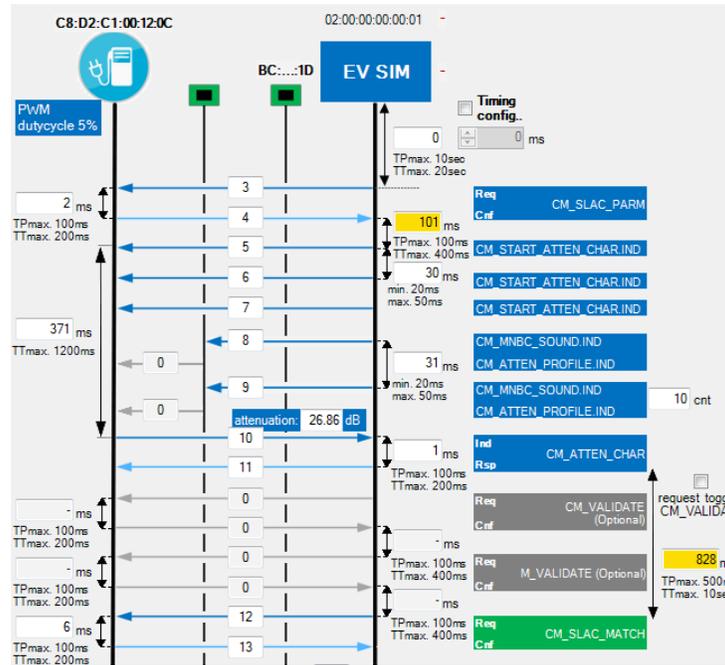


Figure V.1.2 BTC Power SLAC-based Communication

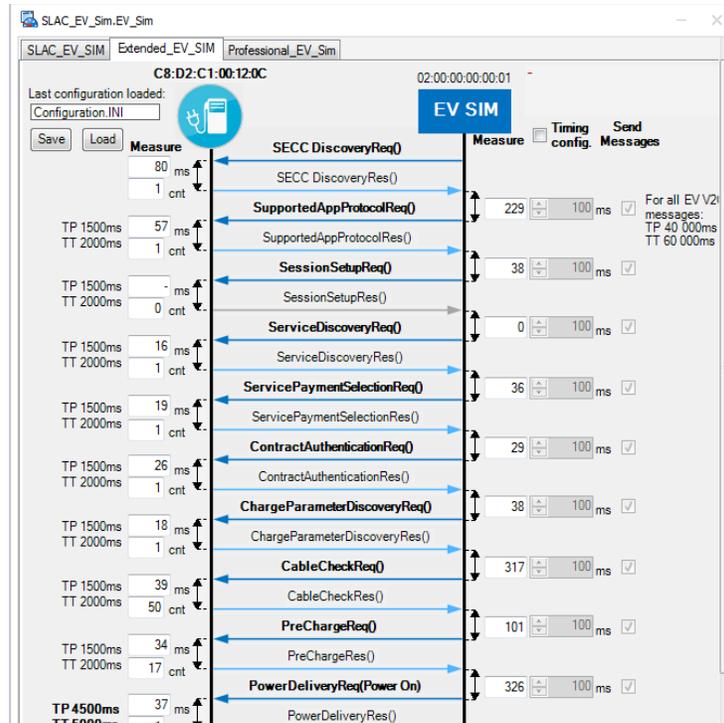


Figure V.1.3 BTCP DCFC Communication Log

**Findings and Issues:** During late Q1 FY2019 the charge system was locked out due to a non-hazardous incident involving an employee EV. The incident resulted in a CHAdeMO connector being stuck in an employee EV. The station was out-of-service from incident occurrence to mid-Q3 FY 2019 when the cable was replaced. Since re-commissioning the charge system has been operating without issue. As of this annual report submission there have been 71 successful OCPP transactions with ANL employee EVs.

**Future work:** Testing charge sessions beyond 50kW, testing with industry- and standards-based testing libraries and evaluating the OCPP smart charging profile.

### **Dual 350kW Charging System**

Phase 1 of the installation was completed in FY18, including transformer station placement, medium and low voltage electrical infrastructure installation. Delivery of the balance of the system (power, cooling and user units) and phase 2 installation was postponed and ultimately cancelled. A replacement system has been procured; delivery and installation are expected in Q2 FY 2020.

### **Findings and Issues:**

- US national electrical code violations associated with the transformer building
- The transformer/charge system was not representative of the vendor's other installations in the US
- Transformer design limited the ability to integrate the charge system with commercial battery energy storage systems, a requirement for the high power charging mitigation and grid integration studies
- Vendor was not able to provide a system that was certified in the US.

**Future Work:** Argonne has procured a dual 400kW system from a US vendor that is consistent with the equipment deployed by Electrify America. The system will be paired with a Battery Energy Storage System (BESS) and integrated with CIP.io to support grid integration and peak power mitigation studies. A candidate BESS solution was identified that meets power, energy and communication requirements to support the Plaza and local grid. Argonne has initiated a lease agreement to allow for advances in battery technology and avoid issues of disposition after the project is complete.

### **Test Procedures and Equipment**

Argonne has aligned its interoperability test procedures with those of our global testing partners. A significant portion of these procedures and test cases were developed in the Global Interop activity (the precursor to the Global G that included OEM partners in the US and Germany, JRC (Ispra, IT location) and Argonne. This activity led to three companies in Germany developing interoperability test equipment. Both JRC and ANL currently use the Comemso EV Charging Analyzer (EVCA) and have developed proficiency in its use and capabilities.

**Functionality:** The Comemso EVCA has extensive analyzing capability. It can analyze in 3 main modes: EV Simulation mode, EVSE Simulation mode, and as man-in-the-middle analyzer. It is compatible with AC and DC EVSE, as well as proximity circuits in the US and Europe. All three modes are PLC capable with Transport Layer Security (TLS) and the ISO 15118 communication protocol. The EVCA performs analysis and read out of the control pilot signaling as well as DC and AC charging waveform analysis. The EVCA is best used as a diagnostic tool when there is a lack of interoperability between an EV and an EVSE.



Figure V.1.4 Comemso EV Charge Analyzer

**Findings and Issues:** The analyzer has been helpful in diagnosis; however, it requires a suite of test libraries to utilize all its capabilities. This is a shortcoming at the moment due to delays in development of the libraries. And the Comemso EVCA software could benefit from further development to make it more convenient and consistent, as well as to reduce the significant training time required to utilize its capabilities properly.

**Future Work:** There are standard test cases adopted by industry that include ISO- and IEC-based for DC charging as well as DIN 70121 and SAE J2953 for AC charging. The test libraries and test scripts for all these cases are only partially available in the Comemso tool currently but can be acquired at a cost; Argonne is considering the purchase of additional test cases as they are developed. Other vendors offer similar tool topologies and expanded testing libraries to compliment the Comemso EVCA; Argonne is considering multiple solutions and plans to extend testing capability as needed.

## Conclusions

Experience in Argonne's Fast Charging Enabling Technologies project indicates that high power charging systems and test equipment have some development remaining before they can be considered commodities. Argonne's lab partner, JRC, has found this to be the case as well. Argonne and JRC agree that one role of the labs is to uncover 'childhood diseases' in new technology and inform the manufacturer accordingly. But the global demand for high power charging is growing at a rapid pace ... charging technology and associated test equipment is expected to mature at a similar rate by necessity.

Argonne's xFC testing observations are based on experience with only two systems, one of which was not placed in operation. The 200 kW xFC system had a few technical issues early on, but when these issues were addressed by the manufacturer it was found to communicate according to the standards using an industry-standard interoperability test tool. And the results showed the EVSE to be backward compatible with EVs below 50 kW charge levels; the DC communication analysis showed consistent messaging and timing. The results also imply that integration of higher power charging stations in communication networks via OCPP should be accomplished with no more effort than lower power EVSE that communicate using OCPP.

The project also demonstrated the need to continue efforts to formalize testing procedures and processes, e.g., implementation of (globally agreed upon) test libraries. The project has developed a baseline for testing and evaluation that will be enhanced with the additional test libraries. The project will lead to a more comprehensive process as Argonne expands testing capabilities, further aligns procedures with JRC and gains access to additional xFC EVSE.



## V.2 Fast Charging: Grid Impacts and Cyber Security (INL)

### John Smart, Principal Investigator

Idaho National Laboratory

P.O. Box 1625

Idaho Falls, ID 83415

E-mail: [john.smart@inl.gov](mailto:john.smart@inl.gov)

### Lee Slezak, DOE Technology Manager

U.S. Department of Energy

E-mail: [Lee.Slezak@ee.doe.gov](mailto:Lee.Slezak@ee.doe.gov)

Start Date: October 1, 2018

End Date: September 30, 2019

Project Funding (FY19): \$425,000

DOE share: \$425,000

Non-DOE share: \$0

### Project Introduction

As the market for electric vehicles (EVs) matures, the charging infrastructure required for an electrified fleet must be reliable, safe, and secure. Technology and engineering advancements must ensure the charging infrastructure provides benefit to, or at least does not negatively impact, the electric grid. Additionally, the charging infrastructure network must be robust to cyber manipulation to ensure safe, reliable, and secure charging operation for the electrified fleet.

### Objectives

The Fast Charging: Grid Impacts and Cyber Security project objective is to investigate and assess the interaction of fast charging with the grid, based on the power demanded during normal EV charging and also during abnormal operation resulting from a malicious cyber attack.

### Approach

As EV charging energy and power requirements increase, the grid impacts and cybersecurity vulnerabilities of fast charging infrastructure must be understood, in order for researchers and product developers to take steps to ensure security and grid stability. During fiscal year 19, this project completed important tasks foundational tasks necessary to achieve this understanding. First, INL installed and characterized the operation of a commercial-off-the-shelf extreme fast charger (XFC) through testing. The purpose of this characterization was to understand how power flows from the grid, through the XFC, to a vehicle during charging. Testing was conducted using a production light-duty EV and a production electric transit bus. A sophisticated data acquisition system was configured to characterize XFC operation with high fidelity. Second, the project also produced a vehicle emulator that is capable of mimicking vehicles with different charge power capacities. This was necessary to allow charging characterization across a range of power levels, including what may be experienced when vehicles with 350-kW charging capability come to market in the future. This vehicle emulator is an important component of INL's power-hardware-in-the-loop platform that will be used in FY20 to simulate fast charging on the grid in real time.

### Results

#### *Extreme Fast Charger Characterization Testing*

XFC characterization testing was conducted using an ABB Terra HP direct current (DC) fast charger, capable of providing up to 350 kW to properly equipped vehicles [1]. Two light-duty EVs (2014 BMW i3 and 2015 Nissan LEAF) and one 60-foot electric transit bus (2019 New Flyer Xcelsior CHARGE bus) were charged during testing. Figure V.2.1 and Figure V.2.2 show the test setup in INL's Electric Vehicle Infrastructure Laboratory.



Figure V.2.1 350-kW XFC charging a 2014 BMW i3 in INL's Electric Vehicle Infrastructure Lab



Figure V.2.2 350-kW XFC charging a New Flyer 60-foot electric transit bus in INL's Electric Vehicle Infrastructure Lab

The charging characteristics differed greatly for these vehicles. This allowed the characterization of XFC operation across a range of conditions. Figure V.2.3 depicts the efficiency of the XFC when charging the three test vehicles. Efficiency of up to 97% was achieved, but efficiency varied considerably during the course of single charge events as charge power ramped up and ramped down according to requirements of the vehicles' battery management systems.

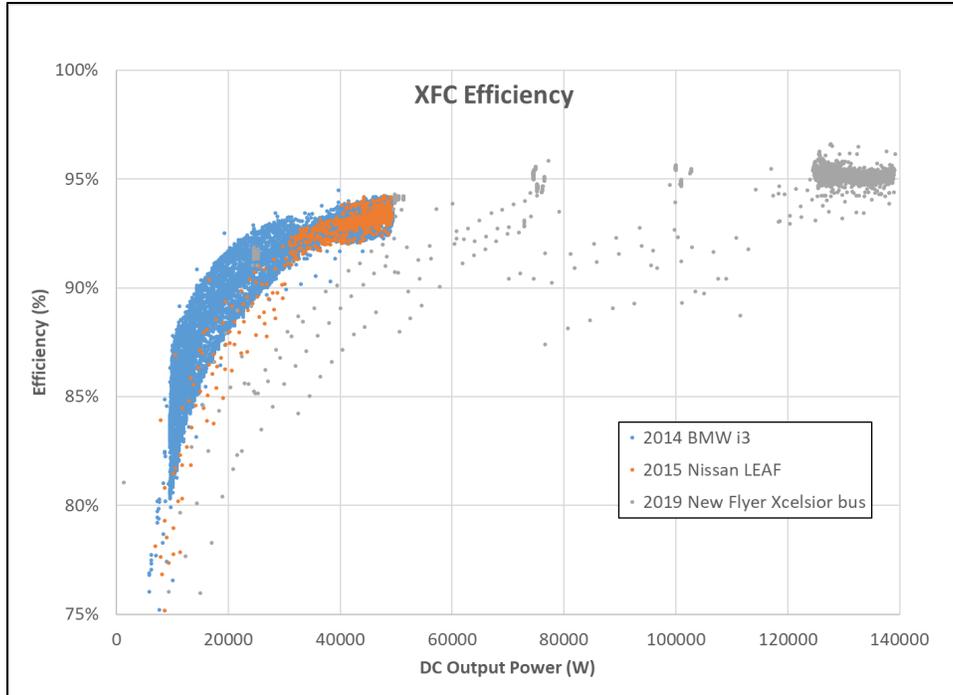


Figure V.2.3 Efficiency of the 350-kW XFC

Time-history power profiles were also generated from test data to understand how each of the three test vehicles received power. The power profile for the 2014 BMW i3 is shown in Figure V.2.4. Peak power is limited by the vehicle's battery management system, not by the fast charger. Therefore, when the 2014 BMW i3 was charged by the ABB Terra HP, charge power peaked at around 50 kW, even though the charger is rated for charging at up to 350 kW. The non-constant power profile of the i3 is typical of DC fast charging profiles. It has a constant-power phase, lasting for about 8 minutes in this case, followed by a constant-voltage phase for the remainder of the charge event. The event ended when the vehicle's battery state of charge reached 80%.

The transient behavior of vehicle charging was the primary focus of characterization testing, because this behavior has the potential to impact grid stability. The XFC's power ramp-up and ramp-down rates were verified to be determined by the vehicle, not by the charger. Ramp-up rates for the three test vehicles are shown in Figure V.2.5. The ramping observed was quite slow and is not expected to create detrimental transients on the grid.

Ramp rates for the three test vehicles charging on the 350-kW XFC were compared to ramp rates for vehicles that were charged on a 50-kW DC fast charger. These are shown in Figure V.2.6. Although the charge ramp-up rate varies greatly from vehicle model to vehicle model, the ramp-up rate is consistent for each vehicle model regardless of charger power capability. This result was expected, because the vehicle actively communicates with the charger during the entire charge event to ensure charge current is delivered as requested by the vehicle's energy storage system.

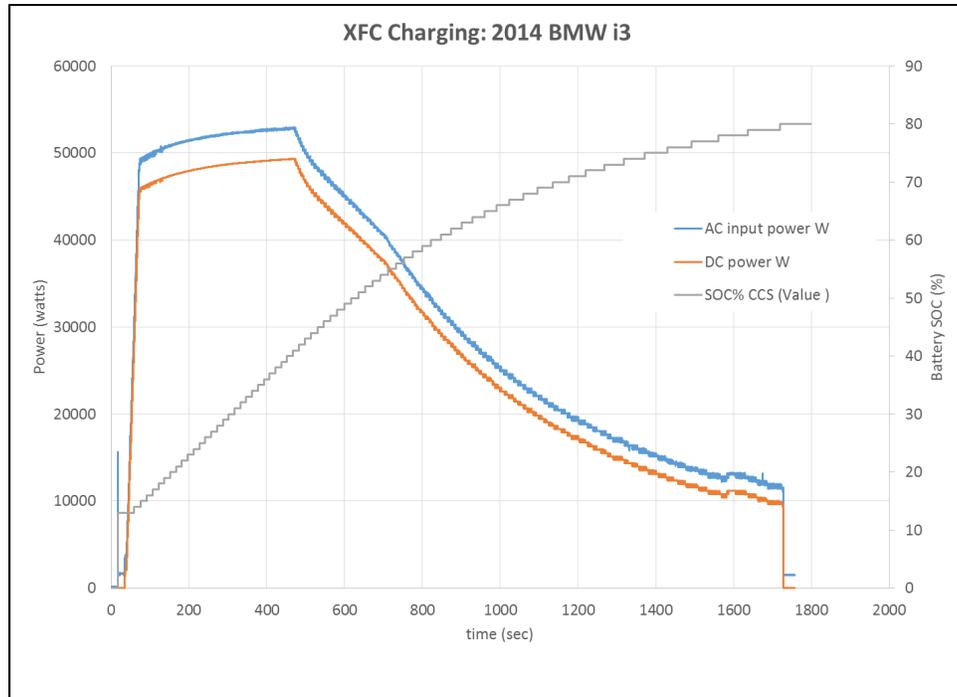


Figure V.2.4 Charge profile of the 2014 BMW i3 connected to the 350-kW XFC

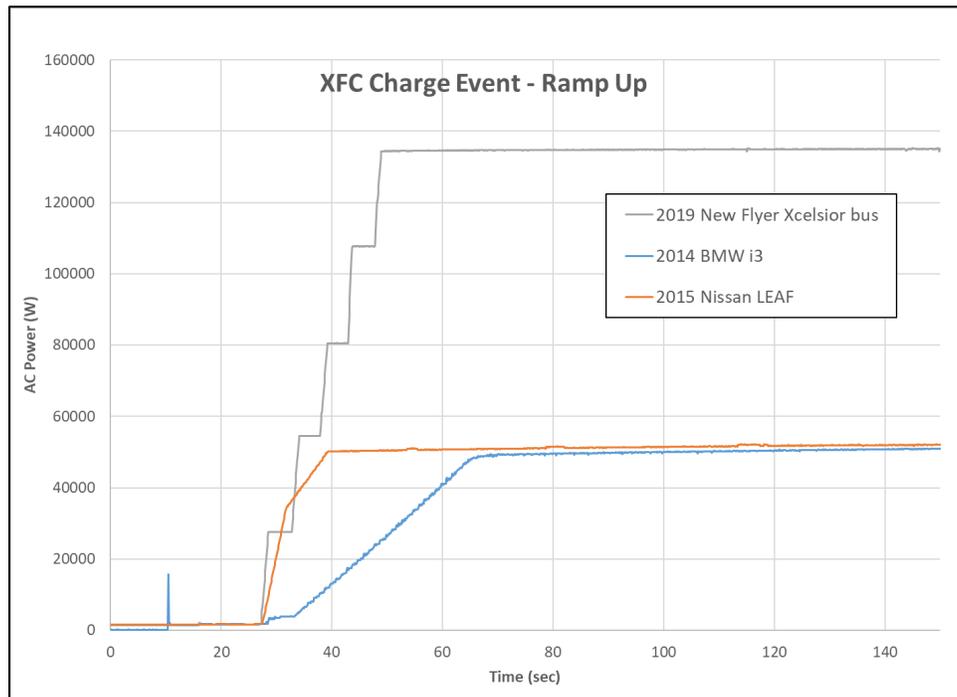


Figure V.2.5 Charge initialization ramp-up characteristics when charging with a 350kW capable XFC

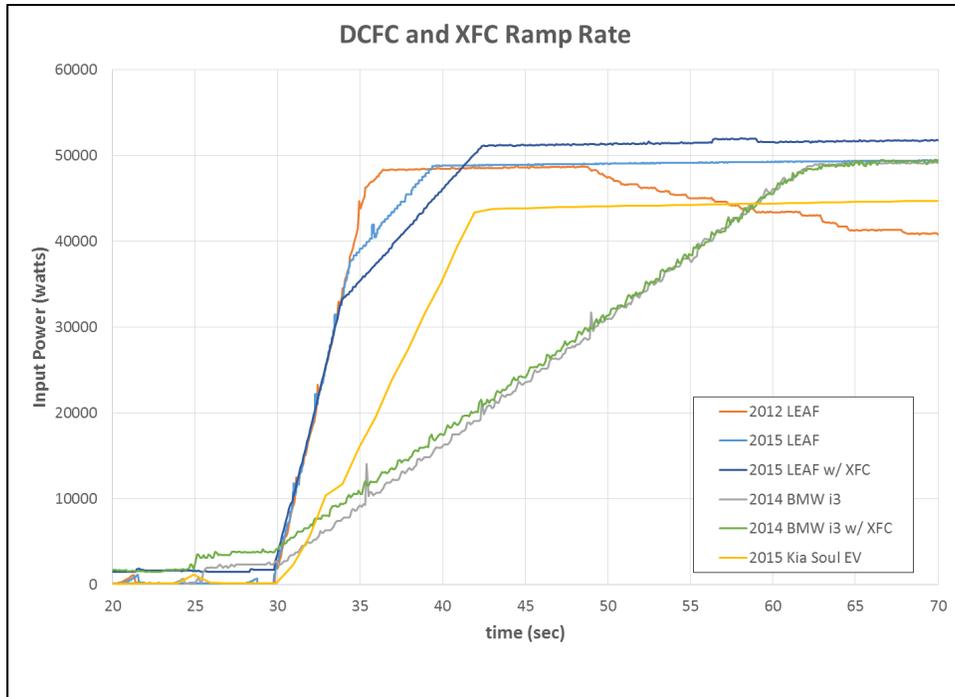


Figure V.2.6 Comparison of charge event initialization and power ramp-up: 50kW DCFC and 350kW XFC

The ramp-down at the end of XFC charge events was also examined. Figure V.2.7 shows that power ramps down exceedingly fast for the Nissan LEAF when a charge on the XFC has finished. This fast shut-off of power is commanded by the XFC to ensure safety. This transient behavior may have a negative effect on grid stability and will be studied in FY20. The likelihood that hackers could cause coordinated chargers to shut-off during a cyber attack and the resulting grid impact is being studied in a sister project titled “Consequence-Driven Cybersecurity for High-Power Charging Infrastructure.”

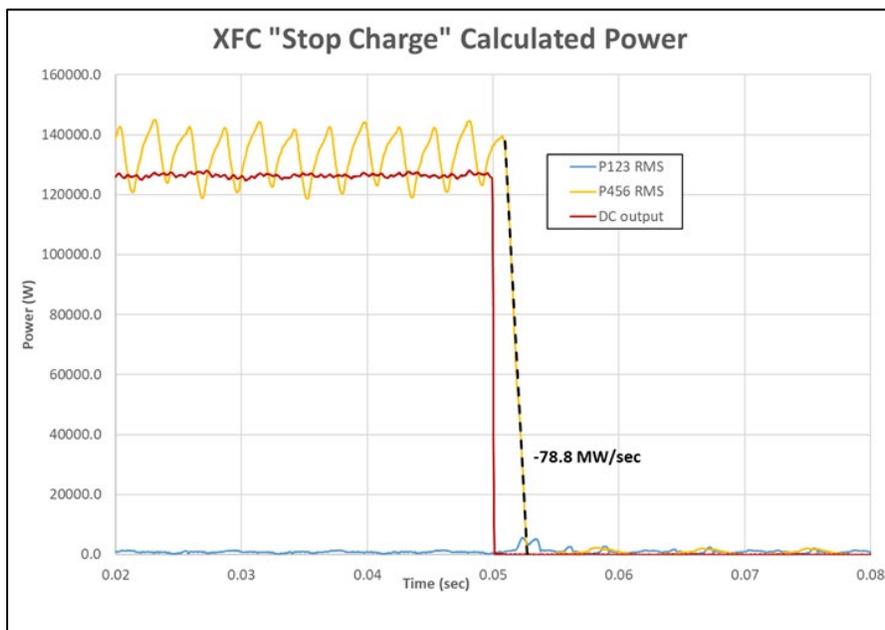


Figure V.2.7 Power ramp-down at the end of a charge on the 350-kW XFC

### Vehicle Emulator Development

A vehicle emulator was developed to facilitate high-power charging using INL's XFC. This was needed because vehicles capable of charging above 150 kW are not available for testing. The vehicle emulator required two components. First, it needed a communications device that is capable of communicating with the XFC through the Combined Charging System (CCS) connector, in accordance with communications standards under development, such as ISO 15118. Second, the vehicle emulator needed a DC load bank capable of absorbing up to 350 kW of power, with current and voltage ratings of 500 amps and 920 volts direct current (VDC). Researchers procured commercial equipment to function as these components and developed necessary interfaces to integrate the components into a system. Figure V.2.8 shows a schematic of the XFC and vehicle emulator.

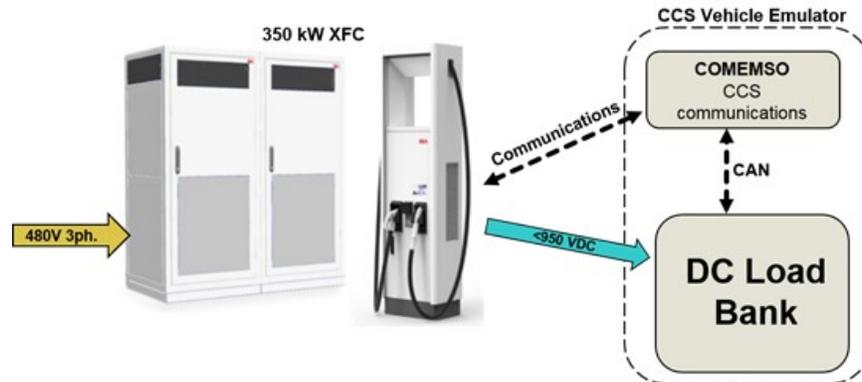


Figure V.2.8 Schematic of vehicle emulator that uses the XFC's Combined Charging System (CCS) connector (Source: INL)

In FY20, this system will be integrated with INL's digital real-time simulator and 540-kW grid emulator to establish a power-hardware-in-the-loop (PHIL) platform. This platform will be used to simulate operation of numerous XFC stations and study the impact to grid stability.

### Conclusions

This project completed important preliminary research that is necessary for understanding the impact of fast charging on grid stability and identifying and mitigating cybersecurity vulnerabilities. Characterization testing of a commercial XFC system with three production vehicles found that efficiency varies widely during individual charging events and across different vehicles; however, this will not cause any negative impact to the grid. On the other hand, a transient characteristic of the XFC was discovered—namely ramp-down rate at the end of charge events—that has the potential to impact grid stability. This extent of the risk that this behavior may present to grid stability during normal operation and as a result of a cyber attack will be studied in FY20. To enable that study, a vehicle emulator was also created to allow PHIL simulation/emulation of vehicles with different charging power capacities, up to 350 kW.

### References

1. ABB High Power Charging Products and Downloads, <https://new.abb.com/ev-charging/products/car-charging/high-power-charging>, accessed Oct 30, 2019.

### V.3 Demand Charge Mitigation Technologies (NREL)

#### Andrew Meintz, Principal Investigator

National Renewable Energy Laboratory  
15013 Denver West Parkway  
Golden, CO 80401  
E-mail: [Andrew.Meintz@nrel.gov](mailto:Andrew.Meintz@nrel.gov)

#### Lee Slezak, DOE Program Manager

U.S. Department of Energy  
E-mail: [Lee.Slezak@ee.doe.gov](mailto:Lee.Slezak@ee.doe.gov)

Start Date: October 1, 2017  
Project Funding: \$450,000

End Date: September 30, 2020  
DOE share: \$450,000

Non-DOE share: \$0

#### Project Introduction

Most commercial buildings or facilities pay for their electricity bills with two types of charges—energy charge and demand charge. Energy charge is the cost for the total energy consumption for the month and demand charge is the charge for the peak power demand of the month. The peak power demand of the month for billing is usually calculated as an average demand in 15-minute time frames. NREL has a contract with the utility at \$0.04/kWh for energy charge and at \$16.79/kW for demand charge in 2017. With this price rate, even 50 kW peak reduction can result in saving more than \$800. Therefore, electricity cost can be lowered not only by using energy efficient products but also by reducing peak demand by distributing power demand throughout the day for flexible devices, specifically plug-in electric vehicles (PEV) charging.

#### Objectives

One of main issues with demand charge mitigation and load control is integration of heterogeneous components and scalability of the existing structure as the number of controllable load devices increases. Distributed control without information on the other devices such as controllable water heater, HVAC, etc. can make the whole system unstable because each device can compete each other due to lack of information on the other devices. Suppose that load control of individual devices is dependent on the total load and are distributed (each control system does not have information on other control systems). Then, if a controller of a device reduces its load during the peak, it will lower the total load. Then, a controller of another device may try to increase its load because total load is reduced, which increases total load again and can make the whole system unstable. Centralized control algorithms [1] can resolve this problem by coordinating each controller together but become complicated and inefficient if the size of the system becomes large. Further, addition of new resources to the system must be scalable to eliminate integration issues.

As an alternative to centralized methods, algorithms using a game theoretic approach were proposed for demand side management [2],[3]. They use real-time pricing information in solving the problem, which is not available in every territory and the conditions for the Nash equilibrium are not always satisfied in real-world conditions. Different from the abovementioned techniques, this project aims to develop a control algorithm combining centralized and distributed methods with the hierarchical and distributed control structure.

#### Approach

One method to resolve the issue described in the previous section is distributed control with hierarchical structure and utilization of energy constraints approach described in [4]. A similar approach in the design of a centrally coordinated distributed control was used in [5]. For PEVs, there is a required energy amount that is needed by departure time. The energy delivered to the car along the time will lie somewhere in the gray area in Figure V.3.1 (a) if we assume that PEV does not discharge to the grid. The upper bound of the plot implies that

the car is charged at the maximum rate as soon as it is plugged in. The lower bound means that the car starts charging as late as possible so that the requested energy amount can be delivered by the departure time. In other words, the upper bound means it uses the maximum available energy at its earliest time and the lower bound means that the energy is used at its latest time. Energy constraints for stationary ESS are different from the ones for PEV because the ESS not only consumes but also provides energy. Examples of energy constraints for ESS and HVAC are illustrated in Figure V.3.1 (b) and (c), respectively. Energy constraints for HVAC have multiple slopes because the power demand by HVAC depends on periodic temperature and circulation requirements. If we have multiple devices, the aggregate energy constraints are represented as the plot in Figure V.3.1 (d). The goal is to find an optimal energy use first at each time step given total energy forecast and then allocate the obtained energy amount to each device depending on its energy need priority.

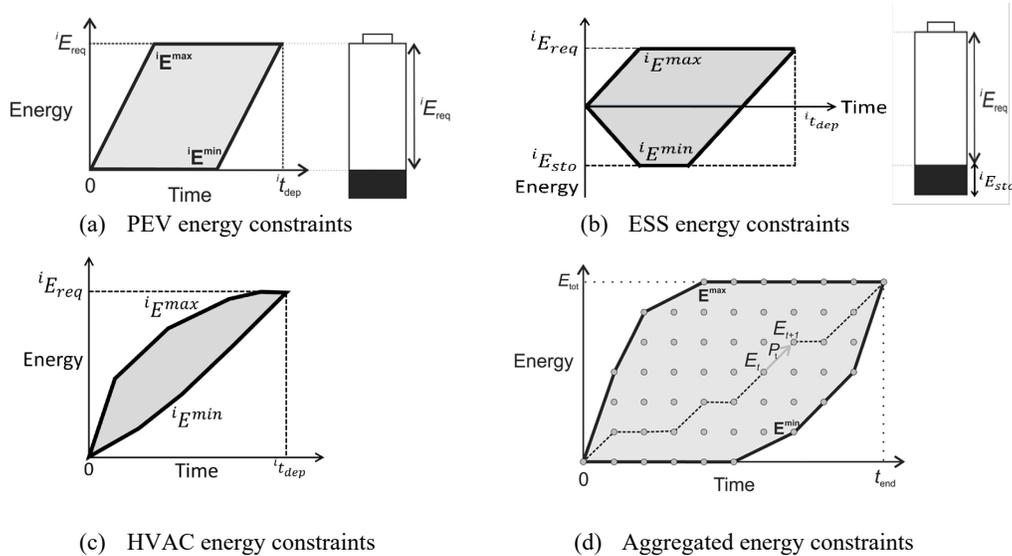


Figure V.3.1 Energy envelop of each device and aggregated energy envelop

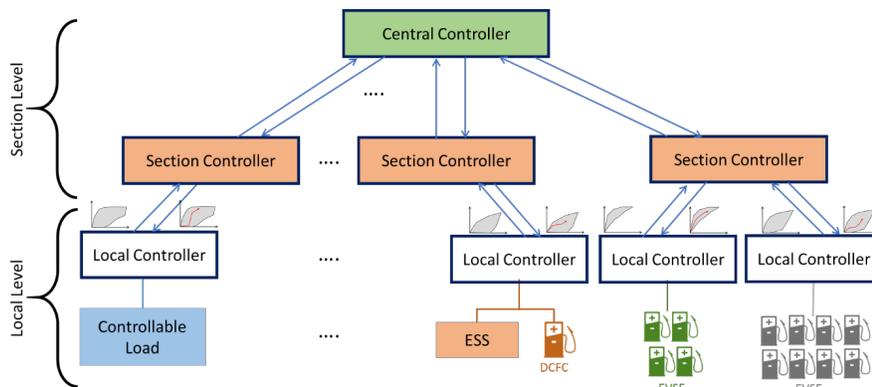


Figure V.3.2 Structure of distributed control with hierarchy

This algorithm can be extended to a system with hierarchy. A diagram of a system with hierarchical control structure is illustrated in Figure V.3.2. The local controllers control each device connected to them. The local controllers have energy constraints of each device connected to them and send aggregate energy constraints to the controller in the above level. The local controllers get energy assignments from the controller right above them and allocate the assigned energy to each device connected to them as previously described. The same thing is repeated in the controllers in the above level. The controllers in the above level will get each aggregated energy constraints from the local controllers, aggregate each aggregated energy constraint, and



send it to the above level. In this way, it can be easily scaled, and the complexity of the system is linearly proportional to the size of the system.

**Results**

The control system for demand charge mitigation is designed to integrate many different types of controllable loads—72 level 2 EVSE’s, a 40-kWh stationary energy storage, and an OCPP 1.6j compatible 50 kW DC fast charger. While all of them have remote communication and control functionality, they do not have a common interface and need an intermediary device to relay messages and commands. Local controllers link each different controllable load and the central controller. Each local controller is built on an individual virtual machine and it is on a dedicated and isolated network for cyber security. The local controllers and the central controller communicate each other through MQTT as a common messaging protocol. The architecture of the system is shown in Figure V.3.3.

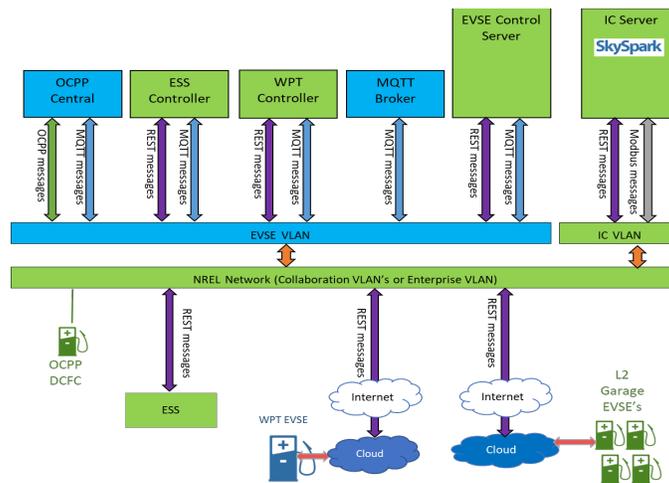


Figure V.3.3 Architecture of integrated control system for EVSE and ESS at NREL

An extended version of the energy constraints approach in [4] is implemented for demand charge mitigation. Each local controller calculates forecasted minimum and maximum energy limits. The energy constraints are transferred to the central controller through MQTT. The central controller solves the following optimization problem based on the energy constraints from each local controller:

$$\begin{aligned}
 & \min_{P_{controllable,k}(t)} \max \left( P_{forecast}(t) + \sum_{k=1}^N P_{controllable,k}(t) \right) \\
 & \text{subject to} \\
 & P_k^{lower\_limit} \leq P_{controllable,k}(t) \leq P_k^{upper\_limit} \quad \forall t \in \{0, \dots, t_{end}\} \\
 & E_k^{min}(t) \leq E_k(t) \leq E_k^{max}(t) \quad \forall t \in \{0, \dots, t_{end}\} \\
 & E_k(t+1) = E_k(t) + P_{controllable,k}(t)\Delta t \quad \forall t \in \{0, \dots, t_{end}\}
 \end{aligned}$$

Here,  $t_{end}$  is the end of the time horizon (6-hour time horizon was used in the experiments),  $P_k^{upper\_limit}$  and  $P_k^{lower\_limit}$  are the physical limits of maximum and minimum power of controllable load  $k$ , respectively. The optimization problem tries to find the optimal power value of each controllable load,  $P_{controllable,k}(t)$ , for  $\forall t \in \{0, \dots, t_{end}\}$  that minimizes the peak of the total load. The value is transferred to each local controller to limit the maximum power allowed to each controller load. The system with this structure can be scaled easily to accommodate additional controllable load such as smart thermostats, lighting, etc.

Each local controller was individually tested and validated first, and then experiments for the integrated system for demand charge mitigation were performed. The testbed includes 72 level 2 EVSE’s at the NREL parking garage used by NREL employees, one 40-kWh stationary energy storage system, and one 50-kW DC fast charger.

### Level 2 EVSE

Total 72 new level 2 EVSE's were installed and operational at the NREL South Table Mountain (STM) parking garage as of September 2019. They have load management capability via REST-based API through a cloud server. The information on miles needed for the planned trips and expected departure time is provided by users and the information is used to calculate the energy constraints for the central controller. The central controller computes a power setpoint value based on the energy constraints from the local controller and transfers the setpoint value to the local controller through MQTT protocol. Once it receives the power setpoint message from the central controller, the local controller translates it into the REST-based API command for the cloud server, which sets up the maximum aggregate power allowed to the EVSE's. The plots in Figure V.3.4 show the energy constraints ( $E_{min}/E_{max}$ ) and the optimal energy profile calculated by the central controller at (a) 9:00am and (b) 11:00am, respectively for the next 6-hour time horizon calculated at each 15-minute time step. The optimal power setpoint value is applied to EVSE power control for the first 15 minutes. During the 15-minute period, the optimization problem calculates the optimal energy profile for the next time interval with updated energy constraints. After completing the current 15-minute interval, the new power setpoint value is applied and the same procedure is repeated every 15 minutes. The right plots in Figure V.3.4 show the optimal L2 EVSE power profile for 6 hours (solid yellow line), the 15-minute average uncontrollable load forecast (solid blue line), and the expected total load when the L2 EVSE power profile is applied (dotted red line) at (a) 9:00am and (b) 11:00am, respectively. Note that the value of the optimal power is zero when a peak load is forecasted less the load by L2 EVSE's should contribute to additional load.

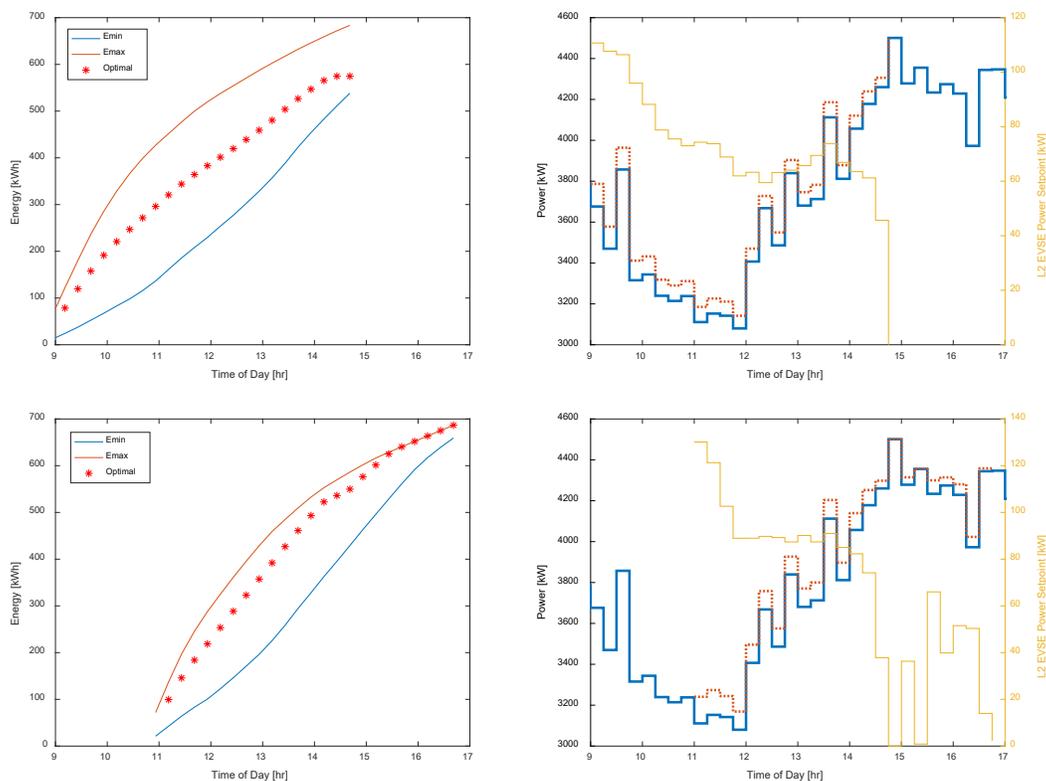


Figure V.3.4 Computed plots at (a) 9:00am (top) and (b) 11:00am (bottom) of the energy constraints and optimal energy profile (left) and the resulting L2 EVSE power profile plan compared to the forecasted load with/without the L2 EVSE load (right)

### DC Fast Charger

The intent of a DC fast charger (DCFCs) is its capability to charge PEVs quickly for immediate departure. In this perspective, it is not desirable to reduce charge power similarly to AC L2 EVSEs because it disregards the main purpose of DCFC. In this regard, the central controller adjusts DCFC power only when the total campus load is close to the historical monthly peak value. The difference between the historical monthly peak value and the real-time campus load value is used in integrating the DCFC with the central controller. The difference implies available power for the DCFC and it is used for calculation of the power setpoint value for DCFC. If the difference is greater than 50 kW, which is the capacity of the DCFC, the DCFC power setpoint is set to 50 kW. Otherwise, the setpoint is set to the difference value in order to alleviate demand charge by the DCFC load. Plots of the difference between the historical monthly peak value and the real-time campus load value and the corresponding DCFC power setpoint are shown in Figure V.3.5 (a).

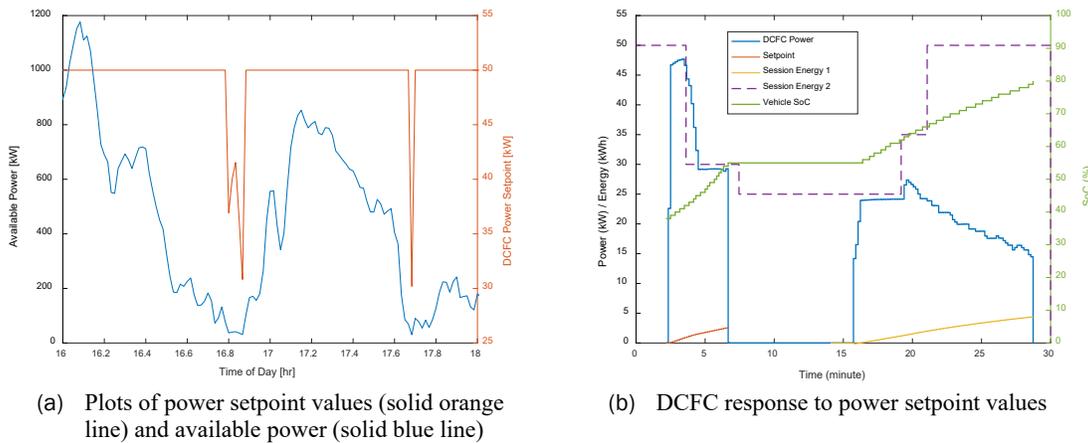


Figure V.3.5 Test results of the DCFC control

An OCPP 1.6 compatible server was developed for communication between the 50-kW DCFC and the central controller. The server was built using Node-RED, a visual tool for wiring the Internet of Things (IoT). The OCPP server can control the power of the charger through SetChargingProfile message defined in OCPP 1.6j. The message consists of a class named ChargingProfile which includes charging schedule and power limit information. The server monitors the status of the charger through MeterValues message from the charger that contains information on power, energy, vehicle battery SOC, current, voltage, and so on. Tests were performed for verification of DCFC’s responses to SetChargingProfile OCPP messages prior to integration to the central controller. SetChargingProfile messages with different power limit setpoint values (30 kW, 25 kW, 35 kW, and 50 kW) were sent to the charger one at a time sequentially in the test. Experiments show (Figure V.3.5 (b)) that the charger responded to the messages quickly and adjusted its maximum charging power accordingly. There were two charging sessions in the test. The first session was ended at about 6 minutes and the second session started at about 15 minutes.

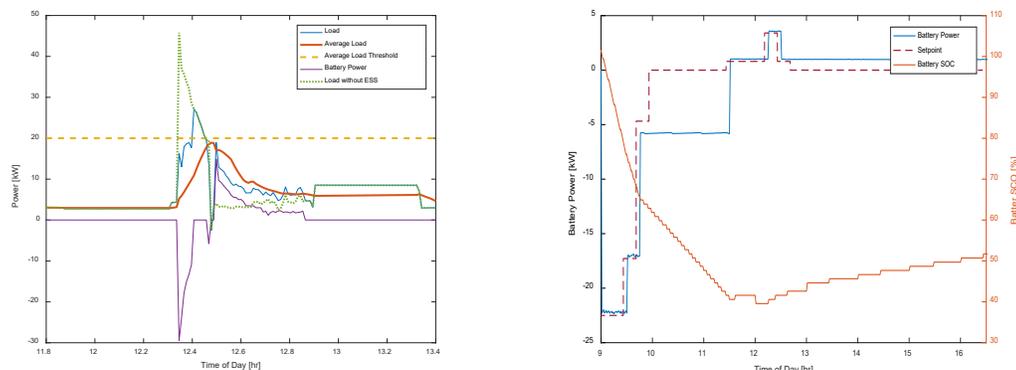
### Stationary Energy Storage System

The 40-kWh stationary energy system is controllable through REST-based API commands to a local server that is directly connected to the battery management system (BMS). There are two API’s that can be used for demand charge mitigation. One API sets a threshold value for the average load and the other sets the current power level for the system. The central controller sends a value for either threshold or current power level through MQTT and the local controller translates the MQTT message into the appropriate API command.

The local server controls the battery for the 15-minute average demand to stay below the threshold value if a threshold value is set. It needs a meter that provides real-time load information in this control mode. Responses of the battery system to the load by setting a threshold value are shown in Figure V.3.6 (a). The battery was discharged very quickly as load increased and approached the threshold value (solid blue line in the plot). The

15-minute average load (solid red line) stayed below the clipping level thanks to the power from the battery to the grid and thus it is useful for demand charge mitigation. One drawback observed from the tests is lack of battery charge control in using this control mode. The system automatically charges the battery (solid purple line) when load decreases.

The API command setting the current power level can be used for battery charge and discharge control. Negative power values denote charge and positive numbers indicate discharge. Test results with the current power level setting are shown in Figure V.3.6 (b). The purple dashed line implies the commanded power setpoint value and the solid blue line denotes the actual battery power. The test demonstrated that the battery follows the command for charge (positive power numbers) or discharge (negative power numbers) quite well but it does not respond to “rest” command (zero power number) and has a tendency to maintain the previous power flow direction (charge or discharge) with a reduced power amount. Therefore, a more sophisticated battery control utilizing both API commands instead of using a single API command can improve the performance of the ESS on demand charge mitigation.



(a) Responses of the ESS by average load threshold

(b) Responses of the ESS by power level setpoint

Figure V.3.6 Test results of the stationary ESS

## Conclusions

NREL has developed a charge management system integrating many different types of controllable loads for demand charge mitigation. The local controllers are connected to the controllable loads with different interfaces. They translate messages in different communication protocols into MQTT messages through which the central controller communicates with the local controllers. This structure facilitates addition of new types of controllable loads without modifying the interface of the central controller. The central controller only needs to add a list of MQTT message topics that are required for the new controllable loads and aggregate the forecasted energy needs of them into the optimization.

NREL has also performed tests on a testbed consisting of level 2 EVSE's, a DC fast charger, and a stationary ESS. The level 2 EVSE's are used by NREL employees without a pre-coordinated test scenario. The drivers use the chargers based on their own schedules. Experiments show that each local controller commanded to reduce power to each controllable load when campus load or forecasted campus load is high and each controllable load decreased load accordingly to not contribute to peak load. Experiments also show that the central controller successfully integrates each local controller through a common communication interface and that it provides an optimal power setpoint value based on expected energy needs and forecasted load.

## References

1. T. Logenthiran, D. Srinivasan, and T. Z. Shun, "Demand side management in smart grid using heuristic optimization," *IEEE Trans. Smart Grid*, vol. 3, no. 3, pp.1244-1252, 2012

2. Z. Ma, D. S. Callaway, and I. A. Hiskens, “Decentralized charging control of large populations of plug-in electric vehicles,” *IEEE Trans. Control Systems Technology*, vol. 21, no. 1, pp.67-78, 2013
3. M. H. K. Tushar, C. Assi, and M. Maier, “Distributed real-time electricity allocation mechanism for large residential microgrid,” *IEEE Trans. Smart Grid*, vol. 6, no. 3, pp. 1353–1363, 2015.
4. S. Vandael, B. Claessens, M. Hommelberg, T. Holvoet, and G. Deconinck, “A scalable three-step approach for demand side management of plug-in hybrid vehicles,” *IEEE Trans. Smart Grid*, vol. 4, no. 2, pp.720-728, 2013
5. Z. Yi, D. Scoffield, J. Smart, A. Meintz, and M. Jun, M. Mohanpurkar, and A. Medam, “A highly efficient control framework for centralized residential charging coordination of large electric vehicle populations,” submitted to *Int. J. of Electrical Power and Energy Systems*

## V.4 Smart Electric Vehicle Charging for a Reliable and Resilient Grid (NREL)

### **Andrew Meintz, Principal Investigator**

National Renewable Energy Laboratory  
15013 Denver West Parkway  
Golden, CO 80401  
E-mail: [andrew.meintz@nrel.gov](mailto:andrew.meintz@nrel.gov)

### **Jesse Bennett, Principal Investigator**

National Renewable Energy Laboratory  
15013 Denver West Parkway  
Golden, CO 80401  
E-mail: [jesse.bennett@nrel.gov](mailto:jesse.bennett@nrel.gov)

### **Lee Slezak, DOE Program Manager**

U.S. Department of Energy  
E-mail: [Lee.Slezak@ee.doe.gov](mailto:Lee.Slezak@ee.doe.gov)

Start Date: October 1, 2018  
Project Funding: \$950,000

End Date: September 30, 2021  
DOE share: \$950,000

Non-DOE share: \$0

### **Project Introduction**

Adoption of plug-in electric vehicles (PEVs) has expanded over the last few years, yet introduction of PEV smart charging has been stalled due to barriers in communication, controls, and an unclear method for determining the value PEVs will bring to the grid. This project will consider the grid impact of a variety of future scenarios, including adoption of different vehicle types, proliferation of extreme fast charging (xFC), expanded adoption of distributed energy resources (DER), and multiple smart charge management approaches. This project will determine how PEV charging at scale should be managed to avoid negative grid impacts, allow for critical strategies and technologies to be developed, and increase the value for PEV owners, building managers, charge network operators, grid services aggregators, and utilities.

The National Renewable Energy Laboratory (NREL) is leading this project, which also includes Sandia National Laboratories (Sandia) and Idaho National Laboratory (INL). NREL will build on past experience in GM0062 and GM0085 and provide expertise in creating and analyzing PEV load profiles using EVI-Pro. These load profiles and other tools will be used for assessing grid and distribution system impacts. NREL will continue using experience integrating building loads to implement charge control strategies at the NREL campus using on-site resources and will provide overall project oversight for this multi-lab project.

### **Objectives**

This project will address benefits and barriers of smart charge management for PEVs at scale through multi-lab collaboration. Taking advantage of their combined cutting-edge facilities, capabilities, and access to data, the team will develop technology for real-world implementation of smart charging. The team will investigate grid resilience and reliability challenges and opportunities presented by mass adoption of PEVs through detailed simulation. Team research will:

- 1) Quantify the effects of uncontrolled charging to understand how increased PEV adoption may negatively impact the grid
- 2) Analyze the effectiveness of multiple control strategies in mitigating negative grid impacts introduced by PEVs at scale

- 3) Rank the benefits and costs of the control strategies in avoiding grid upgrades, providing grid services, and improving resilience, and
- 4) Overcome technical barriers to implementing high-value control strategies.

## Approach

The project is separated into nine tasks to accomplish the four objectives listed above. NREL is involved in the following tasks:

### ***Task 1: Scoping, requirements, and industry engagement***

Identification of regions for the PEVs at scale analysis will be performed to engage utility partners willing to support and provide distribution feeder models, load data, and other analysis or insight into the operation of their distribution system.

### ***Task 2: PEV charging requirements***

Identification of regions for the PEVs at scale analysis will be performed to engage utility partners willing to support and provide distribution feeder models, load data, and other analysis or insight into the operation of their distribution system

### ***Task 3: PEV charging and distribution system modeling***

Develop PEV charging load dataset for two regions in Minnesota and Georgia using GPS travel data from conventional vehicles traveling across each region. This dataset will include charge requirement results for various scenarios that include (1) PEV adoption rates from today (2) a mix of vehicle ranges and (3) a mix of EV charging infrastructure for both home dominant and public dominant charging. The dataset will associate the charging requirement for each PEV to its location to allow load to be disaggregated to individual feeders in the distribution network.

### ***Task 4: Quantifying the impact of uncontrolled charging***

Sandia will apply existing hosting capacity analysis tools to possible PEV charger connections. For each node on the distribution feeder, the maximum charging capacity will be identified. Hosting capacity also resolves the limiting factor (e.g., voltage violations or current limits), which can be used to understand the sensitivity of the feeder.

### ***Task 5: Refining smart charge control strategies***

This task will study the potential of multiple control approaches to mitigate negative impacts of PEV charging at scale and provide grid services. New functionality will be added to control PEVs across multiple distribution feeders and to include bulk grid impacts in the objective function. A series of simulations will be run to compare the efficacy of each control's approach in delivering multiple grid services in various future scenarios.

### ***Task 6: Value of smart charging***

The value of implementing smart charging will be quantified using the same process as in Task 4. The hosting capacity with various methods of smart charging (including controlled ramps up in charging, smart temporal charging, etc.) will be compared to the hosting capacity for uncontrolled charging. The increase in hosting capacity will be compared against the “cost” of smart charging (e.g., slower charging, charge not available when needed, etc.) to determine the value and tradeoff of smart charging.

### ***Task 8: Development of a Charging Decision Model (CDM)***

To overcome two significant barriers to smart charging—understanding driver needs and accurate load forecasting—the team will develop a vehicle-based CDM. This technology will 1) use machine learning to monitor and predict PEV driver charging needs, 2) communicate vehicle charging intentions to infrastructure,

and 3) make decisions on optimal charging time and location based on real-time feedback from charging infrastructure.

***Task 9: Integration of smart charging with building loads***

This effort will build on the GM0062 evaluation of smart workplace charging at the NREL garage and expand on efforts to understand charging behavior (to inform models developed for Task 2 and Task 8), evaluate communication methods for onsite integration with build loads, to incorporate new control methods developed in Task 5, and to develop building load prediction methods to further integrate smart charging into building loads. This testbed will also be used to demonstrate how prior knowledge of vehicle charging needs communicated by the CDM can enhance smart charge management at the building level.

**Results**

Results by task are listed below.

***Task 1: Utility Engagement***

NREL has partnered with Xcel Energy to study the impacts of PEV charging on the Minneapolis-Saint Paul (MSP) region in Minnesota. Through this partnership, NREL has obtained insights and data related to PEV integration and feeders in the MSP region. Through regular communications with Xcel NREL has selected 10 specific distribution feeders for the simulations and analysis throughout this project. These feeders were selected for a number of reasons, including but not limited to; PEV adoption rates, capacity factor, line loading, and customer type (e.g., residential, industrial, or commercial).

***Task 2: PEV charging requirements***

Through the acquisition of INRIX vehicle travel data and the application of EVI-Pro, NREL has compiled a total of 1.9 million vehicle trips. These trips consist of the INRIX recorded travel data for conventional ICE vehicles in MSP for March of 2018 that have been run through EVI-Pro to determine the charge events that would be required for various PEV models.

Due to the disjointed nature of the INRIX data, NREL developed a semi-Markovian synthetic trip chaining methodology to assemble individual vehicle trips into a 24-hour vehicle travel profile. This methodology is broken into three parts and an example of the execution is displayed in Figure V.4.1.

- 1) Procure GPS location of trips within a given city or zone
- 2) Establish probability distributions for:
  - a. Daily trip count
  - b. Vehicle spatial information based off vehicle registration locations
  - c. Time of departure from home locations
  - d. Dwell time as a function of destination land use type and arrival time
- 3) Run simulation
  - a. Select trips from the GPS database in a weighted method to represent the distributions
  - b. Vehicles enter an aggregate zone (TAZ) and their dwell time is determined from the distributions and land use
  - c. The vehicle departs on the next start/end trip pair that is in the same zone and leaves closest to the end of the dwell time



- d. The distance from previous end to next start is added to the daily sum (red)
- e. The vehicle is run in this fashion until it reaches its second to last trip for the day, then the vehicle is sent to its home location (green).

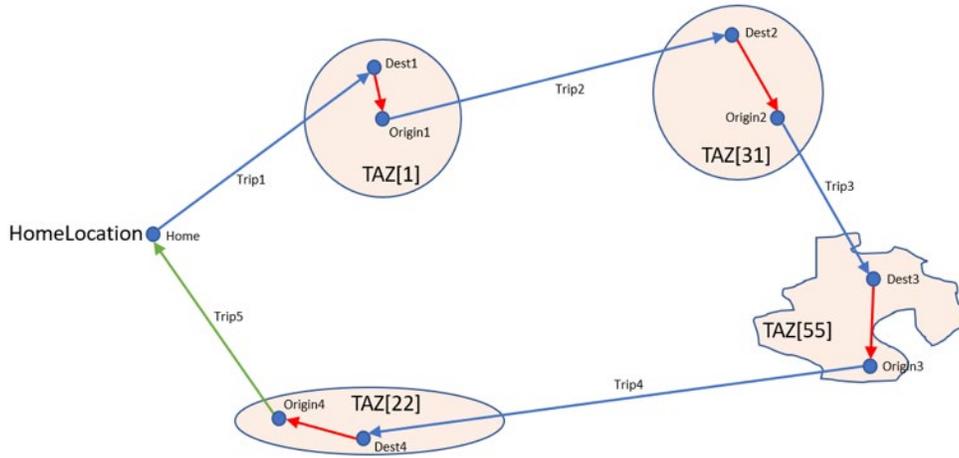


Figure V.4.1 Example of a 5-trip vehicle simulation

**Task 3: Distribution System Modeling**

The NREL team engaged with Xcel Energy (Northern States Power) to perform the grid impact analysis for the Minneapolis-Saint Paul (MSP) region. The Xcel Energy team consists of personnel from customer load research, planning, design & standards, electric vehicle adoption and grid operations groups, from Minnesota and Colorado service territories. The NREL team received data including feeder planning models, historical power and voltage measurements for the feeder, service transformer and secondary network design rules and GIS information for 10 feeders. These feeders were selected due to their unique features as detailed in Table V.4.1. The feeder data was originally shared in SYNERGI format and was converted to OpenDSS format [OpenDSS 2019] to enable the analysis and were validated against the utility-provided feeder models using comparisons of voltage profiles and feeder loading.

**Table V.4.1 Feeder descriptions**

	Description
Feeder 1	Unbalanced phases and evenly mixed customer types
Feeder 2	Heavily residential
Feeder 3	High capacity factor
Feder 4	Unbalanced phases and heavily residential
Feeder 5	Near downtown and heavily residential
Feeder 6	Near downtown with evenly mixed customer types
Feeder 7	Near downtown and heavily residential
Feeder 8	High EV adoption rates
Feeder 9	Downtown commercial and industrial
Feeder 10	Downtown commercial and industrial

#### Task 4: Impact of Uncontrolled Charging

On each of the 10 feeders, NREL performed hosting capacity analysis, which gave the team insight into the feeder's ability to serve a growing PEV load. Hosting capacity analysis considers a new load at each feeder node (customer service points) in addition to the feeder's base load and that load increased until one of the following three violations occurs: 1. voltage at any point in the feeder was out of bound (95 to 105% of the nominal voltage), 2. Loading at any point in the feeder exceeded the thermal loading limit or 3. The loading on the primary distribution network (the main line from the substation) reaches 60% of the thermal loading limit. The third condition above was included in the study per Xcel Energy's planning/operation practices where in 40% of the capacity on primary distribution network is reserved for accommodating any unscheduled outages and emergencies.

The hosting capacity analysis was completed for all the selected feeders. The results for a few select feeders are shown in Figure V.4.2 for illustrating the discussion points articulated below.

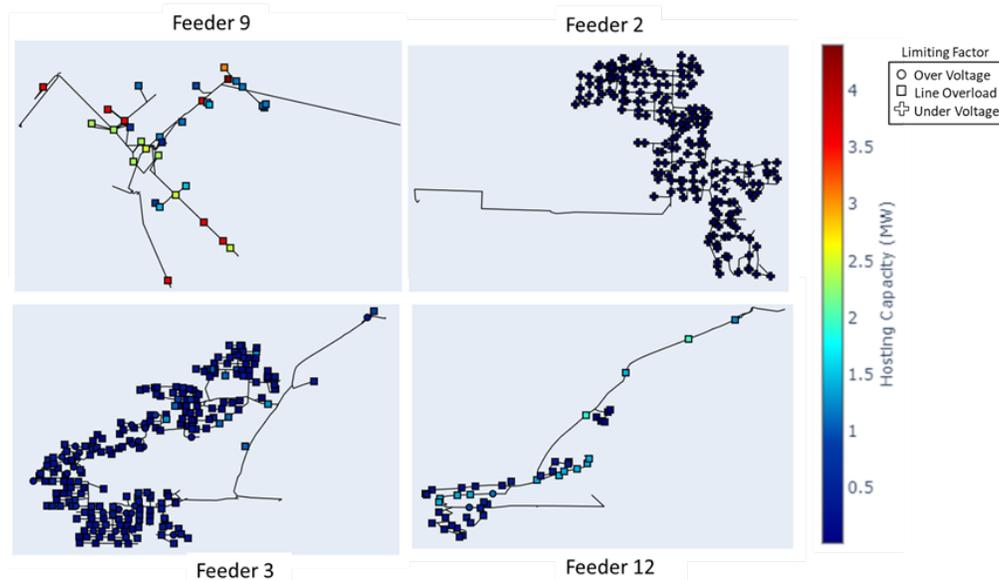


Figure V.4.2 Hosting capacity analysis for four feeders in the MSP region

- Heavily residential Feeder 2 and Feeder 3 show the lowest hosting capacities at existing service points. Addition of substantial charging infrastructure or customer charge loading requires a combination of upgrades including new service points, reconductoring and reconfiguration of the feeders
- Commercial Feeder 9 (located near downtown areas) show higher hosting capacity and offer opportunities for public charging infrastructure including XFC
- For mixed customer-type feeders like Feeder 12, hosting capacity analysis shows select locations where additional charging infrastructure can be accommodated.

#### Task 5: Smart Charge Control Strategies

While hosting capacity analysis details the ability for feeders to serve a new load, uncontrolled charging analysis takes the PEV charging requirements from Task 2 and performs OpenDSS analysis on a specific feeder with the new PEV load added to the existing base load. Depending on the adoption scenario used, such as the EPRI High PEV (EPRI, 2017) adoption scenario the large number of grid violations may best be mitigated through a smart charge control strategy. In this task, we have begun to look at various smart charging solutions and how they have the potential to reduce or eliminate the violations seen in the uncontrolled

charging case. For example, undervoltage violations may be mitigated by introducing control strategies which reduce the charger power during low-voltage times. Similarly, line-loading concerns may be alleviated by limiting simultaneous charging events at a particular location, thus ensuring a particular line never exceeds its rating. In addition to power reductions and temporal shifts in charging events, other control strategies may employ incentives to shift charging geographically, to a node on that feeder with a larger capacity.

#### **Task 6: Impact of Smart Charging**

NREL has started to implement the control strategies considered in Task 5 into the hosting capacity analysis to understand the impact. This work will be continued throughout project year two.

#### **Task 8: Development of a Charging Decision Model (CDM)**

This task is planned for project year three and work has not yet started.

#### **Task 9: Integration of smart charging with building loads**

The approach for developing a forecasting model based on garage charging is both a modeling and data infrastructure one. The overall steps are broken into the 4 steps below:

- Create repository for past and future data
- Clean and transform all historical data
- Creation of persistent anonymized user identification
- Develop both traditional time series statistics models and machine learning models.

Currently all historical data has been cleaned and stored within a database to ensure future usability and data fidelity. Previously unintegrated power meter data has been extracted, cleaned and joined into historical data allowing for a one stop shop for all charging information. The Application Programming Interface (API) that vendor uses has been integrated into NREL scripts to add all new session data. A cost recovery monitoring method has been implemented through JSONLogic as well given a new mandate to recover the energy and operational costs. All users of the system have been anonymized though each user is persistent in the database and joined with their historical usage prior to the newly installed system. This will allow for user behavior to be understood as the costing evolves from a free to charge site to new cost. Machine learning and statistical models have been generated and are being developed to integrate with full campus load predictions for demand charge mitigation.

### **Conclusions**

At the end of the first year of a three-year project, the current progress has considered the limitations of the grid and the impacts of PEV adoption. After acquiring distribution feeder data, the hosting capacity analysis displayed the grid's ability to serve larger loads, such as xFC. This analysis leads into uncontrolled charging simulations in which high levels of PEV adoption begin to create voltage and line loading violations throughout the feeder. These challenges make the case for controlled charging as a way to mitigate these problems. Various control strategies are currently being developed, with the goal to reduce violations by incentivizing charging behaviors that avoid line loading and voltage concerns. These strategies will also account for existing charging behaviors obtained through the research at the NREL garage, which has concluded that personal behavior and habits are the strongest predictor of PEV charging load.

### **References**

1. Open Distribution System Simulator™. Available: <http://sourceforge.net/projects/electricdss/>. Accessed: October 11, 2019.
2. EPRI, *Plug-in Electric Vehicle Market Projections: Scenarios and Impacts*. Available: <https://www.epri.com/#/pages/product/3002011613/>. Published: December 18, 2017.

## V.5 Smart Electric Vehicle Charging for a Reliable and Resilient Grid (Idaho National Laboratory)

### **Don Scofield, Principal Investigator**

Idaho National Laboratory  
775 MK Simpson Boulevard  
Idaho Falls, ID 83415  
E-mail: [John.Smart@inl.gov](mailto:John.Smart@inl.gov)

### **Lee Slezak, DOE Program Manager**

U.S. Department of Energy  
E-mail: [Lee.Slezak@ee.doe.gov](mailto:Lee.Slezak@ee.doe.gov)

Start Date: October 1, 2018  
Project Funding: \$500,000

End Date: September 30, 2021  
DOE share: \$500,000

Non-DOE share: \$0

### **Project Introduction**

Adoption of plug-in electric vehicles (PEVs) has expanded over the last few years, yet introduction of PEV smart charging has been stalled due to barriers in communication, controls, and an unclear method for determining the value PEVs will bring to the grid. This project is considering the grid impact of a variety of future scenarios, including adoption of different vehicle types, proliferation of extreme fast charging (xFC), expanded adoption of distributed energy resources (DER), and multiple smart charge management approaches. This project will determine how PEV charging at scale should be managed to avoid negative grid impacts, allow for critical strategies and technologies to be developed, and increase the value for PEV owners, building managers, charge network operators, grid services aggregators, and utilities.

Idaho National Laboratories (INL) is a team member on this project, which is led by National Renewable Energy Laboratory (NREL) and also includes Sandia National Laboratory (Sandia). INL is focusing on developing and supporting Caldera, a charging infrastructure simulation platform, which will be used by the Sandia and NREL grid groups. Caldera has three components:

1. A library of high-fidelity vehicle charging models for a wide range of vehicles and charging technology (alternating current [AC] Level 2, direct current [DC] fast charging, and xFC)
2. Smart charging strategies that have been developed in multiple projects funded by Vehicle Technologies Office
3. Finally, Caldera has Vehicle artificial intelligence (AI) and Infrastructure AI modules that enable intelligent charging decision management for drivers and automated vehicles.

### **Objectives**

This project is addressing benefits and barriers of smart charge management for PEVs at scale through multi-lab collaboration. Taking advantage of their combined cutting-edge facilities, capabilities, and access to data, the multi-lab team will develop technology for real-world implementation of smart charging. The team will investigate grid resilience and reliability challenges and opportunities presented by mass adoption of PEVs through detailed simulation. The research team will do the following:

1. Quantify the effects of uncontrolled charging to understand how increased PEV adoption may negatively impact the grid
2. Analyze the effectiveness of multiple control strategies in mitigating negative grid impacts introduced by PEVs at scale

3. Rank the benefits and costs of the control strategies in avoiding grid upgrades, providing grid services, and improving resilience, and
4. Overcome technical barriers to implementing high-value control strategies.

## Approach

The project is separated into nine tasks to accomplish the four objectives listed above. INL is involved in the following tasks:

### *Task 1: Scoping, requirements, and industry engagement*

Identification of regions for the PEVs at scale analysis is being performed to engage utility partners willing to support and provide distribution feeder models, load data, and other analysis or insight into the operation of their distribution system.

### *Task 3: PEV charging and distribution system modeling*

Detailed distribution grid models are being implemented to understand the locational impact of PEV charging on distribution grid operations and identify voltage or thermal constraints. This modeling is taking place in OpenDSS, a powerful open-source software conducive to both translating results to commercial software and to releasing developed tools and models to the research community.

### *Task 5: Refining smart charge control strategies*

This task is studying the potential of multiple control approaches to mitigate negative impacts of PEV charging at scale and provide grid services. New functionality is being added to control PEVs across multiple distribution feeders and to include bulk grid impacts in the objective function. A series of simulations are being run to compare the efficacy of each control's approach in delivering multiple grid services in various future scenarios.

### *Task 6: Value of smart charging*

The value of implementing smart charging is being quantified using the same process as in Task 4. The hosting capacity with various methods of smart charging (including controlled ramps up in charging, smart temporal charging, etc.) is being compared to the hosting capacity for uncontrolled charging. The increase in hosting capacity will be compared against the "cost" of smart charging (e.g., slower charging, charge not available when needed, etc.) to determine the value and tradeoff of smart charging.

### *Task 8: Development of a Charging Decision Model*

To overcome two significant barriers to smart charging—understanding driver needs and accurate load forecasting—the team is developing a vehicle-based charging decision mode (CDM). This technology will 1) use machine learning to monitor and predict PEV driver charging needs, 2) communicate vehicle charging intentions to infrastructure, and 3) make decisions on optimal charging time and location based on real-time feedback from charging infrastructure.

## Results

In this project, PEV charging and PEV charging control strategies is enabled by a tool named Caldera. The foundation of Caldera is a library of high-fidelity EV charging models derived from extensive charging and battery testing data that INL has collected over the past decade. Caldera's charging models accurately estimate charge power profiles, efficiency, and power factors for a wide variety of vehicles and charging technologies under varying grid conditions. This capability is critical for predicting charging impact on the grid.

What's more, Caldera enables the co-simulation of the transportation network and the grid. By linking existing simulation tools with Caldera in a co-simulation environment such as HELICS, the grid impact of EV charging demand can be accurately modeled for a variety of future transportation scenarios.

In the RECHARGE project, Caldera is used in conjunction with NREL’s EVI-Pro (a transportation simulation tool) and OpenDSS (a grid simulation tool). In fiscal year 2019 (FY2019), the project team upgraded Caldera with additional capabilities necessary for integration with EVI-Pro and OpenDSS, simulated uncontrolled PEV charging in two metropolitan areas, and created load profiles resulting from PEV charging that the grid would need to serve. Figure V.5.1 depicts the three simulation tools in RECHARGE and the flow of information between them.

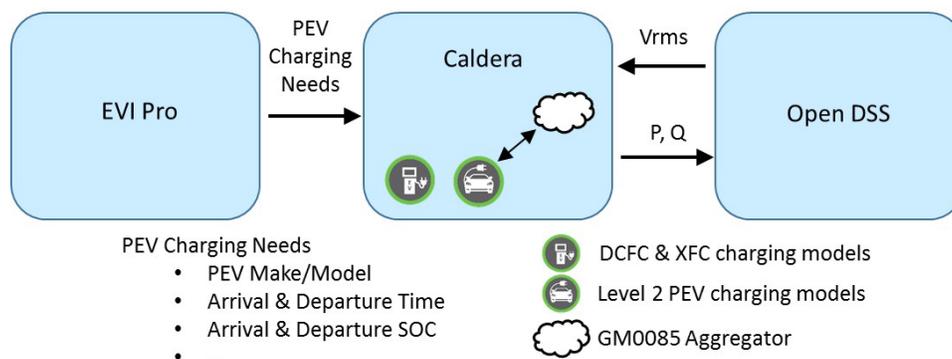


Figure V.5.1 Simulation architecture used in RECHARGE project

### Develop Caldera Charging Models

During FY2019, high-fidelity PEV charging models were developed and integrated into Caldera for AC Level 1 charging, AC Level 2 charging, 50-kW DC fast charging (DCFC), and xFC. These high-fidelity models were based on data collected from extensive laboratory testing of PEV charging systems and batteries. Once the models were developed, they were validated against the lab testing results.

In the RECHARGE project, fast charging models were created and then integrated into Caldera for three types of fast chargers (see Table V.5.1) and five types of PEVs (see Table V.5.2). The charge profile depends on both the charge capabilities of the PEV and the electric vehicle supply equipment (EVSE) that the PEV is connected to. The high-fidelity PEV and EVSE charging models take into account the equipment capabilities and dependencies. Figure V.5.2 shows the charging profiles from the Caldera PEV charging models when the PEVs are connected to a 350-kW capable XFC unit.

Table V.5.1 Types of High-Powered EVSE Used in the Recharge Project

SE Class	Max Charge Rate (kW)	Voltage Class
dcfc_50	50	LV
xfc_150	150	HV
xfc_350	350	HV

**Table V.5.2 Types of PEVs in the RECHARGE Project**

BEV Class	Battery Chemistry	All Electric Range (miles)	Watt hr/mile	Usable Battery Size (kWh)	Rated Battery Size (kWh)	Voltage Class
BEV250_Id2_300kW	NMC	250	350	88	92.1	HV
BEV200_Id4_150kW	NMC	200	475	95	100.0	HV
BEV275_Id1_150kW	NMC	275	300	83	86.8	HV
BEV250_Id1_75kW	NMC	250	300	75	78.9	LV
BEV150_Id1_50kW	NMC	150	300	45	47.4	LV

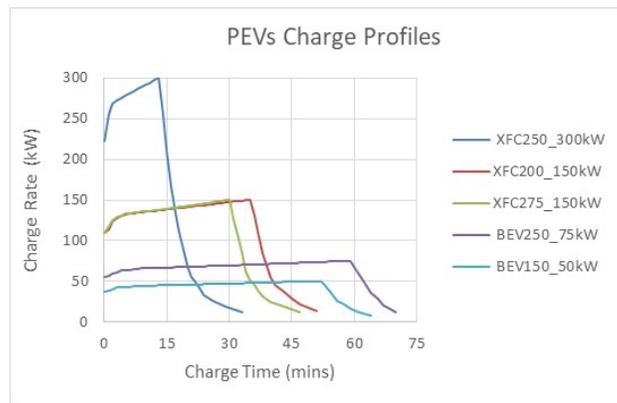


Figure V.5.2 Caldera charging profiles for PEV charging models in when the PEVs are connected to a 350-kW capable XFC unit

***Integrate into Caldera the Centralized Control Strategy from the GM0085 project***

During FY2019, the centralized AC Level 2 charging control strategy developed in the “GM0085” project, funded by Vehicle Technologies Office through the Grid Modernization Laboratory Consortium, was integrated into Caldera. This charging control strategy was able to effectively shift residential PEV charging power from peak grid times to off peak grid times (see Figure V.5.3). This not only nearly eliminated the increase in peak demand for residential level 2 charging, but it also reduced the daily variability in the load profile.

In the RECHARGE project, this centralized Level 2 charging control strategy is the first strategy being used to investigate the benefits of controlled PEV charging.

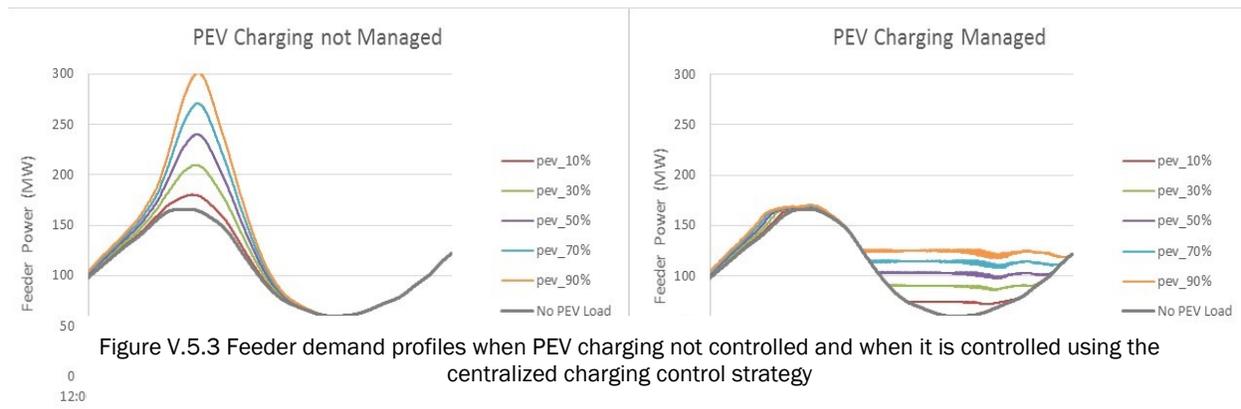


Figure V.5.3 Feeder demand profiles when PEV charging not controlled and when it is controlled using the centralized charging control strategy

### Develop Additional Control Strategies

In FY2019, additional control strategies beyond the GM0085 centralized control strategy were investigated and developed. This process began with a thorough literature review of various architectures for distributed control strategies. This literature review identified three types of approaches that could be used to control Level 2 PEV charging. These three approaches are the aggregator-assisted centralized approach, fully distributed approach, and aggregator-assisted decentralized approach.

The aggregator-assisted centralized approach is capable of achieving a global optimal solution easily. The aggregator dictates precisely when and how much energy every individual PEV will charge. PEVs do not determine their own charging patterns. However, this strategy requires the communication of sensitive information (e.g., arrival and departure times, energy requirements) from PEVs to an aggregator.

The fully distributed strategies generally use a multi-agent framework to facilitate the charging coordination and as a result does not use an aggregator. Each PEV is allowed to make its own charging decisions and communicates directly with other PEVs to reach a consensus. This approach usually works well when relatively few PEVs are controlled, but this strategy is not easily scalable as the number of PEVs increases. The amount of communication needed increases drastically with the number of PEVs.

The aggregator-assisted decentralized strategy is the strategy recommended by INL to use and study in the RECHARGE project. This strategy incorporates the strengths of both the aggregator-assisted centralized and fully distributed approaches and addresses the weaknesses of both strategies. The aggregator in this type of approach serves in a passive role as a coordinator, not a decision maker. Messages communicated with the aggregator would not include any sensitive information about the PEV user, such as arrival time, departure time and required energy of each charging action, which is one of advantages from decentralized strategies. Compared to fully distributed strategies, all PEVs only communicate with the aggregator, not with each other, in aggregator assisted decentralized strategies. This kind of hierarchical communication structure is more easily scalable. Therefore, aggregator-assisted decentralized strategies are feasible to balance the trade-offs between centralized approaches and fully distributed approaches, reducing the risk of sensitive information communication, distributing the computational burden to each PEV and reducing the overall system communication burden.

### Generated Uncontrolled Charging Profiles from EVI-Pro

During FY2019, uncontrolled charging load profiles, made up of both real and reactive power, were created using Caldera for two different scenarios. Caldera created the power profiles using the output from EVI-Pro. EVI-Pro output consisted of when and where PEVs are charged as well as the state of charge of each battery at the beginning of the charge. Uncontrolled charging load profiles were generated for both Atlanta and Minneapolis.

The first scenario was focused on uncontrolled Level 2 residential charging. In Minneapolis, there were 73,029 charge events over a 24-hour period and in Atlanta, there were 94,911 charge events over a 24-hour period. The real and reactive power profiles for PEV charging are displayed in Figure V.5.4. With this many charge events, the peak real power approaches 90 MW in Atlanta and 70 MW in Minneapolis.

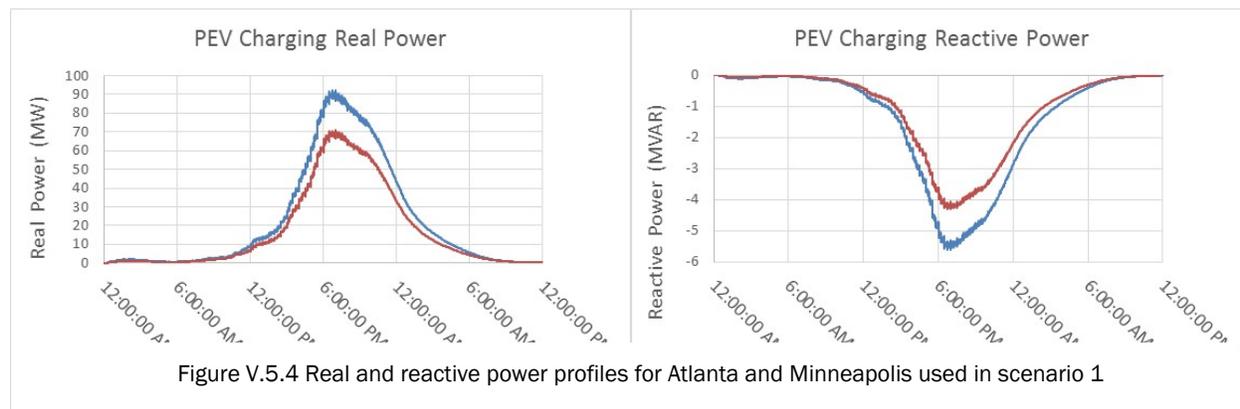


Figure V.5.4 Real and reactive power profiles for Atlanta and Minneapolis used in scenario 1



The second scenario was focused on uncontrolled Level 2 residential and workplace charging with a very small amount of fast charging. In Atlanta, there were 340,000 Level 1 charge events, 300,000 Level 2 charge events, and 20 fast charging events. In Minneapolis, there were 250,000 Level 1 charge events, 240 Level 2 charge events, and 25 fast charging events. The real and reactive power profiles for PEV charging are displayed in Figure V.5.5. This figure shows that with this many charge events, the peak real power approaches 350 MW in Atlanta and 260 MW in Minneapolis.

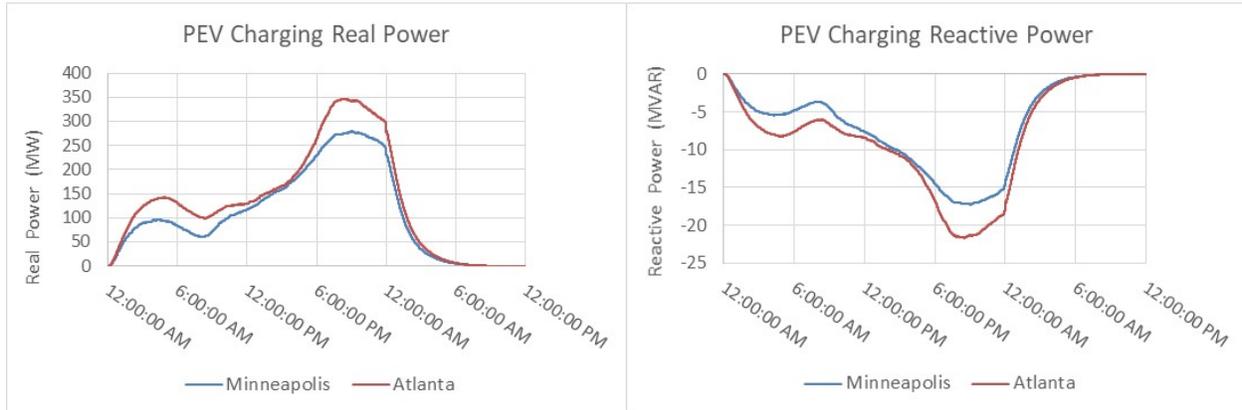


Figure V.5.5 Real and reactive power profiles for Atlanta and Minneapolis used in scenario 2

## Conclusions

While this work is still ongoing (two project years remain), work so far has highlighted the possible challenges in PEV integration if PEV charging is uncontrolled. In order to quantify the effects of uncontrolled charging to understand how increased PEV adoption may negatively impact the grid, and to analyze the effectiveness of multiple control strategies in mitigating negative grid impacts introduced by PEVs at scale, it is essential to have high-fidelity models of PEVs and effective PEV charging control strategies. To this end, high-fidelity charging models have been integrated into Caldera, as have existing control strategies developed in past projects. The work to develop new PEV charging control strategies has begun and will be continued in the next year of the project.

## References

1. Open Distribution System Simulator™. Available: <http://sourceforge.net/projects/electricdss/>. Accessed October 11, 2019.
2. Kersting, W. H. "Distribution feeder voltage regulation control." 2009 IEEE Rural Electric Power Conference. IEEE, 2009.

## V.6 Smart Electric Vehicle Charging for a Reliable and Resilient Grid (Recharge) (SNL)

### Matthew Lave

Sandia National Laboratories  
7011 East Avenue  
Livermore, CA 94550  
E-mail: [mlave@sandia.gov](mailto:mlave@sandia.gov)

### Lee Slezak, DOE Program Manager

U.S. Department of Energy  
E-mail: [Lee.Slezak@ee.doe.gov](mailto:Lee.Slezak@ee.doe.gov)

Start Date: October 1, 2018

End Date: September 30, 2021

Project Funding (FY19): \$550,000

DOE share: \$550,000

Non-DOE share: \$0

### Project Introduction

Adoption of plug-in electric vehicles (PEVs) has expanded over the last few years, yet introduction of PEV smart charging has been stalled due to barriers in communication, controls, and an unclear method for determining the value PEVs will bring to the grid. This project will consider the grid impact of a variety of future scenarios, including adoption of different vehicle types, proliferation of extreme fast charging (xFC), expanded adoption of distributed energy resources (DER), and multiple smart charge management approaches. This project will determine how PEV charging at scale should be managed to avoid negative grid impacts, allow for critical strategies and technologies to be developed, and increase the value for PEV owners, building managers, charge network operators, grid services aggregators, and utilities.

Sandia National Laboratories (Sandia) is a team member on this project, which also includes the National Renewable Energy Laboratory (NREL) and Idaho National Laboratory (INL). Sandia will 1) focus on the grid integration impacts of EV smart charge management, 2) model the interplay of multiple DER to understand how EV smart charging will interact with other grid resources and 3) leverage its electric grid resiliency analysis framework to understand the impact and possible benefits of smart charging during extreme events.

### Objectives

This project will address benefits and barriers of smart charge management for PEVs at scale through multi-lab collaboration. Taking advantage of their combined cutting-edge facilities, capabilities, and access to data, the team will develop technology for real-world implementation of smart charging. The team will investigate grid resilience and reliability challenges and opportunities presented by mass adoption of PEVs through detailed simulation. Team research will:

1. Quantify the effects of uncontrolled charging to understand how increased PEV adoption may negatively impact the grid
2. Analyze the effectiveness of multiple control strategies in mitigating negative grid impacts introduced by PEVs at scale
3. Rank the benefits and costs of the control strategies in avoiding grid upgrades, providing grid services, and improving resilience, and
4. Overcome technical barriers to implementing high-value control strategies.

### Approach

The project is separated into nine tasks to accomplish the four objectives listed above. Sandia is involved in the following tasks:

***Task 1: Scoping, requirements, and industry engagement***

Identification of regions for the PEVs at scale analysis will be performed to engage utility partners willing to support and provide distribution feeder models, load data, and other analysis or insight into the operation of their distribution system.

***Task 3: PEV charging and distribution system modeling***

Detailed distribution grid models will be implemented to understand the locational impact of PEV charging on distribution grid operations and identify voltage or thermal constraints. This modeling will take place in OpenDSS, a powerful open-source software conducive to both translating results to commercial software and to releasing developed tools and models to the research community.

***Task 4: Quantifying the impact of uncontrolled charging***

Sandia will apply existing hosting capacity analysis tools to possible PEV charger connections. For each node on the distribution feeder, the maximum charging capacity will be identified. Hosting capacity also resolves the limiting factor (e.g., voltage violations or current limits), which can be used to understand the sensitivity of the feeder.

***Task 5: Refining smart charge control strategies***

This task will study the potential of multiple control approaches to mitigate negative impacts of PEV charging at scale and provide grid services. New functionality will be added to control PEVs across multiple distribution feeders and to include bulk grid impacts in the objective function. A series of simulations will be run to compare the efficacy of each control's approach in delivering multiple grid services in various future scenarios.

***Task 6: Value of smart charging***

The value of implementing smart charging will be quantified using the same process as in Task 4. The hosting capacity with various methods of smart charging (including controlled ramps up in charging, smart temporal charging, etc.) will be compared to the hosting capacity for uncontrolled charging. The increase in hosting capacity will be compared against the “cost” of smart charging (e.g., slower charging, charge not available when needed, etc.) to determine the value and tradeoff of smart charging.

***Task 7: Resilience Impact***

PEV impacts to grid operations during resilience events may be fundamentally different than impacts during normal operations. This task will investigate how smart charging can adapt to a “coherence of load,” a significant increase in PEV load that happens very rarely. The team will investigate how the power and charging infrastructure and controls can support these extreme scenarios without “gold-plating” the power system.

**Results**

Results by task are listed below.

***Task 1: Utility Engagement***

Sandia has partnered with utilities interested in EV integration. Through these partnerships, Sandia has obtained insights and data related to PEV integration. Sandia has had regular communications with utility employees in power delivery, electric transportation, and distribution systems operations.

***Task 3: Distribution System Modeling***

Through partnerships with distribution utilities, Sandia has received and analyzed distribution system models for 10 feeders. These feeders were converted to OpenDSS format [OpenDSS 2019], as OpenDSS suited to research-level analysis due to its ability to interface with data analysis programs through a COM interface. An overview of the feeders is shown in Table V.6.1.

**Table V.6.1 Feeder Descriptions**

	Description
<b>Feeder 1</b>	Residential
<b>Feeder 2</b>	Residential, some Commercial
<b>Feeder 3</b>	Industrial
<b>Feder 4</b>	Commercial and Residential
<b>Feeder 5</b>	Commercial, some Residential
<b>Feeder 6</b>	Industrial
<b>Feeder 7</b>	Residential and Commercial
<b>Feeder 8</b>	Residential and Commercial
<b>Feeder 9</b>	Commercial
<b>Feeder 10</b>	Commercial, some Residential

***Task 4: Impact of Uncontrolled Charging***

On each of the 10 feeders, Sandia performed hosting capacity analysis. Hosting capacity cycles through each node on the feeder (i.e., each location where a PEV might possibly be connected), adds a new PEV load, and incrementally increases the size of this load until a violation is detected. Violations include excessive loading of lines and under- or over-voltage situations. When a violation is reached, that size of PEV load is recorded as the hosting capacity at that node, the PEV load is removed from the circuit (to return the circuit to the base state with no PEV loads), and the process repeats at the next node.

Figure V.6.1 shows an example hosting capacity result. Feeder nodes along the three-phase backbone of this feeder have large hosting capacities: at least 7MW as indicated by the blue color in Figure V.6.1. Feeder nodes along single-phase laterals of the feeder had much lower hosting capacities, as indicated by the red colors in Figure V.6.1. In some of these areas, the hosting capacity limit was due to larger PEV charge loads exceeding the line rating—single-phase lines typically have smaller capacities. Other areas were affected by undervoltage violations, especially as loads connected to single-phase systems can increase load imbalance between the three phases and quickly reduce the voltage to below the ANSI Range A of within +/- 5% of nominal voltage (i.e., 114-126V for a residential 120V system) [Kersting 2019].

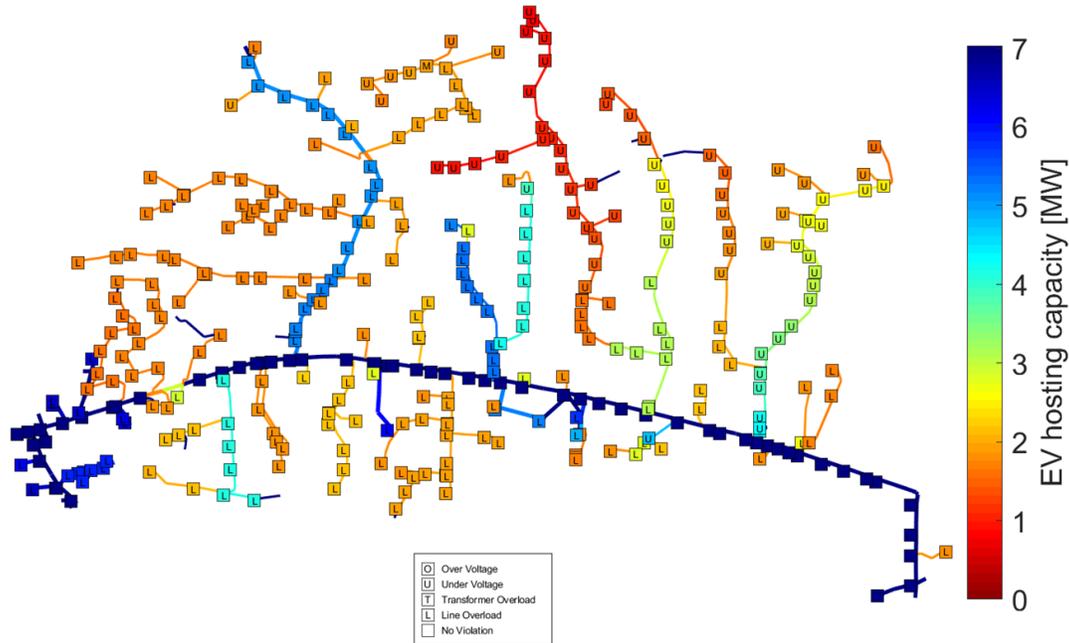


Figure V.6.1 Hosting capacity result for a residential feeder.

#### ***Task 5: Smart Charge Control Strategies***

The uncontrolled charging hosting capacity is a worst-case scenario, where all chargers that exist on the feeder are assumed to be in-use at full capacity. In this task, we have begun to look at the impact that smart charging can have to reduce or eliminate the hosting capacity limits seen in the uncontrolled charging case. For example, when undervoltage violations are the limiting factor, we are looking to introduce control strategies which reduce real power draw during low-voltage times, such as delaying charging slightly to avoid feeder peak demand. Similar controls are being explored to alleviate line-loading concerns—limiting simultaneous charging to ensure that power flow through a particular line never exceeds the line’s rating. Geographic controls shifting charger locations to areas with high hosting capacity are also being explored.

#### ***Task 6: Impact of Smart Charging***

Sandia has started to implement the control strategies considered in Task 5 into the hosting capacity analysis to understand the impact. This work will be continued throughout project year two.

#### ***Task 7: Resilience Impact***

This task is planned for project year three and work has not yet started.

### **Conclusions**

While this work is still ongoing (two project years remain), work so far has highlighted the possible challenges in PEV integration if PEV charging is uncontrolled. With the distribution feeder data obtained, hosting capacity analysis was used to identify grid vulnerabilities. Across all feeders, limits were either line loading or undervoltage, though the size of PEV charge load at which that limit occurred depended on both the feeder and the location of the PEV charger on the feeder. This has highlighted opportunities for controlled charging: controls can both reduce or mitigate line loading and voltage problems by limiting charging during times when the feeder is stressed, and by encouraging geographic movement of charge events to areas without line loading or voltage limitations. The impact of controlling charging in these ways will be explored in project years two and three.

### Key Publications

1. Lave, M. "Towards High Fidelity Modeling of DER Integration to Distribution Grids." *Smart Grid Edge Analytics Workshop*, Atlanta, GA, June 2019. Available: [https://smartgridedgeworkshop.ece.gatech.edu/wp-content/uploads/sites/995/2019/06/S32\\_MattLave\\_SANDIA.pdf](https://smartgridedgeworkshop.ece.gatech.edu/wp-content/uploads/sites/995/2019/06/S32_MattLave_SANDIA.pdf).

### References

1. Open Distribution System Simulator™. Available: <http://sourceforge.net/projects/electricdss/>. Accessed October 11, 2019.
2. Kersting, W. H. "Distribution feeder voltage regulation control." *2009 IEEE Rural Electric Power Conference*. IEEE, 2009.

### Acknowledgements

Sandia National Laboratories is a multimission laboratory managed and operated by National Technology & Engineering Solutions of Sandia, LLC, a wholly owned subsidiary of Honeywell International Inc., for the U.S. Department of Energy's National Nuclear Security Administration under contract DE-NA0003525. SAND2019-13042 R.

## V.7 Development of a Multi-port 1+ Megawatt Charging System for Medium-and Heavy-Duty Electric Vehicles (ORNL)

### Madhu Chinthavali, Principal Investigator

Oak Ridge National Laboratory  
 2360 Cherahala Boulevard  
 Knoxville, TN 37932  
 E-mail: [chinthavalim@ornl.gov](mailto:chinthavalim@ornl.gov)

### Lee Slezak, DOE Program Manager

U.S. Department of Energy  
 E-mail: [Lee.Slezak@ee.doe.gov](mailto:Lee.Slezak@ee.doe.gov)

Start Date: October 1, 2018      End Date: September 30, 2019  
 Project Funding (FY19): \$1,000,000      DOE share: \$1,000,000      Non-DOE share: \$0

### Project Introduction

Electrification of medium and heavy-duty vehicles is creating a demand for extreme fast charging solutions at power rates above 1MW. Existing solutions which depend on parallelization of units of up to 50kW are not scalable to this new demand. This project will address barriers for deployment of 1+MW scale integrated charging stations by identifying the feasibility of higher power building block architectures, integration of distributed energy resources (DERs), and balance of system impacts.

### Objectives

The first-year project objectives include performing a review of existing power electronic topologies that can be applied to 1+MW fast charging applications and performing simulation studies to evaluate feasibility and relative merits of the various candidate architectures. Through these studies, several candidate charger architectures were developed; out of which, three candidates were selected for future detailed simulation and analytical study. The three architectures reflect three diverse approaches integrating grid power with distributed energy resources (DERs), i.e., local storage in the form of batteries and power generation from local solar photovoltaic panels.

### Approach

The first architecture candidate is an AC Coupled architecture where all components are interconnected through a common 480V, 60Hz AC bus. The second is a low-voltage DC Coupled architecture, where are components are interconnected through a common 2kV DC bus. The third is a Medium Voltage (MV) Architecture that connects directly to the medium voltage distribution grid using a cascaded H-Bridge (CHB) converter. The evaluation approach used lumped model analysis to estimate overall system performance attributes to provide a basis of comparison on critical metrics shown in Table V.7.1 across the architecture types for the candidate extreme fast charging (XFC) systems.

**Table V.7.1 1+MW Architecture Evaluation Metrics**

Attribute	Metric
Efficiency	Semiconductor Losses
	Overall System Efficiency
	Standby Efficiency
Performance	Transient DC Voltage Stability
	Grid-side voltage stability

Attribute	Metric
	Advanced Grid Support
	Output current ripple control
	Active device ratings
System Ratings	Low Frequency Stepdown Transformer
	AC-side breaker and switchgear requirements
	Modularity
Scalability	System Scalability

## Results

### Task Summary

In the first phase, overall system level performance metrics were identified for the extremely fast charging (XFC) system with a few of these candidate architectures shown in Figure V.7.1. Based on the estimated overall attributes, the three best architectures were selected for further study: a DC Coupled architecture, an AC-Coupled architecture, and a CHB-based Medium Voltage Architecture. The first two of these connect to the distribution system through a conventional low-frequency transformer similar to existing chargers today. The third topology eliminates this low frequency transformer by using multiple high-frequency transformers driven by individual dual-active bridge converters. The overall system level terminal specifications were also identified and are listed in Table V.7.2.

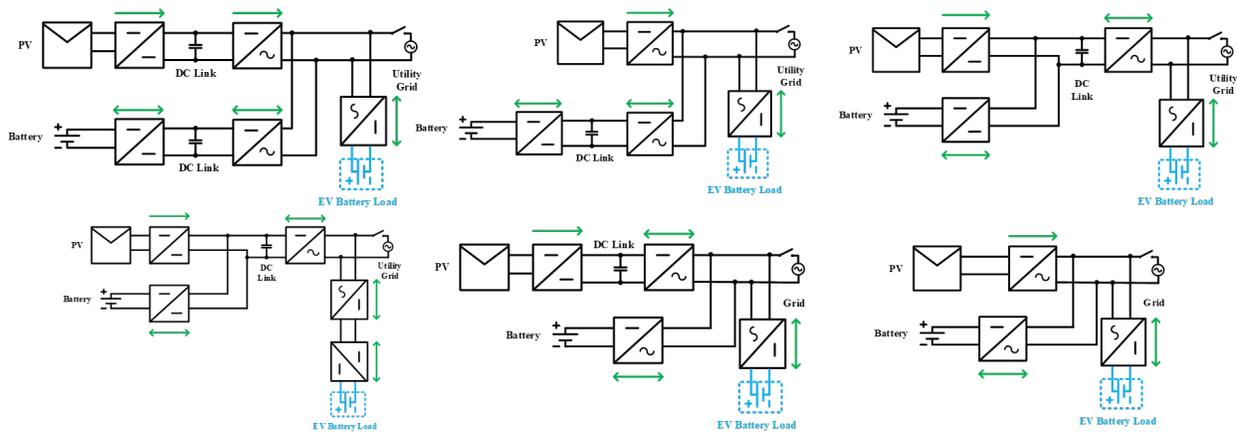


Figure V.7.1 Topology of candidate 1+MW System Architectures

Table V.7.2 System Level Terminal Specifications

	Parameters	Value
Grid	Grid voltage (Low voltage) RMS, $V_{II}(rms)$	480 V
	Grid voltage (Medium voltage) RMS, $V_{II}(rms)$	3.3kV-13.8kV
	Line frequency, $f$	60 Hz



	Parameters	Value
Load	Rated Charging Power, $P_{load}$	1.2 MW
	Battery Voltage, $V_{batt}$	1kV-1.5KV
Charging Unit	Number of charging units, $N$	3
	Power rating of each charging unit, $P_c$	400 KW
	DC bus voltage, $V_{bus}$	2 kV
DERs	PV power rating of each charging unit, $P_{pv}$	200 KW
	Battery power rating of each charging unit, $P_{batt}$	200 KW

In order to improve modularity and scalability for the DC and AC architectures, the entire topology was organized as parallelizable 400kW blocks, enabling the use of multiple such blocks for applications having both aggregated and unitized batteries as shown in Figure V.7.2. In addition, existing products were surveyed to determine voltage, current and power limits of individual components such as lithium ion batteries and photovoltaic panels which helped determine the appropriate system level terminal specifications.

At the same time, the impact of the XFC system on the grid and the distribution system was also considered. A review of the distribution system was conducted in order to model and simulate the upstream feeder network. This preliminary simulation and analysis determined the potential grid impacts using “ideal” fundamental frequency, lumped model of the XFC converter, and the findings will be used to refine and design the control for the XFC in subsequent tasks of this project.

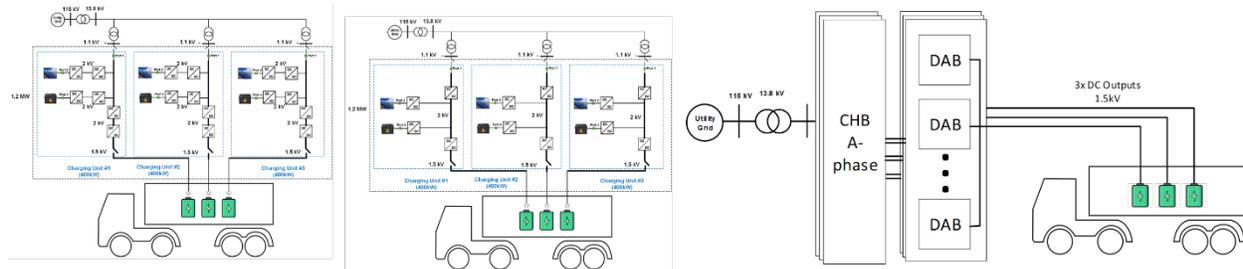


Figure V.7.2

It was seen that conventional voltage regulation using methods such as load tap-changers and voltage regulators is too slow and cannot respond fast enough when multiple XFCs are present on the feeder. Voltage control through reactive power injection, while possible, is limited by the inverter size and is possible within a limited range of power factors. As a result, active power management and load shaping using the available DERs are necessary.

In conjunction with this, active power control was also examined to determine the load demand, the output current ramp rates, and how the individual converters in the architecture respond to changes in the load demand. It was seen that the most challenging case is during fault on the load side, when the entire load may

have to be disconnected. This can cause stability issues which need to be addressed using controller action. These were analyzed finding that the MV topology was best suited to address these issues.

***Architectural Studies:***

The key conclusions of the simulation and analytical study of the XFC Architectures is given below.

- Efficiency Attribute (Semiconductor loss estimation):
  - In AC coupled Architecture, from “efficiency” attribute point of view, semiconductor loss metrics shows worst efficiency numbers since each source/load stage has two power conversion stages
  - Whereas, DC coupled architecture shows better efficiency numbers as it has a smaller number of power conversion stages than AC coupled architecture for each charging unit of 400 kW since the DER converters share a common DC bus with the load converter.
- Reliability Attribute (Single Point Failure):
  - In AC coupled Architecture, loss of load grid-interfacing converter would lead to zero power being supplied to the EV load for each 400 kW charging unit
  - DC Coupled Architecture is much better than AC Coupled Architecture since it can still supply power to the EV Load with the loss of grid interfacing converter.
- Reliability Attribute (EV Fault Response):
  - In AC coupled Architecture, fault in EV Load will impact the load grid interfacing converter node, but the DERs with their own grid interfacing converters will not be significantly impacted by the sudden load shutdown
  - DC Coupled Architecture is worse than AC Coupled Architecture since any EV fault will majorly impact the DER converters; in addition, they are all tied to a common dc bus and might warrant the complete shutdown of all the power electronic converters in the entire 400 kW charging unit.
- Reliability Attribute (Grid Fault Response):
  - In AC Coupled Architecture, grid fault response has the potential of impacting each grid interfacing converters (either Load or DERs) and might cause complete shutdown of the 400 kW charging unit
  - Whereas, in DC Coupled Architecture, grid fault response might cause the grid interfacing converter to disconnect, but the charging unit can still supply load power through the DER converters.
- Reliability Attribute (Grid Voltage Quality):
  - In AC Coupled Architecture, grid voltage quality may be improved from:
    - harmonics standpoint by utilizing the converters in the DERs to provide active grid harmonic elimination
    - voltage sag and swell disturbances through reactive power support to the grid through each grid interfacing converters

- Whereas, in DC Coupled Architecture, the number of grid interfacing converters are less which would result in reduced capability of active harmonic cancellation as well as grid voltage sag and swell disturbances.
- Also, DC coupled Architecture might be limited to one such grid voltage quality functionalities as it has only one grid connected converter for each 400 kW charging unit; as compared to the AC architecture, both the grid functionalities may be pursued at the same time due to the availability of several grid interfacing converters in each 400 kW charging unit
  - From this attribute metric point of view, AC coupled architecture scores better than DC Coupled architecture.
- THD: Grid Connected Converter injects switching harmonics to the grid which is typically attenuated by grid interfacing filter attached to the output of the inverter pole outputs
  - AC coupled architecture is worse than DC coupled architecture since it requires three grid interfacing inverters as compared to on grid interfacing inverter in the DC coupled case. It may also be observed that the three converters would require three grid interfacing filters which would reduce the overall system efficiency of an AC coupled architecture to a much lower value than DC coupled architecture.
- Dynamic Response to EV Load Charging Ramp up / Disconnection Ramp Down Command:
  - In both cases, AC and DC Coupled architecture, in absence of DER, the system dynamic response to such ramp changes in load current has been analyzed. It has been seen that the response is same in both the cases since they have the same power electronic circuit configuration
  - In presence of DER, the system dynamic performance to these ramp load current changes is still under investigation for both the AC and DC coupled architectures.
- Initial System Black Start Transients:
  - In both cases, AC and DC Coupled architecture, in absence of DER, the system dynamic response to such ramp changes in load current has been analyzed. It has been seen that the response is same in both the cases as AC and DC Coupled Architecture have the same power electronic circuit configuration. The methodology that is being used currently is to pre-charge DC bus voltage with a pre-charge circuit up to a certain voltage. Then, implement ramp control command using dc bus voltage control with cascaded current control to achieve desired dc bus voltage. This minimized the initial transients seen at the DC Bus voltage and minimized inrush currents from grid. Also, DC Bus Cascaded Control output to AC current Control is bypassed, and a Power reference command feedforward to current loop has been introduced to further reduce any dc bus voltage transients. Thereby, limiting the voltage variation to less than  $\Delta V = 100 \text{ V}$  (5% of 2 kV DC bus voltage)
  - In presence of DER, the system dynamic performance to such Initial System Black Start Transients is still under investigation for both the AC and DC coupled architectures.

### ***Distribution System Impacts***

The voltage drop caused by multiple XFCs can be a realistic and challenging problem in a distribution system. The voltage drop is directly related to the XFC power consumption and the feeder line resistance of a distribution system. With the line impedance and the distance of a typical distribution system, only 2 MW of XFCs (5 – 400 kW charge block units) would cause 5~7 % of voltage drop as shown in Figure V.7.3. In addition, the voltage drop would appear within very short time due to the rapid charging rate of XFC.

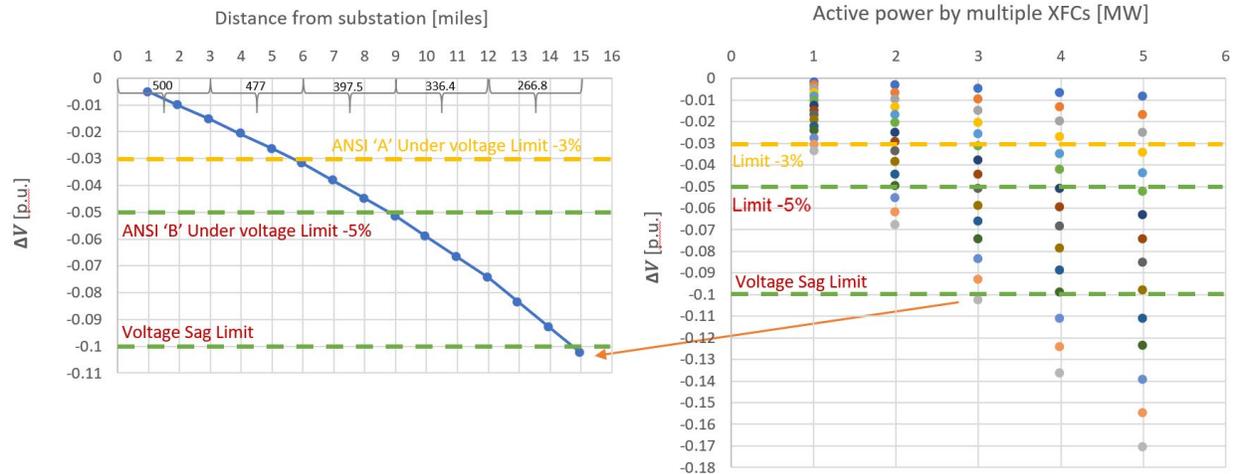


Figure V.7.3 Expected voltage drop introduced by multiple XFCs in a distribution system

In a distribution system, there are conventional voltage regulation equipment such as on-line tap changer (OLTC), step voltage regulator (SVR), and shunt capacitor bank etc. A significant number of algorithms were developed for the optimal voltage regulation. However, these conventional methods might not resolve the voltage drop problem caused by XFCs since the operational delay time is too long to manage the voltage drop properly.

To deal with the voltage drop problem, there can be three possible solutions: voltage regulation support by injecting reactive power at XFC, limited location of XFC to reduce the feeder line resistance, and active power control to reduce the XFC demand. In this research, the voltage support function by injecting reactive power at XFC was studied according to IEEE standard 1547-2018.

According to IEEE 1547-2018, XFC systems are required to provide the voltage regulation function by controlling the output reactive power with four different control modes: constant reactive power mode, voltage-reactive power mode, constant power factor mode, and active power-reactive power mode. Therefore, the controllers were developed for XFC system to perform the four different voltage regulation modes.

In IEEE 1547-2018, the level of the reactive power capability required for voltage regulation is 44% of the rated apparent power of the unit. Since the reactive power capability depends on the number of the grid-connected inverters of the XFC system, the capability was compared with the three different XFC architectures. Based on the comparison, an XFC system with AC architecture has a superior capability for the voltage regulation due to the higher number of grid-connected inverters as shown in Figure V.7.3. However, the possibility of control conflicts needs to be investigated for the regulation performance. To analyze the conflicts of voltage regulation, co-simulation setup was developed by using PSCAD and MATLAB Simulink.

## Conclusions

Based on a lumped model analysis to estimate overall candidate systems attributes, the three candidate architectures listed below were selected for further study:

- DC Coupled architecture: components are interconnected through a common 2kV DC bus
- AC-Coupled architecture: components are interconnected through a common 480V, 60Hz AC bus
- Medium Voltage Architecture: connects directly to the medium voltage distribution grid using a cascaded H-Bridge (CHB) converter

Each of these approaches were investigated from the grid conversion and impact as well as the interaction with DERs (local battery energy storage and photovoltaic panels) and EV load converters. Based on simulations and analytical studies performed in this project, some key relative merits of these three architectures are summarized in Table V.7.3. Taking all factors into account, the Medium Voltage topology using the cascaded H-Bridge (CHB) converter is selected as the most suitable and is therefore chosen for further study in Year 2 and Year 3 of this project.

**Table V.7.3 Summary Metrics for Top Three Candidate Topologies**

Attribute	Metric	Architecture		
		DC Coupled Arch.	AC Coupled Arch.	MV-CHB Arch.
Efficiency	Semiconductor Losses	Lowest in pure-DER mode	Lowest during pure-grid mode	Balanced
	Overall System Efficiency	Better	Good	Best
	Standby Efficiency	Good	Good	Good
Performance	Transient DC Voltage Stability	Better	Good	Best
	Grid-side voltage stability	Best	Poor	Good
	Advanced Grid Support	Comparable	Comparable	Comparable
	Output current ripple control	Good	Good	Best
System Ratings	Active device ratings	Good	Good	Best, Low due to Modular converter structure
	Low Frequency Stepdown Transformer	Required	Required	Not Required
	AC-side breaker and switchgear requirements	High-current AC interface	High-current AC interface	Low-current AC interface
Scalability	Modularity	Good	Good	Best
	System Scalability	Good	Poor	Best

**Acknowledgements**

The following investigators have worked on this project: Pankaj Bhowmik, Namwon Kim, Jongchan Choi, and Abhijit Kshirsagar.

## V.8 Development of a Multiport 1+Megawatt Charging System for Medium- and Heavy-Duty Electric Vehicles (NREL)

### **Andrew Meintz, Principal Investigator**

National Renewable Energy Laboratory  
15013 Denver West Parkway  
Golden, CO 80401  
E-mail: [andrew.meintz@nrel.gov](mailto:andrew.meintz@nrel.gov)

### **Kevin Walkowicz, Principal Investigator**

National Renewable Energy Laboratory  
15013 Denver West Parkway  
Golden, CO 80401  
E-mail: [kevin.walkowicz@nrel.gov](mailto:kevin.walkowicz@nrel.gov)

### **Lee Slezak, DOE Program Manager**

U.S. Department of Energy  
E-mail: [Lee.Slezak@ee.doe.gov](mailto:Lee.Slezak@ee.doe.gov)

Start Date: October 1, 2018

End Date: September 30, 2021

Project Funding (FY19): \$1,000,000

DOE share: \$1,000,000

Non-DOE share: \$0

### **Project Introduction**

Medium-duty (MD) and heavy-duty (HD) electric vehicles (EVs) are being manufactured today and will soon necessitate the use of megawatt (MW)-scale charging systems that can quickly charge large capacity (~800 kWh) battery packs in less than ~30 minutes at an attractive charging cost (\$/kWh). This fast charging time is needed to maximize the revenue-generating operations of commercial MD/HD vehicles. The integration of renewable energy and grid-tied energy storage, coupled with these large and somewhat variable high-power vehicle charge events, will require an integrated system that can be used with minimum impact on the grid.

Many challenges must be met to realize such an integrated system, including 1) understanding and optimizing power demand and management requirements, 2) configuring local infrastructure requirements, 3) designing grid interface converters, 4) managing impacts on grid power quality, 5) developing distribution voltage-level hardware for the point of grid connection, 6) developing safe and robust hardware connections, 7) understanding and overcoming power electronics semiconductor and architecture limitations, 8) developing robust thermal management systems, and 9) assessing and developing vehicle-side power delivery architectures.

This project, in coordination with Oak Ridge National Laboratory (ORNL) and Argonne National Laboratory (ANL), will create hardware and system models as well as power and charge control methods and hardware to address challenges associated with MW-scale charging infrastructure for MD/HD EVs. The primary objective of this project is to develop solutions to enable 1+ MW charging systems for MD/HD EVs of various vocations to maximize utilization of the vehicles and the all-electric miles travelled and improve the return on investment, ensuring industry and consumer acceptance. The project will design and develop a cost-efficient, modular, and reconfigurable power electronics architecture, leveraging current DOE research activities and team members' world-class expertise in power electronics, wide bandgap device-based power electronics converters, vehicle charging and energy storage systems, automated wireless charging systems, and grid modernization. This project will generate DOE-owned intellectual property on high-frequency/high-power inverters, high-frequency AC links, novel integrated magnetic structures and planar transformers, vehicle battery pack thermal management, and connecting mechanisms.

This project will ensure that the United States remains a leader in innovative transportation systems by accelerating adoption of MD/HD EVs and assuring the convenient, flexible, and safe integration of ‘beyond’ extreme fast-charging (XFC) technology with our nation’s grid infrastructure.

### Objectives

This project will 1) address challenges and develop solutions for beyond-XFC (1+ MW) systems through a national laboratory collaboration, 2) overcome barriers to deployment of a 1+ MW- scale integrated charging station and provide answers to fundamental questions associated with the feasibility of the system, 3) identify hardware component needs; 4) develop and test hardware and system designs, 5) develop design guidelines and performance metrics 6) assess potential grid impacts and grid services; 7) develop safe systems and smart energy management techniques including on-site resource sizing and management. This project will ultimately develop a framework to develop a flexible, multi-port 1+ MW fast-charging grid- interconnected system allowing for integration with integrated distributed energy resources (DER) such as photovoltaics and energy storage.

### Approach

This collaborative project is separated into fifteen tasks to accomplish the seven objectives listed above. NREL manages tasks 6-12. Tasks 1-5 (Power Electronics and Power Stage Design) are managed by ORNL and tasks 13-15 (Industry Engagement and Requirements) are managed by ANL and are not discussed in this report. For FY19, NREL completed work on Tasks 6,7,8,9 and 12. These tasks are included in this report.

*Task 1: Literature survey / study of new topologies suitable for >1 MW ultra-fast charger (ORNL)*

*Task 2: Perform simulation study of topologies - evaluate feasibility (ORNL)*

*Task 3: Power stage parameter design and hardware component selection (ORNL)*

*Task 4: Technical assessment of supply equipment for MD/HD EVs and ultra-fast chargers (ORNL)*

*Task 5: Develop host controller for power stage of single multiport MW charging system (ORNL)*

*Task 6: Utilization and facility profile for analysis of charger design (NREL)*

The design space considered for this system will include commercial fleets that tend to operate on predictable, semi-fixed routes or can provide communications to predict charging needs. Analysis will determine the frequency of arrival and the expected charging requirements for the chargers on a vocational basis. NREL’s Fleet DNA tool will be leveraged to determine energy demand and timing based on existing conventional fleets. The introduction of vehicle automation will also be considered in forecasting charge station duty cycles impacting vehicle and station design.

*Task 7: Grid impact analysis (NREL)*

This task focuses first on completing a distribution system analysis of the grid impacts of both individual beyond-XFC chargers and multiple (i.e., truck stop) chargers. For the singular charger, the impacts seen for various interconnection locations will be analyzed. For multiple chargers, the optimization of distribution circuit design and operation will be analyzed. In both cases, the grid services and interconnection capabilities necessary to reduce or eliminate adverse grid impacts will be determined. The desired capabilities of the beyond-XFC chargers will be defined and, based on these requirements, the design and architecture of the beyond-XFC charger (particularly the AC input rectifier section) will be determined. The goal of this task is to evaluate grid impacts and propose technical options to minimize impacts. The options would then influence power electronics topology/control design decisions.

*Task 8: Battery load profile and MPC-based optimal control (NREL)*

This task will develop a real-time MPC-based charge control method that simultaneously optimizes charging for multiple EVs at an XFC station to 1) allow the EVs to share a defined peak power for the station, 2) match the variability of the station load to penalties associated with grid impacts, and 3) minimize each EV’s charging time. The control will be deployed in a power-hardware-in-the-loop (PHIL) test environment where

surrogate battery cells represent the EV battery, cell cyclers represent the fast chargers, and single board computers represent both the battery MPC controller(s) and the station controller.

**Task 9: Design overall site control architecture (central controller) – (Year 2 -NREL)**

This task will define the site control parameters and settings necessary to deliver energy to EVs while achieving rapid throughput and minimizing resulting grid instabilities.

**Task 10: Grid interface development for providing insights into the grid services that must be provided for a given location – (Year 2 - NREL)**

This task will define advanced grid interface features that beyond-XFC stations should provide as part of interconnection. The interface should consider existing protocols such as IEC 61850 as they would apply to multi-MW charging stations to improve the scalability of XFC charging infrastructure.

**Task 11: Functional validation of multiport MW charging system via HIL simulation – (Year 3 NREL)**

This task will verify the advanced functions of a multiport MW charging system in a grid connected and/or HIL environment, including control and communication performance. We will model the DER, load, and power electronics interface of a single multiport MW charging system in a HIL real-time emulator, and then integrate the HIL model with developed power stage host controllers and a center controller for a complete HIL testing system. We will test the basic functions such as charging profile tracking, soft startup, and voltage/current regulation, as well as advanced grid-support functions such as volt/var functions.

**Task 12: Electrical + thermal management design of connector and battery charging (NREL)**

This task will research passive and active thermal management technologies integrated into the charging connector mechanism and charging system to vehicle battery to manage battery and charging component temperatures. Technologies include advanced highly conductive materials, passive two-phase heat transfer, and active-pumped liquid heat transfer. The connector mechanism must be robust, and future work will support the evaluation of the reliability of the connector mechanism through recurring loading and application.

**Results for NREL tasks are listed below**

**Task 6: Utilization and facility profile for analysis of charger design**

Sizing and control of the 1+MW station infrastructure will be informed by the station’s expected duty cycle. Using real-world class 8 tractor data, a national network of charging stations was created, and 2 weeks of operation for 35,469 all-electric trucks was simulated. Vehicles were assigned a battery size of 660, 900 or 1200 kWh based operating envelope. Vehicles that covered less than 600 miles were given the smallest batteries, while vehicles covering more than 1200 miles were given the largest batteries. This method divides the trucks into groups of approximately 9,13 and 13 thousand vehicles respectively. To estimate the fraction of electrification of total truck volume being simulated, simulated driving was aggregated by road segment and compared to vehicle miles traveled from the Freight Analysis Framework (FAF) [1]. This comparison is shown in Table V.8.1 with million miles traveled (daily) shown for simulation and FAF data for each roadway. The ‘% covered’ value represents the % of truck miles simulated for this study.

**Table V.8.1 Driving analysis of roadway segments**

VMT	I-10	I-20	I-45	I-5	I-65	I-70	I-75	I-77	I-80	I-81	I-94
Sim	0.62	0.45	0.05	0.42	0.29	0.55	0.51	0.13	1.12	0.35	0.27
FAF	14.8	8.88	1.39	8.75	7.75	11.3	11.4	3.03	29.0	6.53	6.68
% covered	4.18	5.03	3.51	4.79	3.77	4.89	4.53	4.19	3.86	5.41	4.01



The result of the simulation was an arrival schedule for each charging station identified in the roadway analysis and information on the SOC of each vehicle. The station schedule defines when a vehicle entered the station to charge and what the required energy is to recharge the vehicles. Date, time and required energy are recorded for each charging event. Using a charging rate of 1.2MW, a simulated charging schedule is shown for an example station below (station 410726 is shown in Figure V.8.1). Aggregating the data, ~2PM local time is the busiest time for the station (7 vehicles at 8.4 MW potential total load), with twice the demand for charging of the least busy time, 3 AM.

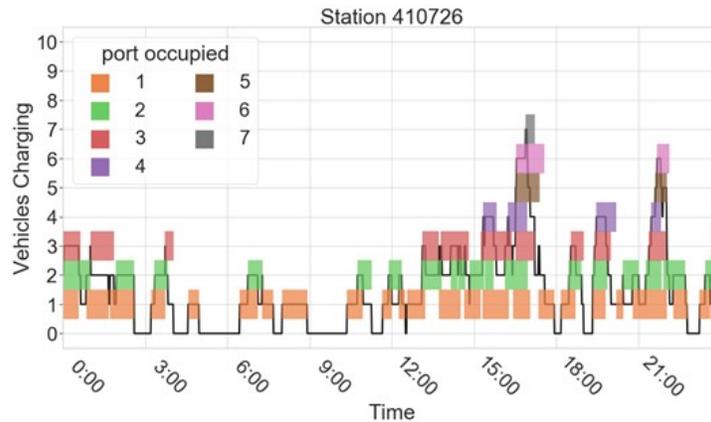


Figure V.8.1 Example of a 5-trip vehicle simulation

### **Task 7: Grid impact analysis**

In this task, we performed grid impact analysis for heavy-duty and medium-duty (HD/MD) electric vehicle (EV) charging stations. We developed a systematic procedure to analyze the potential impact of the placement of charging stations on the distribution grid. Charging load is modeled using a DC 1+MW fast-charging station model developed by the modeling team. A voltage load sensitivity matrix approach is leveraged to investigate the challenges of placing charging stations on the feeder [2]. Given the charging load profiles and suggested charging station locations, time-series simulations are performed on various connection points on the feeder to understand the impact. Analysis was performed on both the IEEE 34-bus system (as an example shown in this report) and an actual feeder from California (not included in this report). Initial mitigation solutions will be developed based on insights from this type of analysis from additional feeders.

**IEEE 34-Bus System Testing:** The nodes at the IEEE 34-node test feeder are sorted out and clustered into different groups. As shown in Figure V.8.2 (a), sample nodes in each group are shown in different colored zones. Four case studies are performed, with the base case representing the case without any charging stations; and Case 1, Case 2, and Case 3 representing good, mediocre, and worst locations, respectively. Five nodes inside each level of location are selected to place the charging stations. Figure V.8.2 (b-c) shows part of the statistical analysis of the 1-day time-series voltage results. Figure V.8.2 (b) shows the distributions of the minimum daily voltage of all the nodes in the system, for all the cases. From Case 1 to Case 3, the number of voltage violations (less than 0.95) increases, which shows that case 1 (good locations) have the best capability to accommodate heavy-duty charging stations. The voltage ramp distribution shown in Figure V.8.2 (c) shows that Case 1 has smaller voltage ramps, whereas cases 2 and 3 have larger voltage ramps.

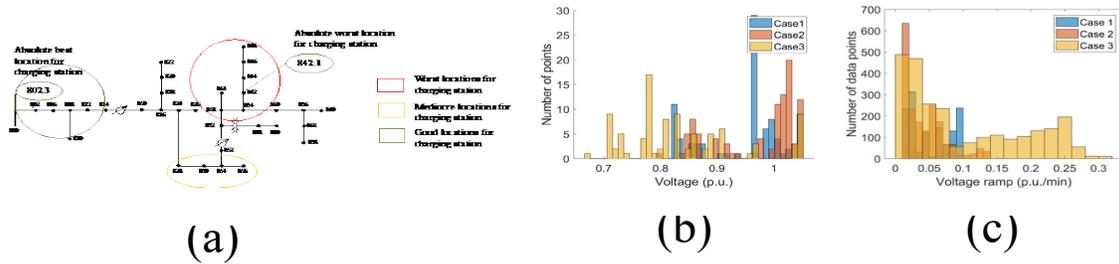


Figure V.8.2 Testing results for IEEE 34-bus system

**Task 8: Battery/station load profile and MPC-based optimal control**

To understand what a station load profile might look like and what type of control would optimize this load, parametric studies were performed by varying three key parameters namely vehicle traffic (vehicles/day), number of ports, and port capacity. It was assumed that the HD vehicle mix at a station consists of equal proportions of 660 kWh, 900 kWh, and 1200 kWh battery-sized vehicles [3],[4] and is charged using the CCCV protocol with a constant current charging rate of 1.5C. One key insight developed through this parametric study is the optimal charging port requirement at a station and the associated trade-offs. Figure V.8.3 (a) shows the variations of peak power demand of a DCFC station with vehicle traffic and the number of installed charging ports. The horizontal lines are the station power capacity for a given number of charging ports. The optimal station design is achieved when the gap between the peak power and station capacity is minimum, but the peak power is not constrained by the station capacity.

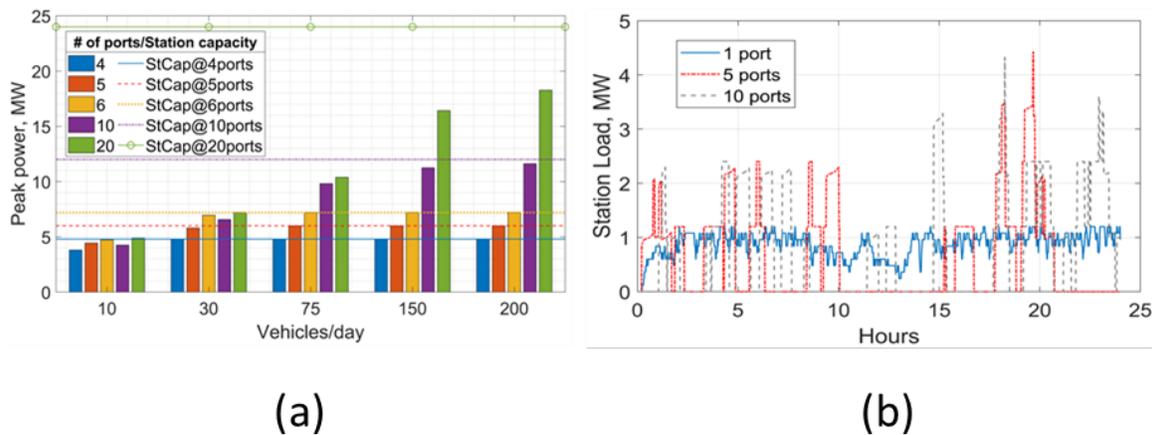


Figure V.8.3 Station load profiles for stations with 30 vehicles / day

A perusal of the resultant station load profiles generated also indicated the presence of an optimal station design for a given vehicle traffic. Figure V.8.3 (b) shows the station load profiles of a station when the number of ports is varied from 1 to 10 while keeping the traffic volume constant at 30 vehicles per day. Capacity of each port is assumed to be 1.2 MW. The similarity between the station loads for 5 and 10 ports in terms of the magnitude of their peaks indicate that for 30 vehicles per day, the charging demand can be met by 5 installed ports or less. Further analysis shows that the average charging time at the station is independent of the vehicle traffic volume but is dependent on the vehicle mix (i.e., vehicle battery size and proportion of each) and infrastructure specifications (i.e., port capacity). Average waiting time, on the other hand, is a traffic volume phenomenon and can be significantly reduced by adding more charging ports. For example, for a traffic of 200 vehicles/day, average wait time decreases to 1.42 minutes from several hours by increasing the number of charging ports from 4 to 10. Charging time can be improved by either increasing the capacity of the charging

ports (provided the batteries can accept the additional power) or by deploying advanced charging algorithms into the battery management system (BMS).

**Task 12: Electrical + thermal management design of connector and battery charging (charger-to-truck)**

The primary focus of the FY19 Task 12 activities focused on a literature review associated with high power charging systems and initial modeling to understand thermal management challenges. The literature review fed the development of a modeling framework and process to build a foundation for year 2 (FY20) activities including numerical modeling of high-power connectors and identifying experimental capabilities with NREL for experimentally characterizing high power connector performance. The work also supported analysis to quantify charge system challenges associated with heat generation. In addition, in support of the CharIN high power commercial vehicle charging (HPCVC) task force, NREL participated in meetings and shared data and results from this project. It is anticipated that NREL will assist with the development and optimization of the new high-power charging standards being developed within CharIN.

*Connector Analysis:* During FY2019 a literature study on power connector mechanisms was conducted to collect information on the characterization and modeling of electrical connectors. Round-shaped pin and socket connectors, which are commonly used in current EV/HEV charging connectors, were selected to further study using numerical analysis tools. A CAD model was created using SOLIDWORKS based on the dimensions of the connectors inside a Phoenix Contact CCS type 1 DC charger cable (model #: 1623634). An indirect coupled mechanical-thermoelectric modeling process was applied to study the coupler. First, the mechanical coupling process of the pin/socket pair was simulated in ANSYS Mechanical. The deformation of socket slits was observed, and a stress-strain profile of the socket was established (Figure V.8.4 (a)). The deformed structure (pin/socket) was then imported into the thermoelectrical module in ANSYS for further analysis with a feeding of constant current (Figure V.8.4 (b)). The model can be used to analyze the impact of heat transfer within the electrical connector. For example, the impact of both the magnitude of the heat transfer coefficient and the location of the cooling within the connector was modeled. An example showing the impact of cooling location on the temperature rise within the connector is shown in Figure V.8.5 (b). The results from the preliminary FEA is more qualitative because there are a few key parameters remaining unknown: thermal contact resistance and electrical contact resistance. Therefore, our next focus in FY20 is to experimentally measure the electrical and thermal contact resistance to quantify the electrical connectors for accurate model-based predication of its performance.

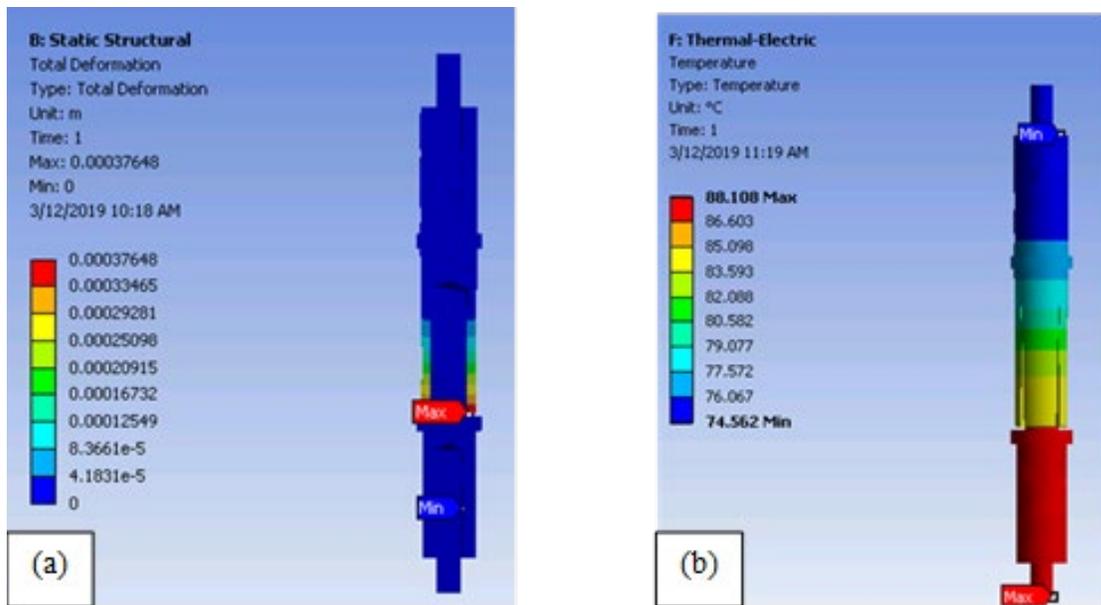


Figure V.8.4 (a) Deformation of connector after insertion process, and (b) temperature distribution of the connector with constant current

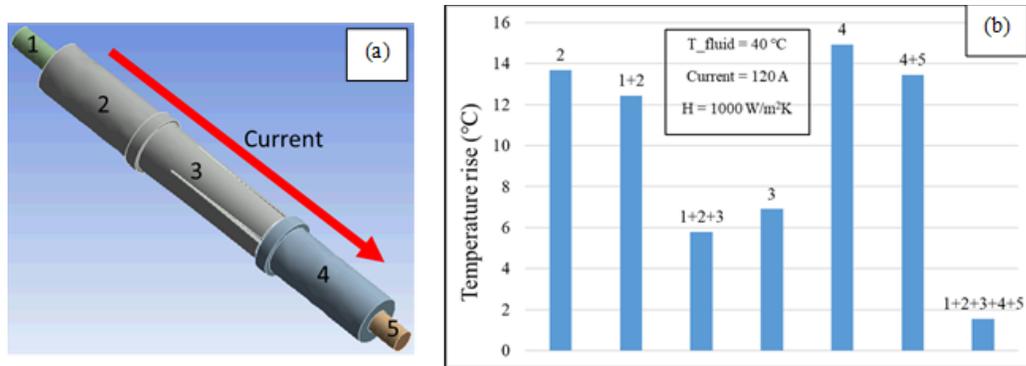


Figure V.8.5 (a) A schematic of the pin/socket coupler showing various locations to apply the convective heat transfer boundary condition, and (b) Results of temperature rise variation with combination of locations to apply heat transfer boundary condition.

*Quantification of Available Excess Heat during Charging Event:* At high power levels of DC fast charging, the amount of heat generated due to inefficiencies (resistance) in vehicle batteries and EVSE hardware requires significant effort for removal and dissipation (or potentially beneficial use) of waste heat at the charging station. For quantification of the available excess heat, multiple charging cable/connector pin configurations were compared to quantify potential thermal loads within the charging system. Below, two scenarios are compared. The first corresponds to the Combined Charging System (CCS) Type 1 Combo connector currently in use for DC fast charging, and the second assumes a larger cable copper cross-sectional area and connector pin size. To reach high current and power levels it is assumed that cooling technologies incorporated into the cable and connector can maintain temperatures within necessary limits and the focus is to compare the magnitude of the station heat loads. The summary results below highlight an example of a 1.2MW (1000V) charging power and typical efficiencies for key EVSE equipment components were used for the analysis.

Table V.8.2 and Figure V.8.6 provide a breakdown of estimated total waste heat generation at a charging port during fast-charge event for key EVSE components (power electronics, isolation transformer) and two charging cable/connector pairs with conductor's cross-sectional areas of (a) 35mm<sup>2</sup> and (b) 95mm<sup>2</sup> at 1.2MW (1200A/1000V) charging level. The cable with cross-sectional area of 35mm<sup>2</sup> approximates a CCS Type 2 Combo cable. A larger cable and connection pin diameter with a cable cross-sectional area of 95mm<sup>2</sup> is intended to approximate a system with 350A rated capability with air-cooling (and higher with liquid-cooling) suitable for higher power DC charging. It is worth noting that with increasing power (current) throughput requirement, charging cable weight increases considerably. For illustration purposes, 5m charging cable with only two DC conductors with 35mm<sup>2</sup> cross-sectional area would weigh  $2 \cdot 0.358\text{kg/m} \cdot 5\text{m} = 3.58\text{ kg}$  (without accounting for signal wiring, cooling tubing/fluid and external insulation) and a 95mm<sup>2</sup> cross-sectional area cable would weigh  $2 \cdot 1.178\text{kg/m} \cdot 5\text{m} = 11.78\text{ kg}$ ! This clearly illustrates the need for shorter, actively liquid-cooled DCFC cables.

**Table V.8.2 Waste Heat by Cable/Connector Type**

Heat Source	Power Requested (kW)	Typical Efficiency (%)	Power Delivered (or Accepted by Battery) (kW)	Losses (%)	Waste Heat (kW)	Contribution (%)	See Note
Batteries on vehicle	1200.0	90%	1080.0	10%	120.0	56.5%	1
<b>Cable/Connector (a): A=35mm<sup>2</sup>/8mm pins</b>							
Connector to vehicle	1200.4	99.96%	1200.0	0.04%	0.4	0.2%	2
Charging cables	1208.9	99.30%	1200.4	0.70%	8.5	3.9%	3
Power electronics cabinet	1272.6	95%	1208.9	5%	63.6	29.1%	4
Isolation transformer	1298.5	98%	1272.6	2%	26.0	11.9%	
<b>Total estimated (per port) waste heat at DCFC station at maximum load:</b>					<b>218.5</b>	<b>kW</b>	
<b>Cable/Connector (a): A=95mm<sup>2</sup>/12mm pins</b>							
Connector to vehicle	1200.2	99.98%	1200.0	0.02%	0.2	0.1%	2
Charging cables	1203.4	99.74%	1200.2	0.26%	3.1	1.5%	3
Power electronics cabinet	1266.7	95%	1203.4	5%	63.3	29.8%	4
Isolation transformer	1292.5	98%	1266.7	2%	25.9	12.2%	
<b>Total estimated (per port) waste heat at DCFC station at maximum load:</b>					<b>212.5</b>	<b>kW</b>	
<b>Notes:</b>							
1. Accepted power is lower due to 70%-90% charging efficiency of batteries							
2. Value from charging connector heat generation estimation table							
3. Value from charging cable heat generation estimation table							
4. Efficiency at full load from datasheets of ABB Terra HP and Efacec HV175/350							

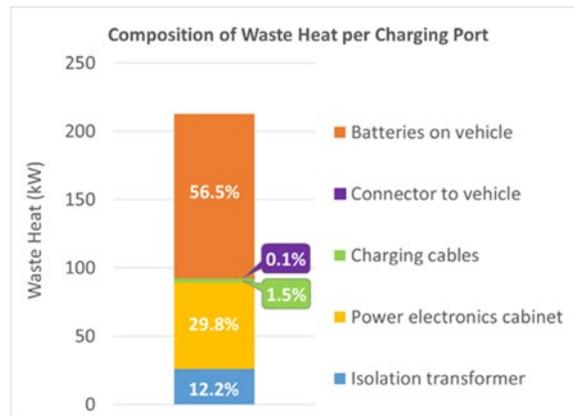


Figure V.8.6 Composition of Waste Heat

**Conclusions**

At the end of the first year of a three-year project, current activities have 1) considered various use cases and travel patterns to develop / quantify expected vehicle loads at a multi-MW station, 2) analyzed and optimized charge port control and battery requirements in a multi-MW station, 3) developed a framework to analyze grid impacts of various multi-MW stations at the distribution level, 4) Analyzed and quantified connector and charging system electrical and thermal requirements. Specific conclusions on task 6,7,8 and 12 are as follows:

*Task 6:* Real-world operating data from class 8 tractor trailers was used to generate a feasible set of stations located within the continental US and to simulate the charging demand schedule for each station. Comparing vehicle data to VMT from FAF, about 5% of all on-road truck traffic is captured in the simulation and is not significantly biased toward any region or corridor. Location, time of day, charging energy, etc. for each station and charge event was disseminated to other tasks in the project in order to provide representative duty cycles for further design, modeling and testing of charging infrastructure.

*Task 7:* The developed grid analysis method was tested on two distribution systems: the IEEE 34-bus system and a California realistic feeder model. The results demonstrated the voltage impact that the charging station might bring to the system. The proposed analysis approach is not system-dependent and can be generalized to other distribution feeders. Based on the analysis results, an initial mitigation plan using smart charger was proposed and tested. A comprehensive impact mitigation plan using both a smart charger and on-site distributed energy resources will be developed in the future.

*Task 8:* A modeling and data analysis framework was developed to gain insights into the design considerations needed to develop a public DCFC station for HD vehicles. Using this framework, informed trade-offs can be made to maximize station utilization. For example, this framework shows that for a station experiencing a vehicle traffic of 30-75 vehicles/day (of a given vehicle mix), the optimal number of ports would be six. This will result in an average wait time between 0-5 minutes and a peak power closer to the station limit, which indicates proper utilization of the installed resources. Higher wait time can be decreased by adding more ports or augmenting port capacities.

*Task 12:* Based on extensive literature study, a numerical models of round pin/socket coupler to investigate the impact of cooling on the thermal performance of connector was developed. A few key parameters, such as the heat transfer coefficient, and the location of cooling were both studied. Test standards were also identified and will be exercised in FY20 to measure the thermal and electrical properties of the connectors. The experimental results will be applied in numerical models for validation, and the validated models will benefit the development of high-performance electrical connectors. The analysis of the thermal management and charge systems showed that the magnitude of heat generated in vehicle batteries and EVSE infrastructure during charging with high currents and power levels poses a challenge for DC fast charging and deserves due attention. Using active liquid cooling for power electronics and charging cables is unavoidable at these power levels. The amount of generated waste heat warrants careful consideration of its beneficial use.

### Key Publications

1. Xiangqi Zhu, Barry Mather, and Partha Mishra, "Grid impact analysis of heavy-duty electric vehicle charging stations", submitted to ISGT 2020, Washington, DC.
2. Partha Mishra, Eric Miller, Shivam Gupta, Shriram Santhanagopalan, Kevin Bennion, Andrew Meintz, Kevin Walkowicz, "A Framework to Analyze the Requirements of a Multiport Megawatt-Level Charging Station for Heavy-Duty Electric Vehicles," accepted in Transportation Research Board Annual Meeting 2020, Washington D.C.

### References

1. Freight Analysis Framework (FAF). Available: [https://ops.fhwa.dot.gov/freight/freight\\_analysis/faf/](https://ops.fhwa.dot.gov/freight/freight_analysis/faf/)
2. Zhu, X., Wang, J., Lu, N., Samaan, N., Huang, R., & Ke, X. (2018). A hierarchical vlsn-based demand response strategy for coordinative voltage control between transmission and distribution systems. IEEE Transactions on Smart Grid.
3. Z. Gao, Z. Lin, S. Davis and A. Birky, "Quantitative Evaluation of MD/HD Vehicle Electrification using Statistical Data," Transportation Research Record, vol. 2672, no. 24, pp. 109-121, 2018.
4. I. Mareev, J. Becker and D. Sauer, "Battery dimensioning and life cycle costs analysis for a heavy-duty truck considering the requirements of long-haul transportation," Energies, vol. 11, no. 55, pp. 1-23, 2018.

## V.9 Development of a Multiport 1+ Megawatt Charging System for Medium and Heavy-Duty Electric Vehicles (ANL)

### Theodore Bohn, Principal Investigator

Argonne National Laboratory  
9700 S Cass Avenue  
Lemont, IL 60439  
E-mail: [tbohn@anl.gov](mailto:tbohn@anl.gov)

### Lee Slezak, DOE Program Manager

U.S. Department of Energy  
E-mail: [Lee.Slezak@ee.doe.gov](mailto:Lee.Slezak@ee.doe.gov)

Start Date: October 1, 2018	End Date: September 30, 2021	
Project Funding (FY19): \$1,000,000	DOE share: \$1,000,000	Non-DOE share:

### Project Introduction

**Problem Statement** – Medium-duty (MD) and heavy-duty (HD) electric vehicles (EVs) are being manufactured today which will soon necessitate the use of megawatt and above (MW+) scale charging systems that can quickly charge large capacity (~800 kWh) battery packs in less than ~30 minutes at an attractive charging cost per unit of energy (\$/kWh). Light duty electric vehicles are parked up to 23 hours of the day while commercial MD/HD vehicles are only available for charging when not in use, often five hours per day. The 30 minute charging time is required to maximize the revenue-generating operations by keeping the electric buses and MD/HD trucks in use more of the day. Integration of renewable energy and grid-tied energy storage, coupled with these large and somewhat variable high-power vehicle charge events, will require an integrated charging control system that can operate with minimum impact on the grid.

The Topic 3E Multiport MW+ lab call project has complementary tasks recorded in the DOE SharePoint project tracking/management system, with separate reports by ANL, NREL (#6-12) and ORNL (#1-5) tasks. The ANL scope of work on this topic cover task areas 13, 14, 15 for electric heavy duty truck, bus, and DC as a Service power delivery charging requirements. Many challenges exist to realize such an integrated system at these power delivery rates. These challenges include understanding and optimizing power demand along with demand management requirements. Charging equipment power density at existing DC charging system levels are insufficient to scale to multiport megawatt charging levels i.e., more parallel charging supply equipment takes up more facility space than is generally available at a charging location. This equipment needs to be higher power density (kilowatts per cubic meter) for smaller equipment footprint, and most likely shared DC overhead distribution to minimize floor space required for the composite EV charging equipment.

### Objectives

#### Primary goals –

The ANL portion of the joint NREL-ORNL-ANL project focuses on building an ‘information nexus’ on megawatt level charging system requirements which can be discussed with industry stakeholders and leading to a MW+ multiport EV charging requirements document. This requirements document can be used as a roadmap for future work on standards, components, systems and system control/safety functions that address MW+ multiport charging of ‘commercial electric vehicles at scale’. The scope of the requirements study and resulting report are constrained to MW+ multiport charging use cases for;

- Class 8 Heavy Duty Electric Trucks (depot and on-road/truck stop)
- Electric Buses (depot and on-route)
- DC as a Service central power conversion and DC distribution to isolated dispensers at each vehicle

The diverse set of topics covered in the requirements study for these charging use cases and interactions of technical systems are illustrated in the Venn diagram below. The center circle focuses on charging systems and functions at the 1 MW and above level. The tangential circles (outside the central purple circle) address technologies that can be leveraged for ‘high power’ charging systems that are under 1MW but not directly applicable for MD and HD electric vehicle charging. These represent depot charging where vehicles are stationary overnight or while out of service during low vehicle usage/demand during the day. These represent the counter-argument that more power is always more beneficial. Slower charging rates when possible, including battery swapping are often a better solution for cost/benefit tradeoffs, if sufficient charging dwell time for these vehicles are available. The aggregate of multiple sub-MW charging adds up to multi-MW loads.



Figure V.9.1 Set of topics covered in the requirements study

The scope of the charging requirements report spans energy delivered from utility interconnection at the sub-transmission level, to the on-site conversion of medium voltage AC to  $\sim 1000\text{vdc}$  to distribution of the DC (DC as a Service) power to isolated dispensers at each vehicle to active/passively cooled cables that deliver power to the vehicle battery via standardized MW level couplers. The scope includes connection equipment such as cord handling/cord retriever systems to handle heavy charging cables to mechanized charging systems for both SAE J3105 and CharIN HPCCV couplers with robotic actuators to insert/remove up to 3000A contacts reliably.

This project’s (ANL portion of multi-lab scope; Multi-Performer Project) yearly objectives include:

**Year 1** – Establish an industry work group to discuss and capture MW+ Multiport charging system requirements for MD and HD electric vehicles. Host monthly web based interactive meetings and several in person meetings to gather input and feedback on proposed content of a charging requirements report.

**Year 2** – Leverage year 1 requirements document as well as outputs from the NREL/ORNL year 1 deliverables on charging location/vehicle dispatch modeling and power electronics topologies down selected candidate solutions to create a technology testbed capabilities matrix. This matrix will be used to specify the parameters upon which a mast climbing work platform (expandable from 3 to 30 meters wide; 10,000lb capacity) can



serve as the (literal) foundation for a technology testbed holding cables, cooling, connection systems and power electronics. The goal of the testbed is to serve as a method to evaluate standards gap and collect data.

**Year 3** – Expand on year 1 and year 2 requirements definitions and testbed capabilities to define interoperability test cases as well as testing procedures for megawatt level multiport MD/HD electric vehicle charging. Work with industry representatives from utilities, energy storage, power electronics, EVSE and vehicle manufactures to host an interoperability workshop.

### Approach

Argonne utilizes its industry connections via EV charging related standards work and development of technology for measurement, control and validation testing to assemble a work group to create a consensus based requirements report.

The work group met monthly via web based hour long as well as day long face to face meetings. An archived recording of the web meeting was distributed to those members that had schedule conflicts for these meetings. The topics covered each month started at the source (grid connection) and proceeded incrementally to the destination (vehicle battery) of the charging energy path; from utility sub-transmission interconnection to battery terminals, one section of the power delivery system each month.

The AOP, Multi-Performer Partner, project tasks are divided as 1-5 for ORNL, 6-12 for NREL and tasks 13-15 for ANL. The ORNL and NREL tasks are covered in their respective Annual Report submissions. Bi-weekly coordination meetings were conducted between the ANL-NREL-ORNL teams on this lab call topic, sharing progress and insights in overlapping/complementary subject areas.

The industry engagement work group has grown to over 170 participants that expressed interest as the year progressed and awareness of the value of participation in the work group spread across the EV charging technology community. The value of the insights presented and discussed in each monthly meeting resulted in positive feedback and added insights for the next meeting. The work group meetings and archived materials evolved into an information nexus on challenges, solutions, gaps and state of the industry for megawatt level MD/HD electric vehicle charging and DC as a service power delivery.

The industry work group was subdivided into subteams, based on the stakeholder particular area of relevance in the Venn diagram above, and in general into segments of AC power delivery from sub-transmission interconnection to the vehicle battery terminals. These subgroups include;

- Utilities, planning services, site operators, municipalities
- EVSE, power electronics, couplers/cable systems, energy storage solutions providers
- Vehicle OEMs, end users/customers
- DOE Funded/Lab coordination, contractors to ANL/DOE.

### ***Task 13: Medium Duty/Heavy Duty Electric Truck Charging Requirements***

#### **Barriers:**

- Lack of existing AC or DC EV charging equipment for MD/HD electric trucks at the MW power level
- Lack of knowledge/data on chain of charging requirements power delivery from sub-transmission to vehicle battery terminals along with unknowns on safety issues handling 1 MW+ connections.

#### **Solution:**

Leverage the CharIN High Power Commercial Charging for Vehicles (HPCCV) industry work group to create consensus based specifications for a coupler capable of delivering over one megawatt of charging power. ANL

staff and ANL contractor Mike Coop (Think Smart Grid) along with Kevin Benion of NREL actively participated in weekly CharIN HPCCV coupler industry work group meetings with the goal of a first draft of the capabilities and requirements by January 1, 2019. The group continues these weekly meetings toward physical connector prototypes that can deliver up to 1500vdc at 3000A with liquid cooling and appropriate safety systems. The requirements document has been published by this non-standards defining organization (SDO), with the goal of passing off the industry collective decision to an SDO for publishing as a standard. Coupler and charging equipment manufacturers are already promoting future 2MW charging solutions.

<https://www.charinev.org/news/news-detail-2018/news/charin-is-publishing-a-solution-for-high-power-charging-of-tucks-and-busses-beyond-1-mw/>

<https://thedriven.io/2019/10/23/new-2mw-electric-vehicle-chargers-could-revolutionise-mining-industry/>

The chart below summarizes the array of charging coupler standards for AC, DC and wireless charging methods with only the last two capable of delivering over 1MW, as it pertains to the commercial vehicle charging objectives.

~ 1.9kW	(J1772) L1-AC
~3.3kW~20kW	(J1772) L2-AC
~ 20kW-100kW	(J3068) AC (208/230/480vac three phase, w/onboard chargers)
~4kW-40kW	(J1772) L1-DC (50-500v/80A limit)
~20kW~150kW	(J1772) L2-DC (basic, 50-500v/350A limit)
~150kW-350kW	(J1772) L2-DC (XFC, 200-1000v/350A limit)
3.3kW-22kW	(J2954) WPT1-4 wireless
60kW-590kW	(J2954/2) WPT5-8 heavy duty wireless
~150kW-1200kW	(J3105) L1-L2 DC mechanized coupler 3 formats (250-1000v/600A,1200A limit)
~150kW-4500kW	(HPCCV) DC (work in progress) (1500v/3000A limit)

The two main MD/HD truck charging use cases addressed in the ANL scope of work, that require MW+ charging rates, are at the point of departure (warehouse/port/factory/dispatch yard) and on-route, at the travel plaza to recharge vehicles during driver required service breaks. In the future autonomous trucks will recharge without limits on driver service hours per day/shift.

DOT Estimates that there are ~5000 truck stops in the United States, which imply upgrades of existing facilities to include high power electric truck charging. Power availability to serve multiple ports of MW+ charging stations will be a major expense to bring from 2MW to 10MW (10\*1MW vehicles) to possibly 100MW, and the implication of local generation or peak shaving energy storage to level demand on utilities.

The ANL MW+ multiport charging requirements summary report collates input from the monthly industry work group meetings that identify the current state of technology readiness to deliver MW+ with parallel existing interconnection switch gear/transformer/electronics/dispenser systems and communication with a comparison to the industry desire to reduce the equipment cost, space requirements, and coordination of loads.

ANL is working with manufacturers/pilot fleets from Daimler, Penske, TA-Petro, Frito Lay and others.

#### ***Task 14: Depot and On-Route Electric Bus Charging Requirements***

##### **Barriers:**

- Lack of published and validated electric bus charging standards that reach MW+ charging levels
- Most on-route MW+ (actual/potential) EV bus charging stations only deploy 1-2 stations at any location. More sophistication of coordination, control and power/energy processing are needed to ensure that fleets of dozens to hundreds of buses in one location are all recharged and ready to use.

**Solution:**

Leverage industry collaborations for participation in monthly work group meetings both on the MW+ multiport bus charging requirements, utility sponsored infrastructure working committees (EPRI IWC), and relevant SAE standards meetings (SAE J3105). The SAE J3105 (EV Power Transfer System Using a Mechanized Coupler) was launched in 2012 and will be published as a full standard late in 2019. The table above shows the level 2 J3015 coupler capability of 1000vdc/1200A=1.2MW, which serves this topic's goals. <https://www.sae.org/standards/content/j3105/>

Shown in the photos below is a four station charging mezzanine charging installation at the Daimler bus factory, with SAE J3105 overhead charging pantographs and SAE J1772 CCS charging cord fed from four sets of 150kW charging stations. A single MW+ bus charging installation would require seven sets of power electronics this size. DC as a service power distribution with centralized power conversion and DC dispensing electronics was proposed as a proof of concept with the ANL led industry work group; implemented using a commercially available (safety certified) mast climbing work platform (shown below) as a testbed. This movable platform can be lowered to ground level to attach/debug MW+ multiport charging system equipment and then elevated via electric motors/pinion drive to a height required to test bus charging coupler systems.



Mast climbing modular work platform; rated up to 10000lb payload, 13'-100' span in 1.5m sections



Figure V.9.2 four station charging mezzanine charging installation at the Daimler bus factory

**Task 15: DC As a Service (DCaaS) Power Delivery****Barriers:**

- Existing medium voltage utility interconnections typically utilize conventional 480vac/3500A pad mounted transformers that limit available charging system power to ~ 2.5MW, which serves just over two electric bus or truck MW level charging stations
- Utilities lack validation data on validated 'modern' power conversion systems that is needed for capital equipment investment opportunities that benefit grid stability and improve grid operation efficiency while opening up revenue streams selling energy in DC format which can reduce charging equipment investments by the facility owner/operator
- Lack of formal standards on interconnection and interoperability of system components and load controls that hamper the ability of utilities to integrate of distributed generation and energy storage buffers systems.

**Solution:**

Leverage industry work group activities to coordinate utility and equipment manufacturer stakeholder knowledge to create consensus based definitions of the approach being called 'DC as a Service' where the utility owns power conversion/storage infrastructure assets, to sell DC power/energy to the facility operator. Compare and contrast relevant DC charging standards, including SAE J2894 (charging power quality) and IEEE P2030.10 (DC microgrids) along with DC power distribution component integration system safety.

Leverage NIST Handbook 44-3.40 commercial transaction energy measurement at the point of dispensing.

## Results

Task 13, 14, 15 have overlapping requirements and use cases with the common item of bringing multiport MW+ EV charging power from the utility interconnection to the battery terminals of MD/HD trucks, electric buses, including DC as a Service power delivery methods. The deliverables for these AOP tasks include quarterly progress updates merged with NREL and ORNL quarterly reports. The main deliverable is the draft requirements report that compiles results of monthly industry group decisions, as well as a more readable ten-page digest of the more detailed larger report. The draft digest was peer reviewed at the full-day workshop hosted at ANL in September, with additional presentation materials from key industry subject matter experts. Publication of SAE J3105 enables studies of interoperability, alignment, communication and safety aspects of charging multiple electric buses in parallel at the MW+ power level, along with grid stability data collection.

Firsthand direct engagement with industry stakeholders is a key pathway to accessing state of the technology and utility best practices on high power multi-port charging stations. The list of industry stake holders and outreach events that ANL staff/contractors participated in illustrate the value of going directly to the source. ANL staff presented project objectives and conclusions at EPRI IWC meetings, EV conferences, CharIN face-to-face meetings, trucking industry meetings, IEEE transportation conference and utility sponsored workshops. The go/no-go criteria listed in the SharePoint AOP is a review of the project activities leading to next steps in moving toward industry preparation for multi-port MW+ charging systems for trucks, buses and DCaaS.

## Conclusions

Publishing of SAE J3105 facilitates the deployment of a standardized coupler method for MW+ electric bus charging, but requirements/technology gaps remain in the other areas of power processing and delivery. These include communication signal reliability (EMI) in the presence of high current/voltage charging cables as well as a vehicle alignment and operator interface to initiate the semi-automated MW+ charging process. The work-in-progress CharIN HPCCV coupler specification covers MD/HD electric truck charging connections, with similar remaining requirements gaps in communication reliability, safety interlocks, cooling, cord handling including robotic insertion/removal processes.

The composite notes and references from the 10 monthly meetings and two face to face meetings are compiled in a draft MW+ multiport charging requirements document with index of subjects to organize the materials. A ten page digest was created to highlight the state of readiness of utilities, energy storage system vendors, charging equipment manufacturers, vehicle manufacturers, fleet operators, site operators, municipalities, other stake holders to plan deployment of MW+ multiport EV charging systems, including gaps in standards or data.

## Key Publications

1. Bohn, Theodore. "Scalable Electric Submeter Challenges for Electric Vehicle Charging; Low Level AC to DC Extreme Fast Charging for Commercial Vehicles" Paper presented at the IEEE Transportation Electrification Conference, June 21, 2019.

## References

1. SAE Electric Bus Charging Standards (part 1-3); <https://www.sae.org/standards/content/j3105/>

## Acknowledgements

The work in this report was conducted by researchers in the Advanced Mobility and Grid Integration Technology Section of the Energy Systems Division of Argonne National Laboratory: Ted Bohn, Keith Hardy, along with inputs from (~170 member) working group industry stakeholders. Key subcontractors include ThinkSmartGrid, 2G Engineering and Amzur Technologies.

## V.10 High-Power Inductive Charging System Development and Integration for Mobility (ORNL)

### Omer C. Onar, Principal Investigator

Oak Ridge National Laboratory, Power Electronics and Electric Machinery (PEEM) Group  
National Transportation Research Center, 2360 Cherahala Boulevard  
Knoxville, TN 37932  
E-mail: [onaroc@ornl.gov](mailto:onaroc@ornl.gov)

### Lee Slezak, DOE Program Manager

U.S. Department of Energy  
E-mail: [Lee.Slezak@ee.doe.gov](mailto:Lee.Slezak@ee.doe.gov)

Start Date: October 2018

End Date: October 2021

Project Funding: \$4,707,901

DOE share: \$2,207,901

Non-DOE share: \$2,500,000

### Project Introduction

Extreme fast charging (XFC) is considered one of the most important research topics in the field of electromobility with the potential to significantly reduce charging times. With extreme fast charging, i.e., charge rates higher than or equal to 3C, it is possible to reduce EV charging times to 10 minutes for 50% increase in the battery state-of-charge (SOC). However, there are several challenges for establishing XFC systems, such as logistics and infrastructure requirements, design and deployment of the grid interface converters, grid power quality (power factor and harmonic distortions), availability of the power (integration with renewable energy or energy storage systems if needed), isolation requirements, distribution voltage level at the point of grid connection, hardware connectivity, power electronic semiconductor and architecture limitations, thermal management systems, and the vehicle side power delivery architectures.

High-power wireless power transfer (WPT) is an attractive option for fast charging because the user is not required to handle any heavy and bulky high-power equipment. WPT is also a key enabling technology for autonomous vehicles. However, power transfer capability of WPT systems is closely linked to the size and mass of the transmitter and receiver pads. The feasibility of high-power WPT systems greatly depend on the ability to improve the power density and specific power of wireless charging systems.

The difficulties of high-power wireless charging are exacerbated by the need to meet the same practical constraints associated with vehicle integration as lower power systems. Therefore, more advanced techniques are necessary to improve power density and specific power of wireless charging systems for high-power applications. This paper proposes three-phase inductive WPT systems with bipolar phase windings with significantly increased surface and volumetric power density of the couplers.

The primary objective of this project is to address the challenges of XFC charging systems for electric vehicles that increases their utilization factors, improves the total electric miles travelled, and improves their return on investment that results in industry and consumer acceptance. The project will also reduce the technology costs through a modular and reconfigurable power electronics architecture and by leveraging the current DOE research activities in power electronics, wide bandgap device-based power electronic converters, vehicle systems, wireless charging systems, and modernization of grid infrastructures in order to meet the project goals. This project will also generate DOE-owned intellectual property on high-frequency / high-power inverters, high-frequency AC links, novel integrated and polyphase magnetic structures, and thermal management systems to be used in extreme fast charging of EVs. Technology developed in this project will be transferable to other vehicle classes such as medium-duty and heavy-duty vehicles.

## Objectives

This project is the first research effort that will showcase an inductive XFC charging system with all the outlined functionalities such as using a poly-phase electromagnetic coupling coils and a modular, scalable, reconfigurable grid-interface power electronic converter architecture. The overall goals of the project to address the challenges of XFC charging systems are:

1. Provide a high-technology, fully automated, high-power, modular, scalable, interoperable, high-efficiency plug-less extreme fast charging system
2. Design an inductive coupling system that supports a variety of vehicle ground clearances that is designed for 100 kW and 300 kW nominal power levels
3. Have minimal grid level disruptions with <5% harmonic distortions on the grid current and >95% grid power factor
4. Design and develop a poly-phase electromagnetic coupling coils with optimal geometry for the highest utilization of the coupler surface area
5. Achieve end-to-end high charging efficiencies greater than 90%
6. Integrate vehicle to infrastructure charging communication protocols
7. Understand and address vehicle integration issues of XFC technology, including energy storage impacts and thermal management considerations.

## Approach

Starting from the AC grid to the vehicle battery terminals, the system power converters must be well-designed and operated in order to achieve high efficiency. In addition, power flow control to the secondary system should be resolved where the control parameters (DC link voltage, frequency, duty cycle, phase-shift, etc.) are actively controlled to improve efficiency while meeting the vehicle-side target voltage, current, and/or power. In this project, team used iterative design and utilized finite element analysis (FEA) based modeling for the design optimization of the electromagnetic coupling coils. Vehicle battery and grid voltage and power levels are used for the proper system design and cascaded down to the appropriate subsystems and components. Furthermore, research team modeled and simulated the grid interface (front-end) power blocks based on the DC link voltage requirements of the proposed system and the grid infrastructure parameters. Also, the system power conversion stages are designed in an integrated approach for an optimal system design in terms of complexity and compactness.

Regarding the system tests, all the power conversion stages will be tested and validated individually before the full system integration (for functionality and performance) which is followed by the entire system tests using grid and battery emulators before vehicle integrations. Although it was not required, team also designed and developed a prototype for proof of concept before designing and developing the high power scaled couplers

and converters. The low-power scale prototype was tested up to 50 kW in the laboratory for validating the proposed concept. The system level circuit diagram of the proposed system is given in Figure V.10.1.

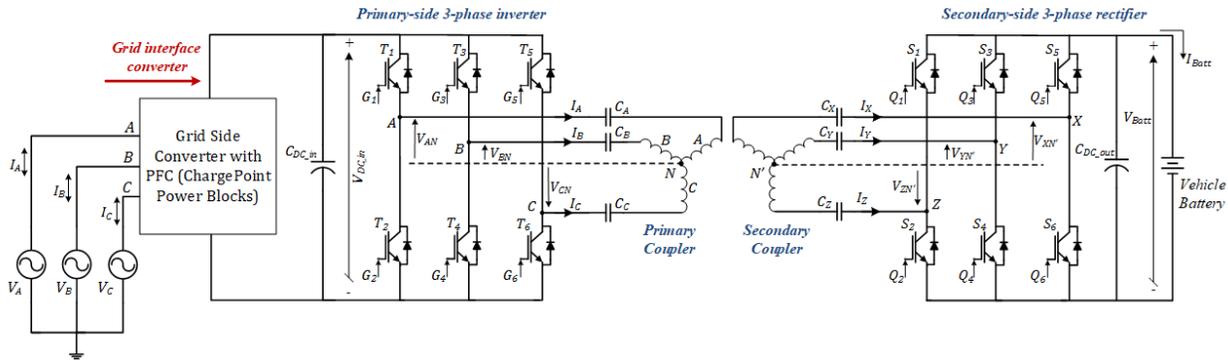


Figure V.10.1 System level diagram of the proposed XFC inductive charging system.

As shown in Figure V.10.1, the ChargePoint power blocks serve as the grid-interface converters with power factor correction for the system with a modular and scalable architecture which consists of 31.25 kW parallel connected power modules. While maintaining high power quality on the grid-side, they can provide a controllable (200-1000V), regulated voltage to the input of the high-frequency poly-phase inverter.

The polyphase inverter is a 3-phase inverter built using the 1200V rated CREE/Wolfspeed phase-leg modules. This inverter takes the DC voltage input from ChargePoint power blocks and applies high-frequency, 3-phase voltage to the resonant stage which consists of the resonant tuning capacitors and the polyphase electromagnetic coupling coils. The inverter 3D design image and its hardware prototype are given in Figure V.10.2 while Table V.10.1 summarizes the inverter parameters. For the rectifier, an identical unit is used with all the switches kept OFF to utilize the body diodes to form a three-phase rectifier.

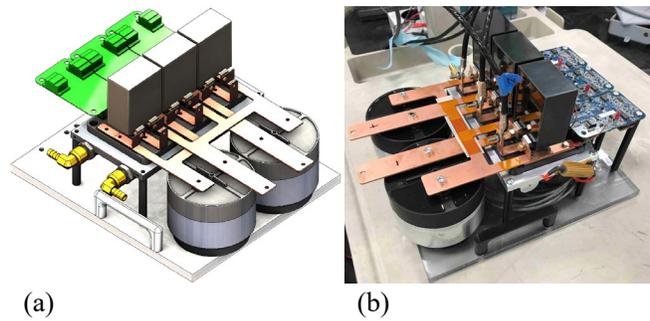


Figure V.10.2 Rendered 3-D image of the inverter design (a) and the actual prototype fabricated (b).

Table V.10.1 High-frequency Power Inverter Parameters

Inverter parameters	Phase-leg module	Cold plate	Gate driver	DC link capacitor	I rating
Value	CAS325M12HM2 CREE/Wolfspeed	CP3009 Microcool	CGD16HB62LP Wolfspeed	947D601K901DCRSN Cornell Dubilier	256A @125 °C T <sub>case</sub> 440A @25 °C T <sub>case</sub>

The polyphase coupler prototype in this project is based on the two-layer winding configuration constructed for experimental validation. This topology was chosen because it results in the system with the largest coil span having balanced inductances. Although resonant tuning can be performed for a system with unbalanced inductances, it is difficult to realize the exact required capacitance values with monolithic induction heating capacitors having high kVA ratings. Rather, low kVA discrete components need to be combined to realize the appropriate capacitances. For systems with balanced inductances, the capacitors can be chosen to locate the actual system resonant frequency as near as possible to the target frequency. A computational model and the physical prototype of the two-layer three-phase coil system are depicted in Figure V.10.3. The initial design of the pad targeted an effective mutual-inductance to achieve 50 kW power transfer for a coupler surface-to-surface separation of 15 cm and a phase current of 73 A<sub>RMS</sub>. This current corresponds to a current density of

5.5 A<sub>RMS</sub>/mm<sup>2</sup> in 6 AWG wire. The design was limited by the 7.4 mm diameter of the Litz wire and the minimum bend radius, which was set to be five times the diameter. A minimum wall thickness of 1.8 mm for mechanical integrity of the additively manufactured wire guides also limited space for additional amp-turns. The resulting system has a vehicle assembly ground clearance of 170 mm and a magnetic airgap of 180 mm. Table V.10.2 provides the inductance readings of the polyphase couplers. The simulation model of the two-layer coupler design and the two-layer prototype built at the PEEM laboratory are shown in Figure V.10.3.

**Table V.10.2 Inductances of the Polyphase Coupler Prototype**

Primary-side inductances [ $\mu\text{H}$ ]	$L_{p_a}$	$L_{p_b}$	$L_{p_c}$	$M_{p_{ab}}$	$M_{p_{bc}}$	$M_{p_{ca}}$			
	34.1	34.3	34.2	-11.2	-11.3	-11.1			
Secondary-side inductances [ $\mu\text{H}$ ]	$L_{s_a}$	$L_{s_b}$	$L_{s_c}$	$M_{s_{ab}}$	$M_{s_{bc}}$	$M_{s_{ca}}$			
	31.1	34.3	34.2	-11.2	-11.3	-11.1			
Primary-to-secondary mutual inductances [ $\mu\text{H}$ ]	$M_{p_a^{sa}}$	$M_{p_b^{sa}}$	$M_{p_c^{sa}}$	$M_{p_b^{sa}}$	$M_{p_b^{sb}}$	$M_{p_b^{sc}}$	$M_{p_c^{sa}}$	$M_{p_c^{sb}}$	$M_{p_c^{sc}}$
	5.65	-3.64	-1.85	-1.85	5.54	-3.57	-3.64	-1.77	5.55

(a)

(b)

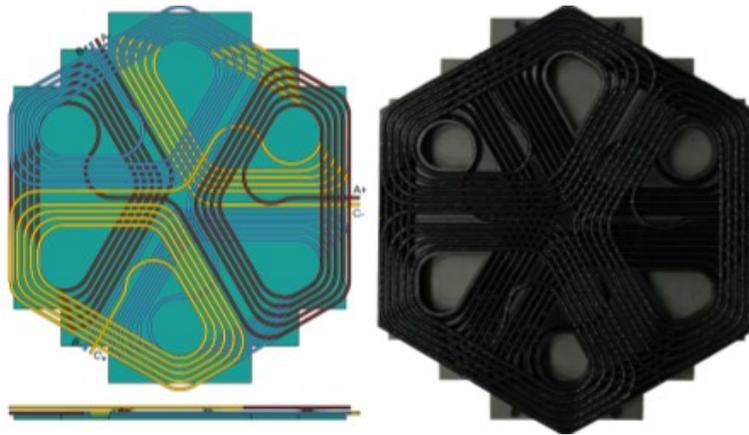


Figure V.10.3 Simulation model of the two-layer coupler design (a) and the fabricated prototype.

The simulation model gives details of the phase winding layout including location of terminals and mechanics for routing the wires to connect the top and bottom layers. The diameter of the Litz wire is scaled to reduce meshing complexities. The bounding box dimensions of the prototype is 47.1×54.4 cm. The total coil mass including ferrite, Litz wire, and wire guides is 13.7 kg. The wire is 6 AWG type 2 Litz with a strand gauge of 38 AWG manufactured by New England Wire. The ferrite backing is constructed from Ferroxcube PLT64/50/5 tiles of 3C94 material (5 mm thick).

In addition to designing, prototyping, and testing this 55 kW coupler, project team also completed the simulation model for this system using the parameters of the prototyped couplers and the inverter. The purpose of developing this simulation model was to increase the model accuracy and confidence for developing the 300 kW system. Both the experimental test results are presented in more details in the Results section.

The grid-interface power block simulation model is given in Figure V.10.4 which is connected to the 480V 3-phase input line and is based on a boost power factor correction rectifier followed by a buck converter in order to regulate the voltage in the range of 200 V to 1000 V. The model of the grid-interface converter helps



understand the controllability and control requirements of the front-end converter. In Figure V.10.5, the simulation model of the developed prototype system is given.

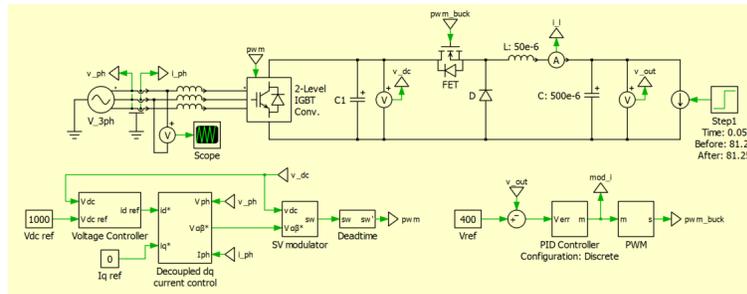


Figure V.10.4 Simulation model of the front-end rectifier and buck converter.

Team also completed the power scaled-up, 300 kW versions of the polyphase coupler designs as well as the power inverters to drive the 300 kW couplers along with their models and simulations. The 300 kW polyphase transmit and receive couplers are shown in Figure V.10.6. These high-power couplers are designed to maintain 315 kW power transfer for up to 125 mm misalignment in any direction. The couplers use 3x 4 AWG Litz wires per phase to improve the current density while maintaining wire flexibility. The specifications of the ground and vehicle coupler are provided in Table V.10.3.

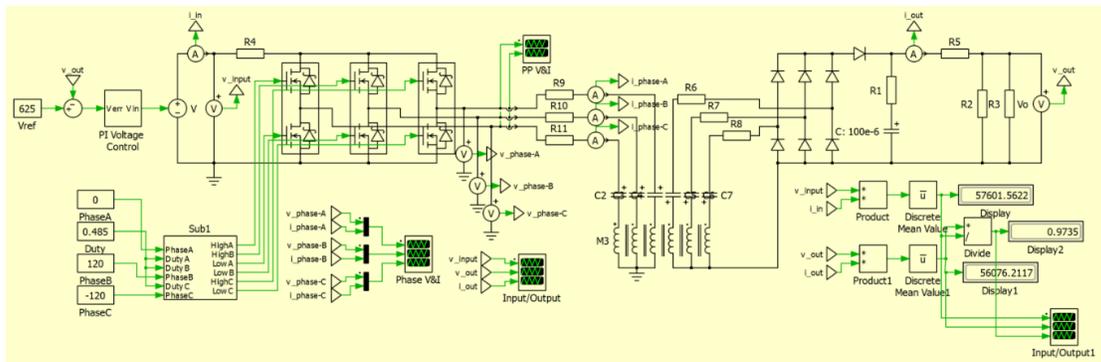


Figure V.10.5 Simulation model of the two-layer three-phase couplers with three-phase inverter/rectifier.

**Table V.10.3 Specifications of the 300 kW Polyphase Couplers**

	Outer Diameter	Current Rating	Phase Voltage	Ferrite Mass	Litz Wire Mass	Total Mass
<b>Ground Coupler</b>	750 mm	321 A <sub>rms</sub>	3.0 kV <sub>rms</sub>	31.8 kg (15mm thick)	12.9 kg	44.7 kg
<b>Vehicle Coupler</b>	500 mm	321 A <sub>rms</sub>	1.2 kV <sub>rms</sub>	11.3 kg (12mm thick)	5.7 kg	17 kg

The 3-D design image of the ground and vehicle-side couplers are shown in Figure V.10.6. The rendered image of the open-ended dual inverter system is given in Figure V.10.7 while the Figure V.10.8 shows the drive system’s circuit schematic.

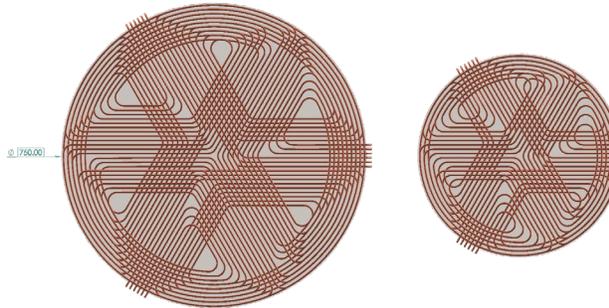


Figure V.10.6 Computational model images of the ground and vehicle couplers.

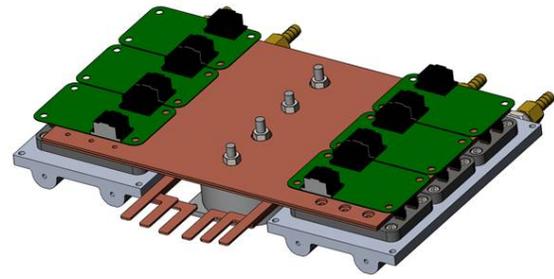


Figure V.10.7 Computational model images of the ground and vehicle couplers.

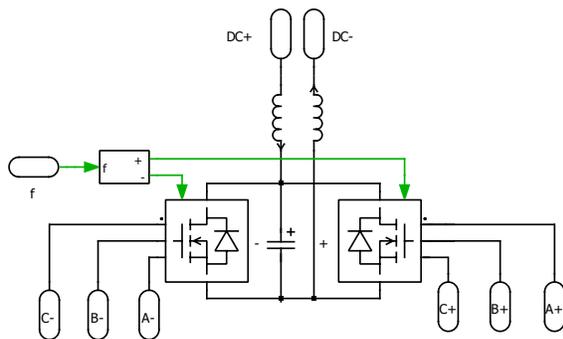


Figure V.10.8 Computational model images of the ground and vehicle couplers.

The drive system uses open winding / six-phase design using two inverters sharing the same DC bus. Using a single three-phase inverter was not possible with 325 kW output power due to current rating and thermal constraints of the semiconductor power devices. Although a second inverter increases number of components and the complexity, the total power rating and the power density of the drive system is significantly increased. This approach doubles the effective output voltage while maintaining DC-link capacitor size reduction compared to a single 3-phase inverter.

## Results

A photograph of the experimental setup is provided in Figure V.10.9 where the primary-side inverter, polyphase coupling coils, secondary-side rectifier, and the resonant tuning capacitors are shown. In this setup an NHR 9300 high-voltage battery test system was used at the input DC source while an additional NHR 9300 was used in parallel with a 14  $\Omega$  resistor bank as the load. A Teledyne Lecroy HDO8108 oscilloscope was used to capture the 3-phase primary side voltage and current waveforms. A Yokogawa DLM4058 oscilloscope was used to capture the 3-phase secondary-side voltage and current waveforms. A Yokogawa WT1806E power analyzer was used to measure the DC input power, DC output power, and DC-to-DC efficiency of the system while a Yokogawa PX800 power analyzer was used to measure the coil-to-coil efficiency using two-Wattmeter method. Both the primary and secondary windings are Y connected with series resonant tuning capacitors. Table V.10.4 summarizes the experimental test results including the input DC voltage, output DC voltage, equivalent load resistance, inverter input and load power, and the dc-to-dc efficiency.

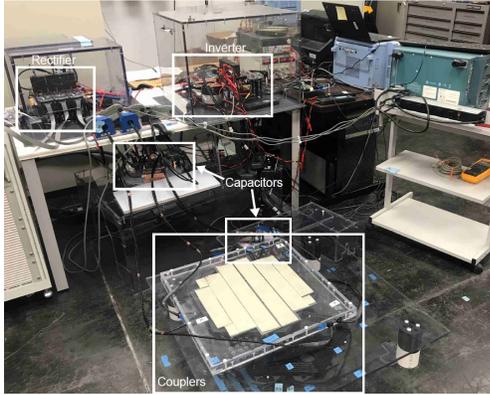


Figure V.10.9 Experimental test setup.

Table V.10.4 Experimental Test Results

Parameter	Aligned	$\Delta\phi=30^\circ$	$\Delta x=-10\text{ cm}$ $\Delta y=-10\text{ cm}$
$V_{dc,input}$	554.9 V	555.9 V	312.7 V
$V_{dc,output}$	584.9 V	585.0 V	265.8 V
$R_{eq,load}$	6.839 $\Omega$	6.842 $\Omega$	6.764 $\Omega$
$P_{dc,input}$	52.60 kW	52.53 kW	11.79 kW
$P_{dc,output}$	50.03 kW	50.02 kW	10.44 kW
$\eta_{dc-to-dc}$	95.1 %	95.2 %	88.5 %

As shown in Table V.10.4, in aligned and rotational misaligned cases, about 50 kW is delivered to the load with dc-to-dc efficiencies greater than 95%. Under x and y directional misalignment conditions (both 10 cm), the power transfer drops to 10.44 kW with an efficiency reduction to 88.5 %. The power analyzer results for an example test case is provided in Figure V.10.10 where (a) shows the dc input and output readings and (b) shows the two-Wattmeter method phase-to-phase voltage and line current readings.

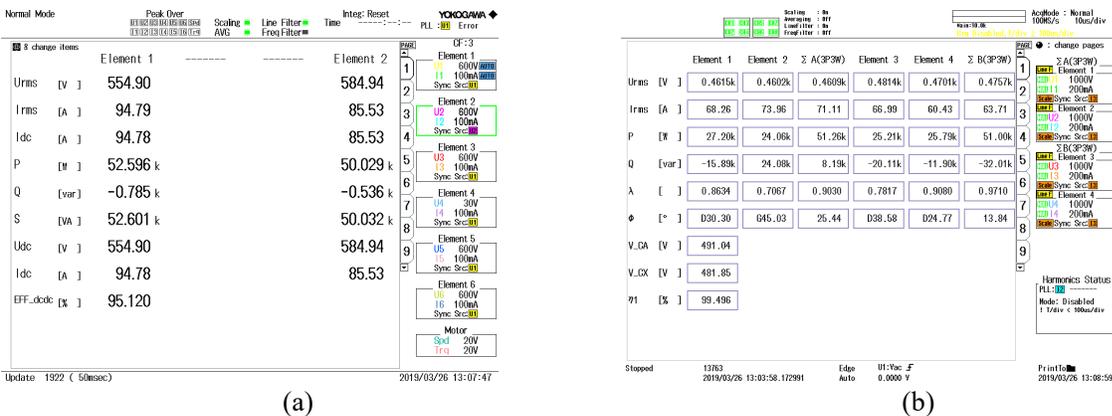


Figure V.10.10 Results for an example test case with 50 kW output.

Based on these two efficiency numbers shown in Figure V.10.10 (dc-to-dc and coil-to-coil), inverter efficiency is 97.5% and rectifier efficiency is 98.1% according to the cascaded power flow.

### Conclusions

During the first budget period of the project, the team worked on modeling, simulations, analysis, and design of the system power conversion stages and control systems and completed the design and simulations of the 300 kW inductive charging system. Since proposed concept is new, a relatively low-power, scaled-down version of the couplers were developed and tested to validate the concept and the operation. The prototype was tested with ~95% dc-to-dc efficiency with ~50 kW output. Simulation results agreed with the experimental results for improved confidence for the 300 kW system.

### Key Publications

1. “A 50 kW Three-Phase Wireless Power Transfer System Using Bipolar Windings and Series Resonant Networks for Rotating Magnetic Fields,” *IEEE Transactions on Power Electronics*, accepted for publication, early access available online: <https://ieeexplore.ieee.org/document/8863954>

## **Acknowledgements**

Project team would like to thank Mr. John Jason Conley of the National Energy Technology Laboratory for his continuous support and guidance on this project. The project team also acknowledges the leadership of David E. Smith, Director, Center for Transportation Analysis, ORNL Program Manager.

## VI Grid and Infrastructure High Power Wireless Charging

### VI.1 High Power and Dynamic Wireless Charging of EVs (ORNL)

#### **Veda Prakash Galigekere, Principal Investigator**

Oak Ridge National Laboratory  
2360, Cherahala Boulevard  
Knoxville, TN 37932  
E-mail: [galigekerevn@ornl.gov](mailto:galigekerevn@ornl.gov)

#### **Lee Slezak, DOE Program Manager**

U.S. Department of Energy  
E-mail: [Lee.Slezak@ee.doe.gov](mailto:Lee.Slezak@ee.doe.gov)

Start Date: October 1, 2018	End Date: September 30, 2019	
Project Funding (FY19): \$4,000,000	DOE share: \$4,000,000	Non-DOE share: \$0

#### **Project Introduction**

Range anxiety continues to be a critical challenge for mass adoption of electric vehicles (EVs). Increasing the on-board battery capacity increases the useable range of EVs but also increases the vehicle cost and reduces the power transfer efficiency due to additional weight. Dynamic wireless charging of EVs based on dynamic wireless power transfer (DWPT) has significant potential to considerably alleviate or even eliminate range anxiety associated with present day EVs. The appropriate power transfer levels for light duty EVs and suitable roadway types which will enable an economically efficient DWPT system is identified based on a high-level cost study. The technology gaps of the existing state-of-the-art (SOA) DWPT systems as compared to the specifications corresponding the economically viable solution are also presented. Preliminary analytical and simulation studies are conducted to identify a viable candidate DWPT system architecture including suitable coil geometries.

#### **Objectives**

The overall objective of the three-year project is to identify, design, build and validate an optimized high power (200 kW+) dynamic wireless charging system suitable for LD vehicles. In the first project year (FY19), feasibility study and technology gap analysis will be carried out to identify a viable overall DWPT system configuration to enable an economically viable system, and preliminary analytical and simulation studies will be conducted to identify the suitable architecture.

The specific goals for FY 2019 were:

- Conduct a high-level cost study to identify key targets (power transfer level, efficiency, coil surface power density) that must be met to enable an economically feasible dynamic WPT system
- Analyze the existing SOA dynamic wireless charging systems to identify the technology gaps and barriers to economic viability
- Develop analytical and simulation models to predict the behavior of dynamic WPT systems with the objective of identifying candidate WPT coupler and resonant architectures to enable feasible high power dynamic WPT

- Identify and evaluate novel technologies and materials to enable high-power density and high misalignment tolerant WPT coupler mechanisms to enable feasible high power dynamic wireless charging.

### Approach

The overall approach can be classified in to three categories: a) Feasibility study including a high level cost study to identify the technical targets to enable economically viable DWPT system b) Technology gap assessment of SOA DWPT systems, and c) analytical and simulation study to identify DWPT architecture including candidate coil designs which will lead to an optimal high-power dynamic EV charging system.

**Feasibility study** – A high-level cost study was conducted to evaluate the effect of power transfer level on roadway coverage required, infrastructure cost and vehicle cost were analyzed. In Figure VI.1.1, Primary roadways are classified as interstate and other freeways and expressways, Secondary roadways are classified as other principal arterial and minor arterial roadways, and the rest of the roadways are termed as local roadways. Primary roadways account for 1.6 % of the total 4.2 million paved miles in the USA but account for 32.9 % of the total annual driven miles [1].

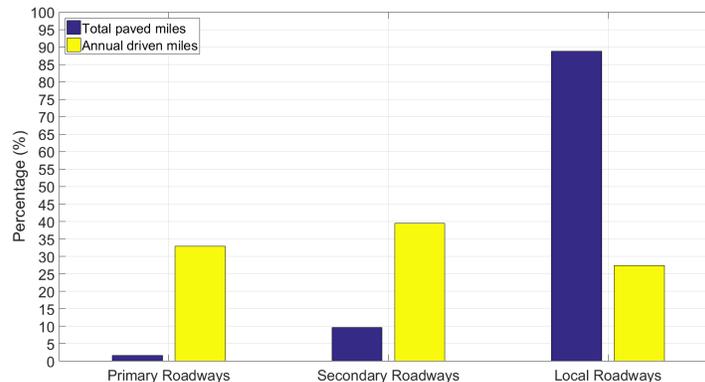


Figure VI.1.1 Percentage of total paved miles and annual driven road-miles for primary, secondary, and local roadways in USA.

The objective of the feasibility study is to identify the deployment scenario which could eliminate range anxiety for light-duty EVs on primary roadways. It is also considered that the EV should have considerable (150 miles) non-dynamic WPT range as well. The components included in the formulation of the cost function can be classified into road component and vehicle component costs. The road component cost includes 1) Grid interface and connection cost, 2) Road installation and retrofitting cost, and 3) Roadside unit power electronics and materials cost. The vehicle component cost includes the 1) Vehicle assembly and power electronics and 2) Onboard battery. The key findings of the high-level cost study and the feasibility study are presented below, and the detailed outcomes are presented in the next section.

**Technology gap assessment** – the SOA dynamic wireless EV charging systems were assessed in terms of the feasibility targets identified by the high-level cost study. The key specifications which were compared are the power transfer level, efficiency, and the coil surface power density. The SOA systems considered from the European consortium Feasibility Analysis and Development of On-Road Charging Solutions for Future Electric Vehicles (FABRIC) include the Qualcomm, POLITO, and SAET Spa systems for light duty (LD) vehicles [Fabric]. Project VICTORIA, OLEV KAIST and Scania Bombardier systems for buses [2] and [3]. It should be noted here that Scania Bombardier system which was used for an EV bus is a tightly coupled inductive system and the other systems were loosely coupled inductive systems.



Figure VI.1.2 Dynamic wireless EV charging in an electrified roadway

**Analytical and simulation study** – Figure VI.1.2 depicts the components involved in an electrified roadway based dynamic wireless EV charging system. The following studies were carried out with the aid of commercially available FEA and circuit simulation packages,

- Power transfer profile study of DWPT coils
- Grid impact study for high-power DWPT systems
- Dynamic modeling of high-frequency resonant inverter used in DWPT systems.

**Power transfer profile study** – Square (uni-polar) and DD (bi-polar) coils are the two types of couplers that are suitable for and typically used for wireless EV charging. 200 kW Square and DD reference coil pairs were designed and a Finite element analysis (FEA) simulation study was conducted to evaluate the power transfer profile, specific power, and energy transfer efficiency. Initially, single transmitter and receiver coil pair were simulated to recreate dynamic charging profile with a coil-to-coil gap of 250 mm and 75 mph. In the second case, three transmitter coil system and a single vehicle coil system was simulated. It was observed that the energy transfer efficiency of multiple (three) transmitter system was close to 90 % as compared to single transmitter system (~ 80 %).

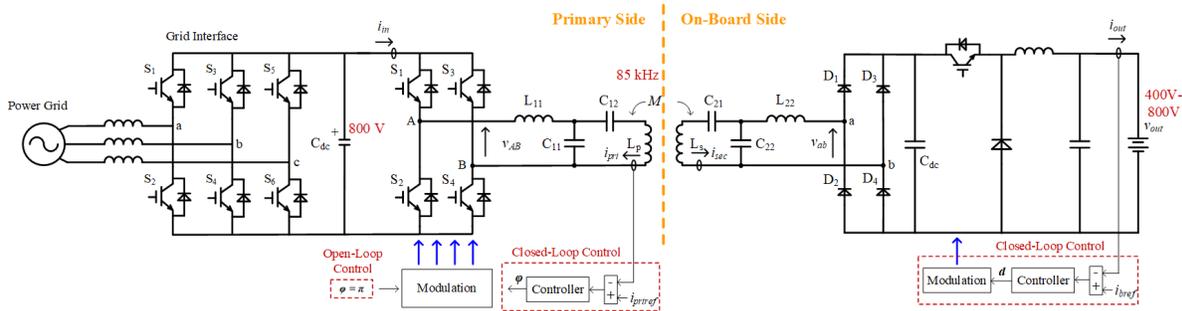


Figure VI.1.3 Dynamic wireless EV charging in an electrified roadway

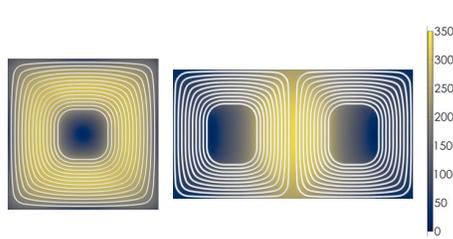


Figure VI.1.4 Reference wireless power transfer pads showing coil layout and peak ferrite flux density (mT):(Left) Square pad, (Right) DD pad

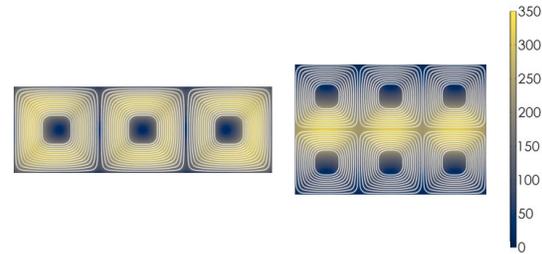


Figure VI.1.5 Reference pad transmitter showing coil layout, peak ferrite flux density (mT), and travel direction:(Left) Square pad system, (Right) DD pad system

**Grid impact study** – High-power dynamic wireless charging for electric vehicle has a unique load profile caused by the high-power demand in a short time duration, To understand the impact on the grid of dynamic EV charging, a 480 V power-grid was modeled and included in the simulation model and the circuit is shown in Figure VI.1.3. The effect of the pulse-like power demand on the grid was evaluated for a 200 kW DWPT system.

**Dynamic modeling of high-frequency resonant inverter** – Figure VI.1.3 shows the schematic of double side LCC tuned DWPT system with a secondary side dc-dc step-down converter. To realize practical real-world dynamic EV charging systems, it is imperative to have accurate dynamic models of the wireless power transfer (WPT) system to scientifically design a controller to regulate the primary coil current and the battery charging current seamlessly as the EV is in motion. Existing dynamic models are not suitable for high frequency (HF) resonant inverters used in dynamic wireless power transfer applications as they do not meet the small ripple approximation. A small-signal linear control-to-primary coil current transfer function was derived by applying direct envelope tracking method and the derived results were validated by simulation.

**Results**

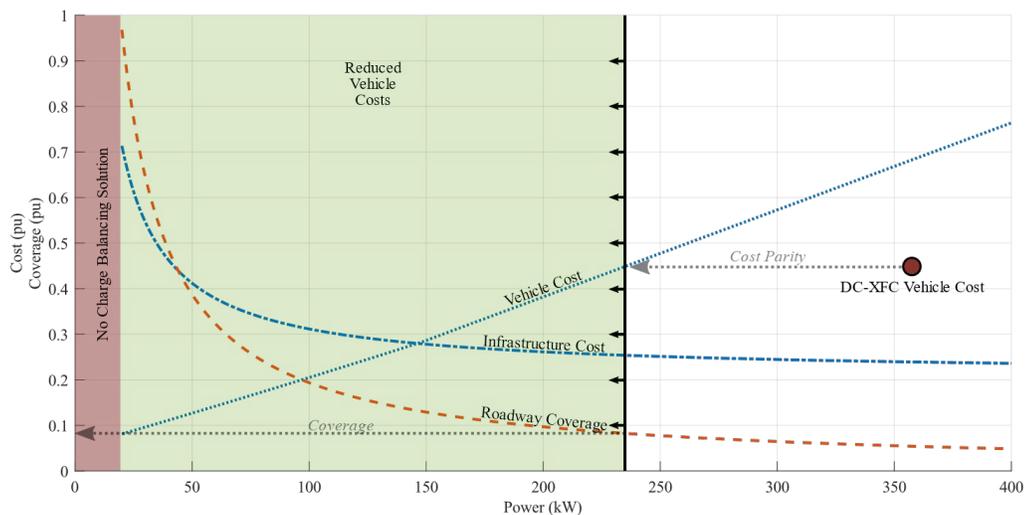


Figure VI.1.6 Dynamic wireless EV charging in an electrified roadway.

**Feasibility Study Results** – The key outcomes of the feasibility study based on real-world energy consumption for LD vehicles (like Nissan Leaf) traveling at an average speed of 65 MPH as depicted in Figure VI.1.6 are:



- The percentage of roadway coverage required to achieve charge-balancing mode of operation decreases significantly with increase in the magnitude of power transferred dynamically.
- If the power transferred is less than 20 kW, it is not possible to achieve charge-balancing solution or eliminate range anxiety. This region is indicated as the ‘no charge balancing solution’ in Figure VI.1.6.
- In Figure VI.1.6, it can be noted that at 235 kW dynamic power transfer level, the vehicle cost is at parity with a corresponding cost of a vehicle which can handle DC extreme fast charging. If the power level is increased beyond this point, it leads to an increased vehicle cost. As a result, 235 kW power transfer level can be inferred as the minimum coverage solution for charge-balanced mode of operation without penalizing the vehicle cost as compared to DC extreme fast charging. The roadway coverage corresponding to minimum coverage solution is 0.82 pu or 8.2 %.
- It can be concluded that for considerable range extension or charge balancing mode of operation, the power transfer level required is between 150 kW and 235 kW.

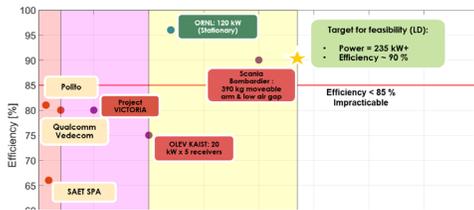


Figure VI.1.7 Dynamic power transfer level and efficiency of the SOA DWPT systems.

LD vehicles (Yellow), (Impractical for LD vehicles) (Red), (Impractical for DWPT) (Green)

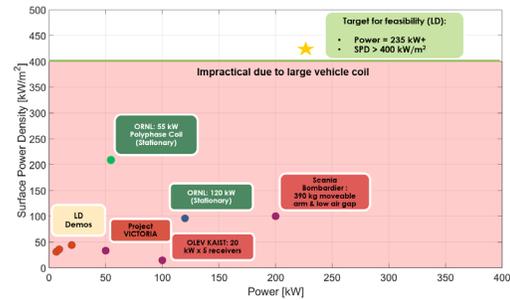


Figure VI.1.8 Dynamic power transfer level and surface power density of the vehicle coil of the SOA DWPT systems

Compared to the feasibility targets identified for LD vehicles on primary roadways, it can be inferred that the SOA LD systems are considerably lower power as shown in Figure VI.1.7 (Highest power SOA LD system 20 kW as compared to needed 150 kW+ system), have poor efficiency (SOA LD system with the best efficiency is 80 % as compared to desired 90 %), and poor SPD (SOA LD system with the nest SPD is 43.95 kW/m<sup>2</sup> which is an order of magnitude lesser than the required 400 kW/m<sup>2</sup>). The MD or the SOA systems corresponding to the buses are impractical for LD vehicles because of their large size and volume. This is reflected in the poor SPD. For example, both Project VICTORIA and the KAIST system have SPDs less than 50 kW/m<sup>2</sup> as compared to the required SPD of 400 kW/m<sup>2</sup>. Scania Bombardier system has an SPD of 100 kW/m<sup>2</sup> but this system has a 390 kg moveable arm adapted from railway technology which renders it impractical [2] and [3].

**Power Transfer Profile Study of DWPT Coils** – Table VI.1.1 shows the comparison of key results of a simulation study which was conducted to evaluate the performance of DD and Square coils designed for 200 kW DWPT. optimized to operate at 85 kHz. It can be seen from Table VI.1.1 that the square coil system has a better surface power density and specific power as compared to the DD coil although the DD coil has slightly better efficiency. it can also be noted that both the DD and the square coils meet the surface power density target of 400 kW/m<sup>2</sup> and are both close to the 90 % efficiency target. The power transfer profile of the DD and the Square coil as a function of time for a vehicle travelling at 70 mph is shown in Figure VI.1.9

**Table VI.1.1 Comparison of simulation results of DD and square coil three-coil transmitter system for 200 kW dynamic WPT**

Receiver Coil	Three transmitters & single receiver coil system	
	Square	DD
Surface Power Density [kW/m <sup>2</sup> ]	733	656
Specific Power [kW/kg]	20.7	14.3
Simulated Energy Transfer Efficiency [%]	87.9	89.7

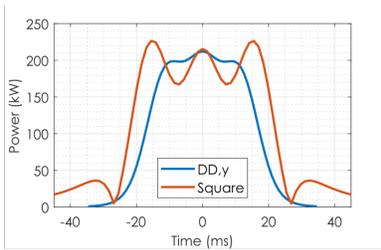


Figure VI.1.9 Reference pad profiles assuming a vehicle velocity of 75 mph.

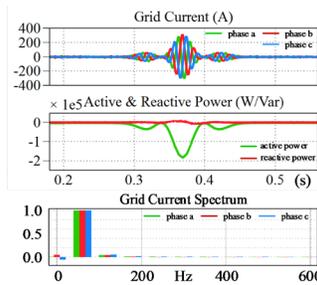


Figure VI.1.10 Grid current, active and reactive power and current spectrum for vehicle traveling at 20 mph with DWPT

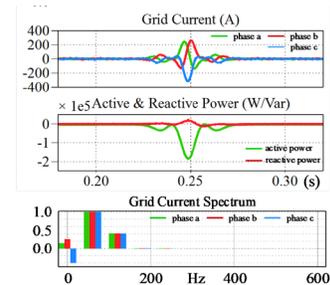


Figure VI.1.11 Grid current, active and reactive power and current spectrum for vehicle traveling at 70 mph with DWPT

**Grid Impact Study** – The load profile of DWPT system to utility grid is analyzed, as shown in Figure VI.1.10 and Figure VI.1.11, respectively. Under different vehicle speeds, they have similar pulse-like shapes but different grid currents. From the spectrum analysis, the grid current has large harmonic component. Such a variable vehicle-speed-related pulse-like load profile and 2nd harmonics may cause considerable stress to the ac grid, especially in the case of low-voltage distribution network.

**Dynamic Modeling of HF Resonant Inverter** – A primary side LCC tuned and secondary series tuned DWPT system capable of transmitting 200 kW with the following parameters is considered as a reference design to obtain the magnitude and phase plots (Bode): operating frequency  $f_o = 85$  kHz, primary tuning inductor  $L_{11} = 4.85$   $\mu$ H, primary tuning capacitor  $C_{11} = 0.72$   $\mu$ F, primary and secondary coil inductance (aligned case)  $L_c = 31.69$   $\mu$ H.

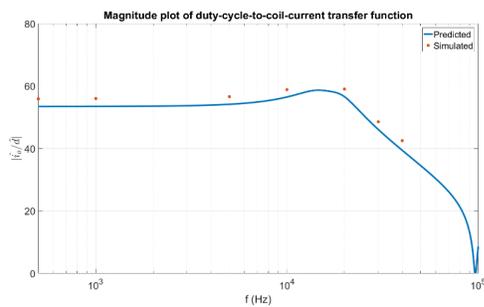


Figure VI.1.13. The magnitude of the derived and simulated control-signal-to-coil current transfer function as a function of frequency

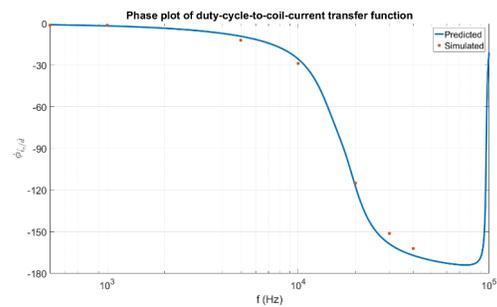


Figure VI.1.12. The phase of the derived and simulated control-signal-to-coil current transfer function as a function of frequency

Figure VI.1.12 and Figure VI.1.13 show the theoretically predicted and simulated magnitude and phase response of the small-signal control-to-coil-current transfer function, respectively.

### Conclusions

1. The targets to achieve an economically feasible dynamic wireless EV charging system applicable to LD vehicles and primary roadways are:
  - Power transfer level for range extension: 150 kW – 235 kW
  - Efficiency: 90 %
  - Surface power density (SPD): 400 kW/m<sup>2</sup>.
2. The minimum roadway coverage solution for primary roadways for a LD vehicle such as Nissan Leaf requires power transfer at 235 kW and a corresponding roadway coverage of 8.2 %.
3. SOA dynamic wireless charging systems are limited to 20 kW power transfer capability and 80 % efficiency for LD vehicles with an SPD of less than 50 kW/m<sup>2</sup>. This is significantly lesser than the required 235 kW, at 90 % efficiency with an SPD of 400 kW/m<sup>2</sup>.
4. Two candidate coil reference designs (square and DD coil systems) have been identified and evaluated in terms of performance as applied to 200 kW dynamic charging application. The preliminary simulation results indicate the coils meet the determined feasibility targets.
5. Direct envelope tracking method has been applied to derive the control-to-coil-current transfer function. This transfer function is important to design an accurate controller for high-power DWPT systems. The derived model was validated (preliminary) by circuit simulation in Saber Sketch platform.

### Key Publications

1. V. Galigekere et al., “Direct Envelope Modeling of Load-Resonant Inverter for Wireless Power Transfer Applications,” Accepted for presentation at *2020 IEEE Applied Power Electronics Conference and Exposition (APEC)*, New Orleans, LA, USA, 2020.

### References

1. Office of Highway Policy Information. (2014). Public road length- 2014: Miles by type of surface and ownership/functional system national summary.
2. Review of Existing Solutions, Feasibility Analysis and Development of On-Road Charging Solutions for Future Electric Vehicles (FABRIC), [www.fabric-project.edu](http://www.fabric-project.edu).  
[https://www.fabric-project.eu/www.fabric-project.eu/images/Deliverables/FABRIC\\_D33\\_1\\_V2\\_Review\\_of\\_existing\\_charging\\_solutions\\_submitted.pdf](https://www.fabric-project.eu/www.fabric-project.eu/images/Deliverables/FABRIC_D33_1_V2_Review_of_existing_charging_solutions_submitted.pdf).
3. “FABRIC Final Event”, [www.fabric-project.edu](http://www.fabric-project.edu).  
[https://www.fabric-project.eu/www.fabric-project.eu/images/Final\\_Event/PRESENTATIONS/3\\_FABRIC\\_final\\_event.pdf](https://www.fabric-project.eu/www.fabric-project.eu/images/Final_Event/PRESENTATIONS/3_FABRIC_final_event.pdf)

### Acknowledgements

Project team would like to thank Lee Slezak and Manish Mohanpurkar from the U. S. Department of Energy and Jason Conley from National Energy Technology Laboratory for their continued guidance and support on this project.

## VI.2 High Power and Dynamic Wireless Charging for EVs (INL)

### Richard “Barney” Carlson, Principal Investigator

Idaho National Lab  
775 MK Simpson Boulevard  
Idaho Falls, ID 83415  
E-mail: [Richard.carlson@inl.gov](mailto:Richard.carlson@inl.gov)

### Lee Slezak, DOE Program Manager

U.S. Department of Energy  
E-mail: [Lee.Slezak@ee.doe.gov](mailto:Lee.Slezak@ee.doe.gov)

Start Date: October 1, 2018	End Date: September 30, 2021	
Project Funding (FY19): \$675,000	DOE share: \$675,000	Non-DOE share: \$0

### Project Introduction

Although the benefits of electrified transportation are well known, electrified transportation is yet to achieve wide acceptance or gain critical momentum due to range anxiety, heavy weight, and high cost. Dynamic wireless charging has the potential to reduce the EV battery size and therefore reduce cost as well as concurrently increasing the vehicle driving range as it enables the EV to pick up energy on the go. The net energy delivered to the vehicle in dynamic charging is a function of the product of power transmission level, the vehicle speed, and the duration in which power is transferred to the vehicle. This translates to the fraction of the roadway embedded with transmitting coils. Current state-of-the-art light duty wireless power transfer systems (WPT) have a power transmission rate capable of approximately 20 kW. This leads to a large section of the roadway to be embedded with coils there by significantly increasing the capital requirements. A dynamic wireless power transfer (dWPT) system capable of transmitting 200 kW with optimized secondary coils to pick up the maximum possible energy based on the volume, thermal, and safety constraints will lead to a system that optimizes the range and battery size for a given class of EV.

There are several challenges present with wireless charging that hinder the safety and adoption of this technology for electric vehicle charging. These challenges include electromagnetic field safety around the WPT system, debris / foreign object interaction with the electromagnetic field, and high speed dynamic alignment and automated power transfer. INL is working on technologies, strategies, and solutions to conquer these system challenges, thereby enabling wireless charging for electric vehicles to become safer and more reliable.

### Objectives

The objectives for INL’s scope of work for this ORNL-led project includes the advancement of safe, high-power transfer for both static and dynamic WPT systems. The primary safety concern with WPT is stray electromagnetic fields (EM fields) originating from the high-power WPT system. Stray EM fields can interact with living beings and metallic objects, resulting in potentially hazardous conditions. To reduce the magnitude of these stray EM fields to within public safety limits, advanced shielding solutions are needed. Currently, solutions exist for light-duty WPT systems up to 20 kW, but further advancement is needed for safe, high-power, light-duty WPT and dWPT operation.

INL is also developing data collection systems and methodologies for the evaluation and analysis of the advanced WPT and dWPT systems developed in this project. This includes developing a data acquisition system, evaluation requirements, and test procedures to characterize the operational and safety performance of the WPT and dWPT systems in the later stages of this project, in collaboration with ORNL.

## Approach

Through modeling and simulation, using advanced magnetics 3-D finite element modeling tools, new EM field mitigation solutions and designs can be designed and evaluated for performance and effectiveness. Additionally, laboratory hardware testing and evaluation is used to validate the modeling results therefore providing high levels of confidence in the effectiveness of future designs developed via modeling and simulation methods.

Data acquisition requirements and methodologies are developed using the anticipated electrical parameters and performance design considerations. Due to the vehicle speed during power transfer for in-motion dWPT (i.e., 70-mph vehicle speed), the data acquisition system must have very high sampling rate capabilities in order to accurately capture the electrical, magnetic, and power transfer performance of the dWPT system. The design approach in this task includes using commercially available sensors, meters, and data acquisition tools to minimize costs and accelerate development time.

## Results

### *EM-field Shaping and Shielding Solutions*

Advanced magnetics 3-D finite element modeling tools were used to develop and analyze the EM field surrounding a 200-kW light-duty WPT system. The new EM-field shaping design uses innovated geometry of ferrite placement around the WPT to effectively shape the EM field therefore reducing the stray EM field surrounding the WPT system. Figure VI.2.1 shows a final design concept which includes a full ferrite backing for each coil and a segmented “tooth-edge” design of wrap-around ferrite which helps to shape the field inwards, therefore inherently reducing the stray magnetic field. The tooth-edge design enables EM-field shaping with a minimal increase in mass and cost.

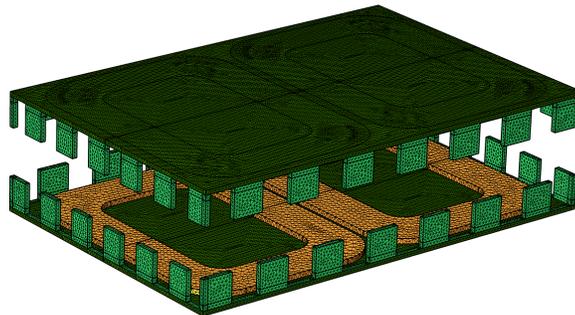


Figure VI.2.1 Light duty 200kW WPT with Tooth-Edge Ferrite Design

Analysis of this segmented “tooth-edge” design in comparison to the traditional ferrite backing design (no wrap-around edge ferrite) is shown in Figure VI.2.2 for 200kW operation. The new segmented “tooth-edge” design shows a 46% reduction in magnetic field strength from 52.6  $\mu\text{T}$  to 24.2  $\mu\text{T}$  when primary and secondary coils are aligned. This is within the industry safety limits of 27  $\mu\text{T}$  for public exposure. This field magnitude comparison was chosen at 0.8m from the coil center because 0.8m is the recognized industry recommended distance. This reference distance was defined with respect to the width of a small light duty car. With a WPT centrally installed on the bottom of a 1.6m wide EV, the closest a person can come in proximity to an operating WPT is 0.8m, without crawling under the vehicle. Therefore, if the EM-field strength at a distance of  $\geq 0.8\text{m}$  is below the industry safety limit, the WPT operation is considered to be safe for public charging operation.

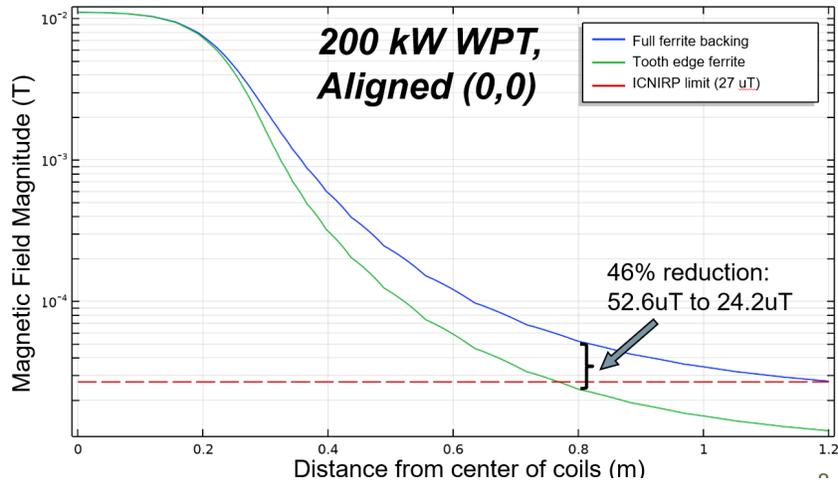


Figure VI.2.2 Magnetic field magnitude for 200kW light duty WPT with and without Tooth-Edge ferrite design

***dWPT Data Acquisition Requirements and Methodology***

INL completed the development of the data acquisition requirements to evaluate high power WPT and dWPT operation. The data acquisition will measure the power transfer, input power quality, EM-field emissions, and transient response characteristics of the dWPT system during static, quasi-static, and in-motion operation. In order to accomplish this goal, measurement systems will be required on both the ground-side and the vehicle-side of the dWPT system. Additionally, the data from the multiple sources will need to be recorded and aligned to enable data analysis.

The purpose of data acquisition is to measure and record accurate data and results from the operation of the system under evaluation. For a dWPT the primary data and results required are:

- Power transferred (full system and sub-systems)
- Efficiency of power transfer
- Power quality characteristics at AC grid input node
- Electromagnetic field emissions surrounding the dWPT system
- Relative position of the two coils during operation (position and velocity)
- Response characteristic of the system to aid development and controls improvements.

In order to accomplish the above requirements, four categories of data acquisition rate are shown in dependent upon Table VI.2.1. The purpose of the data collected and the operating condition.

**Table VI.2.1 Four Sample Rate Ranges for dWPT Evaluation**

Sample Rate Range	Stationary WPT Measurements	Dynamic WPT Measurements	Development & Debug for WPT or dWPT
Cumulative / Bulk Energy	X	X	
10 Hz - 100 Hz	X		
2 kHz - 10 kHz		X	
1 MHz - 5 MHz			X

For static WPT testing, bulk energy measurements and 10 Hz sample rate measurements have been previously utilized since the WPT and EV are stationary and the WPT operates at nearly steady state. Previously, measurements were accomplished by an electromagnetic field meter and a single power meter capable of recording measurements from both the ground-side and vehicle-side components of the WPT system. For dWPT, since the duration of the power transfer event may be very short (example 0.004 seconds), the data acquisition measurement system must have a very high higher sampling rate. The dWPT sampling rate must be of  $>1$  kHz in order to record meaningful data from the DC bus on the ground-side installation as well as the DC output of the dWPT system on the vehicle. Figure VI.2.3 shows a representative measurement of a dWPT with coils of 100mm length operating at 75 mph. At a 3 kHz sample rate, only 9 measurements occur during the time of the full power transfer. Note the 60Hz waveform for input power does not complete a single cycle within the period of power transfer therefore accurately measuring the 60Hz AC input power is extremely challenging during this short duration of power transfer.

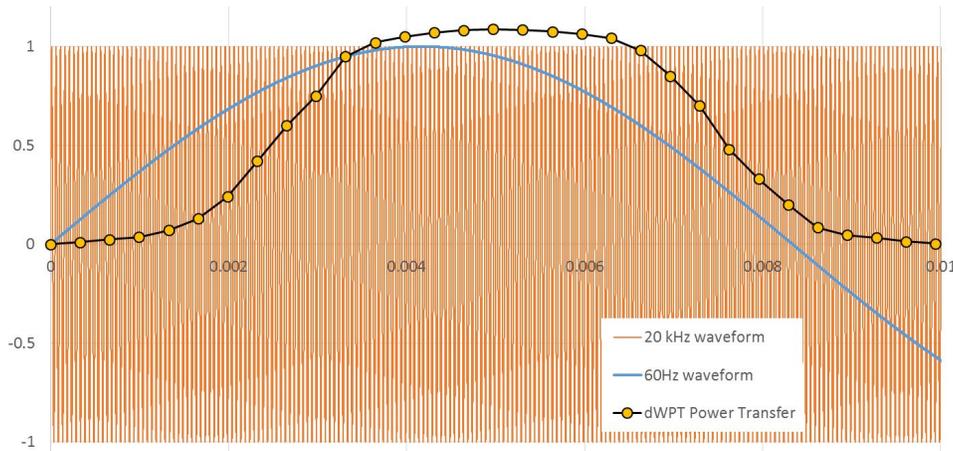


Figure VI.2.3 Representative electrical waveform during in-motion wireless power transfer

During controls development or debug of the power transfer waveform (20kHz or 85kHz), the 3kHz sample rate is not adequate since the operating frequency of the dWPT is 85kHz. Therefore, a much higher sampling rate is required. To avoid aliasing, the measurement sampling rate should be at least ten times greater the operating frequency ( $>850$  kHz). This high sampling rate will allow analysis and development of the power transfer controls system.

## Conclusions

INL has successfully completed several tasks in support of the dynamic and high-power wireless power transfer project. This successful progress enables the project to be on track to successfully demonstrate safe, high-power, dynamic wireless power transfer for a light-duty electric vehicle.

Solutions for EM-field shaping and shielding have been developed and modeled to enable safe, stationary, 200-kW wireless power transfer in a light-duty vehicle. The new EM-field shaping design uses innovated geometry of ferrite placement around the WPT to effectively shape the EM field, thereby reducing the stray EM field surrounding the WPT system. The result is a design that enables 200-kW WPT operation with stray EM-field levels below the industry safety limits of  $27 \mu\text{T}$ .

INL has completed the requirements for a data acquisition system to enable the development, characterization, and evaluation of dynamic wireless power transfer systems. This system utilizes three ranges of sampling rates, enabling the evaluation of static, quasi-static, and in-motion WPT. The data acquisition system incorporates several commercially available pieces of measurement equipment that are utilized both on the vehicle-side WPT and the ground-side WPT. This data acquisition system will provide valuable data from the performance

and operation of the dynamic high-power wireless power transfer system developed within this collaborative project led by ORNL.

### **Key Publications**

Zhang, Bo; et. al.; “*Challenges of Future High Power Wireless Power Transfer for Light-Duty Electric Vehicles—Technology and Risk Management*”; eTransportation Elsevier; 2019.

### **References**

1. ICNIRP\_2010; <https://www.icnirp.org/cms/upload/publications/ICNIRPLFgdl.pdf>



## VII Grid and Infrastructure Cyber Security

### VII.1 Consequence-Driven Cybersecurity for High-Power Charging Infrastructure (INL)

#### **Richard “Barney” Carlson, Principal Investigator**

Idaho National Lab  
775 MK Simpson Boulevard  
Idaho Falls, ID 83415  
E-mail: [Richard.carlson@in.gov](mailto:Richard.carlson@in.gov)

#### **Lee Slezak, DOE Program Manager**

U.S. Department of Energy  
E-mail: [Lee.Slezak@ee.doe.gov](mailto:Lee.Slezak@ee.doe.gov)

Start Date: October 1, 2018

End Date: September 30, 2021

Project Funding (FY19): \$430,000

DOE share: \$430,000

Non-DOE share: \$0

#### **Project Introduction**

With the emergence of electrified transportation, there is a desire for faster recharge times and integrated energy management for charging infrastructure. The development and deployment of extreme fast charging (XFC) and wireless power transfer (WPT) chargers emphasizes the need for cybersecurity of these high-power EV charging systems. The use of high voltage, high current, and high magnetic fields for high power charging systems presents potential public safety hazards if not controlled properly. Additionally, many advanced control systems and communication networks are utilized to maximize the efficiency of this high-power EV charging infrastructure. With these safety and energy management controls systems, cybersecurity vulnerabilities may be present.

Cybersecurity research being conducted at Idaho National Lab includes the analysis and evaluation of cybersecurity of high power conductive and wireless charging infrastructure. INL is leading a project in collaboration with ORNL, NREL, ABB, Tritium, and Electrify America focused on prioritizing and securing cybersecurity vulnerabilities and threats for high power EV charging infrastructure. The purpose of this research project is to first conceptualize possible disruptive events caused by cyber means related to XFC and WPT systems, secondly evaluate the impact severity potential of these events, and thirdly develop mitigation solutions to secure the infrastructure. The impact-based framework methodology used prioritizes disruptive events based on severity of impact and cyber manipulation complexity, leading to defined high consequence events (HCEs). In later stages of the project, preliminary mitigation strategies and solutions will be identified and investigated to defend, identify, and resolve cyberattacks.

Charging infrastructure is designed to meet EV energy transfer requirements with safe, high efficiency operation at a low cost, but often cybersecurity is not at the forefront of the design process when engineering such systems. By identifying and prioritizing potential disruptive cybersecurity events into a list of HCEs, cybersecurity research efforts can be focused on the highest priority events. Using input from industry manufacturing, engineering, cybersecurity, and electric sector subject matter experts, a comprehensive list of HCEs has been developed for high-power EV charging infrastructure.

#### **Objectives**

Charging infrastructure is a system of systems, including physical, communication, and control layers. Physical systems include vehicles, charging equipment, supporting electrical equipment at the charging site (e.g., power converters, transformers, etc.), distributed energy resources (DERs) such as stationary energy storage and solar photovoltaic (PV) arrays that support XFC charging stations, and the distribution feeder

electrical equipment that services charging sites. The objective of this project is to develop solutions and recommendation for the highest prioritized events to secure vulnerabilities, means to detect attacks, and methodologies to respond and restore from an HCE.

### Approach

The impact and consequence-based cybersecurity analysis framework use in this project will first prioritize high consequence events caused by cybersecurity manipulation that can cause physical adverse effects to the EV charging infrastructure. This prioritization is accomplished using an internally developed scoring matrix based on impact severity and cyber manipulation complexity. Secondly, the severity and complexity of these potential events will be evaluated using laboratory equipment to validate the prioritization and to investigate the vulnerabilities and attack pathways leading to the high consequence events. Third, mitigation solutions and strategies will be developed to secure vulnerabilities and threats. Recommended response strategies and methodologies based on the analysis done will also be developed. Lastly, publication of recommendations, project findings, and a stakeholder action plan will be published to inform industry of the solutions developed to secure high power charging infrastructure.

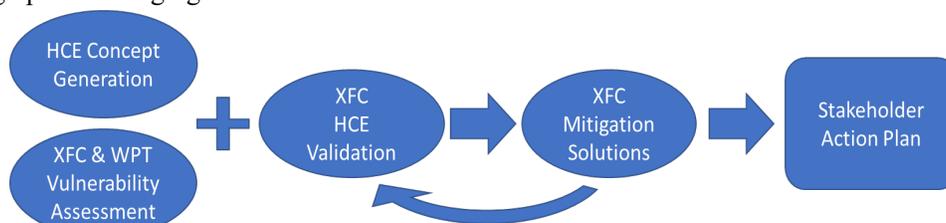


Figure VII.1.1 Project tasks flow chart

Cybersecurity vulnerability and cyber-attack path assessment in this project will be focused on device-level and supervisory control systems and the sophisticated communication they require within and between vehicles, EVSE, DERs, building and other third-party controllers, utilities, and/or other entities. Assessment of the electric grid's cybersecurity vulnerabilities is addressed by other programs and is therefore out of the scope of this project. However, this project will assess threats to the local distribution network and broader grid stability caused by compromised high power charging infrastructure.

The effort required for the success of this three-year project led by Idaho National Lab involves the collaboration of two other National Labs (National Renewable Energy Lab, Oak Ridge National Lab) and three collaborative industry partners (ABB, Tritium, Electrify America). Together the expertise and capabilities of these partners will enable the successful outcome for this project.

### Results

The impact and consequence-based analysis framework used during this project draws on elements of the Consequence-driven Cyber-informed Engineering (CCE) methodology developed by Idaho National Laboratory (Freeman et al. 2019). The CCE methodology was developed to assist private and public organizations examine their own operational technology environment, identify and prioritize potential HCEs, enumerate possible methods by which an adversary could affect a physical process via cyber means, and implement mitigation strategies via engineering to minimize the risk of cyber-attack. A foundational assumption of the CCE methodology is if an entity is targeted by an advanced cyber adversary, it will be compromised. The only question is when. Drawing from this established CCE analysis framework, researchers created a comprehensive list of potential HCEs for the XFC and WPT charging infrastructure. Results of these efforts will be shared with the appropriate XFC and WPT control system manufacturers to develop engineering strategies to mitigate the potential consequence.

Based on cyber manipulation and physical effects, possible HCEs are conceived. Input was provided from automotive, charging infrastructure, cybersecurity, and power systems experts to provide a comprehensive list

of events. The events identified in this project are organized into five categories: loss of service or reduced capacity, injury or loss of life, hardware damage, adverse impacts to the electric grid, and data theft or alteration. Organizing the events into these categories aid the research team in analyzing the different types of effects and allows project managers to assign certain categories of HCEs to subject matter experts for evaluation. Note that some scenarios fit into more than one category.

**High Consequence Events Scoring Methodology**

The impact severity criteria matrix was created based on the specific needs of this project to quantify the impact severity for each event. For the purposes of this project, the point of view for the scoring is from the combined viewpoint of the charging site owner/operator, the charging network operator, and the charger equipment manufacturer. The other stakeholders of a high-power charge site such as the EV owner, vehicle manufacturer, site host, electric grid utility company, and government regulatory agencies were also considered. The criteria are evaluated on a Likert scale from low to high with values ranging from 1 to 5, respectively. A weighting factor for each ranking criterion was determined based on input from stakeholders since some criteria are significantly more important than other criteria. The criteria that are considered the most impactful to the stakeholder are given a higher weighting so the final score would reflect the events of most concern. Table VII.1.1 shows the criteria descriptions for the impact severity scoring. The HCEs are scored by team members using the weighted impact severity criteria matrix. The average of these results is calculated to determine a final weighted impact severity score for each high consequence event.

**Table VII.1.1 Impact Severity Scoring Matrix**

Criteria	Not Applicable (N/A) (0)	Low (1)	Medium (3)	High (5)
<b>Level of Impact</b>	N/A	Single unit affected (EV, XFC, or WPT)	Multiple units at a single site affected (EV, XFC and/or WPT)	Multiple unit at multiple sites affected (EV, XFC and/or WPT)
<b>Magnitude (proprietary / standardized)</b>	N/A	Manufacturer-specific protocol implementation (EV or EVSE)	>1 manufacturer protocol implementation (supply chain) (EV or EVSE)	Across all standardized systems (both EVSE and EVs)
<b>Duration</b>	N/A	<8 hours	>8 hours to <5 days	>5 days
<b>Recovery Effort</b>	Automated recovery without external intervention	Equipment can be returned to operating condition via reset or reboot (performed remotely or by onsite personnel)	Equipment can be returned to normal operating condition via reboot or servicing by offsite personnel	Equipment can be returned to normal operating condition only via hardware replacement
<b>Safety</b>	No risk of injury or death	Risk of minor injury (no hospitalization), but NO risk of death	Risk of serious injury (hospitalization), but low risk of death	Significant risk of death
<b>Costs</b>	No costs incurred	Cost of event is significant, but well within the organization's ability to absorb	Cost of event will require multiple years for financial (balance sheet) recovery	Cost of event triggers a liquidity crisis that could result in bankruptcy of the organization
<b>Effect Propagation Beyond EV or EVSE</b>	N/A	Localized to site	Within metro area	Regional
<b>EV Industry Confidence, Reputation Damage</b>	No impact to EV adoption	Minimal impact to EV adoption	Stagnant EV adoption	Negative EV adoption

A complexity multiplier is determined for each scenario based on the anticipated ease of cyber manipulation through the potential vulnerabilities to cause the event. The complexity multiplier is derived from three attributes. First, the number of systems or functions that are required to be accessed and manipulated concurrently to create the event. Second, the state of the system at the time of the cyber-attack. Examples of the state of the system includes the number and power level of charging systems concurrently operating, the loading of the distribution feeder, the extent of interaction with the public, and other factors. Finally, the skills and experience of the malicious adversary that are required to successfully access and manipulate the vulnerability in order to cause the event. These three groupings of attributes are used to determine the cyber complexity multiplier.

The final score for each high consequence event is determined by multiplying the weighted impact severity score by the cyber complexity multiplier.

$$HCE\ Score = Weighted\ Impact\ Severity \times Complexity\ Multiplier$$

The list of events is prioritized with the highest scored HCE at the top of the list. This prioritized HCE list can aid the direction and focus of future research efforts for cybersecurity of high-power EV charging infrastructure as well as the development of mitigation strategies and solutions.

### Prioritized High Consequence Events

The HCE prioritization process has generated a prioritized list of over fifty possible high consequence events to guide future research tasks. Table VII.1.2 shows the top twelve prioritized high consequence events.

**Table VII.1.2 Top Dozen Prioritized High Consequence Events**

	Category	HCE Description
1	Grid Impacts	Power Outage(s) due to sudden, concurrent load shed from multiple XFCs.
2	Safety	Injury or loss of life due to electrocution, electrical shock, or burns from exposed conductors of the XFC cord set cable caused by manipulated XFC thermal controls systems resulting in insulation failure
3	Grid Impacts	Power Outage(s) due to sudden load shed or load increase from on-site energy storage or other DER manipulation.
4	Safety	Medical device failure or injury caused by exposure to high electromagnetic field to implanted medical devices (applies only to wireless chargers).
5	Grid Impacts	Damage to equipment within the feeder distribution area (transformers, switch gear, harmonics, overload capacitor bank, high reactive power)
6	Grid Impacts	The charger and DER at the site are not able to provide grid service (curtail, VAR support, etc.) when needed causing decreased stability/reliability of the grid
7	Loss of Service	System shutdown (EVSE or charging site) due to creation of software error state resulting in vehicle(s) not charging.
8	Safety	Burns caused by hot cord set due to cyber manipulation of the XFC cooling system
9	Loss of Service	System shutdown due to network outage (Wi-Fi or other communications disruption or outage)
10	Hardware Damage	Hardware damage to the charger over very long duration of elevated temperature
11	Hardware Damage	(WPT Only) Induced voltage (high V/m) on vehicle components or electrical wiring harnesses may damage electrical components not associated with WPT system. Vehicle components that are not rated or shielded from high magnetic field levels may be vulnerable.
12	Data Theft / Alteration	Theft or alteration of PII-type data transmitted between vehicle, EVSE, EV driver, network operator, etc.

### ***Laboratory Preparation for Vulnerability Assessment and HCE Evaluation***

Significant laboratory preparation has been completed to enable the vulnerability assessment of high-power charging infrastructure as well as the evaluation of HCE impact severity and cyber manipulation complexity. Additionally, the laboratory capabilities will enable the development of mitigation solutions and strategies to prevent high consequence events.



Figure VII.1.2 350kW Extreme Fast Charger at Idaho National Lab

Preliminary evaluation of the XFC operation to understand the impact severity of a few HCEs was conducted. Specifically, the HCE #1 involving the grid impact of sudden load shed due to concurrently stop charging of multiple XFCs was evaluated. This preliminary evaluation included the operational characteristics of a 50kW light duty vehicle and a 125kW electric bus.

Several means of ending a charge event were realized including one of many software errors, broadcasting a “end charge” message, or even the correct method by using the public user interface touchscreen “stop” button. All of these methods to stop a charge event resulted in the same response. The XFC power ramp down characteristic for both the 50kW and the 125kW was measured to be between 0.003 and 0.002 seconds from full power to the stand-by power. The variation in stop duration appeared to be dependent upon the condition of the charge event when the stop charge event was initiated. Figure VII.1.3 shows the “stop charge” event duration is 0.002 seconds when operating at 125 kW output. These results will be used during later stages of the project to determine the possible extent of impacts to a distribution feeder if multiple XFC are manipulated to stop charging concurrently. This will likely depend upon how many XFC stop charging concurrently and the state of the distribution feeder providing power to the XFCs in question.

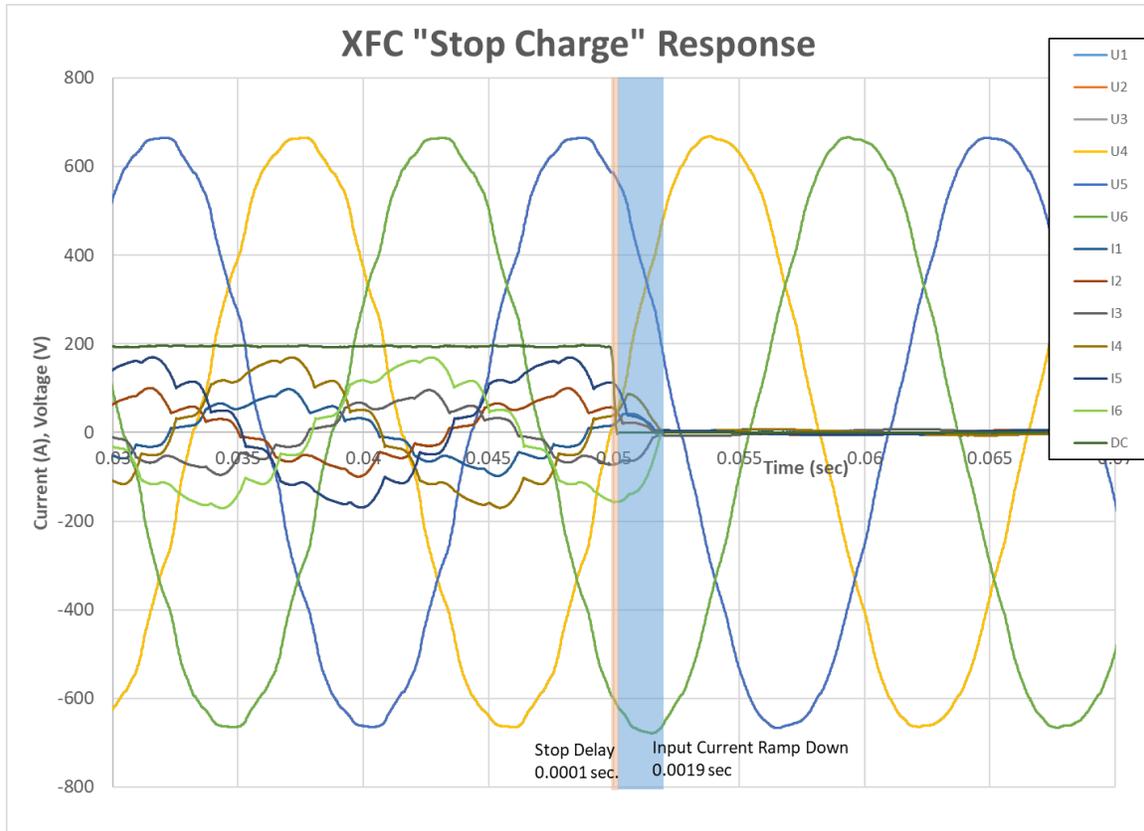


Figure VII.1.3 350kW Extreme Fast Charger stop charge response characteristics

An initial red team assessment of the XFC commenced once the equipment was operational in the laboratory. To prepare the system for the assessment, a private network was established to connect the XFC wired (Ethernet) network. This provides the network services required for the XFC to communicate with the INL OCPP server. Once the OCPP server is configured properly, the assessment will include the analysis of this potential attack vector. Several hardware assessment tools from INL's Hardware Exploitation (HEX) laboratory are now connected to the XFC for an in-depth analysis of the many XFC subsystems. Once firmware is successfully extracted from the XFC, an automated vulnerability analysis will begin. Future activities include leveraging capabilities from the Wireless Testbed at INL to intercept and manipulate the cellular traffic from the XFC. This analysis will allow the assessment team to determine the security level of the remote communications to the charging infrastructure networks.

Thus far the assessment results of the XFC are very encouraging. The security posture of the XFC is much better than previous versions of DC Fast Chargers from the same vendor. Compromise of this XFC will require very specialized expertise which increases the cybersecurity complexity and therefore reduces the potential for unauthorized access leading to system manipulation.

## Conclusions

As high-power EV charging infrastructure is deployed and further established, the need for cybersecurity is vital for safety, robustness, and consumer confidence. Traditional cybersecurity efforts focus on keeping cyber adversaries out of system networks through authorization, firewalls, and encryption. However, this project is conducted under the assumption that a determined, well-resourced adversary will eventually gain access to almost any network. Research efforts for this project are therefore focused on trying to prevent high consequence manipulation and misuse of EV charging infrastructure. In order to effectively do so, researchers first conceptualized events that could be brought about by cyber manipulation to create a physically adverse

effect on high-powered charging infrastructure, EVs, and/or the electric grid. Researchers then quantitatively scored the events using an impact severity scoring matrix and complexity multiplier. The high consequence events were scored and prioritized based upon this quantitative method. This prioritization ranking allows researchers to focus their efforts on identifying and securing attack pathways enabling the most severe HCEs, then working to develop mitigation solutions to prevent and identify the cyber threats potentially leading to those HCEs.

Next steps for this project include validating the HCE priority list through laboratory cybersecurity assessments and determining the complexity of cyber manipulation to evoke these events. This also involves determining available pathways adversaries could use. In the final phase of the project, mitigation strategies and solutions will be developed that can detect, mitigate, or even prevent the cyber threats. The findings and solutions developed in this project will be published to advise industry on methods to improve cybersecurity for high power EV charging infrastructure.

## References

1. Freeman, Sarah G., Curtis St Michel, Robert Smith, and Michael Assante. 2019. *Consequence-driven cyber-informed engineering (CCE)*. October 18. Accessed February 18, 2019. doi:doi:10.2172/1341416

## VII.2 CyberX: Cybersecurity for Grid Connected eXtreme Fast Charging Station (Idaho National Laboratory)

### **Don Scoffield, Principal Investigator**

Idaho National Laboratory  
775 MK Simpson Boulevard  
Idaho Falls, ID 83415  
E-mail: [Don.Scoffield@INL.Gov](mailto:Don.Scoffield@INL.Gov)

### **Lee Slezak, DOE Program Manager**

U.S. Department of Energy  
E-mail: [Lee.Slezak@ee.doe.gov](mailto:Lee.Slezak@ee.doe.gov)

Start Date: October 1, 2018

End Date: September 30, 2020

Project Funding (FY19): \$500,000

DOE share: \$500,000

Non-DOE share: \$0

### **Project Introduction**

Deployment of electric vehicle (EV) charging devices, also known as electric vehicle supply equipment (EVSE), requires widespread infrastructure to meet market demand at the different places where cars travel, such as homes, public/private establishments, or near the highway. The impact of individual or grouped chargers on the distribution system can be neglected for small charging stations with only a few chargers; however, when many EVs are charging simultaneously at an EVSE installation site, the aggregate energy demand may provide a significant grid impact to a distribution or other energy delivery system. As charging power levels and charging speeds increase over time with newly manufactured EVSEs, EVs, and battery storage, this cumulative EV charging load can become a greater issue. The synchronous charging of multiple EVs at an extreme fast charging (XFC) station may cause potential adverse impacts to distribution network components (e.g., distribution transformer, distribution line/cable, circuit breaker, and fuse). These impacts may lead to issues on the larger grid, such as voltage instability, phase unbalance, and heating problems within utility or network operator systems. In response, network operators or utilities would then need to shed loads in their system while maintaining cost-optimized economic dispatch.

These grid impact events are being explored within the project through the following two key milestones: (1) the XFC station design and (2) the threat analysis report based on System Theoretic Process Analysis (STPA).

XFC station design considered in this project is a public or private site or depot where multiple EVSE units are capable of providing high-power charging to multiple EVs simultaneously. Such a XFC station design provides a simplified representation of a distribution system that may experience the potential negative impacts of high-power charging that may be seen elsewhere on the grid. Additionally, many of ABB's EV charging products provide an EVSE charge point and point of sale (similar to the pump of traditional fueling stations) and remote power supply cabinet(s) for power electronics equipment, power conversion equipment, and protection devices. This system must be protected against potential targets for cyber-attack. The threat analysis milestone being conducted in this project aims to provide attack trees focused on the EVSE, supporting electrical system equipment, and other integrated systems such as Battery Energy Storage Systems (BESS).

### **Objectives**

Idaho National Laboratory partnered with ABB, as the project's prime contractor, along with APS Global and XOS Trucks, to perform research, development, and demonstration of a security domain layer that enables an XFC station to detect and defend against cyber-attacks. The project team will develop algorithms that defend against cyber-attacks that aim to disrupt electric power service and/or charging station operation.



## Approach

ABB and the project team will design and test a defense system to improve cyber-security situational awareness in EVSE through a connected XFC Management System (XMS). The project team aims to achieve robust performance capability with component-level validation in a laboratory setting with power hardware-in-the-loop simulators. In some cases, new functionality such as BESS integration and optimization, will be prototyped to demonstrate new use cases that more fully display potential grid impact and the importance of secure communications in the face of increasing demands for connected utility services at the XFC station level. Finally, the project will demonstrate the system in a testbed environment and validate timing and security aspects. The outcome of this project will enhance XFC station management systems and other devices with new hardware and firmware/software functions to support detection and defense mechanisms.

In order to assist the development of CyberX strategies, experts at INL have supported ABB in this project through the following tasks:

1. Develop high-fidelity PEV charging models to accurately represent XFC as a load on the grid
2. Develop Matlab PowerSim model to interface high-fidelity charging models with Opal-RT Simulation
3. Install and commission the ABB Terra HP extreme fast charger in INL's Electric Vehicle Infrastructure (EVI) Laboratory.

## Results

### *Develop High-fidelity Charging Models*

Experts at INL have developed high-fidelity PEV charging models for extreme fast chargers derived from extensive charging and battery testing data that INL has collected over the past decade. These models have been consolidated into a library in Caldera, INL's charging infrastructure simulation platform. Caldera charging models accurately estimate charge power profiles, efficiency, and power factors for a wide variety of vehicles and charging technologies under varying grid conditions.

High-fidelity charging models are important when designing and debugging systems like Cyber-X that are capable of detecting anomalies in PEV charging power profiles. XFC charging profiles can be very volatile due to short charging times, high charge rates, and fast ramp rates. This volatile behavior creates a risk of erroneous identification of cyber-attacks (so-called false positives) in anomalies detection systems. This underscores the need for highly accurate charging models.

In this project, INL developed high-fidelity charging models for the ABB Terra HP system (350 kW) and ABB Terra 53 system (50 kW). Using the Terra HP model, INL simulated 24 hours of operation of six 350-kW ABB Terra HP fast chargers at a single site. The aggregate power profile of the simulated site is shown in Figure VII.2.1. The figure shows that the load profile is extremely volatile. The load changes from less than 200 kilowatts to over 1.5 megawatts many times during the day. One reason for this volatility is the change in power when a PEV stops charging occurs very quickly. Lab tests performed on ABB's Terra HP fast charger determined that this ramp rate can exceed 140 MW per second, which is very fast for power systems. Figure VII.2.2 shows the same power profile over a 2-hour period, making obvious the abrupt changes in power that occur when individual PEVs begin and end charging.

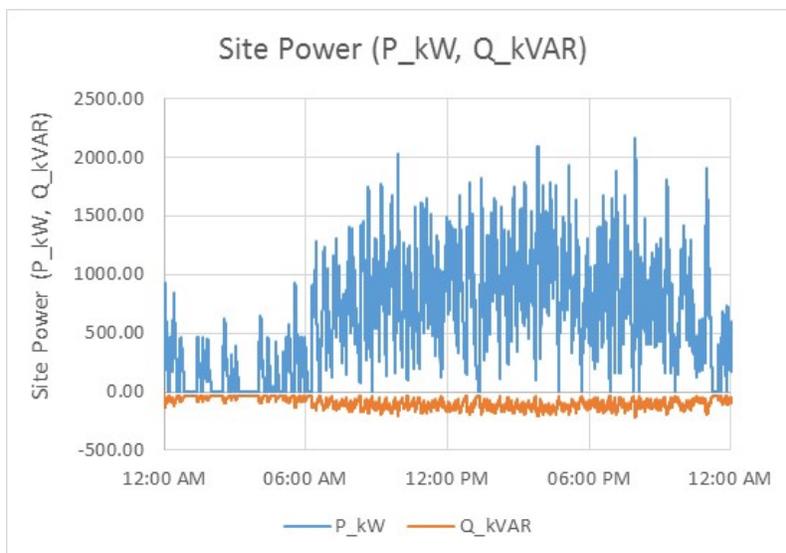


Figure VII.2.1 Charging power profile for a fast charging site with high fidelity models for six 350 kW ABB Terra HP fast chargers over a 24-hour period

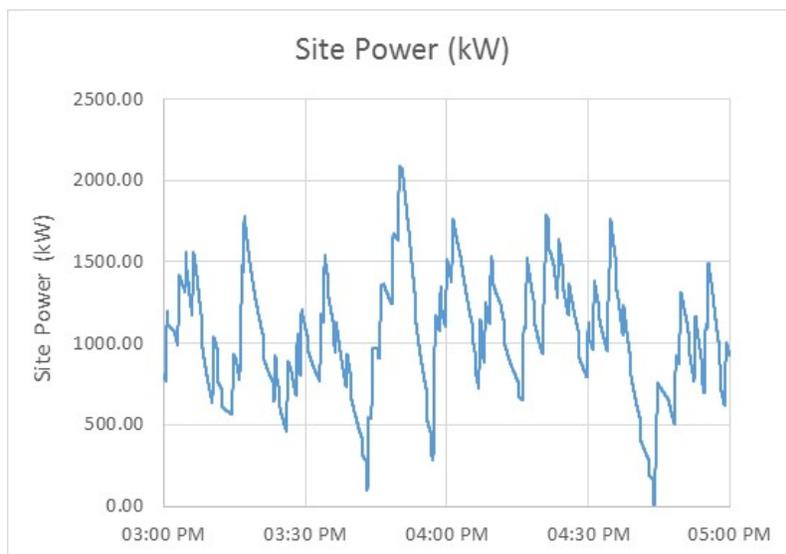


Figure VII.2.2 Charging power profile for a fast charging site with high fidelity models for six 350 kW ABB Terra HP fast chargers over a 2-hour period

***Develop Matlab PowerSim Model to Interface High Fidelity Charging Models with Opal-RT Simulation***

In this project, ABB is using an Opal-RT hardware-in-the-loop (HIL) simulation platform to model a XFC station and supporting electrical equipment. INL’s high-fidelity charging models are being integrated into the HIL platform. To facilitate this integration, INL has coded its models in the Matlab PowerSim library and shared these models with ABB.

***Install and Commission the ABB Terra HP Extreme Fast Charger at INL***

In the second year of the project, the CyberX system will be integrated into an ABB Terra HP charger located in INL’s EVI laboratory and demonstrated in a HIL environment. In preparation for this demonstration, in FY2019, INL acquired, installed, and commissioned an ABB Terra HP charger in its EVI laboratory (see Figure VII.2.3). Under the “Fast Charging: Grid & Cybersecurity” project, the ABB Terra HP charger was

characterized through lab testing. Data from this testing was used to validate the high-fidelity charging model of the ABB Terra HP charger.



Figure VII.2.3 ABB Terra HP extreme fast charger installed in the EVIL lab located at INL

## Conclusions

The INL team is supporting ABB to perform research, development, and demonstration of a security domain layer that enables an XFC station to detect and defend against cyber-attacks. INL staff developed high-fidelity PEV charging models for extreme fast chargers derived from extensive charging and battery testing data that INL has collected over the past decade, including data from a state-of-the-art ABB Terra HP charger. Due to the large amount of variability in XFC charging loads, these high-fidelity charging models are necessary when developing the Cyber-X system to avoid false positives in anomaly detection. These charging models accurately estimate charge power profiles, efficiency, and power factors for a wide variety of vehicles and charging technologies under varying grid conditions. The INL team is also preparing a HIL testbed in INL's EVI Laboratory that will be used to demonstrate and test the Cyber-X system developed by ABB in the second year of this project.

### VII.3 Threat Model of Vehicle Charging Infrastructure (ANL)

#### **Roland Varriale, Principal Investigator**

Argonne National Laboratory  
9700 S Cass Avenue  
Lemont, IL 60439  
E-mail: [rvarriale@anl.gov](mailto:rvarriale@anl.gov)

#### **Lee Slezak, DOE Program Manager**

U.S. Department of Energy  
E-mail: [Lee.Slezak@ee.doe.gov](mailto:Lee.Slezak@ee.doe.gov)

Start Date: October 1, 2018

End Date: September 30, 2020

Project Funding (FY19): \$400,000

DOE share: \$400,000

Non-DOE share: \$0

#### **Project Introduction**

Within the *Threat Model of Vehicle Charging Infrastructure* project's considerations, understanding the application of previous secure architectures and how threat actors have approached them is paramount. Charging infrastructure, although in its infancy from a security perspective, exhibits qualities that are well-documented and addressed within the cyber security space. Understanding the technologies implemented by charging manufacturers and pinpointing key functionality and processes will identify critical processes and increase resiliency. ANL's participation within this project has been mainly in two areas: (1) informing team members of best practices and well-known approaches to architecture deployments within cyber-physical systems, and (2) assisting with experimental testing of charging infrastructure and networking deployments.

#### **Objectives**

The main objective of this project lies within the understanding and documenting of risk—composed of threats, vulnerabilities, and consequences—to electrical vehicle charging infrastructure. This work will assist in the enumeration of use cases and functionality to create more detailed threat models and inform experimental security testing.

#### **Approach**

The original scope of Argonne's effort included penetration testing utilizing the high-power DC charging equipment (200 kW DC) installed at the Smart Energy Plaza. However, the manufacturer invited the project participants to their facility and the initial assessment was conducted there.

ANL participated in the team that inspected theoretical and experimental attacks against electric vehicle charging infrastructure. The findings from this activity have informed the other DOE project team members to incorporate these attack paths and considerations when documenting risks and architectures associated with electric vehicles, vehicle charging systems, and the building/utility infrastructure. Documentation was provided to all participants which highlighted key findings, mitigating measures, and potential consequences.

#### **Results**

As a result of contributions this fiscal year, the work performed has informed the threat model for this project as well as security considerations for more secure charging infrastructure development. Furthermore, coordination with other DOE VTO project participants motivates the production of a reference architecture that will encompass the breadth of work being performed within this project, and others. The threat model, incorporating the Microsoft STRIDE [1] threat model, showed promise during field testing. This testing enumerated several consequences to charging infrastructure that best practices within cyber security – such as NIST-SP800 [2], NIST Cyber Security Framework [3], or ISACA's COBIT [4] framework – may mitigate.

Although initial field-testing results showed several areas of improvement and low cyber maturity [5], additional test facilities should be incorporate in the coming year to identify the heterogeneity of charging infrastructure components and architectures.

By coupling the theoretical work performed by the team on WEC outage simulations with the experimental work performed on security risks to charging infrastructure, risks to charging infrastructure on the whole can be more accurately assessed. Furthermore, this work promotes the ability to assess criticality of load, distribution/concentration of EVSE, and substation utilization to minimize outages due to possible compromise. Work performed during this past year also contributed towards the DOT Volpe Center’s Extreme “Fast Charging (XFC) Cybersecurity Threats, Use Cases and Requirements for Medium and Heavy-Duty Electric Vehicles” document [6].

### Conclusions

The work started during this period of performance has been instrumental in starting conversations around secure architectures for charging infrastructure. Results and high-level findings from this work have been disseminated at meetings promoting security requirements to charging infrastructure at many levels (Level 1/2, xFC [6], Megawatt+). The current sample size for the experimental testing and analysis work is small, and the previous work has sound foundation to extend to additional charging equipment manufacturers.

### References

1. [https://msdn.microsoft.com/en-us/library/ee823878\(v=cs.20\).aspx](https://msdn.microsoft.com/en-us/library/ee823878(v=cs.20).aspx)
2. <https://www.nist.gov/itl/nist-special-publication-800-series-general-information>
3. <https://www.nist.gov/cyberframework>
4. <http://www.isaca.org/Knowledge-Center/COBIT/Pages/Overview.aspx>
5. <https://www.energy.gov/ceser/activities/cybersecurity-critical-energy-infrastructure/energy-sector-cybersecurity-0>
6. Extreme Fast Charging (XFC) Cybersecurity Threats, Use Cases and Requirements for Medium and Heavy-Duty Electric Vehicles, 26 July 2019. Department of Transportation Volpe Center. 2019. Accessed October 22, 2019. <https://github.com/nmfta-repo/nmfta-hvcs-xfc/blob/master/README.md>.

## VII.4 Securing Vehicle Charging Infrastructure

### Jay Johnson, Principal Investigator

Sandia National Laboratories  
 P.O. Box 5800 MS1033  
 Albuquerque, NM 87185  
 E-mail: [jjohns2@sandia.gov](mailto:jjohns2@sandia.gov)

### Lee Slezak, DOE Program Manager

U.S. Department of Energy  
 E-mail: [Lee.Slezak@ee.doe.gov](mailto:Lee.Slezak@ee.doe.gov)

Start Date: October 1, 2018	End Date: September 30, 2021	
Project Funding (FY19): \$1,000,000	DOE share: \$1,000,000	Non-DOE share: \$0

### Project Introduction

Cybersecurity is essential for interoperable power systems and transportation infrastructure in the US. As the US transitions to transportation electrification, cyber-attacks on vehicle charging could impact nearly all US critical infrastructure. This is a growing area of concern as more charging stations communicate to a range of entities (grid operators, vehicles, OEM vendors, etc.), as shown in Figure VII.4.1. The research challenges are extensive and complicated because there are many end users, stakeholders, and software and equipment vendors. Poorly implemented electric vehicle supply equipment (EVSE) cybersecurity is a major risk to electric vehicle (EV) adoption because the political, social, and financial impact of cyberattacks—or public perception of such—ripples across the industry and has lasting and devastating effects. Unfortunately, there is no comprehensive EVSE cybersecurity approach and limited best practices have been adopted by the EV/EVSE industry. For this reason, there is an incomplete industry understanding of the attack surface, interconnected assets, and unsecured interfaces. Thus, comprehensive cybersecurity recommendations founded on sound research are necessary to secure EV charging infrastructure. This project is providing the automotive industry with a strong technical basis for securing this infrastructure by developing threat models, prioritizing technology gaps, and developing effective countermeasures. Specifically, the team is creating a cybersecurity threat model and performing a technical risk assessment of EVSE assets, so that automotive, charging, and utility stakeholders can better protect customers, vehicles, and power systems in the face of new cyber threats.

### Objectives

The goal of this project is to protect US critical infrastructure and improve energy security through technical analysis of the risk landscape presented by massive deployment of interoperable EV chargers. To improve the vehicle industry's cybersecurity posture, this project is:

- conducting adversary-based assessments of charging equipment,
- creating a threat model of EV charging, and
- analyzing power system impact for different attack scenarios.

This will provide DOE and automotive, EVSE vendor, and utility stakeholders with:

- clear documentation of the gaps in EVSE cybersecurity and the path forward to address those weaknesses,
- a threat model for EVSEs and associated infrastructure and services,

- recommendations for the automotive industry based on EVSE penetration testing, and
- cyber-attack impact analyses of the power system with remediation recommendations.

This project is also generating cybersecurity research solutions and collaborating closely with other government agencies and industry stakeholders to raise awareness of cybersecurity issues and solutions.

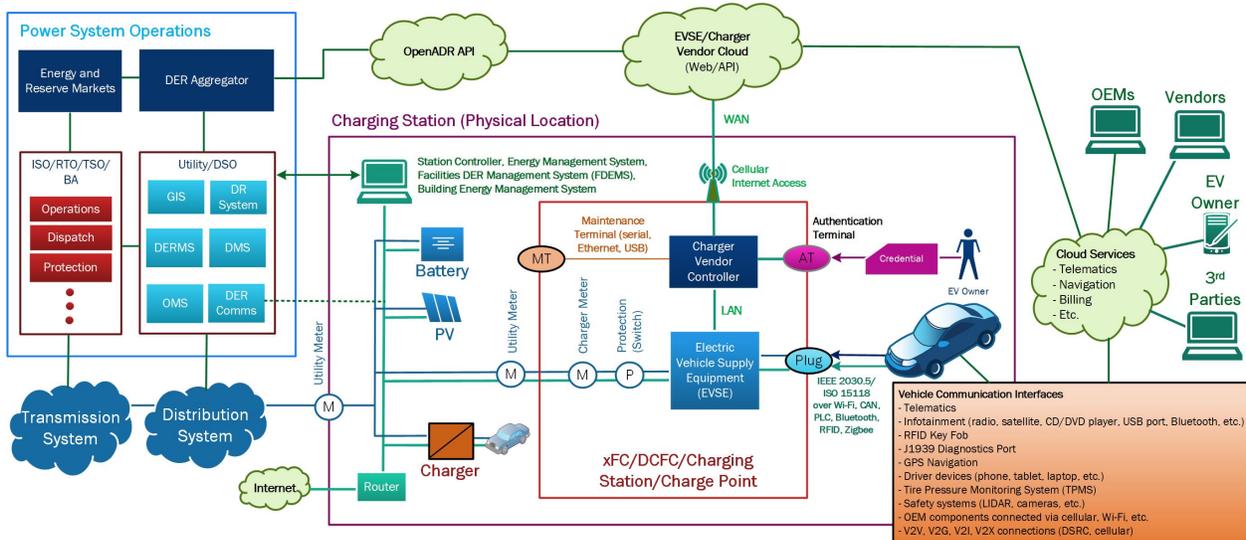


Figure VII.4.1 Electric vehicle communication systems to different components and entities.

**Approach**

The team is executing on the following integrated cybersecurity R&D tasks:

1. Conduct threat modelling based on the STRIDE methodology for EV to understand what potential cyber hazards exist with EVSE communications;
2. Assess the current state-of-the-art cybersecurity posture of EVSE equipment using authorized, adversary-based assessment techniques (red teaming);
3. Establish credible attack vectors based on the red teaming assessments and threat model;
4. Determine the impact of current and potential vulnerabilities on distribution and transmission power systems; and
5. Create a risk matrix to prioritize mitigations that reduce the number of high-consequence/low-threat level attacks.

The task structure of this project is shown in Figure VII.4.2, wherein the left side (blue) estimates the probability of different attack scenarios and the right side (green) estimates the consequence of attack scenarios. The cybersecurity risk of a particular attack is the combination of the likelihood and impact of the attack. By studying a range of attack scenarios, optimal mitigations can be determined to prevent attacks at specific points in the attack kill chain (i.e., the steps to accomplish adversary goals).

**Results**

In the first year of the project, the team evaluated probable attacks based on hands-on cybersecurity assessments with partner organizations and evaluated the probability of success against the skill level required to conduct the attack. A detailed threat model was created for different EVSE chargers with connections to external entities. Attack graphs were revised based on penetration testing of multiple EVSEs. A distribution

simulation of EVSE charging with and without vehicle-to-grid (V2G) functionality was conducted to determine if malicious control of EVSEs could cause high or low voltages on feeder circuits. Transmission simulations of coordinated charging modeled on the WECC were also performed to understand bulk system impact from coordinated cyber-attacks.

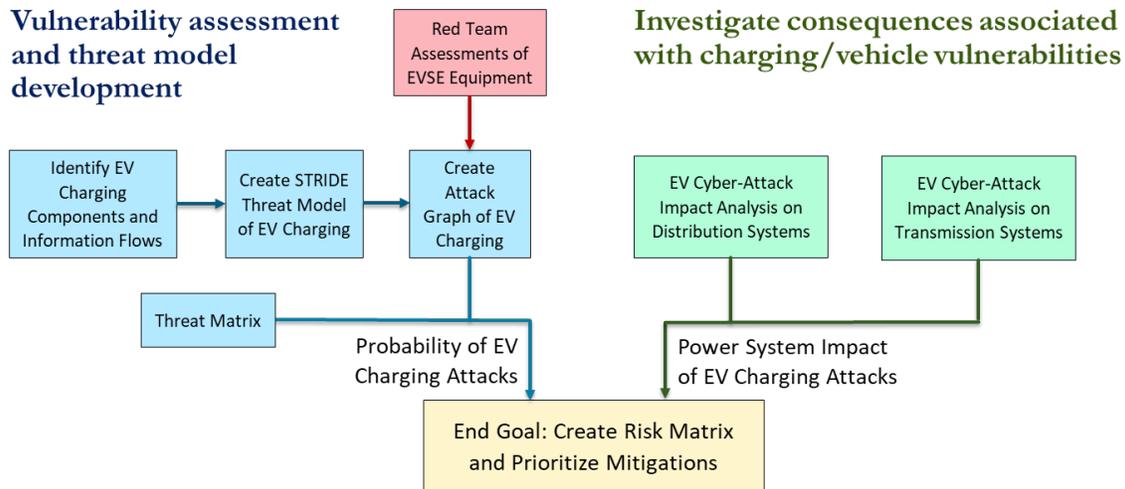


Figure VII.4.2 Project tasking.

### ***STRIDE Threat Model***

STRIDE is a threat modeling methodology used to help identify threats to systems operating in an environment. The team used this methodology to understand the threats to the EV charging ecosystem, including the plug-in electric vehicle, the charging station, charging station owners, and utilities. The threat model, shown in Figure VII.4.3, graphically depicts data flows between components of the electric vehicle charging system. The figure has been simplified to reduce the number of flows and components. The dashed boxes indicate trust boundaries, where the level of trust changes from untrusted (outside the boundary) to trusted (inside the boundary). Components inside the boundary share the same of degree of trust. Using the model, we can reason that a vulnerability to, for example, *P-06 EV Vendor App with Battery Data* can potentially influence EV charging rates. The model also indicates where to mitigate vulnerabilities. For instance, *P-59 EVSE Controller EVSP and DSO* may be an opportune position to implement a mitigation that limits the consequences of an aggregate *App* vulnerability. The team employed the model to consider the potential threats exposed by every data flow through the trust boundaries, and the potential consequences to the ecosystem based on these threats.





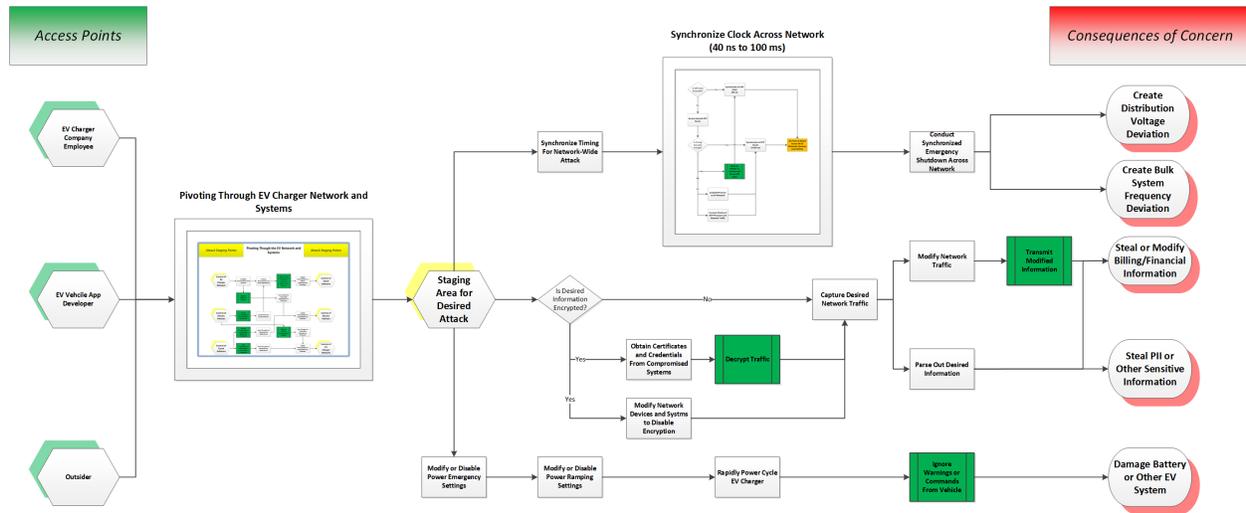


Figure VII.4.4 Attack graph.

### Distribution System Simulations

To better understand the impact on the distribution power system for different penetrations of EVSEs and attack strategies, simulations were conducted on a rural 12 kV distribution feeder in a highly commercial load area. The OpenDSS model contained 215 buses and 39 service transformers and was run for 3-minutes for different charging profiles with reactive power support functionality. The feeder voltage was regulated via substation transformer load tap changer (LTC). Nine 250 kW, 3-phase, 480 V stations were simulated at the end of the feeder. Scenarios included 2.25 MW charging sequences with and without V2G capabilities to generate high and low feeder voltages during peak and min load periods. XFC charging was limited to the SAE J2894/1 ramp rate of 40 amp/sec (i.e., EVSEs reached full output in ~13 seconds). The results for steady-state charging and discharging with different power factors are shown in Figure VII.4.5. The “+0.85 PF Charge+Discharge” scenario was designed to cause the worst overvoltage profile by first charging the EVs, which caused the LTC to tap up, and then discharging the EVs to drive the voltage higher than the steady state solution. In multiple scenarios, the distribution voltage profile exited ANSI C84.1 *American National Standard for Electric Power Systems and Equipment—Voltage Ratings (60 Hz)* voltage ranges.

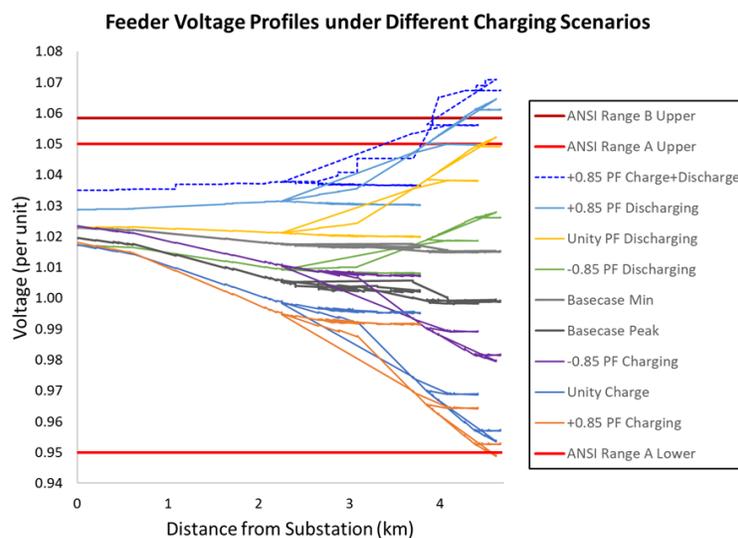


Figure VII.4.5 Different distribution voltage profiles for coordinated charging/discharging of EVSEs totaling 2.25 MW.

**Transmission System Simulations**

With projections of high EV penetration in the US, [1] it is imperative that studies are conducted to fully understand the effect of potential future cyber-attacks on EVs on the North American electric power system. The team evaluated worst-case scenarios in which EV loads were manipulated on a realistic 20,000+-bus representation of the Western Electricity Coordinating Council (WECC) simulated in GE’s PSLF software. The model contained a high-fidelity composite load model that represented motors, lighting, electronic, and associated distribution feeders. The team focused on the stability of the WECC model following the sudden loss of forecasted XFC load. Impacts are analyzed for load distributed system-wide and for load localized in specific areas of interest. (Forecasted EV loads were based on each state attaining a 16.3% conversion from internal combustion engine vehicles to EVs by 2030, calculated based on the percentage of EVs for California to reach its target of five million zero-emission vehicles.)

The load drop disturbance occurred at  $t = 1$  second and the transients were captured for 9 more seconds at a 0.125 s time step to record the primary frequency response. All simulations were run using snapshots of the WECC corresponding to two different operational (seasonal) setpoints: a light spring load profile, and a heavy summer load profile. For the WECC-wide simultaneous EV load tripping events, moderate frequency deviations were observed. Location-specific events corresponding to Los Angeles and Seattle registered much smaller frequency deviations. Given that the light spring load profile will have less generation dispatched initially, we observe that for the same amount of load trip, the lightly-loaded spring case will have a larger frequency deviation than the heavy summer load case. When the “emergency stop charging” command is issued to all EVs in the light spring loading case (worst-case scenario), there is a substantial impact to the power system. A plot of average system frequency, total generation, and total load is shown in Figure VII.4.6 for the cyber-attack. After the attack, the frequency quickly climbs to 60.6 Hz.

In the model, all transmission protection and remedial action schemes were modeled. The North American Electric Reliability Corporation (NERC) defines generator frequency and voltage protective relay settings in PRC-024-2. [2] In the WECC, relays are set to instantaneously trip for frequency deviations less than 57 Hz and greater than 61.7 Hz. Per unit (pu) voltage limits are also defined in PRC-024, where sustained voltages outside of 0.9 pu and 1.1 pu will initiate tripping events to mitigate voltage deviations outside of this range. Fortunately, the does not reach the PRC-024 generator relay trip settings and the power system returns to normal operation by throttling down the synchronous generators. Therefore, the impact to customers is minimal and the generator controls were able to compensate for the XFC disconnect disturbance.

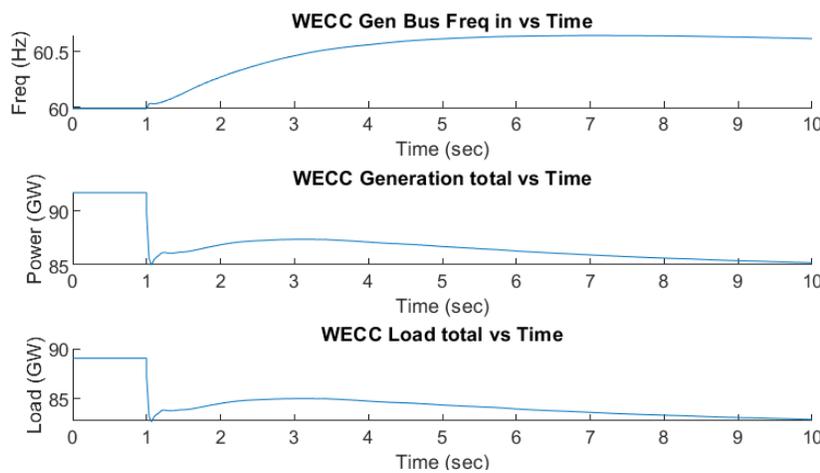


Figure VII.4.6 WECC light spring: system values through time.

## Conclusions

This project is helping identify potential EV charger vulnerabilities and quantify the risk to critical infrastructure when vehicle chargers are maliciously controlled. This risk assessment is only an initial step in a continuous process of hardening charging infrastructure against cyber-attacks. There is much more work to secure charging infrastructure from cyber-attacks, including:

- Developing standardized policies for managing chargers and other assets in the charging ecosystem
- Designing effective perimeter defenses to protect the assets including: firewalls, access control lists, data-in-flight requirements (encryption, node authentication), etc.
- Creating situational awareness systems, intrusion detection systems, and intrusion prevention systems.
- Researching response mechanisms to prevent further adversary actions on the system, nonrepudiation technologies, and dynamic responses.
- Creating hardware- and software-based fallback and contingency operating modes.

## References

1. Edison Electric Institute, "Electric Vehicle Sales Forecast and the Charging Infrastructure Required Through 2030," 2018.
2. NERC, "Standard PRC-024-2 — Generator Frequency and Voltage Protective Relay Settings," Available: <https://www.nerc.com/pa/Stand/Reliability%20Standards/PRC-024-2.pdf>. [Accessed 7 Aug 2019].

## Acknowledgements

DOE and the PI wish to thank the multi-laboratory team for this work: SNL (Brian Wright, Ben Anderson, Russell Graves, Jimmy Quiroz), PNNL (Rick Pratt, Tom Carroll, Lori O'Neil, David Gotthold) and ANL (Roland Varriale, Ted Bohn, and Keith Hardy).

Sandia National Laboratories is a multimission laboratory operated by National Technology and Engineering Solutions of Sandia LLC, a wholly owned subsidiary of Honeywell International Inc., for the U.S. Department of Energy's National Nuclear Security Administration.

(This page intentionally left blank)

U.S. DEPARTMENT OF  
**ENERGY**

*Office of*  
**ENERGY EFFICIENCY &  
RENEWABLE ENERGY**

For more information, visit:  
[energy.gov/vehicles](https://energy.gov/vehicles)

DOE/EE-1989 May 2020